Physics of the Solid State, Vol. 44, No. 8, 2002, pp. 1407–1414. Translated from Fizika Tverdogo Tela, Vol. 44, No. 8, 2002, pp. 1348–1355.

PROCEEDINGS OF THE XI FEOFILOV WORKSHOP "SPECTROSCOPY OF CRYSTALS ACTIVATED BY RARE-EARTH AND TRANSITION-METAL IONS"

(Kazan, Tatarstan, Russia, September 24–28, 2001)

Spectroscopy of Dielectric Nanocrystals Doped by Rare-Earth and Transition-Metal Ions

S. P. Feofilov

Ioffe Physicotechnical Institute, Russian Academy of Sciences, Politekhnicheskaya ul. 26, St. Petersburg, 194021 Russia
e-mail: sergey.feofilov@pop.ioffe.rssi.ru

Abstract—This paper reviews studies on the optical properties of dielectric nanocrystals doped by rare-earth and transition-metal ions. Manifestations of small nanocrystal size in the optical properties of impurity ions are considered. Two types of phenomena are discussed: (i) those associated with modification of the vibrational spectrum of small particles and (ii) those due to the interaction of impurity ions with the medium in which they are embedded. © *2002 MAIK "Nauka/Interperiodica".*

1. INTRODUCTION

A characteristic trend in modern solid-state physics is the increased interest expressed in the properties of low-dimensional objects whose one, two, or three dimensions are limited on the nanometer scale. Spatial confinement markedly affects the structure of electronic states and the vibrational (phonon) properties of crystals. Most publications deal with investigation of the effect of confinement on the electronic bands and excitons in semiconductors (quantum wells, wires, and dots).

Presently, we are witnessing a rising interest in the properties of dielectric nanostructures. The influence of spatial confinement on electronic bands in dielectric nanocrystals, i.e., crystals on the order of a few nanometers in size, is not as significant, since other phenomena play a major role here. The properties of dielectric nanocrystals can reflect the effects associated with modification of their phonon spectrum, with interaction of excitations with the environment, and with the increasing role of the surface. Of particular interest, from the standpoint of optical properties, are dielectric nanocrystals doped by rare-earth and transition-metal ions. Impurity ions can serve as spectroscopic probes to investigate the dynamic processes occurring in nanocrystals. At the same time, the modification of the spectroscopic characteristics of impurity ions caused by spatial confinement is also of interest.

The interest in the optical properties of dielectric nanocrystals doped by rare-earth and transition-metal ions is stimulated to a considerable extent by the application potential of these materials. Indeed, doped crystals and glasses are employed in laser technology and serve as luminophores; therefore, one may expect that the new properties stemming from nanocrystallinity will be of practical value. Actually, it is the interest in nanocrystalline luminophores that has stimulated a large number of papers on the spectroscopy of doped nanocrystals in recent years. We note the most remarkable result in this area, namely, the observation of a strong dependence of the quantum yield of Mn^{2+} fluorescence on the ZnS host particle size [1, 2]; surprisingly, these findings have been neither reproduced nor expanded upon; moreover, they have met with severe criticism [3]. It should be pointed out, however, that paper [1] focused attention on the optical properties of doped nanocrystals and stimulated further studies along these lines. There are presently a number of publications dealing with the optical spectroscopy of doped nanocrystals, with most of them featuring the investigation of luminescence and excitation spectra. It has been found that the spectra of impurity ions in nanocrystals do not, generally speaking, differ much from those obtained on bulk crystals of the same composition and structure, the only essential difference being the large inhomogeneous broadening of spectral lines in nanocrystals. There have been studies of low-frequency Raman scattering of light in nanocrystalline dielectric materials wherein size quantization effects were observed [4–7], but those effects were not related to impurity ions. Nevertheless, it turns out that fluorescence spectroscopy of doped nanocrystals also exhibits a number of effects which are directly associated with the smallness of the nanocrystal size. It is studies in this field that the present review is devoted to. It should be noted that we limit our consideration to nanocrystals, i.e., to objects confined spatially in all three dimensions, and leave thin dielectric films (which also obviously deserve attention) out of our review.

1063-7834/02/4408-1407$22.00 © 2002 MAIK "Nauka/Interperiodica"

2. DIELECTRIC NANOCRYSTALLINE OBJECTS

There is presently a variety of techniques to obtain nanocrystalline dielectric materials doped by rare-earth and transition-metal ions. Among them are the sol-gel technologies [8–13], condensation following laser evaporation (ablation) [14–16], organometallic reactions, and crystallite precipitation in glass [17]. The first three of them permit one to prepare "free" nanocrystals, i.e., nanocrystals surrounded by a gas medium (for instance, air) or in vacuum. Such samples are usually powders consisting of nanocrystal clusters. A particular place among them is occupied by nanocrystalline materials prepared by sol-gel technology; indeed, in this way, one can obtain macromonolithic, highly porous samples exhibiting optical transparency [18]. Unlike free nanocrystals, the crystals prepared by crystallite precipitation in glass are embedded in a glass host. Such host-embedded nanocrystals can also be produced from free nanocrystals by incorporating them in a polymer. While there is a rich variety of chemical compositions of doped nanocrystalline dielectrics, the most frequently used are the oxide and fluoride materials.

Characterization of nanocrystalline objects, i.e., determination of the crystallite shape and size and their distribution in space, is usually done by x-ray structural analysis, small-angle x-ray scattering, and electron and atomic-force microscopy.

3. MODIFIED VIBRATIONAL SPECTRA OF NANOCRYSTALS AND THEIR MANIFESTATIONS IN IMPURITY ION SPECTROSCOPY

The most essential property of acoustic vibrations in a small particle is the existence of minimum size-quantized frequencies corresponding to acoustic resonances of the particle. These vibrations were studied many years ago [19]. The lowest eigenfrequency corresponds to a spherical-particle mode having a higher amplitude on the surface (the surface mode) and is equal to

$$\omega(\mathrm{cm}^{-1}) = 0.85 v_t/ac, \qquad (1)$$

where v_t is the transverse sound velocity and a is the particle diameter. It is to vibrations of this type that one assigns [4, 5] the narrow peak that is observed in the low-frequency Raman scattering spectra of porous a-SiO_2 (aerogel) and shifts by 7 to 30 cm^{-1} with decreasing size of the particles forming the aerogel framework. Similar low-frequency peaks and their shift with variation of the particle size were observed in the Raman spectra of oxide glasses, whose thermal treatment brings about precipitation of nanosized crystal particles [6, 7]. These results are apparently the first observations of size-quantized vibration modes in the optical spectra of small particles. The existence of size-quantized vibrational excitations substantially modifies the density of vibrational states of particles; below the lowest size-quantized frequency, vibrations are impossible in a particle and the density of states is zero, whereas in the frequency region of size-quantized vibrations, the density of vibrational states is higher than that in a bulk crystal [20, 21]. Thus, one may expect the manifestation of confinement effects in doped nanocrystals in processes where low-frequency vibrations play an important part.

3.1. Long-Lived Size-Quantized Vibrational Excitations

In [22], the dynamics of the terahertz-range nonequilibrium vibrational excitations was studied in a γ-Al_2O_3:Cr^{3+} monolithic transparent high-porosity crystalline dielectric prepared by sol-gel technology [18]; the technique used in the measurements was optical detection of phonons from phonon-induced effects in the luminescence spectra of probe impurity ions. The material consisted of interconnected crystal grains about 6 nm in size whose volume fraction was less than one half.

The experimental technique employed was similar to that used earlier in studies of the dynamics of nonequilibrium phonons in disordered oxide crystals and glasses with Cr^{3+} ions [23]. Strong inhomogeneous broadening of the Cr^{3+} R line was used; this broadening is due to the specific structure of the γ-Al_2O_3 crystal lattice, which is similar to that of spinels and whose tetrahedral and octahedral positions are randomly and incompletely occupied by Al ions.

When pumping resonantly into the R line, the Cr^{3+} ions whose lower ($\bar{E}$) or upper ($2\bar{A}$) energy sublevel of the ^2E state coincides with $h\nu_{exc}$ are excited selectively from the ground state $^4A_2$ to the ^2E state by light of frequency ν_{exc}. Anti-Stokes luminescence with frequencies $\nu > \nu_{exc}$ corresponds to transitions from the $2\bar{A}$ states of Cr^{3+} ions, which are selectively excited at the frequency ν_{exc} first to the $\bar{E}$ state and then to the $2\bar{A}$ state in phonon-induced $\bar{E}$–$2\bar{A}$ transitions. At sample temperatures $T \geq 5$ K, anti-Stokes luminescence appears with $\nu > \nu_{exc}$; its intensity grows with increasing T.

Experiments with the generation of nonequilibrium phonons were conducted on samples cooled to T = 2–5 K, i.e., to temperatures at which the equilibrium anti-Stokes luminescence spectrum with $\nu > \nu_{exc}$ is completely frozen out. The nonequilibrium phonons that are generated within the laser beam spot in nonradiative relaxation of electronic excitations are detected from the appearance of anti-Stokes (AS) luminescence with $\nu > \nu_{exc}$. The AS $2\bar{A}$–$^4A_2$ luminescence at a frequency $\nu_{exc} + \omega$ is induced primarily by phonons of frequency ω initiating resonant $\bar{E}$–$2\bar{A}$ transitions in Cr^{3+} ions that are excited into $\bar{E}$ and for which the energy interval

$\Delta_{\bar{E}-2\bar{A}} = h\omega$. Thus, an AS luminescence spectrum can be used to study the behavior of phonons with frequencies ω over a broad frequency interval (up to ~100 cm^{-1}).

At moderate pump intensities of 10–100 mW/mm^2, the observed AS spectrum differs strongly from the equilibrium spectrum measured in stationary experiments at elevated sample temperatures. Figure 1 displays AS spectra induced by intermittent optical pumping and measured at various times Δt after the termination of excitation at frequency ν_{exc}. The millisecond-range times τ_R of the radiative decay of the Cr^{3+} ^2E level in γ-Al_2O_3 permitted observation of the AS luminescence decay kinetics for times up to ~10 ms. As seen from the AS spectrum obtained at Δt = 0–2 ms (Fig. 1), the high-frequency part of the spectrum ($\omega > 30$ cm^{-1}) coincides well with the equilibrium spectrum taken at an elevated sample temperature (T = 20 K in Fig. 1). However, the low-frequency part of the AS spectrum clearly exhibits an additional maximum at 20 cm^{-1}.

The AS spectrum obtained at long delay times Δt = 2–4 ms shows that the low-frequency maximum at $\omega_0 \approx$ 20 cm^{-1} decays in a time of ~1 ms (Fig. 1). As a result, at times >2 ms, the AS spectrum takes on the thermalized Boltzmann shape and falls off thereafter with considerably longer decay times, which are not much shorter than those of the Stokes part of the spectrum determined by the radiative lifetime of the ^2E state. The cooling-off time of the AS spectrum in this thermalized stage can be estimated as 20 ms. Importantly, the decay time of ~1 ms of the maximum at $\omega_0 \approx 20$ cm^{-1} does not depend on the size of the excited volume (the pump laser beam diameter).

The observed frequency of the nonthermalized low-frequency peak in the phonon distribution (Fig. 1), ω_0 = 20 cm^{-1}, is close enough to the lowest surface-mode frequency estimated from Eq. (1) for nanocrystalline particles with the parameters of porous γ-Al_2O_3 ($v_t \approx 6 \times 10^5$ cm/s, a = 6 nm). This suggests that the nonequilibrium phonon distribution peak at ω_0 = 20 cm^{-1} is connected with efficient excitation (due to optical heating of the sample) of the low-energy surface acoustic mode of the particles forming the framework of the porous γ-Al_2O_3.

The connection of the ω_0 = 20 cm^{-1} vibrations with the lowest surface resonant mode of nanocrystalline γ-Al_2O_3 particles can possibly account for the extremely long lifetime (~1 ms) of these vibrations, which exceeds that of the terahertz acoustic phonons in bulk crystals by several orders of magnitude. It appears only natural to assume that such a long lifetime is due to it being difficult for the lowest surface mode to decay into the low-energy vibrations of the porous material (fractons or long-wavelength hypersound).

A theory treating the decay of quantum-confined acoustic vibrations in a nanocrystalline material was proposed in [24], where a special type of localized vibrational states was considered; such a state exists in a porous material consisting of crystallites of approximately equal size. The size and porosity of the materials are such that the lowest frequencies of localized acoustic vibrations of the particles lie substantially higher than the maximum frequency of propagating acoustic phonons (the mobility threshold). The narrow size distribution of the particles implies that the lowest frequencies in the particles are likewise similar. The typical frequency difference is assumed to be below the mobility threshold, so that the energy difference can be taken up by a propagating phonon. At the same time, the typical frequency difference is assumed to be large enough for the neighboring particles to stay out of resonance. The decay rate of a mesoscopic crystalline particle weakly coupled to one or several such particles was calculated. The decay time depends on the width of the particle distribution in size and strength of harmonic and anharmonic interactions. For particles with an average size of 5 nm, the decay time can be as long as a few milliseconds, which is in agreement with the experiments from [22].

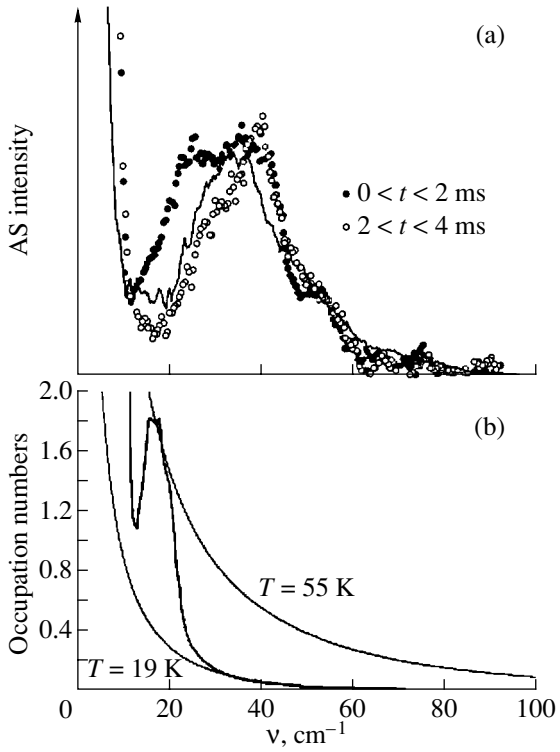

Fig. 1. (a) Normalized anti-Stokes spectra of Cr^{3+} in γ-Al_2O_3 obtained at T = 5 K under intermittent selective optical excitation in two time intervals and (b) phonon occupation numbers in the $0 < t < 2$ ms interval. Solid lines are (a) the experimental thermalized anti-Stokes spectrum measured at T = 20 K and (b) the thermalized distribution calculated for T = 19 and 55 K.

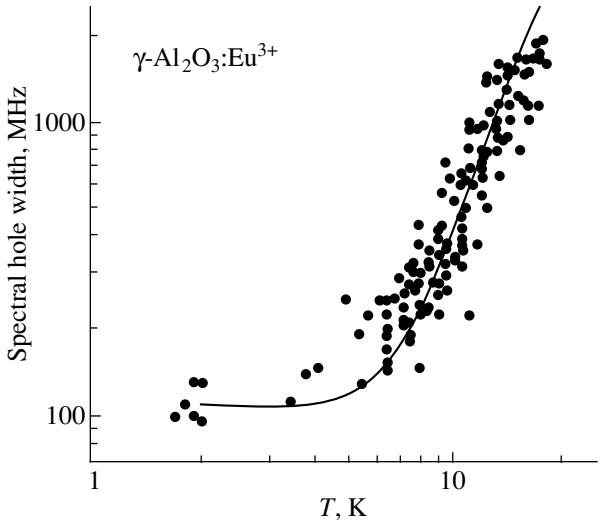

Fig. 2. Temperature dependence of the spectral hole width for the $^5D_0$–$^7F_0$ transition measured in high-porosity γ-Al_2O_3:Eu^{3+}. The solid line is a plot of Eq. (2) for a Raman process involving quantum-confined ω = 25 cm^{-1} vibrations.

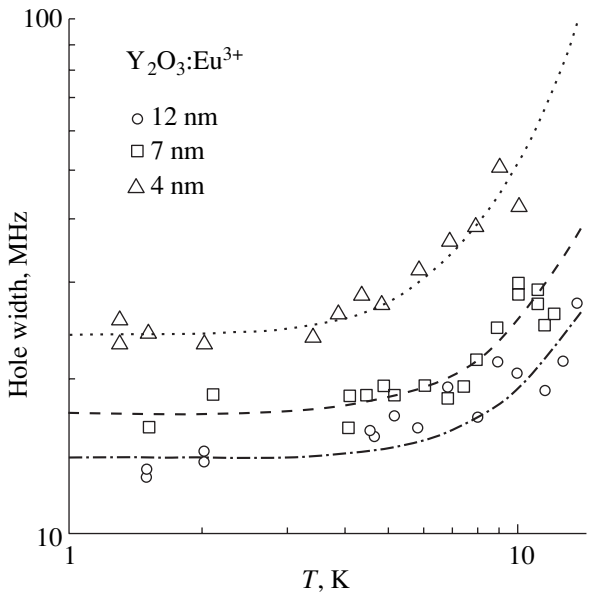

Fig. 3. Temperature dependence of the spectral hole width for the $^5D_0$–$^7F_0$ transition measured in nanocrystalline Y_2O_3:Eu^{3+}.

3.2. Homogeneous Broadening of Spectral Lines in Nanocrystals

The temperature dependence of the homogeneously broadened spectral linewidth Γ(*T*) of electronic transitions in impurity ions is determined by the interaction with phonons and depends on the phonon density of states. At low temperatures, the homogeneous linewidth in ordered crystals scales as $\Gamma(T) \sim T^7$; in glasses, we have $\Gamma(T) \sim T^\alpha$, where $1 < \alpha < 1.3$. In both cases, this relation transforms into $\Gamma(T) \sim T^2$ for higher temperatures. The $\Gamma(T) \sim T^7$ relation observed in crystals is explained as being due to the two-phonon Raman process. The homogeneous linewidth resulting from this process is given by

$$\Gamma \sim \int_{\omega_1}^{\omega_2} |\langle H \rangle|^4 \frac{\rho(\omega)^2 e^{\omega/kT}}{(e^{\omega/kT} - 1)^2} d\omega \qquad (2)$$

for the case of interaction with vibrations whose frequencies lie between ω_1 and ω_2, where *H* is the electron–phonon interaction Hamiltonian and ρ(ω) is the density of vibrational states.

In [25–27], the spectral-hole-burning method was used to study the temperature dependence of the homogeneous width Γ(*T*) of Eu^{3+} spectral lines in nanocrystalline γ-Al_2O_3 obtained by sol-gel technology [25] and in Y_2O_3 and Eu_2O_3 prepared by laser ablation [26, 27] (Figs. 2, 3). The hole burning was achieved through redistribution of the Eu^{3+} ions among the hyperfine-structure components of the ground state. The hole width Γ_{HB} characterizes the homogeneous linewidth $\Gamma(T) = \Gamma_{HB}(T)/2$. It was found that Γ(*T*) for impurity ions in nanocrystalline materials differs radically from that observed in crystals and glasses. This experimental finding can be accounted for as a result of the two-phonon Raman scattering in accordance with Eq. (2), if one includes the modified density of vibrational states ρ(ω) in nanocrystals [25, 28]. It was also found that the vibronic interaction *H* responsible for the homogeneous broadening is substantially stronger than that in bulk crystals.

3.3. One-Phonon Relaxation between Closely-Lying Electronic Levels of Impurity Ions in Nanocrystals

Nonradiative relaxation between closely lying electronic levels (about a few inverse centimeters distant) of impurity ions in bulk crystals involves the emission of one phonon with a frequency equal to the level separation. It is natural to assume that the probability of such processes in nanoparticles, where the phonon spectrum is substantially modified in the low-frequency domain, is essentially different. The relaxation times between closely lying components of the $^5D_1$ multiplet of Eu^{3+} ions in the *C* positions (C_s symmetry) were directly measured in nanocrystalline and bulk monoclinic Y_2O_3 [29, 30]. The energy gaps for which the measurements were performed were 3 and 7 cm^{-1}. The experiment was based on time-resolved measurement of the $^5D_1$–$^7F_3$ luminescence. The size distribution of particles in samples obtained by laser ablation was fairly broad and centered on approximately 13 nm (±5 nm). This particle size is small enough, according to Eq. (1), for the 3-

and 7-cm^{-1} phonons not to be supported by the particles.

It follows from the measurements that in bulk Y_2O_3:Eu^{3+} (the powders used had micron-sized grains), the one-phonon relaxation times between the $^5D_1$-multiplet components of Eu^{3+} ions in the *C* positions are of the order of a few hundreds of nanoseconds, whereas in nanocrystals, this time is 27 and 7 μs for energy gaps of 3 and 7 cm^{-1}, respectively. These relaxation times were found not to depend on temperature within the 1.5- to 10-K interval; this means that two-phonon processes do not play a significant part in the relaxation. Residual relaxation involves, apparently, the vibrational modes of a nanoparticle cluster. Thus, because of the lower density of vibrational states at low frequencies, one-phonon relaxation between closely enough lying electronic levels of impurity ions in nanoparticles is considerably slower than that in bulk crystals.

4. EFFECT OF THE ENVIRONMENT AND OF THE SURFACE ON THE OPTICAL PROPERTIES OF DOPED NANOCRYSTALS

Crystallites of a small enough size can exhibit effects originating from the interaction of impurity ions with the surrounding medium and the surface. Indeed, if the electronic states of an impurity ion interact with the medium in which the nanocrystal is embedded and with its excitations and this interaction is efficient at distances in excess of the nanoparticle dimensions, then the surrounding medium can affect the electronic states and transitions in the impurity ions. The part played by the interaction of impurity ions with the surface is also larger compared with that in bulk crystals, because in a nanocrystalline material all impurity ions are spaced a short distance from the surface.

4.1. Effect of the Surrounding Medium on the Radiative Lifetime of the Impurity-Ion Excited States in Nanocrystals

The smallness of nanocrystal size compared to the wavelength of visible light accounts for a number of interesting effects. Under these conditions, the effective refractive index of the medium in which the impurity ions are located is determined by the refractive indices of both the nanoparticles and of the medium in which the nanoparticles are embedded. The radiative lifetime τ_R of electronic transitions in an ion incorporated in a medium is given by the expression [31]

$$\tau_R \sim \frac{1}{f(ED)} \frac{\lambda_0^2}{\left[\frac{1}{3}(n^2+2)\right]^2 n}, \qquad (3)$$

where $f(ED)$ is the oscillator strength of the electronic dipole transition, λ_0 is the wavelength of light in vacuum, and *n* is the refractive index. The dependence of

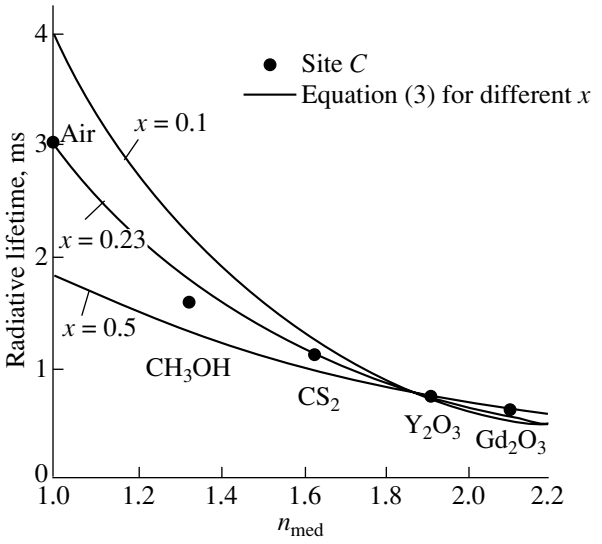

Fig. 4. Radiative lifetime of the $^5D_0$ state of Eu^{3+} ions (*C* centers) in Y_2O_3 nanocrystals plotted vs. refractive index of the surrounding medium n_{med} for $T = 295$ K. Solid lines are plots of Eq. (3) for different volume fractions of the nanocrystals.

τ_R on refractive index is due to two reasons: (i) variation of the density of photon states and (ii) modification of the polarizability of the medium. Because nanocrystals in samples usually occupy a small part of the volume, *n* in Eq. (3) depends substantially on the refractive index of the medium filling the space between the nanocrystals. Thus, the radiative lifetime τ_R, according to Eq. (3), should depend noticeably on the refractive index of the medium in which the nanocrystals are embedded.

In [32], the radiative lifetime of the $^5D_0$ state of Eu^{3+} ions in Y_2O_3 nanocrystals was measured by following the fluorescence decay under intermittent excitation. The samples obtained by laser ablation [14] comprised powders consisting of nanocrystal clusters (7 and 12 nm in size) of monoclinic Y_2O_3:Eu^{3+}. It was shown that at temperatures up to room temperature, the lifetime of the $^5D_0$ state is determined by its radiative decay. Figure 4 plots the lifetimes of the Eu^{3+} $^5D_0$ state measured in nanocrystalline samples embedded in media with different refractive indices (air and various liquids) as functions of the refractive index of the medium n_{med}. Presented for comparison are data obtained for monoclinic Y_2O_3:Eu^{3+} powders containing micron-sized grains and for single-crystal Gd_2O_3:Eu^{3+}, a material in which the structure and spectral properties of the Eu^{3+} centers differ very little from those in Y_2O_3:Eu^{3+}. We readily see that the lifetime of the $^5D_0$ state in nanocrystals is substantially longer than that in bulk samples; indeed, in nanocrystals surrounded by air the lifetime exceeds the time measured in bulk samples

by a factor of more than three. The experimental data were fitted by Eq. (3), with the effective refractive index defined as $n_{\text{eff}}(x) = x n_{Y_2O_3} + (1 - x)n_{\text{med}}$, where x is the volume fraction of nanocrystals (a more accurate definition can be obtained through the Clausius–Mosotti equation, but the difference between the results is small). The best fit to the experimental data was reached for $x = 0.23$, which implies that nanocrystals fill 23% of the sample volume.

Experiments have shown [32] that the radiative lifetimes of the excited states of impurity ions depend strongly on the effective refractive index of the medium consisting of nanocrystals and of the filler medium. As follows from Eq. (3), the impurity-ion lifetime can be longer by a factor of $n(n^2 + 2)^2/9$ compared to that in bulk crystals, if the material is fully dispersed and consists of individual particles in air or vacuum. For Y_2O_3 with $n = 1.91$, this maximum increase in the lifetime is 6.77. The lifetime can be reduced by placing the particles into a medium with a large refractive index. The variation of the lifetime of excited states with the host in which the nanocrystals are embedded can be an important practical feature, for instance, in fluorescent materials consisting of doped nanocrystals in a glass or polymer matrix. The effect of the refractive index on lifetime is usually not observed directly, because a change in the matrix with impurity ions changes the structure of the impurity centers and, hence, the oscillator strength. The situation with nanocrystalline materials is unique in that one can change the refractive index of the surrounding medium without changing the local structure of the centers.

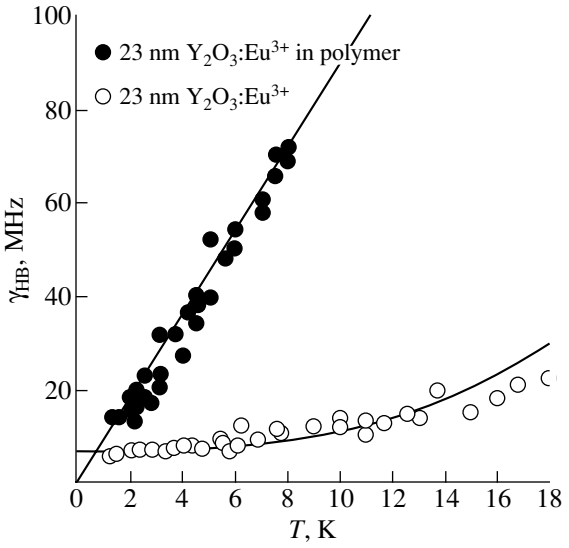

Fig. 5. Temperature dependence of the spectral hole width for Eu^{3+} in Y_2O_3 nanocrystals.

4.2. Interaction of Impurity Ions in Nanocrystals with Two-Level Systems in a Glassy Matrix

It is known that when rare-earth impurity ions are embedded in a glass, their dynamics is governed by interaction with two-level systems (TLS) in the glass. Experiments carried out on many systems have shown that at low temperatures, the homogeneous width γ_h of spectral lines in these systems scales with temperature as $\gamma_h \sim T^\alpha$, where $1 < \alpha < 2$. Theory predicts this behavior in the case where impurity-ion electronic states interact with TLS in glasses [33–37]. It is concluded that the interaction has an elastic dipole–dipole character. Studies with rare-earth ions in nanocrystals embedded in an amorphous matrix permit one to determine the extent to which the impurity-ion interaction with TLS is long-range, because in this case the impurity ions are separated from the TLS by a nanocrystal, which does not contain a TLS.

It has been shown [38, 39] that rare-earth ions in nanoparticles (at least up to 30 nm in size) interact with TLS in an amorphous matrix such that the temperature dependence of the homogeneous linewidth is similar to that in glasses. To determine the homogeneous width γ_h of spectral lines, the spectral-hole-burning method was employed in [38, 39]. Figure 5 shows the temperature dependences of the hole width γ_{HB} (which is intimately related to the homogeneous linewidth through $\gamma_h = \gamma_{HB}/2$) for the ${}^5D_0$–${}^7F_0$ transitions in Eu^{3+} ions in 23-nm Y_2O_3 nanocrystals, both free and embedded in an amorphous polymer matrix [39]. It is seen that when nanocrystals are embedded in a matrix, the temperature dependence of the homogeneous linewidth changes radically to become linear and the homogeneous linewidth increases substantially. This can be accounted for only by Eu^{3+} interaction with the matrix TLS. The dependence of the homogeneous broadening of Eu^{3+} (and Pr^{3+}) spectral lines on nanocrystal size in oxyfluoride glass ceramics was studied in [39] (Fig. 6). We readily see that the line broadening decreases with increasing nanocrystal size, which finds a natural explanation in the larger TLS separation from the impurity ions.

A semiquantitative description of the dependence of homogeneous broadening on nanocrystal size, which is based on the approach considered in [33, 35] in the formalism of [36, 37], was proposed in [39]. In this approach, homogeneous broadening is calculated as a sum of contributions due to all TLSs and the nanocrystal volume (which does not contain TLSs) can be readily excluded from consideration. The homogeneous linewidth can be presented in the form

$$\gamma_h = 4\pi R N_0 \int_0^{r_c} r^2 dr + 2\pi \frac{N_0 A^2}{R} \int_{r_c}^{\infty} r^{-4} dr, \qquad (4)$$

where N_0 is the spatial density of tunneling systems, R is their relaxation rate, and r_c is the critical distance (determined by the ratio $A/r_c^3 = R$) within which the interaction of ions with TLSs can be considered distance-independent. In Eq. (4), the first term describes interaction with closely lying TLSs and the second accounts for more distant TLSs, interaction with which can be treated as having a dipole–dipole character. To exclude the nanocrystal volume, which does not contain TLSs, the integration was performed outside the $r < r_0$ region (r_0 is the nanoparticle radius). On making a few approximations allowable in semiquantitative description, we finally obtain

$$\gamma_h = \begin{cases} 2\pi N_0 A - \dfrac{4\pi}{3} N_0 R r_0^3 & (r_0 < r_c) \\ \dfrac{2\pi N_0 A^2}{3R} r_0^{-3} & (r_0 > r_c). \end{cases} \quad (5)$$

Equation (5) was compared in [39] with experimental data for various r_0; the homogeneous linewidth for ions embedded directly in glass was assumed to correspond to $r_0 = 0$. The critical distance was found to be $r_c = 9$ nm. Thus, the long-range character of the impurity-ion interaction with TLSs finds direct experimental confirmation. It should be pointed out that the experiments described in [38, 39] directly demonstrate the possibility of using nanocrystals with impurity ions as spectroscopic probes to study dynamic processes in disordered media. Such probes have an inherent advantage over ions embedded directly in a medium in that their spectra do not exhibit strong inhomogeneous broadening caused by disorder.

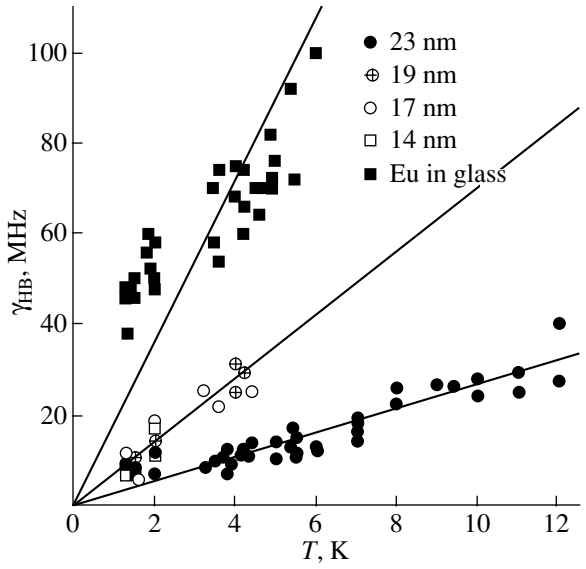

Fig. 6. Temperature dependence of the spectral hole width for Eu^{3+} in LaF_3 nanocrystals of various sizes embedded in oxyfluoride glass ceramics and for Eu^{3+} placed directly in a glass matrix.

4.3. Nonradiative Relaxation of the Excited States of Impurity Ions in Nanocrystals with Inclusion of the Surface Effect

The part played by the surface in nanocrystalline materials is obviously substantially larger than it is in bulk samples. Indeed, all impurity ions in nanocrystals are fairly close to the surface and their interaction with surface states can become manifest in the dynamics of the electronic states.

It was shown in [40] that nonradiative processes associated with the surface can be dominant in the relaxation of impurity-ion excited states in nanocrystals. The material studied was high-porosity γ-Al_2O_3:Yb^{3+} obtained by sol-gel technology. Experiments on the hydration/dehydration of samples revealed that the intensity and lifetime of the Yb^{3+} $^2F_{5/2}$–$^2F_{7/2}$ fluorescence in the 10000- to 11000-cm^{-1} region depends strongly on the number of OH hydroxyl ions in the samples. These observations were assigned to the interaction of Yb^{3+} ions with the OH groups on the nanoparticle surface, which gives rise to nonradiative relaxation of the excited state. It is assumed that the nonradiative process actually consists of energy transfer from Yb^{3+} to a level of the $v = 3$ vibrational mode of the OH group. Three such quanta are required for the nonradiative relaxation to occur. Experimental data [40] stress the importance of surface states for the relaxation characteristics of impurity ions in nanoparticles, where the distances of all impurity ions from the surface are not larger than a few nanometers.

5. CONCLUSIONS

Thus, the experimental studies discussed in the present review revealed and interpreted a number of phenomena in the optics of dielectric nanocrystalline objects doped by rare-earth and transition metals which are directly related to particle smallness. These phenomena can be divided in two classes: (i) those associated with modification of the vibrational spectrum of small particles and (ii) phenomena originating from the interaction of impurity ions with the medium they are embedded in. The available data permit the conclusion that doped nanocrystalline dielectrics constitute a novel type of optical object possessing specific properties. The idea of using nanocrystals with impurity ions as spectroscopic probes to study dynamic processes in disordered materials appears very promising. Some of the features in the optical properties of nanocrystalline materials may turn out to be essential in applications.

ACKNOWLEDGMENTS

The author is indebted to A.A. Kaplyanskiĭ, A.B. Kulinkin, R.I. Zakharchenya, T.N. Vasilevskaya, R.S. Meltzer, W.M. Dennis, W.M. Yen, U. Happek, B.M. Tissue, and M. Dejneka for their cooperation and valuable discussions.

This study was supported by the Russian Foundation for Basic Research (project no. 99-02-18279) and the "Physics of Solid-State Nanostructures" program.

REFERENCES

1. R. N. Bhargava and D. Gallagher, Phys. Rev. Lett. **72**, 416 (1994).
2. R. N. Bhargava, J. Lumin. **70**, 85 (1996).
3. A. A. Bol and A. Meijerink, J. Lumin. **87/89**, 315 (2000).
4. J. Dumas, J. Serughetti, J. L. Rousset, *et al.*, J. Non-Cryst. Solids **121**, 128 (1990).
5. T. Woignier, J. L. Sauvajol, J. Pelous, and R. Vacher, J. Non-Cryst. Solids **121**, 206 (1990).
6. E. Duval, A. Boukenter, and B. Champagnon, Phys. Rev. Lett. **56**, 2052 (1986).
7. V. K. Malinovsky, V. N. Novikov, A. P. Sokolov, and V. G. Dodonov, Solid State Commun. **67**, 725 (1988).
8. R. I. Zakharchenya, I. K. Meshkovskiĭ, and F. S. Kaplan, Dokl. Akad. Nauk SSSR **314**, 393 (1990).
9. R. I. Zakharchenya and T. N. Vasilevskaya, J. Mater. Sci. **29**, 2806 (1994).
10. T. N. Vasilevskaya and R. I. Zakharchenya, Neorg. Mater. **31**, 1 (1995).
11. R. I. Zakharchenya, J. Sol-Gel Sci. Technol. **6**, 179 (1995).
12. T. N. Vasilevskaya and R. I. Zakharchenya, Fiz. Tverd. Tela (St. Petersburg) **38**, 3129 (1996) [Phys. Solid State **38**, 1711 (1996)].
13. B. E. Yoldas, J. Appl. Chem. Biotechnol. **23**, 803 (1973); Am. Ceram. Soc. Bull. **54**, 286 (1975).
14. B. Bihari, H. Eilers, and B. M. Tissue, J. Lumin. **75**, 1 (1997).
15. H. Eilers and B. M. Tissue, Mater. Lett. **24**, 261 (1995).
16. D. K. Williams, B. Bihari, B. M. Tissue, and J. M. McHale, J. Phys. Chem. B **102**, 916 (1998).
17. M. J. Dejneka, MRS Bull. **23**, 57 (1998); J. Non-Cryst. Solids **239**, 149 (1998).
18. S. P. Feofilov, A. A. Kaplyanskii, A. B. Kulinkin, *et al.*, J. Sol-Gel Sci. Technol. **21**, 135 (2001).
19. H. Lamb, Proc. London Math. Soc. **13**, 189 (1882).
20. A. Tamura and T. Ichinokava, J. Phys. C **16**, 4779 (1983).
21. A. Tamura, Phys. Rev. B **52**, 2668 (1995).
22. S. P. Feofilov, A. A. Kaplyanskii, and R. I. Zakharchenya, J. Lumin. **66/67**, 349 (1996); A. A. Kaplyanskiĭ, S. P. Feofilov, and R. I. Zakharchenya, Opt. Spektrosk. **79**, 709 (1995) [Opt. Spectrosc. **79**, 653 (1995)].
23. S. A. Basun, P. Deren, S. P. Feofilov, *et al.*, J. Lumin. **45**, 115 (1990); Fiz. Tverd. Tela (Leningrad) **31** (3), 199 (1989) [Sov. Phys. Solid State **31**, 460 (1989)].
24. V. L. Gurevich and H. R. Schober, Phys. Rev. B **57**, 11295 (1998).
25. S. P. Feofilov, A. A. Kaplyanskii, R. I. Zakharchenya, *et al.*, Phys. Rev. B **54**, 3690 (1996).
26. K. S. Hong, R. S. Meltzer, B. Bihari, *et al.*, J. Lumin. **76–77**, 234 (1998).
27. K. S. Hong, R. S. Meltzer, S. P. Feofilov, *et al.*, J. Lumin. **83/84**, 393 (1999).
28. R. S. Meltzer and K. S. Hong, Phys. Rev. B **61**, 3396 (2000).
29. H.-S. Yang, S. P. Feofilov, D. K. Williams, *et al.*, Physica B (Amsterdam) **263**, 476 (1999).
30. H.-S. Yang, K. S. Hong, S. P. Feofilov, *et al.*, J. Lumin. **83–84**, 139 (1999).
31. B. Henderson and G. F. Imbusch, *Optical Spectroscopy of Inorganic Solids* (Clarendon, Oxford, 1989), p. 173.
32. R. S. Meltzer, S. P. Feofilov, B. Tissue, and H. B. Yuan, Phys. Rev. B **60**, R14012 (1999).
33. S. K. Lyo, Phys. Rev. Lett. **48**, 688 (1982).
34. D. L. Huber, M. M. Broer, and B. Golding, Phys. Rev. Lett. **52**, 2281 (1984); Phys. Rev. B **33**, 7297 (1986).
35. L. W. Molenkamp and D. A. Wiersma, J. Chem. Phys. **83**, 1 (1985).
36. R. Silbey and K. Kassner, J. Lumin. **36**, 283 (1987).
37. D. L. Huber, J. Lumin. **36**, 307 (1987).
38. R. M. Macfarlane and M. J. Dejneka, Opt. Lett. **26**, 429 (2001).
39. R. S. Meltzer, W. M. Yen, Hairong Zheng, *et al.*, Phys. Rev. B **64**, 100201(R) (2001).
40. J. K. Krebs, S. P. Feofilov, A. A. Kaplyanskii, *et al.*, J. Lumin. **83–84**, 209 (1999).

Translated by G. Skrebtsov

Physics of the Solid State, Vol. 44, No. 8, 2002, pp. 1415–1425. Translated from Fizika Tverdogo Tela, Vol. 44, No. 8, 2002, pp. 1356–1366.

PROCEEDINGS OF THE XI FEOFILOV WORKSHOP "SPECTROSCOPY OF CRYSTALS ACTIVATED BY RARE-EARTH AND TRANSITION-METAL IONS"

(Kazan, Tatarstan, Russia, September 24–28, 2001)

Clusters of Group-III Ions in Activated Fluorite-Type Crystals

S. A. Kazanskiĭ and A. I. Ryskin

Vavilov State Optical Institute, St. Petersburg, 199034 Russia
e-mail: kazanski@SK7936.spb.edu
e-mail: alex@ryskin.spb.su

Abstract—The data on optically detected EPR in absorption bands of alkaline-earth fluoride crystals doped with rare-earth (Er, Tm, Yb, Lu) or yttrium activators indicate that these crystals contain clusters similar to Y_6F_{37}, which is the structural unit of the naturally occurring mineral tveitite and of synthetic yttrofluorite $[(CaF_2)_{1-y}(YF_3)_y]$ crystals, whose lattices exhibit a superstructure at certain values of y. Starting from a rare-earth ion concentration of the order of 0.1%, the greater part of the rare-earth impurity is concentrated in these clusters, having a tendency to aggregate into larger clusters. Clusters are also of considerable importance in semiconducting fluorite-structure crystals of CdF_2 doped with Ga, In, or Y ions, as indicated by microwave and IR radiation absorption in these crystals. © *2002 MAIK "Nauka/Interperiodica".*

1. INTRODUCTION

Fluorite-like crystals activated with group-III elements, predominantly by rare-earth (RE) elements and yttrium, are usually investigated by optical and EPR spectroscopy [1]. Many interesting phenomena discovered in activated fluorite crystals, such as cooperative processes in luminescence [2–7], the decreased transition temperature to superionic conduction [8], and the occurrence of low-energy excitations inherent in glasses [9–12], are associated with activator ions ceasing to be randomly distributed over the fluorite lattice and forming clusters. Although clusters have been studied using selective laser spectroscopy [4–7], neutron scattering [13], and ^{19}F NMR [14] and EXAFS measurements [15, 16], their structure is still not completely understood.

We observed the clusterization effect when studying the low-frequency magnetic field absorption by spin–spin interacting subsystems in activated fluorite crystals [17]. It was found that $CaF_2 : Tm^{3+}$ (0.2 mol %) crystals had an increased (in comparison with its initial value) concentration of the paramagnetic impurity with a large magnetic moment in the ground state (at $T = 1.8$ K). At the same time, the EPR spectrum of the Tm^{3+} ion has never been observed in fluorite-like crystals (the ground state of this ion is a singlet for all known Tm^{3+} impurity centers).

Fluorite-like crystals (CaF_2, SrF_2, BaF_2, CdF_2) have the structure of cubic fluorite and can be easily activated with group-III elements, in particular, by RE ions and yttrium [1, 18]. In this case, trivalent impurity ions occupy Ca^{2+} cation sites of the fluorite lattice and the excess (+1) impurity charge is neutralized by F^- ions displaced to the empty cube centers (interstitial sites) of the anion sublattice. If such an interstitial site is the nearest to the impurity ion, we have a simple tetragonal RE^{3+}–F^- center; otherwise, the excess charge is neutralized nonlocally and the impurity ion is in the nearest neighbor environment of cubic symmetry, forming a cubic RE^{3+} center. Such simple centers (with their charge neutralized either locally or nonlocally) manifest themselves in optical spectra associated with transitions in the inner $4f^n$ electron shell of RE ions, as well as in EPR spectra of activated fluorite-like crystals. As a rule, only simple centers exist when the activator concentration is less than 0.1 mol % [6, 7]. (We note that only cubic, i.e., nonlocally neutralized, centers are known to exist in CdF_2 crystals [19].) At a higher activator concentration, RE and F^- ions form clusters in fluorite-like crystals.

The EPR method gives the most reliable information on the structure of impurity centers. Using this method, it was found that the tetragonal centers do not form in fluorides of Ca, Sr, and Ba when the activator concentration is higher than approximately one mole percent. At the same time, the cubic centers persist and are observed in EPR spectra for activator concentrations as high as roughly ten mole percent. However, the EPR spectra do not reveal clusters; therefore, other methods should be used to study them. Using neutron-scattering data [13], models were constructed for clusters of vacancies and interstitials at anion-sublattice sites, which are classified in different types (clusters 2 : 2 : 2, 4 : 3 : 2, etc.) as often cited in the literature. However, those models assume that the activated fluorite-like crystal is strongly disordered, especially for extremely high activator concentrations, which is not in fact the case.

1063-7834/02/4408-1415$22.00

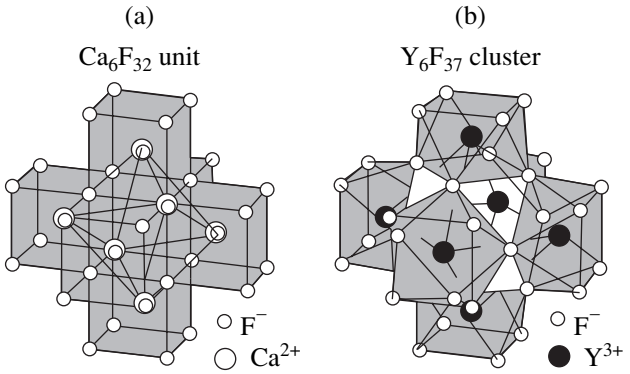

Fig. 1. (a) Inner F_8 cube of F^- anions in the Ca_6F_{32} cluster and (b) cuboctahedron F_{12+1} in the Y_6F_{37} cluster in yttrofluorite solid solutions with a superstructure.

It should be noted that, in terms of crystal chemistry, the crystals under study are yttrofluorite-like nonstoichiometric solid solutions $(CaF_2)_{1-y}(YF_3)_y$ ($0 \le y \le 0.4$) with an excess content of F^- anions. Solid solutions of alkaline-earth fluorides with trifluorides of rare earths and yttrium have been studied comprehensively using the methods of crystal chemistry [18, 20]. X-ray diffraction analysis shows that yttrofluorite possesses a disordered cubic fluorite structure; however, the cation (Ca, Y) sublattice exhibits the same order as the parent fluorite lattice and the nonstoichiometry leads to the appearance of disordered defects on the anion (F^-) sublattice. In the naturally occurring mineral tveitite, as well as in the homologous yttrofluorite series with $y = 5/m$ (m = 13–19) fabricated under special conditions, x-ray diffraction studies reveal a superstructural ordering of the crystal lattice [21]. The superstructure unit is a Y_6F_{37} cluster, which is, in fact, identical (in volume and form) to the Ca_6F_{32} unit of the fluorite lattice and, therefore, is easily incorporated into this lattice, accommodating excess anions. In the Y_6F_{37} cluster, the octahedron Y_6 of six Y^{3+} cations encloses a cuboctahedron F_{12} of twelve F^- anions, within which there is an off-center ion F^- (Fig. 1).

2. INVESTIGATION OF CLUSTERS IN CALCIUM-, STRONTIUM-, AND BARIUM-FLUORIDE CRYSTALS

In what follows, we present optically detected EPR (OD-EPR) [22] spectra of Er^{3+}, Tm^{3+}, and Yb^{3+} ions in crystals of alkaline-earth fluorides, which indicate that clusters in the yttrofluorite-like solid solutions studied are identical to clusters of the Y_6F_{37} type observed in fluorite phases with a superstructure [21].

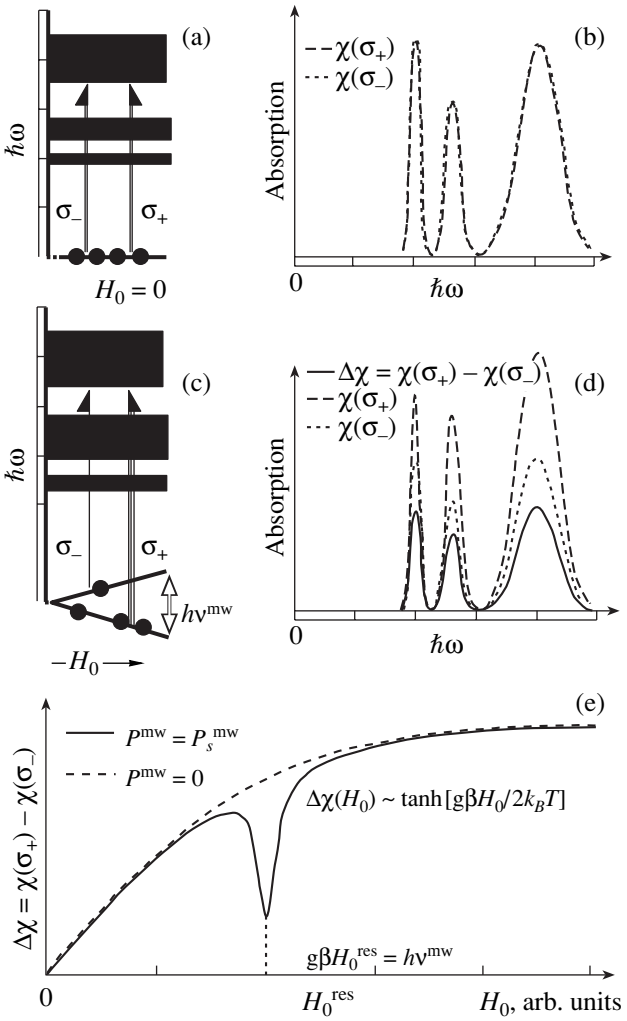

Fig. 2. Occurrence (a, c) of circularly polarized optical spectrum and (b, d) of magnetic circular dichroism of a sample placed in a magnetic field H_0 and (e) the $\Delta\chi(H_0)$ dependence in the absence ($P^{mw} = 0$) and in the presence ($P^{mw} = P_s^{mw}$) of microwave radiation that saturates transitions between the Zeeman sublevels of the ground state of a paramagnetic impurity.

2.1. Optical Detection of EPR by Using Magnetic Circular Dichroism

We briefly describe the method of optical detection of EPR using magnetic circular dichroism (MCD), which we apply in this work in the region of optical absorption of paramagnetic RE ions. Let us consider the simple case of an ion with effective spin $S = 1/2$ in the ground state (Fig. 2).

The magnetic circular dichroic absorption (MCDA) of a sample placed in a dc magnetic field H_0 is equal to the difference $\Delta\chi$ in the absorption χ of light waves with left-hand (σ_-) and right-hand (σ_+) circular polar-

ization propagating along the magnetic-field direction:

$$\Delta\chi = \chi(\sigma_-) - \chi(\sigma_+). \quad (1)$$

In a zero magnetic field ($H_0 = 0$), we have $\Delta\chi = 0$, because the absorption of right-handed and left-handed circularly polarized light are equal. When a magnetic field is applied ($H_0 \neq 0$), the ground state of the paramagnetic impurity is split and, at low temperatures, the lower of the two Zeeman levels is predominantly populated, which gives rise to MCD. The magnetic-field dependence of MCDA (Fig. 2e) has the form (with the tendency to saturate)

$$\Delta\chi(H_0) = \Delta\chi^{\max}\tanh(g\beta H_0/2k_BT), \quad (2)$$

where g is the spectroscopic splitting factor, β is the Bohr magneton, and k_B is the Boltzmann constant.

If the sample is also exposed to microwave (MW) radiation, which can induce transitions between the Zeeman sublevels of the ground state at a certain resonance value of H_0, then the MCDA vs. H_0 curve exhibits a dip at this H_0 value (Fig. 2e) and the change in MCDA caused by the MW radiation is manifested in the OD-EPR spectrum:

$$\delta(\Delta\chi) = \Delta\chi(P^{\mathrm{mw}} = 0) - \Delta\chi(P^{\mathrm{mw}}), \quad (3)$$

where P^{mw} is the MW radiation power.

An OD-EPR spectrometer based on MCD is shown schematically in Fig. 3. As in a conventional EPR spectrometer, samples are placed in a MW cavity; the cavity has windows through which a probe light beam can pass. The polarization of the probe beam is varied at a given frequency ν^{mod} with the help of a circular-polarization modulator positioned behind the monochromator. The photodetector measures the intensity of the light transmitted through the sample and its variations in the case where the MCDA occurs and is affected by MW radiation (which is repeatedly turned on and off). The intensity of the light beam measured by the photodetector can be easily shown to be

$$I \approx I_0\exp(-\chi_0 d) + \frac{I_0}{2}\cos(2\pi\nu^{\mathrm{mod}}t)\Delta\chi, \quad (4)$$

where I_0 is the intensity of the monochromatic light wave incident on the sample, χ_0 is the absorption coefficient of the sample (of thickness d) in the absence of a dc magnetic field, and $\Delta\chi \ll \chi_0$ is the MCDA.

As applied to the problem under study, the OD-EPR method has the following advantages over the conventional EPR method: (1) The EPR spectra are recorded in the region of optical absorption of the paramagnetic centers under study, which allows one to relate the observed EPR spectra to optical spectra of the same centers. (2) The optical channel of signal recording is independent of the MW radiation channel which saturates transitions between the spin sublevels in the presence of a dc magnetic field. This makes it possible to study strongly forbidden transitions in the spin system (in the case where $g_\perp \sim 0$ is very small) by utilizing intense MW radiation and make use of low-Q microwave cavities (with large samples).

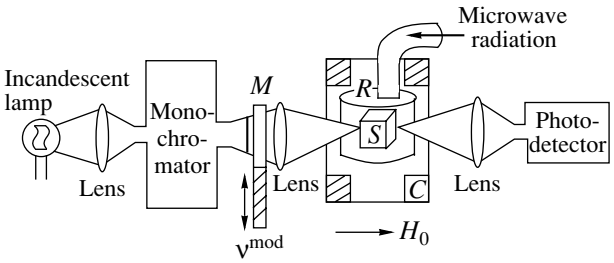

Fig. 3. Experimental setup for measuring MCDA and OD-EPR spectra: (*M*) circular-polarization modulator, (*S*) sample placed in the resonant MW cavity *R*, and (*C*) magnet coil.

2.2. Experimental OD-EPR Spectra

In this work (see also [23, 24]), we studied the MCDA and OD-EPR spectra of yttrofluorite-like solid solutions (at $T = 1.8$ K) containing paramagnetic RE ions, namely, $(MF_2)_{1-x}(R'F_3)_x \equiv MF_2 : R'_x$, where M = Ca, Sr, or Ba and R' = Er, Tm, or Yb. In these crystals, clusters proved to be magnetically concentrated systems with broad-band EPR spectra. In order to suppress the magnetic spin–spin interactions between paramagnetic RE ions in the clusters, the paramagnetic impurities were highly diluted with diamagnetic (R'') ions Lu^{3+} or Y^{3+}. The fraction of the diamagnetic ions reached 90% and higher. Thus, the structure of RE clusters was determined by investigating the MCDA and OD-EPR spectra of paramagnetic R' ions incorporated in clusters of diamagnetic R'' ions in solid solutions $(MF_2)_{1-x-y}(R'F_3)_x(R''F_3)_y \equiv MF_2 : (R'_x, R''_y)$ with $0 \le x \le 0.02$ and $0.001 \le y \le 0.38$. It should be noted that R' and R'' ions (which will be referred to as R ions) are all randomly distributed over the clusters; therefore, it is easy to dilute paramagnetic ions in clusters with diamagnetic ions. The MCDA and OD-EPR spectra of Er, Tm, and Yb ions can be recorded for any transition between the energy levels of the inner $4f^n$ electron shell of these trivalent ions. The electron shells of Lu and Y ions are closed, and these ions have no optical or EPR spectra of their own.

Figure 4 shows the MCDA spectra of CaF_2 crystals doped with Er and Y activators in the region of ${}^4I_{15/2} \longrightarrow {}^4F_{5/2}$ transitions in Er^{3+} ions. When the activator concentration is increased, the optical spectra exhibit broadened bands of clusters of Er^{3+} and Y^{3+} ions on the fluorite crystal lattice instead of narrow lines of simple centers. It is seen from Fig. 4 that the intensities of the absorption bands of Er^{3+} ions in both the clusters

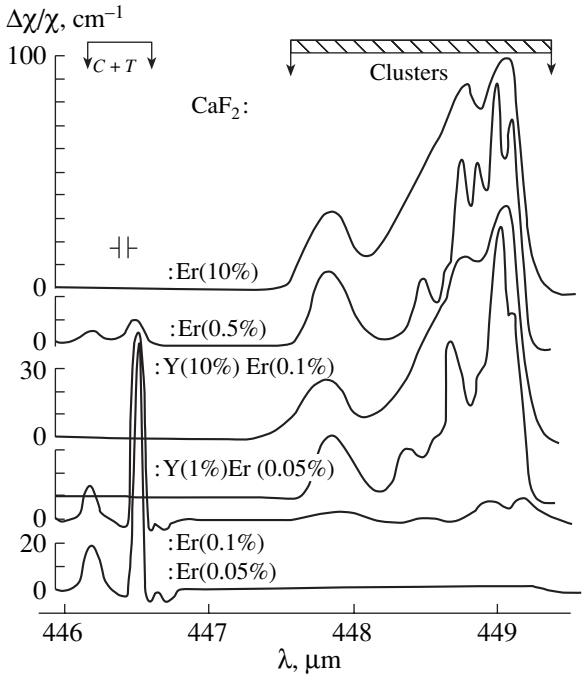

Fig. 4. MCDA spectra of $CaF_2 : Er_xY_y$ in the region of $^4I_{15/2} \longrightarrow {}^4F_{5/2}$ transitions in Er^{3+} ions at 1.8 K for H_0 = 3 kG. *C* and *T* are cubic and tetragonal impurity centers, respectively.

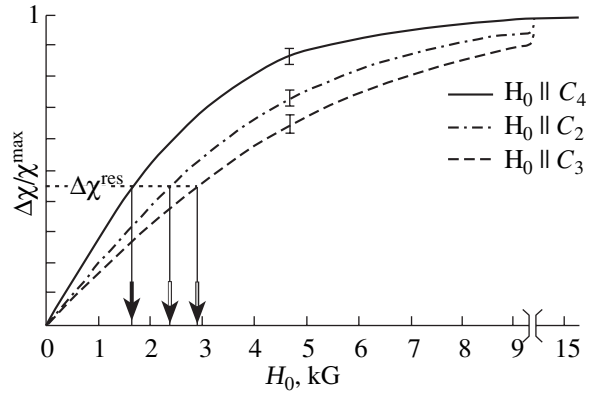

Fig. 5. $\Delta\chi(H_0)$ dependence for $CaF_2 : Er_xY_y$ with $0.002 \le x + y \le 0.02$ for different orientations of the magnetic field relative to the crystal axes. The wavelength of the probing light beam is λ = 449 μm and T = 1.8 K. Arrows indicate the predicted positions of OD-EPR lines for ν^{mw} = 37 GHz and T = 1.8 K; $\Delta\chi^{res} = \tanh(h\nu^{mw}/2k_BT)$.

and simple centers depend on the total $(x + y)$ concentration of the activator (Er^{3+}, Y^{3+}) in the CaF_2 crystal. In other words, clusters can be produced in the crystal by increasing the concentration of both Er^{3+} and Y^{3+} ions.

An investigation of the magnetic-field dependence of the MCDA of paramagnetic ions for different crystal orientations reveals that the crystal field possesses a predominantly tetragonal symmetry for all RE ions in clusters and that the *g* factor of these ions is highly anisotropic. The *g* factor is determined from the $\Delta\chi(H_0)$ curves measured for different orientations of the magnetic field relative to the crystal axes ($\mathbf{H}_0 \parallel C_2, C_3, C_4$) and satisfies the relation $g = g_\parallel \cos\vartheta$, where ϑ is the minimum angle between the magnetic field direction and the C_4 axes of the crystal. Figure 5 shows the $\Delta\chi(H_0)$ dependence for $CaF_2 : (Er_x, Y_y)$ crystals. It is significant that this dependence is the same for different values of *x* and *y*; i.e., it does not vary with dilution of erbium with yttrium over the entire concentration range covered, $0.002 \le (x + y) \le 0.02$. For the *g* factor of the Er^{3+} ions in clusters, this dependence gives the estimate $g_\parallel = 15.5 \pm 1 \gg g_\perp$. From the $\Delta\chi(H_0)$ curves, one can predict the positions of the EPR lines of the cluster centers for different crystal orientations (indicated by arrows in Fig. 5).

Figure 6 shows the OD-EPR spectra of the Er^{3+} ions in clusters. In Fig. 6c, wherein the spectra of the Er^{3+} ions in Y^{3+} clusters are presented, the positions of the spectral lines coincide with those calculated from the $\Delta\chi(H_0)$ curves (indicated by arrows in Fig. 5). The OD-EPR spectrum of Er^{3+} clusters not diluted with *R*" ions is a broad band (Figs. 6a, 6b). The lines of simple centers are also observed in these spectra.

The clearly defined angular dependence of the $\Delta\chi(H_0)$ curves and of the OD-EPR spectra suggests that the RE ions in clusters have a predominantly tetragonal symmetry over the entire composition range of the solid solutions, which argues for the proposed structure of clusters of the Y_6F_{37} (or R_6F_{37}) type in the case where diamagnetic ions of any species in the clusters are randomly replaced by paramagnetic ions and *vice versa*. It is obvious that all positions of *R* ions in the R_6F_{37} clusters are approximately equivalent (except for the position of the off-center F^- ion in the F_{12} cuboctahedron) and the crystal-field symmetry is nearly tetragonal.

Figure 7 shows the OD-EPR spectra of the Tm^{3+} ions in clusters not diluted and diluted with Y^{3+} ions. It is seen that the OD-EPR spectra of Tm^{3+} in undiluted solid solutions containing only paramagnetic ions (Figs. 7a, 7b) are broad and the EPR spectra become noticeably broadened with a proportional increase in the total concentration of the activator above the value $(x + y) = 0.002$ (Figs. 7c, 7d), which suggests that the R_6F_{37} clusters coagulate on the fluorite lattice to form grains of the *R* phase and that the concentration of trivalent *R* ions in the *R* phase is close to the limiting value of the RF_3 solubility in fluorites (~40 mol %). The simplest narrow-line EPR spectra of diluted clusters are observed for intermediate concentrations of *R* ions in fluorites, $(x + y) \sim 0.01$ (Fig. 7e). In this case, the doublet structure of the spectra is likely due to the hyperfine interaction between the Tm^{3+} electron spin and the

Tm^{169} nucleus of spin $I = 1/2$ (isotopic content 100%). The noticeably broadened OD-EPR lines for $\mathbf{H}_0 \parallel C_2$ and C_3, where C_2 and C_3 are the twofold and threefold symmetry axes of the crystal, respectively, suggest that the principal axes of the $g_\parallel$ tensor are not oriented exactly along their preferred orientation, with the misorientation angles being $\varphi \le 5°$ for $(x + y) \le 0.02$ and $\varphi \le 30°$ for $(x + y) \sim 0.38$.

The OD-EPR spectra of the Er and Yb ions in clusters are independent of the wavelength of the probing light wave. At the same time, the MCDA lines of Tm^{3+} ions on the long-wavelength side of the absorption band corresponding to the $^3H_6 \longrightarrow {}^3H_5$ transition (Fig. 8) can be divided into two groups: long-wavelength $\{\lambda_L\}$ and short-wavelength $\{\lambda_S\}$. The $\Delta\chi(H_0)$ dependences measured in these two spectral regions are similar and correspond to tetragonal Tm^{3+} ions with approximately equal values of the $g_\parallel$ factor. However, the OD-EPR spectra of these ions are observed in the $\{\lambda_S\}$ region and not in the $\{\lambda_L\}$ region. The absence of OD-EPR signals in the latter region is apparently explained by the fact that there are at least two nonequivalent positions of Tm^{3+} ions in clusters and that the initial splitting of the non-Kramers doublet of Tm^{3+} ions manifested in the $\{\lambda_L\}$ region is large. The optical-detection methods allow one to estimate the initial splitting (δ_S, δ_L) for the two groups of ions when studying the high-frequency longitudinal magnetic susceptibility of non-Kramers ions [25]. In this paper, the initial splitting for the Tm^{3+} ions in clusters in CaF_2 are estimated using modulation of MCDA signals with an additional longitudinal ac magnetic field.

Thus, the Tm^{3+} ions in clusters in a fluorite-like crystal are divided into groups differing in the initial splitting of the non-Kramers doublet ground state but having the same value of the factor $g_\parallel \approx 14$. A certain disorder in the arrangement of Y_6F_{37}-type clusters in grains, in our opinion, is the only reason for the apparent great diversity (~20) in the types of clusters detected by optical and laser selective spectroscopy [4–7] ("more sensitive" than EPR spectroscopy). It should be noted that we did not observe clusters other than those of the Y_6F_{37} type in the OD-EPR spectra.

The table lists the parameters of the spin Hamiltonian of paramagnetic ions in clusters in CaF_2 studied by us. To within the experimental error, these parameters are roughly the same for clusters in fluorides of Ca, Sr, and Ba. For comparison, the known values of the g factor for the Er^{3+} and Yb^{3+} simple centers in CaF_2 are also presented in the table.

From the table, it is seen that the $g_\parallel$ factor for the ground states of the Er^{3+}, Tm^{3+}, and Yb^{3+} ions in clusters has very large values, which has not been encountered in fluorite-like crystals up to now; these values are close to their upper limit $g^{\lim} = 2Jg_J$, where J is the total angular momentum and g_J is the Landé factor for the lower multiplet of each species of R' ions [26]. Therefore, the ground states of these ions are predominantly doublets $|\pm J\rangle$. This will be the case if the dominant contribution to the axial component of the crystal field comes from the term with constant A_2^0, which is negative in this case. Let us consider the contribution

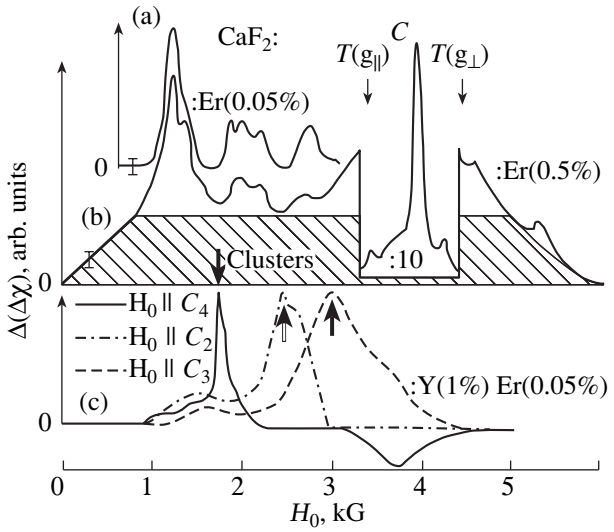

Fig. 6. OD-EPR spectra of (a) $CaF_2 : Er_{0.0005}$, (b) $CaF_2 : Er_{0.005}$, and (c) $CaF_2 : Y_{0.01}Er_{0.0005}$ crystals for different orientations of the magnetic field. Arrows indicate the lines of cubic (C) and tetragonal (T) centers; $\nu^{mw} = 37$ GHz and $T = 1.8$ K.

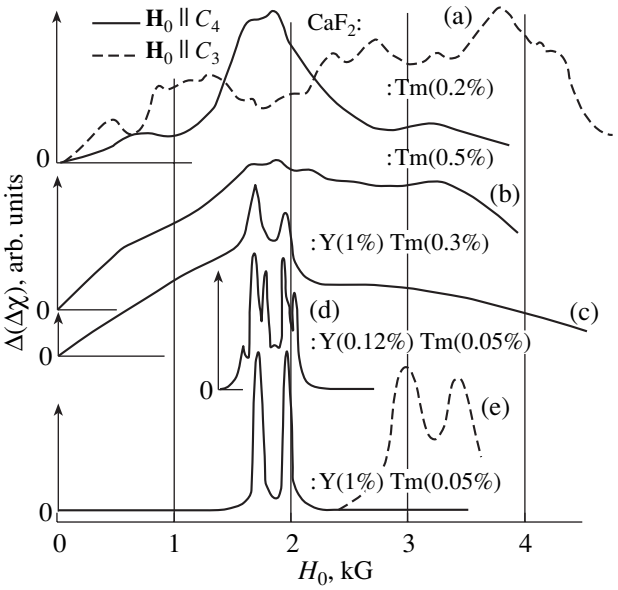

Fig. 7. OD-EPR spectra of Tm^{3+} ions in clusters for $\mathbf{H}_0 \parallel C_4$ (solid line) and $\mathbf{H}_0 \parallel C_3$(dashed line) for (a) $CaF_2 : Tm_{0.002}$, (b) $CaF_2 : Tm_{0.005}$, (c) $CaF_2 : Y_{0.01}Tm_{0.003}$, (d) $CaF_2 : Y_{0.0012}Tm_{0.0005}$, and (e) $CaF_2 : Y_{0.01}Tm_{0.0005}$ crystals. $\nu^{mw} = 36$ GHz and $T = 1.8$ K.

Spin-Hamiltonian parameters for Er^{3+}, Tm^{3+}, and Yb^{3+} ions in clusters and for simple isolated centers in CaF_2

Ions	Clusters in CaF_2 crystals and in solid solutions of CaF_2 with YF_3 or LuF_3 (tetragonal symmetry)		$g_{\parallel}^{\lim}$	Simple centers in CaF_2 [1]		
				cubic	tetragonal	
	$g_{\parallel}$	$g_{\perp}$; δ, cm^{-1}		g	$g_{\parallel}$	$g_{\perp}$
Er^{3+}	16 ± 1	$g_{\perp} \ll g_{\parallel}$	18	6.785	7.78	6.254
Tm^{3+}	≈4	$g_{\perp} = 0$, $\delta_S = 0.25 \pm 0.15$, $\delta_L = 2 \pm 1$	14	–	–	–
Yb^{3+}	7 ± 1	$g_{\perp} \ll g_{\parallel}$	8	3.438	2.423	3.878

$A_2^0 \langle r^2 \rangle \langle J \| \alpha \| J \rangle O_2^0$ to the crystal field, where $\langle r^2 \rangle$ is the mean square radius of the 4*f* orbital and $\langle J \| \alpha \| J \rangle$ is a numerical coefficient that is dependent on the species of *R*' ions. The matrix elements of the spin operators O_2^0 are positive, and their values are maximum for spin sublevels with $J_z = \pm J$. Therefore, in a strong axial crystal field, the ground state will be the doublet $|\pm J\rangle$ if the quantity $A_2^0 \langle J \| \alpha \| J \rangle$ is negative. Usually, $A_2^0 > 0$ for crystals with fluorite structure. However, for the Er^{3+}, Tm^{3+}, and Yb^{3+} ions, we have $\langle J \| \alpha \| J \rangle > 0$; therefore, the value $g_{\parallel} \sim g^{\lim}$ can occur only in anomalous crystal fields for which $A_2^0 < 0$. This is indeed an anomaly, because the EPR spectrum of Tm^{3+} ions has been recorded only for a few systems [27] and has not been observed in crystals with fluorite structure up to now.

2.3. Microwave Investigations of Ionic Two-Level Systems in Fluorite-Like Crystals with Clusters

As already noted, the Y_6 octahedron of six Y^{3+} cations in clusters of the Y_6F_{37} type encloses a cuboctahedron F_{12} of twelve F^- anions, within which there is one off-center ion F^-. We associate possible tunneling of the off-center ion F^- within the cuboctahedron with the

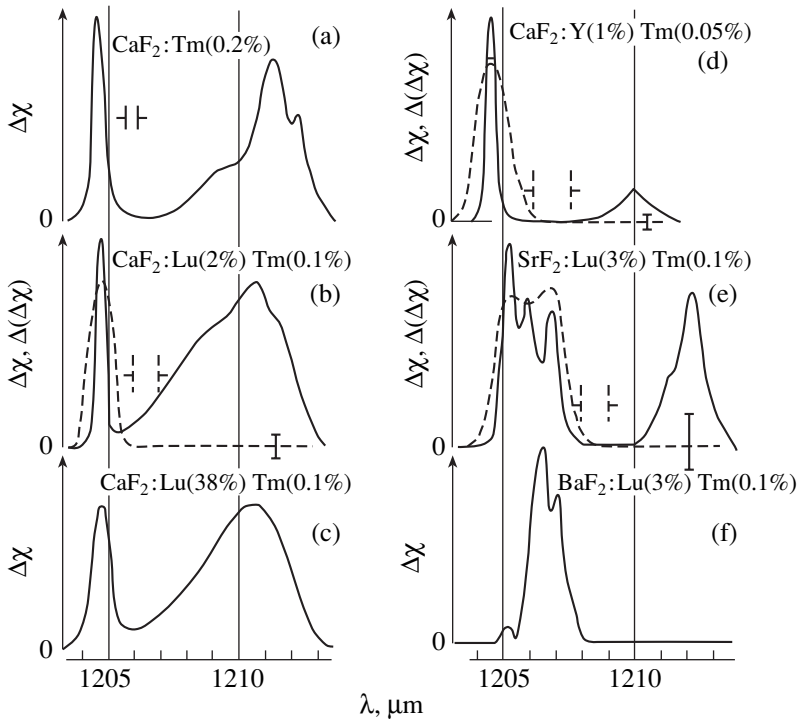

Fig. 8. MCDA spectra (solid lines) on the long-wavelength side of the absorption band $^3H_6 \longrightarrow {}^3H_5$ of Tm^{3+} ions in clusters for solid solutions (a) $CaF_2 : Tm_{0.002}$, (b) $CaF_2 : Lu_{0.02}Tm_{0.001}$, (c) $CaF_2 : Lu_{0.38}Tm_{0.001}$, (d) $CaF_2 : Y_{0.01}Tm_{0.0005}$, (e) $SrF_2 : Lu_{0.03}Tm_{0.001}$, and (f) $BaF_2 : Lu_{0.03}Tm_{0.001}$. Dashed lines show the spectra of the intensity of OD-EPR signals for $\nu^{mw} = 36$ GHz, $T = 1.8$ K.

existence of two-level systems (TLSs), which have been disclosed in solid solutions like yttrofluorite [28].

The ionic TLSs are known to appear when atoms or atomic groups tunnel in amorphous insulators or in disordered, glasslike regions of crystals with "porous" defects [29, 30]. The simplest case of the formation of an ionic TLS is illustrated in Fig. 9. If tunneling is negligible, the ion in a void of an extended defect moves within one of the two potential wells and the wave functions of the ion in the different potential wells do not overlap (panel *1* in Fig. 9). When ion tunneling between the potential wells is possible, the wave function of the ion can be represented, in a zeroth-order approximation, as a superposition of the wave functions for each of the potential wells (panel *2* in Fig. 9). As in the classic case of the ammonia molecule NH_3, tunnel splitting (Δ) of the ground state of the ion (molecule) occurs, with the lower sublevel of the ground state described by an antisymmetric wave function and the upper sublevel described by a symmetric wave function. Therefore, electric dipole transitions are allowed between these sublevels. The TLSs in question are disordered systems with a continuous tunneling-splitting distribution; therefore, resonance absorption of TLSs covers a wide spectral range, from zero to roughly 10–100 cm^{-1} [10–12].

It was found that all yttrofluorite-like solid solutions, both doped and undoped with a paramagnetic impurity, possess high MW dielectric losses (measurements were made at frequencies approximately equal to 9, 36, and 75 GHz). Furthermore, the dielectric losses are resonant in character at $T = 1.8$ K and are saturated with increasing MW radiation power.

We will discuss the experimental data obtained at MW frequencies of ~36 GHz. Measurements were performed with samples placed in a cylindrical reflecting cavity of the TE_{011} type. A empty cavity with a loaded Q factor $Q_{LO} \approx 5000$ was matched with a waveguide and almost entirely absorbed the klystron MW radiation passed through the waveguide. An input power of ~30 mW can be reduced with the help of an attenuator with 0–30 dB. Dielectric losses in the sample led to a decrease in the cavity Q factor and, therefore, to a mismatch between the cavity and the waveguide, which, in turn, caused an increase in the MW radiation power reflected from the cavity with the sample.

Figure 10 shows the klystron MW radiation power reflected from the cavity with a sample as a function of frequency in the frequency range of the klystron radiation (±50 MHz relative to the central frequency $\nu^{mw} \sim$ 36 GHz) for different attenuations of the input power. The absorption line of the cavity with the sample is seen to be near the center of these curves. This line narrows and its intensity increases with increasing input MW radiation power, because the Q factor of the cavity with the sample increases and the cavity and waveguide become better matched as the absorption due to transitions between the lower and upper sublevels of the TLS is saturated.

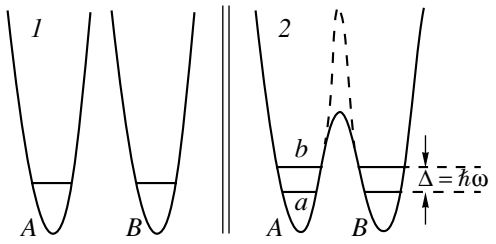

Fig. 9. Ground state of an atom in potential wells A and B (*1*) in the absence and (*2*) in the presence of tunneling between the potential wells. $\Phi^a(R) = [\Phi_A(R) - \Phi_B(R)]/\sqrt{2}$ and $\Phi^b(R) = [\Phi_A(R) + \Phi_B(R)]/\sqrt{2}$ are the wave functions of the atom at the lower and upper sublevels in the A–B double-well potential, respectively, where $\Phi_A(R)$ and $\Phi_B(R)$ are the wave functions of the atom in the isolated potential wells A and B, respectively.

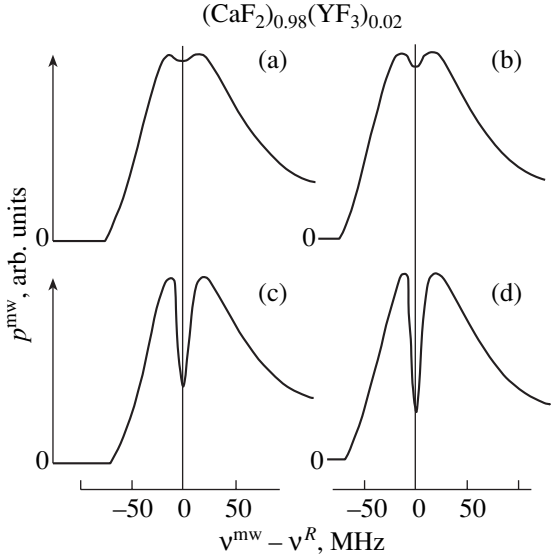

Fig. 10. Frequency dependence of the klystron MW radiation power (~30 mW) reflected from the MW cavity with a sample of $(CaF_2)_{0.98}(YF_3)_{0.02}$ for different attenuation levels of the MW radiation power: (a) 30, (b) 20, (c) 10, and (d) 0 dB. $\nu^{mw} \approx 36$ GHz and $T = 1.8$ K.

The TLSs in yttrofluorite-like solid solutions have been comprehensively studied by IR-absorption and Raman scattering spectroscopy [10–12].

3. EFFECT OF CLUSTERS ON THE SEMICONDUCTOR PROPERTIES OF CdF_2

CdF_2 is the only fluorite-like crystal (and predominantly ionic crystal) that becomes a semiconductor when doped with group-III elements and warmed in a

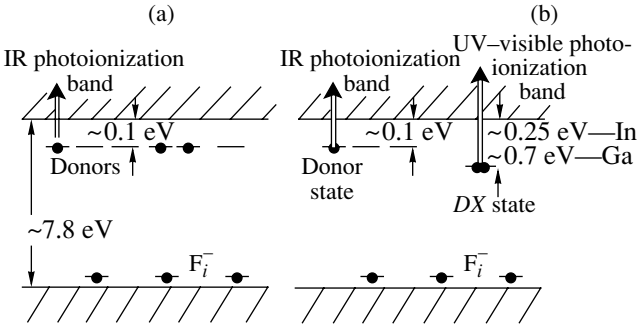

Fig. 11. Energy levels located in the band gap of semiconductor crystals (a) CdF_2 : Y and (b) CdF_2 : In and CdF_2 : Ga.

reducing atmosphere, e.g., in Cd vapors (additive crystal coloration [31]). During this procedure, the F^- ions that compensate the excess charge (+1) of trivalent activator ions diffuse toward the surface, where they recombine with reducing (Cd) atoms, while electrical neutrality is provided by the inverse flow of electrons traveling inward from the surface. Semiconducting CdF_2 crystals are partially compensated *n*-type semiconductors [32, 33] with neutral hydrogen-like donors in which a captured electron occupies an orbital with Bohr radius *a*; the remaining interstitial F^- ions act as acceptors (Fig. 11a). The compensation ratio *K* is defined as $K = N_D^+/N_D$, where $N_D = N_D^+ + N_D^0$ is the total concentration of neutral (N_D^0) and ionized (N_D^+) donors. We note that the donor ionization energy in CdF_2 is roughly 100 meV, which is considerably higher than that in conventional semiconductors. These donor centers are associated with an IR absorption band corresponding to photoionization with a maximum at 7–8 μm.

The Ga and In donor impurities in CdF_2 are of special interest, because these impurities form bistable centers. In addition to a usual shallow hydrogenic state, Ga and In also produce a deep, strongly localized *DX* state (Fig. 11b) which is characterized by large crystal-lattice relaxation, i.e., by a large displacement of the equilibrium position in the configuration-coordinate space [34, 35].

When cooled in the dark, reduced crystals of CdF_2 : Ga and CdF_2 : In are semi-insulating, because the electrons introduced into the crystal during coloration are localized predominantly on deep M^{1+} centers (*M* = Ga, In). These centers are responsible for the UV and visible photoionization absorption band. Illumination of crystals in this spectral band leads to excitation of electrons into the conduction band and their capture by an ionized (empty) center with the formation of a neutral (shallow) donor; in this case, the ionized deep center also transforms spontaneously into a neutral donor. The optical spectra of CdF_2 crystals doped with bistable impurities alter profoundly in the process of conversion of deep centers into shallow ones, which renders the crystals photochromic [32, 33].

In semiconducting CdF_2 crystals, we detected "electronic" TLSs associated with ionized donor pairs in the case where there are ionized and neutral donors in the crystal [36]. We described the ionized donor pairs in terms of the theory of Tanaka *et al.* [37] extended to the case of semiconductors with an arbitrary compensation ratio in a wide frequency range (including the far IR region).

3.1. Ionized Donor Pairs: Modified Tanaka Theory

If two nearest neighbor donors are identical and an electron is captured by this ionized-donor pair, the electron will occupy each of the two donor levels with equal probability (as is the case in the molecular ion H_2^+). The twofold degenerate ground state of such a system is split by an amount *W*, which depends on the distance r_ω between the members of the donor pair. Since the donors are randomly distributed over the crystal, the distribution of donor pairs in distance r_ω is continuous. This leads to the occurrence of broad bands in the far-IR and MW absorption spectra of partially compensated semiconductors, which was first observed in lightly doped Si and Ge [37, 38].

The dependence of the splitting energy *W* and of the corresponding frequency ω on the distance r_ω for $r_\omega > a$ is closely approximated by [37]

$$\hbar\omega = W(r_\omega) \approx (4e^2/3\varepsilon_1 a)\frac{r_\omega}{a}\exp(-r_\omega/a). \qquad (5)$$

Let us introduce the average distance between those donor centers (neutral or ionized) whose concentration is higher:

$$\bar{R} = \left(\frac{4}{3}\pi N_{mj}\right)^{-1/3}, \qquad (6)$$

where $N_{mj} = N_D^0 = N_D(1 - K)$ for $0 \le K \le 0.5$ and $N_{mj} = N_D^+ = N_D K$ for $0.5 \le K \le 1$.

The donor pairs with distances $r_\omega < \bar{R}$ can be considered to be isolated only approximately, because the concentration of charged acceptors (interstitial F^- ions in our case) is high and the energy levels of the members of a donor pair cease to be in resonance, their difference being equal to [37]

$$\Omega \equiv \Omega(r_\omega, R, \sin\theta) = \frac{e^2}{\varepsilon_1 R_B} - \frac{e^2}{\varepsilon_1 R_A} \cong \frac{e^2}{\varepsilon_1 R^2}(R_A - R_B). \qquad (7)$$

Here, ε_1 is the dielectric constant; *e* is the electron charge; R_A, R_B, and *R* are the distances from an F^- ion to the *A* and *B* donors and their center of gravity, respec-

tively; and θ is the angle between the median R and the normal to the A–B axis (Fig. 12).

Following [37], we assume that all donor pairs with $\Omega \le W = \hbar\omega$ make the same contribution to resonant absorption at frequency ω. Further, for any value of ω, there is a limit angle θ_{lim} ($0 \le \theta_{lim} \le \pi/2$) for which $\Omega = W$ for a given value of R and there is a limit distance

$$R_{max}(\omega) \cong \left(\frac{e^2 r_\omega}{\varepsilon_1 \hbar\omega}\right)^{1/2} \quad (8)$$

for which $\theta_{lim} = \pi/2$. (The influence of the charged impurity is negligible for $R \ge R_{max}$.) Let us introduce a function $\Phi(\omega, r)$ which is equal to $\sin\theta_{lim}$ if $R \le R_{max}$ and to unity if $R \ge R_{max}$. Then, the fraction $S(\omega) \le 1$ of the donor pairs with distance r_ω that make a contribution to resonant absorption at frequency ω is given by

$$S(\omega) = \int_0^\infty \frac{3x^2}{\bar{R}^3} \exp[-(x/\bar{R})^3]\Phi(\omega, x)dx. \quad (9)$$

Finally, the frequency dependence of the imaginary part of the dielectric constant due to resonant absorption of ionized donor pairs can be found to be (in the Gauss system of units)

$$\varepsilon_2(\omega) = \frac{\pi^2}{\hbar\omega} N_{min} S(\omega) e^2 \bar{R} a \left(\frac{r_\omega}{\bar{R}}\right)^4 \exp\left[-\left(\frac{r_\omega}{\bar{R}}\right)^3\right] \times (1 + E^2/E_c^2)^{-1/2} \tanh\left(\frac{\hbar\omega}{2k_B T}\right). \quad (10)$$

Here, $\hbar\omega$ is the energy of MW quantum, E is the electric-field amplitude of MW radiation, and E_c is the critical value of this amplitude at which dielectric losses reach saturation. By using the relation

$$\alpha(\omega) = \sqrt{2}\frac{\omega}{c}[(\varepsilon_1^2 + \varepsilon_2^2)^{1/2} - \varepsilon_1]^{1/2} \cong \frac{\omega}{c}\frac{\varepsilon_2(\omega)}{\sqrt{\varepsilon_1}}, \quad (11)$$

we find the frequency dependence of the optical absorption coefficient α(ω).

3.2. Electronic Two-Level Systems in Semiconducting CdF_2 Crystals

Similar to ionic two-level systems, electronic TLSs can be manifested by the tendency of MW radiation absorption to saturate. We detected resonant absorption of ionized donor pairs in semiconducting CdF_2 crystals in the MW region $\lambda \approx 8$ mm. At $T = 1.8$ K, the tendency of dielectric losses to saturate was observed for all CdF_2 crystals doped with Y, Ga, or In when the intensity of the absorption line of the MW cavity with a sample increased with MW radiation power (Fig. 13).

As was the case with ionic TLSs (see above), for a sample of $CdF_2 : Y^{3+}$ (0.5 mol %), the cavity–waveguide matching was partially restored and the fraction of MW radiation power reflected from the cavity was decreased when the electric dipole transitions between the electronic resonant TLS sublevels were saturated with MW radiation power. In photochromic crystals of $CdF_2 : Ga^{3+}$ and $CdF_2 : In^{3+}$, dielectric losses become significantly higher (by roughly an order of magnitude) when samples cooled in the dark from room to liquid-helium temperature are illuminated with UV and visible light , which results in an increased concentration of shallow donors. In CdF_2 crystals not subjected to additive coloration, the electronic TLSs were not detected.

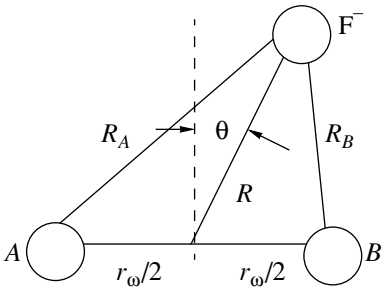

Fig. 12. Ionized A–B donor pair in the field of an interstitial F^- ion.

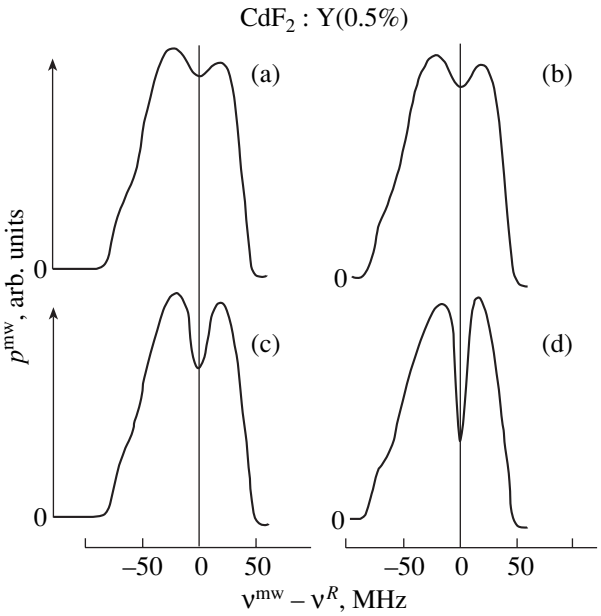

Fig. 13. Frequency dependence of the klystron MW radiation power (~10 mW) reflected from the MW cavity with a semiconductor sample of $CdF_2 : Y$ for different attenuation levels of the MW radiation power: (a) 30, (b) 20, (c) 10, and (d) 0 dB. $\nu^{mw} \approx 36$ GHz and $T = 1.8$ K.

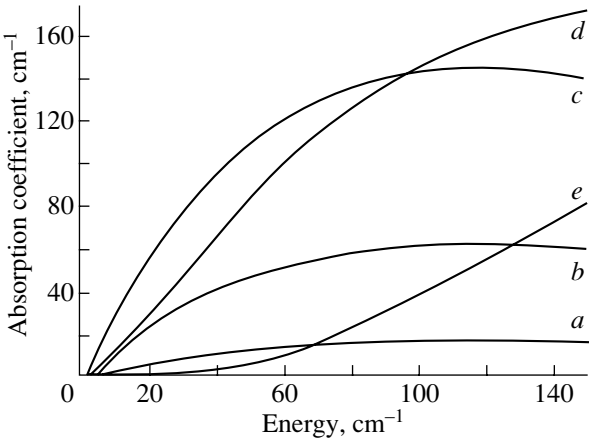

Fig. 14. Calculated far-IR absorption spectra of semiconducting CdF_2 crystals with neutral-donor concentration 2×10^{18} cm^{-3} for donor Bohr radius $a = 7$ Å [33] and compensation ratio K equal to (*a*) 0.1, (*b*) 0.3, (*c*) 0.5, (*d*) 0.7, and (*e*) 0.9.

Our experimental data on MW radiation absorption and the data from [39] on IR absorption can be interpreted in terms of Eqs. (10) and (11), which are given by the theory of resonant absorption of ionized donor pairs for semiconductors with different compensation level. Figure 14 shows absorption spectra in the far IR region calculated for the CdF_2 semiconductor with electron concentration $n_e \sim 2 \times 10^{18}$ cm^{-3}. The calculated IR absorption spectra agree well with the experimental spectra [39] in both shape and absorption intensity.

An analysis of our experimental data on MW and far-IR absorption reveals that the CdF_2 crystals subjected to additive coloration are partially compensated semiconductors ($0.5 \le K \le 0.9$). The total electron concentration $n_e \approx N_D^0 \sim 10^{18}$ cm^{-3} in these crystals was determined from the intensity of the IR band corresponding to shallow centers [32, 33], which allows us to calculate (using the values of K indicated above) the total concentration of donors (neutral and charged) $N_D = n_e/(1 - K) \sim 10^{19}$ cm^{-3}. Since the concentration of donor impurities in CdF_2 can be as high as tens of percent, the above estimate indicates that there are clusters in which activator ions are "bound" and do not participate in electronic processes. It was found, for example, that in the CdF_2 : Y (0.5 mol %) crystals studied by us, the donor concentration N_D, equal to the concentration of isolated Y^{3+} ions on the CdF_2 lattice, is at least five times smaller than the total yttrium concentration in this crystal ($\sim 10^{20}$ cm^{-3}). Thus, no less than 80% of the Y^{3+} ions are in clusters.

By analogy with fluorides of Ca, Sr, and Ba [6, 24], one can assume that there is a limit concentration ($\sim 10^{19}$ cm^{-3}) of donor impurities in CdF_2 that become simple centers randomly distributed over the CdF_2 crystal lattice. Excess impurity forms impurity–fluorine clusters, which manifest themselves clearly in the optical spectra of RE ions with concentration higher than ~0.1 mol % in CdF_2 [7]. High solubility of some elements of the main (boron) subgroup, e.g., indium [40], allows one to suggest that the formation of clusters is a phenomenon typical of the donor impurities in CdF_2.

4. CONCLUSION

Thus, our studies of solid solutions of fluorides of Ca, Sr, and Ba with trifluorides of elements of the second half of the RE series have revealed that nonstoichiometric fluorite phases, which were earlier considered to be fully disordered, can actually accommodate a change in stoichiometry through a fairly regular rearrangement of the fluorite crystal lattice with the formation of the same structural units (clusters of the Y_6F_{37} type) that are observed in the homologous series of fluorite-like superstructures [21]. This is consistent with the well-known tendency for nonstoichiometric compounds of different structural types to preserve a certain order in the crystal lattice through the formation of extended defects, even in the case of small deviations from stoichiometry [41]. This conclusion is supported by the results of other studies. EXAFS studies revealed [15] that the nearest neighbor environment of the Y^{3+} ion in $(CaF_2)_{1-y}(YF_3)_y$ solid solutions is similar in structure to that of the Y^{3+} ion in YF_3 and, as in the Y_6F_{37} clusters, has the form of a square antiprism. Neutron diffraction studies showed [41] that the *R* ions seem to form octahedra in activated fluorite-like crystals. Investigations of the magnetic susceptibility of dipole-spin glasses in the CaF_2 : $Er_{0.01}$ system [43, 44] disclosed that there were regions of high concentration of Er^{3+} ions (not less than 20 mol %) in the samples.

Our results indicate that in CdF_2 crystals activated with group-III elements and subjected to additive coloration, complete chemical reduction and, hence, the full removal of interstitial F^- ions from a crystal seems to be impossible. This suggests that there are clusters that bind "excess" impurity in the crystal and that there are some sources that provide F^- ions in the process of chemical reduction of an impurity. Such sources can be the same impurity–fluorine clusters that are assumed in [6, 7] to be accumulators of interstitial F^- ions. The clusters form during CdF_2 crystal growth and, perhaps, rearrange in the process of thermochemical transformation of the crystal from the semi-insulating to a semiconducting state [7]. These clusters can possess different structure, depending on the impurity, and are responsible for the high solubility of many group-III elements in CdF_2. A major portion of impurities that could be involved in the formation of donor levels is bound together into clusters, which hinders the fabrication of semiconducting CdF_2 with a compensation ratio

$K < 0.5$ and a concentration of free or nearly free electrons higher than roughly $\sim 10^{19}$ cm^{-3}.

ACKNOWLEDGMENTS

This study was supported by US CRDF, grant no. RPI-2096.

REFERENCES

1. W. Hayes, *Crystals with the Fluorite Structure* (Clarendon, Oxford, 1974).
2. V. V. Ovsyankin and P. P. Feofilov, Pis'ma Zh. Éksp. Teor. Fiz. **3** (12), 494 (1966) [JETP Lett. **3**, 322 (1966)].
3. L. D. Livanova, I. G. Saĭtkulov, and A. L. Stolov, Fiz. Tverd. Tela (Leningrad) **11** (4), 918 (1969) [Sov. Phys. Solid State **11**, 750 (1969)].
4. M. D. Kurz and J. C. Wright, J. Lumin. **15** (2), 169 (1977).
5. M. P. Miller and J. C. Wright, J. Chem. Phys. **68** (4), 1548 (1978).
6. D. S. Moore and J. C. Wright, J. Chem. Phys. **74** (3), 1626 (1981).
7. Sun-II Mho and J. C. Wright, J. Chem. Phys. **81** (3), 1421 (1984).
8. C. R. A. Catlow, J. D. Comins, F. A. Germano, *et al.*, J. Phys. C **14** (4), 329 (1981).
9. D. G. Cahill and R. O. Pohl, Phys. Rev. B **39** (14), 10477 (1989).
10. J. Tu, S. A. FitzGerald, J. A. Campbell, and A. J. Sievers, J. Non-Cryst. Solids **203**, 153 (1996).
11. S. A. FitzGerald, J. A. Campbell, and A. J. Sievers, J. Non-Cryst. Solids **203**, 165 (1996).
12. J. J. Tu and A. J. Sievers, Phys. Rev. Lett. **83** (20), 4077 (1999).
13. A. K. Cheetman, B. E. F. Fender, and M. J. Cooper, J. Phys. C **4** (18), 3107 (1971).
14. R. J. Booth and B. R. McGarvey, Phys. Rev. B **21** (4), 1627 (1980).
15. S. P. Vernon and M. B. Stearns, Phys. Rev. B **29** (12), 6968 (1984).
16. J. P. Laval, A. Abaous, B. Frit, and A. Le Bail, J. Solid State Chem. **85** (1), 133 (1990).
17. S. A. Kazanskiĭ, Zh. Éksp. Teor. Fiz. **84** (3), 1202 (1983) [Sov. Phys. JETP **57**, 697 (1983)].
18. *Inorganic Solid Fluorites: Chemistry and Physics*, Ed. by P. Hagenmuller (Academic, London, 1985).
19. P. Eisenberger and P. S. Pershan, Phys. Rev. **167** (2), 292 (1968).
20. A. K. Ivanov-Shits, N. I. Sorokin, P. P. Fedorov, and B. P. Sobolev, Solid State Ionics **31**, 253 (1989).
21. D. J. M. Bevan, J. Strähle, and O. Greis, J. Solid State Chem. **44** (1), 75 (1982).
22. S. Geshwind, in *Electron Paramagnetic Resonance*, Ed. by S. Geshwind (Plenum, New York, 1972), p. 353.
23. S. A. Kazanskiĭ, Pis'ma Zh. Éksp. Teor. Fiz. **38** (9), 430 (1983) [JETP Lett. **38**, 521 (1983)].
24. S. A. Kazanskiĭ, Zh. Éksp. Teor. Fiz. **89** (4), 1258 (1985) [Sov. Phys. JETP **62**, 727 (1985)].
25. V. S. Zapasskiĭ, Fiz. Tverd. Tela (Leningrad) **22** (10), 2906 (1980) [Sov. Phys. Solid State **22**, 1696 (1980)].
26. A. Abragam and B. Bleaney, *Electron Paramagnetic Resonance of Transition Ions* (Clarendon, Oxford, 1970; Mir, Moscow, 1972).
27. J. E. Rouse and J. B. Gruber, Phys. Rev. B **13** (9), 3764 (1976).
28. S. A. Kazanskiĭ, Pis'ma Zh. Éksp. Teor. Fiz. **41** (5), 185 (1985) [JETP Lett. **41**, 224 (1985)].
29. *Amorphous Solids (Low-Temperature Properties)*, Ed. by W. A. Phillips (Springer, Berlin, 1981).
30. W. A. Phillips, Rep. Prog. Phys. **50**, 1657 (1987).
31. P. F. Weller, Inorg. Chem. **4** (11), 1545 (1965); **5** (5), 739 (1966).
32. F. Moser, D. Matz, and S. Lyu, Phys. Rev. **182** (3), 808 (1969).
33. J. M. Langer, Rev. Solid State Sci. **4**, 297 (1990).
34. C. H. Park and D. J. Chadi, Phys. Rev. Lett. **82**, 113 (1999).
35. A. S. Shcheulin, A. I. Ryskin, K. Swiatek, and J. M. Langer, Phys. Lett. A **222**, 107 (1996).
36. S. A. Kazanskii, D. S. Rumyantsev, and A. I. Ryskin, Physica B (Amsterdam) **308–310**, 1038 (2001).
37. S. Tanaka, M. Kobayashi, E. Hanamura, and K. Uchinokura, Phys. Rev. **134** (1), A256 (1964).
38. H. F. Jang, G. Gripps, and T. Timusk, Phys. Rev. B **41** (8), 5152 (1990).
39. P. Eisenberger, P. S. Pershan, and D. R. Bosomworth, Phys. Rev. **188** (3), 1197 (1969).
40. P. Lagassie, J. Grannee, and J.-M. Reau, Rev. Chim. Miner. **24**, 328 (1987).
41. B. G. Hyde, A. N. Bagshaw, Sten Andersson, and M. O'Keefe, Annu. Rev. Mater. Sci. **4** (1), 43 (1974).
42. P. J. Bendall, C. R. A. Catlow, J. Corish, and P. W. M. Jacobs, J. Solid State Chem. **51** (2), 159 (1984).
43. V. A. Atsarkin, V. V. Demidov, and S. Ya. Khlebnikov, Pis'ma Zh. Éksp. Teor. Fiz. **32** (7), 461 (1980) [JETP Lett. **32**, 440 (1980)].
44. T. S. Belozerova and E. K. Khenner, Fiz. Tverd. Tela (Leningrad) **26** (1), 83 (1984) [Sov. Phys. Solid State **26**, 47 (1984)].

Translated by Yu. Epifanov

Physics of the Solid State, Vol. 44, No. 8, 2002, pp. 1426–1432. From Fizika Tverdogo Tela, Vol. 44, No. 8, 2002, pp. 1367–1373.

PROCEEDINGS OF THE XI FEOFILOV WORKSHOP "SPECTROSCOPY OF CRYSTALS ACTIVATED BY RARE-EARTH AND TRANSITION-METAL IONS"

(Kazan, Tatarstan, Russia, September 24–28, 2001)

Parameters of Light-Induced Charge Transfer Processes in Photorefractive Crystals[1]

O. F. Schirmer, C. Veber, and M. Meyer

Fachbereich Physik, Universität Osnabrück, Osnabrück, D-49069 Germany

Abstract—A method is outlined by which the parameters governing light-induced charge transfer processes in photorefractive crystals can be determined. The system $BaTiO_3$:Rh is treated as an example. EPR is used to obtain information on the EPR-active defect charge states. Through simultaneous observation of light-induced EPR- and optical absorption changes, the corresponding optical absorption bands are established as fingerprints of the defect charge states. Consistency arguments make it possible to label EPR-silent absorption bands in this way also, significantly extending the scope of EPR-based defect studies. On this basis, the charge transfer paths taking place under illumination are identified. Quantitatively, the defect concentrations are directly or indirectly derived from the available EPR signals. In addition, the kinetics of the light-induced changes of the densities of the occurring defect charge states are studied. In conjunction with the defect concentrations, this makes it possible to deduce the responsible transfer parameters. © *2002 MAIK "Nauka/Interperiodica".*

The photorefractive effect in a suitable electrooptic material is usually triggered by the photoionization of defects [1]. Under illumination with an inhomogeneous light pattern, the freed charge carriers move in either tie valence or in the conduction band from the brighter regions towards the darker ones, transported by various possible driving mechanisms. A charge pattern results; it is accompanied by the corresponding space charge field, which is transformed into a refractive index pattern by the electrooptic effect. Figure 1 demonstrates the three elementary models under which the occurring charge transfer processes can be subsumed [2]. In the 1-center model, the defects representing source and drain of the charge carriers are identical. In the two other models, the 2-center and 3-valence models, the carriers end at levels different from the initial ones. In the latter situations, photochromism is usually observed, since each of the defect charges absorbs light in different ways. It should be noted that such absorption changes occur also under homogeneous illumination. For a quantitative prediction of the photorefractive performance of a material, it is necessary to know the concentrations of the defects in the various possible charge states and their spatial distributions present under defined illumination conditions. These quantities can be obtained if a set of parameters describing the kinetics of the light-induced charge transfers between the relevant defects is known. In a later section, these parameters will be introduced.

The essential role of defects in the photorefractive effect is obvious. For this reason, the structure and properties of defects in several inorganic photorefractive crystals have been investigated intensively over the last decade, mainly by EPR studies ($BaTiO_3$, $LiNbO_3$, $Sr_{1-x}Ba_xNbO_6$, $KNbO_3$, $Ba_{1-x}Ca_xTiO_3$, $Bi_{12}MO_{20}$ (M = Ti, Ge, Si), etc.) [3–5]. At this point, it is advantageous to demonstrate a way how the charge transfer processes connected with tile defects can be elucidated from the information available on them. If a method can be outlined as to how this knowledge leads to insight into the charge transfer processes connected with defects, an important step towards an understanding of the optical properties of free materials would be achieved. The term "defect" can be used with two different meanings: first, it may stand for a certain chemical entity which interrupts the periodicity of a crystal lattice, and second, for one of the charge states such a perturbation can acquire. For the latter case, we shall talk of "defect charge state," if necessary.

The procedure which we developed to quantitatively assess the role of defects in charge transfer processes, especially in photorefractive crystals, will be exemplified in the following by the system $BaTiO_3$ doped with Rh. This host lattice has high electrooptic coefficients; therefore, only a few transferred charges can already head to measurable index changes, and thus the material offers high photorefractive sensitivity. Doping with Rh increases the infrared response of the system [6–10].

1. METHOD

When applicable, EPR is the most suitable method of obtaining information on the chemical, geometrical, electronic, and energetic structure of defects. However,

[1] This article was submitted by the authors in English.

in many cases, defects are EPR-silent. Since these can likewise be involved in the charge transfer processes, one has to look for ways to obtain information on them also. The method which we introduced is able to achieve this and will eventually allow one to obtain the quantitative information needed to predict the defect-induced photorefractive properties. In this section, the procedure is outlined briefly. The first step is to establish the optical absorption bands as fingerprints of the defects on the basis of the available EPR information. As will be shown, this can be done not only for EPR-active but also for EPR-silent defects. By comparing the defect concentrations deduced from the EPR intensities to the absorption strengths, the optical cross sections of the absorption bands can also be obtained. From here on, all further studies can be based on optical measurements alone. Usually, these can be performed at room temperature, where EPR investigations generally fail, but where photorefractive devices are expected to operate. The changes of the optical absorption bands under illumination with pump light make it possible to draw conclusions about the charge transfer processes taking place at these pump energies. Also, the defect concentrations present under the various experimental illumination conditions can be deduced. Further parameters describing the charge transfer processes can be deduced from the temporal evolution of the defect concentrations occurring after switching the light on or off.

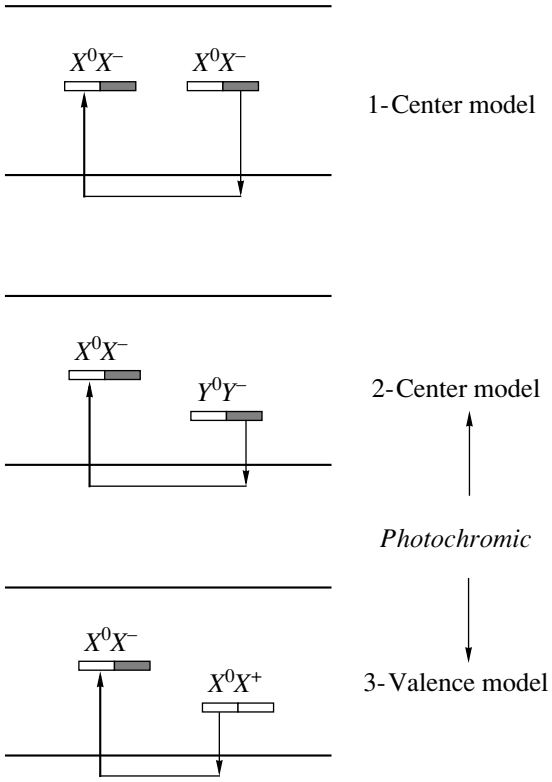

Fig. 1. The three basic models for charge transfer processes between defect gap levels. The lower two lead to light-induced optical absorption under homogeneous illumination.

2. QUALITATIVE IDENTIFICATION OF THE CHARGE TRANSFER PROCESSES

The experimental data mentioned in the following is taken from the investigation of a $BaTiO_3$:Rh crystal grown from a $BaTiO_3$ melt unintentionally containing rhodium. The simultaneous observation of light-induced EPR- and optical absorption changes is performed with a setup described earlier [11] which allows optical absorption measurements to be made within an EPR cavity in a rather flexible way. The scheme is presented in Fig. 2. Absorption changes, resulting when the pump light energy is increased stepwise starting from low energies, can be shown in the conventional way, as given in Fig. 3b. More insight into the phenomena taking place can be derived if the same information is plotted in a pseudo-3D plot, exhibited above that in Fig. 3a. While abscissa and ordinates mark the probe- and pump-light energies, respectively, the grey shading indicates the absorption changes, their calibration being given by the bar at the top. In the experiment, the pump energy is raised successively in steps marked with short horizontal thin lines along the ordinate. The indicated diagonal, defined by identical probe- and pump-light energies $E_{probe} = E_{pump}$, is an important guideline allowing one to organize the features in the plot. The absorption minima or, alternatively, the light-induced transparencies lying on the diagonal have to be attributed to primary processes. Here, a given pump energy photoionizes a defect and the corresponding absorption caused by this charge transfer decreases. Such primary processes are marked by double arrows in Fig. 1. Secondary processes are those triggered by the primary ones; they lie outside the diagonal in Fig. 3a; among them are those given by single arrows in Fig. 1. Along the vertical line in Fig. 3a crossing the minimum at $E_{probe} = E_{pump} = 1.9$ eV, the correlation with the EPR spectra of Rh^{4+} [12] was studied. The intensities of the corresponding EPR and absorption signals are given in Fig. 4. A close correlation is seen, which supports the assignment to Rh^{4+} being converted to Rh^{3+} by photoexcitation of a valence band electron (see lower part of Fig. 4). Also shown is the corresponding process in real space. In this and comparable investigations, it should be kept in mind that the most intense absorption processes, such as charge transfer transitions, dominate over weaker ones, such as crystal field excitations. The latter can thus be neglected. The conversion of Rh^{4+} creates Rh^{3+} and a hole in the valence band. Since the optical absorption band near 3.0 eV rises in parallel to the decrease in the Rh^{4+} absorption near 1.9 eV, it is likely that the band near 3.0 eV has to be attributed to Rh^{3+}. The hole in the valence band is not stable, which means it will be captured at a suitable trap. As Rh is the main impurity in the material, it is likely that the hole is caught at another Rh^{4+}, forming Rh^{5+}. The correspond-

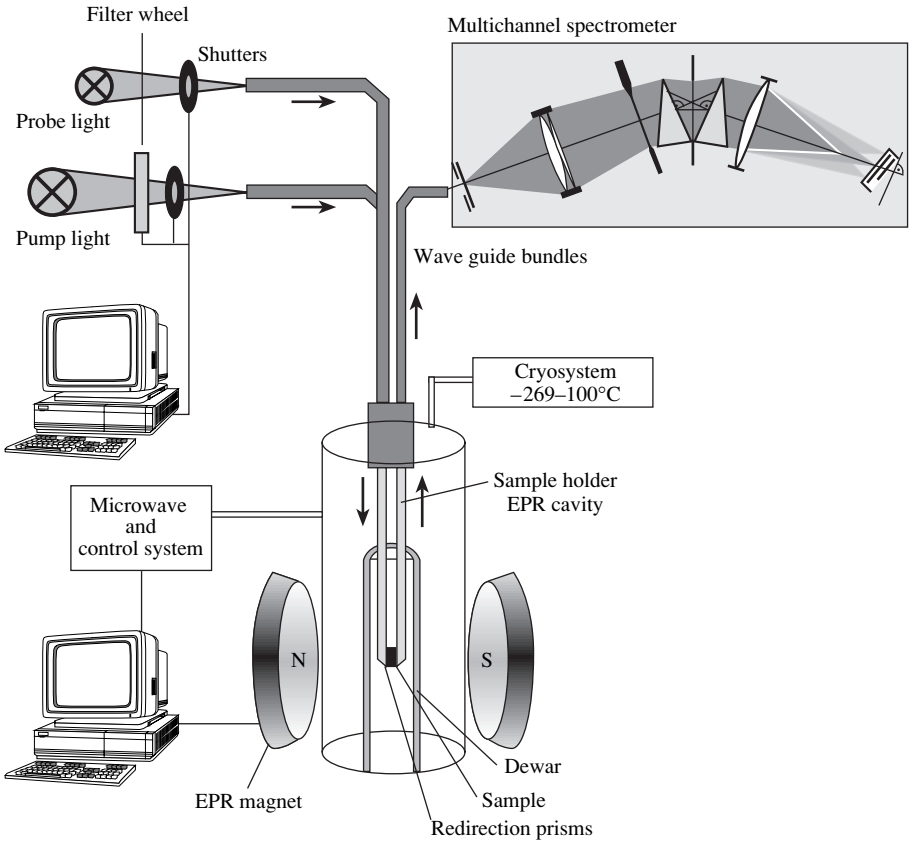

Fig. 2. Setup for combined EPR/optical absorption investigations of light-induced signal changes. The specimen, centered in the EPR cavity between two half-cylindrical quartz rods, is first illuminated by intense monochromatic pump light for typically 60 s; the resulting signal changes are then simultaneously probed by EPR and weak, 1–3 eV, 20 ms pulsed white probe light. The transmitted light, guided by prisms at the quartz rods, is dispersed and registered with a multichannel detector.

ing band, also rising essentially parallel to the decrease in Rh^{4+}, is seen to lie near 1.7 eV. This assignment of the Rh absorption bands is also supported by the fact that the higher valence, Rh^{5+}, has a lower absorption energy than Rh^{3+}. It takes less energy to excite a valence electron to a highly charged cation defect than to a lower charged one. The described primary charge transfer process and its secondary consequences comply with the 3-valence model (Fig. 1). One should note also that the EPR silent charge states Rh^{3+} and Rh^{5+} have become accessible through their optical fingerprints according to this consistent interpretation procedure.

From Fig. 3 it is furthermore seen that not all absorption changes can be attributed to Rh charge states. The presence of unintended Fe background impurities must also be considered. This can be based on previous work on this element in $BaTiO_3$ [4]. There, it was shown that Fe^{4+} is converted to Fe^{3+} near 2.6 eV. Fe^{5+} is recharged to Fe^{4+} near 2.3 eV. The charge transfer absorption of Fe^{3+} to Fe^{2+} peaks at energies higher than 3.5 eV [13] lying above the band edge of $BaTiO_3$, at about 3.2 eV, and thus lies outside of the graph in Fig. 3. The assignment of the features in Fig. 3 includes the Fe^{4+} and Fe^{5+} absorptions. It should be noted that Fig. 3 contains difference spectra; therefore, the extrema in this plot can occur at energies slightly different from those of the component bands.

If the pump energy is changed, other charge transfer transitions will be activated as primary processes. Accordingly, the difference spectra will be composed of varying combinations of the component bands. The graphs at the right side of Fig. 3 illustrate this. As an example, the consequences of the illumination at 2.4 eV are discussed. Here, a primary process involving the low-energy outskirts of the Fe^{4+} absorption, subtracted from the Rh^{3+} band near 3.0 eV, is dominant. Pumping with 2.4 eV thus reduces the tile concentration of Fe^{4+} present in the crystal from the beginning or created from Fe^{3+} by hole capture during the previous illumination with lower pump energies; the valence band holes are captured by Rh^{3+}, forming Rh^{4+}.

A diagram is also given which qualitatively explains the charge transfer processes triggered by 2.9 eV pump light. Here, the fundamental absorptions starts, creating holes which eventually increase the concentrations of the higher valences of Rh and Fe. In assessing the right side of Fig. 3, it must be considered that because of the Franck–Condon principle, optical and thermal levels

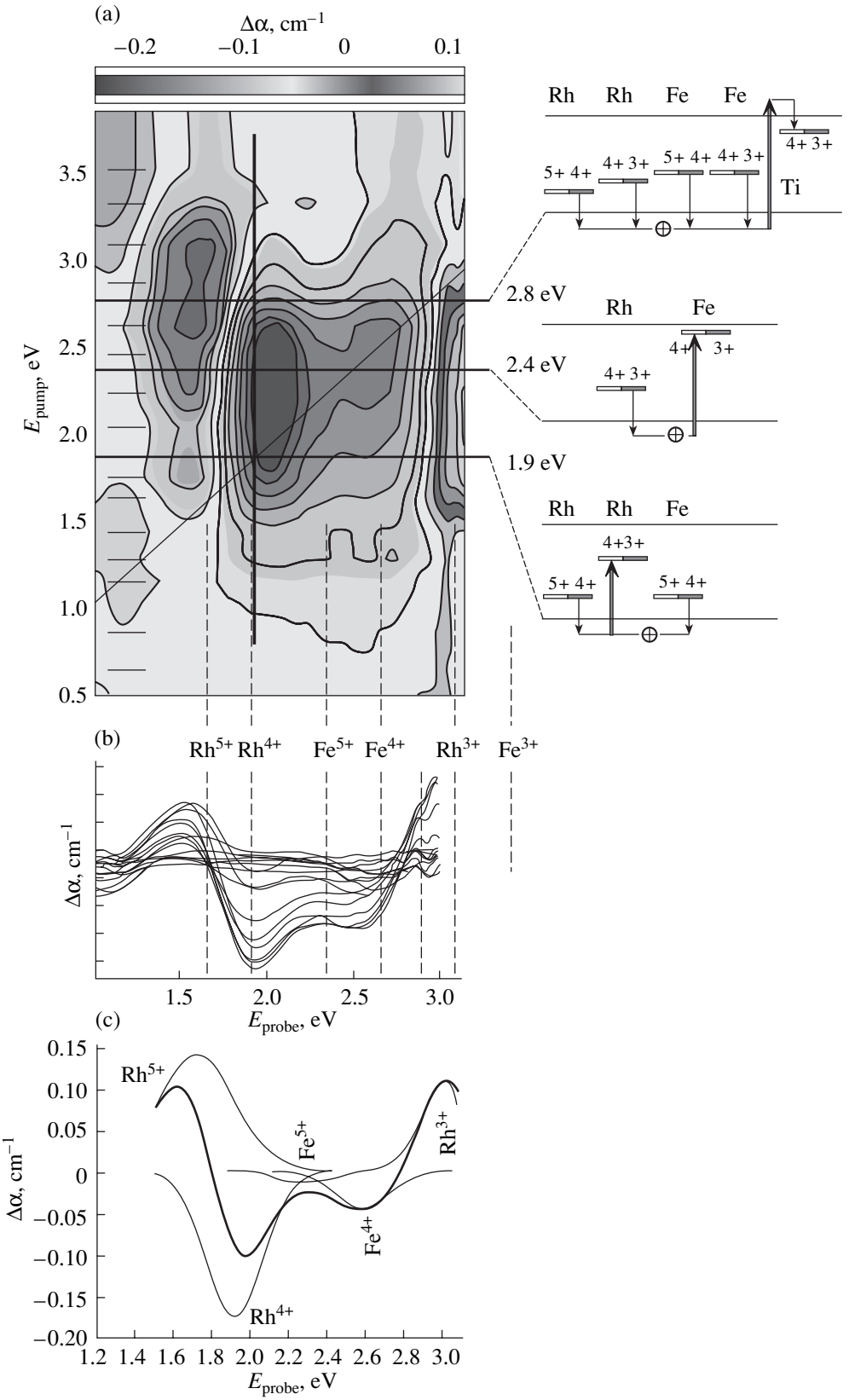

Fig. 3. (b) Optical absorption changes of $BaTiO_3$:Rh after illumination with 17 different pump energies, (a) same information plotted in a pseudo-3D plot. Abscissa: probe light energy. Ordinate: pump light energy. Grey shading: absorption changes, as calibrated by the bar on top. Assignment to the various charge states of Rh and Fe is indicated by the dashed lines. The thick vertical line is addressed in Fig. 4. An analysis of the plot into its component bands is shown in panel *c* (state after 1.9 eV pumping). The variation of the plot under different pumping energies is analyzed on the right using the appropriate level schemes.

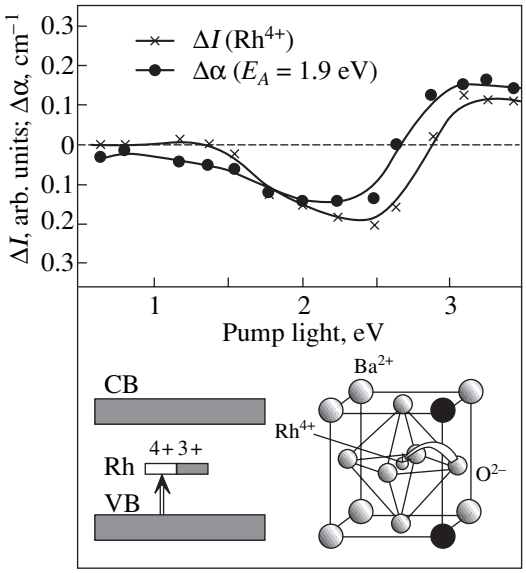

Fig. 4. Comparison of light-induced changes of the Rh^{4+} EPR-signal and the optical absorption along the vertical line in Fig. 3. A close correlation between both signals is seen. The optical absorption band at 1.9 eV can thus be attributed to the indicated transfer of valence electrons to Rh^{4+}, shown in two equivalent ways in the lower panel.

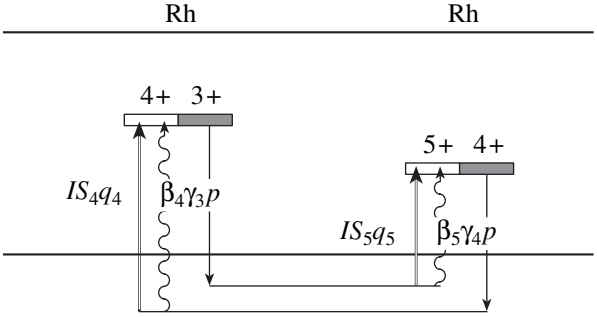

$$Rh^{3+} = (IS_4q_4 + \beta_4)\,Rh^{4+} - \gamma_3 p\,Rh^{3+}$$

$$Rh^{5+} = -(IS_5q_5 + \beta_5)\,Rh^{5+} + \gamma_4 p\,Rh^{4+}$$

$$Rh^{4+} = -Rh^{3+} - Rh^{5+}$$

Fig. 5. 3-Valence model together with the set of differential equations governing the recharging of the Rh levels following thermally (wavy arrows) and optically (double arrows) induced transfer processes. For simplicity, optical and thermal levels are not distinguished.

have to be distinguished: primary transfers excite valence electrons to optical levels, whereas recombination to the valence band starts from thermal levels.

3. QUANTITATIVE ANALYSIS

Assuming that all absorption bands represented by the features in Fig. 5 are caused by the five components Rh^{5+}, Rh^{4+}, Rh^{3+}, Fe^{5+} and Fe^{4+} and, for simplicity, assuming gaussian band shapes, the plot (Fig. 3) can be analyzed into the Rh^{i+} bands shown in Figs. 3c and 6. Since the optical absorption of a defect "*i*" is connected to its density N_i by $\alpha_i(E) = N_i S_i(E)$, the energy dependence of the absorption cross sections $S_i(E)$ is given by that of the component absorption bands in Fig. 6. If the respective defect concentrations N_i are known, the cross sections can be derived quantitatively.

In order to establish this quantitative calibration, the EPR signal of Rh^{4+}, for experimental reasons being given by the first derivative of the resonant microwave absorption, is integrated twice. This number, proportional to the amount of spins in the sample, is compared to the corresponding quantity of a known number of spins of a paramagnetic EPR standard. For this purpose, small single crystals of $CuSO_4 \cdot 5H_2O$ of defined weight were used. On this basis, the Rh^{4+} density in the material is determined [14].

Then, the change in the Rh^{4+} EPR signal under illumination with 1.9 eV light is compared to the correlated change in the Rh^{4+} optical absorption band. Since the decrease in the number of Rh^{4+} ions can be inferred from the previous EPR calibration, the procedure allows one to derive values of the absorption cross section of Rh^{4+}, as given in Fig. 6. Their energy dependence is given by the gaussian fit. Assuming, as an approximation, that the participation of the Fe charge states in Fig. 3 is only a minor effect, the validity of the 3-valence model can be taken as a basis for further arguments. Since in this model two Rh^{4+} ions are converted to Rh^{3+} and Rh^{5+}, respectively, the changes in the concentrations under illumination with 1.9 eV, inducing the Rh^{4+} primary charge transfer process, are $\Delta Rh^{5+} = \Delta Rh^{3+} = -1/2\Delta Rh^{4+}$. By comparing the concentration changes to those of the corresponding absorption bands in Fig. 3, the absorption cross section of Rh^{3+} and Rh^{5+} are derived. They are also given in Fig. 6.

With these quantities available, the concentrations of Rh^{3+}, Rh^{4+}, and Rh^{5+} present in the crystal before illumination can now be determined. From the total absorption of the crystal, one finds the values included in the table. One deduces a total Rh concentration $Rh_T = Rh^{3+} + Rh^{4+} + Rh^{5+}$ of about 40 ppm.

All the parameters governing the charge transfer processes connected with the 3-valence model, as applicable in the first approximation of BT:Rh, are comprised by the corresponding system of differential equations [2] displayed in Fig. 5. These rate equations describe the kinetics of the Rh charge states; the symbols have the following meanings ("*i*" indicating the Rh charge state species): Rh^{i+} is the density of the charge state; *I*, light intensity; S_i, absorption cross sections; q_i, probabilities that the charge state "*i*" is ionized

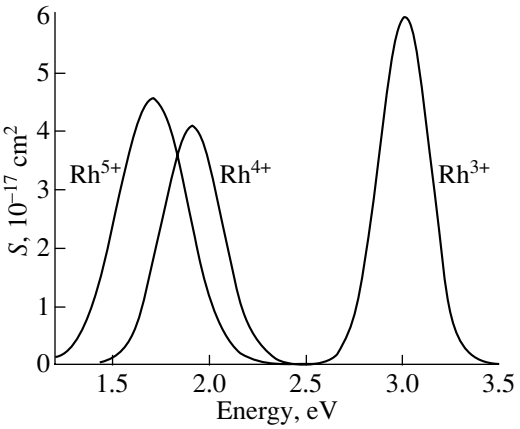

Fig. 6. Energy dependence of the optical absorption cross sections of the three Rh charge states involved.

after absorption; β_i, thermal ionization rates; γ_i, capture coefficients; and p, hole density in the valence band.

Figure 7 displays the corresponding changes of the defect densities induced by illumination with 12 mW/cm^2 HeNe light and their decay after the illumination has ended. It is surprising that at room temperature they do not return to the initial state in the latter situation. Apparently, this represents a metastable nonequilibrium situation caused by a slow back reaction in the dark. The mobility of holes thermally excited to the edge of the valence band is more impeded by potential fluctuations than the mobility of holes light-induced during the forward reaction. This argument is supported by the data taken at 50°C. Here, the changes relax to essentially zero because the hole mobility is increased at elevated temperatures even in the presence of potential fluctuations. Because the recombination processes are then also faster, the steady state amplitudes of the changes are smaller than at room temperature. However, it should be considered that the light-induced absorption changes shown in Fig. 7 amount to only about 1% of the initial Rh^{i+} concentrations. Neglecting this very small relative mismatch between the zero and steady-state values, the parameters listed in the table were identified by fitting the numerical solutions of the rate equations to the data. Analysis of the photorefractive properties of the investigated specimen is in progress. Comparison with present results will take place when the necessary data become available.

4. DISCUSSION

The basis of the presented method is the use of optical absorption bands as fingerprints of existing defects established by means of the available EPR information. As shown, EPR-silent lattice irregularities can also often be labelled and identified in this way. In this manner, the scope of defect studies is extended beyond that accessible to EPR measurements. The range of detectable defects is more than doubled because it is now possible to also verify the presence of the EPR-silent majority of defects. The method is applicable if the light-induced defect recharging leads to a photochromic situation. This is not a serious limitation, however. If not fulfilled at room temperature, this condition is usually valid at low temperatures where shallow traps tend to be populated by charge carriers after photoexcitation, while being empty at room temperature. From defect investigations under such conditions, one can then make an extrapolation to the behavior at room temperature, where photorefractive devices are expected to operate.

There have been previous studies of $BaTiO_3$:Rh in which the charge transfer parameters responsible for the photorefractive properties of the material were derived [9, 10]. The present investigation differs from these studies in two respects: (1) Previously, data from

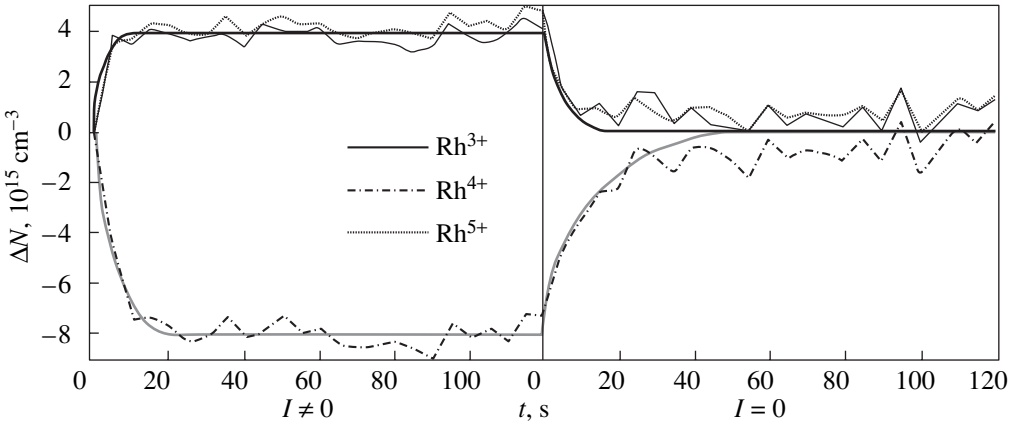

Fig. 7. Rise ($I \neq 0$) and decay ($I = 0$) of the light-induced changes of the Rh^{5+}, Rh^{4+}, and Rh^{3+} concentrations. The metastable deviation of the steady state under $I = 0$ from equilibrium, expected to be zero, is small (about 1%) compared to the uncharged background of Rh^{i+}. Therefore, this small deviation is neglected.

Parameters describing charge transfer processes in $BaTiO_3$ involving Rh charge states

Generally valid parameters		Parameters characteristic for the investigated crystal (initial Rh concentrations)	
q_4	0.5	Rh^{4+}	1.0×10^{17} cm^{-3}
q_5	0.5	Rh^{3+}	4.0×10^{17} cm^{-3}
β_4	9.3×10^{-2} s^{-1}	Rh^{5+}	0.5×10^{17} cm^{-3}
β_5	1.3 s^{-1}	Rh_T	5.5×10^{17} cm^{-3} (=40 ppm)
γ_3	1.4×10^{-12} cm^3/s		
γ_4	3.9×10^{-11} cm^3/s		
$S_i(E)$	See Fig. 6		

photorefractive measurements were used to derive, in a rather indirect way, the densities of the defect charge states involved. Our present treatment obtains these densities independently and can thus eventually check whether the photorefractive data are reproduced. (2) Based on the energy dependence of the defect-related optical cross sections, we can obtain quantitative information on the parameters of the light-induced charge transfer processes for a wide range of light energies. In each of the previous studies, the analysis was limited to one light energy only.

CONCLUSION

In conclusion, we have described a method by which the charge transfer processes occurring in doped insulating crystals can be analyzed with respect to the paths photoexcited charge carriers take between the defects involved. The method allows quantitative determination of the parameters governing such processes. It is entirely based on the EPR information on the defects. Eventually, this could lead to a prediction of the sensitivity of doped photorefractive materials.

REFERENCES

1. *Photorefractive Effects and Materials*, Ed. by P. Günter and J.-P. Huignard (Springer, Berlin, 1988), Top. Appl. Phys. 61.
2. K. Buse, Appl. Phys. B **64**, 273 (1997); **64**, 391 (1997).
3. O. F. Schirmer, H.-J. Reyher, and M. Wöhlecke, in *Insulating Materials for Optoelectronics*, Ed. by F. Agulló-López (World Scientific, Singapore, 1995).
4. O. F. Schirmer, M. Meyer, A. Rüdiger, *et al.*, Opt. Mater. (in press).
5. O. F. Schirmer, in *Defects and Surface-Induced Effects in Advanced Perovskites*, Ed. by G. Borstel, A. Krumins, and D. Millers (Kluwer, Dordrecht, 2000), p. 75.
6. G. W. Ross, P. Hribek, R. W. Eason, *et al.*, Opt. Commun. **11**, 60 (1993).
7. B. A. Wechsler, M. B. Klein, C. C. Nelson, and R. N. Schwartz, Opt. Lett., 536 (1994).
8. M. Kaczmarek and R. W. Eason, Opt. Lett., 1850 (1995).
9. N. Huot, J. M. C. Jonathan, and G. Roosen, Appl. Phys. B **65**, 489 (1997).
10. L. Corner, R. Ramos-Garcia, A. Petris, and M. J. Damzen, Opt. Commun. **143**, 168 (1997).
11. H. Kröse, R. Scharfschwerdt, A. Mazur, and O. F. Schirmer, Appl. Phys. B **67**, 79 (1998).
12. E. Possenriede, P. Jacobs, H. Kröse, and O. F. Schirmer, J. Phys.: Condens. Matter **4**, 4719 (1992).
13. H. J. Reyher, N. Hausfeld, and M. Pape, J. Phys.: Condens. Matter **12**, 10599 (2000).
14. J. A. Weil, J. R. Bolton, and J. E. Wertz, *Electron Paramagnetic Resonance: Elementary Theory and Practical Applications* (Wiley, New York, 1994), p. 498.

Physics of the Solid State, Vol. 44, No. 8, 2002, pp. 1433–1439. From Fizika Tverdogo Tela, Vol. 44, No. 8, 2002, pp. 1374–1379.

PROCEEDINGS OF THE XI FEOFILOV WORKSHOP "SPECTROSCOPY OF CRYSTALS ACTIVATED BY RARE-EARTH AND TRANSITION-METAL IONS"

(Kazan, Tatarstan, Russia, September 24–28, 2001)

Structure and Charge Transfer Dynamics of Uranyl Ions in Boron Oxide and Borosilicate Glasses[1]

G. K. Liu*, H. Z. Zhuang*, J. V. Beitz*, C. W. Williams*, and V. S. Vikhnin**

** Chemistry Division, Argonne National Laboratory, Argonne, IL 60439, USA*

*** Ioffe Physicotechnical Institute, Russian Academy of Sciences, Politekhnicheskaya ul. 26, St. Petersburg, 194021 Russia*

e-mail: gkliu@anl.gov

Abstract—Laser spectroscopic experiments, molecular dynamics simulation, and charge transfer-lattice interaction modeling have been conducted for studying the electronic and structural properties of the uranyl ion UO_2^{2+} in boron oxide and borosilicate glasses. The charge transfer electronic and vibrational energy levels for uranyl ions in the glass matrices were obtained from laser excitation and fluorescence spectra of UO_2^{2+}. A model structure for uranyl ions in the glass matrices was established using the method of molecular dynamics (MD) simulation in comparison with the results of extended x-ray absorption fine structure (EXAFS) for U^{6+} ions in the glasses we studied. The formation and stabilization of uranyl clusters in glass matrices are interpreted in terms of charge transfer-lattice interactions on the basis of self-consistent charge transfer accompanied by lattice distortion. The latter is in the framework of the simultaneous action of pseudo-Jahn–Teller and pseudo-Jahn–Teller analog effects on charge transfers between oxygen and uranium ions. © *2002 MAIK "Nauka/Interperiodica".*

From uranium to americium, the lighter elements in the actinide series often bind with two oxygen anions to form actinyl ions. The uranyl ion, UO_2^{2+}, is extraordinarily stable in solutions as well as in crystals and glasses. Under blue or shorter wavelength light illumination, it emits visible fluorescence in the region of 500 to 700 nm. The fluorescence and spectral properties of uranyl in canary glass have been studied since the 19th century. After extensive and systematic investigation of actinyl properties began in the middle of the last century, many current studies of the spectroscopic properties of actinyl species have sought primarily to interpret their electronic structure and bonding and eventually to provide a fundamental understanding of the chemical and mechanical properties of nuclear waste-related phases.

Since Jørgensen's initial work in 1957 [1] and subsequent studies by others [2–4], it has been well understood that optical absorption and emission in the uranyl ion are due to oxygen-to-uranium charge transfer excitations. A significant contribution to uranium-related impurity center studies was made by Feofilov and coauthors [5, 6]. The optical transitions are due to electronic excitation primarily from the 2*p* state of the ligands to the 5*f* state of the uranium ion. The intense vibronic features and absence of zero-phonon lines in the optical transitions indicate that the charge transfer transition is strongly coupled to lattice vibrational modes. Therefore, the uranyl optical transitions indirectly probe the properties of local structure. Depending on the host materials, the lowest excited charge transfer state of UO_2^{2+} is on the order from 19000 to 21000 cm^{-1} and the vibrational energy of the O–U–O symmetric stretch mode is typically 750 to 900 cm^{-1} for its ground state and much lower in its excited states. The lowering of vibrational energy in the excited uranyl states suggests strong structure distortion induced by charge transfer-lattice interaction [7, 8]. Strong charge transfer-lattice interaction also results in large, different equilibrium positions of the uranyl potential that prevent the observation of zero-phonon transitions and change the lifetime of the uranyl fluorescence.

It is also well known that vibronic states originating from the charge transfer-lattice interaction are quite localized. As a result, the absorption and emission spectra of the UO_2^{2+} ion in single crystals such as $Cs_2UO_4Cl_4$ indeed exhibit extremely sharp lines [9]. At low temperature, optical lines are as narrow as ~1 cm^{-1}; as a result, energy levels of various vibrational modes and even the isotopic shift resulting from substitution of oxygen-18 for exygen-16 are clearly observable [10]. However, due to structural disorder in amorphous environments, inhomogeneous line broadening is often significant and obscures the spectral structure of vibronic transitions. The inhomogeneous line broadening,

[1] This article was submitted by the authors in English.

which often can be partially eliminated using selective laser excitation [11], provides "fingerprint" information about the uranyl local structure. Namely, one expects to observe sharp lines in the absorption and emission spectra of uranyl ions in crystalline phases [9], where the charge transfer transitions can be so broad that the characteristic vibronic features become obscured for uranyl ions in amorphous phases. It has been realized that lanthanide and actinide ions in oxide glasses, such as borosilicate glass, have an ordered local structure [11, 12]. This means that an *f*-element ion has a definite coordination number and bond distance with its first shell ligands, although there is no long-range order in the glass matrix.

Although the electronic properties of uranyl itself and its bonding in crystalline phases have been extensively studied [4], there is still a lack of knowledge on its bonding property in glasses. In the present paper, we report the results of experimental investigation and theoretical modeling of uranyl coordination in boron oxide and borosilicate glasses. It is shown that the uranyl ions have a well-defined local structure that includes four additional oxygen ions in its equatorial plane to form a UO_6 tetrahedral cluster in the glass matrix. A model structure of uranyl in boron oxide and borosilicate glasses is established using a molecular dynamics (MD) simulation method. The symmetry and stability of the uranyl cluster are interpreted based on the microscopic mechanisms of charge transfer-lattice interaction.

1. EXPERIMENTAL RESULTS AND DISCUSSION

Samples of boron oxide (B_2O_3) and borosilicate (12%B_2O_3, 63%SiO_2, 20%Na_2O, 5%Al_2O_3, by weight) glass containing 0.1 and 1% (weight) uranium were prepared for this work. After the host glasses were made, a nitric acid solution of natural isotopic abundance uranium as uranyl was added to the ground glass and the mixture was melted in a furnace by heating up to 1000°C for the boron oxide glass and 1600°C for the borosilicate glass before quenching to room temperature. Laser excitation and fluorescence spectra and fluorescence decay were recorded for the samples with 0.1 and 1% (by weight) uranium at room temperature and liquid helium temperature.

As shown in Fig. 1 for 0.1% UO_2 in the boron oxide glass, the fluorescence spectrum consists of 5 sharp bands from 20278 to 16722 cm^{-1} that are due to vibronic transitions from the excited state to the ground state of the uranyl charge transfer configuration. Figure 1 also includes a section of the excitation spectrum that shows the lowest two groups of excited states, one centered at 21030 cm^{-1} and another at 21570 cm^{-1}. No zero-phonon line was observed in the fluorescence spectrum. The spectrum is remarkably sharp and little inhomogeneous line broadening due to structure disorder was observed. No significant differences were registered between the spectra of the 0.1 and 1% uranyl samples. Uranyl ions in samples of different concentration have the same line width and positions. The results shown in Fig. 1 suggest that UO_2^{2+} in the B_2O_3 glass matrix has a well-defined local environment This means that the uranyl ions have the same coordination number and local crystalline lattice and that disorder in the first shell of ligands is insignificant.

The lifetime of the uranyl ion in the lowest excited state is longer than 1 ms, which is extremely long in comparison with the microsecond scale of fluorescence decay dynamics for many other uranyl compounds. As shown in Fig. 2, the fluorescence decay curves of uranyl in the B_2O_3 glass are nonexponential immediately following the laser pulse due to the energy transfer and

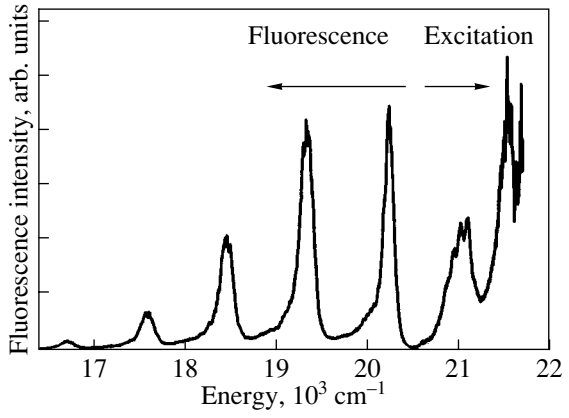

Fig. 1. Ambient temperature excitation and fluorescence spectra of uranyl in B_2O_3 glass that contained 0.1% uranium.

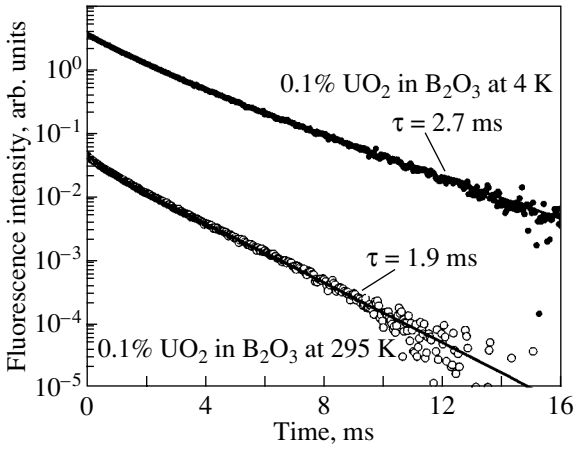

Fig. 2. Fluorescence decay of uranyl in boron oxide glass.

approach a single exponential decay time of 2.7 ms at 4 K and 1.9 ms at room temperature. The single exponential decay suggests that most uranyl ions have similar local environments in the sample we studied. The uranyl fluorescence decay in the boron oxide glass decay curves is not sensitive to temperature from ambient temperature to 4 K. The initial decay rate at room temperature is slightly larger than that at low temperatures. Without considering this faster decay at short times, the decay curves are not sensitive either to temperature or uranium concentration. This result indicates that the two most common relaxation mechanisms, namely, phonon relaxation and energy transfer between uranyle ions, are not strong in the samples we studied. Without much contribution from these two relaxation mechanisms, the millisecond-scale lifetime of uranyl in the lowest excited state confirms that the charge transfer state is metastable and the recombination process with electronic relaxation to the ground states is extremely slow. This will be discussed later with regard to the mechanisms of charge transfer-lattice interaction.

As expected for uranyl ions in the borosilicate glass, the lines of the fluorescence spectrum are much broader than those in the boron oxide glass. Figure 3 (curve *1*) shows the fluorescence spectrum recorded at 4 K and with laser excitation at 28170 cm^{-1}. It is apparent that uranyl ions have a common local structure in which they have different electronic energy levels and vibronic energies than in the B_2O_3 glass. It is also clearly shown in Fig. 3 (curves *2*, *3*) that selective excitation at lower laser energies resulted in fluorescence line narrowing and distinguished four different types of uranyl species that evidently arc due to UO_2 at different local environments. These site-resolved spectra are shifted from each other by approximately 200 cm^{-1} and have similar vibronic peaks that are separated by 750 to 760 cm^{-1}. In comparison with the broad spectrum obtained with 28170 cm^{-1} excitation, the strongest set of peaks in Fig. 3 (curve *2*) is attributed to uranyl ions surrounded by SiO_2, the major constituent of the glass compositions. The other three groups of lines of weaker intensity likely arise from uranyl ions that are coordinated with the other three constituents of the glass, namely, Na_2O, Ba_2O_3, and Al_2O_3. One also anticipates that in borosilicate glass a uranyl ion may be coordinated with more than one type of these four metal oxides; more possibly, there will be present a different type of metal oxide near the uranyl cluster that is coordinated with one type of the metal oxides in its first shell. The mixture of the surrounding metal oxides is expected to shift the uranyl electronic energy levels. In the spectra obtained from our sample, only four sets of spectra can be identified, although emission line shifting was observed when the laser excitation energy was varied. We believe that the line shifting, indicative of inhomogeneous line broadening, is largely due to the mixtures of different metal oxides in the surrounding environment of uranyl ions.

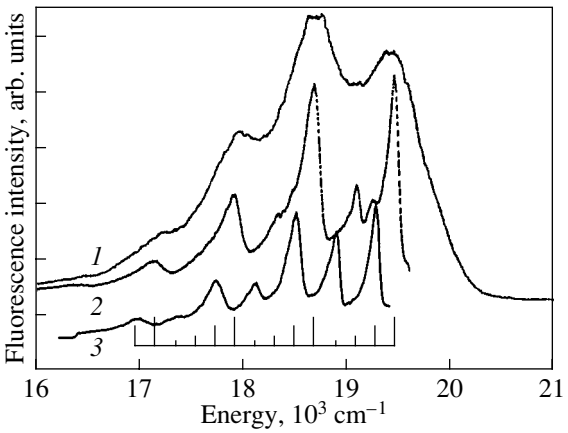

Fig. 3. Fluorescence spectra of uranyl in borosilicate glass that contained 0.1% uranium with laser excitation at (*1*) 28169, (*2*) 19806, and (*3*) 19550 cm^{-1}. All spectra were recorded at 4 K.

It should be pointed out that in contrast to our selective laser excitation spectra revealing four types of different uranyl sites plus significant inhomogeneous line broadening on each set of the site-resolved spectra, the EXAFS data [13, 14] suggest that only one type of uranyl cluster exists in the same borosilicate glass. This is presumably because the EXAFS is not capable of resulting in site selective spectra and has a sensitivity much less than that of laser-induced fluorescence detection; as a result, minor sites were not resolved in the EXAFS spectrum. Given that the three sets of laser-detect uranyl sites indeed have much weaker intensity in comparison with the major site shown in Fig. 3 (curves *1*, *2*), these results can be interpreted consistently with the assumption that in the borosilicate glass most of the uranyl ions coordinate with four SiO_2 tetrahedra in their equatorial plane. This means that a uranyl ion tends to bond with SiO_2 and excludes other metal oxides in the formation of a uranyl tetrahedral cluster. This hypothesis was verified in MD simulation.

2. MOLECULAR DYNAMICS SIMULATION

It is generally believed that there is no long-range order in glasses, even though short-range structural order is common. This usually means that the structure order is limited to a metal ion and its nearest neighbor ligands. In B_2O_3 glass, for example, the BO_3^{3-} cluster in the form of a plane triangle is the basic unit of the disordered glass matrix. The present results show that for uranium in the glasses that we studied, not only is the linear structure of the uranyl ion well defined and stable, but also structure ordering extends to the next nearest neighbors to from a larger crystalline cluster. At present, EXAFS and laser spectroscopic experiments provide the best experimental techniques for resolving the structure of uranyl clusters diluted in glasses in

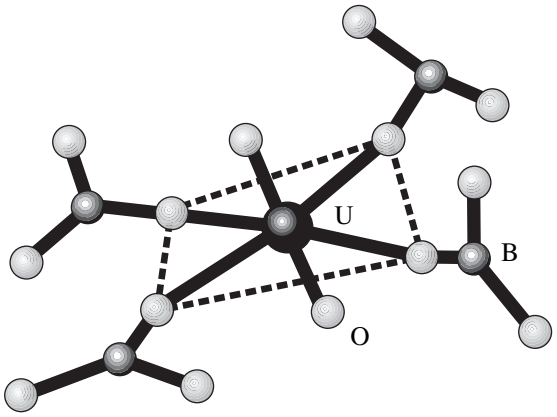

Fig. 4. Model structure of uranyl cluster in B_2O_3 glass established using a molecular dynamics simulation.

detail. The structure and vibrational spectrum of uranyl in vitreous glass have been studied using a MD simulation method [15–17].

Our MD calculations utilize the Born–Mayer–Huggins and Coulomb pair potentials and the Stillinger–Weber three-body potential [18]. We simulated two systems, UO_2–B_2O_3 and UO_2–(70 mol %)SiO_2(30 mol %)B_2O_3. The first system contained 2124 atoms including four U^{6+} ions, and the second contained 3000 atoms including nine U^{6+} ions. For the procedure of MD simulation, an effective charge of –2 is assigned to each axial oxygen ion in the uranyl ions and –1.5 to the other four oxygen ions located as the nearest ligands of the uranium. The same structure configuration was always obtained in our MD simulations regardless of initial conditions as long as the emulated system underwent virtual quenching from the initial temperature at 6000 to 1000°C and then from 1000°C to room temperature in 10^5 time steps (0.5 fs/step). Partial random distribution functions (RDFs) of ion pair distances were calculated from the MD model systems for structure identification and comparison with EXAFS experiments [13, 14].

From the simulated glass systems, we can visualize the exact atomic structure in which a uranyl is centered. Figure 4 shows the cluster structure of uranyl in the B_2O_3 glass matrix. In addition to the six oxygen ions that are directly coordinated with the core uranium ion, we see four boron ions in connection with additional oxygen ions in the form of four BO_3 triangles. The BO_3 triangle units that are bonded with the uranyl are slightly bent and twisted, which is understood because these BO_3 groups are connected with other such groups that are randomly oriented in the glass matrix. The B–O bond length of the four BO_3 groups in the uranyl cluster varies from 0.132 to 0.153 nm, in comparison with 0.136–0.138 nm for the intrinsic B–O bond. It is always the case that the two axial oxygen ions are not actively bonded with any boron (or Si) ions in the glass matrix. In agreement with this observation, calculations of molecular bonding using quantum theory also suggest that no stable bonding can be established on the top of an actinyl ion along its axis [19]. The model structure is based, of course, on the agreement between the EXAFS data and the calculated RDF for the uranium ion and its ligands and the agreement between the simulated glass matrices and that previously established by Raman and neutron scattering techniques. The calculated ion pair distances are listed in the table in comparison with those obtained from EXAFS [14] and *ab initio* calculations [20]. The model structure is also supported by comparison between the vibrational energies measured in the laser spectra and those calculated for the simulated system of uranyl in B_2O_3 glass [21].

3. THE MECHANISM OF CHARGE TRANSFER-LATTICE INTERACTION

While our MD simulations provide a model structure for uranyl clusters in boron oxide and borosilicate glasses that is in excellent agreement with experimental observation, one of the main purposes of the present work is to construct a theoretical model of charge transfer-lattice interaction that would help to explain the formation of uranyl clusters in glass environments. The basic consideration is to take into account ionic-covalent bonding between the six oxygen ions, as well as between uranium and oxygen ions, both with charge transfer-lattice interaction in the UO_6 cluster (see Fig. 5). The mechanism of charge transfer-lattice interaction can be realized based on the following phenomena being simultaneously active.

The first phenomenon is a self-consistent charge transfer-lattice distortion. There are three actual channels of charge transfer in the UO_6 cluster, namely, oxy-

Pair distances between U and its ligands in various uranyl phases (pm)

Ion pair	$UO_2B_2O_3$ MD/EXAFS [14]	$UO_2SiO_2^*$ MD/EXAFS [14]	$UO_2(NO_3)(H_2O)_2$ [20]	$UO_2(SO_4)(H_2O)_2$ [20]
$U–O_{ax}$	176/180	182/182	174	180
$U–O_{eq}$	248/249	222/223	249	264
U–B (Si, N, S)	340/335	367/	304	308

* Borosilicate glass studied in this work.

gen 2*p*–oxygen 2*p* charge transfer (q_1) between the six active oxygen ions, oxygen 2*p*, 2*s*–uranium 6*p* (q_2), and oxygen 2*p*–uranium 5*f* (q_3) charge transfers. Such charge transfers are self-consistent with the local lattice displacements. The latter is due to the vibronic-type charge transfer-lattice interaction proposed recently in the framework of consideration of the problem of charge transfer vibronic excitons (CTVE) [7, 8]. The CTVE is an electronic polaron–hole polaron correlated pair with strong vibronic interaction of polaronic origin [7]. Namely, the small polaron nature of the electronic and hole states of CTVE is responsible for the high strength of the vibronic interaction in the case of the uranyl cluster.

The important peculiarity of CTVE in the uranyl system is the charge transfer being between the same type of active ions. This is mainly due to the possible strong equilibrium charge transfer between different oxygen ions within the degenerated states, which significantly reduces the quadratic increasing of cluster energy with charge transfer and, hence, produces rather soft conditions for the CTVE formation even in the ground charge transfer state.

The oxygen 2*p*(2*s*)–uranium 6*p* charge transfer should also be considered. It induces additional strengthening of the CTVE effect in the cluster under discussion. The pseudo-Jahn–Teller type mechanism of such charge transfer presumably exists in the present case. The equilibrium charge transfer in the oxygen–uranium channel becomes important when taking into account the simultaneous action of the charge transfer analog of the pseudo-Jahn–Teller effect (PJTE) and PJTE on the active tetragonal distortion of the cluster. Both types of PJTE are realized in the framework of the oxygen 2*p*, 2*s*–uranium 6*p* states mixing. Moreover, this type of charge transfer is responsible for the effective indirect and two step mechanism of the oxygen 2*p*–oxygen 2*p* charge transfer resulting from the oxygen 2*p*–uranium 6*p*–oxygen 2*p* charge transfer via the intermediate uranium 6*p* state.

Last but not least, the classical [1–4] oxygen 2*p*–uranium 5*f* charge transfer also plays an important role in the uranyl formation. Here, the PJTE mechanism of charge transfer also has an actual contribution. Again the equilibrium charge transfer becomes significant when taking into account the simultaneous action of the charge transfer analog of the PJTE width oxygen 2*p*–uranium 5*f* states mixing, as well as PJTE, on structure-distortion with the same active electronic states. The strong local displacements of oxygen ions that were detected in the experiments on the uranyl cluster need very definite conditions for charge transfer-lattice interaction even in the frame of the CTVE-model. This situation takes place within the second phenomenon mentioned above. Namely, there is an increase in the ionicity of the two active oxygen ions of UO_2^{2+} due to the charge transfer under consideration (tending to O^{2-} final states where the ionic radius is decreased). Correspondingly, a decrease in the Born–Mayer repulsion radius with increasing ionicity will lead to significant softening of the quasi-local vibration for these two oxygen ions. The latter induces local configurational instability (LCI) caused by the charge transfer-lattice interaction under discussion. Such LCI is accompanied by strong equilibrium tetragonal lattice distortion for the UO_6 cluster in the glass matrix (with displacements of two axial oxygen ions toward each other). Therefore, the microscopic nature of the above-mentioned charge transfer-lattice interaction (the direct influence of charge transfer on the local vibrational dynamics of active ions) explains the uncommonly strong increase in vibronic interaction with charge transfer. It is important to underline that this CTVE-effect is mainly formed by the competition between the cluster energy increasing due to oxygen–oxygen charge transfer and cluster energy decreasing due to lattice distortion as a result of LCI.

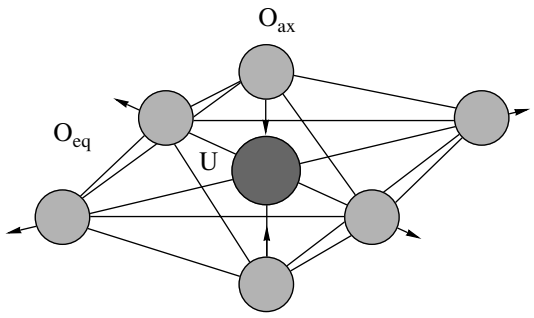

Fig. 5. Charge transfer channels and vibronic distortion in the UO_6 cluster that contains uranyl. The lines indicate charge transfer channels, and the arrows indicate distortion modes.

The uranyl ground state structure can be treated as an oxygen-related CTVE-pair trapped by the central U^{6+} ion. The tetragonal structure of such a CTVE-pair leads to a cluster energy minimum due to Coulomb repulsion between two electronic polarons (two oxygen ions with increased negative charges and a correspondingly high ionicity). Another origin of the geometry with tetragonal symmetry for the UO_6 cluster is connected with the specific hybridization of the states in the framework of PJTE. The role of the central U^{6+} ion is essential in the construction of the uranyl structure. Because of significant U–O state overlapping, the indirect mechanism of O(1)–O(2) effective charge transfer between two different oxygen ions via successive O(1)–U and U–O(2) channels of state mixing becomes important. The latter strongly decreases the electronic part of the cluster energy, which is characterized by enhancement in the charge transfer. As a result, the energy of the localized CTVE-pair of O–O type decreases due to softening of the corresponding CTVE-pair trapping by the U^{6+} ion.

It should be stressed that there is another important source of the U^{6+} ion influence on the uranyl structure and properties. This is the PJTE due to the mixing of the 6*p*–5*f* uranium ion states induced by linear vibronic interaction with active tetragonal distortion of the cluster coordinate. This PJTE-mechanism of the 6*p*-5*f* states mixing accompanied by an equilibrium distortion can explain the linear geometry of the uranyl structure. It should be also pointed out that the importance of the 6*p*–5*f* hybridization for the stability of linear geometry was discussed for the uranyl ion in the review article [4]. We have proposed here the microscopic mechanism of such a phenomenon. The CTVE-effect under discussion can be described in the framework of a semiphenomenological approach. The latter is based on the cluster potential expansion into powers of active variables. It corresponds to the strong PJTE case and to the two successive adiabatic approximations within the hierarchy of the characteristic rates of active subsystems. Namely, the latter hierarchy is realized within the interactive "very fast" subsystem of electronic degrees of freedom of ionic states, the "intermediately fast" subsystem of charge transfer degrees of freedom, and the "slow" subsystem of quasi-local vibrations of the ionic cluster under consideration. A solution for the problem can be found from analysis of the successive potential energy minimization in accordance with the subsystem hierarchy mentioned above. The intermediate adiabatic potential of a UO_6 cluster embedded in the matrix of B_2O_3 (or SiO_2) contains the leading charge transfer-lattice interaction and depends on three types of charge transfer variables $\{q_1, q_2, q_3\}$, as well as on the slow vibration variable x. We obtain the adiabatic potential for the slow subsystem after minimization of the intermediate potential on the $\{q_1, q_2, q_3\}$ variables. Its expansion in powers of x-displacements can be presented in the usual form but with coefficients strongly renormalized by charge transfer:

$$U = D(x)^2 + \beta(x)^4 + \gamma(x)^6 + \ldots. \quad (1)$$

Here, two different types of solutions are realized. Namely, in the case of $D < 0$, $\beta > 0$ (LCI of the second order), we have to deal with equilibrium cluster distortion accompanied by the corresponding equilibrium charge transfer, both induced by leading vibration instability. This is the case of CTVE trapped to the ground state. In contrast to this case, in the situation of $D > 0$, but with $\beta < 0$, $\gamma > 0$, a pure CTVE-type solution is realized (with equilibrium charge transfer in the corresponding anharmonic excited state of the system). Both solutions are possible depending on the parameter values. However, the first case is adequate to the real situation for uranyl ions. Strong vibronic charge transfer-lattice interaction is responsible here for a sufficiently strong equilibrium charge transfer and cluster distortion within the LCI phenomenon. The model proposed in the present work is in agreement with EXAFS and MD simulation and can explain the stability of the uranyl cluster on the basis of uncommonly high CTVE-pair lattice distortion. In addition, the long lifetime of the uranyl fluorescence also finds explanation in vibronic reduction appearing in the framework of the recombination process with electronic transition between states with strongly different equilibrium positions of cluster ions. The latter results from strong lattice distortion in the framework of the CTVE-effect.

Thus, we have investigated experimentally and theoretically the formation of a locally ordered structure of uranyl ions in B_2O_3 glass and borosilicate glass. Our experimental results show an ordered local structure in which a UO_2^{2+} ion is coordinated with its surrounding ligands, consisting of four BO_3 triangles in the case of boron oxide glass and SiO_4 tetrahedra in the borosilicate glass. Our MD simulations reproduced the EXAFS results and demonstrated that a U^{6+} ion in vitreous B_2O_3 and SiO_2 matrices has a strong capacity to form a crystalline-like, ordered UO_6 cluster, which consists of a linear uranyl ion with an additional four oxygen ions in its equatorial plane in a tetragonal symmetry. This crystalline-like cluster is very stable in the glass matrix, although the U–O distances vary (depending on the O-B (or O-Si) bonding strength). It is also observed that in the borosilicate glass, uranyl primarily coordinates with four metal oxide ligand units of the same type, mainly four SiO_4 tetrahedra. The model of charge transfer-lattice interaction explains the stability of the uranyl cluster on the basis of uncommonly high CTVE-pair lattice distortion. In the framework of this theoretical model, charge transfer channels in the uranyl ion (UO_2) and a larger cluster (UO_6) are considered to be important in the formation of a crystalline-like cluster. The predicted structural and electronic properties for the uranyl cluster are in agreement with the spectroscopic experiments and MD simulation. In addition, the long lifetime of the uranyl fluorescence is also explained based on the vibronic reduction of the recombination process in the electronic transitions between states with strongly differing equilibrium positions of cluster ions.

ACKNOWLEDGMENTS

Work performed at the Argonne National Laboratory was supported by the US DOE Office of Basic Energy Science, Division of Chemical Sciences, and by DOE EMSP Programs, under contract no. N W-31-109-ENG-38. One of the authors (V.S.V.) was supported in Germany and Russia by the German DAAD and RFBR programs (no. 00-02-16875) and by NATO (PST. CLG, 977348).

REFERENCES

1. C. K. Jørgensen, Acta Chem. Scand. **11**, 166 (1957).
2. C. Gorller-Walrand and L. G. van Quikenborne, J. Chem. Phys. **54**, 4178 (1971).

3. C. K. Jørgensen and R. Reisfeld, Chem. Phys. Lett. **35**, 441 (1975).
4. R. G. Denning, in *Complexes, Clusters, and Crystal Chemistry* (Springer, Berlin, 1992), Structure and Bonding, Vol. 79, p. 215.
5. L. M. Belyaev, G. F. Dobrzhanskii, and P. P. Feofilov, Izv. Akad. Nauk SSSR, Ser. Fiz. **25** (4), 548 (1961).
6. P. P. Feofilov and A. A. Kaplyanskii, Usp. Fiz. Nauk **76** (2), 201 (1962) [Sov. Phys. Usp. **5**, 79 (1962)].
7. V. S. Vikhnin, Ferroelectrics **199**, 25 (1997); Z. Phys. Chem. **201**, 201 (1997); Ferroelectr. Lett. **25**, 27 (1999).
8. V. S. Vikhnin, H. Liu, W. Jia, and S. Kapphan, J. Lumin. **83–84**, 91 (1999).
9. R. G. Denning, T. R. Snellgrove, and D. R. Woodwark, Mol. Phys. **30**, 1819 (1976).
10. R. G. Denning, C. N. Ironside, J. R. G. Thorne, and D. R. Woodwark, Mol. Phys. **44**, 209 (1981).
11. G. K. Liu, V. V. Zhorin, M. R. Antonio, *et al.*, J. Chem. Phys. **112**, 1489 (2000).
12. M. R. Antoio, L. Soderholm, and A. J. G. Ellison, J. Alloy Compd. **250**, 536 (1997).
13. B. W. Veal, J. N. Mundy, and D. J. Lam, in *Handbook on the Physics and Chemistry of Actinides*, Ed. by A. J. Freeman and G. H. Lander (North-Holland, Amsterdam, 1987), p. 271.
14. G. K. Liu, H. Z. Zhuang, M. R. Antoio, and L. Soderholm, to be published.
15. D. Frenkel and B. Smith, *Understanding Molecular Simulation* (Academic, New York, 1996).
16. D. J. Evans and G. P. Morris, Comput. Phys. Rep. **1**, 297 (1984).
17. D. C. Rapaport, *The Art of Molecular Dynamics Simulation* (Cambridge Univ. Press, Cambridge, 1995).
18. F. H. Stillinger and T. A. Weber, Phys. Rev. B **31**, 5262 (1985).
19. J.-P. Blaudeau, private communication.
20. J. S. Craw, M. A. Vincent, I. H. Hiller, and A. L. Wallwork, J. Phys. Chem. **99**, 10181 (1995).
21. H. Z. Zhuang and G. K. Liu, to be published.

Physics of the Solid State, Vol. 44, No. 8, 2002, pp. 1440–1444. From Fizika Tverdogo Tela, Vol. 44, No. 8, 2002, pp. 1380–1384.

PROCEEDINGS OF THE XI FEOFILOV WORKSHOP "SPECTROSCOPY OF CRYSTALS ACTIVATED BY RARE-EARTH AND TRANSITION-METAL IONS"

(Kazan, Tatarstan, Russia, September 24–28, 2001)

Charge Transfer Bands in the Eu^{3+} Luminescence Excitation Spectra of Isomeric Europium Pyridine-Dicarboxylates[1]

L. N. Puntus*, V. F. Zolin*, V. A. Kudryashova*, V. I. Tsaryuk*, J. Legendziewicz, P. Gawryszewska**, and R. Szostak****

** Institute of Radio Engineering and Electronics, Russian Academy of Sciences, pl. Vvedenskogo 1, Fryazino, Moscow oblast, 141120 Russia*

e-mail: art225@ire216.msk.su

*** Faculty of Chemistry, University of Wrocław, F. Joliot-Curie Str. 14, Wrocław, 50-383 Poland*

Abstract—A ligand–cation charge transfer band was observed in the region of 360–400 nm in the Eu^{3+} luminescence excitation spectrum of europium 3,4-pyridine-dicarboxylates, but was absent in the spectra of europium 2,6- and 2,3-pyridine-dicarboxylates. This band is due to noticeable energy transfer through a charge-transfer state formed owing to the high polarizability of the ligand in the former compound. Energy transfer through the excited ligand–lanthanide charge-transfer state can explain the well-known effect of luminescence quenching by redox-sensitive lanthanide ions. *© 2002 MAIK "Nauka/Interperiodica".*

1. INTRODUCTION

Studies of the intra- and intermolecular charge and energy transfer in organometallic complexes [1, 2] lead to the opinion that hydrogen bonds and proton transfer [3, 4] play a prominent role in these processes. Among systems of this kind are photosynthetic aggregates, which are oxidation–reduction enzymes of mitochondria and calcium-binding proteins such as cod parvalbumin. Quenching of luminescence of the tryptophan residue was observed in the latter protein when calcium ions were substituted by europium or ytterbium ions with a low redox potential [1]. Quantitative investigations of energy transfer processes in cryptates and related systems have been reported, and the role of the charge transfer (CT) states has been analyzed [5, 6]. In this work, the energy transfer to coordinated europium ions was studied in three isomeric [7] europium pyridine-dicarboxylates (H_2PDA). We report on the dependence of the intensity and position of the ligand–europium CT band in the luminescence excitation spectra of europium 2,6-, 2,3-, or 3,4-pyridine-dicarboxylates (salts of dipicolinic, quinolinic, and cinchomeronic acids) on the structure of the isomeric pyridine-dicarboxylic ligands, which influences the intramolecular CT and the polarizability and zwitter-ionic properties of the ligands [7, 8]. Manifestation of the ligand–europium CT band in the luminescence excitation spectra of the salts investigated is equivalent to a demonstration of energy transfer to the redox-sensitive lanthanide cations (Eu^{2+}/Eu^{3+}, Yb^{2+}/Yb^{3+}) or to the ligand luminescence quenching by these cations.

[1] This article was submitted by the authors in English.

2. EXPERIMENTAL

The lanthanide salts of dipicolinic, quinolinic, and cinchomeronic acids [dipic, quin, and cinch, respectively (H_2PDA)] were obtained from water solutions of the corresponding acids and lanthanide oxide, hydroxide, or chloride. In the case of dipicolinic and cinchomeronic acids, the ligand–metal molar relation was 3 to 1 and the mixed solution was brought to a neutral pH value by introducing alkali hydroxide. In this way, we obtained binary salts $M_3Ln(PDA)_3 \cdot nH_2O$ (with M = Li, Na, K, Cs), $HLn(quin)_2 \cdot 3H_2O$, and $Na_3Nd(dipic)_3 \cdot nH_2O$ (with Ln = Eu, Tb) for salts of dipicolinic, quinolinic, and cinchomeronic acids, respectively. Samples of the salts of quinolinic and dipicolinic acids are photosensitive and change in color from white to light blue with time. In the case of dipicolinic salts, the samples can loose a part of the water molecules in storage and the water content can decrease from 14 to about 4–5. We also prepared sodium salts of the PDA, $Na_2PDA \cdot nH_2O$. We did not determine the water content in the sodium salts.

The luminescence, luminescence excitation, and absorption spectra of compounds were measured on an SLM Aminco SPF-500 spectrofluorimeter and DFS-12 and SPECORD UV–VIS spectrometers at 300 and 77 K. Raman spectra were recorded at 300 K with a Nicolet FT Raman module attached to a Nicolet Magna 860 FTIR spectrometer. IR absorption spectra of mulls in Nujol and hexachlorobutadiene were measured on a UR-20 spectrophotometer at 300 K.

1063-7834/02/4408-1440$22.00 © 2002 MAIK "Nauka/Interperiodica"

3. RESULTS AND DISCUSSION

The data on the structure of $Na_3Nd(dipic)_3 \cdot nH_2O$ with $n = 14$ are presented in [9]. Three-dentate $dipic^{2-}$ anions form a three-capped trigonal prism, which is the coordination polyhedron of Nd^{3+}; the coordination number of this cation is nine. The structure and spectroscopy of some of the europium dipicolinic salts were also presented in [10–14]. The luminescence spectra of the europium pyridine-dicarboxylates synthesized by us are presented in Fig. 1. Judging by the relative intensities of lines in the Eu^{3+} spectra, the site symmetry of the Eu^{3+} ions seems to be the same in the dipicolinic and cinchomeronic salts and is lower in the case of the quinolinic salt. In the latter case, an appreciable value of the overall Stark splitting of the $^7F_1$ level and relatively high intensity of the zero-phonon line of the $^5D_0$–$^7F_0$ transition are observed.

In the luminescence spectra recorded with high resolution, we observed a number of vibronic bands: (1) low-frequency satellites of the $^5D_0$–$^7F_0$ line with Stokes shifts roughly equal to 80–180 cm^{-1} attributed to metal–ligand vibrations (region of 585–590 nm); (2) a band related to the C–C stretching vibration in the region of 605–610 nm; the Stokes shift for this band is 835 cm^{-1} for $Na_3Eu(dipic)_3 \cdot 14H_2O$, 850 cm^{-1} for $HEu(quin)_2 \cdot 3H_2O$, and 845 cm^{-1} for $Na_3Eu(cinch)_3 \cdot 10H_2O$; and (3) Stokes satellites of the $^5D_0$–$^7F_0$ line in the region of 630–640 nm and of the $^5D_0$–$^7F_2$ line in the region of 670–685 nm. These last satellites correspond to symmetric and antisymmetric stretching vibrations of carboxyl groups, and their Stokes shifts lie in the region of 1390–1660 cm^{-1}. Judging by the relative intensities of the vibronic bands in the spectra of the various europium salts, the electron–phonon interaction is the strongest in the case of the dipicolinic salt; this interaction is somewhat weaker in the quinolinic salt and is 4–5 times weaker in the cinchomeronic salt.

The luminescence excitation spectra of the samples of sodium–europium and sodium–terbium pyridine-dicarboxylates in glass ampules are shown in Figs. 2–4. The europium spectra are normalized by the $^7F_0$–$^5D_1$ magnetic dipole transition intensity. All the excitation spectra of the terbium salts studied are alike (curves *b*

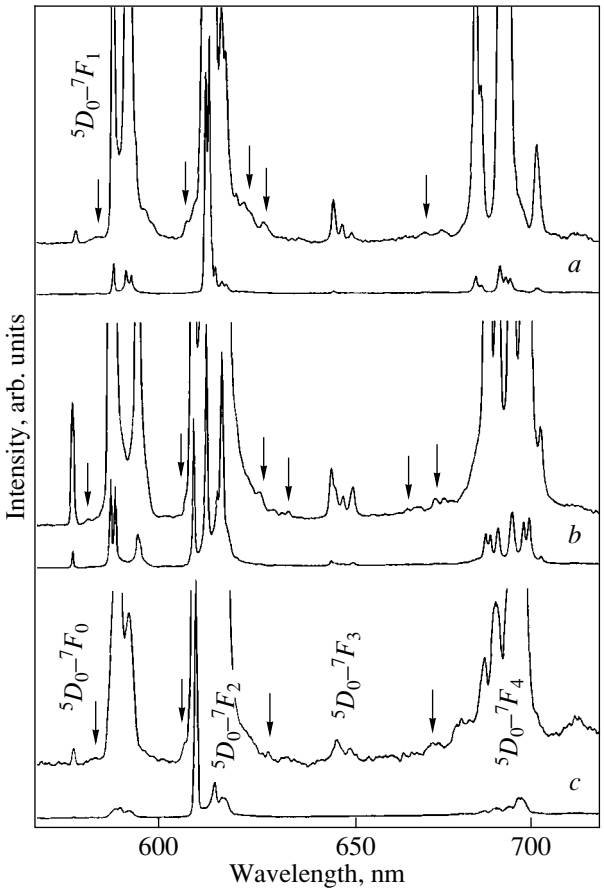

Fig. 1. Luminescence spectra of (*a*) $Na_3Eu(dipic)_3 \cdot 14H_2O$, (*b*) $HEu(quin)_2 \cdot 3H_2O$, and (*c*) $Na_3Eu(cinch)_3 \cdot 10H_2O$ at 77 K. Arrows mark the most intense vibronic bands.

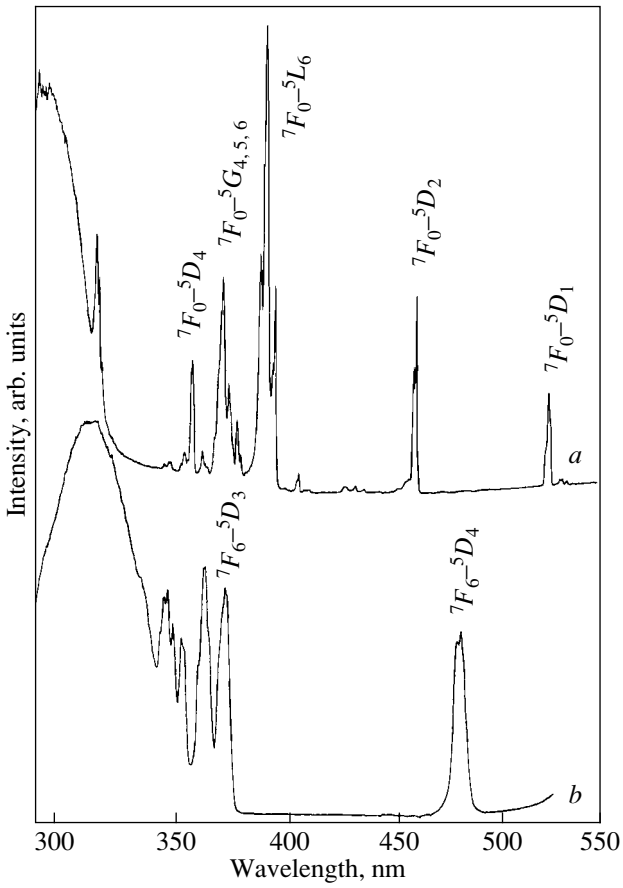

Fig. 2. Luminescence excitation spectra of (*a*) $Na_3Eu(dipic)_3 \cdot 14H_2O$ and (*b*) $HTb(quin)_2 \cdot 3H_2O$ at 77 K.

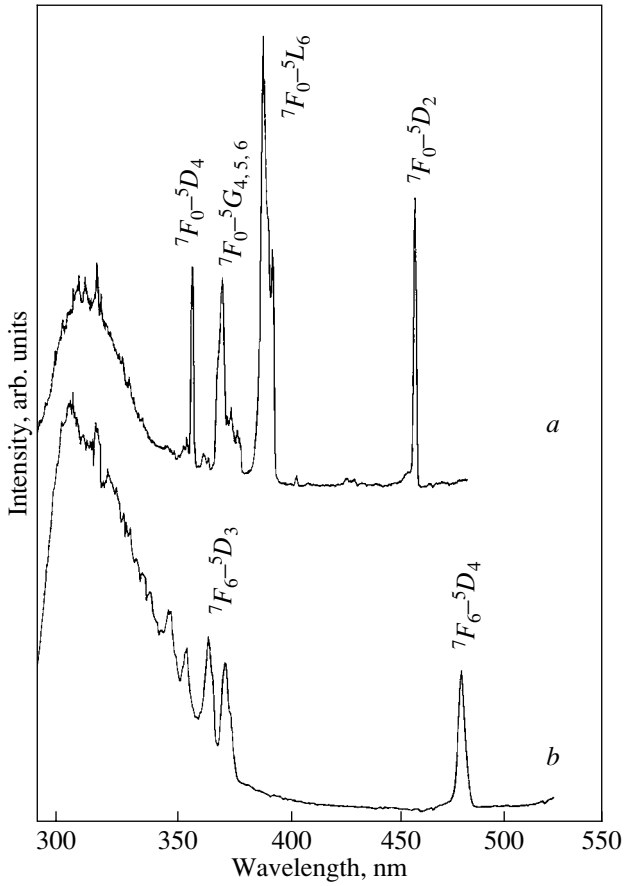

Fig. 3. Luminescence excitation spectra of (*a*) $HEu(quin)_2 \cdot 3H_2O$ and (*b*) $Na_3Tb(cinch)_3 \cdot 10H_2O$ at 77 K.

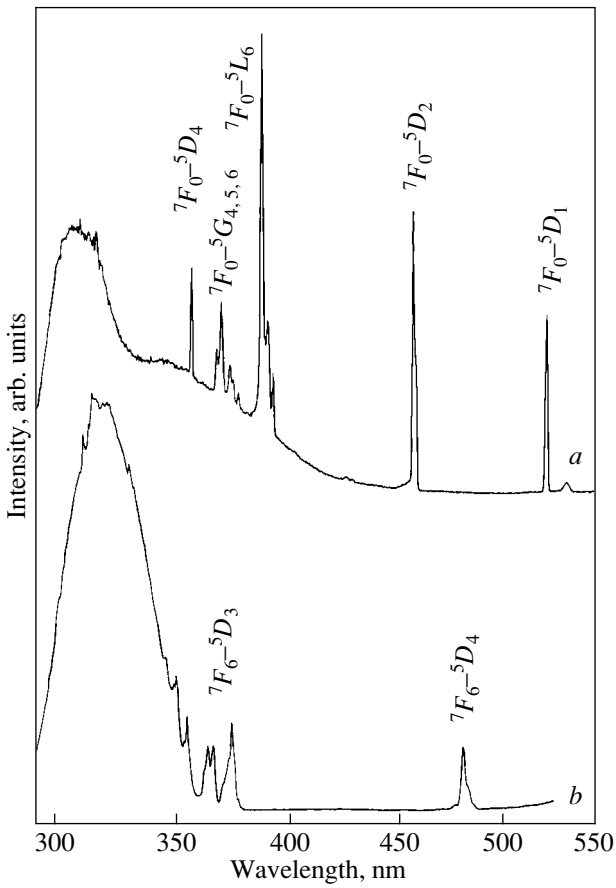

Fig. 4. Luminescence excitation spectra of (*a*) $Na_3Eu(cinch)_3 \cdot 10H_2O$ and (*b*) $Na_3Tb(dipic)_3 \cdot 10H_2O$ at 77 K.

in Figs. 2–4). These spectra have a wide high-frequency band formed by overlapping bands of ligand absorption and of Tb^{3+} *f–d* transitions and also have sharp Tb^{3+} *f–f* lines. The sloping low-frequency edge of the wide band ends somewhere between 370 and 375 nm. A band observed in the region of 350–410 nm of the europium excitation spectrum of $Na_3Eu(cinch)_3 \cdot 10H_2O$ (Fig. 4, curve *a*) corresponds to a ligand–Eu^{3+} CT state, because this band is absent in the spectrum of the corresponding sodium–terbium salt. Earlier, the same CT band was observed in absorption spectra of other europium salts and complexes [8, 15–18]. Emission from the CT states of ytterbium compounds was discussed in [19]. The ligand–lanthanide CT states and their influence on the spectra of the lanthanide ions have been discussed in many papers, in particular, in [20–23]. The energy of the CT state can depend on the ligand optical electronegativities [24] and on the structure of complexes of these ligands [25]. The influence of a CT state on the europium emission is conditioned both by the position of the minimum and by the form of the potential-energy curve for the CT state [26, 27].

To understand the origin of the low-frequency ligand–europium CT band in spectra of the cinchomeronic salt, we analyzed the vibration spectra of the salts investigated.

Raman spectra of sodium and sodium–terbium salts of dipicolinic, quinolinic, and cinchomeronic acids are presented in Fig. 5. As the spectra of europium and terbium salts are almost the same, only the latter are shown in Fig. 5. The effective cross section of the Raman scattering by water molecules [28] in the region of 200–1800 cm^{-1} is substantially smaller than that of the pyridine derivatives. This can be demonstrated by comparing the Raman spectra with IR absorption spectra, where the bands of vibrations of water molecules are much stronger.

The Raman spectra of the salts investigated provide data on the coordination and polarizability of the ligands which can be obtained from the intensity distribution, position, shifts, and the structure of the Raman bands. We assigned the bands in the region 770–900 cm^{-1} to the δ(C–H) out-of-plane and δ(C–C) stretching vibrations; in the region of 1010–1070 cm^{-1}, to the breathing vibration mode of the heterocyclic

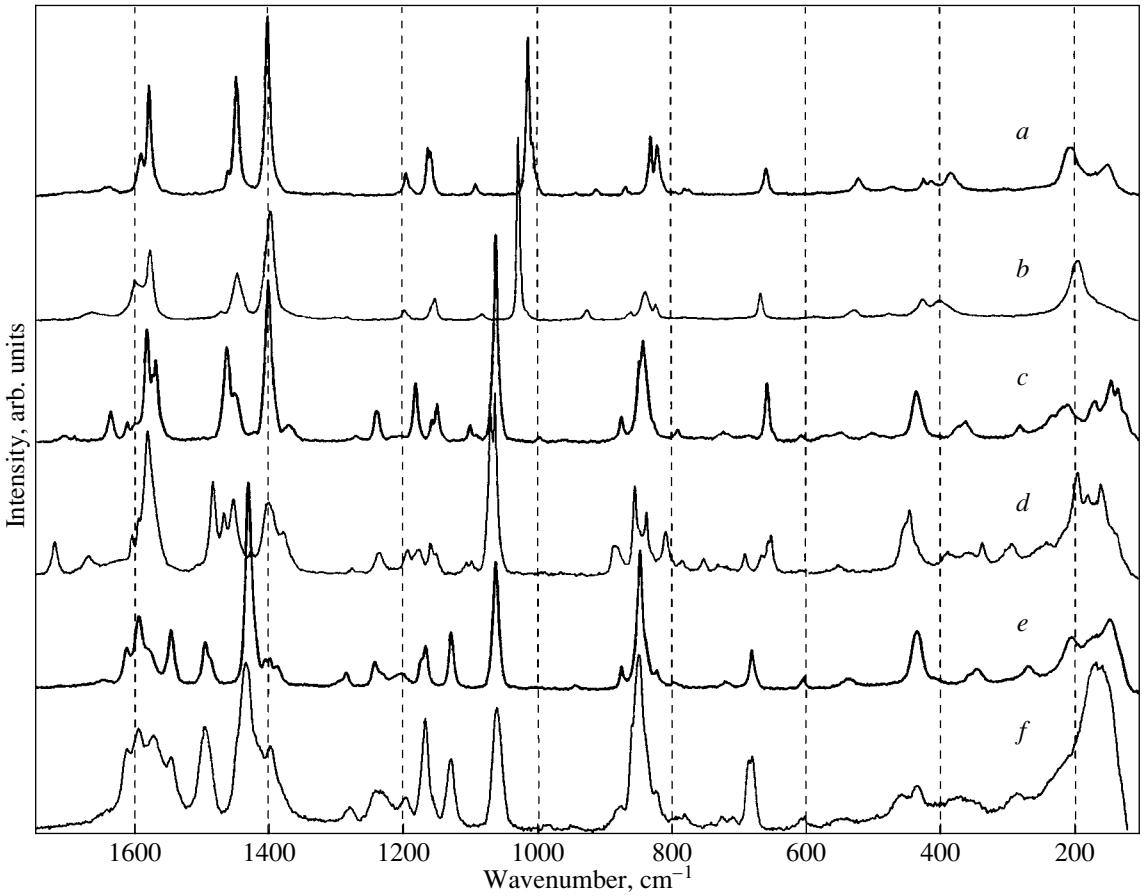

Fig. 5. Raman spectra of (*a*) $Na_2(dipic) \cdot nH_2O$, (*b*) $Na_3Tb(dipic)_3 \cdot 14H_2O$, (*c*) $Na_2(quin) \cdot nH_2O$, (*d*) $HTb(quin)_2 \cdot 3H_2O$, (*e*) $Na_2(cinch) \cdot nH_2O$, and (*f*) $Na_3Tb(cinch)_3 \cdot 10H_2O$ at 300 K.

ring; and the bands in the region of 1370–1630 cm^{-1}, to the ν(C=C) and ν(C=N) [with the participation of δ(C–H)] in-plane vibrations and to ν(COO^-) stretching vibrations. The most intense lines in the Raman spectra of dipicolinic salts are attributed to the breathing vibration mode of a heterocyclic ring and to symmetric stretching vibrations ν(COO^-). In the spectra of the cinchomeronic salts, the most intense are the lines of the carboxyl symmetric stretching vibration modes.

Peculiarities of coordination of the carboxyl groups by a metal ion can be obtained by analyzing the positions of the ν(COO^-) bands. The value of the splitting of the ν(COO^-) stretching vibration mode correlates with the oxygen effective charges and with the degree of polarization and polarizability of these anions. By using the Raman and IR spectra to determine the frequencies of the symmetric (Raman) and antisymmetric (IR) stretching vibration modes, we found out that the value of the splitting of ν(COO^-) exceeds 200 cm^{-1} in the case of dipicolinic and quinolinic salts and is minimum (smaller than 170 cm^{-1}) for cinchomeronic salts.

Judging from the x-ray diffraction data [9], as well as from the Raman and IR spectra, the ligands in the dipicolinic salts are tridentate coordinated and equivalent. The ligands have monodentate coordinated carboxyl groups (as indicated by the large value of the splitting of the ν(COO^-) stretching vibration modes) and a coordinated nitrogen atom [as indicated by the high-frequency shift of the breathing vibration band of the heterocyclic ring [29] in the Raman spectra of the sodium–lanthanide salts (Fig. 5, curve *b*) in comparison to that of the sodium salt (Fig. 5, curve *a*)]. The ligands in the cinchomeronic salts also seem to be equivalent (Fig. 5, curve *f*), but the role played by the carboxyl groups is different from that in the dipicolinic salts (bidentate-cyclic or bidentate-bridging instead of monodentate coordinated carboxyl groups) and the coordination of the nitrogen atoms is absent (fourdentate coordinated ligands). In the case of the quinolinic salts (Fig. 5, curve *d*) the ligands are inequivalent due to the presence of a proton. The proton probably participates in the hydrogen bond between one of the carboxyl groups and the nitrogen atom (as indicated by the doublet structure of the breathing vibration band in the spectra of the sodium–lanthanide salts). The increase in the relative intensities of the Raman lines in the regions of 845 and 1430 cm^{-1} seems to indicate an increase in

the polarizability of ligands in the cinchomeronic salts. This can be explained by the influence of the relative positions of the ring heteroatom and of the carboxyls as substituents on the polarizability and intramolecular CT [7].

The increase in the polarizability of the ligands, which is maximal in the case of the cinchomeronic salts, promotes the ligand–europium CT. The contribution from the ligand-to-Eu^{3+} CT band to the luminescence excitation spectra of Eu^{3+} reflects an increase in the efficiency of the energy transfer to the redox-sensitive lanthanide ions through the excited ligand–cation CT state. This may be related to the luminescence quenching of the tryptophan residue in the cod parvalbumin by redox-sensitive europium and ytterbium ions [1]. This luminescence quenching and the energy transfer may be conditioned by the high probabilities of the energy transfer from the ligand to the CT state and from this state to the cation due to delocalization of the CT state and to the high oscillator strength of the corresponding electric dipole transitions (the probability of radiative transitions from the CT state is roughly 10^7 s^{-1} [19]).

4. CONCLUSION

Sensitization of europium luminescence through the ligand–europium charge transfer state has been observed in the spectra of the sodium–europium salt of cinchomeronic acid. This sensitization was assigned to the increased efficiency of the energy transfer to the redox-sensitive lanthanide ions through the excited ligand–cation charge transfer state.

ACKNOWLEDGMENTS

The work was supported by the Russian Foundation for Basic Research (project no. 01-02-16837), the Russian Federal Program on Laser Physics (project no. 08.01.099 ph), and the Polish State Committee for Scientific Research.

REFERENCES

1. R. M. Supkowski, J. P. Bolender, W. D. Smith, *et al.*, Coord. Chem. Rev. **185–186**, 307 (1999).
2. M. C. Ghosh, J. W. Reed, R. N. Bose, and E. S. Gould, Inorg. Chem. **33**, 73 (1994).
3. M. Neumann, M. Johnson, L. von Laue, and H. P. Trommsdorff, J. Lumin. **66–67**, 146 (1996).
4. G. Zundel, in *Advances in Chemical Physics*, Ed. by I. Prigogine and S. A. Rice (Wiley, New York, 2000), Vol. III, p. 1.
5. L. Prodi, M. Maestri, V. Balzani, *et al.*, Chem. Phys. Lett. **180**, 45 (1991).
6. P. Gawryszewska, L. Jerzykiewicsz, M. Pietraszkiewicz, *et al.*, Inorg. Chem. **39**, 5365 (2000).
7. N. L. Glinka, *General Chemistry* (Khimiya, Leningrad, 1985).
8. B. L. Davydov, L. D. Derkacheva, V. V. Lunina, *et al.*, Pis'ma Zh. Éksp. Teor. Fiz. **12**, 24 (1970) [JETP Lett. **12**, 16 (1970)].
9. S. Petoud, J.-C. G. Bunzli, Th. Glanzman, *et al.*, J. Lumin. **82**, 69 (1999).
10. A. Mondry and P. Starynowicz, J. Alloys Compd. **225**, 367 (1995).
11. D. H. Metcalf, S. W. Snyder, J. H. Demas, and F. S. Richardson, J. Am. Chem. Soc. **112**, 5691 (1990).
12. D. H. Metcalf, J. M. M. Stewart, S. W. Snyder, *et al.*, Inorg. Chem. **31**, 2445 (1992).
13. D. H. Metcalf, S. W. Snyder, J. N. Demas, and F. S. Richardson, J. Am. Chem. Soc. **112**, 469 (1990).
14. J.-G. Kim, S. K. Yoon, and J.-G. Kang, Bull. Korean Chem. Soc. **17**, 854 (1996).
15. J.-G. Kim, S. K. Yoon, Y. Sohn, and J.-G. Kang, J. Alloys Compd. **274**, 1 (1998).
16. J. C. Barnes, J. Chem. Soc., 3880 (1964).
17. V. L. Ermolaev, N. A. Kazanskaya, A. A. Petrov, and Yu. A. Kheruze, Opt. Spektrosk. **28**, 113 (1970).
18. G. D. R. Napier, J. D. Neilson, and T. M. Shepherd, Chem. Phys. Lett. **31**, 328 (1975).
19. L. S. Villata, E. Wolcan, M. R. Feliz, and A. L. Capparelli, J. Phys. Chem. A **103**, 5661 (1999).
20. L. van Pieterson, M. Heeroma, E. de Heer, and A. Meijerink, J. Lumin. **91**, 177 (2000).
21. L. S. Gaigerova, O. F. Dudnik, V. F. Zolin, and V. A. Kudryashova, in *Luminescence of Crystals, Molecules, and Solutions*, Ed. by F. Williams (Plenum, New York, 1973), p. 514.
22. D. Hommel and J. Langer, J. Lumin. **18–19**, 281 (1979).
23. I. Gerard, J. C. Krupa, E. Simoni, and P. Martin, J. Alloys Compd. **207–208**, 120 (1994).
24. E. Huskowska, J. Legendziewicz, and P. Drożdżewski, Acta Phys. Pol. A **90**, 447 (1996).
25. J. D. Ryan and C. K. Jørgensen, J. Phys. Chem. **70**, 2845 (1966).
26. J. Legendziewicz, G. Oczko, and B. Keller, Bull. Acad. Pol. Sci. **34** (5–6), 257 (1986).
27. C. W. Struck and W. H. Fonger, J. Lumin. **1–2**, 456 (1970).
28. G. Blasse, Mater. Chem. Phys. **31**, 3 (1992).
29. M. H. Brooker, G. Hancock, R. C. Rice, and J. Shapter, J. Raman Spectrosc. **20**, 683 (1989).
30. S. P. Sinha, Z. Naturforsch. A **20**, 835 (1965).

Physics of the Solid State, Vol. 44, No. 8, 2002, pp. 1445–1449. Translated from Fizika Tverdogo Tela, Vol. 44, No. 8, 2002, pp. 1385–1389.

PROCEEDINGS OF THE XI FEOFILOV WORKSHOP "SPECTROSCOPY OF CRYSTALS ACTIVATED BY RARE-EARTH AND TRANSITION-METAL IONS"

(Kazan, Tatarstan, Russia, September 24–28, 2001)

Photoluminescence and Tunneling Charge Transfer in $CaF_2 : RE^{2+}$–CdF_2 Superlattices on Si(111)

S. V. Gastev*, S. É. Ivanova, N. S. Sokolov*, S. M. Suturin*, and E. M. Langer*****

** Ioffe Physicotechnical Institute, Russian Academy of Sciences, ul. Politekhnicheskaya 26, St. Petersburg, 194021 Russia*
e-mail: gastev@fl.ioffe.rssi.ru

*** Institute of Physics, St. Petersburg State University, ul. Pervogo Maya, Petrodvorets, 199034 Russia*

**** Institute of Physics, Polish Academy of Sciences, Warsaw, 02-668 Poland*

Abstract—The nonstationary behavior of Eu^{2+} and Sm^{2+} photoluminescence in continuously optically pumped CaF_2:RE^{2+}–CdF_2superlattices was considered. The transient character of the photoluminescence is due to spontaneous electron tunneling from the excited 4*f*5*d* states into the conduction band of the adjacent CdF_2 layer. Coupled balance equations were constructed and numerically analyzed. It is shown that photoionization energies of the 4*f*5*d* states can be derived from the experimentally measured variation of the photoluminescence intensity in superlattices with CaF_2 and CdF_2 layers 10 to 20 monolayers thick. © *2002 MAIK "Nauka/Interperiodica".*

1. INTRODUCTION

Charge transfer between rare-earth ions occurring in photochemical reactions in solids has been attracting the attention of researchers for many years; it will suffice to cite the pioneering studies of Feofilov [1] and Welber [2], as well as some recent publications [3, 4]. In bulk crystals, this transfer occurs primarily in the course of photoexcitation of carriers into the conduction band of the crystal matrix, followed by their capture by traps.

Charge transfer plays a noticeable part in various fluoride-based nanostructures. At the X Feofilov symposium, the first observations of the transient behavior of the Sm^{2+} and Eu^{2+} luminescence in heterostructures with fluoride layers were reported [5] and a possible connection between this effect and charge transfer processes was discussed. The tunneling mechanism of electron transfer from the $4f^6 5d$ excited state of Eu^{2+} ions present in the CaF_2 layers of CaF_2:Eu–CdF_2 superlattices through the CaF_2/CdF_2 interface into the conduction band of the adjacent CdF_2layers was demonstrated to play an important part [6]. This effect was studied in superlattices (SL) with selectively europium-doped layers [7]. Later, a similar effect was observed in CaF_2:Sm–CdF_2 superlattices [8]. The photochemical reaction initiated by optical excitation in such structures can be written as $RE^{2+} + h\nu = RE^{3+}$ + a conduction-band electron in the CaF_2 layer, where RE = Eu or Sm. Spontaneous tunneling of electrons through the interface turns out to be possible because of the SL energy bands [9] and the rare-earth ion levels being arranged in a specific way (Fig. 1). Tunneling reduces the number of rare-earth ions in the divalent state; this is what accounts for the falloff of the RE^{2+} photoluminescence (PL) intensity under stationary pumping with photon energies less than the RE^{2+} optical ionization energy in CaF_2. Thus, CaF_2:RE–CdF_2 superlattices offer a unique possibility of experimental optical investigation of the essentially quantum effect of under-barrier spontaneous electron tunneling. Based on an analysis of our earlier studies [5–8], we present here a more general mathematical description of the physical model of the effect and make a qualitative comparison of the calculations with available experimental data.

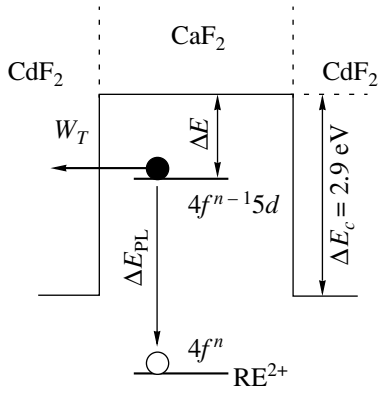

Fig. 1. Energy diagram of the SL conduction bands and CaF_2–CdF_2 interfaces.

1063-7834/02/4408-1445$22.00 © 2002 MAIK "Nauka/Interperiodica"

2. EXPERIMENTAL RESULTS AND THE PHYSICAL MODEL OF THE EFFECT

Earlier [5–8], we studied the evolution of the Eu^{2+} and Sm^{2+} luminescence intensity in CaF_2:RE–CdF_2 superlattices under stationary optical pumping. The thickness of the RE-doped fluoride layer d_{CaF_2} was 10–60 monolayers (ML) (3–19 nm). SLs with equal thickness of the CaF_2 and CdF_2 layers adding up to a total thickness of 100–350 nm were molecular-beam epitaxy (MBE) grown [10], and their structural characteristics were studied by high-resolution x-ray diffractometry [11].

Stationary optical excitation of such SLs revealed a substantial decrease in the RE^{2+} luminescence intensity with increasing sample exposure. Figure 2 shows the evolution of the Eu^{2+} luminescence intensity in CaF_2:Eu^{2+}–CdF_2 superlattices [7]. In SLs with d_{CaF_2} = 60 ML, the luminescence intensity decreased by a factor of more than two over a period of a few minutes. The effect became stronger with decreasing fluoride layer thickness, such that for d_{CaF_2} = 20 ML, the observed decrease in the initial PL intensity became as large as 20–50 times. In SLs with d_{CaF_2} = 10 ML, virtually no luminescence was seen. Remarkably, this effect was observed within a broad temperature interval, from room to liquid-helium temperature.

We analyzed possible reasons for the decrease in the PL intensity, such as tunneling through the interfaces and two-step RE^{2+} photoionization; the possible physical degradation of the SL was also investigated. An important argument in favor of the tunneling mechanism of photoionization in the SL was the experimentally proven one-photon character of the RE^{2+} ionization process. In this case, when the excitation intensity was increased (decreased) and the time scale was simultaneously stretched (compressed) by the same factor, the normalized time dependences of the PL intensity did not change for SLs with a fixed CaF_2 layer thickness. This behavior of the PL for the SLs doped by Eu and Sm ions is shown in Figs. 3a and 3b, respectively.

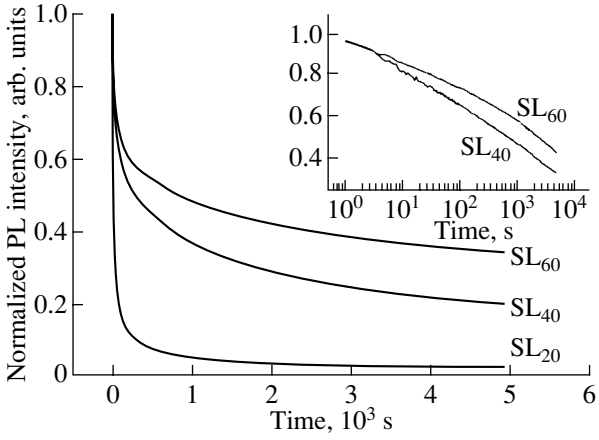

Fig. 2. Eu^{2+} photoluminescence of an SL with CaF_2 layers 20, 40, and 60 ML thick under stationary Ar laser pumping (λ = 361 nm) at an excitation density of 0.5 W/cm^2. Inset: same PL relations for SLs with CaF_2 layer thicknesses of 60 and 40 ML drawn on a logarithmic time scale. T = 300 K [7].

In addition to the absence of any visible defects on the SL surface produced by its irradiation, the independence of the effect on temperature and the possibility of hole burning in the zero-phonon band of the Eu^{2+} absorption spectrum in such SLs also argue against the surface degradation as the reason for the PL decay [12, 13]. A specific feature of the above experiments is the need of using a new spot on the sample surface for each new measurement, because the exposed spot retains the memory of the illumination for at least a few days.

The effect under discussion was treated theoretically in [6] within a quantum-mechanical problem of under-barrier tunneling. The probability of an electron tunneling from the excited state of an RE^{2+} ion located at a distance z from the nearest interface to the CdF_2 conduction band was found for the case of tunneling through a square potential barrier of width z in a one-dimensional approximation and a quasi-classical formalism and has the form

$$W_T = \frac{2\Delta E}{\pi\hbar}\exp\left(-\frac{z}{z_0}\right) = W_0\exp\left(-\frac{z}{z_0}\right),$$
$$z_0 = \frac{\hbar}{\sqrt{8m^*\Delta E}}. \quad (1)$$

Here, ΔE is the barrier height, which is equal to the photoionization energy of the excited RE^{2+} $4f^{n-1}5d$ level; m^* is the electron effective mass; and $\hbar$ is the Planck constant. Estimation of the parameter z_0 from Eq. (1) by assuming ΔE = 1 eV and $m^* = m_0$ yields z_0 = 0.1 nm. Because the thickness of 1 ML in the SLs studied here is 0.315 nm, the tunneling probability changes by more than 20 times with z changing by 1 ML; hence, the ionization can be considered to be a layer-by-layer process. As a result of the tunneling, the rare-earth ion charge changes from +2 to +3, thus reducing the RE^{2+} PL intensity; this process can be simulated by solving simple coupled balance equations:

$$\frac{dN_0}{dt} = -I_{exc}\sigma N_0 + \frac{1}{\tau}N_1,$$
$$\frac{dN_1}{dt} = I_{exc}\sigma N_0 - \left(W_T + \frac{1}{\tau}\right)N_1. \quad (2)$$

Here, N_0 and N_1 are the populations of the ground ($4f^n$) and excited ($4f^{n-1}5d$) states, respectively; I_{exc} is the pump light intensity; σ is the photoionization cross section of the RE^{2+} $4f^n \longrightarrow 4f^{n-1}5d$ transition; and τ is the PL lifetime; the initial conditions for $t = 0$ are $N_0 = 1$ and $N_1 = 0$.

Assuming the tunneling probability to be small such that $W_T \ll I_{exc}\sigma \ll 1/\tau$, the coupled equations (2) reduce to one equation describing the variation of the number of RE^{2+} ions due to tunneling ionization of excited states. The solution to this equation can be written as

$$N(RE^{2+}) = N(RE)\exp\{-tI_{exc}\sigma\tau W_0 \exp(-z/z_0)\}, \quad (3)$$

where N(RE) is the total rare-earth ion concentration and t is the time elapsed from the beginning of optical excitation of the system. From Eq. (3), one readily obtains the relation for the propagation of the RE^{2+} photoionization front from the interface boundary into the CaF_2 layer:

$$z(t) = z_0 \ln(tI_{exc}\sigma\tau W_0), \quad (4)$$

which shows that the distance of the ionization front from the interface increases proportionately to the logarithm of time. Because, as shown above, photoionization occurs in a layer-by-layer manner, the luminescence intensity of the layer as a whole is proportional to the thickness of the layer with RE^{2+} ions not subjected to further ionization; the variation of this intensity with time can be written as

$$\begin{aligned} I(t) &= I_0[1 - 2z(t)/d_{CaF_2}] \\ &= I_0[1 - (2z_0/d_{CaF_2})\ln(tI_{exc}\sigma\tau W_0)], \end{aligned} \quad (5)$$

where I_0 is the initial PL intensity (at $t = 0$). As follows from Eq. (5), the tunneling parameter z_0 can be determined from the slope of a PL decay curve on a logarithmic time scale:

$$z_0 = (d_{CaF_2}/2)[I(t_1)/I_0 - I(t_2)/I_0]/[\ln t_2 - \ln t_1]. \quad (6)$$

It was found that in many cases, experimental curves are fitted quite well by the logarithmic dependence (5) (see inset to Fig. 2), which provides an important argument for the validity of the above physical scenario. However, estimates of the characteristic tunneling length made using Eq. (6) are noticeably larger than the expected figures from Eq. (1) [6, 7]. Furthermore, this very pictorial but certainly simplified model of the effect does not explain the absence of RE^{2+} luminescence in SLs with $d_{CaF_2} = 10$ ML. Therefore, we carried out a numerical analysis of the coupled balance equations (2) without making the assumptions $W_T \ll 1/\tau$ and $W_T \ll I_{exc}\sigma$, which do not correlate well with real experimental conditions.

Obviously enough, the space charge forming in the course of RE^{2+} ionization gives rise to an electrostatic potential and band bending. Because the ionization is a layer-by-layer process, a CaF_2 layer in the space charge region can be considered to be fully depleted in RE^{2+}. Estimates of the band bending yield ~0.1 eV at an RE^{2+} concentration $N_0 = 0.1$ mol %. Because such a change ΔE affects the tunneling parameters only weakly, we shall disregard it in our subsequent analysis.

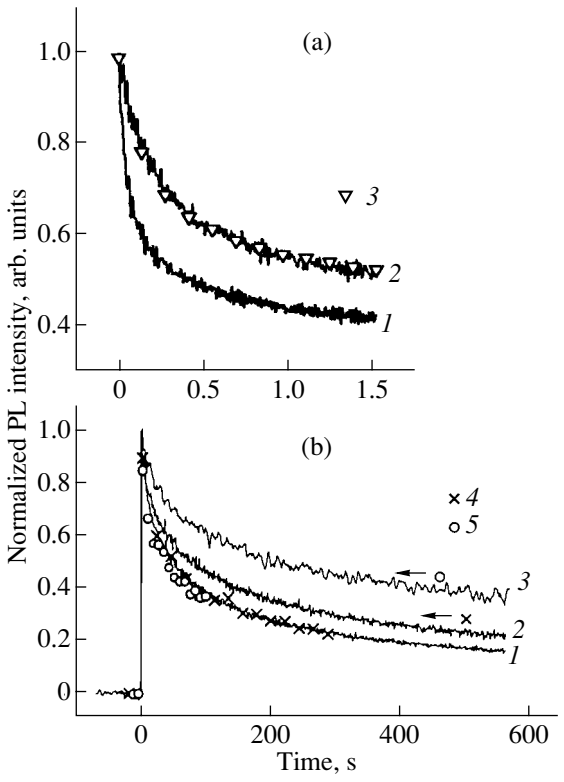

Fig. 3. Photoluminescence of (a) europium ions [6] and (b) samarium ions [8] measured at different stationary pumping intensities. (a) Excitation wavelength $\lambda = 351$ nm, (*1*) $I_{exc} = I_0$, (*2*) $I_{exc} = 0.2I_0$, and (*3*) initial part of curve *1* extended in time 1/0.2 times; and (b) $\lambda = 633$ nm, (*1*) $I_{exc} = I_0$, (*2*) $I_{exc} = 0.55I_0$, (*3*) $I_{exc} = 0.18I_0$, (*4*) initial part of curve *2* compressed in time 1/0.55 times, and (*5*) initial part of curve *3* compressed in time 1/0.18 times. $T = 300$ K.

3. SOLUTION OF THE BALANCE EQUATIONS

The coupled balance equations (2) are easier to solve if presented in the matrix form

$$\frac{d\bar{\mathbf{N}}(t)}{dt} = A(z)\bar{\mathbf{N}}(t),$$

$$A(z) = \begin{pmatrix} -I_{exc}\sigma & \frac{1}{\tau} \\ I_{exc}\sigma & -\frac{1}{\tau} - W(z) \end{pmatrix}. \quad (7)$$

The solution can be written as

$$\bar{\mathbf{N}}(t) = \overline{\mathbf{C}^0}\exp(\lambda_0 t) + \overline{\mathbf{C}^1}\exp(\lambda_1 t), \quad (8)$$

where λ_0 and λ_1 are the eigenvalues of the matrix $A(z)$ and $\overline{\mathbf{C}^{(0,1)}}$ are the eigenvectors corresponding to the above initial conditions. This yields the following relation for the exact solution to Eq. (7) for the excited-state population:

$$N_1(z, t) = \frac{I_{\text{exc}}\sigma}{\text{Tr}AD} \times \left[\exp\left\{\frac{1+D}{2}t\text{Tr}A\right\} - \exp\left\{\frac{1-D}{2}t\text{Tr}A\right\}\right], \quad (9)$$

$$D = \sqrt{1 - \frac{4\det A}{(\text{Tr}A)^2}}.$$

Solution (9) can be simplified by accepting the following approximations, which are in agreement with the experimental conditions: (i) $I_{\text{exc}}\sigma \ll 1/\tau$, which permits one to retain only the linear terms in the expansion of the square roots D involved in the argument of the exponentials into a Taylor series, to replace D with unity in the prefactor denominator, and to neglect $I_{\text{exc}}\sigma$ compared to $1/\tau$ in TrA, and (ii) $t \gg \tau$, which allows one to drop the first exponential term in square brackets. After these simplifications and substitution of Tr$A(z)$ and det$A(z)$ of matrix (7) in an explicit form, Eq. (9) reduces to an approximate solution,

$$N_1(z, t) \approx \frac{I_{\text{exc}}\sigma\tau}{1 + W_T\tau}\exp\left\{-\frac{I_{\text{exc}}\sigma W_T\tau}{1 + W_T\tau}t\right\}. \quad (10)$$

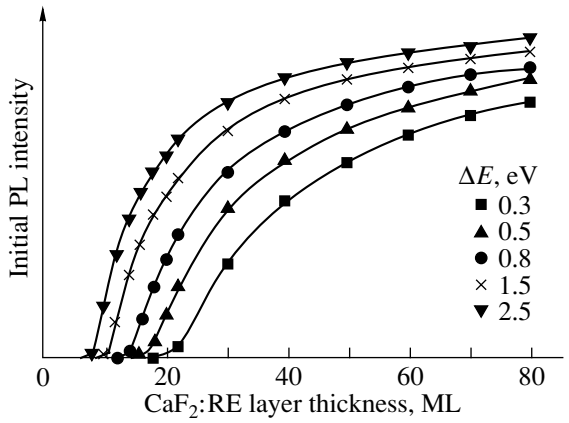

Fig. 4. Initial RE^{2+} photoluminescence intensities in SLs with CaF_2 layers of various thicknesses calculated for various values of the parameter ΔE. $m^* = m_0$.

Equation (10) is seen to transform into Eq. (3) if one accepts the $W_T \ll 1/\tau$ approximation. For subsequent calculations, we include the contributions from the possible electron tunneling in both directions in W_T (which is essential for SLs with layer thicknesses from 10 to 20 ML):

$$W_T(z, d_{\text{CaF}_2}) = W_0\left\{\exp\left(\frac{-z}{z_0}\right) + \exp\left(\frac{d_{\text{CaF}_2} - z}{z_0}\right)\right\}. \quad (11)$$

The evolution of the integrated PL intensity with time can be written as

$$I(t, d_{\text{CaF}_2}) = N(\text{RE})n\int_0^{d_{\text{CaF}_2}} N_1(z, d_{\text{CaF}_2}, t)dz, \quad (12)$$

where N(RE) is the ion concentration in the SL CaF_2 layers and n is the number of CaF_2:RE^{2+} layers. Equation (12) permits numerical calculation of the time dependences of the RE^{2+} PL intensity and the initial intensities I_0.

Reliable experimental data on the electron effective masses in the CaF_2 and CdF_2 conduction band are virtually lacking. It is assumed that because the conduction band of fluorides is derived from *s* orbitals and the band separation is large (~10 eV), the electron masses in the fluoride conduction band are close to the free electron mass [14, 15]. Therefore, we accept $m^* = m_0$ in our calculations. It was shown in [16, 17] that the optical ionization energies of Eu^{2+} and Sm^{2+} excited states in CaF_2 are about 1.5 eV. Experiments on the photoconductivity in CaF_2:Eu^{2+} yield, however, ΔE = 0.8 eV [18].

We carried out calculations for these values of m^* and ΔE using the MATHCAD code. The calculated values of I_0, obtained by extrapolating the time dependences in Eq. (12) to $t = 0$ for ΔE = 0.3, 0.5, 0.8, 1.5, and 2.0 eV, are presented graphically in Fig. 4. We readily see that for ΔE less than 0.3 eV, no RE^{2+} luminescence should be observed in SLs with CaF_2:RE layers 10 and 20 ML thick. Experiments revealed, however, strong RE^{2+} luminescence in SLs with d_{CaF_2} = 20 ML. Thus, ΔE is larger than 0.3 eV. On the other hand, in order to reconcile the calculations with the experimentally shown absence of PL in SLs with d_{CaF_2} = 10 ML, ΔE has to be less than 1.5 eV. The threshold character of the relations displayed in Fig. 4 suggests that if experimental data for SLs with layer thicknesses between 10 and 20 ML are made available, one will be able to obtain a more accurate value for ΔE.

Thus, we believe that the effect described above can also become manifest in other heterostructures with deep impurity centers and large band offsets at the interfaces, as well as give rise to a new efficient nonradiative recombination channel. We note that even the

more general consideration of the effect presented here is actually very simplified. The wave function of the rare-earth ion excited state, which is the initial state for the tunneling transition, has the electronic configuration $4f^n5d$. The final state of the transition is the $4f^{n-1}$ electron shell and an electron in the CdF_2 conduction band. As a result of the ionization event, the lattice contracts in the vicinity of the rare-earth ion to release an energy of up to 2 eV. Therefore, a more consistent theoretical analysis should include multiphonon lattice relaxation processes. On the other hand, more complete experimental data on the dependence of the initial PL intensity on the thickness of the doped layer in the small thickness region (10–20 ML) would provide a possibility of more accurate determination of the tunneling parameters.

Obviously enough, the effect considered here allows for a local recording of optical information. The experimental data on optical reflection from structures undergoing photoionization appear very promising for the reading of this information [19]. Of particular interest would be finding a means to erase the recorded information.

ACKNOWLEDGMENTS

The authors are indebted to I.N. Yassievich for her contribution to the development of the original model and helpful discussions of the results obtained.

This study was supported by INTAS (grant no. 97-10528), the Swiss Scientific Society (grant no. 7SUPJ062359), and the Ministry of Industry and Science of the RF.

REFERENCES

1. P. P. Feofilov, Opt. Spektrosk. **12**, 531 (1962).
2. B. Welber, J. Chem. Phys. **42**, 4264 (1965).
3. D. S. McClure, Proc. SPIE **2706**, 315 (1996).
4. S. A. Basun, S. P. Feofilov, A. A. Kaplyanskii, *et al.*, Phys. Rev. B **61**, 12848 (2000).
5. S. V. Gastev, J. C. Alvarez, V. V. Vitvinsky, *et al.*, Proc. SPIE **2706**, 67 (1996).
6. N. S. Sokolov, S. V. Gastev, A. Yu. Khilko, *et al.*, Phys. Rev. B **59**, R2525 (1999).
7. S. M. Suturin, S. A. Basun, S. V. Gastev, *et al.*, Appl. Surf. Sci. **162–163**, 474 (2000).
8. S. V. Gastev, A. V. Krupin, N. S. Sokolov, and S. M. Suturin, in *Proceedings of the Conference "Nanotechnology-2000," Nizhni Novgorod, 2000*, p. 266.
9. A. Izumi, Y. Hirai, K. Tsutsui, and N. S. Sokolov, Appl. Phys. Lett. **67**, 2792 (1995).
10. A. Yu. Khilko, S. V. Gastev, R. N. Kyutt, *et al.*, Appl. Surf. Sci. **123–124**, 595 (1998).
11. R. N. Kyutt, A. Yu. Khil'ko, and N. S. Sokolov, Fiz. Tverd. Tela (St. Petersburg) **40**, 1563 (1998) [Phys. Solid State **40**, 1417 (1998)].
12. D. M. Boye, Y. Sun, R. S. Meltzer, *et al.*, J. Lumin. **72–74**, 290 (1997).
13. S. V. Gastev, A. Yu. Khilko, N. S. Sokolov, *et al.*, in *Proceedings of the 6th International Symposium "Nanostructures: Physics and Technology," St. Petersburg, Russia, 1998*, p. 16.
14. *Crystals with the Fluorite Structure*, Ed. by W. Hayes (Clarendon, Oxford, 1974), Chap. 1.
15. A. M. Stoneham, *Theory of Defects in Solids: The Electronic Structure of Defects in Insulators and Semiconductors* (Clarendon, Oxford, 1975; Mir, Moscow, 1979), Chap. 2.
16. J. F. Owen, P. B. Dorain, and T. Kobayasi, J. Appl. Phys. **52** (3), 1216 (1981).
17. J. K. Lawson and S. A. Payne, J. Opt. Soc. Am. B **8**, 1404 (1991).
18. C. Pedrini, F. Rogemond, and D. S. McClure, J. Appl. Phys. **59**, 1196 (1986).
19. N. S. Sokolov, S. V. Gastev, A. Yu. Khilko, *et al.*, in *Proceedings of 10th Conference on Semiconducting and Insulating Materials (SIMC-X), Berkeley, California, 1998*, p. 305.

Translated by G. Skrebtsov

Physics of the Solid State, Vol. 44, No. 8, 2002, pp. 1450–1454. Translated from Fizika Tverdogo Tela, Vol. 44, No. 8, 2002, pp. 1390–1394.

PROCEEDINGS OF THE XI FEOFILOV WORKSHOP "SPECTROSCOPY OF CRYSTALS ACTIVATED BY RARE-EARTH AND TRANSITION-METAL IONS"

(Kazan, Tatarstan, Russia, September 24–28, 2001)

Charge Ordering and Lattice Dimerization in α'-NaV_2O_5: One or Two Phase Transitions?

M. N. Popova*, A. B. Sushkov*, E. P. Chukalina*, E. A. Romanov*, M. Isobe, and Y. Ueda****

** Institute of Spectroscopy, Russian Academy of Sciences, Troitsk, Moscow oblast, 142190 Russia*
e-mail: popova@isan.troitsk.ru
*** Institute for Solid State Physics, The University of Tokyo, 5–1–5 Kashiwanoha, Kashiwa, Chiba, 277-8581 Japan*

Abstract—The charge redistribution and the structural change in the α'-NaV_2O_5 quasi-one-dimensional magnet that are initiated at the transition to the low-temperature charge-ordered, structurally dimerized nonmagnetic phase was studied by optical Fourier spectroscopy. Polarized far-infrared transmission spectra obtained in the temperature region T = 6–300 K were used to measure the temperature dependences of the charge-ordering-induced variation of the refractive index and of the intensity of the folded phonon mode which forms in the doubling of the lattice period. The charge-ordering and the structural phase-transition temperatures were found to coincide, $T_{co} \approx T_c \approx 34$ K. © *2002 MAIK "Nauka/Interperiodica".*

1. INTRODUCTION

Low-dimensional oxide magnets have recently been attracting considerable interest in connection with the discovery of such interesting phenomena as high-temperature superconductivity, the spin-Peierls transition in a system of antiferromagnetic Heisenberg chains of half-integer spins ($CuGeO_3$ [1]), and the Haldane gap in integer-spin chains (Y_2BaNiO_5 [2]). The sodium vanadate α'-NaV_2O_5 was established to be the second known inorganic spin-Peierls compound (besides $CuGeO_3$); the temperature dependence of its magnetic susceptibility was measured, and it was shown that at high temperatures, its susceptibility passes through a broad maximum characteristic of antiferromagnetic chains, to subsequently drop abruptly at $T_c \approx 34$ K [3]. This is accompanied by the formation of a gap $\Delta \approx$ 10 meV in the magnetic excitation spectrum [4] and by the lattice period doubling along the *a* and *b* axes and quadrupling along the *c* axis [5].

The α'-NaV_2O_5 structure has double chains (ladders) of distorted corner-sharing VO_5 pyramids arranged along the *b* axis. The adjacent double chains join common edges to form layers in the *ab* plane (Fig. 1). The Na atoms are sandwiched between the layers. Based on the $P2_1mn$ space symmetry group for the high-temperature (HT) α'-NaV_2O_5 structure with two inequivalent vanadium positions, the chains of the V^{4+} magnetic ions were assumed to alternate with those of the nonmagnetic V^{5+} ions [6]. This pattern provided a reasonable explanation for the one-dimensional magnetic properties and the spin-Peierls transition in this intermediate-valence ($V^{4.5+}$) compound. However, the anomalously large value $2\Delta/kT_c \approx 6.5$ and the giant thermal-conductivity anomaly [7], as well as the very weak dependence of T_c on magnetic field [8], revealed in subsequent experiments were at odds with the classical pattern of the spin-Peierls transition. It was soon found that (a) the HT α'-NaV_2O_5 structure belongs, in actual fact, to the *Pmmn* group, in which there is only one position for vanadium, $V^{4.5+}$ [9–14], so that one electron in a molecular orbital of the V_2O complex is situated on a ladder rung [9, 15], and (b) in the low-temperature (LT) phase, charge ordering follows a zigzag pattern [16]. At the same time, the detailed charge distribution pattern remains unclear. In some models, the charge is ordered on each ladder [17, 18], in other models, on each alternate ladder [19, 20], as shown in Fig. 1.

An NMR study suggested that the phase transition with charge ordering occurs at T_{co} = 37 K and that it precedes a phase transition involving lattice dimerization and spin-wave energy gap formation at T_c = 34.7 K [21]. Our studies showed that both processes manifest themselves in the IR spectra of α'-NaV_2O_5; namely, the charge ordering gives rise to a dielectric anomaly, which can be detected from an interference fringe shift and from a change in the absorption coefficient α in a broad low-frequency band [16], whereas the lattice dimerization initiates the formation of new vibrational modes coupled genetically with Brillouin zone-edge modes of the HT phase (folded modes) [22–24]. The purpose of this study was to determine the temperatures T_{co} and T_c by measuring the interference fringe posi-

1063-7834/02/4408-1450$22.00 © 2002 MAIK "Nauka/Interperiodica"

tions (and absorption α) and the intensity of the folded modes on the same sample.

2. EXPERIMENT

Crystals of stoichiometric α'-NaV_2O_5 were melt-grown using a $NaVO_3$ flux [25]. The single crystals measured $1 \times 5 \times 0.5$ to $3 \times 17.3 \times 1.6$ mm along the *a*, *b*, and *c* axes, respectively. Three samples with thicknesses of 110.7, 14, and 7.5 μm were prepared by cleaving perpendicular to the *c* axis for transmission measurements in the $k \parallel c$, $E \parallel a$ and $E \parallel b$ configurations. In the $k \parallel a$ and $E \parallel c$ measurements, two samples, 1.3 mm and 150 μm thick, were used. The latter sample was prepared by embedding it in epoxy resin and grinding it off to a specified thickness.

X-ray, magnetic, and EPR measurements revealed a phase transition at $T_c \approx 34$ K in all the samples. The samples were placed in a helium-vapor optical cryostat on a holder designed so as to compensate temperature-induced variations of the cryostat length.

Normal-incidence, polarized transmission spectra were recorded on a BOMEM DA3.002 Fourier spectrometer in the region 25–300 cm^{-1} with a resolution of 0.05–1 cm^{-1} at temperatures of 6–300 K stabilized to within ±0.1 K. A reference spectrum was obtained at each temperature. The refractive index *n* and the absorption coefficient α ($\alpha = 4\pi\nu\kappa$, where κ is the imaginary part of the complex refractive index $\bar{n} = n + i\kappa$) were derived from the experimental interference pattern in a plane-parallel sample using the relations

$$\Delta\nu = \frac{1}{2dn}, \tag{1}$$

$$Tr_{\max} = \frac{(1-R)^2 e^{-\alpha d}}{(1-Re^{-\alpha d})^2}, \tag{2}$$

$$R = \left(\frac{n-1}{n+1}\right)^2. \tag{3}$$

Here, Δν is the separation (in wavenumber) between adjacent maxima in the interference fringe pattern, $Tr_{\max}$ is the sample transmission at the frequency corresponding to the interference maximum, *d* is the sample thickness, and *R* is the reflection coefficient for one face. Equations (1)–(3) are valid for $n \gg \kappa$, a condition satisfied in our case. We fitted the fringe pattern observed in the range 30–120 cm^{-1} to the relation [26]

$$Tr = \left|\frac{4\bar{n}}{(\bar{n}+1)^2 e^{-i\beta d} - (\bar{n}-1)^2 e^{i\beta d}}\right|^2, \tag{4}$$

where $\beta = 2\pi\nu\bar{n}$ and $n(\nu)$ and $\kappa(\nu)$ were fitted at each temperature by expressions of the type $a + b(\nu - \nu_0)^2$.

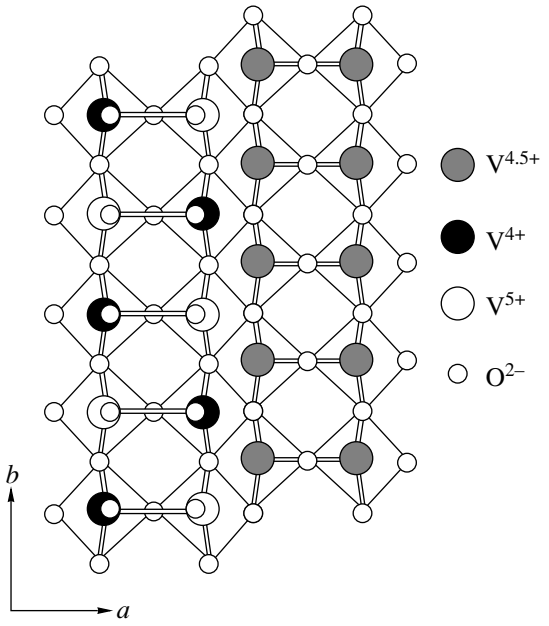

Fig. 1. Projection of two adjacent ladders in a vanadium–oxygen sheet of the α'-NaV_2O_5 sodium vanadate structure on the *ab* plane. In the HT phase, all vanadium atoms occupy equivalent positions and are in the $V^{4.5+}$ valence state (the right-hand ladder). In the LT phase, zigzag ordering sets in (the left-hand ladder). It remains unclear whether all of the ladders or only alternate ones are ordered (as shown in the figure).

The parameters *a* and *b* obtained in the fitting were used subsequently to calculate the integral

$$I(T) = \int_{\nu_1}^{\nu_2} \frac{\alpha(\nu, T)}{\nu_1 - \nu_2} d\nu. \tag{5}$$

For the *c* polarization, in which no interference was observed, the absorption was characterized by the quantity

$$\tilde{\alpha} = \frac{1}{d}\ln\frac{1}{Tr}; \tag{6}$$

we also calculated the integral

$$\tilde{I}(T) = \int_{\nu_1}^{\nu_2} \frac{\tilde{\alpha}(\nu, T)}{\nu_1 - \nu_2} d\nu. \tag{7}$$

The integration here was performed within the region 30–120 cm^{-1}, with subtraction of the intensity of the new line in this region at about 70 cm^{-1}, which increased with decreasing temperature.

In order to find the intensity of any new phonon mode of the LT phase, its contribution Δε to the dielec-

tric permittivity $\varepsilon = \bar{n}^2$ was described in terms of the oscillator model as

$$\Delta\varepsilon = \frac{4\pi f \omega_0^2}{\omega_0^2 - \omega^2 - i\gamma\omega}, \quad (8)$$

where ω_0, γ, and f are the oscillator frequency, damping constant, and the oscillator strength, respectively, and a fit to the experimental spectrum was performed for each temperature using Eq. (4). The oscillator strength thus found was taken as a measure of the mode intensity.

3. RESULTS AND DISCUSSION

Figure 2 displays far-infrared transmission spectra of polarized light obtained on an α'-NaV_2O_5 single crystal at temperatures both above and below T_c. The $E \parallel a$ and $E \parallel b$ polarized spectra clearly exhibit interference in the plane-parallel sample (d = 110.7 μm). Only one phonon mode of the HT phase (ω_0 = 140 cm^{-1}, $E \parallel a$) falls into the frequency interval considered [12]. The new (folded) phonon modes of the LT phase [22–24] are specified by arrows. In the *a* polarization, the HT phase exhibits a strong continuum of long-wavelength absorption [12, 22, 27] which disappears in the LT phase; the transmission of the crystal increases, and the interference fringes become deeper and shift. The *c*-polarized spectra also exhibit an order-of-magnitude weaker continuum absorption (we note that the *c*-polarization spectrum was measured on a sample 12 times thicker than the one used in the *a* polarization). The phase-transition-induced changes in the absorption coefficient and refractive index (or, what amounts to the same thing, the dielectric permittivity $\varepsilon = \varepsilon' + i\varepsilon''$) of α'-$NaV_2O_5$ at low frequencies is associated with charge ordering [16, 28].

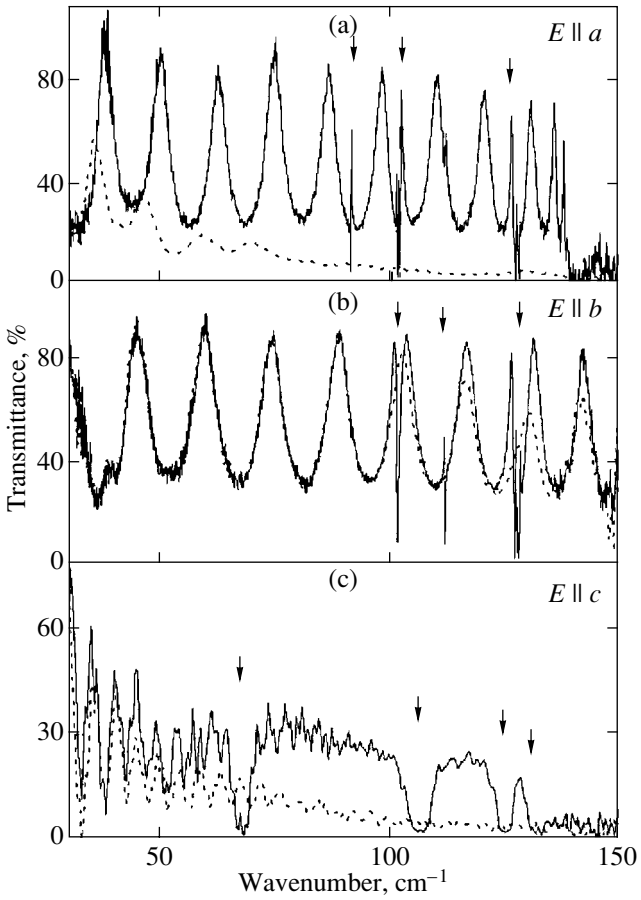

Fig. 2. Transmission spectra of α'-NaV_2O_5 measured at temperatures $T \approx 40$ K > T_c (dashed line) and T = 8 K < T_c (solid line). The *a* and *b* polarized spectra ($k \parallel c$) were obtained on a sample with d_1 = 110.7 μm. The *c*-polarized spectra ($k \parallel a$) relate to another sample (with d_2 = 1.3 mm). The arrows specify the new lines appearing in the low-temperature phase.

Figure 3 shows temperature dependences of the refractive index in the *a* and *b* polarizations and of the intensity of one of the folded phonon modes initiated in the LT phase by the lattice dimerization. The shelf-shaped anomaly in n_a (and ε'_a), combined with the absence of any change in n_b, originates from zigzag charge ordering on the ladder rungs oriented along the *a* axis, which is an ordering of the antiferroelectric type [16, 28]. The temperature of the phase transition involving charge ordering in the *ab* plane, as found from the kink in the $n_a(T)$ relation, is $T_{co} = 33.6 \pm 0.4$ K. This temperature coincides, within the measurement error, with the temperature of the structural phase transition $T_c = 33.9 \pm 0.3$ K derived from the position of the inflection point in the temperature dependence of the 101-cm^{-1} folded mode intensity.

The nonzero intensity of the folded mode for $T > T_c$ (see inset to Fig. 3) and the changes in the refractive index seen to occur for $T > T_{co}$ are associated with short-range order [29]. This order manifests itself much stronger in the $n_a(T)$ dependence, which characterizes charge ordering, than in the $I(T)$ behavior connected with structural changes. This can be accounted for by the fact that charge fluctuations are two-dimensional, whereas structural fluctuations near a transition point occur in three dimensions [30], and the part played by short-range order increases for low-dimensional systems [29]. We note that the effect of charge fluctuations in α'-NaV_2O_5 at temperatures up to ≈100 K was detected in [31] from the softening of the transverse ultrasonic mode C_{66} (*a*-polarized and propagating along the *b* axis), which interacts with zigzag-type charge fluctuations.

Thus, our data do not provide grounds for maintaining, as was done in [21], that charge ordering in α'-NaV_2O_5 occurs as a separate phase transition at a tem-

perature 2–3 K higher than that of the subsequent structural–magnetic transformation.

Because no interference occurs in the *c* polarization, we have not succeeded here in directly measuring the variation of the refractive index with temperature. However, because the real and the imaginary parts of $\bar{n}$ (or of ε) are coupled through the Kramers–Kronig relations and vary similarly [32], we attempted to study the behavior of n_c from the variation of the continuum absorption. The temperature behavior of absorption in the long-wavelength continuum is presented graphically in Fig. 4. The variation of absorption in the *a* polarization follows the same pattern as that of the refractive index, with an inflection point at $T_{co} = 33.6 \pm 0.4$ K (compare Figs. 3, 4). In the *c* polarization, one observes a peak at 33.0 ± 0.3 K. The peak seen in the temperature dependence of the dielectric permittivity is characteristic of a transition to the ferroelectric phase. Such a phase could form for $T < T_c$ if all the $V^{4.5+\delta}$ ions are displaced along the *c* axis in one direction and all the $V^{4.5-\delta}$ ions are displaced in the opposite direction, as follows from [13, 19]. That the temperature position of the peak differs from T_{co} is most probably connected with a scatter in the sample quality, rather than with the charge ordering in the *ab* plane and along the *c* axis occurring at different temperatures. The samples we have at our disposal do not, unfortunately, permit one to measure the temperature dependences of ε_a and ε_c on the same sample.

We note that temperature dependences of the dielectric permittivity of α'-NaV_2O_5 exhibiting a shelf in ε_a and a peak in ε_c were observed earlier at frequencies of 1 kHz [33], 1 MHz–1 GHz [34], and 16.5 GHz [32]. Measurements of $\varepsilon_a(T)$ and $\varepsilon_c(T)$ on the same sample revealed both relations to have anomalies at the same temperature (34.4 K [33] and 33 K [32]). A comparison of the data on ε_c obtained at 1 kHz [33], 1 MHz–1 GHz [34], and 1–3 THz [12] shows ε to have no dispersion up to the terahertz range. Therefore, from the relation $\omega\tau \ll 1$, we obtain an estimate for the dielectric relaxation time $\tau < 1.6 \times 10^{-13}$ s.

That the charge, structural, and magnetic states of sodium vanadate undergo a change in the same phase transition is accounted for by the specific features of this compound. In α'-NaV_2O_5, one *d* electron is shared by two vanadium atoms, thus providing an additional electronic degree of freedom. The probability of an electron hopping along the ladder rung is substantially higher than that along the ladder or between ladders [9, 15]. The zigzag charge ordering in the *ab* planes at low temperatures can be considered to be antiferroelectric ordering of dipoles on ladder rungs [16, 28]. Because each electron possesses a spin ($S = 1/2$), the charge and spin degrees of freedom are intimately coupled. Mostovoy and Khomskii proposed a spin–isospin model for description of the processes occurring in sodium vanadate and used it to show that zigzag charge ordering

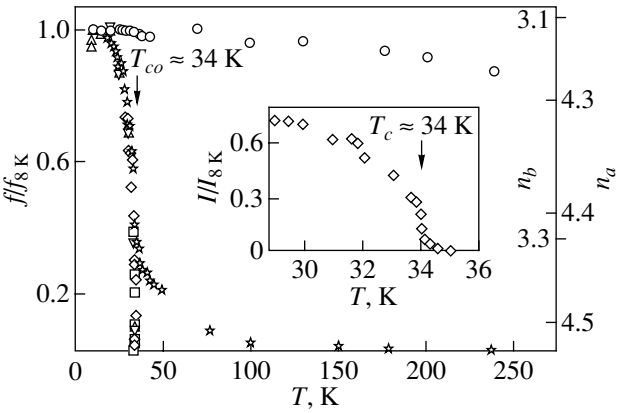

Fig. 3. Temperature dependences of the relative intensity of the folded mode with a frequency of approximately 101 cm^{-1} (different symbols refer to different series of measurements) and of the refractive indices measured at a frequency near 82 cm^{-1} in the $E \parallel a$ and $E \parallel b$ polarizations (asterisks and circles, respectively). Inset shows the behavior of the intensity in the vicinity of the phase-transition point on an expanded scale.

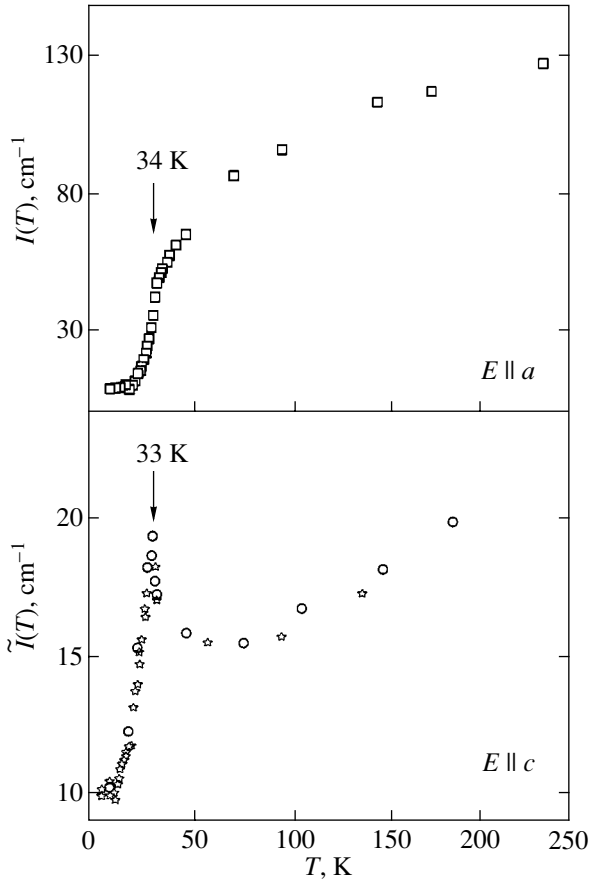

Fig. 4. Temperature dependences of the intensity of the long-wavelength absorption continuum obtained in the *a* and *c* polarizations (measured on different samples with thicknesses $d_1 = 110.7$ μm for $E \parallel a$ and $d_2 = 1.3$ mm for $E \parallel c$). The functions $I(T)$ and $\tilde{I}(T)$ were calculated using Eq. (5) with $\nu_1 = 30$ cm^{-1} and $\nu_2 = 120$ cm^{-1} for $E \parallel a$ and Eq. (7) with $\nu_1 = 30$ cm^{-1} and $\nu_2 = 100$ cm^{-1} for $E \parallel c$, as explained in the text.

opens a gap in the magnetic excitation spectrum [28, 35]. The quasi-one-dimensional spin system in their model is coupled strongly with the exciton-type low-energy antiferroelectric mode (isospin mode), and the observed charge ordering is indicative of softening of this mode. The isospin excitation is softened at the Q point (1/2, 1/2, 1/4) of the Brillouin zone, which corresponds to the wave vector of the LT-phase lattice superstructure [28]. A change in the radii of the vanadium electron clouds brings about displacements of the equilibrium positions of the surrounding oxygen ions, which corresponds to a structural phase transition. Thus, the charge, spin, and lattice degrees of freedom of the sodium vanadate are intimately coupled; as a result, charge ordering and a change in the magnetic state and in the lattice structure in the same phase transition appear only natural.

ACKNOWLEDGMENTS

This study was supported by the Russian Foundation for Basic Research (project no. 01-02-16329) and INTAS (grant no. 99-0155).

REFERENCES

1. M. Hase, I. Terasaki, and K. Uchinokura, Phys. Rev. Lett. **70** (23), 3651 (1993).
2. J. Darriet and L. P. Regnault, Solid State Commun. **86** (7), 409 (1993).
3. M. Isobe and Y. Ueda, J. Phys. Soc. Jpn. **65** (5), 1178 (1996).
4. T. Yoshihama, M. Nishi, K. Nakajima, *et al.*, Physica B (Amsterdam) **234–236**, 539 (1997).
5. Y. Fujii, H. Nakao, T. Yoshihama, *et al.*, J. Phys. Soc. Jpn. **66**, 326 (1997).
6. A. Carpy and J. Galy, Acta Crystallogr. B **31**, 1481 (1975).
7. A. N. Vasil'ev, V. V. Pryadun, D. I. Khomskii, *et al.*, Phys. Rev. Lett. **81** (9), 1949 (1998).
8. W. Schenelle, Yu. Grin, and R. K. Kremer, Phys. Rev. B **59** (1), 73 (1999).
9. H. Smolinski, C. Gros, W. Weber, *et al.*, Phys. Rev. Lett. **80**, 5164 (1998).
10. A. Meetsma, J. L. de Boer, A. Damascelli, *et al.*, Acta Crystallogr. C **54**, 1558 (1998).
11. H. G. von Schnering, Y. Grin, M. Kaupp, *et al.*, Z. Kristallogr. **213**, 246 (1998).
12. M. N. Popova, A. B. Sushkov, S. A. Golubchik, *et al.*, Zh. Éksp. Teor. Fiz. **115** (6), 2170 (1999) [JETP **88**, 1186 (1999)].
13. J. Lüdecke, A. Jobst, S. van Smaalen, *et al.*, Phys. Rev. Lett. **82** (18), 3633 (1999).
14. T. Ohama, H. Yasuoka, M. Isobe, and Y. Ueda, Phys. Rev. B **59** (5), 3299 (1999).
15. P. Horsch and F. Mack, Eur. Phys. J. B **5**, 367 (1998).
16. A. I. Smirnov, M. N. Popova, A. B. Sushkov, *et al.*, Phys. Rev. B **59** (22), 14546 (1999).
17. T. Ohama, A. Goto, T. Shimizu, *et al.*, J. Phys. Soc. Jpn. **69** (9), 2751 (2000).
18. H. Nakao, K. Ohwada, N. Takesue, *et al.*, Phys. Rev. Lett. **85** (20), 4349 (2000).
19. J. L. de Boer, A. M. Meetsma, J. Baas, and T. T. M. Palstra, Phys. Rev. Lett. **84** (17), 3962 (2000).
20. S. van Smaalen and J. Lüdecke, Europhys. Lett. **49** (2), 250 (2000).
21. Y. Fagot-Revurat, M. Mehring, and R. K. Kremer, Phys. Rev. Lett. **84** (18), 4176 (2000).
22. M. N. Popova, A. B. Sushkov, A. N. Vasil'ev, *et al.*, Pis'ma Zh. Éksp. Teor. Fiz. **65** (9), 711 (1997) [JETP Lett. **65**, 743 (1997)].
23. M. N. Popova, A. B. Sushkov, S. A. Golubchik, *et al.*, Physica B (Amsterdam) **284–286**, 1617 (2000).
24. M. N. Popova, A. B. Sushkov, S. A. Klimin, *et al.*, Phys. Rev. B **65**, 144303 (2002).
25. M. Isobe, C. Kagami, and Y. Ueda, J. Cryst. Growth **181**, 314 (1997).
26. M. Born and E. Wolf, *Principles of Optics* (Pergamon, Oxford, 1969; Nauka, Moscow, 1970).
27. S. A. Golubchik, M. Isobe, A. N. Ivlev, *et al.*, J. Phys. Soc. Jpn. **66** (12), 4042 (1997); **68** (1), 318 (1999).
28. M. V. Mostovoy, J. Knoester, and D. I. Khomskii, Phys. Rev. B **65**, 064412 (2002).
29. L. J. de Jongh and A. R. Miedema, Adv. Phys. **23** (1), 6 (1974).
30. S. Ravy, J. Jegoudez, and A. Revcolevschi, Phys. Rev. B **59** (2), R681 (1999).
31. H. Schwenk, S. Zherlitsyn, B. Lüthi, *et al.*, Phys. Rev. B **60** (13), 9194 (1999).
32. M. Poirier, P. Fertey, J. Jegoudez, and A. Revcolevschi, Phys. Rev. B **60** (10), 7341 (1999).
33. Y. Sekine, N. Takeshita, N. Möri, *et al.*, Technical Report of ISSP, Ser. A, No. 3371 (Japan, 1998).
34. S. V. Demichev, A. A. Pronin, N. E. Sluchanko, *et al.*, Fiz. Tverd. Tela (St. Petersburg) **43** (2), 307 (2001) [Phys. Solid State **43**, 320 (2001)].
35. M. V. Mostovoy and D. I. Khomskii, Solid State Commun. **113**, 159 (1999).

Translated by G. Skrebtsov

Physics of the Solid State, Vol. 44, No. 8, 2002, pp. 1455–1458. Translated from Fizika Tverdogo Tela, Vol. 44, No. 8, 2002, pp. 1395–1398.

PROCEEDINGS OF THE XI FEOFILOV WORKSHOP "SPECTROSCOPY OF CRYSTALS ACTIVATED BY RARE-EARTH AND TRANSITION-METAL IONS"

(Kazan, Tatarstan, Russia, September 24–28, 2001)

Exciton Luminescence in Orthorhombic-Structure MnF_2 Epitaxial Films

N. S. Sokolov*, O. V. Anisimov*, A. G. Banshchikov*, S. V. Gastev*, C. Dyroff, R. J. Reeves**, X. Wang***, and W. M. Yen******

** Ioffe Physicotechnical Institute, Russian Academy of Sciences, ul. Politekhnicheskaya 26, St. Petersburg, 194021 Russia*
e-mail: nsokolov@fl.ioffe.rssi.ru
*** Department of Physics & Astronomy, University of Canterbury, Christchurch, New Zealand*
**** Department of Physics, Georgia Southern University, Statesboro, GA 30460 USA*
***** Department of Physics & Astronomy, University of Georgia, Athens, GA 30602 USA*

Abstract—The low-temperature photoluminescence (PL) of 100 to 300-nm thick MnF_2 epitaxial films of the α-PbO_2-type orthorhombic structure was studied. The PL spectrum consists mainly of a broad band peaking around 575 nm and a slowly decaying long-wavelength wing. The short-wavelength part of the main band revealed relatively weak spectral features, which are due to magnon replicas of the Mn^{2+} excitonic line perturbed by Mg and Ca impurities. These features were found to shift toward shorter wavelengths by 12 nm relative to their position in bulk MnF_2 crystals. The shift can be accounted for by a change in the crystal field acting on the Mn^{2+} ions in the orthorhombic phase. © *2002 MAIK "Nauka/Interperiodica".*

1. INTRODUCTION

We are witnessing presently an increasing interest in magnetically ordered thin films and related multilayer heterostructures, as they exhibit considerable application potential in magnetoelectronics. The crystal structure and physical properties of thin films differ quite frequently, however, from the bulk characteristics of the corresponding materials, and revealing these differences requires comprehensive studies. Obviously enough, the size effect in films should be investigated using well-studied model compounds. Among such compounds is MnF_2 with a clearly pronounced antiferromagnetic ordering below 67 K, which possesses interesting optical properties [1–5]. The presence of a orthorhombic crystal field, as well as the spin–orbit and exchange couplings, brings about a 17-cm^{-1} shift and splitting of the Mn^{2+} degenerate excited level ($^4T_{1g}$) into two lowest levels, commonly denoted by E_1 and E_2. Optical excitation is delocalized in the Mn^{2+} lattice because of the strong coupling between adjacent Mn^{2+} ions and propagates as a Frenkel exciton. An important step in the spectroscopic investigation of MnF_2 was the observation of spin waves or magnon replicas of the E_1 and E_2 electronic absorption bands. The exciton and the magnon appear in absorption simultaneously, and their strong interaction results in renormalization of the magnon band energy. In emission, however, the excitations appear one after another and, hence, there is no renormalization.

At low temperatures, MnF_2 exhibits strong fluorescence, which is connected, even in very pure crystals, primarily with Mn^{2+} ions perturbed by impurities. The energy levels of such perturbed ions lie below those of the ions residing in a regular environment, as a result of which free excitons are captured. Some researchers (see, for instance, [1, 5]) report the observation of narrow lines originating from radiative exciton and exciton–magnon transitions from the E_1 level of Mn^{2+} ions perturbed by positively charged Mg^{2+}, Ca^{2+}, and Zn^{2+} ions of residual impurities.

Under normal conditions, bulk MnF_2 crystals are known to have a rutile-type tetragonal structure. In addition, as shown in [6] and other publications of the same authors, manganese fluoride can also crystallize in other phases at high temperatures and pressures. It was later established that the first three MnF_2 monolayers grow coherently with the CaF_2/Si(111) pseudomorphic heteroepitaxial substrate and adopt its cubic crystal structure [7, 8]. It has been demonstrated recently [9, 10] that comparatively thick MnF_2 films (100–300 nm) in the metastable α-PbO_2 rhombic phase can be grown using molecular-beam epitaxy (MBE). We report here on a study of the low-temperature photoluminescence (PL) and its excitation spectra in the rhombic phase of manganese fluoride.

1063-7834/02/4408-1455$22.00

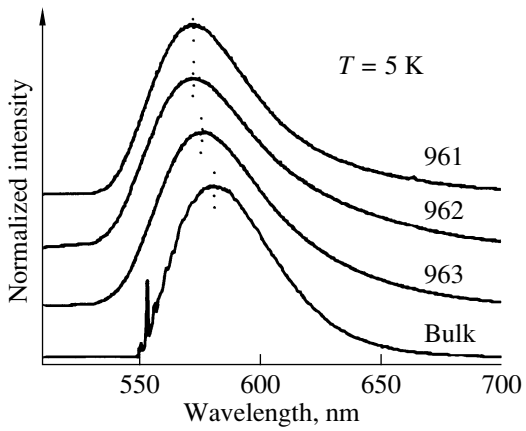

Fig. 1. Photoluminescence of a bulk MnF_2 single crystal and of manganese fluoride films measured at $T = 5$ K. The figures adjoining the curves refer to epitaxial-structure nos (see table).

2. EXPERIMENT

Epitaxial layers of manganese fluoride were grown at the Ioffe Physicotechnical Institute, RAS, on a setup for MBE of fluorides [7]. CaF_2 buffer layers were deposited on Si(111) substrates which were first cleaned chemically in air and then heated in ultrahigh vacuum. A 40- to 50-nm thick MnF_2 film was deposited on CaF_2 at $T = 100$°C and annealed subsequently for 1–2 s at $T = 550$°C. This procedure of manganese fluoride growth was repeated until the films grew to 100–200 nm in thickness. The films thus prepared were coated by a CaF_2 cap layer up to 10 nm thick. The characteristics of the structures grown and studied in this work are listed in the table.

The PL was measured at various temperatures using an Oxford helium cryostat. The PL was excited by an Ar^+ ion laser ($\lambda = 488$ nm) at excitation densities of about 3 W/cm^2. The PL was collected at right angles to the sample surface and propagated through a fiber waveguide system to a spectrometer with a focal length of 0.3 m interfaced to a CCD camera. The PL excitation spectra were obtained with a continuously tunable laser operating on Coumarin 540 dye.

3. RESULTS AND DISCUSSION

The PL spectrum of MnF_2 films represents a broad asymmetric band near 575 nm, with a long-wavelength wing extending to 700 nm. The PL band in the film resembles very much in shape the PL band in bulk MnF_2 crystals, where it is due to phonon and magnon transitions associated with the Mn^{2+} sublattice [1]. This suggests that the PL spectra of films and bulk crystals have the same nature. Figure 1 presents low-temperature PL spectra of three films and of a bulk single crystal. The film PL band is seen to be shifted toward shorter wavelengths by about 10 nm, and this shift is the largest for the thinner films, nos. 961 and 962.

When scaled down in wavelength, the short-wavelength wing of the main PL band of bulk MnF_2 and of the films shows a number of superposed narrow lines (Fig. 2). These lines were identified earlier in bulk crystals as being due to the emission of Mn^{2+} ions perturbed by Mg^{2+} and Ca^{2+} impurity cations. A recent study of the luminescence of MnF_2 films [11] did not report observation of such lines; only kinks were resolved at somewhat different wavelengths on the short-wavelength wing of the main band. This difference in the fine structure of the spectra should be apparently assigned to differences in the growth regimes of the films studied in [11] and this work.

To establish the nature of the fine structure in the PL spectra of MnF_2 films, we studied their temperature behavior. Figure 3a shows emission spectra of sample no. 962 measured from 1.7 to 40 K. We readily see that the intensity of the 535.4-nm line decreases rapidly with increasing temperature. At the same time, the 540-nm line intensity grows with temperature up to 8 K, after which a further increase in temperature brings about a weakening of this line (Fig. 3b). The temperature behavior of these line spectra resembles the one observed for radiative recombination of Mn^{2+} ions perturbed by closely located Mg^{2+} and Ca^{2+} impurities in bulk manganese fluoride crystals [1].

Based on the similar temperature dependence of the PL intensity and spectral positions, the transitions observed in the films at 535.4 and 540.0 nm were assigned by us to Mn^{2+} ions having Mg^{2+} and Ca^{2+} ions, respectively, in their nearest environment. It is also very likely that it is these lines that are electric-dipole allowed magnon replicas of the forbidden pure-electron magnetic-dipole transitions. The shift of about 10 nm

Main growth characteristics of the MnF_2 epitaxial layers studied in this work

Epitaxial-structure no.	Growth characteristics
961	30 nm, growth at 100°C, anneal at 550°C, 75 nm, growth at 400°C
962	(25 nm, growth at 100°C, anneal at 550°C) 4 times
963	(25 nm, growth at 100°C, anneal at 550°C) 11 times

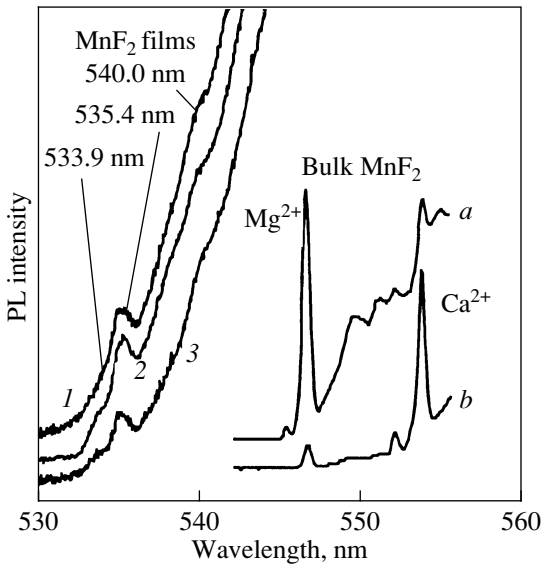

Fig. 2. Fine structure of the photoluminescence spectra of MnF_2 epitaxial films. Left: (*1*) sample no. 961; (*2*) sample no. 962; and (*3*) sample no. 963. Right: Line structure of the short-wavelength edge of the main luminescence band of an MnF_2 bulk single crystal obtained at T equal to (a) 5 and (b) 15 K.

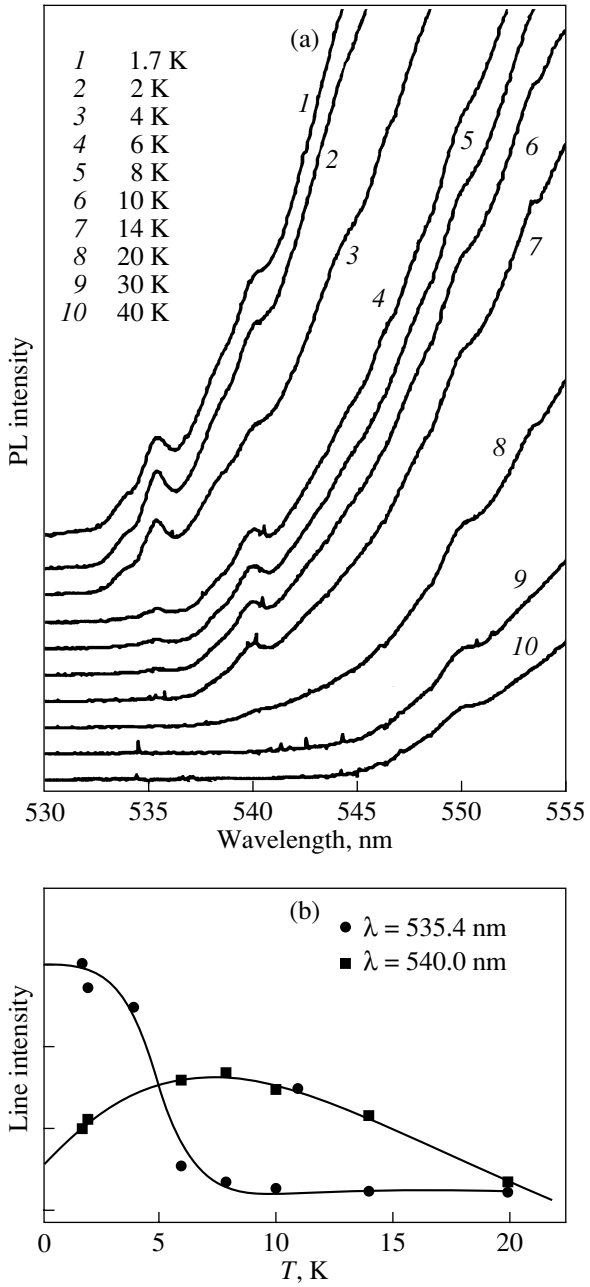

Fig. 3. Temperature dependences of (a) the PL spectrum at the short-wavelength edge of the main band measured on epitaxial film no. 962 and (b) fine-structure line intensities at 535.4 and 540.0 nm.

relative to the corresponding lines in bulk crystals can be attributed to a change in the crystal field around Mn^{2+} ions occurring in the rhombic phase of manganese fluoride.

The PL spectra of films shown in Figs. 2 and 3a exhibit, in addition to the strong 535.4-nm line, a weaker line at 533.9 nm. The splitting is about 60 cm^{-1}, and the intensities of both lines behave in the same way with temperature (Fig. 3a), thus demonstrating their similar nature. The magnon band observed in the luminescence of bulk MnF_2 crystals is shifted to longer wavelengths by 58 cm^{-1} from the purely electronic line. Thus, the weaker line at 533.9 nm observed in the PL of the films can be assigned to the forbidden pure electron magnetic-dipole transition.

We also studied PL excitation spectra in films and compared them with the corresponding spectrum obtained from a bulk MnF_2 single crystal. Figure 4 presents excitation spectra of the 575-nm luminescence measured at 2 K on film no. 962 and on a bulk MnF_2 single crystal. The spectral slit width of the entrance monochromator was 3 nm. The inset to the figure shows the PL excitation spectrum of a bulk MnF_2 single crystal scaled down in wavelength. The spectrum clearly reveals exciton (E_1, E_2) and magnon (σ_1, σ_2) transitions [3]. Taking into account the above data on the PL of films and assuming the PL excitation spectra in films and single crystals to be similar, one can expect there to be a maximum in the excitation spectrum of films near 530 nm. As follows from examination of Fig. 4, however, the experimental PL excitation spectrum of the film has a different shape. The clearly pronounced spectral maximum at 544 nm is located at lower energies than the fine structure in the PL spectrum that is associated with magnon excitation (dashed line). This implies the operation of an additional efficient mechanism of luminescence excitation at 575 nm in films, which is probably connected with their having deep levels that are absent in bulk single-crystal samples.

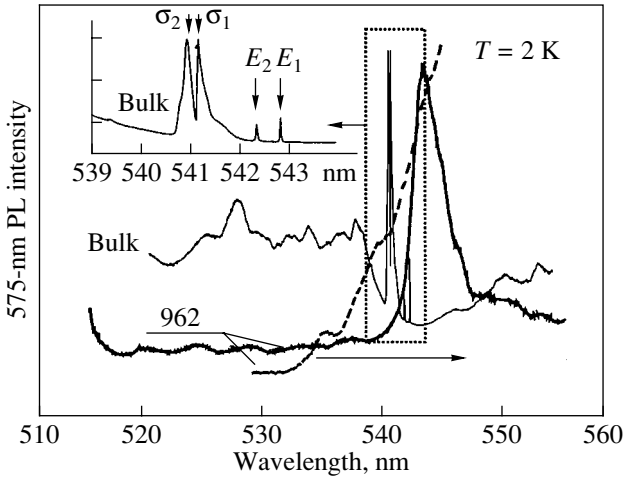

Fig. 4. Excitation spectra of the 575-nm luminescence in an MnF_2 bulk crystal and epitaxial film no. 962 measured at 2 K. Shown for comparison is the short-wavelength part of the luminescence spectrum of the same film (dashed curve). Inset shows the fine structure of the luminescence excitation spectrum of a bulk crystal (expanded in wavelength).

4. CONCLUSION

Thus, low-temperature PL spectra of MBE-grown MnF_2 epitaxial films of α-PbO_2-type rhombic structure are dominated by a broad phonon band peaking at about 575 nm, which resembles in shape the PL band seen in bulk single crystals but is shifted by ~10 nm toward shorter wavelengths. A relatively weak but clearly pronounced fine structure was detected in the short-wavelength part of the main PL band of films. The temperature behavior of the fine-structure line intensities confirms the existence of magnon transitions in Mn^{2+} ions perturbed by closely located Mg^{2+} and Ca^{2+} impurities. These lines are also shifted toward shorter wavelengths by ~10 nm from the corresponding positions in the spectra of bulk MnF_2 crystals as a result of the change in the crystal field in the rhombic phase. An analysis of the PL excitation spectra of MnF_2 films measured in this study revealed the existence of at least two contributions to the luminescence near the maximum of the main band. In addition to the contribution associated with exciton excitation in unperturbed Mn^{2+} ions, there is an appreciable contribution originating from the presence of deeper states, which accounts for the new band in the excitation spectrum with a maximum near 544 nm.

ACKNOWLEDGMENTS

This study was supported by the National Science Foundation, USA (grant no. DMR-9986693); Canterbury University (New Zealand); the National Science Foundation of Switzerland (grant no. 7SUPJ062359); and the Ministry of Industry and Science of the RF.

REFERENCES

1. R. L. Greene, D. D. Sell, R. S. Feigelson, *et al.*, Phys. Rev. **171** (2), 600 (1968).
2. R. L. Greene, D. D. Sell, W. M. Yen, *et al.*, Phys. Rev. Lett. **15** (4), 656 (1965).
3. D. D. Sell, R. L. Greene, and R. M. White, Phys. Rev. **158** (2), 489 (1967).
4. R. E. Dietz, A. E. Meixner, and H. J. Guggenheim, J. Lumin. **1–2**, 279 (1970).
5. A. Misetich, R. E. Dietz, and H. J. Guggenheim, *Localized Excitations in Solids* (Plenum, New York, 1968), p. 379.
6. S. S. Kabalkina, L. F. Vereshchagin, and L. M. Lityagina, Zh. Éksp. Teor. Fiz. **56** (5), 1497 (1969) [Sov. Phys. JETP **29**, 803 (1969)].
7. O. V. Anisimov, A. G. Banshchikov, A. V. Krupin, *et al.*, Thin Solid Films **367** (1–2), 199 (2000).
8. H. Ofuchi, M. Tabuchi, A. G. Banshchikov, *et al.*, Appl. Surf. Sci. **159-160**, 220 (2000).
9. N. S. Sokolov, O. V. Anisimov, A. G. Banshchikov, *et al.*, in *Proceedings of the Conference "Nanophotonics-2001," Nizhni Novgorod, 2001*, p. 277.
10. A. G. Banshchikov, O. V. Anisimov, N. F. Kartenko, *et al.*, in *Proceedings of the 9th International Symposium "Nanostructures: Physics and Technology," St. Petersburg, Russia, 2001*, p. 25.
11. A. G. Banshchikov, S. V. Gastev, M. Ichida, *et al.*, J. Lumin. **87–89**, 519 (2000).

Translated by G. Skrebtsov

Physics of the Solid State, Vol. 44, No. 8, 2002, pp. 1459–1462. Translated from Fizika Tverdogo Tela, Vol. 44, No. 8, 2002, pp. 1399–1402.

PROCEEDINGS OF THE XI FEOFILOV WORKSHOP "SPECTROSCOPY OF CRYSTALS ACTIVATED BY RARE-EARTH AND TRANSITION-METAL IONS"

(Kazan, Tatarstan, Russia, September 24–28, 2001)

Luminescence of Impurity-Bound Excitons in Corundum

B. R. Namozov, V. A. Vetrov, S. M. Muradov, and R. I. Zakharchenya

Ioffe Physicotechnical Institute, Russian Academy of Sciences, ul. Politekhnicheskaya 26, St. Petersburg, 194021 Russia

e-mail: namozov@pop.ioffe.rssi.ru

Abstract—The luminescence characteristics of $M^{3+}:Al_2O_3$ crystals, where M^{3+} stands for an isoelectronic cation impurity with a filled electron shell, namely, Sc^{3+}, Y^{3+}, or La^{3+}, were studied. The luminescence of excitons bound (BE) to these impurities was detected. The position of the BE energy states at the long-wavelength absorption edge as a function of the M^{3+} ionic radius was established. The energies of the long-wavelength BE creation threshold and of the maximum of the BE luminescence band were approximated empirically by third-order polynomials of the Toyozawa polynomial type, which describes electron–phonon interaction. The energy and spatial structure of the BE was found to be similar to that of a self-trapped exciton (STE). The BE and STE states are separated by an energy barrier, and energy transfer from the STE to BE is frozen at low temperatures.

1. INTRODUCTION

Isoelectronic impurities Sc^{3+} and Ga^{3+} incorporated in crystalline Al_2O_3 produce intense UV luminescence bands which are stable at high temperatures. These bands are assigned to excitons localized at an impurity (bound excitons, BE) [1, 2]. Exciton localization depends substantially on the size and structure of the outer electron shell of the impurity ion. To exclude the influence of the impurity valence electrons and establish the part played by impurity size in exciton localization, isoelectronic ions with filled outer shells were doped into corundum.

Although the radius of the La^{3+} ion is twice that of Al^{3+}, they were incorporated into the corundum structure [3]. We report here on spectroscopic and kinetic studies of electronic excitations in Al_2O_3 samples containing impurities with filled outer shells, more specifically, Sc^{3+}, Y^{3+}, and La^{3+}. The ionic radii of these impurities are substantially larger than that of Al^{3+} (R = 0.57 Å) and increase from Sc^{3+} to La^{3+} as 0.81, 0.97, and 1.06 Å, respectively.

2. RESULTS

Polycrystalline samples of corundum with the substituting cations Y^{3+}, Sc^{3+}, and La^{3+} were prepared by sol-gel technology [4]. The material of the samples was a dense α-Al_2O_3 ceramic containing nanocrystalline particles 50–100 nm in size. In addition, single-crystal $Sc:Al_2O_3$ samples were grown by the Czochralski method at 2050 ± 50°C. The optical spectra of the samples were studied on an experimental setup described elsewhere [2].

The absorption spectra were measured on $Sc^{3+}:Al_2O_3$ single-crystal samples (Fig. 1). We readily see that, when Sc^{3+} is introduced into corundum, a shelf, i.e., an absorption band (at 8.3 eV), is formed at the long-wavelength absorption edge, more specifically, in the 8.0- to 8.6-eV region.

Stationary x-ray or electron-beam excitation of $Sc:Al_2O_3$ samples gives rise to a strong luminescence

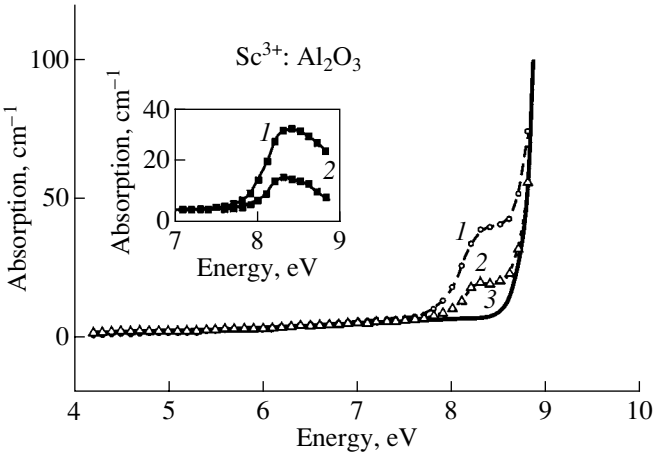

Fig. 1. Absorption spectra of corundum single crystals: (*1*) Al_2O_3:Sc (0.02%), (*2*) Al_2O_3:Sc (0.01%), and (*3*) nominally pure Al_2O_3. The inset shows scandium-induced absorption spectra *1* and *2* relative to the spectrum of nominally pure sample.

1063-7834/02/4408-1459$22.00 © 2002 MAIK "Nauka/Interperiodica"

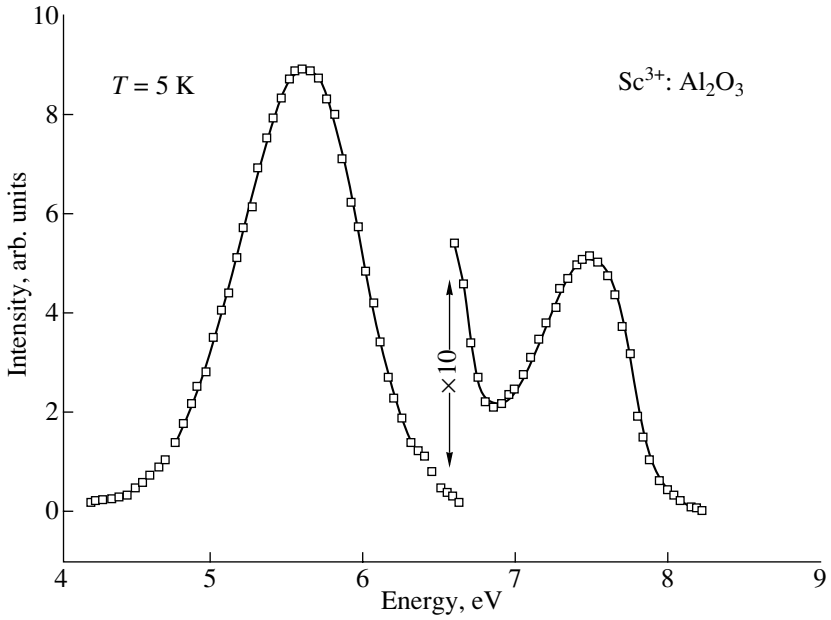

Fig. 2. Luminescence spectra of a single-crystal Al_2O_3:Sc (0.02%) sample obtained under x-ray excitation.

band that peaks at 5.6 eV and to a weak luminescence band at 7.5 eV due to a self-trapped exciton (STE) whose hole component is the O^- relaxed ion [5] (Fig. 2). For equal impurity concentrations, the intensities of these luminescence bands in polycrystalline samples are weaker by an order of magnitude than those of a single crystal. Nevertheless, the ratio of the 5.6- to 7.5-eV band intensities does not change. When pumped by a short electron-beam pulse ($\tau_{ex} \sim 1$ ns), the 5.6-eV luminescence band, as measured during the first 20 ns after the pulse termination, consists of three components at 6.25, 5.75, and 5.25 eV; after ~100 ns, the band at 5.6 eV becomes identical to the steady-state one. The decay of the 5.6-eV band in the 4- to 100-K temperature range follows an exponential law with the time constant $\tau_1 \approx 160$ μs. For $T \geq 120$ K, τ decreases strongly, and at 300 K, we have $\tau_2 \approx 0.5$ μs (curve *1* in Fig. 3) and $\tau_3 \approx 100$ ns.

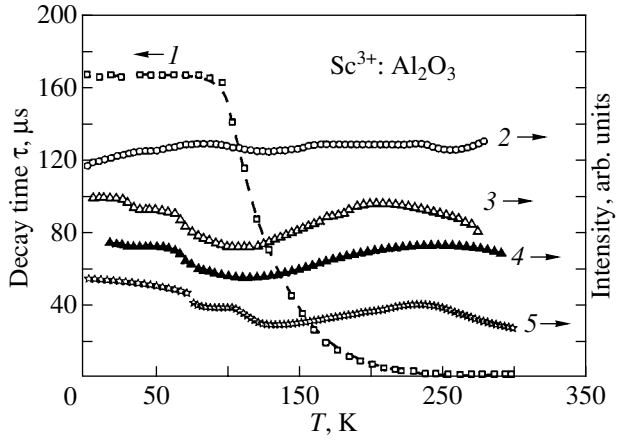

Fig. 3. Temperature dependences of (*1*) the decay time τ and (*2–5*) integrated intensity of the 5.6-eV luminescence band of the Al_2O_3:Sc (0.02%) sample under excitation by photons of energy (*2*) 8.3, (*3*) 9.0, (*4*) 8.7, and (*5*) 10.0 eV.

The 5.6-eV luminescence band is polarized with the degree of polarization being maximum (~30%) at room temperature and with the polarization vector being perpendicular to the trigonal crystal axis. Below 100 K, the degree of polarization drops to 5%. A comparison of the temperature dependences of the degree of polarization and luminescence decay kinetics shows them to be in anticorrelation; i.e., the short decay time occurs at a high degree of luminescence polarization. The STE luminescence band in corundum was found [5] to consist of three spectrally unresolved components with different decay times ($\tau \sim 22$, 230, 2500 ns). The degree of STE polarization in the 7.5-eV band is high (≥30%), and the polarization vector is likewise perpendicular to the trigonal axis of the crystal [5]. Thus, the spatial and energy structures of the BE and STE luminescence in corundum are similar.

The excitation spectrum of the 5.6-eV luminescence band is primarily a sum of the two bands at 8.3 and 9.0 eV, which coincide with the scandium-induced absorption band and the excitonic band, respectively (curve *2*' in Fig. 4).The excitation efficiency of the 5.6-eV luminescence in the 8.3-eV band is high and does not depend on temperature (curve *2* in Fig. 3). When excited in the 9.0-eV band, the temperature dependence of the 5.6-eV luminescence is nonmonotonic; namely, as the temperature is decreased below 200 K, the intensity first decreases and then, for $T \leq$

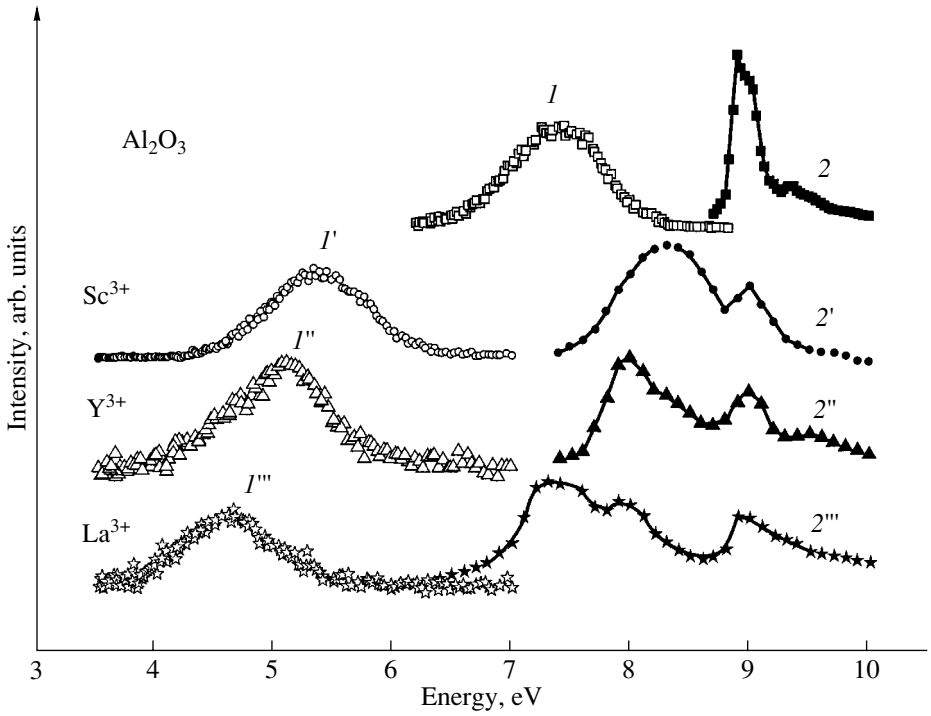

Fig. 4. Normalized spectra of (*1*, *1*', *1*'', *1*''') luminescence and (*2*, *2*', *2*'', *2*''') absorption of various samples; (*1*, *2*) STE in Al_2O_3, (*1*', *2*') Al_2O_3:Sc (0.5%), (*1*'', *2*'') Al_2O_3:Y (0.5%), and (*1*''', *2*''') Al_2O_3:La (0.5%).

120 K, rises in steps, at 65 and 30 K (curve *3* in Fig. 3). The initial decrease is due to the existence of an energy barrier between the BE and STE states. For $T \le 200$ K, the STE luminescence intensity increases and energy transfer to the BE stops (because of the energy barrier) [5]. The rest of the 5.6-eV luminescence (when excited at ≥9.0 eV), observed for $T \le 100$ K, is due to the 7.5-eV STE luminescence band overlapping strongly with the BE absorption band at 8.3 eV (reabsorption; curves *1*, *2*' in Fig. 4). The intensity rise at 65 and 30 K is due to a growth in intensity of the second and third STE luminescence band components, which partially excite the 5.6-eV luminescence through reabsorption. When excited at 10.0 eV, the 5.6-eV band intensity reveals indications of the first and second corundum STE luminescence components rising in intensity at 110 and 65 K (curve *5* in Fig. 3).

The luminescence bands of the Y^{3+}:Al_2O_3 and La^{3+}:Al_2O_3 samples (curves *1*'', *1*''' in Fig. 4) and the temperature dependences of their intensities are similar to the 5.6-eV band and its temperature dependence in Sc^{3+}:Al_2O_3 (curve *1*' in Fig. 4, curve *4* in Fig. 3). The only difference consists in the spectral positions of the bands, namely, 5.2 and 4.6 eV, respectively. As seen from the excitation spectra, their long-wavelength excitation threshold is also shifted toward lower energies. This shift is larger, the larger the ionic radius of the impurity compared to that of the regular cation Al^{3+}.

3. DISCUSSION OF RESULTS

An anion vacancy in alkali halide crystals induces additional α and β absorption bands at the long-wavelength absorption edge [6]. These absorption bands were assigned to exciton formation near such a vacancy. Doping corundum with transition-metal impurities induces additional absorption bands of other types, namely, those involving charge transfer from the impurity to the lattice [7].

The onset of additional absorption at 8.3 eV in scandium-doped corundum was interpreted as being associated with an optical transition of an electron from oxygen ions to the aluminum ion in the nearest environment of the impurity [1]. Indeed, when the matrix cation is replaced by scandium with a larger ionic radius than that of Al^{3+}, the impurity perturbs its oxygen environment and, thus, pushes the O^{2-} valence levels up into the crystal band gap.

On the other hand, the Sc^{3+} ion has a filled argon shell with $3s^2 3p^6$ configuration, which, by our estimates, cannot create electronic levels with an energy less than 12 eV relative to the corundum valence-band top. Such levels lie approximately 3 eV above the conduction-band bottom (the band gap width of corundum is $E_g = 9.3$ eV). Hence, Sc^{3+}:Al_2O_3 cannot form a charge transfer band in the band gap. We believe that the absorption band at 8.3 eV is associated with the $O2p^5$–$Al3s^1$ electronic transition in the nearest lattice environ-

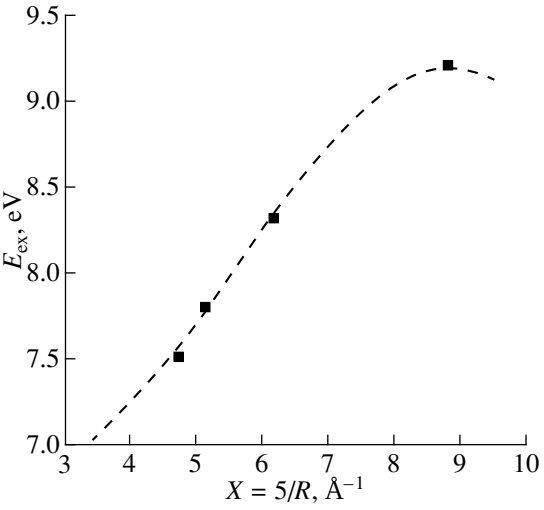

Fig. 5. Position of the maximum of the impurity-induced absorption band in corundum (squares) plotted vs. impurity ionic radius, and its approximation (dashed line).

ment of Sc^{3+}. This electronic transition can be identified with the exciton bound at an impurity. Thus, the 5.6-eV band is actually BE luminescence, because it is observed to be directly related to excitation in the 8.3-eV absorption band (curves *1*', *2*' in Fig. 4).

The luminescence and excitation bands observed by us in the Y^{3+}:Al_2O_3 and La^{3+}:Al_2O_3 samples are similar in nature to the electronic excitations in Sc^{3+}:Al_2O_3 (Fig. 4). Their long-wavelength shift depends on the magnitude of the ionic radii and supports our conclusion that if the cation impurity has a large radius, then the valence oxygen levels of the impurity environment are pushed up more strongly, thus reducing the energy of the $O2p^5$–$Al3s^1$ optical transition.

Figure 5 plots the position of the maximum of the impurity-induced absorption bands as a function of inverse ionic radius *R*. Also shown is the best-fit curve for this relation obtained for $X = 5/R$ and described by

$$E_{ex} = 7.8 - 0.99X + 0.28X^2 - 0.02X^3. \quad (1)$$

The luminescence bands can be fitted by the relation

$$E_{lum} = 5.2 - 1.3X + 0.3X^2 - 0.02X^3. \quad (2)$$

A generalized expression for Eqs. (1) and (2) can be written in the form

$$E \sim (k_1R^{-2} - k_2R^{-3} - k_3R^{-1}), \quad (3)$$

which includes the deformation (k_2R^{-3}) and polarization (k_3R^{-1}) energies of the lattice and the kinetic energy (k_1R^{-2}) both for the carriers (electron and hole) and for the exciton in the strained region of the lattice. Such an expression was proposed by Toyozawa to describe the electron–phonon interaction in polar crystals [8]. According to this theory, the polarization and deformation components are responsible for the negative part of the energy (the attractive potential), whereas the kinetic part of the energy creates the repulsive potential for charge carriers or the exciton. Therefore, this polynomial describes an equilibrium minimum in energy; the exciton (its electron or its hole) is localized in this minimum.

ACKNOWLEDGMENTS

The authors are indebted to A.A. Kaplyanskiĭ for helpful discussions.

Support from the Ministry of Science and Technologies of the RF is gratefully acknowledged.

REFERENCES

1. B. R. Namozov, R. I. Zakharchenya, M. P. Korobkov, and V. V. Myurk, Fiz. Tverd. Tela (St. Petersburg) **40** (4), 653 (1998) [Phys. Solid State **40**, 599 (1998)].
2. A. Lushchik, E. Feldbach, M. Kirm, *et al.*, J. Electron Spectrosc. Relat. Phenom. **101–103**, 587 (1999).
3. C. Verdozzy, D. R. Jennison, P. A. Schults, *et al.*, Phys. Rev. Lett. **80** (25), 5615 (1998).
4. R. I. Zakharchenya and T. N. Vasilevskaya, J. Mater. Sci. **29**, 2806 (1994).
5. B. R. Namozov, M. É. Fominich, R. I. Zakharchenya, and V. V. Myurk, Fiz. Tverd. Tela (St. Petersburg) **40** (5), 910 (1998) [Phys. Solid State **40**, 837 (1998)].
6. F. Seitz, Rev. Mod. Phys. **26** (1), 7 (1954).
7. H. H. Tippins, Phys. Rev. B **1** (1), 126 (1970).
8. Y. Toyozawa, Prog. Theor. Phys. **26** (1), 29 (1961).

Translated by G. Skrebtsov

Physics of the Solid State, Vol. 44, No. 8, 2002, pp. 1463–1467. Translated from Fizika Tverdogo Tela, Vol. 44, No. 8, 2002, pp. 1403–1406.

PROCEEDINGS OF THE XI FEOFILOV WORKSHOP "SPECTROSCOPY OF CRYSTALS ACTIVATED BY RARE-EARTH AND TRANSITION-METAL IONS"

(Kazan, Tatarstan, Russia, September 24–28, 2001)

Exciton–Magnon Interactions in $Ni_cMg_{1-c}O$ Single Crystals

N. Mironova-Ulmane*, V. Skvortsova*, A. Kuzmin*, and I. Sildos**

** Institute of Solid State Physics, Latvian University, ul. Kengaraga 8, Riga, LV-1063 Latvia*

e-mail: ulman@latnet.lv

*** Institute of Physics, Tartu, EE-2400 Estonia*

Abstract—The effect of chemical composition and temperature on exciton–magnon interactions in $Ni_cMg_{1-c}O$ single crystals was studied using optical absorption spectra in the region of the magnetic-dipole $^3A_{2g}(G) \longrightarrow {}^3T_{2g}(F)$ and electric-dipole $^3A_{2g}(F) \longrightarrow {}^1E_g(D)$ transitions. The two zero-phonon lines at ~7800 and ~7840 cm^{-1} on the low-energy side of the magnetic-dipole transition band were assigned to a pure exciton transition and an exciton–one-magnon transition at the center of the Brillouin zone. The intensity of the exciton–one-magnon peak decreases rapidly with increasing magnesium ion concentration and/or temperature, to vanish altogether at $T = 6$ K for $c < 0.95$ and at $T = 130$ K for $c \geq 0.99$. Thus, the contribution of long-wavelength magnons in optical absorption spectra of $Ni_cMg_{1-c}O$ becomes negligible at temperatures substantially lower than the Néel point T_N (the antiferromagnetic ordering temperature). This observation can be explained as being due to a substantial decrease in the characteristic spin–spin interaction length with increasing concentration of the diamagnetic magnesium impurity ions (static disorder) and/or with increasing amplitude of thermal atomic vibrations (dynamic disorder). At the same time, the peak at ~14500 cm^{-1}, which lies in the electric-dipole transition region and corresponds to excitation of an exciton and two magnons at the Brillouin zone edge, remains visible up to the Néel temperature. This is accounted for by the short-wavelength magnons being sensitive to short-range magnetic order, which persists up to T_N. © *2002 MAIK "Nauka/Interperiodica".*

1. INTRODUCTION

Pure nickel oxide NiO is an antiferromagnet of the second kind with a Néel temperature $T_N = 523$ K. Substitution of a part of nickel ions by magnesium ions produces a continuous series of $Ni_cMg_{1-c}O$ solid solutions [1]. The magnetic phase diagram of the $Ni_cMg_{1-c}O$ system, which has been established earlier by elastic neutron scattering [1] and SQUID magnetometry [2], indicates the existence of four regions (Fig. 1) [1]: (1) a homogeneous antiferromagnet ($0.63 \leq c \leq 1$), (2) a cluster antiferromagnet ($0.4 \leq c < 0.63$), (3) a spin-glass-type structure ($0.25 \leq c < 0.4$), and (4) a paramagnet ($c \leq 0.2$). We note that both of the experimental methods mentioned above [1, 2] are sensitive to long-range magnetic order. Microscopic studies [3] of the effect of composition and temperature on the domain structure of $Ni_cMg_{1-c}O$ single crystals provided additional information. It was established in [3] that a domain structure exists at temperatures substantially below T_N (Fig. 1) and that it is more sensitive to the solid-solution composition than the Néel temperature. Magnetic order in the $Ni_cMg_{1-c}O$ solid solutions was also investigated by optical absorption [4], luminescence [5], and Raman spectroscopy [6].

This publication reports on a study of the contribution of exciton–magnon interactions to the optical absorption spectra of $Ni_cMg_{1-c}O$ single crystals. Attention is focused on the dependence of the one- and two-magnon contributions on the solid-solution composition and temperature.

2. SAMPLES AND EXPERIMENTAL TECHNIQUE

$Ni_cMg_{1-c}O$ single crystals were grown by chemical transport reactions [7, 8] on (100)-oriented MgO substrates. The samples were of a greenish color, whose intensity depended on the nickel content and varied from green for $c = 1$ to light green for small c. The chemical composition of the solid solutions was checked by neutron activation analysis [9]; it was found that the nickel content was stoichiometric to within ±0.01%. The optical absorption spectra were measured on a Jasco V-570 double-beam spectrophotometer with a tungsten lamp serving as a light source. The absorption spectra were recorded by a photomultiplier tube and a PbS photocell in the energy intervals 11110–18500 and 7600–12500 cm^{-1}, respectively. The temperature of the samples, fixed in a helium cryostat, was measured in the 5-to 293-K range to within ±1 K.

1063-7834/02/4408-1463$22.00 © 2002 MAIK "Nauka/Interperiodica"

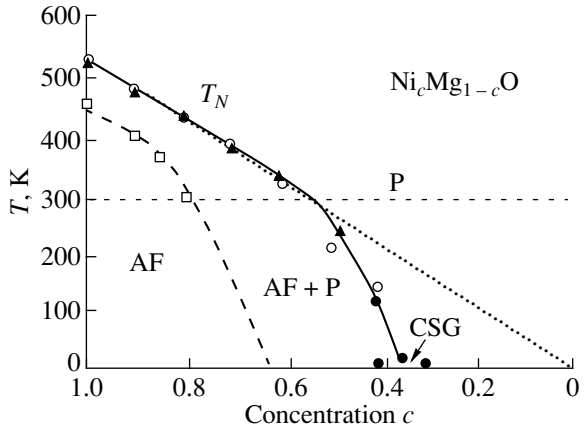

Fig. 1. Magnetic phase diagram of the $Ni_cMg_{1-c}O$ solid solutions obtained using elastic neutron scattering [1] and SQUID magnetometry data [2]. The region of an infinite antiferromagnetic cluster [3] is specified by open squares. P denotes the region of the paramagnetic phase, AF is the antiferromagnetic phase, and CSG indicates the cluster spin glass region.

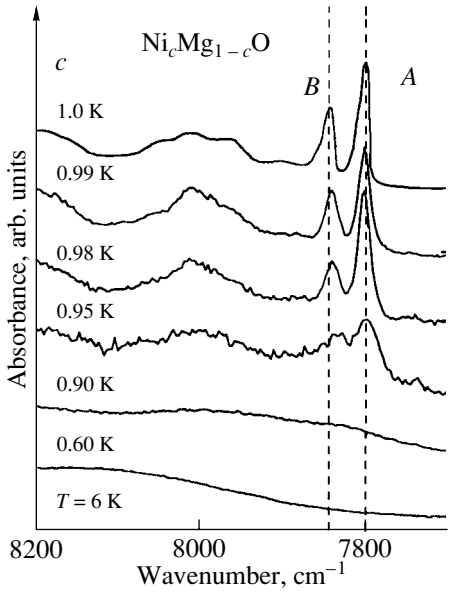

Fig. 2. Low-energy part of the ${}^3A_{2g}(F) \longrightarrow {}^3T_{2g}(F)$ magnetic-dipole absorption band in $Ni_cMg_{1-c}O$ single crystals measured at $T = 6$ K. The peaks corresponding to the pure exciton and the exciton–one-magnon transitions are denoted by *A* and *B*, respectively.

3. RESULTS AND DISCUSSION

The optical absorption spectra of the NiO nickel oxide and $Ni_cMg_{1-c}O$ solid solutions can be interpreted using the energy level diagram of a free nickel ion Ni^{2+} ($3d^8$) in a cubic crystal field. The observed absorption bands are related to parity-forbidden *d*–*d* transitions, three of which, ${}^3A_{2g}(F) \longrightarrow {}^3T_{2g}(F)$, ${}^3A_{2g}(F) \longrightarrow {}^3T_{1g}(F)$, and ${}^3A_{2g}(F) \longrightarrow {}^3T_{1g}(P)$, are spin-allowed ($\Delta S = 0$), whereas the others are forbidden. We will consider the two lowest bands, which correspond to the magnetic-dipole transition ${}^3A_{2g}(F) \longrightarrow {}^3T_{2g}(F)$ at ~8800 cm^{-1} and the electric-dipole transition ${}^3A_{2g}(F) \longrightarrow {}^1E_g(D)$ at ~13800 cm^{-1}.

At low temperatures ($T < 100$ K), the magnetic-dipole absorption band ${}^3A_{2g}(F) \longrightarrow {}^3T_{2g}(F)$ of NiO consists of two narrow, zero-phonon lines (peaks *A*, *B* in Figs. 2, 3) and a broad vibronic band with several maxima corresponding to simultaneous excitation of an exciton and phonons [4, 10]. Peak *A* at ~7800 cm^{-1} is due to the exciton transition, and peak *B* at ~7840 cm^{-1} is associated with exciton–one-magnon excitation involving a magnon with $k = 0$, i.e., at the Brillouin zone center [4, 10]. The magnon energy is determined by the interval separating peaks *A* and *B* [10]. Variation of temperature and substitution of magnesium for nickel result in homogeneous and inhomogeneous broadening of the absorption band, respectively, which affects the intensity and position of both the *A* and *B* peaks and the vibronic band [11].

Figure 3 displays the temperature dependence of the absorption due to the ${}^3A_{2g}(F) \longrightarrow {}^3T_{2g}(F)$ magnetic-dipole transition in NiO and the $Ni_{0.99}Mg_{0.01}O$ solid solution. In both cases, peak *B* disappears at ~110 K, i.e., substantially below the Néel temperature T_N ~ 523 K. The separation between peaks *A* and *B* (Fig. 4a) does not vary with temperature, which implies a constant magnon energy. Nevertheless, the positions of both peaks, as well as of the absorption band maximum, shift to lower energies, which may be attributed to a change in the crystal field strength resulting from lattice expansion [8]. Another interesting observation is the nonlinear variation of the $I(B)/I(A)$ amplitude ratio of peaks *A* and *B* (Fig. 4b). A comparison of the two graphs in Fig. 4 reveals that the $I(B)/I(A)$ ratio varies faster below 60 K, where the *A* and *B* peaks do not change position. At the same time, the two peaks change position toward lower energies above 60 K, although their amplitude ratio remains constant to within the experimental error.

The absorption originating from excitation of the long-wavelength magnon (at the center of the Brillouin zone) is sensitive to long-range magnetic order; therefore, peak *B* and the magnetic structure of nickel oxide and of the solid solutions are related. Substitution of magnesium ions for nickel (up to 10%, $c > 0.9$) strongly reduces the peak *B* intensity already at $T = 6$ K (Fig. 2), i.e., substantially below the temperature of the phase transition from the antiferromagnetic to paramagnetic state (Fig. 1) [1, 2]. To within the experimental error, the magnon energy in $Ni_cMg_{1-c}O$ for $c > 0.95$ remains constant and equal to the value for pure NiO, $\omega_{1M} \approx 41$ cm^{-1}. A decrease in ω_{1M} by ~8 cm^{-1} was observed to occur for $c = 0.95$ (Fig. 2). While the one-magnon pro-

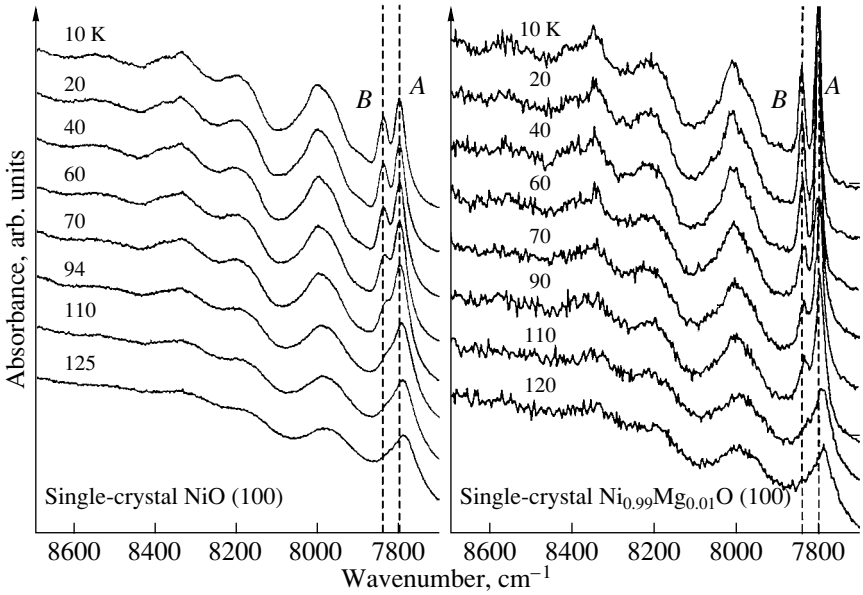

Fig. 3. Temperature dependence of the ${}^3A_{2g}(F) \longrightarrow {}^3T_{2g}(F)$ absorption in NiO and $Ni_{0.99}Mg_{0.01}O$ single crystals. Peak *A* corresponds to the exciton transition, and peak *B* corresponds to the exciton–one-magnon excitation.

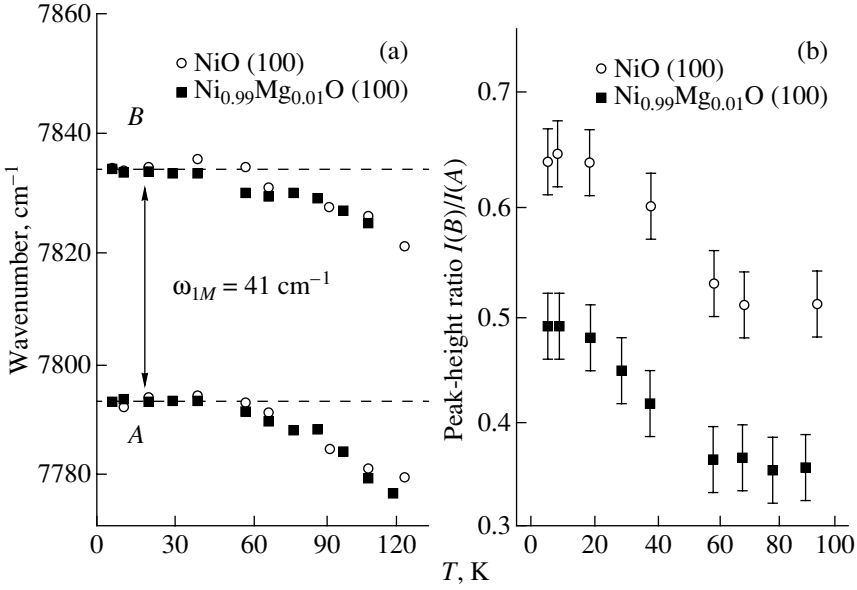

Fig. 4. (a) Variation of the *A* and *B* peak positions with temperature in NiO and $Ni_{0.99}Mg_{0.01}O$ single crystals. The separation between the two peaks remains constant and equal to the magnon energy $\omega_{1M} = 41$ cm^{-1}. (b) ${}^3A_{2g}(F) \longrightarrow {}^3T_{1g}(F)$, ${}^1E_g(D)$ ratio of the *A* and *B* peak amplitudes in NiO and $Ni_{0.99}Mg_{0.01}O$ single crystals.

cess does not produce a contribution in the form of a single peak for $c \leq 0.9$ at 6 K, the $Ni_{0.90}Mg_{0.10}O$ sample nevertheless reveals a strongly smeared feature in place of peaks *A* and *B* (Fig. 2). According to the magnetic phase diagram (Fig. 1), antiferromagnetic order at 6 K is observed in $Ni_cMg_{1-c}O$ solid solutions for $c \gtrsim 0.4$ [1, 2]; moreover, for $c \gtrsim 0.6$, a continuous antiferromagnetic domain structure exists [3]. In pure NiO or in solid solutions with low magnesium content, a continuous antiferromagnetic domain structure is observed to persist up to ~450 K [3], whereas antiferromagnetic order exists substantially above room temperature, up to

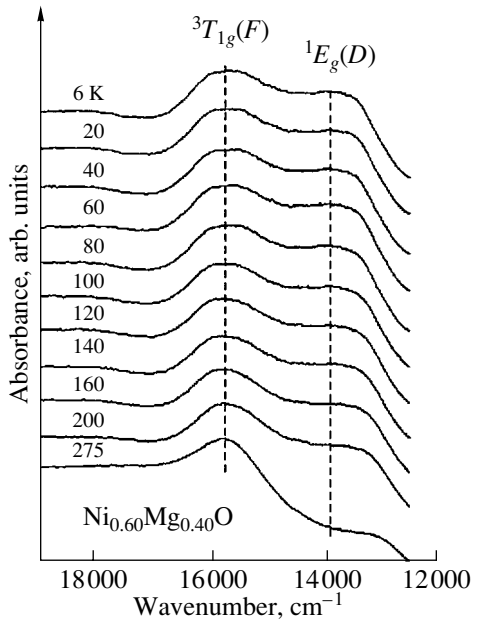

Fig. 5. Temperature dependence of the $^3A_{2g}(F) \longrightarrow {}^3T_{1g}(F)$ and $^1E_g(D)$ absorption in a $Ni_{0.60}Mg_{0.40}O$ single crystal.

523 K. These results reflect the macroscopic magnetic properties of NiO and $Ni_cMg_{1-c}O$, whereas optical absorption spectra are sensitive to magnetic interactions at a microscopic level. Our observations suggest that the long-wavelength magnons at the center of the Brillouin zone are very sensitive to violations of the long-range spin–spin correlations, which occur with increasing temperature and/or dilution by nonmagnetic ions.

Figure 5 shows the temperature dependence of the absorption due to the $^3A_{2g}(F) \longrightarrow {}^1E_g(D)$ electric-dipole transition in $Ni_{0.60}Mg_{0.40}O$. The $^1E_g(D)$ absorption band is seen to overlap partially with the transition to the $^3T_{1g}(F)$ level lying close to 15700 cm^{-1}. The $^1E_g(D)$ band intensity decreases sharply in the 200- to 275-K temperature interval, somewhat below the Néel point $T_N \sim 320$ K. Our previous studies [12] of a similar absorption band in single-crystal $KNiF_3$ permit the conclusion that the shape of the $^1E_g(D)$ band is governed by vibronic processes, in which an exciton and one or several phonons are excited simultaneously, and by an exciton–two-magnon process, which involves excitation of an exciton and two magnons at the Brillouin zone edge. No pure exciton transition is observed in the absorption spectrum, because this transition is both parity- and spin-forbidden; it should lie near 12500 cm^{-1}. The zone-edge excited magnons are short in wavelength and, thus, sensitive to short-range magnetic order. Therefore, the absorption corresponding to the exciton–two-magnon process is observed to occur up to the Néel temperature (Fig. 5). The two-magnon contribution was found earlier to behave in a similar way in Raman spectra of NiO [6] and $KNiF_3$ [13]. The energy ω_{2M} needed to excite two magnons in NiO is approximately ~1400 cm^{-1}, i.e., substantially higher than that in $KNiF_3$ (ω_{2M} = 813 cm^{-1}) [12]. The difference between the two energies is due to the superexchange interaction between nickel ions, which is stronger in NiO.

4. CONCLUSION

Thus, we have studied the temperature and concentration dependences of optical absorption spectra of NiO and $Ni_cMg_{1-c}O$ single crystals grown on MgO(100) substrates. Attention was focused on the magnon contribution in the absorption bands associated with the magnetic-dipole $^3A_{2g}(F) \longrightarrow {}^3T_{2g}(F)$ (~8800 cm^{-1}) and electric-dipole $^3A_{2g}(F) \longrightarrow {}^1E_g(D)$ (~13800 cm^{-1}) transitions. It was found that the two-magnon absorption contribution varies in close correspondence with the magnetic phase diagram for $Ni_cMg_{1-c}O$, whereas the one-magnon contribution is observed only at temperatures substantially below the Néel point. The results obtained were interpreted as being due to different magnons being involved in the processes. The two-magnon absorption involves zone-edge magnons, whereas the magnon taking part in one-magnon absorption is excited at the center of the Brillouin zone. Because the zone-edge magnons are short in wavelength, they are sensitive to the short-range magnetic order, which persists at fairly high temperatures and for large dilutions of nickel oxide by magnesium ions. At the same time, the zone-center magnon is long in wavelength and, therefore, particularly sensitive to thermal and/or structural magnetic order violations, which arise already at fairly low temperatures and for a 10% substitution.

ACKNOWLEDGMENTS

The partial support of the Latvian Government (grant nos. 01.0806, 01.0821) and of the Estonian Science Foundation (grant no. 3453) is gratefully acknowledged.

REFERENCES

1. A. Z. Menshikov, Yu. A. Dorofeev, A. G. Klimenko, and N. A. Mironova, Phys. Status Solidi B **164**, 275 (1991).
2. Z. Feng and M. S. Seehra, Phys. Rev. B **45**, 2184 (1992).
3. N. A. Mironova, A. I. Belyaeva, O. V. Miloslavskaya, and G. V. Bandurkina, Ukr. Fiz. Zh. **34**, 848 (1981).
4. N. A. Mironova, G. A. Grinvald, V. N. Skvortsova, and U. A. Ulmanis, Fiz. Tverd. Tela (Leningrad) **23**, 1498 (1981) [Sov. Phys. Solid State **23**, 874 (1981)].
5. G. A. Grinvald and N. A. Mironova, Phys. Status Solidi B **99**, K101 (1980).

6. R. E. Dietz, G. I. Parisot, and A. E. Meixner, Phys. Rev. B **4**, 2302 (1971).
7. N. A. Mironova and G. V. Bandurkina, Izv. Akad. Nauk Latv. SSR, Ser. Fiz. Tekh. Nauk, No. 4, 14 (1975).
8. N. A. Mironova and U. A. Ulmanis, *Radiation-Induced Defects and Metal Ions of Iron-Group Elements in Oxides* (Zinatne, Riga, 1988).
9. D. V. Riekstinya, I. É. Tsirkunova, and G. Ya. Églite, Izv. Akad. Nauk Latv. SSR, Ser. Fiz. Tekh. Nauk, No. 1, 3 (1975).
10. N. Mironova, V. Skvortsova, A. Kuzmin, I. Sildos, and N. Zazubovich, in *Defects and Surface-Induced Effects in Advanced Perovskites*, Ed. by G. Borstel, A. Krumins, and D. Millers (Kluwer, Dordrecht, 2000), p. 155.
11. K. K. Rebane, in *Zero-Phonon Lines and Spectral Hole Burning in Spectroscopy and Photochemistry*, Ed. by O. Sild and K. Haller (Springer, Berlin, 1988), p. 1.
12. N. Mironova-Ulmane, V. Skvortsova, A. Kuzmin, and I. Sidos, Ferroelectrics **258**, 177 (2001).
13. S. R. Chinn, H. J. Zeiger, and J. R. O'Connor, Phys. Rev. B **3**, 1709 (1971).

Translated by G. Skrebtsov

Physics of the Solid State, Vol. 44, No. 8, 2002, pp. 1468–1470. Translated from Fizika Tverdogo Tela, Vol. 44, No. 8, 2002, pp. 1407–1409.

PROCEEDINGS OF THE XI FEOFILOV WORKSHOP "SPECTROSCOPY OF CRYSTALS ACTIVATED BY RARE-EARTH AND TRANSITION-METAL IONS"

(Kazan, Tatarstan, Russia, September 24–28, 2001)

Jahn–Teller Effect in Low-Spin Ni^{3+} in the $LaAlO_3$ Ceramic

T. A. Ivanova*, V. E. Petrashen'*, N. V. Chezhina, and Yu. V. Yablokov*****

** Kazan Physicotechnical Institute, Kazan Scientific Center, Russian Academy of Sciences, Sibirskiĭ trakt 10/7, Kazan, 420029 Russia*

e-mail: alex@dionis.kfti.knc.ru

*** Institute of Physics, St. Petersburg State University, ul. Pervogo Maya, Petrodvorets, 199034 Russia*

**** Institute of Molecular Physics, Polish Academy of Sciences, Poznan, 60-179 Poland*

Abstract—This paper reports on an EPR study of $LaAl_{1-x}Ni_xO_3$ solid solutions with $x \le 0.12$ made in the 4.2- to 300-K temperature range. In the *X* range, the broadening of the single EPR line with $g_{eff} = 2.148$ was observed at temperatures below ~40 K. In the *Q* range, a slightly anisotropic EPR line with $g'_\perp = 2.145 \pm 0.002$ and $g'_\parallel = 2.154 \pm 0.002$ transforms to a rhombic-symmetry spectrum with $g_1 = 2.183 \pm 0.002$, $g_2 = 2.143 \pm 0.002$, and $g_3 = 2.118 \pm 0.002$. It is shown that the observed low-temperature effects are due to the lowered symmetry of the complex under the combined action of the tetragonal Jahn–Teller distortions and of the trigonal component of the crystal field. © *2002 MAIK "Nauka/Interperiodica".*

1. INTRODUCTION

Most studies of the Jahn–Teller (JT) effect in an orbitally degenerate electronic doublet have been made for the Cu^{2+} ion (d^9 configuration), with the EPR method playing a dominant part in the investigation of this phenomenon [1–3]. The information on EPR studies of vibronic interactions in d^7 ions is much scarcer. JT distortions of the Ni^{3+} octahedral complexes were observed in $KTaO_3$, $SrTiO_3$, and some fluorides with elpasolite structure [4–6]. A dynamic JT effect was found to exist above 77 K in MgO, CaO, Al_2O_3, and $SrTiO_3$ [7–9].

We report here on a study of low-spin Ni^{3+} EPR centers at octahedral sites with slight trigonal distortions. The combined action of the trigonal crystal-field component and of the JT effect, which produces tetragonal distortions, should lower the EPR spectrum symmetry down to rhombic [10]. We are aware of two publications dealing with an experimental study of this situation [8, 11], in which no rhombic distortions were detected in the EPR spectra.

2. $LaAlO_3$ STRUCTURE

$LaAlO_3$ has a slightly distorted perovskite structure. The angle α between the edges of the rhombohedral unit cell is $\alpha = 60.13°$ at room temperature. When heated, the crystal undergoes a second-order phase transition to cubic symmetry, with the angle α decreasing to become 60.00° at ~500°C [12]. The Al position is an octahedron with slight trigonal distortions along the [111] axis. According to [13], when the temperature is lowered below the phase transition point, the octahedron turns about the [111] axis; however, within the 4.2- to 200-K interval, the turn angle does not change within the experimental error.

3. EPR OF LOW-SPIN Ni^{3+} IN $LaAl_{1-x}Ni_xO_3$ SOLID SOLUTIONS

EPR studies of $LaAl_{1-x}Ni_xO_3$ ceramic samples with $x = 0.009$, 0.06, 0.07, and 0.126, made in the *X* range within the 4.2- to 300-K range, revealed a single line with $g_{eff} = 2.148 \pm 0.002$, a magnitude characteristic of low-spin Ni^{3+}. Figure 1 shows the variation with temperature of the linewidth ΔH_{eff}. The linewidth is seen to increase with decreasing temperature below ~40 K in all the samples studied. Taking into account the possible JT effect in the octahedral low-spin Ni^{3+} complexes, we believe this temperature behavior to be associated with stabilization of low-symmetry distortions at the minima of the adiabatic potential, i.e., with a transition from the dynamic to the static JT effect. The observed spectrum becomes anisotropic; however, because of the small anisotropy of the *g* factor compared to the linewidth, the signal anisotropy is not seen in the spectrum and brings about only an increase in the effective EPR line width. We note that the stabilization temperature does not depend on the paramagnetic-center concentration for the compositions studied. The slight increase in the linewidth with increasing concentration (at a fixed temperature) is probably associated with an enhancement of the dipole–dipole interactions. The signal broadening in the high-temperature part of the curves

1063-7834/02/4408-1468$22.00

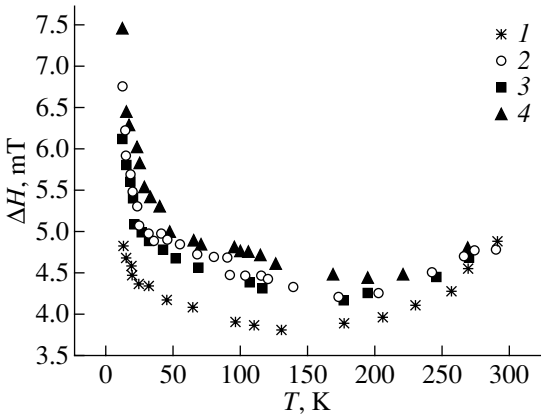

Fig. 1. Temperature dependence of the EPR linewidth ΔH of low-spin Ni^{3+} in $LaAl_{1-x}Ni_xO_3$ samples measured for x equal to (*1*) 0.009, (*2*) 0.06, (*3*) 0.07, and (*4*) 0.12 at a frequency ν = 9.43 GHz.

(Fig. 1) can be accounted for by an increasing contribution from the relaxation-induced broadening.

Measurements in the Q range confirmed the JT nature of the observed centers. At T = 77 K, we observed a slightly anisotropic EPR line, which can be satisfactorily described by the parameters $g'_\perp = 2.145 \pm 0.002$ and $g'_\parallel = 2.154 \pm 0.002$ (Fig. 2a). The spectrum obtained at $T = 4.2$ K corresponds to rhombic symmetry (Fig. 2b) with $g_1 = 2.183 \pm 0.002$, $g_2 = 2.143 \pm 0.002$, and $g_3 = 2.118 \pm 0.002$. The spectral parameters do not depend on the paramagnetic-ion concentration (Figs. 2b, 2c).

4. DISCUSSION OF RESULTS

The Ni^{3+} ion substituting for Al^{3+} is in a low-spin state. It is in a crystal field of octahedral symmetry with small trigonal component. If the spin–orbit coupling is negligible, the trigonal crystal-field component leaves the ground-state orbital doublet degenerate, such that the symmetry of the complex should decrease to tetragonal due to the JT effect. Combined action of the trigonal crystal-field component and of the tetragonal JT distortions lowers the symmetry of the complex to C_i; thus, at low temperatures, one should observe an EPR spectrum corresponding to rhombic symmetry. The resulting deflection of the principal g-tensor axes from the fourfold axes is characterized by the angle $\Delta\gamma = \gamma - \gamma_0$, where γ is the angle between the principal g-tensor axis and the C_3 crystal axis; for a zero trigonal crystal-field component, we have $\gamma_0 = 54.7°$. As the temperature increases, the tetragonal JT component of the crystal field averages out and the symmetry of the complex increases to C_{3v}. The relations connecting the parameters of the low-temperature spectrum g_1, g_2, and g_3 with

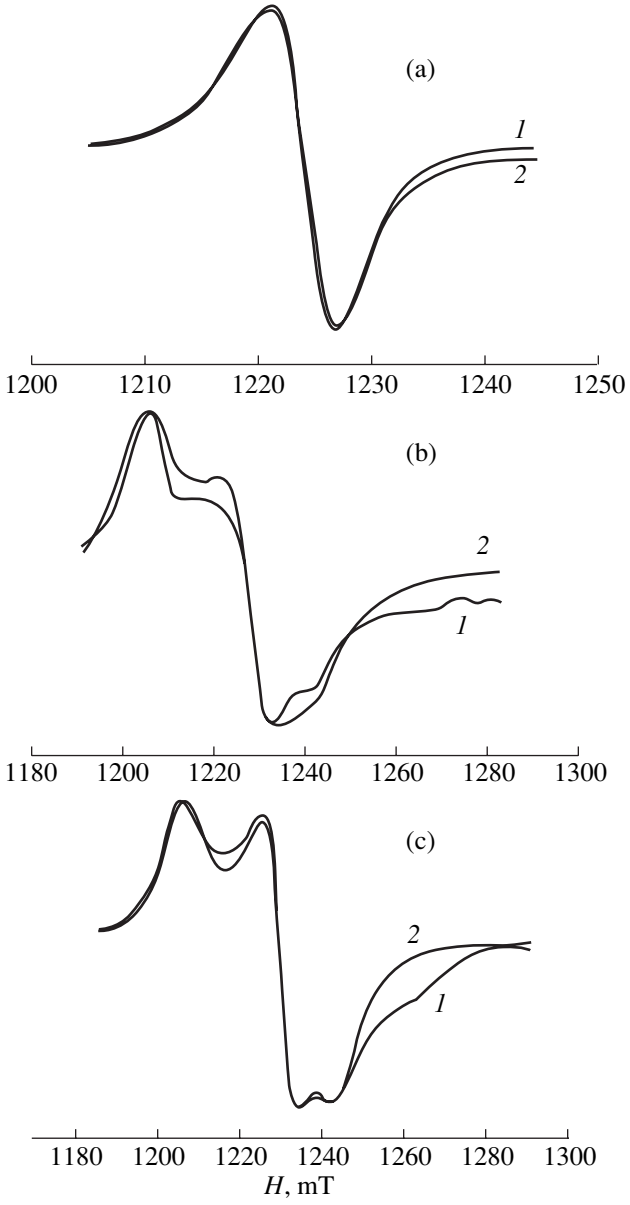

Fig. 2. Q-range EPR spectra of $LaAl_{1-x}Ni_xO_3$ samples: (*1*) experiment and (*2*) theoretical spectrum constructed with Gaussian-shape lines and the following parameters: (a) $x = 0.07$, $T = 77$ K, $g'_\perp = 2.145$, $g'_\parallel = 2.154$, $\Delta H_\perp = 4.6$ mT, and $\Delta H_\parallel = 5.6$ mT; (b) $x = 0.07$, $T = 4.2$ K, $g_1 = 2.183$, $g_2 = 2.143$, $g_3 = 2.118$, $\Delta H_1 = 6.7$ mT, $\Delta H_2 = 6.2$ mT, and $\Delta H_3 = 12.0$ mT; and (c) $x = 0.009$, $T = 4.2$ K, $g_1 = 2.183$, $g_2 = 2.140$, $g_3 = 2.114$, $\Delta H_1 = 6.8$ mT, $\Delta H_2 = 6.5$ mT, and $\Delta H_3 = 8.3$ mT.

the parameters of the averaged high-temperature spectrum $g'_\perp$ and $g'_\parallel$ permit one to determine the value of γ:

$$g'_\parallel = g_\parallel \cos^2\gamma + g_\perp \sin^2\gamma,$$
$$g'_\perp = (g_\parallel \sin^2\gamma + g_\perp \cos^2\gamma + g_\perp)/2, \quad (1)$$

where $g_\perp = (g_x + g_y)/2$.

With $g_\parallel = g_1$ and $g_\perp = (g_2 + g_3)/2$, a fit to experimental data gives $\Delta\gamma$ equal to approximately 6.7°.

The g factors for d^7 ions in a strong crystal field of octahedral symmetry were found in [14]. Deriving similar expressions for lower symmetries encounters formidable calculational difficulties. Assuming the axial crystal-field component to be substantially smaller than the cubic one, which is suggested by structural data, we will use the results reported in [14] to estimate the crystal field parameter Dq and the energy intervals between the ground and the excited states. As follows from the relative magnitude of the g factors of the high-temperature spectrum ($g'_\perp < g'_\parallel$), the unpaired electron resides on the $d_{x^2-y^2}$ orbital in the trigonal crystal field (for averaged JT interaction). In this case, we have

$$\begin{aligned} g'_\parallel &= 2 + 4\xi/E + 2\xi^2/\delta^2, \\ g'_\perp &= 2 + \xi/E + 2\xi^2/\delta^2, \\ 1/E &= 1/E_3 + 1/E_4 + 0.38(1/E_3 - 1/E_4), \end{aligned} \tag{2}$$

where ξ is the spin–orbit coupling constant for a single d electron; E_3 and E_4 are the lowest and the highest $^2T_2$ components of the excited t^5e^2 configuration, respectively; and δ is the energy of the lowest $^4T_1$ level; the splitting of this level by spin–orbit interaction and by low-symmetry fields is disregarded. Using the spin–orbit coupling parameter weakened by covalent bonding, $\xi = 520$ cm^{-1} and the Racah parameter calculated with due account of the covalency, $B = 660$ cm^{-1} [4], we obtain from Eqs. (2) an estimate $\delta = 1950$ cm^{-1}, which corresponds to $Dq/B = 2.5$ on the Tanabe–Sugano diagram. However, the value of E providing the experimentally observed g-factor anisotropy is about an order of magnitude larger than that expected from the diagram. Apparently, Eqs. (2) require refinement near the crossover point; namely, one should take into account the splitting of the $^4T_1$ level. For estimation of Dq, we use the average g factor $\langle g\rangle = (2g'_\perp + g'_\parallel)/3 = 2.148$, which should be less sensitive to the axial splitting of the $^4T_1$ level. From the $\langle g\rangle = 2 + 2(\xi/E + (\xi/\delta)^2)$ relation, we obtain that the experimental value of $\langle g\rangle$ can be brought in agreement with the values of E and δ in the diagram by accepting $Dq/B = 2.4$ and $(\xi/\delta)^2 = 0.05$, which yields $Dq = 1600$ cm^{-1}.

ACKNOWLEDGMENTS

This study was supported by the Russian Foundation for Basic Research, project no. 01-03-32266.

REFERENCES

1. A. Abragam and B. Bleaney, *Electron Paramagnetic Resonance of Transition Ions* (Clarendon, Oxford, 1970; Mir, Moscow, 1972, 1973), Vols. 1, 2.
2. F. S. Ham, *Jahn–Teller Effects in Electron Paramagnetic Resonance* (Plenum, New York, 1972), p. 1.
3. Yu. V. Yablokov, A. E. Usachev, and T. A. Ivanova, in *Radiospectroscopy of Condensed Media* (Nauka, Moscow, 1990), p. 141.
4. D. M. Hannon, Phys. Rev. **164**, 366 (1967).
5. K. A. Müller, W. Berlinger, and R. S. Rubins, Phys. Rev. **186**, 361 (1969).
6. D. Reinen, C. Fribel, and V. Propach, Z. Anorg. Allg. Chem. **408**, 187 (1974).
7. U. Hochli, K. A. Müller, and P. Wysling, Phys. Lett. **15**, 5 (1965).
8. S. Geshwind and J. P. Remeika, J. Appl. Phys. Suppl. **33**, 370 (1962).
9. R. S. Rubins, W. Low, K. A. Müller, *et al.*, in *Proceedings of the First International Conference on Paramagnetic Resonance* (Academic, New York, 1963).
10. Yu. N. Tolparov, G. L. Bir, L. S. Sochava, and N. N. Kovalev, Fiz. Tverd. Tela (Leningrad) **16**, 895 (1974) [Sov. Phys. Solid State **16**, 573 (1974)].
11. P. Ganguly, G. Demazzeau, J. M. Dance, and P. Hagenmuller, Solid State Commun. **73**, 617 (1990).
12. H. M. O'Bryan, P. K. Gallagher, G. W. Berkstresser, and C. D. Brandle, J. Mater. Res. **5**, 183 (1990).
13. K. A. Müller, W. Berlinger, and F. Waldner, Phys. Rev. Lett. **21**, 814 (1968).
14. R. Lacroix, U. Hochli, and K. A. Müller, Helv. Phys. Acta **37**, 627 (1964).

Translated by G. Skrebtsov

Physics of the Solid State, Vol. 44, No. 8, 2002, pp. 1471–1479. Translated from Fizika Tverdogo Tela, Vol. 44, No. 8, 2002, pp. 1410–1417.

PROCEEDINGS OF THE XI FEOFILOV WORKSHOP "SPECTROSCOPY OF CRYSTALS ACTIVATED BY RARE-EARTH AND TRANSITION-METAL IONS"

(Kazan, Tatarstan, Russia, September 24–28, 2001)

The Influence of Local Distortions on the Static and Dynamic Properties of Copper and Silver Eightfold-Coordinated Jahn–Teller Complexes in Mixed Crystals with a Fluorite-Type Structure

V. A. Ulanov, M. M. Zaripov, and E. P. Zheglov

Zavoĭskiĭ Physicotechnical Institute, Kazan Scientific Center, Russian Academy of Sciences, Sibirskiĭ trakt 10/7, Kazan, 420029 Tatarstan, Russia

e-mail: ulanov@dionis.kfti.kcn.ru

Abstract—The influence of local distortions on the structure and properties of copper and silver impurity Jahn–Teller complexes in mixed crystals, namely, $Ca_xSr_{1-x}F_2 : Me^{2+}$ and $Sr_{1-x}Ba_xF_2 : Me^{2+}$ ($0 \le x \le 1$, $Me^{2+} = Cu^{2+}$ or Ag^{2+}), is investigated using electron paramagnetic resonance (EPR) spectroscopy at frequencies of 9.3 and 37 GHz in the temperature range 4.2–250 K. Local distortions of the tensile and compressive types are induced by Ca^{2+}, Sr^{2+}, and Ba^{2+} impurity ions incorporated into the first or second coordination sphere of the cationic environment of the Me^{2+} impurity ion during crystal growth. © *2002 MAIK "Nauka/Interperiodica".*

1. INTRODUCTION

It is known that Cu^{2+} and Ag^{2+} ions in a free state are characterized by the ground configuration nd^9 (n = 3 and 4) with a sole term ^2D (the total orbital momentum L is equal to 2, and the total spin moment S is 1/2). In crystal fields of cubic symmetry, the quintuply degenerate orbital states of the ^2D term are split into the triplet ^2T and the doublet ^2E. In the case when the coordination polyhedron of the Me^{2+} ion (nd^9) has the form of an octahedron, the orbital doublet ^2E_g appears to be ground. If the Me^{2+} ion (nd^9) coordination polyhedron has the form of a cube or tetrahedron, the ground state represents the orbital triplet $^2T_{2g}$. In both cases, it can be expected that the Jahn–Teller effect will manifest itself due to strong interactions between the degenerate electronic states of the impurity ion and vibrations of the surrounding lattice sites. The orbital doublet states are characterized by efficient interactions of the $(E \times e)$ type. For the orbital triplet T_2, there exist several possible variants. When the spin–orbit interaction is substantially stronger than the vibronic interaction, the Jahn–Teller effect can be completely suppressed and the nuclear configuration of the complex remains undistorted. Otherwise, there occur interactions of the $(T_2 \times e)$, $(T_2 \times t_2)$, and $T_2 \times (e + t_2)$ types which correspond to tetragonal, trigonal, and orthorhombic distortions of the high-symmetry nuclear configuration of the complex [1].

Our earlier investigations of Cu^{2+} and Ag^{2+} eightfold-coordinated impurity ions in CdF_2, CaF_2, SrF_2, and BaF_2 crystals of the fluorite group revealed three types of impurity complexes [2–4]. It was found that the $CdF_2 : Ag^{2+}$, $CaF_2 : Ag^{2+}$, and $SrF_2 : Ag^{2+}$ crystals contain $[AgF_2F_6]^{6-}$ trigonal complexes; the $CdF_2 : Cu^{2+}$, $CaF_2 : Cu^{2+}$, and $BaF_2 : Ag^{2+}$ crystals involve $[MeF_4F_4]^{6-}$ orthorhombic complexes; and the $SrF_2 : Cu^{2+}$ and $BaF_2 : Cu^{2+}$ crystals contain $[CuF_4F_4]^{6-}$ tetragonal complexes, in which the impurity ions are substantially (by ~1 Å) displaced from the centers of their coordination cube toward the ⟨001⟩ axis. Although the temperature dependences of the electron paramagnetic resonance (EPR) spectra of these complexes were not analyzed in detail and explicit manifestations of the Jahn–Teller effect were not revealed in these works, the observed distortions of coordination cubes of the impurity ions involved were assigned to the Jahn–Teller effect. This inference was made reasoning from the fact that the studied crystals were grown from high-purity reactants; hence, foreign impurities could not be responsible for the above distortions. Moreover, we took into account that the change in the growth conditions did not bring about the formation of additional paramagnetic centers, because the crystals under investigation invariably contained only single-type centers differing solely in the orientation of their magnetic axes (the principal axes of the spin Hamiltonian tensors). In this respect, it is highly improbable that the observed distortions of molecular structures of the studied com-

1063-7834/02/4408-1471$22.00

plexes are caused by defects of the interstitial or vacancy type. If the inference regarding the Jahn–Teller origin of these distortions holds true, vibronic interactions of the $(T_{2g} \times t_{2g})$, $T_{2g} \times (e_g + t_{2g})$, and $(T_{2g} + A_{2u}) \times (e_g + t_{1u})$ types should occur in the first, second, and third cases, respectively [5].

Bill *et al.* [6] carried out EPR investigations into the structure of silver impurity centers in $SrCl_2$ crystals with a fluorite-type lattice. It was revealed that, in these crystals, an Ag^{2+} impurity ion is also incorporated into the coordination cube of a Sr^{2+} host cation. However, in $SrCl_2$ crystals, unlike alkaline-earth fluoride crystals, the Ag^{2+} ion is located at the off-center position; i.e., it is displaced by ~1 Å from the center of the coordination cube toward the center of the cube face. It is evident that, in this case, as for a copper impurity ion in BaF_2, the tetragonal-type vibrations appear to be the most efficient; i.e., the Jahn–Teller interaction $(T_{2g} \times e_g)$ accompanied by the pseudo-Jahn–Teller interaction with normal vibrations of the t_{1u} type takes place. It is these interactions with the aforementioned odd vibrations that are responsible for the displacement of the Ag^{2+} ion to the off-center position. It should be noted that the efficiency of interactions of this type in $SrCl_2$ crystals increases drastically compared to that in fluoride crystals, because the coordination cube of the lattice cation replaced by an Ag^{2+} impurity ion upon doping of the former crystals is substantially larger than that of the latter crystals.

The experimental data obtained in [2–6] indicate that the parameters of vibronic interactions depend on the ratio

$$\eta = \frac{2(r_{imp} + r_{an})}{\sqrt{3}a_0},$$

where a_0 is the size of the coordination cube and r_{imp} and r_{an} are the ionic radii of the impurity paramagnetic ion and the lattice anion, respectively. It turns out that variations in the parameter η in a relatively narrow range $(0.79 \le \eta \le 0.83)$ lead to radical changes in the parameters of vibronic interactions. It seems likely that, in the case when the size of the coordination cube of an impurity ion residing in the nd^9 electron configuration corresponds to the critical values, the complex becomes very sensitive to various external perturbations. This implies that the parameters of vibronic interactions in crystals can change, for example, under external pressure or in an external electric field. In particular, these changes can be caused by mechanical deformations of the crystal lattice at the nd^9 impurity ion site. In turn, the mechanical deformations can be produced by impurity diamagnetic ions that are chemically identical to the lattice ions but differ from them in ionic radius. For alkaline-earth ions serving as diamagnetic impurities, the highest probability that such an ion will replace one of the twelve lattice cations involved in the first coordination sphere of the cationic environment of the nd^9 impurity ion is observed at a relative impurity ion concentration of ~5%. Consequently, the majority of the nd^9 impurity ions in the crystal appear to be in crystal fields of the orthorhombic symmetry (C_{2v}) with the crystallographic axis $C_2 \parallel \langle 110 \rangle$ and the symmetry plane (110). Under these conditions, the impurity complex is involved in the interaction with one normal mode of the trigonal symmetry t_{2g}, whereas interactions with all the other modes are suppressed. The incorporation of small- and large-sized impurity diamagnetic alkaline-earth ions into the crystal lattice brings about distortions of the tensile and compressive types, respectively.

In our previous work [7], we investigated the influence of the aforementioned local distortions of the crystal structure on the properties of Cu^{2+} impurity complexes with the $3d^9$ electron configuration. In [7], we used CaF_2 and SrF_2 crystals as matrices in which local distortions were accomplished through the incorporation of Sr^{2+} and Ca^{2+} ions, respectively. It was found that the most efficient compressive-type local distortions are induced by large-sized impurity diamagnetic alkaline-earth ions adjacent to the Cu^{2+} ions. The diamagnetic impurities incorporated into the second coordination sphere of the cationic environment of the Cu^{2+} ion give rise primarily to low-symmetry distortions of the copper complex. Owing to the large number of cationic positions in this coordination sphere, the impurity diamagnetic cations are involved in different combinations; hence, the resultant distortions are random in character.

The aim of the present work was to elucidate how the local distortions of the crystal lattice of mixed crystals, namely, $Ca_xSr_{1-x}F_2$ and $Sr_{1-x}Ba_xF_2$ $(0 \le x \le 1)$, affect the parameters of magnetic interactions in $[CuF_8]^{6-}$ and $[AgF_8]^{6-}$ impurity Jahn–Teller complexes at low temperatures and the temperature dependence of these parameters.

2. EXPERIMENTAL TECHNIQUE

The mixed crystals $Ca_xSr_{1-x}F_2 : Me^{2+}$, $Ca_{1-x}Sr_xF_2 : Me^{2+}$, and $Sr_{1-x}Ba_xF_2 : Me^{2+}$ (Me^{2+} = Cu^{2+} or Ag^{2+}) were grown by the Czochralski method in a helium atmosphere with small fluorine additives (~2%). Silver and copper in the form of finely dispersed metallic powders were added to the batch. It would be ineffective to use fluorides of these metals, because, at growth temperatures, they rapidly decompose into the metal and fluorine. Since metallic silver and copper were virtually insoluble in the fluoride melt, the addition of gaseous fluorine to the helium atmosphere used in the crystal growth provided conditions for a certain equilibrium between the formation and decomposition of silver (copper) fluorides. In all the crystals grown in this manner, the impurity silver was in the univalent state. In

order to transform silver into the bivalent state, the silver-containing crystal samples were exposed to x-ray radiation at room temperature for 20–30 min. X-ray radiation was generated using an x-ray tube with a tungsten cathode (anode voltage, 30 kV; current, 20 mA). Unlike silver, the introduced copper was in the bivalent state; hence, there was no need for x-ray irradiation of the copper-containing samples.

The electron paramagnetic resonance measurements were performed on an E-12 Varian spectrometer in the *X* and *Q* bands (9.3 and 37 GHz, respectively) in the temperature range 4.2–250 K.

3. EXPERIMENTAL RESULTS

3.1. Silver complexes. The majority of the studied mixed crystals with silver impurities (exposed to preliminary x-ray irradiation) contain bivalent silver centers with trigonal symmetry of the magnetic properties. The resonance lines in the EPR spectra of these centers are substantially (approximately four or five times) broader than those for mixed crystals free of diamagnetic impurities. Figure 1 shows the EPR spectrum of Ag^{2+} paramagnetic centers in the $Ca_{1-x}Sr_xF_2$: Ag (x = 0.05) crystal in which the trigonal axis is aligned parallel to the external dc magnetic field $\mathbf{B}_0$. The EPR spectrum exhibits a pronounced ligand hyperfine structure due to interaction of the electron magnetic moment of the Ag^{2+} impurity ion with nuclear magnetic moments of two axial fluorine ions (the splitting is approximately equal to 25 mT) and six fluorine ions whose coordinate vectors deviate from the trigonal axis of the impurity center by ~71° and 109°. The superhyperfine splittings of the resonance lines in the EPR spectrum are caused by the interaction with the latter group of ligands and, for the given orientation of the impurity center, are equal to 2.1 mT. Apparently, the broadening of the lines in the EPR spectrum of silver complexes in the $Ca_{1-x}Sr_xF_2$: Ag crystal can be attributed to random compressive distortions induced by strontium impurity diamagnetic ions at the Ag^{2+} paramagnetic ion site. An increase in the concentration of strontium impurity ions leads to an increase in both the spectral line width and the temperature range in which the EPR spectra of the trigonal centers are observed. Indeed, for the studied crystals free of diamagnetic impurities, the EPR spectrum disappears at a temperature of ~35 K. At the same time, the EPR spectra of the crystals containing diamagnetic impurities at a concentration x = 0.05 are observed up to $T \approx 85$ K. It is worth noting that, in this case, the parameters of the electronic Zeeman, hyperfine, and superhyperfine interactions remain unchanged (to within the error in the determination of these parameters). A similar situation is observed for trigonal silver impurity centers in $Ca_xSr_{1-x}F_2$ and $Sr_{1-x}Ba_xF_2$ ($x \le$ 0.05) crystals.

An unexpected result was obtained for $Ca_{0.5}Sr_{0.5}F_2$: Ag crystals, in which, even after x-ray irradiation, no paramagnetic centers that could be assigned to the Ag^{2+} centers were revealed. The grown crystals (prior to x-ray irradiation) had a yellow color typical of Ag^+ ions in fluorites. Therefore, the lack of electron paramagnetic resonance of the impurity centers under consideration cannot be explained by the absence of impurity silver ions in the crystals.

It was found that, in addition to the trigonal silver centers, the $Sr_{1-x}Ba_xF_2$: Ag ($x \le 0.05$) crystals contain impurity centers with orthorhombic symmetry of the magnetic properties. The concentration of orthorhombic centers is several times higher than that of trigonal silver centers, and the EPR spectra of the orthorhombic centers are observed up to 200 K. The parameters of magnetic interactions in the observed silver complexes remain nearly constant over the entire temperature range covered.

Figures 2 and 3 display the EPR spectra recorded for two (most important) orientations of the crystal with respect to the external magnetic field, namely, $\mathbf{B}_0 \parallel \langle 110 \rangle$ and $\mathbf{B}_0 \parallel \langle 001 \rangle$, respectively. The most informative spectrum is depicted in Fig. 2. This spectrum contains three groups of lines attributed to the resonance transitions between electronic–nuclear levels of six sets of impurity centers that are similar in structure but differ in their orientations with respect to the vector $\mathbf{B}_0$. Line *I*, which exhibits neither hyperfine nor superhyperfine structures, is associated with the impurity centers in which the principal magnetic axis Z_i is parallel to the vector $\mathbf{B}_0$. Lines of group *III* are assigned to the impurity centers with the axis $X_i \parallel \mathbf{B}_0$. In the magnetic coordinate system of four sets of magnetically equivalent centers responsible for the appearance of resonance lines of group *II*, the magnetic field vector does not coincide with any one of the principal axes of the paramagnetic center. For one of these sets of paramagnetic centers, the magnetic field vector in the intrinsic coordinate system can be represented as the row matrix $(1/2B_0, 1/\sqrt{2}B_0, 1/2B_0)$. For the other three sets of paramagnetic centers, the representation of the vector $\mathbf{B}_0$

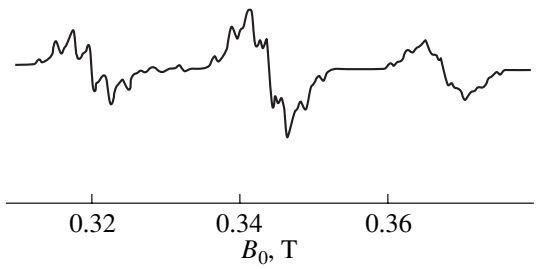

Fig. 1. EPR spectrum of trigonal bivalent silver centers in the $Ca_{0.95}Sr_{0.05}F_2$: Ag^{2+} crystal (9.3 GHz, 77 K). The external dc magnetic field $\mathbf{B}_0$ is aligned parallel to the trigonal axis of the complex.

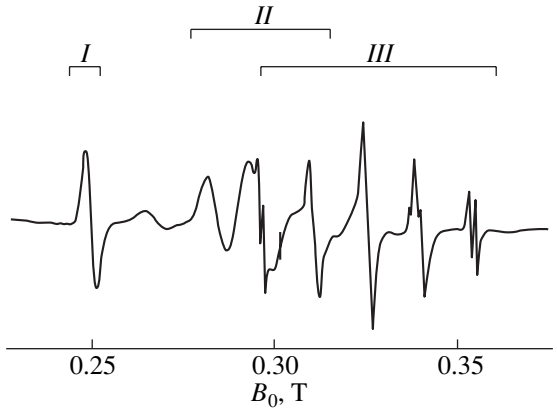

Fig. 2. EPR spectrum of the $Sr_{0.95}Ba_{0.05}F_2 : Ag^{2+}$ sample (9.3 GHz, 77 K, $\mathbf{B}_0 \parallel \langle 110 \rangle$).

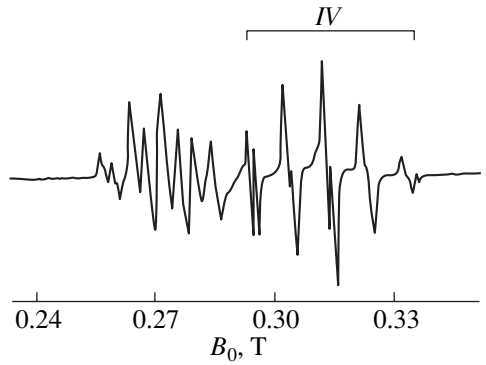

Fig. 3. EPR spectrum of the $Sr_{0.95}Ba_{0.05}F_2 : Ag^{2+}$ sample (9.3 GHz, 77 K, $\mathbf{B}_0 \parallel \langle 001 \rangle$).

can be obtained using cubic symmetry operations. The broad line located between lines of groups *I* and *II* corresponds to trigonal silver centers. Therefore, from analyzing the EPR spectrum shown in Fig. 2, we can determine two principal components of the *g* tensor, namely, the g_z and g_x components. The third principal component of the *g* tensor (g_y) can be obtained from the EPR spectrum displayed in Fig. 3. In this figure, resonance lines of group *IV* correspond to the g_y component of the *g* tensor. Analysis of the superhyperfine structure of the EPR spectrum of the impurity centers with the axis $X_i \parallel \mathbf{B}_0$ (lines of group *III* in Fig. 2) shows that, in this case, we deal with the electron–nucleus magnetic interaction involving F^- ligands of two groups (each group contains two F^- ions) which are characterized by slightly different interaction parameters. All four ligands are located in the *XOY* plane of the intrinsic magnetic coordinate system of the impurity center in such a way that ligands of both pairs are symmetrically arranged with respect to the *X* axis.

Apart from the superhyperfine structure, the EPR spectra exhibits a hyperfine structure caused by the interaction between the electron magnetic moment of the impurity center and the magnetic moment of the silver nucleus. For both silver isotopes (^{107}Ag and ^{109}Ag), the nuclear spin is equal to 1/2; however, their isotopic splitting is not observed by virtue of the relatively large inhomogeneous broadening of the spectral lines. For this reason, the hyperfine structure of the EPR spectrum is characterized by the averaged components of the hyperfine structure tensor.

In the intrinsic magnetic coordinate system, the spin Hamiltonian of the silver centers under investigation can be represented in the form

$$\mathbf{H}_s = \beta_e(\mathbf{B}_0 \cdot \mathbf{g} \cdot \mathbf{S}) + (\mathbf{S} \cdot \mathbf{a} \cdot \mathbf{I}_{\mathrm{Ag}}) + \sum_i [(\mathbf{S} \cdot \mathbf{A}_{\mathrm{F}(i)} \cdot \mathbf{I}_{\mathrm{F}(i)}) - g_n^F \beta_n (\mathbf{B}_0 \cdot \mathbf{I}_{\mathrm{F}(i)})], \quad (1)$$

where *g* is the tensor of the electron Zeeman interaction between the external magnetic field B_0 and the electron magnetic moment of the silver center, **S** is the operator of the electron spin moment ($S = 1/2$), $\mathbf{I}_{\mathrm{Ag}}$ is the operator of the nuclear spin moment of the Ag^{2+} impurity ion, $\mathbf{I}_{\mathrm{F}(i)}$ is the operator of the nuclear spin moment of the *i*th ligand, **a** is the tensor of the hyperfine interaction between the electron magnetic moment of the silver center and the nuclear magnetic moment of the Ag^{2+} impurity ion, $\mathbf{A}_{\mathrm{F}(i)}$ is the tensor of the superhyperfine interaction with the nucleus of the *i*th ligand, β_e is the Bohr magneton, β_n is the nuclear magneton, and g_n^{F} is the nuclear *g* factor of fluorine. The Zeeman interaction with the nuclear moment of the Ag^{2+} impurity ion was disregarded because of its smallness.

Table 1 presents the tensor components of the spin Hamiltonian (1) as obtained from analyzing the angular dependence of the position of the resonance lines in the EPR spectrum.

Reasoning from the results obtained, we proposed a model of the impurity center under consideration. In general terms, this model is similar to the model of an Ag^{2+} center in BaF_2 crystals [4]. The difference lies in the fact that an impurity center formed in $Sr_{1-x}Ba_xF_2$ crystals has monoclinic (rather than orthorhombic) symmetry. This additional lowering of the symmetry is associated with the fact that, in the nearest cationic environment of the Ag^{2+} impurity ion (in the direction of the *X* axis), the Sr^{2+} cation is replaced by a Ba^{2+} cation whose ionic radius exceeds the ionic radius of Sr^{2+}. A fragment of the cross section of the Ag^{2+} coordination polyhedron in the *XOY* plane of the magnetic coordinate system of the impurity center is depicted in Fig. 4. This figure also shows the two diamagnetic cations nearest to the silver ion, one of which is the Ba^{2+} impurity cation. Under the effect of the repulsive potential of the Ba^{2+} impurity cation, the surrounding atoms

are displaced to new equilibrium positions. The directions of atomic displacements (shown by arrows in Fig. 4) are radial with respect to the Ba^{2+} nucleus. The atomic displacements (cited near the arrows in Fig. 4) were calculated within the Born–Mayer–Huggins model (see, for example, [8, 9]) in terms of the pair interaction potential

$$V_{\alpha\beta} = Z_\alpha Z_\beta \frac{e^2}{4\pi\varepsilon_0 r} + A_{\alpha\beta}\exp\left(-\frac{r}{\rho_{\alpha\beta}}\right) - C_{\alpha\beta}\frac{1}{r^6}. \quad (2)$$

Here, Z_α and Z_β are the charges of the αth and βth interacting ions (in terms of elementary charge), respectively; r is the distance between these ions; and the interaction parameters $A_{\alpha\beta}$, $\rho_{\alpha\beta}$, and $C_{\alpha\beta}$ are as follows [8]:

Ca^{2+}–F^-: A = 794.4 eV, ρ = 0.3179 A, C = 0;
Sr^{2+}–F^-: A = 715.3 eV, ρ = 0.3422 A, C = 0;
Ba^{2+}–F^-: A = 681.1 eV, ρ = 0.3574 A, C = 0;
F^-–F^-: A = 1127.7 eV, ρ = 0.2753 A, C = 15.83 eV A^6.

Since the parameters $A_{\alpha\beta}$, $\rho_{\alpha\beta}$, and $C_{\alpha\beta}$ for the potentials of interaction between the silver ion and the surrounding ions were unknown, the displacements of the lattice sites were calculated for the case when the lattice contained only one alkaline-earth impurity ion and the other cation sites were occupied by the host cations. To put it differently, we calculated the external disturbance with respect to the Ag^{2+} impurity ion. It is evident that the results of this approximate calculation are also applicable to the copper impurity ion. The response of the impurity Jahn–Teller ion to this disturbance will be qualitatively examined in the next section.

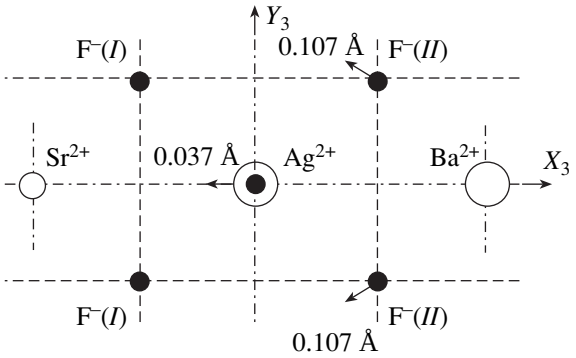

Fig. 4. A fragment of the section of the $Sr_{0.95}Ba_{0.05}F_2$: Ag^{2+} crystal lattice in the plane aligned parallel to the crystallographic plane (110) and passing through the Ag^{2+} and Ba^{2+} impurity cations. Arrows indicate the directions of atomic displacements. Numbers near the arrows are the atomic displacements calculated in the framework of the Born–Mayer–Huggins model.

3.2. Copper complexes. The basic results of our investigations of bivalent copper complexes in $Ca_xSr_{1-x}F_2$ ($0 \le x \le 1$) mixed crystals were published in our recent paper [7]. For this reason, we will consider some additional experimental data obtained in the study of $Sr_{1-x}Ba_xF_2$: Cu^{2+} (x = 0.05 and 0.5) crystals.

Table 1. Components of the tensors of the spin Hamiltonian (1) for $[AgF_8]^{6-}$ complexes (parameters of the hyperfine and superhyperfine interactions are given in MHz)

Parameter	CaF_2	$Ca_{0.95}Sr_{0.05}F_2$	$Ca_{0.05}Sr_{0.95}F_2$	SrF_2	$Sr_{0.95}Ba_{0.05}F_2$	BaF_2	Parameter
	1	2	3	4	5	6	
$g_\perp$	2.5840 ± 0.0005	2.581 ± 0.002	2.579 ± 0.002	2.5780 ± 0.0005	2.064 ± 0.003	2.085 ± 0.001	g_x
					2.097 ± 0.003	2.109 ± 0.001	g_y
$g_\parallel$	1.9071 ± 0.0002	1.911 ± 0.001	1.920 ± 0.001	1.9235 ± 0.0002	2.756 ± 0.003	2.687 ± 0.001	g_z
$a_\perp$	28 ± 3	~30	31 ± 5	33 ± 3	51 ± 5	63 ± 2	a_x
					38 ± 5	64 ± 3	a_y
$a_\parallel$	0 ± 2	~0	17 ± 3	21 ± 1	~15	40 ± 3	a_z
$A_\perp(I)$	55 ± 3	50 ± 5	35 ± 5	32 ± 3	350 ± 10	420 ± 10	$A_{xx}(I)$
					43 ± 10	56 ± 10	$A_{yy}(I)$
$A_\parallel(I)$	702 ± 3	700 ± 5	695 ± 5	692 ± 3	440 ± 10	480 ± 10	$A_{zz}(I)$
					270 ± 10	195 ± 10	$A_{xz}(I)$
$A_{xx}(II)$	8.1 ± 2	8 ± 4	8 ± 5	7.6 ± 2	360 ± 10	–	$A_{xx}(II)$
$A_{yy}(II)$	31.3 ± 2	31.4 ± 4	34 ± 5	35.6 ± 2	45 ± 10	–	$A_{yy}(II)$
$A_{zz}(II)$	45.6 ± 2	4.4 ± 4	41 ± 5	39.8 ± 2	430 ± 10	–	$A_{zz}(II)$
$A_{xz}(II)$	44.8 ± 2	45 ± 4	45 ± 5	45.7 ± 2	260 ± 10	–	$A_{xy}(II)$

Note: The data presented in columns 1–4 refer to trigonal silver complexes, and the data cited in columns 5 and 6 relate to orthorhombic silver complexes.

Table 2. Components of the tensors of the spin Hamiltonian (3) for $[CuF_8]^{6-}$ complexes (parameters of the hyperfine and superhyperfine interactions are given in MHz)

Parameter	CaF_2	$Ca_{0.95}Sr_{0.05}F_2$		$Ca_{0.5}Sr_{0.5}F_2$		$Ca_{0.05}Sr_{0.95}F_2$		SrF_2	$Sr_{0.95}Ba_{0.05}F_2$
	1	2	3	4	5	6	7	8	9
g_x	2.099 ± 0.001	2.098 ± 0.001	2.101 ± 0.001	2.098 ± 0.001	2.20 ± 0.01		2.493 ± 0.001	2.493 ± 0.001	2.49 ± 0.01
g_y	2.147 ± 0.001	2.145 ± 0.001	2.141 ± 0.001	2.139 ± 0.001	2.20 ± 0.01		2.493 ± 0.001	2.493 ± 0.001	2.49 ± 0.01
g_z	2.802 ± 0.001	2.795 ± 0.001	2.792 ± 0.001	2.756 ± 0.001	2.36 ± 0.01	2.751 ± 0.001	2.084 ± 0.001	2.084 ± 0.001	2.08 ± 0.01
a_{xx}	97 ± 3	98 ± 10	100 ± 20	70 ± 10			26 ± 5	26 ± 5	~25
a_{yy}	96 ± 3	96 ± 10	100 ± 20	70 ± 10			26 ± 5	26 ± 5	~25
a_{zz}	76 ± 3	71 ± 10	70 ± 20	≈0		≈0	362 ± 5	362 ± 5	360 ± 15
Q	–11 ± 3	–10 ± 5	–10	–7 ± 5			–8 ± 5	–8 ± 3	~7
A_{xx}	221 ± 5	230 ± 15	230 ± 20	235 ± 15			95 ± 10	99 ± 3	100 ± 20
A_{yy}	136 ± 5	130 ± 15	130 ± 20	115 ± 15			380 ± 15	380 ± 8	380 ± 20
A_{zz}	58 ± 3	60 ± 10	60 ± 20	70 ± 10		60 ± 20	125 ± 15	127 ± 5	120 ± 20
A_{ij}	89 ± 5	80 ± 15	80 ± 20	80 ± 15			85 ± 15	87 ± 5	85 ± 20

Note: The data presented in columns 1–4 and 6 refer to the orthorhombic centers (*ij–xy*), and the data cited in columns 5 and 7–9 relate to the trigonal centers (*ij–xz*).

Unlike the silver centers, which are stable in the univalent state in the grown crystals, the copper centers are located at lattice sites of fluorite crystals in the bivalent state. The same situation is observed for impurity ions in the mixed crystals under investigation. In actual fact, the copper complexes exhibit EPR spectra without additional irradiation of the samples. It was revealed that the incorporation of Ba^{2+} impurity ions in small amounts ($x = 0.05$) only slightly affects the properties of off-center bivalent copper complexes, which are usually formed in SrF_2 : Cu crystals and have the C_{4v} symmetry.

The magnetic properties of the bivalent copper impurity complexes in $Ca_xSr_{1-x}F_2$ ($0 \le x \le 1$) and $Sr_{1-x}Ba_xF_2$ ($x = 0.05$) crystals can be adequately described by the spin Hamiltonian

$$\begin{aligned}\mathbf{H}_s &= \beta_e(\mathbf{B}_0 \cdot \mathbf{g} \cdot \mathbf{S}) \\ &+ [(\mathbf{S} \cdot \mathbf{a} \cdot \mathbf{I}_{\mathrm{Cu}}) - g_n^{\mathrm{Cu}}\beta_n(\mathbf{B}_0 \cdot \mathbf{I}_{\mathrm{Cu}})] \\ &+ \sum_i [(\mathbf{S} \cdot \mathbf{A}_{\mathrm{F}(i)} \cdot \mathbf{I}_{\mathrm{F}(i)}) - g_n^{\mathrm{F}}\beta_n(\mathbf{B}_0 \cdot \mathbf{I}_{\mathrm{F}(i)})].\end{aligned} \tag{3}$$

The tensor components of the spin Hamiltonian (3) for $Sr_{0.95}Ba_{0.05}F_2$: Cu^{2+} crystals are almost identical to those for SrF_2 : Cu^{2+} crystals. However, compared to the latter crystals, the resonance lines in the EPR spectra of the $Sr_{0.95}Ba_{0.05}F_2$: Cu^{2+} crystals are four or five times broader and have an asymmetric shape. The last circumstance clearly indicates that there is a certain scatter in the directions of the principal axes of the electron Zeeman and hyperfine interaction tensors due to a random distribution of Ba^{2+} impurity ions in the second coordination sphere of the cationic environment of the Cu^{2+} ion. In addition to the tetragonal copper complexes, the $Sr_{0.95}Ba_{0.05}F_2$: Cu^{2+} crystals involve orthorhombic centers (C_{2v}) that are similar to those revealed in the $Ca_{0.05}Sr_{0.95}F_2$: Cu^{2+} samples [7]. The concentration of orthorhombic centers is 20–25 times less than that of tetragonal copper complexes. Consequently, we observed only the EPR spectrum of the copper impurity centers in the orientation $C_2 \parallel \mathbf{B}_0$. The spectra of the impurity centers in other orientations were unresolved against the background of the intense spectra of the tetragonal copper complexes.

As regards the $Sr_{0.5}Ba_{0.5}F_2$: Cu^{2+} crystals, we observed the EPR spectra of the copper impurity centers with a nearly tetragonal symmetry of the magnetic properties. These spectra resemble the spectra of off-center copper complexes in the BaF_2 crystal but exhibit considerably more broadened lines. X-ray diffraction analysis revealed that the $Sr_{0.5}Ba_{0.5}F_2$: Cu^{2+} samples consist of a large number of differently oriented grains with diffuse boundaries.

Table 2 presents the magnetic parameters of the copper impurity centers revealed in $Ca_xSr_{1-x}F_2$ ($0 \le x \le 1$) [7] and $Sr_{1-x}Ba_xF_2$ ($x = 0.05$). These parameters characterize the static properties of the copper complexes and their dependence on the composition of the mixed crystals.

4. THE JAHN–TELLER EFFECT IN COPPER AND SILVER COMPLEXES WITH THE ORBITAL GROUND STATE T_{2g} UNDER STRAIN

For a qualitative analysis of the influence of local distortions on the shape of the lower sheet of the adiabatic potential for $[MeF_8]^{6-}$ ($Me = Cu^{2+}$ or Ag^{2+}) impurity complexes in $Ca_xSr_{1-x}F_2$ and $Ba_xSr_{1-x}F_2$ crystals, we used the Opik–Pryce method [10]. The Hamiltonian of the studied complex in the cluster approximation can be represented as the sum of two terms:

$$H = H_0 + H_1. \tag{4}$$

Here, the first term describes the cubic crystal field acting on the impurity ion and can be written in the form

$$H_0 = B_4(O_4^0 + 5O_4^4). \tag{5}$$

and the second term characterizes the perturbation of the states of this ion,

$$\begin{aligned} H_1 = {} & \frac{1}{2\mu_E}(P_\varepsilon^2 + P_\vartheta^2) + \frac{1}{2\mu_T}(P_{xy}^2 + P_{yz}^2 + P_{zx}^2) + V_T(Q^T) \\ & + V_E(Q^E) + U_T(Q^T) + U_E(Q^E) + H_{\text{strain}} + H_{LS}. \end{aligned} \tag{6}$$

According to [11], the perturbation operator (6) includes the kinetic energies of the nuclei involved in the impurity complex (the first two terms); the potential energies of the Jahn–Teller interaction with the trigonal (V_T) and tetragonal (V_E) vibrational modes,

$$V_T(Q^T) = V_T(Q_{xy}T_{xy} + Q_{yz}T_{yz} + Q_{zx}T_{zx}) \tag{7}$$

$$V_E(Q^E) = V_E(Q_\varepsilon E_\varepsilon + Q_\vartheta E_\vartheta); \tag{8}$$

and the elastic energies of the lattice due to Jahn–Teller distortions of the trigonal (U_T) and tetragonal (U_E) types,

$$U_T(Q^T) = \frac{\mu_T\omega_T^2}{2}(Q_{xy}^2 + Q_{yz}^2 + Q_{zx}^2), \tag{9}$$

$$U_E(Q^E) = \frac{\mu_E\omega_E^2}{2}(Q_\varepsilon^2 + Q_\vartheta^2). \tag{10}$$

In the perturbation operator (6), the lattice strains induced by alkaline-earth impurity ions are represented by the operator

$$\begin{aligned} H_{\text{strain}} = {} & V_{TS}(e_{xy}T_{xy} + e_{yz}T_{yz} + e_{zx}T_{zx}) \\ & + V_{ES}(e_\varepsilon E_\varepsilon + e_\vartheta E_\vartheta), \end{aligned} \tag{11}$$

and the spin–orbit interactions are described by the operator

$$H_{LS} = \lambda(L_XS_X + L_YS_Y + L_ZS_Z). \tag{12}$$

The Jahn–Teller interaction constants were calculated within the point crystal-field approximation [12]:

$$V_E = \frac{\sqrt{2}|e|q\langle r^4\rangle}{21\pi\varepsilon_0 a_0^6}\left[\frac{20}{9} + 3\frac{\langle r^2\rangle}{\langle r^4\rangle}a_0^2\right], \tag{13}$$

$$V_T = \frac{\sqrt{3}|e|q\langle r^4\rangle}{21\pi\varepsilon_0 a_0^6}\left[\frac{100}{27} + 3\frac{\langle r^2\rangle}{\langle r^4\rangle}a_0^2\right]. \tag{14}$$

The components of the displacement vectors for ligands of the impurity ion were calculated with the pair interaction potential (2). These components were used to construct the three-dimensional vector of collective displacements R. After a linear transformation, the vector R was decomposed into the strain tensor components e_{xy}, e_{yz}, e_{zx}, e_ε, and e_ϑ.

The shape of the lower sheet of the adiabatic potential was analyzed for the case when only one alkaline-earth impurity ion is involved in the nearest cationic environment of the nd^9 ion. It was found that the strain tensor components for tensile strains are approximately 1.7 times less than those for compressive strains. According to our calculations, the interaction energy is approximately equal to 2400 cm^{-1} for strains of the first type and 4100 cm^{-1} for strains of the second type.

Analysis of the adiabatic potential surface shape demonstrates that, in the case when the Jahn–Teller interaction energy E_{JT} is substantially higher than the strain energy $E_{\text{strain}}(e_{xy})$, the lower sheet of the adiabatic potential for the trigonal silver complexes remains a quadruple-well sheet (as is the case with CdF_2, CaF_2, and SrF_2 crystals); however, the potential wells have different depths. The bottoms of two potential wells are located below the bottoms of the other two wells; correspondingly, the barrier between the potential wells decreases in height. An increase in the Jahn–Teller interaction energy E_{JT} leads to the disappearance of the barriers between the potential wells and the formation of a single well corresponding to a static orthorhombic distortion of the complex under consideration.

The sextuple-well adiabatic potential for the orthorhombic copper complexes in CdF_2 and CaF_2 crystals is characterized by more complex distortions. It turned out that appreciable changes in the parameters of the low-temperature EPR spectra of these complexes can be achieved only if the strain energy is 1.5–2 times higher than the Jahn–Teller interaction energy.

Thus, we estimated the upper limits of the Jahn–Teller interaction energy for trigonal silver complexes in CdF_2, CaF_2, and SrF_2 crystals and for orthorhombic copper complexes in CdF_2 and CaF_2 crystals. The lower limits of the Jahn–Teller interaction energy are determined by the spin–orbit interaction energies for Ag^{2+} and Cu^{2+} ions. This inference stems from the fact that the main features of the strong Jahn–Teller interaction are observed experimentally and that no indications of the suppression of the Jahn–Teller effect through the spin–orbit interaction are revealed in the EPR spectra.

It should be noted that the strains induced by alkaline-earth impurity ions bring about changes not only in the relative depths of the wells of the adiabatic potential but also in their relative positions in the system of normal coordinates. In turn, this leads to changes in the overlap integrals of the vibrational functions corresponding to the vibronic states in the adjacent wells of the adiabatic potential of the complex under investigation and, consequently, to changes in the tunneling probabilities. However, the temperature dependences of these probabilities are strongly affected by the relative shifts of the vibronic energy levels in the adjacent wells of the adiabatic potential [13, 14]. It is worth noting that the tunneling transitions between the wells of the adiabatic potential can occur without and with a spin flip. In the former case, an increase in the temperature is accompanied by gradual variations in the electron Zeeman interaction tensor components in the EPR spectra toward the mean value $(g_x + g_y + g_z)/3$. As a result, the isotropic EPR line should arise at sufficiently high temperatures. In the latter case, the temperature dependences of these parameters are associated primarily with the thermal expansion of the crystal lattice and an increase in the tunneling rate results in a decrease in the spectral intensity due to a decrease in the number of impurity centers involved in resonance absorption of microwave energy. This can be explained by the fact that, over one period of oscillations of the microwave field created by the spectrometer generator, rapidly tunneling centers repeatedly violate the phase conditions for resonance absorption of microwave energy. According to Zaritskiĭ *et al.* [14], the probability of the tunneling spin-flip transition in Jahn–Teller complexes, which are characterized by triply degenerate orbital ground states and high energies of spin–orbit interactions, is larger than the probability of the tunneling transition without spin flip.

5. DISCUSSION AND CONCLUSIONS

The results obtained in this work and in our earlier investigations [2–4, 7] demonstrate that the parameters of the vibronic interactions in eightfold-coordinated complexes with the nd^9 electron configuration ($n = 3$ and 4) can radically change both with variations in the size of the coordination cube of the impurity ion and upon distortion of this cube. In the experiments performed, the volume changes in the coordination cube were accomplished through the incorporation of nd^9 ions into ionic crystals belonging to the same structural group (the fluorite family). By ignoring the overlap between the electron shells of the nd^9 ion and the electron shells of the alkaline-earth ions involved in the first coordination sphere of the cationic environment of this ion, we can make the inference that, in this crystal family, the most essential differences in the properties of the nd^9 paramagnetic complexes are associated primarily with changes in the distance between the impurity ion and the ligand.

According to x-ray diffraction analysis of the mixed crystals $Ca_xSr_{1-x}F_2$ ($0 \le x \le 1$) [7], the mean distances between impurity ions and the ligands can also change with variations in the relative content of cations in the crystals. However, this gives rise to considerable lattice distortions in the neighborhood of the paramagnetic ion.

As follows from the results obtained in the present work, the introduced parameter η makes it possible to predict certain properties of nd^9 eightfold-coordinated cubic complexes. The values of $\eta = 0.79$ and 0.83 can be considered to be critical. This is evident from the noticeable differences in the spin Hamiltonian parameters for orthorhombic copper complexes in $Ca_{0.5}Sr_{0.5}F_2$ and CaF_2 crystals and also from drastic changes in the magnetic properties of bivalent silver centers in $Sr_{0.95}Ba_{0.05}F_2$ crystals. It should be noted that the compressive strains induced in the $Ca_{0.95}Sr_{0.05}F_2$ crystals bring about the formation of orthorhombic bivalent silver centers rather than trigonal centers. At the same time, no orthorhombic centers are observed in the $Ca_{0.5}Sr_{0.5}F_2$ crystals.

The theoretical analysis (briefly outlined in the preceding section) allowed us to estimate the Jahn–Teller interaction energies for the orthorhombic copper complexes and trigonal silver complexes. The estimated energies are as follows: $E_{JT}(Cu^{2+}) \approx 1200$–$1600$ cm^{-1} and $E_{JT}(Ag^{2+}) \approx 2000$–$2500$ cm^{-1}. It is evident that, in the case of so strong a Jahn–Teller interaction, the over-barrier transitions between the potential wells cannot occur at temperatures of ~35 K. Therefore, the disappearance of the EPR spectra of the conventional (unmixed) crystals at these temperatures [2–4] can be explained in terms of tunneling transitions. Since the location of the resonance lines in the EPR spectra is virtually independent of temperature, the tunneling transitions between the potential wells are most likely attended by spin flip.

The angular dependences of the EPR spectra of the trigonal silver centers and orthorhombic copper centers in the conventional crystals correspond to static distortions of these centers, and the relative intensities suggest a small tunneling splitting of the ground vibronic levels ($\delta < 0.5$ cm^{-1}). Moreover, judging from the x-ray diffraction data, the energy of random strains in our samples (CaF_2 and SrF_2 crystals) cannot exceed 2–3 cm^{-1}. Hence, the disappearance of the EPR spectra of the conventional crystals can be explained by spin-flip tunneling through the excited vibronic energy levels lying approximately 25–35 cm^{-1} (35–50 K on the temperature scale of energy) above the ground levels.

As was noted above, the temperature at which the EPR spectra can be observed increases to 85 K for Ag^{2+} trigonal centers and to 120 K for Cu^{2+} orthorhombic centers [7]. Apparently, this can be associated with the relative shifts of the vibronic energy levels by approximately 35 and 60 cm^{-1}, respectively. However, the sur-

prising thing is that the strains induced by alkaline-earth impurity cations of the second coordination sphere of the cationic environment more strongly affect the state of the copper ion as compared to that of the silver ion, even though the silver ion is characterized by a larger constant of interaction with strains. Let us attempt to explain this disagreement between the experimental data and the results of the theoretical analysis. First, we should note that the interaction parameters were estimated within the point model of the crystal field of ligands without regard for the covalence effects. Since the fundamental electron functions for silver and copper ions differ in the complexes under investigation, the covalence of the bonds between these ions and the surrounding ligands can manifest itself in a different manner. Another reason for the above disagreement can reside in the fact that the linear approximation used in our consideration disregards both the higher terms in the expansion of the Jahn–Teller interaction operator and the anharmonicity of vibrations of nuclei involved in the cluster. Moreover, we should take into account that, in the course of crystal growth, different distributions of alkaline-earth impurity cations can be formed in the second coordination sphere of the cationic environment of the silver and copper ions. This can be due to the fact that, during crystallization, silver and copper ions are incorporated into the crystal lattice in different valence states. However, it is clear that the influence of strains induced by impurity diamagnetic ions of the second coordination sphere is reduced to relatively small distortions of the wells of the adiabatic potential and to shifts of the vibronic levels in these wells by 25–60 cm^{-1}. As follows from the above experimental data on the Ag^{2+} trigonal complexes, these shifts of the energy levels lead to changes in the tunneling rate of the Jahn–Teller complex through the barriers between the potential walls but cannot induce vibronic interactions with tetragonal vibrational modes.

ACKNOWLEDGMENTS

We would like to thank B.Z. Malkin and A.E. Nikiforov for their participation in discussions of the experimental results and for many pieces of helpful advice.

REFERENCES

1. I. B. Bersuker, *The Jahn–Teller Effect and Vibronic Interactions in Modern Chemistry* (Plenum, New York, 1984; Nauka, Moscow, 1987).
2. M. M. Zaripov and V. A. Ulanov, Fiz. Tverd. Tela (Leningrad) **30** (5), 1547 (1988) [Sov. Phys. Solid State **30**, 896 (1988)].
3. M. M. Zaripov and V. A. Ulanov, Fiz. Tverd. Tela (Leningrad) **31** (10), 251 (1989) [Sov. Phys. Solid State **31**, 1796 (1989)]; Fiz. Tverd. Tela (Leningrad) **31** (10), 254 (1989) [Sov. Phys. Solid State **31**, 1798 (1989)].
4. M. M. Zaripov, V. A. Ulanov, and M. L. Falin, Fiz. Tverd. Tela (Leningrad) **31** (2), 248 (1989) [Sov. Phys. Solid State **31**, 319 (1989)]; Fiz. Tverd. Tela (Leningrad) **31** (11), 289 (1989) [Sov. Phys. Solid State **31**, 2004 (1989)].
5. S. K. Hoffmann and V. A. Ulanov, J. Phys.: Condens. Matter **12**, 1855 (2000).
6. H. Bill, C. M. Millert, and R. Lacroix, in *Proceedings of the XVII Congress AMPERE "Magnetic Resonance and Related Phenomena," 1972*, Ed. by V. Hovi (North-Holland, Amsterdam, 1973), p. 233.
7. V. A. Ulanov, M. M. Zaripov, V. A. Shustov, and I. I. Fazlizhanov, Fiz. Tverd. Tela (St. Petersburg) **40**, 445 (1998) [Phys. Solid State **40**, 408 (1998)].
8. D. Bingham, A. N. Cormack, and C. R. A. Catlow, J. Phys.: Condens. Matter **1**, 1205 (1989).
9. R. C. Baetzold, Phys. Rev. B **36**, 9182 (1987).
10. U. Opik and M. H. L. Pryce, Proc. R. Soc. London, Ser. A **238**, 425 (1957).
11. A. Abragam and B. Bleaney, *Electron Paramagnetic Resonance of Transition Ions* (Clarendon, Oxford, 1970; Mir, Moscow, 1973), Vol. 2.
12. C. A. Bates, Phys. Rep. **35** (3), 187 (1978).
13. V. S. Vikhnin, Fiz. Tverd. Tela (Leningrad) **20** (5), 1340 (1978) [Sov. Phys. Solid State **20**, 771 (1978)].
14. I. M. Zaritskiĭ, V. Ya. Bratus', V. S. Vikhnin, *et al.*, Fiz. Tverd. Tela (Leningrad) **18** (11), 3226 (1976) [Sov. Phys. Solid State **18**, 1883 (1976)].

Translated by O. Borovik-Romanova

Physics of the Solid State, Vol. 44, No. 8, 2002, pp. 1480–1483. From Fizika Tverdogo Tela, Vol. 44, No. 8, 2002, pp. 1418–1420.

PROCEEDINGS OF THE XI FEOFILOV WORKSHOP "SPECTROSCOPY OF CRYSTALS ACTIVATED BY RARE-EARTH AND TRANSITION-METAL IONS"

(Kazan, Tatarstan, Russia, September 24–28, 2001)

The Plasticity of the $Cu(H_2O)_6^{2+}$ Jahn–Teller Complex Affected by Lattice Strains and Cooperative Interactions[1]

M. A. Augustyniak-Jabłokow*, K. Łukaszewicz, A. Pietraszko**, V. E. Petrashen**, and Yu. V. Yablokov**

** Institute of Molecular Physics, Polish Academy of Sciences, Poznań, 60-179 Poland*

e-mail: yablokov@ifmpan.poznan.pl

*** Institute of Low Temperature and Structural Research, Polish Academy of Sciences, Wrocław, 50-950 Poland*

**** Zavoĭskiĭ Kazan Physical Technical Institute, Russian Academy of Sciences, Kazan, Tatarstan, 420029 Russia*

Abstract—The EPR spectra evolution of $Cs_2Zn_{1-x}Cu_x(ZrF_6)_2 \cdot 6H_2O$ (x = 0.01, 0.6, 0.8, and 1.0) in the temperature range 4.2–330 K and the x-ray structure analysis of the compound with x = 1.0 in the range 150–327 K show that the Jahn–Teller (JT) complex $Cu(H_2O)_6$ coordination sphere undergoes a plastic deformation. The observed effect is due to the combined influence of small lattice strains existing in the paraphase and a new one appearing as a result of a ferroelastic phase transition and increasing with decreasing temperature below T_c. It is proved that both cooperative interactions between JT complexes and ferroelastic strain stabilize a certain JT configuration. The problem of instability of a JT configuration compressed at $T \sim 265$ K is discussed. © *2002 MAIK "Nauka/Interperiodica".*

EPR study of a series of compounds $Cs_2Zn_{1-x}Cu_x(ZrF_6)_2 \cdot 6H_2O$ ($0.01 \le x \le 1$) for $x \ge 0.6$ has shown an extremely strong temperature dependence of the resonance line positions [1]. Temperature dependences of all three principal values of the *g*-factor indicate very weak lattice deformations of the position occupied by the Jahn–Teller (JT) $Cu(H_2O)_6^{2+}$ complex, i.e., very small differences in the energy of its possible JT configurations. Such a situation remains weakly investigated and presents interesting possibilities in the study of JT dynamics.

Recently, new light was cast on this problem by structural and EPR studies [2, 3]. It was found that the ferroelastic phase transition take place in $Cs_2Cu(ZrF_6)_2 \cdot 6H_2O$ at 320 K followed by a gradual change in the $Cu(H_2O)_6$ configuration from tetragonal elongated along one C_4 (Cu–$O_3 \equiv R_3$) direction through tetragonal compressed along another C_4 axis (Cu–$O_1 \equiv R_1$) at ~265 K to elongated again along a third C_4 axis (Cu–$O_2 \equiv R_2$) at ~150 K. The temperature dependences of the R_k are shown in Fig. 1, wherein the main structural results of the paper [3] are collected. On the basis of these data, the EPR results were interpreted in the framework of continuous transformation of the adiabatic potential surface of the weakly deformed complex. Ferroelastic strains appearing after phase transitions and cooperative JT interactions were considered to be the reasons behind the dramatic changes in the structure and EPR parameters. Here, we analyze these processes in more detail, focusing our attention on the reasons for and mechanisms of the transformations in question. The EPR data of the diluted compounds will be taken into consideration. *X*- and *Q*-band EPR studies were performed in the temperature range 4.2–330 K.

RESULTS AND DISCUSSION

The temperature dependences of *g*-values for the compounds with x = 0.8 and 0.6 compared with data for x = 1 and 0.01 are shown in Fig. 2. We shall analyze them in the way described previously [3].

The universal factors stabilizing the definite JT configuration and determining the JT complex dynamics are low symmetry strains in the crystal and cooperative interactions between JT complexes [4]. The octahedral complex is elongated along R_3 in the paraphase of the $Cs_2Cu(ZrF_6)_2 \cdot 6H_2O$ crystal with symmetry *Pmnn*. The corresponding minimum on the adiabatic potential surface in the $\rho_0\varphi$ coordinate space corresponds to φ =

[1] This article was submitted by the authors in English.

$\varphi_0 = 0$ and is lower than the other two by $\delta E_{3-1(2)} \equiv \delta_{31(2)} = 230$ cm^{-1} (Fig. 3). The ferroelastic transition to the phase with $P2_1/n$ symmetry leads to the appearance of some additional deformation, which sharply arises at $T_c \cong 320$ K and then gradually increases in the temperature interval 320–(~180–200) K and results in a smooth change in the $g_2(R_2)$ and $g_3(R_3)$ values. The spontaneous strain appearing below the ferroelastic phase transition has a certain component along R_2 with $\varphi = \varphi_0 + 120°$ and increases with decreasing temperature. The resulting deformation also increases with decreasing temperature. Its direction changes from $\varphi = 0$ and at about 265 K, leads to a configuration compressed along R_1 (with $R_2 = R_3$) for $\varphi = 60°$. With a further decrease in temperature, the resulting deformation changes to resemble the behavior of the *b*, *c* and monoclinic angle β (Fig. 1). The last one can be considered the phase transition order parameter. At low temperatures, the $Cu(H_2O)_6$ complex configuration is again nearly tetragonal, but it is elongated along R_2 with $\varphi = 120°$. All these transformations result in a change in the adiabatic potential surface; this change can be treated as a manifestation of plasticity of the JT complex coordination sphere [4].

In the discussed transformations, the cooperative JT interactions are also taken into consideration. Their existence is proved directly by the differences in the temperature dependences of $g_k(T)$ for various copper concentrations (Fig. 2). Decreasing of the JT ion concentration moves the interval of strong $g_{2,3}(T)$ changes from the 180–250 K region for $x = 1$ to regions of 80–180 K for $x = 0.8$ and of 70–170 K for $x = 0.6$, respectively. According to [1], the cooperative interactions in $Cs_2Cu(ZrF_6)_2 \cdot 6H_2O$ occur through the phonon field, i.e., through the vibrations of the crystal lattice. They diminish because of the increase in the distances between JT ions and thermal vibrations of the crystal lattice.

In the $Cs_2Zn_{1-x}Cu_x(ZrF_6)_2 \cdot 6H_2O$ crystals with $x < 1.0$, the cooperative interactions stabilize the same configuration elongated along R_2, as in the crystal with $x = 1.0$. This was shown by x-ray investigations of the crystals with $x = 1$ [3] and by an EPR study of the crystal with $x = 0.01$ [5]. The equality of the low temperature $g_i(T)$-values (at 4.2 K) and nearly equal high temperature $g_i(T)$-values (at 300 K) in all considered crystals allow us to extend this conclusion to the $x = 0.6$ and 0.8 cases. These facts lead to the conclusion that both ferroelastic strains and cooperative JT interactions stabilize the same configuration of the JT $Cu(H_2O)_6$ complex. The ferroelastic deformation does this smoothly; the cooperative interactions result in sharp dependences of the $g_k(R_r)$ parameters. This action of the cooperative interaction was confirmed by theoretical analysis [1]. The energy of the cooperative interactions E_{coop} can be estimated due to the analysis of the temperature behavior of the intervals between different JT

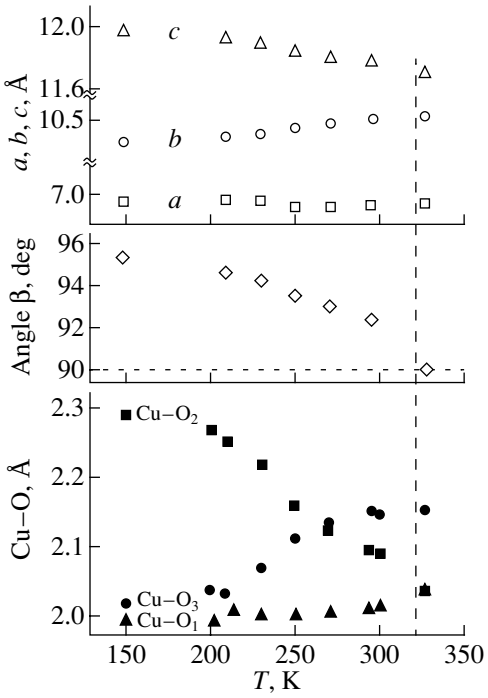

Fig. 1. Temperature dependences of the unit cell parameters and Cu–O distances.

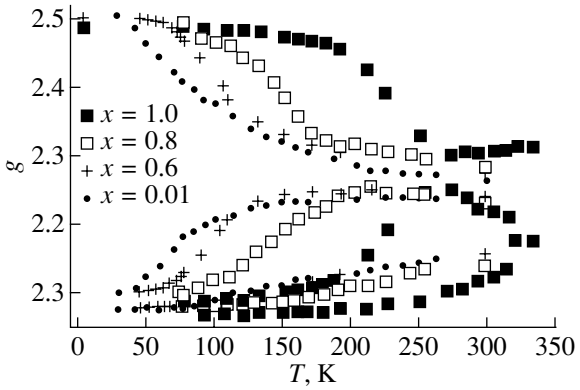

Fig. 2. Temperature dependences of the principal values of the *g*-factor in $Cs_2Zn_{1-x}Cu_x(ZrF_6)_2 \cdot 6H_2O$ with $x = 0.01$, 0.6, 0.8 and 1.0.

configurations [3]. As is shown in Fig. 3, the values of $\delta 23$ (between the ground and first excited configuration) diminish from ≈420 cm^{-1} in $Cs_2Cu(ZrF_6)_2 \cdot 6H_2O$, E_{coop} down to ~200 cm^{-1} in the crystal with $x = 0.8$ and down to ~180 cm^{-1} for $x = 0.6$.

Since the crystal with $x = 0.01$ has shown ferroelastic properties [5], the character of the $g_k(T)$ dependences (the intermediate *g*-value increases up to 225–

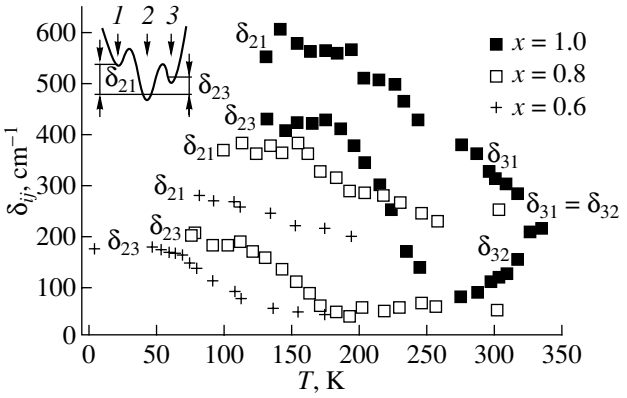

Fig. 3. Temperature dependences of the energy intervals δ_{mn} between JT configurations corresponding to minimums of the adiabatic potential surface for $x = 0.6$, 0.8, and 1.0.

250 K and then decreases above 250 K) allows us to postulate the existence of a hypothetical phase transition at $T_c \sim 550$ K in this crystal. The collected EPR data suggest the presence of such a phase transition also in the crystals with $x = 0.8$ and 0.6. First of all, we take into consideration the analogous convergence of the $g_{2,3}$ (g-large and g-intermediate) components in these crystals with $x = 0.6$, 0.8, and 1.0 and the mentioned tendency of the diminishing of the g-intermediate (it should be equal to g_1 (g-small) at $T > T_c$). EPR does not allow one to make a direct determination if a change in the axes directions occurs in these crystals. This can be done only by structural studies, which are presently in progress. However, a positive answer to this question can be obtained in the indirect way from other data. We shall discuss this situation in more detail.

Structural studies of $Cs_2Cu(ZrF_6)_2 \cdot 6H_2O$ show the equalizing and reversing of R_2 and R_3 bond lengths, but EPR studies do not show the expected equalizing of $g_{2,3}$-components. It would appear that the compressed configuration with $R_2 = R_3$ is stable under the conditions of structure determination but is not stable from the EPR point of view, as it tumbles down into configurations with $R_2 > R_3$ or $R_3 > R_2$. Let us return to the $x = 1$ crystal. From T_c down to approximately 280 K, the g_3-value decreases when the g_2-value increases. The g_1-value also decreases, but we concentrate on the two first values. Then, within an interval of about 20°, these g-components are relatively close but no crossing is observed. We call this interval the range of instability. Here, the configuration of the octahedron is very close to compressed and we postulate that the configuration of the compressed octahedron is unstable. One can conclude that this is a manifestation of a more general feature of instability in the conditions of degeneration. As concerns the x-ray diffraction data, we should point out that this method cannot distinguish between dynamic and space averaging. If the instability results in the simultaneous existence of weakly deformed complexes with different directions of elongation, the diffraction averages out this difference to zero, giving the same result as the dynamic averaging. The supposition that a similar situation occurs for the crystals with $x = 0.8$ and 0.6 is reasonable. It is obvious that at low temperatures, $Cu(H_2O)_6$ octahedrons are elongated along R_2 in all crystals. It does not seem realistic that at high temperatures the configuration of the $Cu(H_2O)_6$ complex elongated along R_3 for $x = 1$ (the hypothetic configuration for the paraelastic phase for $x = 0.01$) would be different for crystals with $x = 0.8$ and 0.6. Transition from the high temperature to the low temperature configuration requires the existence of a transitional range with a principal compression along R_1. The character of the $g_k(T)$ dependences in the corresponding ranges in the crystals with $x = 0.8$ and 0.6 are very similar. This is not surprising since the temperature changes of the ferroelastic deformations are very small in these compounds and the cooperative stabilization starts at lower temperatures.

Thus, the main result of the study of the $Cs_2Zn_{1-x}Cu_x(ZrF_6)_2 \cdot 6H_2O$ crystals is the discovery of continuous changes in the JT complex configuration initiated by temperature dependent ferroelastic strains and supported by cooperative vibronic interactions. This fact is a manifestation of the plasticity of the JT complex coordination sphere as one of the fundamental properties of its behavior. The concept of plasticity was introduced to describe the JT complex's unusual ability to adapt to the conditions produced by various crystal lattices [4, 6] when changes of axial and plane bond lengths are mutually dependent. In the crystal studied, the plasticity of the coordination sphere was first observed directly as a modification of the complex shape reflecting the lattice changes.

The correlated influence of ferroelastic strains and cooperative JT interactions on the stabilization of a definite JT configuration in the crystal in question should be accented. It was also concluded that cooperative JT interactions in the crystal studied are not the reason for the ferroelastic phase transition. However, at the same time, the JT $Cu(H_2O)_6$ complexes were shown to very strongly influence the temperature of the phase transition.

Of special interest is the question of the structural instability of the JT configuration compressed as a result of external factors. Of course, the reasons for the nonaveraging of the two rhombic configurations at relatively high temperature should be analyzed. We suppose that this effect is connected with the ferroelastic properties of the compounds studied. The existence of the ferroelastic domains and boundaries between them can produce heterogeneous or random strains, which strongly influence the EPR spectra of the JT ion [7]. It is important that the conditions of the formal degeneration of two JT configurations be exactly fulfilled in the

crystals studied. This allows accurate consideration of the posed problem.

REFERENCES

1. M. V. Eremin, A. Yu. Zavidonov, V. E. Petrashen', *et al.*, Fiz. Tverd. Tela (Leningrad) **29** (11), 3426 (1987) [Sov. Phys. Solid State **29**, 1962 (1987)].
2. P. E. Tomaszewski, A. Pietraszko, K. Łukaszewicz, and M. A. Augustyniak-Jabłokow, in *Abstracts of the 19th European Crystallographic Meeting, Nancy, France, 2000*, p. 427.
3. M. A. Augustyniak-Jabłokow, Yu. V. Yablokov, K. Łukaszewicz, *et al.*, Chem. Phys. Lett. **344** (3–4), 345 (2001).
4. I. B. Bersuker, J. Coord. Chem. **34**, 289 (1995).
5. M. Hitchman, Yu. V. Yablokov, V. E. Petrashen, *et al.*, Inorg. Chem. (in press).
6. I. B. Bersuker, *The Jahn–Teller Effect and Vibronic Interactions in Modern Chemistry* (Plenum, New York, 1984; Nauka, Moscow, 1987).
7. M. A. Augustyniak-Jabłokow, J. Phys. Chem. Solids **62**, 1319 (2001).

Physics of the Solid State, Vol. 44, No. 8, 2002, pp. 1484–1490. Translated from Fizika Tverdogo Tela, Vol. 44, No. 8, 2002, pp. 1421–1427.

PROCEEDINGS OF THE XI FEOFILOV WORKSHOP "SPECTROSCOPY OF CRYSTALS ACTIVATED BY RARE-EARTH AND TRANSITION-METAL IONS"

(Kazan, Tatarstan, Russia, September 24–28, 2001)

Ab initio Theory of the Electronic Structure and Spectra of Impurity *nl* Ions

N. A. Kulagin

Kharkov National University of Radio Electronics, National Academy of Sciences of Ukraine, Kharkov, 61045 Ukraine
e-mail: kulagin@kture.kharkov.ua

Abstract—The fundamentals of the theory of the electronic structure of impurity clusters and the results of numerical calculations for the iron-, lanthanum-, and actinium-group ions in $Me^{+n}:[L]_k$ clusters are presented. The effects of the interionic distance and ligands in the $Me^{+n}:[L]_k$ clusters on the electronic structure of the nl^N and $nl^{N-1}n'l'$ configurations of the 3*d*, 4*f*, and 5*f* ions are considered. The correspondence between the optical and x-ray spectra of different impurity crystals is also analyzed. © *2002 MAIK "Nauka/Interperiodica".*

1. INTRODUCTION

The electronic structure and the intensity of the intrashell $nl \longleftrightarrow nl$ transitions, forbidden within the dipole approximation, as well as other peculiarities of ions with a partly filled *nl* shell, are usually studied and calculated taking into account the influence of the nearest neighbor ions (ligands) and the effect of the excited configurations of opposite parity [1–5]. The direct influence of these configurations (via the dipole transition operator), as well as their indirect influence (through the crystal potential), is considered. The theory of the excited configurations is used, for example, in investigations of x-ray spectra [6, 7].

The difference in the electron density between a free ion and the ion in a solid or a cluster can be taken into account by using the X_α method [1–5] (the self-consistent-field method for clusters [6, 7]). However, the electronic structure of solids and the intensities of the spectral lines of impurity ions are often calculated using the free-ion functions found within the Hartree–Fock approximation [3, 4, 8].

It is well known that in solids, a significant redistribution of the electron density occurs in both the outer and inner electron shells of the iron-, lanthanum-, and actinium-group ions. This leads to a shift of the characteristic x-ray spectral lines [7, 9]. However, it is obvious that the wave functions of the excited configurations $3d^{N-1}4p$ and $3d^{N-1}4s$ of 3*d* ions and $4f^{N-1}5p$ and $4f^{N-1}6s$ of rare-earth ions are changed most significantly.

The analysis performed in [10, 11] revealed that the relative energy of the exited configurations of Me^{+n} and RE^{+n} ions is changed nonmonotonically [11–15]. It should be noted that investigation of the dependence of the electronic structure of $Me^{+n}:[L]_k$ clusters on the interionic distance makes it possible to determine the change in the spectral characteristics of the impurity crystals under pressure very accurately [16, 17].

In this paper, we continue the investigations of the electronic structure of impurity clusters started in [18] and consider the dependence of the electrostatic parameters and the energies of the ground-state and excited configurations and the x-ray spectra of Cr, Cu, and, partially, Fe, Ni, and Co ions, as well as of Nd, Eu, U, and a number of other *nl* ions in $Me^{+n}:[O^{-2}]_k$, $Me^{+n}:[F^-]$, and $Me^{+n}:[Cl^-]_k$ clusters with $k = 4, 5, 6$ on the interionic distance *R* in the range 1.7–2.5 Å.

2. THE SELF-CONSISTENT-FIELD METHOD FOR CLUSTERS

The self-consistent-field method for clusters is an extension of the Hartree–Fock–Pauli method [6, 8, 19] to clusters and solids [6, 7, 20, 21]; this method gives correct results in all the cases considered.

First, we consider the electronic structure of the *Me* ion in an $Me^{+n}:[L]_k$ cluster consisting of a central *Me* ion with the nl^N or $n'l^{N-1}n'l'$ configuration surrounded by *k* ions of the ligands *L* at a distance *R*. The ligand ions (O^{-2}, F^-, or Cl^-) have a configuration consisting of completely occupied nl^{4l+2} electron shells. The cluster symmetry corresponds to the symmetry of the crystal fragment under investigation.

Using the one-electron approximation and the central-field functions, the energy of the cluster can be written as [6, 7]

$$E(Me^{+n}:[L]_k) = E_0 + kE_1 + k'(E_z + E_c + E_{ex}), \quad (1)$$

where E_0 and E_1 are the energies of the central ion and ligand in the free state, respectively; E_z is the interaction energy between the electrons and a neighbor

nucleus; E_c and E_{ex} are the Coulomb and exchange interaction energies between the electrons of the central ion and the ligands, respectively; and k' is a coefficient depending on the symmetry of the cluster [7].

Minimizing functional (1) with respect to the radial parts (radial orbitals) of the one-electron wave functions of the central ion and the ligands gives the system of equations

$$\left[\frac{d^2}{dr^2} + \frac{2}{r}Y'(nl|r) - \varepsilon_{nl} - \frac{l(l+1)}{r^2}\right]P(nl|r) = X'(nl|r) + \sum_{n' \neq n}\varepsilon_{n'l}P(n'l|r), \quad (2)$$

which defines the radial orbitals of the central ion $P(nl|r)$ and those of the ligands $P(n'l'|r^*)$. Here, $Y'(nl|r)$ and $X'(nl|r)$ are the Coulomb and exchange potentials, respectively, and ε_{nl} is the one-electron energy. The system of equations (2) is similar to the Hartree–Fock system [19], but its solutions depend on the wave functions of all ions of the cluster. Equations for $Y'(nl|r)$ and $X'(nl|r)$ differ from the standard equations in having additional potentials (self-consistent potentials of the cluster):

$$\begin{aligned}\Delta Y(nl|r) &= r/2\sum_{k, k_1, n'l'}[a_{ll'}^{kk_1}Y_{kk_1}(n'l', n'l'|r) + b_{ll'}^{kk_1}Y_{kk_1}(nl, n'l'|r)],\\ \Delta X(nl|r) &= -\sum_{k, k_1, n'l'}[\alpha_{ll'}^{kk_1}Y_{kk_1}(nl, n'l'|r) + \beta_{ll'}^{k}r^{k_1}]P(n'l'|r);\end{aligned} \quad (3)$$

the tensor function $Y_{kk_1}(nl, n'l'|r)$ is defined in [11, 12]. The coefficients $a_{ll'}^{kk_1}$, $b_{ll'}^{kk_1}$, $\alpha_{ll'}^{kk_1}$, and $\beta_{ll'}^{k}$ are presented in [7] and have a sufficiently simple form for closed shells. For an individual cluster, the system of equations (2) can be used with the boundary conditions for a free atom $P(nl|r) \longrightarrow 0$ and $dP(nl|r)/dr \longrightarrow 0$ for $r \longrightarrow 0$. For a crystal, the Wigner–Seitz conditions $P(nl|r) \longrightarrow 0$ and $dP(nl|r)/dr|_{r \to a} \longrightarrow 0$ (a is the radius of the cluster) are more correct.

When deriving the equations for the additional potentials $Y(nl|r)$ and $X(nl|r)$, we expanded the ligand wave functions (chosen in the form of Roothaan functions [22]) in terms of functions centered on the central ion. The additional potentials and energy parameters of the cluster ions were calculated using the program described in [7].

It should be noted that for the iron-group ions, the relativistic effects are comparable in magnitude with the influence of the surroundings. For this reason, we used the Hartree–Fock–Pauli approximation, which takes into account the basic relativistic effects, such as the velocity dependence of the electron mass and the contact and spin contact interactions [1–3, 8]. Taking into account the relativistic effects leads to renormalization of the radial integrals. The method used for calculating the electronic structure of impurity ions gives results which are in reasonable agreement with the experimental data on both the optical spectra of impurity crystals and the energies of the characteristic x-ray spectral lines [6, 7].

Taking into account the Stark splitting of the free-ion levels within the crystal-field approximation, we represent the energy of the Stark components in the form

$$E(nl^N|\alpha\alpha' LSJ\Gamma) = E_0 + \sum_k f_k(l^N, \alpha\alpha' LS)F_k(nl, nl) + \chi(LSL'S'J)\eta(nl) + \sum_{k, q, i}B_{kq}Y_{kq}(\Theta_i, \Phi_i). \quad (4)$$

Here, the crystal-field parameters can be determined from the reference values $B_{kq\,\mathrm{test}}$ by using the formula

$$B_{kq} = B_{kq\,\mathrm{test}}\frac{(nl|r^k|nl)}{(nl|r^k|nl)_{\mathrm{test}}}\frac{R_{\mathrm{test}}^{k+1}}{R^{k+1}} \quad (5)$$

and the change in the distribution of the electron density is taken into account by varying the values of $(nl|r^k|nl)$ and R.

First, we solve the problem for the cluster consisting of an *Me* ion and ligands, because the influence of the ions of the more distant coordination shells on the radial wave functions is relatively small (about 1%) and can be neglected at the first step. At the same time, there is no restriction on the number of ions in the cluster under consideration.

3. THE ELECTRONIC STRUCTURE OF THE *nl* IONS IN Me^{+n} : $[O^{-2}]_k$ CLUSTERS

Using the Cr^{+n} ions in the Cr^{+n} : $[O^{-2}]_6$ cluster as an example, let us consider the change in the *d–p*(*s*)- and *f–d*(*p*)-interaction energy when a free *nl* ion is incorporated into a crystal or subjected to hydrostatic pressure, which changes the interionic distances in the cluster. Table 1 shows the values of the radial integrals required to determine the energy-level diagram of the $3d^N$ configuration and the values of the integrals specifying the energy of the 3*d*–4*p* interaction, $F^k(3d, 4p)$ and $G^k(3d, 4p)$, for the Cr^{+3} ion in the free state and in the cluster. The data obtained for the $3d^N$ configuration are seen to be in good agreement with known results.

It follows from Table 1 that as free chromium ions are incorporated into a crystal, the values of the radial integrals decrease by 25 to 700%. The decrease in the

Table 1. Theoretical values of the radial integrals for the Cr^{+3} ion in the $Cr^{+3}:[O^{-2}]_6$ cluster at different values of R

Integral	Free ion	R, Å				
		2.1	1.96	1.9	1.8	1.5
Configuration $3d^3$						
$F^2(3d, 3d)$, cm^{-1}	87080	72010	58448	50932	45863	44795
$F^4(3d, 3d)$, cm^{-1}	54582	42380	35644	30881	27796	29599
$\eta(3d)$, cm^{-1}	290.9	245.1	220.2	194.8	167.5	74.9
$(3d\|r\|3d)$, a.u.	1.093	1.351	1.561	1.721	1.839	2.100
Configuration $3d^24p$						
$F^0(3d, 4p)$, cm^{-1}	91284	65490	69606	71629	74294	
$F^2(3d, 4p)$, cm^{-1}	22295	9455	12485	14705	21010	
$G^1(3d, 4p)$, cm^{-1}	7778	2513	4924	7046	12430	
$G^3(3d, 4p)$, cm^{-1}	7193	2001	3838	5471	11135	
$\eta(3d)$, cm^{-1}	331.9	322.1	303.8	288.7	238.1	
$\eta(4p)$, cm^{-1}	642.0	97.6	129.6	153.3	198.8	
$(3d\|r\|3d)$, a.u.	1.018	1.064	1.148	1.219	1.474	
$(4p\|r\|4p)$, a.u.	2.734	3.538	3.314	3.210	3.045	
$\Delta E(3d^3 \longrightarrow 3d^24p)$, eV	17.8	21.8	16.1	9.9	11.6	

Table 2. Dependence of the energy levels (cm^{-1}) of the Cr^{+3} ion in the $Cr^{+3}:[O^{-2}]_6$ cluster on R_{Cr-O}

R_{Cr-O}, Å (calculation)	Energy level					
	^2E	$^2T_1$	$^4T_2$	$^2T_2$	$^4T_1(t_2^2e)$	$^4T_1(t_2e^2)$
2.0	14850	15652	16500	22171	24229	37661
1.96	14220	14969	18100	21538	25811	40324
1.9	12500	13113	20500	19392	27659	44176
Data for ruby						
Experiment	14433	15087	18133	21318	24767	39067
Semiempirical calculation	14354	14989	18108	21355	24843	39362

values of the parameters specifying the *d–p*-interaction energy is larger than the decrease in the parameters of the 3*d* shell. As might be expected, the most significant difference is observed between the changes in the average radii of the 3*d* and 4*p* shells. At $R = 2.1$ Å, the value of $\langle r\rangle_{3d}$ increases by 5% in comparison with that for the free ion and then grows by 46%. The values of $\langle r\rangle_{4p}$ increase by 14% at $R = 2.1$ Å.

As the interionic distance R decreases, the relative energy of the $3d^{N-1}4p$ configuration changes significantly; when the free ions are incorporated into the crystal ($R = 2.1$ Å), this energy increases from 17.8 to 21.8 eV and then decreases down to 9.9 eV as the radius of the coordination shell diminishes to 1.9 Å. It should be noted that the distance $R = 1.9$ Å corresponds to the size of the impurity $Cr^{+3}:[O^{-2}]_6$ cluster in ruby.

The experimental dependence of the optical spectrum of ruby on external pressure is well described by the theoretical data presented in Table 2 for the $Cr^{+3}:[O^{-2}]_6$ energy diagram, which changes as R decreases. The calculated parameters B, C, and Dq (Table 3) at different R are compared with the data for the $Cr^{+3}:[O^{-2}]_6$ clusters in different laser crystals.

It should also be noted that by estimating the change in the *d–p*-interaction energy as the ratio of the squared value of the radial integral $F^3(3d, 4p)$ to the energy of the excited configuration, we obtain a nonlinear change in the *d–p*-interaction energy; at $R = 1.9$ Å, the energy decreases by 10–15% in comparison with the data for the free ion.

The behavior of bivalent and quadrivalent chromium ions is similar to the behavior of the trivalent chromium ion described above, with the appropriate

Table 3. Semiempirical and theoretical values of the integrals *B*, *C*, and *Dq* (cm^{-1}) for the Cr^{+3} ions in different crystals

Integral	α-Al_2O_3	$Y_3Al_5O_{12}$	$Gd_3Sc_5O_{12}$	$Cd_3Sc_2Ga_3O_{12}$	$Cr^{+3}:[O^{-2}]_6$
B	682	725	740	740	789
C	3120	3373	3578	3578	2829
Dq	1787	1650	1500	1500	1750

Table 4. Values of the radial integrals for the Cu^{+3} and Cu^{+2} ions in the $Cu^{+n}:[O^{-2}]_6$ clusters

Integral	Free ion	*R*, Å				
		2.5	2.0	1.95	1.9	1.8
			Cu^{+3}			
E, a.u.	–1636.7563	0.7564	0.7539	0.7551	0.7551	0.7557
ε_{3d}, a.u.	2.2391	2.2175	2.1578	2.1436	2.1273	2.1042
$(3d\|r\|3d)$, a.u.	0.8422	0.8414	0.8427	0.8434	0.9445	0.8463
$F^2(3d, 3d)$, cm^{-1}	129327	99498	98753	98711	98662	98618
$F^4(3d, 3d)$, cm^{-1}	80874	62188	61719	61680	61660	61625
$\eta(3d)$, cm^{-1}	925.2	910.8	909.5	909.3	908.8	908.1
			Cu^{+2}			
E, a.u.	–1638.1232	0.0841	0.0839	0.035	0.0832	0.0723
ε_{3d}, a.u.	1.4789	1.4477	1.3872	1.3735	1.3532	1.3356
$(3d\|r\|3d)$, a.u.	0.8837	0.8989	0.9013	0.9025	0.9043	0.9070
$F^2(3d, 3d)$, cm^{-1}	119110	93078	91987	91987	91796	91569
$F^4(3d, 3d)$, cm^{-1}	74806	58120	57495	57495	57365	57251
$\eta(3d)$, cm^{-1}	845.9	825.0	820.8	820.8	818.9	815.1

correction for the valency: the changes for the Cr^{+4} ions are 3–5% larger than those for the trivalent ions, while for the Cr^{+2} ions, the changes are smaller. In addition, a significant decrease in the relative energy of the $3d^3 4p$ configuration is observed for the Cr^{+2} ions, which leads to a sharp increase in the *d–p*-interaction energy. It should be noted that the transition energies in the $Cr^{+4}:[O^{-2}]_6$ cluster are consistent with the spectrum of ruby after irradiation by γ-rays [23]. Thus, under irradiation, some of the Cr^{+3} ions in ruby transform into Cr^{+4}, which was previously revealed through a shift in the Cr$K_{\alpha 1}$ x-ray spectral lines [21, 23].

The problem of the *d–s* interaction is also of importance in investigating the intensity of optical spectral lines (in the presence of the indirect influence of strong *s–p* interaction) and in explaining high-temperature superconductivity. We considered the change in the *d–s*-interaction energy within the approach chosen. In our opinion, the most interesting results are obtained for the Cu^{+2} and Cu^{+3} ions in the $Cu^{+n}:[L]_k$ clusters (for O^{-2}, F^-, Cl^-; $k = 4, 5, 6$); these results are presented in Tables 4 and 5. For these clusters, the relative energy of the excited $3d^{N-1}4s$ configuration averaged over all terms [6] shows a nonlinear dependence on the values of *k* and *R*, whereas the other quantities, such as the Slater integrals and the spin–orbit-coupling integrals, vary almost linearly. As a result, extreme values of the interaction energy are observed at certain values of the coordination number and interionic distance for bivalent and trivalent copper ions. The minimum relative energy of the excitation of a 3*d* electron to the 4*s* shell is achieved at the interionic distance *R* equal to 1.85 Å for Cu^{+3} at $k = 6$ and to 1.95 Å for Cu^{+2} at $k = 4$. The 40% decrease in the excitation energy of a 3*d* electron to the 4*s* shell obtained for the Cu^{+2} ion in the tetrahedral surroundings is a very important result. Due to a sharp decrease in the relative energy of the $3d^9 4s$ configuration of the Cu^{+2} ion and to a growth in the values of the radial integrals $F^0(3d, 4s)$ and $G^2(3d, 4s)$, the *d–s* interaction energy increases by almost 2 times. There is reason to believe that the existence of the absolute maximum of the *d–s*-interaction energy in the Cu^{+2} ions surrounded by four oxygen ions at $R = 1.95$ Å is directly related to the appearance of high-temperature superconductivity, because such an extremum was not observed for the other ions considered by us (Fe, Co, Ni, Zn).

By comparing the calculated dependences of the radial integrals on the interionic distance for the Me

Table 5. Theoretical values of the radial integrals and the energy of the $3d \longrightarrow 4s$ excitation for the Cu^{+2} ions in the $3d^8 4s$ configuration in the $Cu^{+2} : [O^{-2}]_4$ clusters at different values of R

Integral	R, Å				
	2.01	1.89	1.8	1.7	1.6
ε_{3d}, a.u.	1.7045	1.6715	1.6378	1.5895	1.5269
ε_{4s}, a.u.	0.9977	0.9939	0.9912	0.9884	0.9861
$(3d\|r\|3d)$, a.u.	0.8297	0.8345	0.8484	0.8507	0.8556
$(4s\|r\|4s)$, a.u.	2.3414	2.3516	2.3592	2.3678	2.3758
$F^0(3d, 4s)$, cm^{-1}	0.4852	0.4836	0.4812	0.4789	0.4767
$G^2(3d, 4s)$, cm^{-1}	0.0439	0.0434	0.0431	0.0430	0.0434
$E(3d^9 \longrightarrow 3d^8 4s)$, eV	1.892	1.713	1.428	1.632	1.784

Table 6. Theoretical values of the radial integrals for UIII and FmIV and for the $Me^{+n} : [L]_k$ cluster (with ligands F^-, O^{-2}, Cl^-) at different values of R

Integral	UIII	R, Å		
		2.2	2.37	2.4
		$U^{+2} : [F^-]_9$	$U^{+2} : [O^{-2}]_{12}$	$U^{+2} : [Cl^-]_9$
ε_{5f}, a.u.	0.8935	0.9104	0.9218	0.9342
ε_{6p}, a.u.	1.3552	1.3662	1.3796	1.3815
$F^2(5f, 5f)$, cm^{-1}	75169	65785	60560	59200
$F^4(5f, 5f)$, cm^{-1}	48895	42890	39406	38496
$F^6(5f, 5f)$, cm^{-1}	35810	31370	28850	28190
η_{5f}, cm^{-1}	2161.1	2086.7	2040.0	2011.8
$\langle r\rangle_{5f}$, a.u.	1.3249	1.4611	1.4784	1.4814
$\langle r\rangle_{6p}$, a.u.	1.9452	2.0977	2.1831	2.2212
	FmIV	$Fm^{+3} : [F^-]_9$	$Fm^{+3} : [O^{-2}]_{12}$	$Fm^{+3} : [Cl^-]_9$
ε_{5f}, a.u.	1.9516	1.9741	1.9940	1.9985
ε_{6p}, a.u.	2.3189	2.3267	2.3377	2.3406
$F^2(5f, 5f)$, cm^{-1}	103218	100380	99560	98330
$F^4(5f, 5f)$, cm^{-1}	68043	66180	65730	64900
$F^6(5f, 5f)$, cm^{-1}	48891	47670	47180	46870
η_{5f}, cm^{-1}	5294.7	5258.8	5105.4	5007.0
$\langle r\rangle_{5f}$, a.u.	0.9746	1.0376	1.0490	1.0572
$\langle r\rangle_{6p}$, a.u.	1.7297	1.7421	1.7568	1.7589

ions surrounded by oxygen, fluorine, and chlorine ions, we revealed significant differences in the electronic structure between the corresponding clusters. For the oxygen surroundings, the average radius of the 3*d* shell in the cluster is larger than that of the free ion and increases with decreasing R. For the fluoride surroundings, the changes caused by the incorporation of the free ion into the crystal are not so large, because the localization of the fluorine and oxygen 2*p* functions is different. For *Me* ions in the fluorine surroundings, the size of the 4*s*(*p*) shells increases with decreasing R down to 1.5 Å, whereas the average radius of the 3*d* shell first decreases and then, starting from R = 1.9 Å, the values of $\langle r\rangle_{3d}$ for oxides increase. As the interionic distance R becomes smaller than 1.6 Å, a compression of the 3*d* shell occurs due to the significant overlap of the oxygen 2*p* functions and 3*d* (4*s*, 4*p*) orbitals of the iron-group ion and due to the onset of strong repulsion between the electrons of the nearest neighbor ions due to the Pauli exclusion principle [24]. For the same reason, the values of $\langle r\rangle_{3d}$ and $\langle r\rangle_{4s}$ in chlorides start to decrease at $R \le 2.0$ Å.

An important feature of the fluoride clusters is the decrease in the *d*–*s*-interaction energy with decreasing *R* (with increasing pressure). The results of calculations for the $Ni^{+2} : [F^-]_6$ cluster at $R = 2.1$–1.7 Å are presented in [25]. It should be noted that the values of $F^0(3d, 4s)$ for oxides depend on *R* only weakly. For chlorides, this quantity increases sharply with decreasing *R*.

The radial integrals and the *d*–*s*-interaction energy exhibit a nearly linear dependence on the number of ligands for all types of the surroundings considered. An anomalous behavior is observed only for the $Cu^{+2} : [O^{-2}]_6$ clusters.

Interesting results are obtained for actinides, in particular, for the uranium ions in different clusters. When free actinium-group ions are incorporated into a crystal, the electronic structure of the ions changes (both qualitatively and quantitatively) in the same way as the electronic structure of 3*d* ions does. Some results obtained are presented in Table 6 for the basic configurations of the 5*f* ions in the free state and in clusters. The calculated energies of the characteristic x-ray spectral lines are listed in Table 7. For heavy ions, these energies change rather strongly; for actinides in clusters, these changes are due to the strong interaction of the 5*f* electrons with the ligands. The results obtained are in good agreement with the experimental data on both the energy-level diagrams and the energies of the x-ray *K* and *L* lines.

It should be noted that for rare-earth ions, the method suggested is efficient when the Hartree wave functions are used as the zeroth-order approximation.

Table 7. Theoretical values of the energies (eV) of the K_α and L_α lines for a number of 4*f* and 5*f* ions in the $Me^{+n} : [O^{-2}]_8$ cluster at $R = 2.37$ Å

Ion	$K_{\alpha 1}$	$K_{\beta 1}$	$L_{\alpha 1}$
Nd^{+2}	37337.290	42250.942	5370.985
Nd^{+3}	37336.610	42248.875	5369.708
Nd^{+4}	37335.741	42246.471	5368.449
Eu^{+2}	40071.174	45371.500	5852.357
Eu^{+3}	40070.420	45369.567	5848.793
Eu^{+4}	40069.405	45367.192	5847.622
Gd^{+2}	42921.661	48620.131	6062.622
Gd^{+3}	42920.521	48618.235	6063.971
Gd^{+4}	42920.118	48615.998	6060.614
Yb^{+2}	52156.939	58580.850	7421.563
Yb^{+3}	52155.897	58578.564	7426.668
Yb^{+4}	52155.077	58576.031	7429.100
U^{+2}	95912.345	108809.007	13639.793
U^{+3}	95912.037	108808.394	13239.528
U^{+4}	95911.663	108807.659	13639.200
Np^{+2}	98307.960	111517.588	13970.953
Np^{+3}	98307.642	111516.963	13970.674
Np^{+4}	98307.262	111516.221	13970.346
Bk^{+2}	108277.894	122779.219	15339.303
Bk^{+3}	108277.543	122778.545	15339.005
Bk^{+4}	108277.142	122777.775	15338.668

4. X-RAY SPECTRA OF *nl* IONS IN CLUSTERS

X-ray spectra are usually considered under the assumption that the transition energy of the inner electrons does not depend on the surroundings of the *nl* ion. At the same time, it is well known that a change in the type of the chemical bond of the compound and a change in the electronic state (valency) of the *nl* ion cause the x-ray spectral lines of 3*d* and 4*f* ions to shift; this effect is known as the chemical shift of x-ray spectral lines [9].

The valence shift of x-ray spectral lines caused by a change in the ion valency in solids under the influence of radiation or thermal treatment has been observed experimentally [11, 21, 23].

An electron transition in an ion with nl^N configuration in which inner $n'l'$ and $n''l''$ electrons are involved can be written in the standard form as $n'l'^{-1}nl^N \longrightarrow n''l''^{-1}nl^N$. It is obvious that the energy of the x-ray spectral lines is determined by the difference between the energies of the center of gravity of the initial ($n'l'^{-1}nl^N$) and final ($n''l''^{-1}nl^N$) configurations:

$$E_x = E^N_{n'l'} - E^N_{n''l''}. \quad (6)$$

The calculations showed that the energy of the excited state of the *nl* ion changes by approximately 100 a.u., whereas the change in the energy quantum of x-rays is 1–10 eV. In investigating the change in the valency of the ions, the valence shift of the energy of an x-ray spectral line

$$\Delta E_x = E_x^{+n} - E_x^{+n-1}, \quad (7)$$

rather than the energy itself, is the most important quantity, whose value should be calculated theoretically with the maximum degree of accuracy; this value often determines the accuracy of calculation of the concentration of ions with changed valency.

The theoretically calculated energies of the $K_{\alpha 1,2}$ ($1s_{1/2}nl^N \longrightarrow 2p^5_{1/2,3/2}nl^N$), K_β ($1s_{1/2}nl^N \longrightarrow 3p^5_{1/2,3/2}nl^N$), L_α ($2p^5_{1/2,3/2}nl^N \longrightarrow 3d^5_{3/2,5/2}nl^N$), and other x-ray spectral lines of the ions of the iron, lanthanum, and actinium groups in different clusters are in good agreement with the experimental data (the relative deviation is of the order of 0.1%); this agreement suggests that the calculated valence shifts of the x-ray spectral lines are highly accurate. As an example, the energies of the x-ray spectral lines for a number of lanthanum- and actinium-group ions are listed in Table 7. It should be

noted that similar data for other ions of the iron, lanthanum, and actinium groups are presented in [25].

5. CONCLUSIONS

Thus, the calculations performed for the $Me^{+n} : [L]_k$ clusters at different values of R and different types of ligands make it possible to draw the following conclusions.

First, the available experimental data on both optical and x-ray spectra of the impurity ions of the iron and actinium groups can be completely described within our approach [6, 7].

In oxygen-containing clusters, the relative energy of the excited $3d^{N-1}4s$ and $3d^{N-1}4p$ configurations decreases as R changes from 2.0 to 1.9–1.8 Å. The most interesting results were obtained for copper ions: a sharp decrease in the excitation energy and an increase in the d–s-interaction energy are observed for a Cu^{+2} ion surrounded by four oxygen ions at distances corresponding to the structure of high-temperature ceramics. This result has been obtained only for Cu^{+2} ions and is not observed for Cu^{+3} ions or other $Me^{+n} : [L]_k$ clusters considered. The strong d–s interaction between the Cu^{+2} ions must lead to a deformation of the conduction band and, probably, to the formation of a band based on the wave functions of these ions. Probably, a similar situation occurs in the $SrTiO_3$ perovskite crystals; in these crystal, the Ti^{+4} ions are partially changed into the Ti^{+3} state [26].

It should be noted that such a phenomenon is not observed for Ni and Zn ions surrounded by oxygen atoms; in this case, as well as for the Cu^{+2} and Cu^{+3} ions with fluorine and chlorine ligands, the dependences of the excitation energy and the d–s-interaction energy are virtually linear. For fluorides, the d–s-interaction energy decreases with increasing pressure by several percent, while for chlorides, this energy increases by 1–2%.

The energies of the characteristic x-ray spectral characteristic lines of the nl ions and the valence shift of these lines calculated within our approach are close to the experimental values. This makes it possible to use x-ray spectral lines for investigation of the changes in the valence of the host and impurity nl ions in solids.

ACKNOWLEDGMENTS

This work was supported by GB NIR program no. 115-3.

REFERENCES

1. J. C. Slater, *Quantum Theory of Molecules and Solids*, Vol. 4: *The Self-Consistent Field for Molecules and Solids* (McGraw-Hill, New York, 1975; Mir, Moscow, 1978).
2. J. Morrison, *Many-Body Calculation* (Springer, New York, 1987).
3. R. D. Cowan, *The Theory of Atom Structure and Spectra* (Univ. of California Press, Berkeley, 1981).
4. N. A. Kulagin and D. T. Sviridov, in *Problems of Crystallography* (Nauka, Moscow, 1987).
5. F. Bassani and G. Pastori Parravicini, *Electronic States and Optical Transitions in Solids* (Pergamon, New York, 1975; Nauka, Moscow, 1982).
6. N. A. Kulagin and D. T. Sviridov, *Methods of Calculation of Electronic Structures of Free and Impurity Ions* (Nauka, Moscow, 1986).
7. N. A. Kulagin and D. T. Sviridov, *Introduction to the Physics of Activated Crystals* (Vyshcha Shkola, Kharkov, 1990).
8. Ch. Fisher, *The Hartree–Fock Method for Atoms* (Wiley, New York, 1977).
9. O. I. Sumbaev, Usp. Fiz. Nauk **124**, 281 (1978) [Sov. Phys. Usp. **21**, 141 (1978)].
10. N. Kulagin, J. Phys. B **16**, 1695 (1983).
11. N. A. Kulagin and V. F. Sandulenko, Fiz. Tverd. Tela (Leningrad) **31** (1), 243 (1989) [Sov. Phys. Solid State **31**, 133 (1989)].
12. N. A. Kulagin, Physica B (Amsterdam) **222**, 173 (1996).
13. N. A. Kulagin, Physica B (Amsterdam) **245**, 52 (1998).
14. J. Jorgensen, H. Schuttler, D. Hinks, *et al.*, Phys. Rev. Lett. **58**, 1024 (1987).
15. L. Matheiss, Phys. Rev. Lett. **58**, 1032 (1987).
16. Ya. O. Dovgiĭ, L. T. Kadillyuk, I. V. Kityk, and R. V. Lutsiev, Fiz. Tverd. Tela (Leningrad) **32**, 3099 (1990) [Sov. Phys. Solid State **32**, 1798 (1990)].
17. N. A. Kulagin and D. T. Sviridov, Dokl. Akad. Nauk SSSR **266**, 616 (1982) [Sov. Phys. Dokl. **27**, 744 (1982)].
18. N. A. Kulagin, Fiz. Tverd. Tela (Leningrad) **27**, 2039 (1985) [Sov. Phys. Solid State **27**, 1223 (1985)].
19. D. Hartree, *The Calculation of Atomic Structures* (Wiley, New York, 1957; Inostrannaya Literatura, Moscow, 1960).
20. N. A. Kulagin, Opt. Spektrosk. **63**, 964 (1987) [Opt. Spectrosc. **63**, 566 (1987)].
21. N. A. Kulagin and D. T. Sviridov, J. Phys. C **17**, 4539 (1984).
22. E. Clementi and C. Roetti, At. Data Nucl. Data Tables **14**, 177 (1974).
23. I. I. Zalyubovskiĭ, N. A. Kulagin, L. A. Litvinov, and L. P. Podus, Fiz. Tverd. Tela (Leningrad) **23**, 846 (1981) [Sov. Phys. Solid State **23**, 480 (1981)].
24. P. Gombás, *Theorie und Lösungsmethoden des Mehrteilchenproblems der Wellenmechanik* (Birkhäuser, Basel, 1950; Inostrannaya Literatura, Moscow, 1953).
25. N. Kulagin, J. Alloys Compd. **300–301**, 56 (2000).
26. N. A. Kulagin, Fiz. Tverd. Tela (Leningrad) **25**, 3392 (1983) [Sov. Phys. Solid State **25**, 1952 (1983)].

Translated by A. Poushnov

Physics of the Solid State, Vol. 44, No. 8, 2002, pp. 1491–1495. From Fizika Tverdogo Tela, Vol. 44, No. 8, 2002, pp. 1428–1431.

PROCEEDINGS OF THE XI FEOFILOV WORKSHOP "SPECTROSCOPY OF CRYSTALS ACTIVATED BY RARE-EARTH AND TRANSITION-METAL IONS"

(Kazan, Tatarstan, Russia, September 24–28, 2001)

Anharmonic $T \otimes \varepsilon$ Jahn–Teller Coupling in $LiCaAlF_6 : Cr^{3+}$*

Gh. E. Drăgănescu, C. N. Avram, and N. M. Avram

Department of Physics, University of the West of Timişoara, Timişoara, 1900 Romania
e-mail: ghed@physics.uvt.ro
e-mail: acalin@physics.uvt.ro
e-mail: avram@physics.uvt.ro

Abstract—For an octahedral system, we analyzed the coupling between the triple degenerate electronic states of a transition metal ion and the double degenerate vibration of the ligands of the host matrix. The vibrations of the ligands of the lattice are described by new anharmonic coherent states of the Morse potential. For the linear coupling between electronic states and anharmonic vibrations, we built the matrix elements from the interaction Hamiltonian and corresponding energy levels. © *2002 MAIK "Nauka/Interperiodica".*

In the last twenty years, considerable attention has been paid to the linear octahedral Jahn–Teller system $T \otimes (\varepsilon + \tau_2)$, in which an electronic state T of the transition metal ion is equally coupled to the vibrational normal modes ε and τ_2 of the ligands, each of which corresponds to a common angular frequency [1–5].

The strong coupling limit has been explored by means of the Glauber state by Judd [6] and Judd and Vogel [7]. Studies of the Jahn–Teller effect using coherent states, as well as some applications to particular systems, are well known [8–11].

In all cases, the coupling of double and triple degenerate electronic states with harmonic vibrations described by harmonic coherent states was considered. For laser crystals doped with transitional metal ions, the vibronic interactions are higher than other types of interactions and explain the experimental data concerning vibronic transitions. This is the case of $LiCaAlF_6 : Cr^{3+}$.

In the cluster model [12], for the Cr^{3+} ion incorporated in LiCaAlFe in an octahedral site, the interaction of the triple degenerate electronic state ${}^4T_2$ of d^3 configuration of the chromium ion with τ_{2g} (three-dimensional) vibrations of the ligands was neglected since the ε_g (two-dimensional) mode of the octahedron of the ligands interacts more strongly with the same electronic states of the ion.

This is true because the ε_g mode of an octahedron which involves radial motion of the ligand ions can couple to σ-bonding orbitals and should therefore couple more strongly than the τ_{2g} modes, which only involve tangential motion and couple only to π-orbitals. Thus, vibronic $T \otimes \varepsilon$ interaction is present here.

In this paper, we studied the general case of an octahedral Jahn–Teller system of type $T \otimes \varepsilon$ having triple degenerate electronic states coupled with the double degenerate anharmonic vibrational states, the latter being described by the Morse potential.

For the Morse oscillator [13, 14], there are different types of coherent states [15]. We used these states in order to extend the analytical treatment of the Jahn–Teller effect of the $E \otimes \varepsilon$ interaction in Jahn–Teller octahedral symmetries [16] presented in our previous paper to the case of $T \otimes \varepsilon$ coupling for the same symmetry.

1. HAMILTONIAN OF THE SYSTEM

The Hamiltonian of the octahedral Jahn–Teller $T \otimes \varepsilon$ system is

$$H = H_e + H_v + H_{JT}, \tag{1}$$

where H_e represent the Hamiltonian of the electronic part of the system, H_v is the Hamiltonian of a double Morse oscillator, and H_{JT} is the Hamiltonian of the Jahn–Teller interaction between the triple degenerate electronic state T of the metal ion and the double degenerate vibrations of the ligands of a laser crystal.

The electronic Hamiltonian of the system is well known. We denote by $|\theta\rangle$ and $|\varepsilon\rangle$ uncoupled electronic wave-functions that transform according to a two-dimensional irreducible representation of the octahedral group. In order to obtain an analytic expression for the quantities of interest, such as the energy of the levels of the Ham factors, it is necessary to use the wave functions of the Hamiltonian $H_e + H_v$ from Eq. (1). Such wave functions are products of the electronic wave functions $|\theta\rangle$, $|\varepsilon\rangle$ and the wave functions which describe the vibrations of ligands.

* This article was submitted by the authors in English.

1063-7834/02/4408-1491$22.00 © 2002 MAIK "Nauka/Interperiodica"

For the vibrations of ligands, we suppose that the vibration Hamiltonian H_v is described by

$$H_v = H_{v1} + H_{v2} = \sum_{k=1}^{2}\left[\frac{p_k^2}{2m} + V_0(e^{-2\alpha x_k} - e^{-\alpha x_k})\right], \quad (2)$$

where $\alpha > 0$ is the anharmonicity constant of the oscillator, m is the mass of the oscillator, p_k is the momentum operator of the k oscillator, x_k is the displacement from the equilibrium position of the k oscillator, and V_0 is a positive constant.

We use the notation

$$\nu = \sqrt{\frac{8mV_0}{\alpha^2\hbar^2}} \quad (3)$$

and introduce the variables

$$y_k = \nu\exp(-\alpha x_k), \quad k = 1, 2. \quad (4)$$

The energy levels of the single Morse oscillator described by H_{vk} are

$$E_0(n_k) = -\hbar\Omega\left(n_k - \frac{\nu-1}{2}\right)^2, \quad (5)$$

where $k = 1, 2$; $\hbar\Omega = V_0/\nu^2$; $n_i = 0, 1, 2, \ldots, N = \left[\frac{\nu-1}{2}\right]$, with $[\mu]$ representing the entire part of μ.

The eigenfunctions of the Hamiltonian H_{0k} (where $k = 1, 2$) are

$$\psi_{n_k}(y_k) = c_k y^{s_k} e^{-y_k/2} F(-n_k, 2s_k + 1, y_k), \quad (6)$$

where $2s_k + 1 = \nu - 2n_k$, $c_k = \frac{1}{\Gamma(\nu - 2n_k)}\sqrt{\frac{\Gamma(\nu - n_k)}{n_k!}}$ is a normalization constant, and F represents the confluent hypergeometric function.

The vibrational states of the two-dimensional Morse oscillator are

$$|n_1 n_2\rangle = \psi_{n_1}(y_1)\psi_{n_2}(y_2). \quad (7)$$

These states have orthonormalization properties as follows:

$$\langle n_1 n_2 | n_1' n_2'\rangle = \delta_{n_1 n_1'}\delta_{n_2 n_2'}. \quad (8)$$

In the linear approximation, the Jahn–Teller Hamiltonian of interaction H_{JT} has the form

$$H_{JT} = \kappa\hbar\Omega(\mu^+\mu)^{(E)}(x_1 + x_2), \quad (9)$$

where κ is the strength of the Jahn–Teller coupling μ^+ and μ represents the creation and annihilation operators of the triple degenerate electronic states of the vibronic system. The label (E) indicates that operators act on the electronic states of the system.

2. THE ALGEBRA OF THE ANHARMONIC OSCILLATOR

In our previous papers [15], we established the creation operator B_+, the annihilation operator B_-, and the operator B_0 for the one-dimensional Morse oscillator. The results of [15] will be extended to the two-dimensional isotropic Morse oscillator by introducing the creation operators B_{+k}, the annihilations operators B_{-k}, and the operators B_{0k} ($k = 1, 2$), which have the analytical expressions

$$B_{\pm k} = (2s_k \mp 1)\frac{\partial}{\partial y_k} \pm \frac{s_k(2s_k \mp 1)}{y_k} \mp \frac{\nu}{2}, \quad (10)$$

$$B_{0k} = -y_k\frac{\partial^2}{\partial y_k^2} - \frac{\partial}{\partial y_k} + \frac{s_k^2}{y_k} + \frac{y_k}{2} - s_k + \frac{\nu}{2} - 1. \quad (11)$$

The operators obey the commutation relations

$$[B_{+k}, B_{-l}] = 2B_{0k}\delta_{kl}, \quad [B_{\pm k}, B_{0l}] = \pm B_{\pm k}\delta_{kl}, \quad (12)$$

where $k, l = 1, 2$.

Instead of operators (10) and (11), which are s_k dependent, we introduce new operators which are independent of s_k. For this reason, the dynamic system can be expressed with the aid of auxiliary variables $\xi_k \in [0, 2\pi]$ (where $k = 1, 2$) of the extra-phase type. According to this method, the new operators are

$$a_{\pm k} = e^{\mp i\xi_k}\left\{\left[\frac{2}{i}\frac{\partial}{\partial\xi_k} \mp 1\right]\frac{\partial}{\partial y_k} \pm \frac{1}{y_k}\left[\frac{1}{i}\frac{\partial}{\partial\xi_k}\left(\frac{2}{i}\frac{\partial}{\partial\xi_k} \mp 1\right)\right] \mp \frac{\nu}{2}\right\}, \quad (13)$$

$$a_{0k} = \frac{1}{i}\frac{\partial}{\partial\xi_k}. \quad (14)$$

The commutators of the operators a_{0k} and $a_{\pm k}$ are

$$[a_{+k}, a_{-l}] = 2a_{0k}\delta_{kl}, \quad [a_{\pm k}, a_{0l}] = \pm a_{\pm k}\delta_{kl}, \quad (15)$$

and

$$[a_{0k}, e^{\pm i\xi_l}] = \pm e^{\pm i\xi_k}\delta_{kl}, \quad (16)$$

where $k, l = 1, 2$.

The new eigenfunctions of the Hamiltonian H_{v_k} will be

$$\Phi_{n_k}(y_k, \xi_k) = e^{is_k\xi_k}\psi_{n_k}(y_k), \quad (17)$$

instead of $\psi_{n_k}(y_k)$ given by (6).

The action of the operators $a_{\pm k}$, a_{0k} on the eigenstates Φ_{n_k} is

$$a_{+l}\Phi_{n_k}(y_k, \xi_k) = \sqrt{(n_k+1)(\nu - n_k - 1)}\Phi_{n_k+1}(y_k, \xi_k)\delta_{kl},$$
$$a_{-l}\Phi_{n_k}(y_k, \xi_k) = -\sqrt{n_k(\nu - n_k)}\Phi_{n_k-1}(y_k, \xi_k)\delta_{kl}, \quad (18)$$
$$a_{0l}\Phi_{n_k}(y_k, \xi_k) = s_k\Phi_{n_k}(y_k, \xi_k)\delta_{kl},$$

where $k, l = 1, 2$.

The Hamiltonian H_ν can be expressed in terms of the operators a_{01} and a_{02}:

$$H_\nu = -\hbar\Omega(a_{01}^2 + a_{02}^2). \quad (19)$$

3. THE JAHN–TELLER INTERACTION

In order to express the Jahn–Teller interaction Hamiltonian H_{JT} in terms of the dynamic group operators $\{a_{\pm 1}, a_{\pm 2}, a_{01}, a_{02}\}$, we start with the relations [16]

$$\frac{\partial}{\partial y_k} = -\frac{1}{2}\sum_{n=0}^{\infty}(2a_{0k})^n \times\left[e^{i\xi_k}a_{+k} + \frac{\nu}{2} - (-1)^n\left(e^{-i\xi_k}a_{-k} - \frac{\nu}{2}\right)\right], \quad (20)$$

$$\frac{1}{y_k} = -\sum_{n=0}^{\infty}(2a_{0k})^{n-1} \times\left[e^{i\xi_k}a_{+k} + (-1)^n e^{-i\xi_k}a_{-k} + \frac{\nu}{2}[1-(-1)^n]\right]. \quad (21)$$

The coordinate x_k from Hamiltonian (9) can be written as

$$x_k = \frac{1}{\alpha}[\ln\nu - \ln y_k] = \frac{\ln\nu}{\alpha} - \frac{1}{\alpha}\sum_{n=1}^{\infty}\frac{1}{n}\left(1 - \frac{1}{y_k}\right)^n$$
$$= \frac{1}{\alpha}\left\{\ln\nu - \sum_{n=1}^{\infty}\frac{1}{n}\left[1 + \nu\sum_{m=0}^{\infty}(2a_{0k})^{2m}\right.\right. \quad (22)$$
$$\left.\left. + \sum_{m=0}^{\infty}(2a_{0k})^{m-1}(e^{i\xi_k}a_{+k} + (-1)^m e^{-i\xi_k}a_{-k})\right]^n\right\}.$$

The Hamiltonian H_{JT} in terms of operators $a_{\pm k}$ and a_{0k} has the final form

$$H_{JT} = \frac{1}{\alpha}\kappa\hbar\Omega(\mu^+\mu)^{(E)}$$
$$\times\left\{2\ln\nu - \sum_{k=1}^{2}\sum_{n=0}^{\infty}\frac{1}{n}\left[1 + \nu\sum_{m=0}^{\infty}(2a_{0k})^{2m}\right.\right. \quad (23)$$
$$\left.\left. + \sum_{m=0}^{\infty}(2a_{0k})^{m-1}[e^{i\xi_k}a_{+k} + (-1)^n e^{-i\xi_k}]\right]^n\right\}.$$

4. THE COHERENT STATES

For the Morse oscillator, different kinds of coherent states [15, 17] can be built. The two types of coherent states are useful for study of the Jahn–Teller interaction.

The first-type states are the displacement-operator coherent states defined as the states obtained by action of the displacement operator D on the vacuum state of the one-dimentional Morse oscillator:

$$|\alpha\rangle = D(\alpha)|0\rangle = \exp[i(\alpha a_+ - \alpha^* a_-)]|0\rangle, \quad (24)$$

where $\alpha \in C$ is a complex valued parameter.

We extended these states to the case of the Morse double-oscillator as

$$|\alpha\rangle = D(\alpha_1)D(\alpha_2)|00\rangle$$
$$= \exp[i(\alpha_1 a_{+1} - \alpha_1^* a_{-1})]\exp[i(\alpha_2 a_{+2} - \alpha_2^* a_{-2})]|00\rangle,$$

where $\alpha_1, \alpha_2 \in C$ and $|n_1 n_2\rangle = |n_1\rangle|n_2\rangle$. Annihilation operator coherent states designed by $|\lambda\rangle$ (where $\lambda \in C$) are another type of coherent state. These are states which have the following property:

$$a_-|\lambda\rangle = \lambda|\lambda\rangle. \quad (25)$$

For the one-dimensional Morse oscillator, these states are

$$|\lambda\rangle = c_0\sum_{n=0}^{N}\frac{(-1)^n(\lambda a_+)^n}{n!(\nu - n)_n}|0\rangle, \quad (26)$$

where

$$c_0 = \left(\sum\frac{|\lambda|^{2n}}{n!(\nu - n)_n}\right)^{-1/2}$$

is the normalization constant.

The states (25) can also be extended to the Morse double-oscillator case. We denote these states as $|\lambda\rangle = |\lambda_1\rangle|\lambda_2\rangle$, where $\lambda_1, \lambda_2 \in C$.

The general expression for these coherent states is

$$|\lambda\rangle = |\lambda_1\rangle|\lambda_2\rangle$$
$$= c_0^2\sum_{n,m=0}^{M}\frac{(-1)^n(\lambda_1 a_{+1})^n}{n!(\nu - n)_n}\frac{(-1)^m(\lambda_2 a_{+2})^n}{m!(\nu - m)_m}|00\rangle.$$

5. THE GENERALIZED COHERENT STATES AND THE JAHN–TELLER INTERACTION

In order to establish the states which correspond to non-vanishing average values of the H_{JT} energy, Judd [6] generalized the coherent states (24) by introducing wavefunctions of the electron–phonon system with

vibronic interaction. For the case of an $E \otimes \varepsilon$ system, Judd defined its coherent states as the overlap

$$|\beta nz\rangle = \int_0^{2\pi} d\varphi |\beta\rangle e^{iz\varphi} e^{i\kappa b^+} (b^+ - \kappa)^n |00\rangle, \quad (27)$$

where β refers to the lower branch ($\beta = l$) or to the upper branch ($\beta = u$).

Thus,

$$|l\rangle = \cos\frac{\varphi}{2}|\theta\rangle - \sin\frac{\varphi}{2}|\varepsilon\rangle, \quad (28)$$

$$|u\rangle = \sin\frac{\varphi}{2}|\theta\rangle + \cos\frac{\varphi}{2}|\varepsilon\rangle, \quad (29)$$

and the creation operator b^+ is defined by

$$b^+ = a_{+1}^{HO}\cos\varphi + a_{+2}^{HO}\sin\varphi. \quad (30)$$

The operators $a_{\pm k}^{HO}$ are the creation and annihilation operators for the double harmonic oscillator, φ is an arbitrary angle, and the parameter z in (27) is characterized by the type of coupling. For example, $z = 1/2$ corresponds to the states accessible to electric dipole radiation from the zero-phonon ground state.

Thus, the generalized coherent states (27) correspond to the case of Jahn–Teller interaction in the presence of harmonic vibrations. In their papers, Judd [6] and Chancey [8, 9] studied the Jahn–Teller interaction for systems with different symmetries in harmonic approximation.

We generalized the results of Judd and Chancey for the case of Morse anharmonic vibrations, considering the corresponding operators for Morse oscillator (13) and (14) instead of the creation and annihilation operators for the harmonic oscillator

The first result was reported in [16], where we studied the case of $E \otimes \varepsilon$ for anharmonic vibrations.

For the anharmonic vibrations in (30), instead of the operators $a_{\pm k}^{HO}$ we use the corresponding operators $a_{\pm k}$, introduced in (13), corresponding to the Morse oscillators. Thus, the operator b^+ became

$$b^+ = a_{+1}\cos\varphi + a_{+2}\sin\varphi, \quad (31)$$

where the operators $a_{\pm k}$ are given in (13).

We note that the operators (30) and (31) act on a state $|n\rangle$ of the double anharmonic oscillator defined by

$$|n\rangle = |n_1 + n_2\rangle = |n_1\rangle|n_2\rangle. \quad (32)$$

We define a new set of generalized anharmonic coherent states as follows:

$$|\beta nz\rangle = \int_0^{2\pi} d\varphi |\beta\rangle e^{i\varphi z} (b^+ - \kappa)^n |\kappa\rangle, \text{ with } \kappa \in C, \quad (33)$$

where $|\beta\rangle$ are the electronic states of the system and can be $\beta = (jmu)$ or $\beta = (jml)$, with $j = 1$ and $m = 0, \pm 1$; l refers to the lower branch and u to the upper branch of the electronic states. As in (27), z represents a coupling parameter.

In (33), $|\kappa\rangle$ represents the annihilation operator coherent states

$$|\kappa\rangle = c_0 \sum_{n=0}^{N} \frac{(-1)^n (\kappa b_+)^n}{n!(\nu - n)_n} |0\rangle, \quad (34)$$

where the state $|0\rangle$ represents the state $|n\rangle$ from (32) for $n = 0$.

In the case $z = 0$, the states (33) correspond to the uncoupled case

$$|\beta nz\rangle_0 = |\beta\rangle (b - \kappa)^n |\kappa\rangle. \quad (35)$$

We can expand the states $|\beta nz\rangle$ in terms of uncoupled $|\beta nz\rangle_0$ states as follows:

$$\begin{aligned} |\beta nz\rangle &= c_0 \sum_{l=0}^{N} \sum_{j=0}^{n} \int_0^{2\pi} d\varphi e^{i\varphi\nu} |\beta\rangle \\ &\times C_n^j \frac{(-1)^{l+j} \kappa^{l+j} (b^+)^{n+l-j}}{j!(\nu - j)_j} |0\rangle \\ &= c_0 \sum_{l=0}^{N} \sum_{j=0}^{n} C_n^j \frac{(-1)^{l+j} \kappa^{l+j}}{j!(\nu - j)_j} |\beta, n + l - j, z\rangle_0. \end{aligned} \quad (36)$$

The states (36) make it possible to calculate the average value of the Jahn–Teller interaction energy. We obtain

$$\begin{aligned} E_{JT} &= c_0^2 \sum_{l=0}^{N} \sum_{j=0}^{n} \sum_{l'=0}^{N} \sum_{j'=0}^{n} C_n^j C_n^{j'} \frac{(-1)^{l+j} \kappa^{l+j}}{j!(\nu - j)_j} \\ &\times \frac{(-1)^{l'+j'} \kappa^{l'+j'}}{j!(\nu - j')_{j'}} \\ &\times {}_0\langle \beta, n + l' - j', z | H_{JT} | \beta, n + l - j, z\rangle_0. \end{aligned} \quad (37)$$

The final form of Eq. (37) is

$$\begin{aligned} E_{JT} &= \frac{1}{\alpha} \kappa \hbar \Omega c_0^2 \sum_{l=0}^{N} \sum_{j=0}^{n} \frac{|\kappa|^{2(j+l)} (C_n^j)^2}{[j!(\nu - j)_j]^2} \\ &\times {}_0\langle \beta | (\mu^+ \mu)^{(E)} | \beta \rangle \\ &\times \left\{ 2\ln\nu - \sum_{k=1}^{2} \sum_{p=0}^{\infty} \frac{1}{p} \left[1 + \nu \sum_{m=0}^{\infty} (s_{n+l-j})^{2m} \right] \right\}. \end{aligned} \quad (38)$$

Thus, we studied the vibronic coupling between the triple degenerate electronic states of a transition metal ion incorporated in a crystal laser and the double degenerate vibration states of the ligands of a crystal for octahedral symmetry.

We introduced a new type of coherent states by generalizing annihilation operator coherent states in order to describe the vibrations of ligands.

We used a new representation of the dynamic group of the system by introducing an auxiliary variable ξ_k of extra-phase type. In this representation, the eigenfunctions, the observables, and the Hamiltonian of anharmonic vibrations were expressed. The eigenfunctions of the Hamiltonian of the system, in the absence of interaction, are built using the overlap of the electronic states and these new anharmonic coherent states.

The results show that the anharmonic effects on Jahn–Teller interaction can be expressed in a rigorous form containing a dependence on the anharmonicity of the system.

ACKNOWLEDGMENTS

The authors acknowledge the CNCSIS (Romania) for their financial support under grant no. 12625/1 (1998).

REFERENCES

1. W. Moffit and W. Thorson, Phys. Rev. **108**, 1251 (1957).
2. U. Öpik and M. H. L. Price, Proc. R. Soc. London, Ser. A **238**, 425 (1957).
3. R. Romstein and Y. Merlé d'Aubigné, Phys. Rev. B **4**, 4611 (1971).
4. M. C. M. O'Brien, Phys. Rev. **187**, 407 (1969); J. Phys. C **4**, 2524 (1971); **9**, 3153 (1976).
5. F. S. Ham, Phys. Rev. **138**, A1727 (1965).
6. B. R. Judd, Can J. Phys. **52**, 999 (1974).
7. B. R. Judd and E. E. Vogel, Phys. Rev. B **11**, 2427 (1975).
8. C. C. Chancey, J. Phys. A **17**, 3183 (1984); **20**, 2753 (1987).
9. C. C. Chancey and B. R. Judd, J. Phys. A **16**, 875 (1983).
10. J. Rivera-Iratchet, Manuel A. de Orúe, M. L. Flores, and E. E. Vogel, Phys. Rev. B **47**, 10164 (1993).
11. M. C. M. O'Brien and C. C. Chancey, Am. J. Phys. **61**, 688 (1993); H. G. Reik, J. Phys. A **26**, 6549 (1993).
12. M. D. Sturge, in *Solid State Physics*, Ed. by F. Seitz, D. Turnbull, and H. Ehrenreich (Academic, New York, 1967), Vol. 20.
13. L. D. Landau and E. M. Lifshitz, *Course of Theoretical Physics*, Vol. 3: *Quantum Mechanics: Non-Relativistic Theory* (Nauka, Moscow, 1974; Pergamon, New York, 1977); R. G. Wybourne, *Classical Groups for Physicists* (Wiley, New York, 1974); P. Cordero and S. Hojman, Lett. Nuovo Cimento **4**, 1123 (1970).
14. C. C. Gerry, Phys. Rev. A **33**, 2207 (1986); C. C. Gerry, Phys. Rev. A **31**, 2721 (1985).
15. N. M. Avram, Gh. E. Drăgănescu, and C. N. Avram, J. Opt. B **2**, 214 (2000); Gh. E. Drăgănescu and N. M. Avram, Z. Phys. Chem. (Munich) **200**, 51 (1997).
16. N. M. Avram, Gh. E. Drăgănescu, and M. Kibler, Int. J. Quantum Chem. **88**, 303 (2002).
17. A. Perelomov, *Generalized Coherent States and Their Applications* (Springer, Berlin, 1986).

Physics of the Solid State, Vol. 44, No. 8, 2002, pp. 1496–1499. Translated from Fizika Tverdogo Tela, Vol. 44, No. 8, 2002, pp. 1432–1434.

PROCEEDINGS OF THE XI FEOFILOV WORKSHOP "SPECTROSCOPY OF CRYSTALS ACTIVATED BY RARE-EARTH AND TRANSITION-METAL IONS"

(Kazan, Tatarstan, Russia, September 24–28, 2001)

Structural Asymmetry of Kramers Clusters as a Consequence of Time-Reversal Symmetry

I. I. Geru

Moldova State University, ul. Mateevicha 60, Chisinau, MD 2009 Moldova

e-mail: geru@usm.md

Abstract—Asymmetry of Kramers magnetic clusters is shown to be dictated by the structure of magnetic four-color point groups. Factorization of the time-reversal operator is performed for Kramers systems. © *2002 MAIK "Nauka/Interperiodica".*

1. INTRODUCTION

Highly symmetric polyatomic molecules and atomic and molecular clusters with an orbitally degenerate ground state are distorted and their symmetry is reduced owing to the Jahn–Teller effect [1]. Structural distortions can also occur in polyatomic systems of other physical nature. For example, this is the case with many-particle systems with an odd number of particles of spin 1/2, whose energy levels are degenerate in accordance with Kramers theorem. Kramers systems belong to magnetic symmetry groups which can be obtained by extending the classical point groups with the help of the second-order cyclic group *2*': $\{K, K^2 = e\}$, where K is the time-reversal operator and e is the identity element of the group [2, 3]. The number of black-and-white (or junior [4]) magnetic symmetry groups is 58. In the case of Kramers systems, however, such an extension is not correct and, instead of group *2*', one should use the fourth-order cyclic group *4*': $\{K, K^2, K^3, K^4 = e\}$. The magnetic symmetry groups thus obtained are four-color groups rather then two-color ones, as in the previous case, and there are four such groups rather than 58 [5]. It should be remembered that double classical symmetry groups should be extended when the spin is taken into account.

In this paper, it is shown that the specific structure of four-color magnetic point groups dictated by the time-reversal symmetry is the reason for distortions of the geometrical structure of Kramers molecules and clusters in comparison with the structure that would arise in the absence of magnetic interactions between atoms (or between magnetic nuclei in the case of nuclear magnetic ordering in condensed media [6]). In the last section, we discuss the factorization of the time-reversal operator.

2. MAGNETIC SYMMETRY GROUPS OF KRAMERS SYSTEMS

The known 58 magnetic point groups are inadequate for describing the magnetic properties of Kramers systems, because the behavior of systems with half-integer spin under time reversal is different from that of systems with integer spin. The necessity of using group 4' instead of 2' in order to extend the classical point symmetry groups to the magnetic symmetry groups for Kramers systems was discussed in [5, 7]. It was shown in [5] that, with the help of group 4', the classical point symmetry groups can be extended to the following four four-color symmetry groups: $4^{(4'_z)}$, $\bar{4}^{(4'_z)}$, $4^{(4'_z)}/m^{(1)}$ and $4^{(4'_z)}/m^{(2)}$, where the overscribed bar indicates a mirror rotation and the prime denotes an antirotation. The first two groups are generated using groups 4 and $\bar{4}$, respectively, while the other two groups are generated with the help of group $4/m$. The symbols $m^{(1)}$ and $m^{(2)}$ denote the generating elements of groups $4^{(4'_z)}/m^{(1)}$ and $4^{(4'_z)}/m^{(2)}$ that generate the symmetry transformations $4'^4_z m = em$, $4'^2_z m = 2_z m$ and $4'_z m$, $4'^3_z m = 4'_z 2_z m$, respectively.

Let us expand the full wave function of the system with total spin S in terms of the spinor basis vectors $\xi^{(S)}_\sigma$:

$$\psi = \sum_{\sigma=-S}^{S} \psi_\sigma \xi^{(S)}_\sigma, \qquad (1)$$

1063-7834/02/4408-1496$22.00 © 2002 MAIK "Nauka/Interperiodica"

where

$$\xi_S^{(S)} = \begin{pmatrix} 1 \\ 0 \\ \vdots \\ 0 \end{pmatrix}, \quad \xi_{S-1}^{(S)} = \begin{pmatrix} 0 \\ 1 \\ \vdots \\ 0 \end{pmatrix}, \quad \ldots,$$

$$\xi_{-S+1}^{(S)} = \begin{pmatrix} 0 \\ \vdots \\ 1 \\ 0 \end{pmatrix}, \quad \xi_{-S}^{(S)} = \begin{pmatrix} 0 \\ \vdots \\ 0 \\ 1 \end{pmatrix}.$$

Under the action of the time-reversal operator K, the wave function of Eq. (1) is transformed into [8]

$$K\Psi = \sum_{\sigma=-S}^{S} (-1)^S \psi_\sigma^* \xi_{-\sigma}^{(S)}.$$

In the case of a half-integer S, the action of operators K, K^2, K^3, and $K^4 = e$ on the wave function Ψ corresponds to four successive antirotations of the point representing the state Ψ through an angle of 90° in the function space spanned by the basis vectors $\xi_\sigma^{(S)}$ [5]. The axis of the antirotation passes through the origin of coordinates and is perpendicular to the plane of the square whose corners correspond to the states $K\Psi$, $K^2\Psi = -\Psi$, $K^3\Psi = -K\Psi$, and $K^4\Psi = \Psi$. The opposite corners of the square (Ψ, $-\Psi$; $K\Psi$, $-K\Psi$) are equivalent, while any adjacent corners are inequivalent and colored differently (Fig. 1).

In the case of a half-integer spin, the coloration of the square corners that correspond to functions $K\Psi$ and $K^3\Psi = -K\Psi$ is the anti-identity transformation of the spinor Ψ into the conjugate spinor Ψ^+ ($\psi_\sigma \longrightarrow \psi_\sigma^*$, $\xi_\sigma^{(S)} \longrightarrow (-1)^S \xi_{-\sigma}^{(S)}$). In the case of an integer spin, only the coloration of the corner of the $(2S + 1)$-dimensional cube corresponding to the state $K\Psi$ is the anti-identity transformation.

The correspondence of the operators K, K^2, K^3, and K^4 to the symmetry elements $4_z'$, $4_z'^2$, $4_z'^3$, and $4_z'^4 = e$ of the square with black-and-white corners, respectively, is shown graphically in Fig. 1a for the case of $S = 1/2$. Such a correspondence cannot be depicted graphically in the case of a half-integer spin $S > 1/2$, that is, in a space of dimensionality higher than three. Nevertheless, using the properties of the unitary part of the operator K, it can be shown that in this case, the geometric transformations corresponding to the elements of group 4' are also four antirotations $4_z'$ [5].

If, in addition to the antirotations forming the cyclic group 4', we take into account the other four generalized-symmetry elements of the square with inequivalent adjacent corners (mirror reflections $m_{xy}^{(i)}$ from the diagonals and antireflections $m_x'^{(i)}$ from the straight lines passing through centers of opposite sides; $i = 1, 2$), then the extension of the classical point groups should be performed with the help of group 4'$m'm$. Among all 32 point symmetry groups, only groups 422, 4mm, and $\bar{4}2m$ can be extended with the help of group 4'$m'm$. In this more general case, there are also four junior point generalized-symmetry groups (four-color symmetry groups): $4^{(4_z')}2^{(m_x')}2^{(m_{xy})}$, $4^{(4_z')}m^{(m_x')}m^{(m_{xy})}$, $\bar{4}^{(4_z')}2^{(m_x')}m^{(m_{xy})}$, and $\bar{4}^{(4_z')}2^{(m_{xy})}m^{(m_x')}$ [5]. The first two magnetic symmetry groups are generalized with the help of groups 422 and 4mm, respectively, while the other two groups are generalized by using group $\bar{4}2m$. In the symmetry group 4'$m'm$, reflections $m_{xy}^{(i)}$ and antireflections $m_x'^{(i)}$ ($i = 1, 2$) in the spinor basis are described by operators σ_x, $-\sigma_x$ and $\sigma_z K_0$, $-\sigma_z K_0$, respectively, where K_0 is the complex-conjugation operator. Thus, group 4'$m'm$ is composed of operators $i\sigma_y K_0$, $-e$, $-i\sigma_y K_0$, e, σ_x, $-\sigma_x$, $\sigma_z K_0$, and $-\sigma_z K_0$. The multiplication table for them is presented in the table.

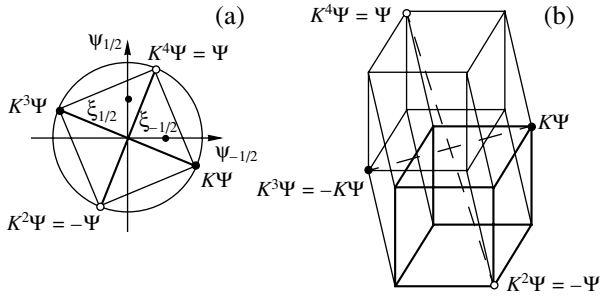

Fig. 1. Action of operators K, K^2, K^3, and K^4 on the wave function Ψ in the case of spin S equal to (a) 1/2 and (b) 3/2.

In order to elucidate the structure of group 4'$m'm$, we use g_i and g_k to denote the elements of subgroup 4' (g_i, $g_k \in 4'$) and h_i and h_k to denote the remaining elements of group 4'$m'm$ that constitute the set H (h_i, $h_k \in H$). Then, we have

$$g_i g_k \in 4', \quad h_i h_k = g_l \in 4'; \quad g_i h_k \in H, \quad h_i g_k \in H. \quad (2)$$

As seen from Eq. (2), any product of the elements of the set H belongs to subgroup 4'.

3. STRUCTURAL DISTORTIONS OF KRAMERS MAGNETIC CLUSTERS AS A CONSEQUENCE OF TIME-REVERSAL SYMMETRY

Among the elements of the magnetic point groups obtained by extending the classical point symmetry groups with the help of the cyclic group 4', there are no threefold, fivefold, or sixfold (proper and mirror) rota-

Multiplication table for the elements of group $4'm'm$

Element of the group	$i\sigma_y K_0$	$-e$	$-i\sigma_y K_0$	e	σ_x	$-\sigma_x$	$\sigma_z K_0$	$-\sigma_z K_0$
$i\sigma_y K_0$	$-e$	$-i\sigma_y K_0$	e	$i\sigma_y K_0$	$\sigma_z K_0$	$-\sigma_z K_0$	$-\sigma_x$	σ_x
$-e$	$-i\sigma_y K_0$	e	$i\sigma_y K_0$	$-e$	$-\sigma_x$	σ_x	$-\sigma_z K_0$	$\sigma_z K_0$
$-i\sigma_y K_0$	e	$i\sigma_y K_0$	$-e$	$-i\sigma_y K_0$	$-\sigma_z K_0$	$\sigma_z K_0$	σ_x	$-\sigma_x$
e	$i\sigma_y K_0$	$-e$	$-i\sigma_y K_0$	e	σ_x	$-\sigma_x$	$\sigma_z K_0$	$-\sigma_z K_0$
σ_x	$-\sigma_z K_0$	$-\sigma_x$	$\sigma_z K_0$	σ_x	e	$-e$	$-i\sigma_y K_0$	$i\sigma_y K_0$
$-\sigma_x$	$\sigma_z K_0$	σ_x	$-\sigma_z K_0$	$-\sigma_x$	$-e$	e	$i\sigma_y K_0$	$-i\sigma_y K_0$
$\sigma_z K_0$	σ_x	$-\sigma_z K_0$	$-\sigma_x$	$\sigma_z K_0$	$i\sigma_y K_0$	$-i\sigma_y K_0$	e	$-e$
$-\sigma_z K_0$	$-\sigma_x$	$\sigma_z K_0$	σ_x	$-\sigma_z K_0$	$-i\sigma_y K_0$	$i\sigma_y K_0$	$-e$	e

tion axes, as well as no other high-symmetry elements, which means that the local symmetry of magnetic clusters cannot be high. For example, in the practically important case of trimer magnetic clusters, a triangle whose vertices are occupied by 3*d* or 4*f* ions of a half-integer spin in the ground state cannot be equilateral. On the whole, this prediction is supported by x-ray diffraction, magnetic-susceptibility, EPR spectroscopy, spin heat capacity, Mössbauer spectroscopy, and neutron diffraction studies [9–13]. In many cases, the experimental data are interpreted in terms of the Dzyaloshinskiĭ–Moriya antisymmetric-exchange model [9]. In the cases where the experimentally measured sides of the triangle (or exchange interaction constants between magnetic ions) appear to be equal, to within experimental error, the magnetic ions are inequivalent, which can be revealed by more precise measurements.

The magnetic symmetry groups that are obtained by extending the classical point groups with the help of group $4'm'm$ (which contains group $4'$ as its subgroup) are also of low symmetry. Among the symmetry elements of these groups, there are no threefold, fivefold, or sixfold (proper and mirror) rotation axes. Therefore, magnetic clusters in this case are also of low symmetry.

Thus, the structural asymmetry of magnetic clusters with Kramers-degenerate energy levels is dictated by the time-reversal symmetry, which leads to the specific structure of four-color magnetic symmetry groups.

4. FACTORIZATION OF THE TIME-REVERSAL OPERATOR

The time-reversal operator K is a symmetry element of the non-Abelian group $4'm'm$ ($K \in 4'm'm$) and can be represented as the product of elements $\sigma_z K_0$, and σ_x:

$$K = i\sigma_y K_0 = \sigma_z K_0 \sigma_x,$$

which is the factorization of operator K in terms of the operators $K_1 = \sigma_z K_0$ and $K_2 = \sigma_x$,

$$K = K_1 K_2. \tag{3}$$

The operators K_1 and K_2, as well as K, are defined to within an arbitrary multiplying constant and belong to the symmetry group $4'm'm$ ($K_1, K_2 \in 4'm'm$); therefore, these operators commute with the Hamiltonian H of the system and the following invariance relations hold:

$$KHK^{-1} = H, \quad K_1 H K_1^{-1} = H, \quad K_2 H K_2^{-1} = H.$$

The spin-projection operators S_x, S_y, and S_z $\left(\mathbf{S} = \frac{1}{2}\boldsymbol{\sigma}\right)$ go into their negatives under the time reversal. We will refer to the simultaneous change of sign of all operators S_x, S_y, and S_z under the action of operator K as the complete reversal of motion and to the operator K as the complete time-reversal operator. As follows from the relations

$$K_1 S_x K_1^{-1} = -S_x, \quad K_1 S_y K_1^{-1} = S_y, \quad K_1 S_z K_1^{-1} = S_z, \tag{4}$$

$$K_2 S_x K_2^{-1} = S_x, \quad K_2 S_y K_2^{-1} = -S_y, \quad K_2 S_z K_2^{-1} = -S_z, \tag{5}$$

only S_x changes its sign under the action of operator K_1 and only S_y and S_z change sign under the action of operator K_2. Therefore, K_1 and K_2 are incomplete time-reversal operators; these operators obey the relations ($(K_1K_2)^2 = -e$ and $K_1^2 = K_2^2 = e$).

In the presence of an external magnetic field, the Hamiltonian will remain invariant under the action of operators K_1 and K_2 (characterized by Eqs. (4) and (5)) if the sign of the x component and the signs of the y and z components of the magnetic field, respectively, are reversed. However, problems involving invariance under the action of operators K_1 and K_2 should be considered separately.

REFERENCES

1. H. A. Jahn and E. Teller, Proc. R. Soc. London, Ser. A **161**, 220 (1937); H. A. Jahn, Proc. R. Soc. London, Ser. A **164**, 117 (1938).
2. B. A. Tavger and V. N. Zaĭtsev, Zh. Éksp. Teor. Fiz. **30** (3), 564 (1956) [Sov. Phys. JETP **3**, 430 (1956)].
3. M. Hamermesh, *Group Theory and Its Applications to Physical Problems* (Addison-Wesley, Reading, 1962; Mir, Moscow, 1966).
4. A. M. Zamorzaev, Kristallografiya **2** (1), 15 (1957) [Sov. Phys. Crystallogr. **2**, 10 (1957)].
5. I. I. Geru, Dokl. Akad. Nauk SSSR **268** (6), 1392 (1983) [Sov. Phys. Dokl. **28**, 99 (1983)].
6. A. Abragam and M. Goldman, *Nuclear Magnetism: Order and Disorder* (Clarendon, Oxford, 1982; Mir, Moscow, 1984), Vol. 1.
7. I. I. Geru, in *Proceedings of the All-Union Symposium on the Theory of Symmetry and Its Generalizations, Kishinev, 1980*, p. 42.
8. E. P. Wigner, *Group Theory and Its Application to the Quantum Mechanics of Atomic Spectra* (Academic, New York, 1959; Inostrannaya Literatura, Moscow, 1961).
9. B. S. Tsukerblat and M. I. Belinskiĭ, *Magnetochemistry and Radiospectroscopy of Exchange Clusters* (Shtiintsa, Kishinev, 1983).
10. Tagano Mikio, J. Phys. Soc. Jpn. **33** (5), 1312 (1972).
11. J. F. Duncan, C. R. Kanekar, and K. F. Mok, J. Chem. Soc. A, No. 3, 480 (1969).
12. J. J. Long, W. T. Robinson, W. P. Tappmeyer, and D. L. Bridges, J. Chem. Soc., Dalton Trans., No. 6, 573 (1973).
13. K. I. Turta, A. O. Solonenko, I. I. Bulgak, *et al.*, J. Radioanal. Nucl. Chem. **190** (2), 347 (1995).

Translated by Yu. Epifanov

Physics of the Solid State, Vol. 44, No. 8, 2002, pp. 1500–1504. Translated from Fizika Tverdogo Tela, Vol. 44, No. 8, 2002, pp. 1435–1438.

PROCEEDINGS OF THE XI FEOFILOV WORKSHOP "SPECTROSCOPY OF CRYSTALS ACTIVATED BY RARE-EARTH AND TRANSITION-METAL IONS"

(Kazan, Tatarstan, Russia, September 24–28, 2001)

Induced Resonant Transparency of Magnetic Materials for Gamma Radiation: Propagation Dynamics

A. V. Mitin and D. A. Roganov

Kazan State Technological University, ul. Karla Marksa 68, Kazan, 420015 Tatarstan, Russia
e-mail: mitin@knet.ru

Abstract—The theory of spatiotemporal dynamics of gamma radiation in a resonant medium upon excitation of two-frequency gamma magnetic resonance in magnetic materials is considered. The radiation absorption at the fundamental frequency and the harmonic generation are investigated under conditions when the frequency of gamma radiation is shifted by the half-sum or half-difference of the frequencies of radio-frequency magnetic fields. It is shown that the propagation of gamma radiation through an absorber is characterized by a steady-state gamma intensity (resonant transparency). A consistent radio-frequency spectral analysis demonstrates that the intensities of harmonics drastically change at the transparency region boundaries due to nonlinear interference. The theory of quantum and dynamical beats of synchrotron radiation under conditions of induced resonant transparency is proposed. © *2002 MAIK "Nauka/Interperiodica".*

1. INTRODUCTION

A new direction in nonlinear optics, coherent population trapping, has been developed in recent years [1]. Considerable research in this field is currently aimed at attaining resonant transparency in different media. In particular, resonant transparency has been achieved in a medium through the interaction of an atomic quantum system with two laser fields, namely, a strong laser field saturating the atomic transition [2] and a weak probing field used for analyzing the material. In the optical range, the use of sufficiently high-power lasers makes it possible to fill excited levels; however, the intensity of gamma radiation is too low to accomplish these ends. At the same time, the magnetic moments of Mössbauer nuclei in the ground and excited isomeric states can actively interact with radio-frequency magnetic fields (RFMFs) and induce interference effects. They can arise from both the excitation of gamma magnetic resonance (magnetic quantum beats at frequencies multiple to RFMF frequencies) [3] and the interference between RFMF-dressed Zeeman states of the isomeric levels of the Mössbauer nuclei [3–6]. These findings gave impetus to a successful solution of the problem associated with induced resonant transparency in the gamma range of electromagnetic waves through gamma irradiation of a Mössbauer absorber (in the form of a single-domain ferromagnet) subjected to two resonant RFMFs (two-frequency gamma magnetic resonance). In our recent work [7], we succeeded in achieving resonant transparency of the studied material for gamma rays.

At present, significant advances have been made in Mössbauer spectroscopy owing to the use of synchrotron radiation in analyzing time spectra. Hastings *et al.* [8] developed an approach providing a means for treating the nuclear resonant forward scattering gamma-ray spectra in the framework of the Fourier representation. Shvyd'ko *et al.* [9] and Smirnov [10] found that the time spectra observed for thick Mössbauer absorbers are characterized by a superposition of quantum beats associated with the hyperfine structure of the energy levels and dynamical beats induced by interference of gamma rays due to spatial phase incursion in the case of resonance absorption. In this respect, it is of interest to analyze the time spectra of a Mössbauer absorber under conditions of induced resonant transparency. Moreover, it is necessary to investigate in more detail the nonlinear evolution of the Doppler and radio-frequency spectra of the gamma intensity and to perform a comparison with their analogs in the optical range.

2. THE THEORY

2.1. The stationary case. Using ^{57}Fe nuclei in pure iron as an example, we consider the propagation of a gamma wave upon excitation of two-frequency gamma magnetic resonance. Simultaneous solution of the Maxwell equations and equations for the density matrix of a ^{57}Fe nucleus [7] makes it possible to analyze two variants: (i) symmetric excitation under conditions when the frequency of gamma radiation is shifted by $\Omega_s = (\Omega_2 + \Omega_1)/2$ and (ii) antisymmetric excitation under conditions when the frequency of gamma radiation is shifted by $\Omega_a = (\Omega_2 - \Omega_1)/2$. Here, Ω_2 and Ω_1 are the cyclic RFMF frequencies, which are resonant with respect to the Larmor frequencies of the ground and

1063-7834/02/4408-1500$22.00

excited states, respectively. In either of these variants, the intensity of a gamma wave propagating through a sample is described by six harmonics, including the zeroth harmonic; that is,

$$h^p(s,t) = \sum_{m=1}^{6} h_m^p(s) \times \exp(i[q(\Omega_1 t + \varphi_1)] + r(\Omega_2 t + \varphi_2)), \quad (1)$$

where m specifies the values of q and r (Table 1).

In relationship (1), we changed over to a dimensionless quantity, namely, the optical path $s = (1/2)\sigma_0 n_0 z(2L+1)/(2L_e+1)$. Here, σ_0 is the resonance cross section of absorption of gamma-ray photons (for the 14.4-keV gamma transition of a ^{57}Fe nucleus, $\sigma_0 = 1.48\times10^5\delta$, n_0 is the number of Mössbauer nuclei per unit volume, z is the distance passed by gamma radiation, L is the radiation multipolarity (for ^{57}Fe, $L = 1$), and $I_e(I_g)$ is the nuclear spin in the excited (ground) state (for ^{57}Fe, $I_e = 3/2$ and $I_g = 1/2$).

The harmonic amplitudes for the symmetric and antisymmetric excitation variants satisfy the set of equations

$$-\frac{d\tilde{h}_m^p(s)}{ds} = \sum_{m'=1}^{6}\sum_{p'=\pm1} R_{mm'}^{pp'}\tilde{h}_{m'}^{p'}(s), \quad (2)$$

$$R_{mm'}^{pp'} = \sum_{e,g}\frac{{}^pL_m^{eg\,p'}L_{m'}^{eg}}{i[a_e e - a_g g + \Omega_{s,a} + D] + 1}. \quad (3)$$

Here, we carried out the change $\tilde{h}_m^p = h_m^p\exp(ip\psi)$.

In both variants, the factors ${}^pL_m^{eg}$ are defined as follows:

$$\begin{aligned}
{}^pL_1^{eg} &= \frac{1}{2}d_{e,3/2}^{(3/2)}(\beta_e)d_{g,1/2}^{(1/2)}(\beta_g),\\
{}^pL_4^{eg} &= \frac{1}{\sqrt{12}}d_{e,-1/2}^{(3/2)}(\beta_e)d_{g,1/2}^{(1/2)}(\beta_g),\\
{}^pL_2^{eg} &= \frac{-p}{\sqrt{3}}d_{e,1/2}^{(3/2)}(\beta_e)d_{g,1/2}^{(1/2)}(\beta_g),\\
{}^pL_5^{eg} &= \frac{-p}{\sqrt{3}}d_{e,-1/2}^{(3/2)}(\beta_e)d_{g,-1/2}^{(1/2)}(\beta_g),\\
{}^pL_3^{eg} &= \frac{1}{\sqrt{12}}d_{e,1/2}^{(3/2)}(\beta_e)d_{g,-1/2}^{(1/2)}(\beta_g),\\
{}^pL_6^{eg} &= \frac{1}{2}d_{e,-3/2}^{(3/2)}(\beta_2)d_{g,-1/2}^{(1/2)}(\beta_g),
\end{aligned} \quad (4)$$

where $d_{e,e'}^{(3/2)}(\beta_e)$ and $d_{g,g'}^{(1/2)}(\beta_g)$ are the Wigner functions; e and g are the magnetic quantum numbers of spins 3/2 and 1/2, respectively; and the angles β_e and β_g are determined from the following equations:

$$\begin{aligned}
a_e\sin\beta_e &= \frac{1}{2}\omega_{1e}, \quad a_e\cos\beta_e = \omega_{0e} + \Omega_1;\\
a_g\sin\beta_g &= \frac{1}{2}\omega_{1g}, \quad a_g\cos\beta_g = \omega_{0g} - \Omega_2.
\end{aligned} \quad (5)$$

The calculations will be perform for $\omega_{1e}/(\Gamma/2) = 3$ and $\omega_{1g}/(\Gamma/2) = 5.25$. The boundary conditions for the symmetric and antisymmetric variants can be written in the form

$$h_m^p(s)\big|_{s=0} = \delta_{m,5}h^p(0), \quad h_m^p(s)\big|_{s=0} = \delta_{m,3}h^p(0), \quad (6)$$

where $\delta_{m,m'}$ is the Kronecker symbol.

For unpolarized incident radiation, the intensity I_{st} of the zeroth harmonic and the intensities I_h of the harmonics of quantum beats can be represented as

$$I_{st}(s) = \frac{I_0}{2}\sum_m\sum_{p,p'}[(e^{-Rs})_{mm_0}^{pp'}(e^{-R^*s})_{mm_0}^{pp'}], \quad (7)$$

$$I_h(s,t) = \frac{I_0}{2}\sum_{mm'}\sum_{p,p'}[(e^{-Rs})_{mm_0}^{pp'}(e^{-R^*s})_{m'm_0}^{pp'}] \times e^{i[\Phi_m(t)-\Phi_{m'}(t)]}. \quad (8)$$

According to the analysis performed earlier in [7], the highest intensities are observed for the *a* harmonic in the symmetric case and the *f* harmonic in the antisymmetric case. It is worth noting that the quantum beat components of the symmetric *a* harmonic are composed of harmonics 1–3, 2–5, and 4–6 (Table 2) and that, for small angles β_e and β_g, these pairs are governed by the selection rule $\Delta(e+g) = 2$, whereas the antisymmetric *f* harmonic follows the selection rule $\Delta(e+g) = 0$ (see [7]). It is these harmonics that will be considered below.

Table 1. Notation for the index m

m	$(q, r)_s$	$(q, r)_a$
1	2.1	1.1
2	1.1	0.1
3	1.0	0.0
4	0.1	–1.1
5	0.0	–1.0
6	–1.0	–2.0

2.2. The stationary spectra. First, we analyze how the detuning δ (with respect to the Doppler shift) of the collective gamma-resonance [7], which arises in a system of Zeeman levels (dressed by two RFMFs) of the ground and excited states of the Mössbauer nucleus, affects the transparency of the medium. It can be seen

Table 2. Harmonics of quantum beats of the gamma wave under consideration

Phase	Superposition of harmonics
a. $(\Omega_1 + \varphi_1) + (\Omega_2 t + \varphi)$	1–3, 2–5, 4–6
b. $(\Omega_1 t + \varphi_1)$	1–2, 2–4, 3–5, 5–6
c. $(\Omega_2 t + \varphi_2)$	2–3, 4–5
d. $2(\Omega_1 t + \varphi_1)$	1–4, 3–6
e. $2(\Omega_1 t + \varphi_1) + (\Omega_2 t + \varphi_2)$	1–5, 2–6
f. $(\Omega_1 t + \varphi - 1) - (\Omega_2 t + \varphi_2)$	3–4
g. $3(\Omega_1 t + \varphi_1) + (\Omega_2 t + \varphi_2)$	1–6

from Figs. 1 and 2 that, upon symmetric (*a* harmonic) and antisymmetric (*f* harmonic) excitations, the detuning leads to a substantial decrease in the transparency (by a factor of approximately three at $\delta = 10$ as compared to that at $\delta = 0$). The sharpness of the peaks in the vicinity of the transparency region boundaries decreases significantly.

The radio-frequency spectra were obtained using consistent detuning, that is,

$$\Omega_1 = |\omega_{0e}| + y + \delta/2, \quad \Omega_2 = |\omega_{0g}| - y + \delta/2. \quad (9)$$

In this case, the detuning of collective gamma-resonance is characterized by the parameter δ. The dependence of the intensity on the RFMF frequency was derived by changing the variable *y*. For this purpose, we analyzed different points of the spectra depicted in Figs. 1 and 2. The results obtained demonstrate that the sharpest changes in the spectra take place at the points marked by arrows in Fig. 1. Further examination of the spectra with respect to these points (Fig. 3) allows us to make the inference that the intensity of the spectrum changes most drastically when the detuning parameter δ is equal to zero. Orriols [11] also observed a sharp change in the optical spectrum of induced transparency. This suggests that the interference exhibits a nonlinear behavior due to mixing of the Raman and parametric processes in two-frequency gamma magnetic resonance [12]. These abrupt changes in the gamma-ray spectra under conditions of induced resonant transparency can be used for precise determination of the hyperfine fields and other parameters of the interaction between nuclei and the environment. In optics, a magnetometric method based on the induced transparency effect has already been devised [13–15].

2.3. The time spectra. Now, we consider the case when a pulse of gamma waves is incident on the edge of the Mössbauer absorber. For the harmonic amplitudes of the gamma wave intensity, we can use the Fourier representation

$$\tilde{h}^p_m(s, t) = \frac{1}{2\pi}\int_{-\infty}^{\infty} d\nu \exp(-i\nu t)\tilde{h}^p_m(s, \nu). \quad (10)$$

By ignoring the delay effect, the time dependence of the harmonic amplitudes can be represented by the equation

$$\tilde{h}^p_m(s, t) = \frac{1}{2\pi}\sum_{p' = \pm 1}\int_{-\infty}^{\infty} d\nu \exp(-i\nu t) \times \{\exp(-\hat{R}(\nu)s)\}^{pp'}_{mm_0}\tilde{h}^{p'}_{m_0}(0, \nu), \quad (11)$$

$$R^{pp'}_{mm'} = \sum_{e, g}\frac{{}^pL^{eg}_m x^{p'}L^{eg}_{m'}}{i[a_e e - a_g g + \Omega_{s, a} + D - \nu] + 1}, \quad (12)$$

where $m_0 = 5$ and 3 for the symmetric and antisymmetric variants, respectively, according to the boundary

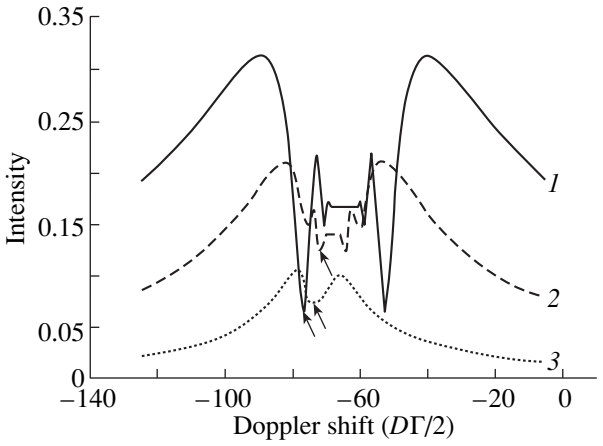

Fig. 1. Doppler spectra of the intensity of the *a* harmonic upon symmetric excitation for δ = (*1*) 0, (*2*) 5, and (*3*) 10.

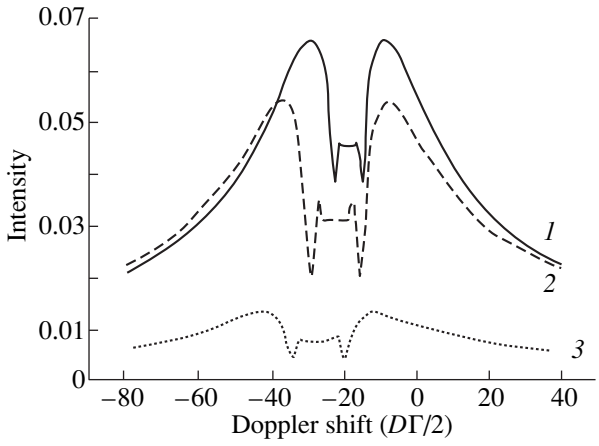

Fig. 2. Doppler spectra of the intensity of the *f* harmonic upon antisymmetric excitation for δ = (*1*) 0, (*2*) 5, and (*3*) 10.

conditions (6). For convenience, let us introduce the following designations:

$$\{e, g\} \equiv j, \quad \binom{p}{m} \equiv r, \quad \hat{L}(j) = \{L(j)\}_{rr'},$$
$$A_j(\nu) = ia_j(\nu) + 1, \quad a_j(\nu) = a_j - \nu, \qquad (13)$$
$$a_j = a_e e - a_g g + \Omega_{s,a} + D, \quad \{\hat{\Phi}(j)\}^{pp'}_{mm'} = {}^{p}L^{egp'}_{m}L^{eg}_{m'}.$$

Moreover, we can write the relationship

$$[\hat{R}(j)]^n = \frac{(l^2)^{n-1}}{(A_j(\nu))^n}\hat{\Phi}(j), \qquad (14)$$

where $l^2 = \sum_r (L^r)^2$.

Since the incident synchrotron pulse has a duration $T < nc$, it is reasonable to represent this pulse in the form $H\delta(t - t_0)$, where $\delta(t - t_0)$ is the delta function. According to the combinatorial analysis, we can write the relationship

$$h^p_m(t, s) = H\delta(t - t_0) + \sum_{n=1}^{\infty}\frac{(-s)^n}{(n-1)!n!}\sum_{j1}\{\hat{\Phi}(j_1)\}^{pp'}_{mm_0}(l^2)^{n-1} \times \int_0^{\infty} dx_1 (x_1)^{n-1}\exp(-A_{j1}(0)x_1)\delta(x_1 - t) + \sum_{n=2}^{\infty}(-s)^n \sum_{k_1+k_2=n}\sum_{j_1\neq j_2}\frac{\{[\hat{\Phi}(j_1)]^{k_1}[\hat{\Phi}(j_2)]^{k_2}\}^{pp'}_{mm_0}}{(k_1-1)!k_1!(k_2-1)!k_2!} \times \int_0^{\infty} dx_1 (x_1)^{k_1-1} e^{-A_{j_1}(0)x_1} \times \int_0^{\infty} dx_2 (x_2)^{k_2-1} e^{-A_{j_2}(0)x_2}\delta(x_1 + x_2 - t) + \ldots. \qquad (15)$$

The combinatorial analysis is based on the account of the number of terms involved in products that are not coincident with each other. These terms are designated by $j_1, j_2, \ldots, j_h$ where $h_{\max} = (2I_g + 1)(2L_e + 1)$. For a ^{57}Fe nucleus, $h_{\max} = 8$ is determined by the number of possible Rabi levels. Note that the higher the Rabi frequencies, the faster the convergence of the expansion in terms of the contributions with a particular h.

Since the experimental setup does not respond to very fast variations in time, the zero contribution ($h = 0$) with the delta function is rejected and the second contribution is defined by an expression similar to that given in [16]; that is,

$$\tilde{h}^p_m(s, t) = -\frac{sJ_1(2\sqrt{sl^2}t)}{\sqrt{sl^2}t} \times \sum_{j_1}\sum_{p'}\{\Phi(j_1)\}^{pp'}_{mm_0}\tilde{h}^{p'}_{m_0}(0, 0)\exp(-A_{j_1}(0)t), \qquad (16)$$

where $J_1(2\sqrt{sl^2}t)$ is the Bessel function of the first kind and $t_0 = 0$.

Expression (16) corresponds to the case of small s, because, at $s \longrightarrow \infty$, we obtain the relationship $J_1(\sqrt{s}) \sim 1/\sqrt[4]{s}$; hence, $\tilde{h}^p_m \sim \sqrt[4]{s}$; i.e., the gamma wave intensity increases as $\sqrt{s}$ with an increase in the passed path.

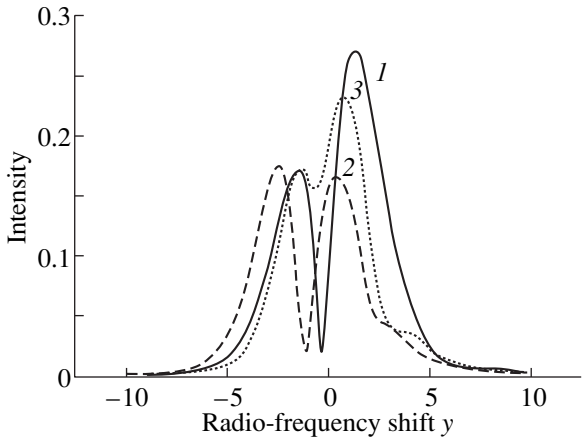

Fig. 3. Radio-frequency spectra of the intensity of the a harmonic upon symmetric excitation for δ = (*1*) 0, (*2*) 5, and (*3*) 10.

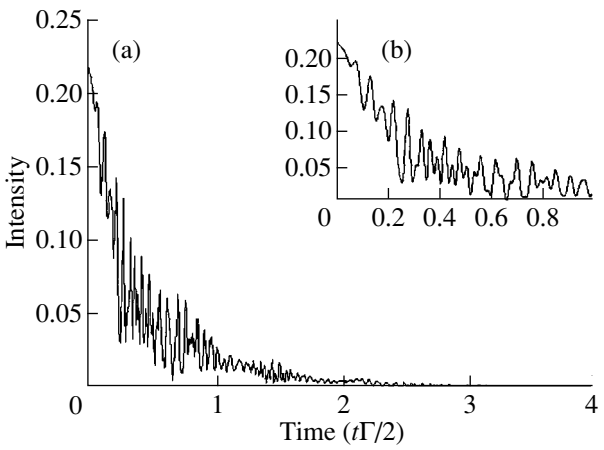

Fig. 4. (a) The time spectrum of the intensity of gamma radiation upon symmetric excitation and (b) a spectral fragment on an enlarged scale.

However, this situation is unjustified physically. At the same time, for large Rabi splittings and $s \leq 1$, some tentative estimates can be made using relationship (16). The intensity of the time spectra is determined by the square of the magnitude of the sum of harmonics of the magnetic gamma wave intensity averaged over the polarization of incident radiation.

Figure 4 displays the time spectrum of the intensity of gamma radiation from a synchrotron source under conditions of resonant transparency induced by two-frequency gamma magnetic resonance (at the optical path $s = 1$). As can be seen, this spectrum represents a superposition of the time Mössbauer spectra attributed not only to the quantum and dynamical beats but also to the beats of radio-frequency harmonics. Further analysis should be performed with due regard for the other contributions in expansion (15). Another approach involves solution of the problem for gamma pulses of finite duration.

3. CONCLUSION

The above analysis demonstrated that nonlinear interference phenomena can substantially affect the character of the resonant interaction between gamma radiation and nuclei. It is reasonable to expect that the induced resonant transparency effect can be used in total external reflection techniques and nuclear Bragg scattering in crystals containing Mössbauer nuclei with an energy spectrum characterized by a hyperfine structure. This makes it possible to reveal the contribution of the inelastic channels and those associated with them, including conversion electron emission. The nonlinear character of induced resonant transparency can find application in improving the resolution of gamma-resonance spectra. Performing experiments for the purpose of attaining induced resonant transparency in different media with the use of a synchrotron source of gamma radiation holds considerable promise. Another aspect of the practical use of the induced resonant transparency effect is associated with the development of nonlinear gamma-ray optics. Moreover, the induced resonant transparency effect can be used in designing gamma-ray cavities and gamma-ray lasers.

REFERENCES

1. B. A. Agap'ev, N. B. Gornyĭ, B. G. Matisov, and Yu. V. Rozhdestvenskiĭ, Usp. Fiz. Nauk **163** (9), 1 (1993) [Phys. Usp. **36**, 763 (1993)].
2. S. E. Harris, Phys. Today **50** (7), 36 (1997).
3. A. V. Mitin, Phys. Lett. A **84** (5), 278 (1981).
4. V. K. Voĭtovetskiĭ, S. M. Cheremisin, A. Yu. Dudkin, and E. G. Ploskirev, Pis'ma Zh. Éksp. Teor. Fiz. **36** (9), 322 (1982) [JETP Lett. **36**, 393 (1982)].
5. A. V. Mitin, E. F. Makarov, and N. V. Polyakov, Zh. Éksp. Teor. Fiz. **90** (6), 1931 (1986) [Sov. Phys. JETP **63**, 1130 (1986)].
6. A. V. Mitin, Izv. Akad. Nauk, Ser. Fiz. **56** (7), 186 (1992).
7. A. V. Mitin and D. A. Roganov, Izv. Akad. Nauk, Ser. Fiz. **65** (7), 941 (2001).
8. J. B. Hastings, D. P. Siddons, U. van Bürck, *et al.*, Phys. Rev. Lett. **66** (6), 770 (1991).
9. Yu. V. Shvyd'ko, U. van Bürck, W. Potzel, *et al.*, Phys. Rev. B **57** (6), 3552 (1998).
10. G. V. Smirnov, Hyperfine Interact. **123/124**, 31 (1999).
11. G. Orriols, Nuovo Cimento B **53** (1), 1 (1979).
12. A. V. Mitin, Phys. Lett. A **213**, 207 (1996).
13. M. O. Scully and M. Fleischhauer, Phys. Rev. Lett. **69**, 1360 (1992).
14. M. O. Scully, Phys. Rev. Lett. **67**, 1855 (1991).
15. A. S. Zibrov, M. D. Lukin, L. Hollberd, *et al.*, Phys. Rev. Lett. **76**, 3935 (1996).
16. Yu. M. Kagan, A. M. Afanas'ev, and V. G. Kohn, J. Phys. C **12**, 615 (1979).

Translated by O. Borovik-Romanova

Physics of the Solid State, Vol. 44, No. 8, 2002, pp. 1505–1509. Translated from Fizika Tverdogo Tela, Vol. 44, No. 8, 2002, pp. 1439–1443.

PROCEEDINGS OF THE XI FEOFILOV WORKSHOP "SPECTROSCOPY OF CRYSTALS ACTIVATED BY RARE-EARTH AND TRANSITION-METAL IONS"

(Kazan, Tatarstan, Russia, September 24–28, 2001)

Quantum Interference of Mössbauer Gamma-Radiative Transitions in Magnetic Materials

É. K. Sadykov, L. L. Zakirov, A. A. Yurichuk, and V. V. Arinin

Kazan State University, ul. Lenina 18, Kazan, 420008 Tatarstan, Russia
e-mail: esad@ksu.ru

Abstract—A method is developed for calculating the resonance fluorescence spectrum of coherent radiation with a finite linewidth from a system whose energy levels are coupled through a strong field. In this case, the shape of the spectrum is essentially affected by quantum interference. The results obtained give impetus to investigations into quantum interference of Mössbauer gamma-radiative transitions in magnetic materials under conditions of induced coherent magnetization dynamics. © *2002 MAIK "Nauka/Interperiodica".*

1. INTRODUCTION

In the last decade, noticeable advance has been made in the theoretical and experimental study of quantum interference (QI) of optical transitions [1–4]. Particular attention has been given to the QI phenomenon in the spectral region of Mössbauer (gamma) radiation [5], where this effect can be used for coherent inversionless amplification. This is of fundamental importance, because it is unfeasible to create a gamma-ray laser by using the schemes typical of visible-light lasers.

In our earlier paper [6], the QI of Mössbauer transitions was studied in a four-level system of electron–nucleus states, where this effect leads to the occurrence of regions of destructive and constructive interference in the spectrum of spontaneous gamma radiation caused by a coherent field acting on the electron degrees of freedom and mixing the electron–nucleus states. The QI effect essentially depends on the initial state of the system. For example, in [6], it was assumed that the Mössbauer energy level is selectively populated by incoherent radiation. In this case, the coherence effect manifests itself as an insignificant change in the line shape due to QI. The objective of this paper is to show that the QI effect becomes noticeable and can be easily measured experimentally when the selective excitation is caused by coherent or fairly narrow-band radiation.

2. THE DENSITY MATRIX METHOD (THREE-LEVEL SCHEME): ALLOWANCE FOR PUMPING-FIELD PHASE FLUCTUATIONS

By way of illustration, we consider the three-level system (Fig. 1). Level *1* and the other two levels (*2*, *3*) are different states of a nucleus between which gamma-radiative transitions can occur. A strong coherent field with energy quantum Ω_0 (which is a hyperfine-structure field in nature) is induced by an external radio-frequency (RF) field and mixes spin sublevels *2* and *3*. The feasibility of generation of such a strong field in magnetic materials has been demonstrated experimentally (see, e.g., [7]). The density matrix for this system in the interaction representation satisfies the equation

$$\frac{d\hat{\rho}'}{dt} = -\frac{i}{\hbar}[\hat{H}'\hat{\rho}'] + \Lambda\hat{\rho}'. \qquad (1)$$

The Hamiltonian $\hat{H}'$ is defined as

$$\hat{H}' = \exp(i\hat{H}_0 t)(\hat{H}^d + \hat{H}^p)\exp(-i\hat{H}_0 t), \qquad (2)$$

where $\hat{H}_0$, $\hat{H}^d$, and $\hat{H}^p$ are the zeroth-approximation

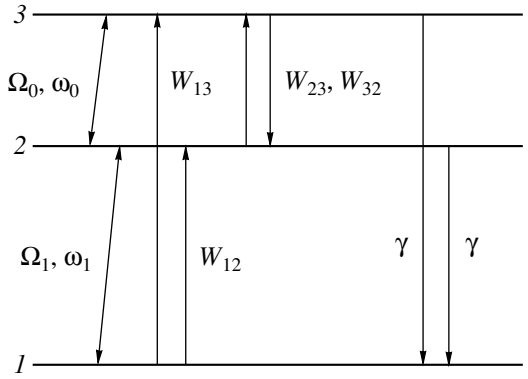

Fig. 1. Three-level system. Ω_0 and Ω_1 are the mixing field and the pumping field, respectively; W_{12} and W_{13} are the parameters of the incoherent pumping radiation; W_{23} and W_{32} are the spin relaxation rates; and γ is the gamma-decay constant.

Hamiltonian, the strong RF field, and the pumping field, respectively, which are given by [8, 9]

$$\hat{H}_0 = \sum_{i=1}^{3} \varepsilon_i \hat{a}_i^+ \hat{a}_i, \tag{3}$$

$$\hat{H}^d = \hbar\Omega \exp(-i\omega_0 t)\hat{a}_3^+ \hat{a}_2 + \hbar\Omega_0^* \exp(i\omega_0 t)\hat{a}_2^+ \hat{a}_3, \tag{4}$$

$$\begin{aligned}\hat{H}^p = \hbar[&\Omega_1 \exp(i\theta(t))\hat{a}_2^+ \hat{a}_1 \exp(-i\omega_1 t) \\ &+ \Omega_1^* \exp(-i\theta(t))\hat{a}_1^+ \hat{a}_2 \exp(i\omega_1 t)].\end{aligned} \tag{5}$$

Here, $\hat{a}_i$ and $\hat{a}_i^+$ are Fermi operators.

In Eq. (5), the phase of the pumping field is assumed to fluctuate and $\theta(t)$ is a random function subject to a Wiener–Levy process. The line shape of such a field can be described by a Lorentzian function of width $2D$ and is found from the equation [10, 11]

$$\langle \dot{\theta}(t)\dot{\theta}(t')\rangle = 2D\delta(t-t'). \tag{6}$$

Preparatory to solving Eq. (1) with interaction given by Eq. (5), we will first write out a solution to this equation in the case where there are no fluctuations in the interaction in Eq. (5) [8, 9]:

$$\frac{d}{dt}\mathbf{\Psi} = \mathbf{L}\mathbf{\Psi} + \mathbf{I}. \tag{7}$$

Here, $\mathbf{L}$ and $\mathbf{I}$ are a matrix and a vector, respectively (see table), which are time-independent functions of Ω_0, Ω_1, and of the parameters of irreversible processes [the second term in Eq. (1)], and $\mathbf{\Psi}$ is a column vector with the following components:

$$\begin{aligned}&\Psi_1 = \rho'_{12}\exp(-i\Delta_1 t), \quad \Psi_2 = \rho'_{13}\exp(-i(\Delta_1+\Delta)t), \\ &\Psi_3 = \rho'_{21}\exp(i\Delta_1 t), \quad \Psi_4 = \rho'_{22}, \\ &\Psi_5 = \rho'_{23}\exp(-i\Delta t), \quad \Psi_6 = \rho'_{31}\exp(i(\Delta_1+\Delta)t), \\ &\Psi_7 = \rho'_{32}\exp(i\Delta t), \quad \Psi_8 = \rho'_{33}.\end{aligned} \tag{8}$$

Here, $\Delta = \omega_0 - \omega_{32}$ and $\Delta_1 = \omega_1 - \omega_{21}$ are detunings of the respective frequencies relative to the corresponding transition frequencies.

The solutions to Eq. (7) enable one to calculate the correlation functions and the radiation spectrum [8, 9].

When interaction (5) with a pumping field with fluctuating phase is included in Eq. (1), the structure of Eq. (7) is grossly changed. We will demonstrate the extension of the theory developed in [6, 8, 9] to this case on the example of the three-level system in calculating the required correlation functions.

The spectrum of spontaneous radiation associated with a *j–i* transition is given by the Fourier transform of the double-time correlation function:

$$\gamma(\tau_1, \tau_0) \propto \langle \hat{P}^{(-)}(\tau_1)\hat{P}^{(+)}(\tau_0)\rangle, \tag{9}$$

where $\hat{P}^{(+)} = \mu_{ij}\hat{a}_i^+ \hat{a}_j$ is the transition polarization operator. We consider only gamma-radiative transitions, namely, *3–1* and *2–1*.

We calculate the correlation function in Eq. (9) with the help of the quantum-regression theorem. For this purpose, we first calculate the equal-time average:

$$\begin{aligned}\langle \hat{P}^{(-)}(\tau_1)\rangle = \mathrm{Tr}[\mu_{ij}\hat{a}_j^+ \hat{a}_i \hat{\rho}] = \mu_{13}\exp(i\omega_1\tau + i\omega_0\tau) \\ \times \Psi_2(\tau_1) + \mu_{12}\exp i\omega_1\tau \Psi_1(\tau_1).\end{aligned} \tag{10}$$

Matrix **L** and column vector **I**

	1	2	3	4	5	6	7	8	**I**
1	$-\Gamma_{12}$	$i\Omega_0$	0	$-2i\Omega_1^*$	0	0	0	$-i\Omega_1^*$	$i\Omega_1^*$
2	$i\Omega^*$	$-\Gamma_{13}$	0	0	$-i\Omega_1^*$	0	0	0	0
3	0	0	$-\Gamma_{21}$	$2i\Omega_1$	0	$-i\Omega_0^*$	0	$i\Omega_1$	$-i\Omega_1$
4	$-i\Omega_1$	0	$i\Omega_1^*$	$-\Gamma_{22}$	$i\Omega_0$	0	$-i\Omega_0^*$	$W_{32}-W_{12}$	W_{12}
5	0	$-i\Omega_1$	0	$i\Omega_0^*$	$-\Gamma_{23}$	0	0	$-i\Omega_1^*$	0
6	0	0	$-i\Omega_0^*$	0	0	$-\Gamma_{31}$	$i\Omega_1$	0	0
7	0	0	0	$-i\Omega_0$	0	$i\Omega_1^*$	$-\Gamma_{32}$	$i\Omega_0$	0
8	0	0	0	$W_{23}-W_{13}$	$-i\Omega_0$	0	$i\Omega_1^*$	$-\Gamma_{33}$	W_{13}

Note: $\Gamma_{12} = (W_{12} + W_{13} + \gamma + W_{23})/2 + i\Delta_1$, $\Gamma_{21} = \Gamma_{12}^*$; $\Gamma_{13} = (W_{12} + W_{13} + \gamma + W_{32})/2 + i(\Delta_1 + \Delta)$, $\Gamma_{31} = \Gamma_{13}^*$; $\Gamma_{23} = (2\gamma + W_{23} + W_{32})/2 + i\Delta$, $\Gamma_{32} = \Gamma_{23}^*$; $\Gamma_{22} = \gamma + W_{23} + W_{12}$; and $\Gamma_{33} = \gamma + W_{32} + W_{13}$.

The quantities $\Psi_1(\tau_1)$ and $\Psi_2(\tau_1)$ are the components of the vector $\mathbf{\Psi}' = (\Psi_1, \Psi_2, \Psi_3^{--}, \Psi_4^-, \Psi_5^-, \Psi_6^{--}, \Psi_7^-, \Psi_8^-)$, which, in turn, is determined by the components given by Eq. (8),

$$\Psi_i^- = \Psi_i \exp(-i\theta(t)), \quad \Psi_i^+ = \Psi_i \exp(i\theta(t)). \quad (11)$$

The column vector $\mathbf{\Psi}'$ satisfies the matrix equation

$$\frac{d}{dt}\mathbf{\Psi}' = [\mathbf{L} - i\dot{\theta}(t)\mathbf{L}']\mathbf{\Psi}' + \mathbf{I}\exp(-i\theta(t)). \quad (12)$$

The matrix $\mathbf{L}$ and vector $\mathbf{I}$ are the same as those in Eq. (7). The diagonal matrix $\mathbf{L}'$ has the following nonzero components: $L'_{33} = L'_{66} = 2$ and $L'_{44} = L'_{55} = L'_{77} = L'_{88} = 1$.

Equation (12) is a stochastic differential equation with coefficients which are random functions of time. Since we consider the stationary case, Eq. (12) should be averaged over the stochastic variables, which gives [10, 11]

$$\begin{aligned}\frac{d}{dt}\langle\mathbf{\Psi}'\rangle &= [\mathbf{L} - D(\mathbf{L}')^2]\langle\mathbf{\Psi}'\rangle + \mathbf{I}\langle\exp(-i\theta(t))\rangle \\ &= \mathbf{L}_1\langle\mathbf{\Psi}'\rangle + \mathbf{I}\langle\exp(-i\theta(t))\rangle.\end{aligned} \quad (13)$$

A solution to this equation can be written in the form (we drop the stochastic-average sign for the quantities $\mathbf{\Psi}'$ in what follows)

$$\begin{aligned}\mathbf{\Psi}'(\tau_1) &= \exp[\mathbf{L}_1(\tau_1 - \tau_0)]\mathbf{\Psi}'(\tau_0) \\ &+ \int_{\tau_0}^{\tau_1} d\tau' \exp[\mathbf{L}(\tau_1 - \tau')]\mathbf{I}\langle\exp(-i\theta(\tau'))\rangle.\end{aligned} \quad (14)$$

By making the substitution of variable $\tau = \tau_1 - \tau_0$ and using the relation $\langle\exp(-i\theta(\tau')\rangle = \exp(-D(\tau' - \tau_0))\langle\exp(-i\theta(\tau_0))\rangle$, we find

$$\begin{aligned}\mathbf{\Psi}'(\tau_1) &= \exp[\mathbf{L}_1(\tau)]\mathbf{\Psi}'(\tau_0) \\ &+ \int_0^{\tau} d\tau' \exp[\mathbf{L}(\tau - \tau')]\mathbf{I}\langle\exp(-i\theta(\tau_0))\rangle \\ &\times \exp(-D\tau') = \exp[\mathbf{L}_1(\tau)]\mathbf{\Psi}'(\tau_0) \\ &+ \frac{\exp(\mathbf{L}_1\tau) - \exp(-\mathbf{D}\tau)}{\mathbf{L}_1 + \mathbf{D}}\mathbf{I}\langle\exp(-i\theta(\tau_0))\rangle.\end{aligned} \quad (15)$$

Here, $\mathbf{D}$ is the number D multiplied by the unit matrix of the same order as the matrix $\mathbf{L}$.

The quantities $\Psi'_j(\tau_0)$ can be expressed in terms of the system operators at time $\tau = \tau_0$. For example, we have

$$\begin{aligned}\Psi'_2(\tau_0) &= \langle\exp(-i\omega_1\tau_0)\rho_{13}(\tau_0)\rangle \\ &= \langle\exp(-i\omega_1\tau_0)\langle|3\rangle\langle 1|\rangle_{\tau_0}\rangle.\end{aligned} \quad (16)$$

The double-time average $\langle\langle P^{(-)}(\tau_1)P^{(+)}(\tau_0)\rangle\rangle$ [see Eq. (9), which is now also subjected to stochastic averaging] can be calculated from $\langle\langle P^{(-)}(\tau_1)\rangle\rangle$ with the help of the quantum-regression theorem by replacing $\langle\langle|i\rangle\langle j|\rangle_{\tau_0}\rangle$ and $\langle\exp(-i\theta(\tau_0))\rangle$, $\langle\langle|i\rangle\langle j|\hat{P}^{(+)}(\tau_0)\rangle_{\tau_0}\rangle$ and $\langle\exp(-i\theta(\tau_0))\hat{P}^{(+)}(\tau_0)\rangle$, respectively. This replacement leads to the occurrence of variables that are not involved in the vector $\mathbf{\Psi}'$. In order to find them, we introduce a vector $\mathbf{\Psi}'' = (\Psi_1^+, \Psi_2^+, \Psi_3^-, \Psi_4, \Psi_5, \Psi_6^-, \Psi_7, \Psi_8)$ which satisfies the matrix equation

$$\frac{d}{dt}\langle\mathbf{\Psi}''\rangle = [\mathbf{L} - D(\mathbf{L}'')^2]\langle\mathbf{\Psi}''\rangle + \mathbf{I} = \mathbf{L}_2\langle\mathbf{\Psi}''\rangle + \mathbf{I}. \quad (17)$$

Here, $\mathbf{L}''$ is a diagonal matrix with the following nonzero elements: $L''_{11} = L''_{22} = 1$ and $L''_{33} = L''_{66} = -1$.

Next, we take the limit $\tau_0, \tau_1 \longrightarrow \infty$ in such a way that the difference $\tau = \tau_1 - \tau_0$ is finite and then take the Laplace transform of the required correlation function in Eq. (9). The radiation spectrum is proportional to the real part of the expression thus found:

$$S(\omega) \propto S_1(\omega) + S_2(\omega), \quad (18)$$

where

$$\begin{aligned}S_1(\omega) = \mathrm{Re}\Bigg[&\sum_{j=1}^{2} M_{1j}(z_1)\Psi''_{j+3}(\infty) \\ &+ \sum_{j=1}^{8} N_{1j}(z_1)I_j\Psi''_3(\infty)\Bigg],\end{aligned} \quad (19)$$

$$\begin{aligned}S_2(\omega) = \mathrm{Re}\Bigg[&\sum_{j=1}^{2} M_{2j}(z_2)\Psi''_{j+6}(\infty) \\ &+ \sum_{j=1}^{8} N_{2j}(z_2)I_j\Psi''_6(\infty)\Bigg].\end{aligned} \quad (20)$$

Here, we introduced the following notation: $\mathbf{M}(z) = (\mathbf{z} - \mathbf{L}_1)^{-1}$, $\mathbf{\Psi}''(\infty) = \mathbf{L}_2^{-1}\mathbf{I}$, $\mathbf{N}(z) = (\mathbf{L}_1 + \mathbf{D})^{-1}[(\mathbf{z} - \mathbf{L}_1)^{-1} - (\mathbf{z} + \mathbf{D})^{-1}]$, $\mathbf{z}$ is equal to z multiplied by the unit matrix of the same order as that of the matrix $\mathbf{L}$, $z_1 = i(\omega - \omega_{21})$, and $z_2 = i(\omega - \omega_{31})$.

3. ANALYSIS OF THE RESULTS

The technique developed in [8, 9] for calculating coherent-fluorescence spectra ignores the elastic (Rayleigh) scattering, which is described by a δ function. In [8], such an approach was justified, because the emphasis was on the spontaneous emission that occurs under conditions of double coherent mixing of the states of a system and exhibits an unusual narrowing of its spec-

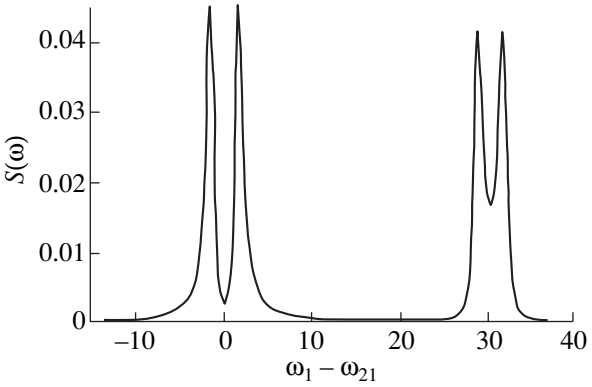

Fig. 2. Fluorescence spectrum in the case of incoherent pumping radiation. $\Omega_0 = 1.5$, $\Omega_1 = 0$, $W_{12} = 0.1$, $W_{13} = 0$, $W_{32} = W_{23} = 0.01$, and $\gamma = 1$.

trum. When the predictions made in [8] were verified experimentally in [12], precautions were also taken to remove the Rayleigh scattering component.

In the preceding section, we extended the technique employed in [6, 8, 9] to the case of a finite line width of pumping radiation. In this case, the Rayleigh scattering (including the Raman component) is represented in the fluorescence spectrum by lines of finite width. It turns out that the behavior of these lines essentially depends on the coherent properties of the system. First, let us consider the case of incoherent pumping radiation. It is seen from Fig. 2 that the spectrum consists of two spontaneous-emission lines, which are Rabi doublets distorted by QI. The case of coherent pumping radiation with finite line width differs fundamentally from the above case; now, in addition to the Rabi doublets, lines of a width comparable to the pump line width appear in the spectrum (Fig. 3). These lines are the Rayleigh lines in the scattering spectrum that had the form of δ functions and were neglected when the case of coherent pumping radiation was considered in [8, 9]. Figure 3 shows two fluorescence spectra which differ in their pumping energy quantum; this energy quantum is exactly equal to the *2–1* transition energy in Fig. 3a and differs from this value by Ω_0 in Fig. 3b. The difference in intensity of the extra lines is easy to understand. In the first case, both "dressed" states resulting from mixing of states *2* and *3* are excited, which leads to interference between Rayleigh scattering amplitudes from these two states. In the second case, only one dressed state is excited and there is no interference. This spectral feature can be characterized by the intensity ratio σ_2/σ_1, where σ_1 and σ_2 are determined experimentally as the areas under the fluorescence spectral curves in the regions of the *2–1* and *3–1* transitions, respectively. It is seen from Fig. 4 that with increasing Ω_0, the ratio σ_2/σ_1 can exceed unity in the case of resonant pumping radiation and only tends to unity in the case where the deviation of the pump frequency from its resonance value is equal to Ω_0. The difference in the behavior of σ_2/σ_1 is due to the different influence of QI on the Rayleigh scattering in these two cases. Therefore, in the case of narrow-band pumping radiation, the regions of the maximum QI effect in the fluorescence spectrum can be found by varying the pumping radiation fre-

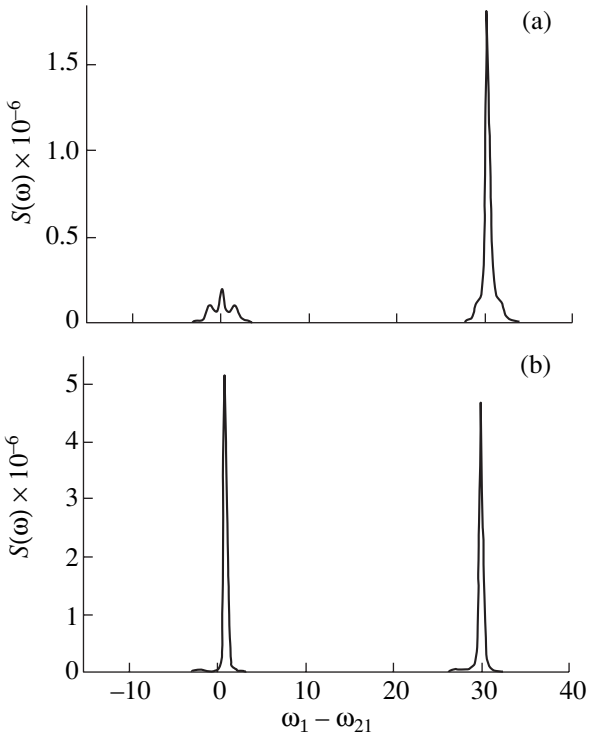

Fig. 3. Fluorescence spectrum in the case of pumping radiation with finite line width. $\Omega_0 = 1.5$, $\Omega_1 = 0.001$, $W_{12} = W_{13} = 0$, $W_{32} = W_{23} = 0.01$, $\gamma = 1$, and $D = 0.2$. The pump frequency (a) exactly equals the *1–2* transition frequency and (b) differs from this value by Ω_0.

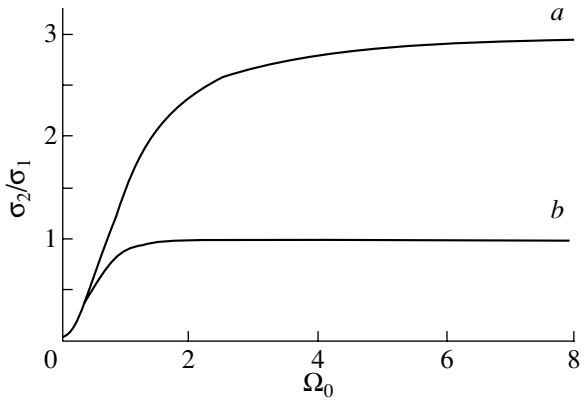

Fig. 4. Intensity ratio σ_2/σ_1 for the case of $\Omega_1 = 0.001$, $W_{12} = W_{13} = 0$, $W_{32} = W_{23} = 0.01$, $\gamma = 1$, and $D = 0.5$. The pump frequency (*a*) exactly equals the *1–2* transition frequency and (*b*) differs from this value by Ω_0.

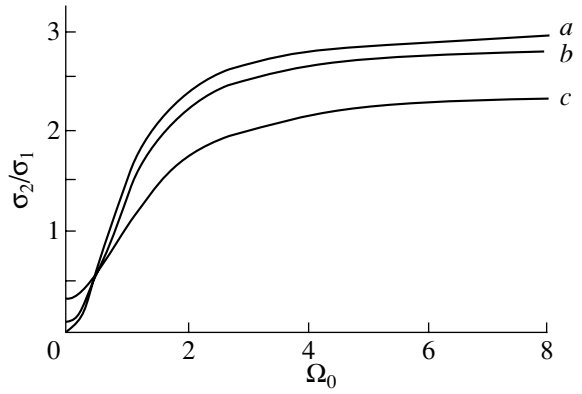

Fig. 5. Intensity ratio σ_2/σ_1 for the case of $\Omega_1 = 0.001$, $W_{12} = W_{13} = 0$, $\gamma = 1$, $D = 0.5$, and spin relaxation rates $W_{32} = W_{23}$ equal to (*a*) 0.01, (*b*) 0.1, and (*c*) 0.5.

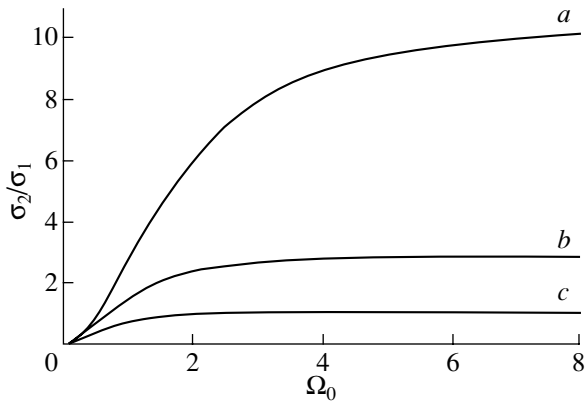

Fig. 6. Intensity ratio σ_2/σ_1 for the case of $\Omega_1 = 0.001$, $W_{12} = W_{13} = 0$, $W_{32} = W_{23} = 0.01$, $\gamma = 1$, and the parameter D equal to (*a*) 0.1, (*b*) 0.5, and (*c*) 10.

quency. Figure 5 demonstrates the effect of spin relaxation on the area ratio, while Fig. 6 shows the dependence of this ratio on the value of D. With increasing D, the effect of coherent pumping radiation becomes progressively similar to that of incoherent radiation. Therefore, the induced coherence in the system and the QI effects can be judged from the experimentally measured ratio between the areas σ_1 and σ_2.

Now, let us discuss possible observation of the effects predicted in this paper by using conventional Mössbauer spectroscopy. In [6], we restricted our consideration to the case of incoherent pumping radiation, because there are no currently available sources of coherent gamma radiation. However, the consideration in [6] is inadequate for describing a conventional Mössbauer experiment wherein the Mössbauer atom resonant fluorescence involves Mössbauer hyperfine-structure levels coupled by a strong field. This last case can be adequately described in terms of the model proposed in this paper (by putting $D = 0.5$), at least, when the Mössbauer radiation is sufficiently weak.

ACKNOWLEDGMENTS

This study was supported by the Russian Foundation for Basic Research (project no. 01-02-17502), NI-OKR RT (project no. 06-6.1-21/2001), and CRDF (grant no. REC-007).

REFERENCES

1. O. Kocharovskaya and P. Mandel, Phys. Rev. A **42**, 523 (1990).
2. K.-J. Boller, A. Imamoglu, and S. E. Harris, Phys. Rev. Lett. **66**, 2593 (1991).
3. H. Lee, P. Polynkin, M. O. Scully, and S.-Y. Zhu, Phys. Rev. A **55**, 4454 (1997).
4. S.-Y. Zhu, L. M. Narducci, and M. O. Scully, Phys. Rev. A **52**, 4791 (1995).
5. R. Coussement, M. van den Bergh, G. S'heeren, *et al.*, Phys. Rev. Lett. **71**, 1824 (1993).
6. E. K. Sadykov, L. L. Zakirov, and A. A. Yurichuk, Laser Phys. **11**, 409 (2001).
7. F. G. Vagizov, Hyperfine Interact. **61**, 1359 (1990).
8. L. M. Narducci, M. O. Scully, G.-L. Oppo, *et al.*, Phys. Rev. A **42**, 1630 (1990).
9. A. S. Manka, H. M. Doss, L. M. Narducci, *et al.*, Phys. Rev. A **43**, 3748 (1991).
10. A. H. Toor, S.-Y. Zhu, and M. S. Zubairy, Phys. Rev. A **52**, 4803 (1995).
11. J. Gea-Banacloche and M. S. Zubairy, Phys. Rev. A **42**, 1742 (1990).
12. D. J. Gauthier, Y. Zhu, and T. W. Mossberg, Phys. Rev. Lett. **66**, 2460 (1991).

Translated by Yu. Epifanov

Physics of the Solid State, Vol. 44, No. 8, 2002, pp. 1510–1512. Translated from Fizika Tverdogo Tela, Vol. 44, No. 8, 2002, pp. 1444–1445.

PROCEEDINGS OF THE XI FEOFILOV WORKSHOP "SPECTROSCOPY OF CRYSTALS ACTIVATED BY RARE-EARTH AND TRANSITION-METAL IONS"

(Kazan, Tatarstan, Russia, September 24–28, 2001)

Nonequilibrium Dynamic Effects within a Quantum Droplet Model of Ising Spin Glass

R. V. Saburova, E. A. Yanvarev, and V. G. Sushkova

Kazan State Power University, Kazan, 420066 Tatarstan, Russia

e-mail: saburov@mi.ru

Abstract—The real and imaginary parts of the dynamic linear magnetic susceptibility at very low temperatures are found within the quantum droplet model of Ising spin glass, and their temperature and frequency dependences are calculated analytically and numerically. The nonequilibrium theory of the response of quantum-mechanical systems is used. The slow, quasi-equilibrium dynamics and the divergence of the dynamic linear susceptibility are investigated. Numerical calculations illustrate the crossover between the low-frequency and high-frequency regimes. A transition to the glasslike state is assumed to occur at a nonzero temperature. At zero temperature, the results are identical to those obtained earlier. The spin-glass ageing is considered briefly in the model at hand. © *2002 MAIK "Nauka/Interperiodica".*

1. INTRODUCTION

In recent years, there has been a growing interest in theoretical and experimental studies of quantum spin glasses [1–4]. The problem of phase transition in spin glasses can be treated in terms of the dynamic magnetic susceptibility $\chi_1(\omega, T)$, where ω is the angular frequency of an external ac magnetic field and T is the temperature of the spin glass.

In this paper, we calculated the low-temperature dynamic linear magnetic susceptibility (the real and imaginary parts), as well as the linear susceptibility in the ageing regime, which gives important information on the dynamic behavior of glasslike systems. The nonequilibrium dynamics has been studied in the spin glass AgMn by measuring the dynamic linear susceptibility $\chi_1(\omega, T)$ at low frequencies [4]. The $\chi_1(T)$ temperature dependence for this glass has been discussed in terms of the classical droplet model of spin glasses [2]. Here, we employ a quantum droplet theory of spin glasses [3] based on the model Hamiltonian of a d-dimensional Ising spin glass in a transverse magnetic field

$$H = -\sum_{ij} J_{ij}\sigma_i^z\sigma_j^z - \Gamma\sum_i \sigma_i^x, \qquad (1)$$

where σ_i^x and σ_i^z are the Pauli matrices for a spin at site i and Γ is the magnetic field strength; summation in Eq. (1) is performed over the nearest neighbors, whose interaction J_{ij} is a random variable with zero average and the standard deviation $J = (\overline{J_{ij}})^{1/2}$. This model approximately describes, e.g., the diluted dipole magnet $LiHo_xY_{1-x}F_4$ [4].

2. DYNAMIC LINEAR SUSCEPTIBILITY

It was shown in [3] that, at very low temperatures, the quantum-mechanical Hamiltonian (1) can be represented as a sum of the Hamiltonians of independent quantum two-level systems (low-energy droplets):

$$H = \frac{1}{2}\tilde{\sum_L}\sum_{D_l}(\varepsilon_{D_L}s_{D_L}^z + \Gamma_L s_{D_L}^x), \qquad (2)$$

where $s_{D_L}^z$ and $s_{D_L}^x$ are the Pauli matrices, representing two states of a droplet D_L; summation is performed over all droplets D_L of length L and over all lengths L. The summation can be represented as $\tilde{\sum_L} \equiv \sum_{k=0}^{\infty} \sim \int_{L_0}^{\infty}\frac{dL}{L_0}$, where $L = 2^kL_0$ and L_0 is the cut-off length; ε_{D_L} is the energy of one droplet, which is an independent random variable. It is assumed that $\varepsilon_{D_L} \sim L^\theta$, where θ is an exponent satisfying the condition $\theta \le (d-1)/2$. The droplet length L is of the order of the correlation length, and $\Gamma_L = \Gamma_0\exp(-\sigma L^d)$ is the droplet tunneling rate, with Γ_0 being the microscopic tunneling rate; the coefficient σ is assumed to be the same for all droplets.

We use the general theory of the linear response of a quantum magnetic system to a weak external ac magnetic field. If a weak magnetic field $h(t) = h\cos\omega t$ is applied along the z axis, then the induced magnetic moment of the sample is

$$M(t) = [\chi_1'(\omega)\cos\omega t + \chi_1''(\omega)\sin\omega t]hV, \qquad (3)$$

1063-7834/02/4408-1510$22.00

where V is the sample volume and $\chi_1(\omega) = \chi_1'(\omega) - i\chi_1''(\omega)$ is the complex dynamic linear susceptibility.

Let us consider the case where the system is placed in a weak dc magnetic field h and is at equilibrium at $t \le 0$. If at the instant $t = 0$ the field is switched off, then the macroscopic magnetization at $t \ge 0$ can be represented in the form $M(t) - M(0) = \psi(t)h$, where $M(0)$ is the equilibrium magnetization in zero field and $\psi(t)$ is the relaxation function, which can be written as [3]

$$\psi(t) = \int_0^\beta \mathrm{Tr}[\rho_0 s^z \exp[i(t + i\lambda)H]s^z \times \exp[-i(t + i\lambda)H]]d\lambda - \beta(\mathrm{Tr}[\rho_0 s^z])^2, \quad (4)$$

where $\beta = (k_B T)^{-1}$, $\rho_0 = \dfrac{\exp(-\beta H)}{\mathrm{Tr}\exp(-\beta H)}$ is the equilibrium density matrix, and $\chi_1(\omega) = \psi(0)/V(i\omega/V)\int_0^\infty \psi(t)e^{-i\omega t}dt$.

In the quantum regime ($T \longrightarrow 0$, $\beta\Gamma_L \gg 1$, $\varepsilon_{D_L} > k_B T$), the real part $\chi_1'(\omega, T)$ of the linear susceptibility is given by

$$\chi_1'(\omega, T) - \chi_1'(0, T) \sim -\frac{q_{EA}\sigma^{\theta/d}}{4\gamma\theta}\left|\log\frac{\omega}{\Gamma_0}\right|^{-\theta/d} - \frac{2\sqrt{2\pi}}{\gamma\theta}q_{EA}\sigma^{\theta/d}\sqrt{\beta\omega}e^{-\beta\omega}\left|\log\frac{\omega}{\Gamma_0}\right|^{-\theta/d} \sim -\frac{q_{EA}\sigma^{\theta/d}}{4\gamma\theta}\left|\log\frac{\omega}{\Gamma_0}\right|^{\theta/d}(1 + 8\sqrt{2\pi\beta\omega}e^{-\beta\omega}), \quad (5)$$

where q_{EA} is the order parameter for the spin glass [4].

Using the well-known relation [4] $\chi_1''(\omega) = -\dfrac{\pi}{2}\dfrac{\partial\chi_1'(\omega)}{\partial(\log\omega)}$, we find the following expression for the imaginary part $\chi_1''(\omega, T)$ of the dynamic susceptibility:

$$\chi_1''(\omega, T) \sim \frac{\pi}{2}\frac{q_{EA}\sigma^{\theta/d}}{4\gamma\theta}\left|\log\frac{\omega}{\Gamma_0}\right|^{-\theta/d} - \frac{2\sqrt{2\pi}}{\gamma\theta}q_{EA}\sigma^{\theta/d}\sqrt{\beta\omega}e^{-\beta\omega}\left|\log\frac{\omega}{\Gamma_0}\right|^{\theta/d} \sim \frac{q_{EA}\sigma^{\theta/d}}{4\gamma\theta}\left|\log\frac{\omega}{\Gamma_0}\right|^{-\theta/d}(1 + 8\sqrt{2\pi\beta\omega}e^{-\beta\omega}). \quad (6)$$

Equations (5) and (6) describe the spin-glass dynamics in a transverse magnetic field at low temperatures.

Now, we treat the nonequilibrium process of ageing in terms of our spin-glass model. In this case, a sample is cooled in a zero magnetic field for a so-called waiting time t_w down to a temperature $T < T_g$, where T_g is the spin-freezing temperature [4]. Then, a probing weak ac magnetic field is applied and the dynamic susceptibility $\chi_1(t + t_w, t_w)$ is measured as a function of time at a fixed temperature. This problem is of interest, because most measurements on spin glasses are made under nonequilibrium conditions and, therefore, the experimental data have to be carefully analyzed. The real part of the dynamic linear susceptibility (or of the integrated response) has the form

$$\chi_1(t + t_w, t_w) = \int_{t_w}^{t + t_w} dt' R(t + t_w, t'),$$

$$R(t, t') = \left.\frac{\partial\langle\overline{S^z(t)}\rangle}{\partial h(t')}\right|_{h=0}.$$

Here, $\langle\ldots\rangle$ signifies a thermal average and $\overline{S(t)}$ is the configuration average (over possible values of ε_L and L). Using the general theory of nonequilibrium linear response to the first order in perturbation $h(t)$, we obtain (for the case of $\ln t > \ln t_w$)

$$\chi_1(t + t_w, t_w) \sim \frac{q_{EA}\sigma^{\theta/d}}{4\gamma\theta} \times \frac{\ln\left(\dfrac{t_w}{t + t_w}\right)}{\ln[\hbar^{-1}\Gamma_0(t + t_w)]\ln(\hbar^{-1}\Gamma_0 t_w)}. \quad (7)$$

This nonequilibrium dynamic linear susceptibility is similar to that derived in the conventional classical droplet model of the Ising spin glass.

3. DISCUSSION

The temperature and frequency dependences given by Eqs. (5) and (6) are fairly intricate. We performed numerical calculations for $\theta = 0.5$, $d = 3$, $q_{EA} = 0.5$, $\Gamma_0 = 10^{10}$ s^{-1}, and $\gamma = 10^{-15}$ erg. The linear susceptibility χ_1' at very low temperatures (~0.1–1 K) is, on the whole, a monotonic function of frequency and follows a logarithmic law. Therefore, there is a wide spread in the tunneling rates. The temperature dependence of χ_1' at a fixed frequency is described by a curve which passes through a minimum; the magnitude of the minimum is frequency-independent, but its position in temperature varies with frequency.

The temperature dependence of χ_1'' on cooling exhibits a broad maximum whose position shifts to higher temperatures with increasing frequency. The maximum of χ_1'' corresponds to the minimum point of χ_1'. The frequency dependence of χ_1'' is also remarkable; the imaginary part of the susceptibility increases with frequency, then passes through a maximum and decreases as the frequency increases further. It should

be noted that our results at $T = 0$ are identical to those reported in [3].

Preliminary calculations of the ageing effect in the quantum spin glass also revealed that the nonequilibrium dynamics is very slow at low temperatures. However, since theoretical results of this kind are new and the available experimental data are relatively meager, we can only conclude that there is qualitative agreement between the theory and experiment [4].

ACKNOWLEDGMENTS

This study was supported by the Russian Foundation for Basic research, project no. 01-02-16368.

REFERENCES

1. T. Jonsson, K. Jonason, P. Jonsson, and P. Nordblad, Phys. Rev. B **59** (13), 8770 (1999).
2. D. S. Fisher and D. A. Huse, Phys. Rev. B **38** (1), 386 (1988).
3. M. J. Thill and D. A. Huse, Physica A (Amsterdam) **241** (2), 321 (1995).
4. J. A. Mydosh, *Spin Glasses: An Experimental Introduction* (Taylor and Francis, London, 1993), p. 293.

Translated by Yu. Epifanov

Physics of the Solid State, Vol. 44, No. 8, 2002, pp. 1513–1518. Translated from Fizika Tverdogo Tela, Vol. 44, No. 8, 2002, pp. 1446–1451.

PROCEEDINGS OF THE XI FEOFILOV WORKSHOP "SPECTROSCOPY OF CRYSTALS ACTIVATED BY RARE-EARTH AND TRANSITION-METAL IONS"

(Kazan, Tatarstan, Russia, September 24–28, 2001)

Structure and Dynamics of the Pure and Mixed Fluorites MeF_2 (*Me* = Ca, Sr, Ba, and Pb)

A. E. Nikiforov, A. Yu. Zakharov, V. A. Chernyshev, M. Yu. Ougryumov, and S. V. Kotomanov

Ural State University, pr. Lenina 51, Yekaterinburg, 620083 Russia

e-mail: Vladimir.Chernyshev@usu.ru

Abstract—The structure and dynamics of the crystal lattice of MeF_2 fluorites (*Me* = Ca, Sr, Ba, and Pb) under external hydrostatic compression (0–3.5 GPa) are calculated within the shell model in the pair potential approximation. The first-order structural phase transition from the cubic to the orthorhombic phase in these crystals under pressure is investigated. The effect of chemical pressure on the BaF_2 crystal is analyzed by the simulation of mixed crystals, namely, $Ba_{1-x}Ca_xF_2$ and $Ba_{1-x}Sr_xF_2$. It is demonstrated that the supercell method, as applied to the simulation of mixed crystals, results in a lower lattice energy per formula unit as compared to the lattice energy obtained by the virtual-crystal method. © *2002 MAIK "Nauka/Interperiodica".*

1. INTRODUCTION

The considerable interest expressed by researchers in fluorites is due to the wide application of these materials in different areas of physics and engineering. Fluorites are used as solid electrolytes in electric batteries [1] and as optical materials [2, 3]. The particular attention paid to the study of fluorites is caused by the use of these crystals with rare-earth ion impurities in scintillators. The understanding of the nature of the physical processes occurring in excited impurity centers in crystals requires knowledge of the electron–phonon interaction responsible for the time of trap de-excitation [3].

Some fluorites (for example, PbF_2 and BaF_2) exist in two modifications (the cubic β phase and the orthorhombic α phase) which can be transformed into each other under external compression and heat treatment. In this case, the cubic β phase of PbF_2 is metastable. Investigation of the phase transition between these modifications is of practical interest because a similar phase transition can occur in epitaxial films of alkaline-earth fluorides when the thermal expansion coefficients of the film and the substrate are different [4]. In this respect, the evaluation of the critical pressure of the phase transition and comparison of this estimate with the degree of deformation of the crystal structure of fluorite in the film are topical problems.

Mixed crystals (solid solutions) of fluorites are used to change the location of the luminescence lines in the spectrum through changes in the impurity concentration [5]. The structure of an impurity center can be modified by varying the impurity concentration (for example, the displacement of an impurity Cu^{2+} ion in the mixed crystal $Ca_xSr_{1-x}F_2 : Cu^{2+}$ depends on the concentration *x* [6]).

The structure and dynamics of the crystal lattice of fluorites have been investigated in a number of theoretical works. The first calculations of the structure and dynamics of the crystal lattice of fluorites with impurity rare-earth ions were carried out in [7–9]. One of the first calculations of the structure of alkaline-earth fluorites with defects was performed in the framework of the shell model by Catlow [10]. However, the orthorhombic α phase of fluorites has been studied only in a few works. In particular, Bazhenov *et al.* [11] investigated the phonon spectrum of the PbF_2 orthorhombic phase experimentally and theoretically and calculated the phonon spectrum of this phase at the Γ point within the rigid ion approximation. As far as we know, neither the structural phase transition from the cubic to the orthorhombic phase in fluorites under hydrostatic pressure nor the phonon spectrum of the α phase of fluorites has been simulated in the framework of the shell model. Furthermore, theoretical studies concerned with the simulation of mixed crystals and calculations of their phonon spectra are absent.

The purpose of the present work was to simulate the structural phase transition from the cubic to the orthorhombic phase in fluorites under external hydrostatic compression and to simulate mixed fluorites in the framework of the shell model.

2. MODEL CALCULATION OF THE ENERGY OF A CRYSTAL

The parameters of the equilibrium crystal structure under external hydrostatic pressure can be determined by minimizing the crystalline enthalpy $H = E + PV$, where E is the lattice energy, P is the external hydrostatic pressure, and V is the volume of the unit cell.

1063-7834/02/4408-1513$22.00 © 2002 MAIK "Nauka/Interperiodica"

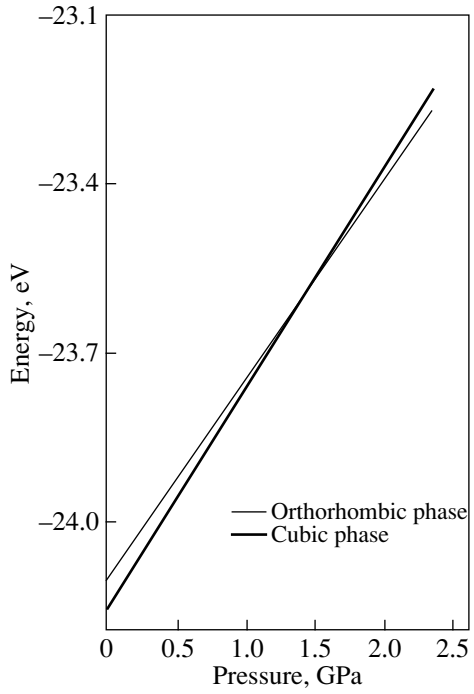

Fig. 1. Pressure dependences of the unit cell energy of PbF_2.

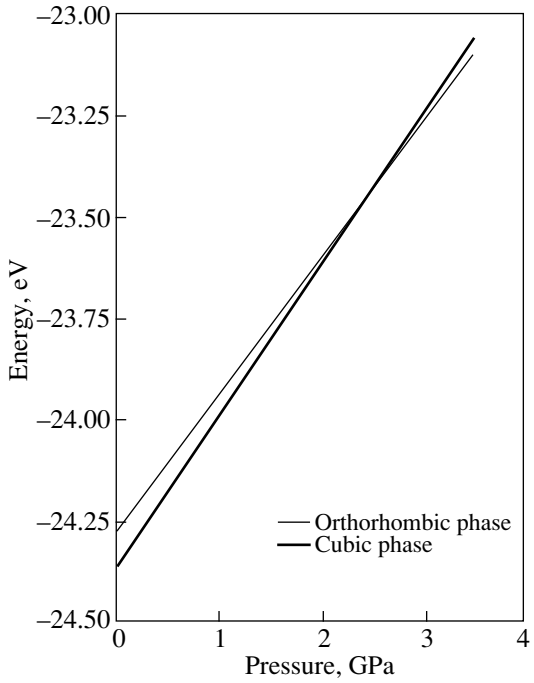

Fig. 2. Pressure dependences of the unit cell energy of BaF_2.

Within the shell model in the pair potential approximation, the lattice energy can be represented in the form

$$E_{\text{lat}} = \frac{1}{2}\sum_{i,\,j,\,j\neq j} V_{i,\,j} + \frac{1}{2}\sum_{i} k_i|\mathbf{s}_i|^2, \qquad (1)$$

where the subscript i refers to ions of the unit cell, the subscript j refers to ions of the crystal, k_i is the constant of the core–shell interaction, and $\mathbf{s}_i$ is the displacement of the shell of the ith ion with respect to the core. The pair potential of the ion–ion interaction V_{ij} has the form

$$\begin{aligned} V_{ik} = {} & \frac{X_iX_j}{r} + \frac{Y_iX_j}{|\mathbf{r}_{ij}-\mathbf{s}_i|} + \frac{X_iY_j}{|\mathbf{r}_{ij}+\mathbf{s}_j|} + \frac{Y_iY_j}{|\mathbf{r}_{ij}-\mathbf{s}_i+\mathbf{s}_j|} \\ & + C_{ij}\exp(-D_{ij}|\mathbf{r}_{ij}-\mathbf{s}_i+\mathbf{s}_j|) \\ & - \lambda_{ij}/|\mathbf{r}_{ij}-\mathbf{s}_i+\mathbf{s}_j|^6 + f_{ij}(r), \end{aligned} \qquad (2)$$

where X_i and Y_i are the charges of the core and the shell of the ith ion, respectively ($Z_i = X_i + Y_i$), and $r = |\mathbf{r}_{ij}|$ is the distance between the ion nuclei. The function

$$f_{ij}(r) = -A_{ij}\exp(-B_{ij}r)/r \qquad (3)$$

characterizes the short-range screening of the electrostatic interaction of the ion cores, and the expression

$$C_{ij}\exp(-D_{ij}|\mathbf{r}_{ij}-\mathbf{s}_i+\mathbf{s}_j|) - \lambda_{ij}/|\mathbf{r}_{ij}-\mathbf{s}_i+\mathbf{s}_j|^6$$

describes the short-range repulsion between the ion shells in the form of the Born–Mayer potential and the van der Waals interaction. The interaction parameters C_{ij}, D_{ij}, λ_{ij}, k_i, A_{ij}, and B_{ij} and the procedures of their determination are described in our previous works [12, 13].

Table 1. Critical pressure P_c and the pressure-induced change in the unit cell volume of β-MeF_2 crystals (*Me* = Ca, Sr, Ba, and Pb)

Crystal	P_c, GPa		Change in the unit cell volume at P_c, %	Change in the unit cell volume of the epitaxial film [4], %
	calculation	experiment	calculation	
BaF_2	2.5	2.6 [14]	3.36	
PbF_2	1.3	0.48 [16]	1.84	
SrF_2	3.0		3.31	
CaF_2	2.9		2.67	2.40

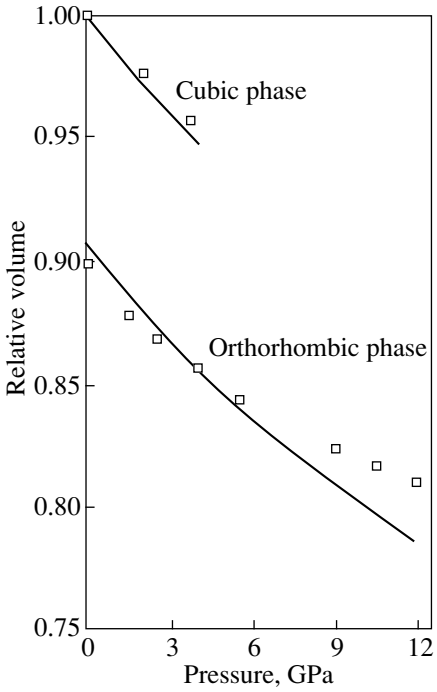

Fig. 3. Pressure dependences of the relative volume of the BaF_2 unit cell. Points are the experimental data taken from [14].

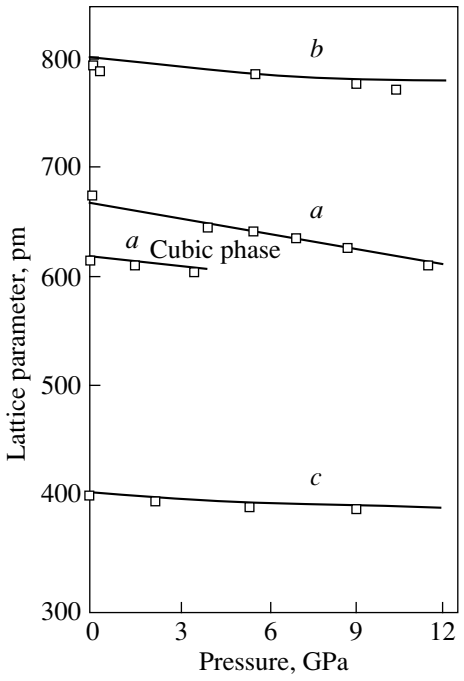

Fig. 4. Pressure dependences of the lattice parameter of BaF_2. Points are the experimental data taken from [14].

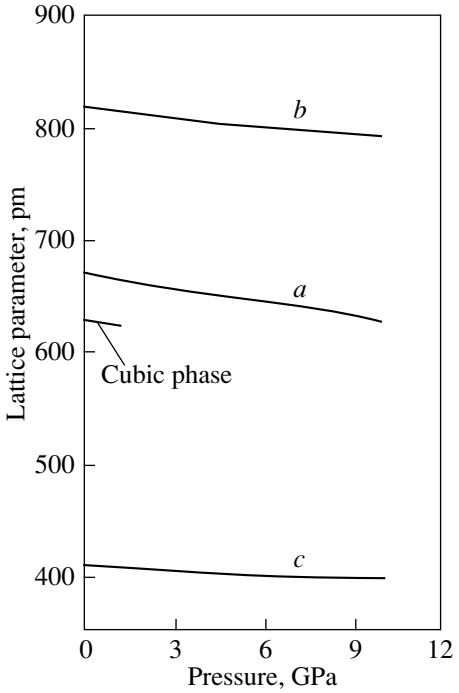

Fig. 5. Pressure dependences of the lattice parameter of PbF_2.

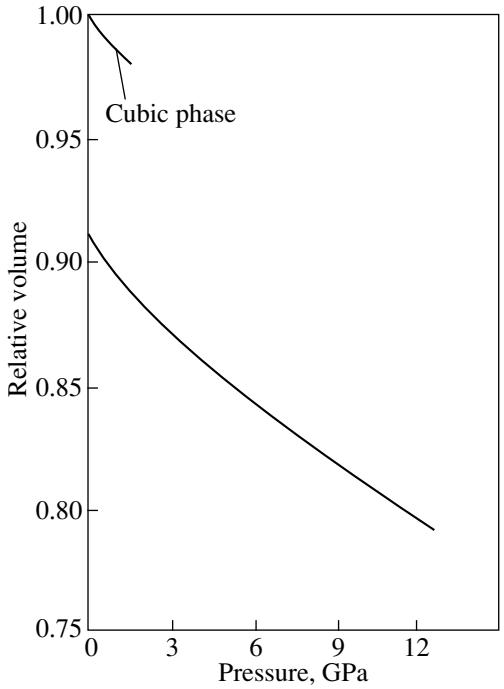

Fig. 6. Pressure dependences of the relative volume of the PbF_2 unit cell.

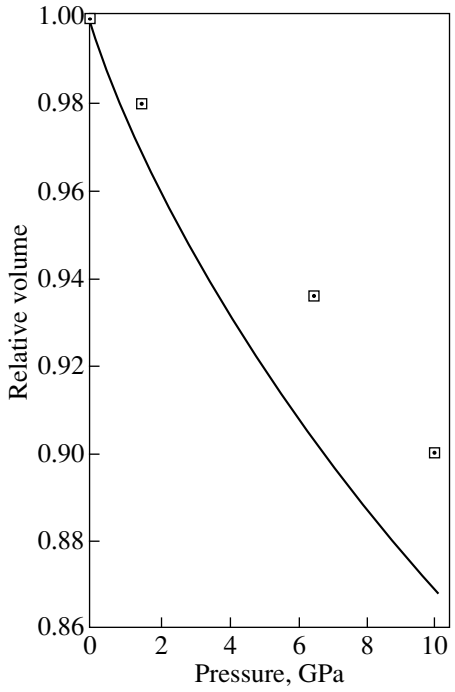

Fig. 7. Pressure dependence of the relative volume of the unit cell of the PbF_2 orthorhombic phase. Points are the experimental data taken from [15].

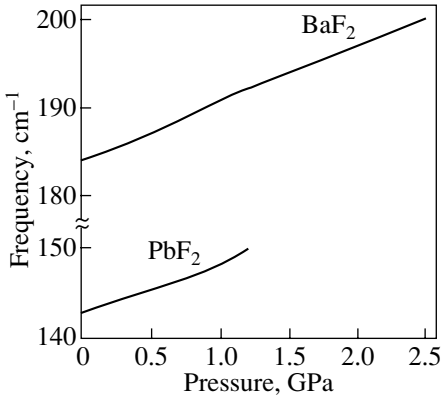

Fig. 8. Pressure dependences of the frequency of the F_{1u} mode.

3. RESULTS AND DISCUSSION

3.1. Structural phase transition under pressure. As was already mentioned, PbF_2 and BaF_2 crystals exist either in the cubic phase with space group O_h^5 (the so-called β phase) or in the orthorhombic phase with space group D_{2h}^{16} (the so-called α phase). The orthorhombic phase is characterized by a higher density and larger coordination number (for the α and β phases, the coordination numbers are 9 and 8, respectively). The primitive cell in the β phase contains four formula units. The structural phase transition from the β phase to the α phase occurs at a critical pressure P_c. At higher pressures, these crystals undergo a structural phase transition to even a more low-symmetry phase with denser packing [14, 15]. In the present work, we calculated the unit cell energy as a function of the pressure for both phases (Figs. 1, 2) and predicted a similar phase transition in CaF_2 and SrF_2 crystals. The results of our calculations in comparison with the experimental data are presented in Table 1. The pressure dependences of the lattice parameter and the unit cell volume for both phases are shown in Figs. 3–7. The nonlinearity in the pressure dependence of the unit cell volume in the orthorhombic phase can be attributed to the denser packing of this phase and to the stronger short-range interaction. Upon the phase transition from the β phase to the α phase in MeF_2 crystals (*Me* = Ca, Sr, Ba, and Pb), the volume per formula unit decreases by 3.3–3.5%. This phase transition is a first-order phase transition. The changes in the unit cell volume of the β phase of these crystals under a critical pressure corresponding to the phase transition are given in Table 1. It is seen from Table 1 that the change in the unit cell volume of the CaF_2 epitaxial film due to the interaction with a silicon substrate is close to the change in the unit cell volume at the critical pressure of the phase transition.

3.2. Pressure-induced changes in the phonon spectra of BaF_2 and PbF_2 crystals. Crystals of MeF_2 (*Me* = Ca, Sr, Ba, and Pb) are superionic conductors [1, 17]. At temperatures above the critical point, the anionic sublattice of these crystals undergoes disordering. The phonon spectrum of the cubic phase of the MeF_2 crystals is characterized by modes attributed to only the anions (the Raman-active F_{2g} mode) and modes associated with both the cations and anions (the dipole-active F_{1u} mode). The phonon spectrum of fluorites has been investigated for many years [16, 18]. According to the experimental data [17], the temperature of the transition to the superionic state in MeF_2 crystals (*Me* = Ca, Sr, Ba, and Pb) is proportional to the frequency of the F_{1u} mode. The pressure effect on the superionic conductivity is associated with the change in the phonon frequency, which, in turn, determines the activation jump [19]. We analyzed the dependences of the frequencies of the F_{2g} and F_{1u} modes at the Γ point on the hydrostatic pressure (Figs. 8–10). As follows from our calculations, the frequencies of the phonon modes increase with an increase in the pressure. Therefore, we can assume that, in these crystals, the temperature of the transition to the superionic state also increases with an increase in the pressure.

3.3. The influence of chemical pressure on the BaF_2 crystal. The influence of chemical pressure on the BaF_2 crystal was investigated by simulating the mixed crystals $Ba_{1-x}Ca_xF_2$ and $Ba_{1-x}Sr_xF_2$ in which

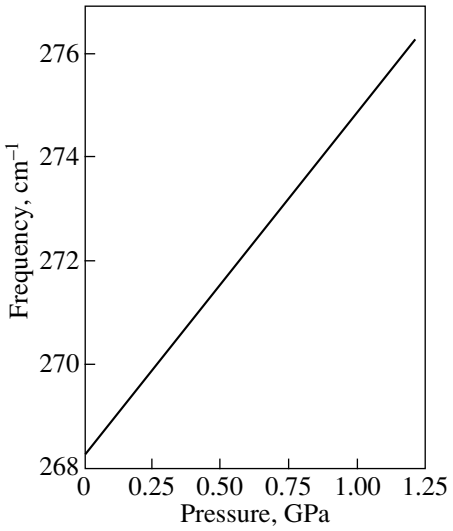

Fig. 9. Pressure dependence of the frequency of the F_{2g} mode in the PbF_2 cubic phase.

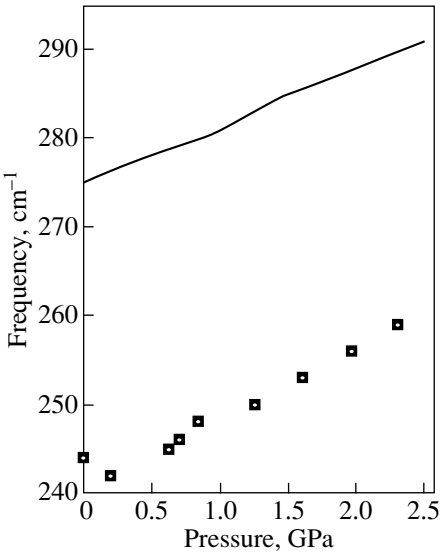

Fig. 10. Pressure dependence of the frequency of the F_{2g} mode in the BaF_2 cubic phase. Points are the experimental data taken from [16].

some Ba^{2+} ions were isovalently replaced by ions of smaller radii. In our calculations, we used two approaches, namely, the virtual-crystal and supercell methods. Within the virtual-crystal approximation, the parameters of the pair interaction can be represented in the form

$$A_{\mathrm{CaBa-F}}(x) = (1-x)A_{\mathrm{Ba-F}} + xA_{\mathrm{Ca-F}}, \qquad (4)$$

where A is the parameter of the pair interaction and A_{CaBa} is the parameter of the pair interaction for the lattice site in which the Ca and Ba ions are located with the probabilities x and $(1-x)$, respectively.

The supercell method consists in replacing part of the ions of a given sort by ions of another sort in the unit cell of the crystal. Since, upon this replacement, the translational symmetry of the crystal is lost, the unit cell must be enlarged in the directions of the lattice constants (along which the translational symmetry is violated) by such a factor that the crystal with the new (extended) unit cell will retain the translational symmetry. From this circumstance, it follows that the supercell method can be used only for certain impurity concentrations x. Moreover, the requirement of translational symmetry conservation makes the calculations with disordered distribution of impurity ions over the crystal lattice impossible. For a given symmetry of the crystal with a specified concentration of impurity ions, there are several possible types of impurity ion distribution in the primitive cell. All these types correspond to the same lattice energy. We calculated the lattice energy of the mixed crystal $Ba_{1-x}Ca_xF_2$ ($Ba_{1-x}Sr_xF_2$) within the virtual-crystal and supercell approximations for impurity concentrations $x = 0.25$, 0.5, and 0.75. These calculations demonstrated (Table 2) that the supercell method gives a lower lattice energy per formula unit than the lattice energy obtained by the virtual-crystal method.

Table 2. Difference in the lattice energies (per formula unit) calculated within the supercell and virtual-crystal approximations (meV) for mixed crystals

x, %	$Ba_{1-x}Ca_xF_2$	$Ba_{1-x}Sr_xF_2$
25	–84.7	–28.2
50	–127.7	–40.2
75	–108.1	–32.5

4. CONCLUSION

Thus, the shell model in the pair potential approximation, as applied to the calculation of the crystal energy, makes it possible to describe adequately the structural phase transition in MeF_2 fluorides (*Me* = Ca, Sr, Ba, and Pb), to obtain the phonon spectra of these crystals under pressure, and to simulate the structure of the mixed crystals $Ba_{1-x}Ca_xF_2$ and $Ba_{1-x}Sr_xF_2$. The above calculations have demonstrated that, upon the structural phase transition from the β phase to the α phase in PbF_2 and BaF_2 crystals, the volume per formula unit decreases by 3.5%. A similar phase transition is predicted to occur in CaF_2 and SrF_2 crystals.

According to our calculations, the supercell method used in the simulation of mixed crystals leads to a lower lattice energy per formula unit than the energy obtained by the virtual-crystal method.

ACKNOWLEDGMENTS

This work was supported by the Ministry of Education of the Russian Federation (project no. E00-3.4-227) and the American Foundation for Civilian Research and Development for the promotion of cooperation with scientists from the New Independent States of the former Soviet Union (grant no. REC-005 CRDF).

REFERENCES

1. Yu. I. Gurevich and Yu. I. Kharkats, Usp. Fiz. Nauk **136** (4), 693 (1982) [Sov. Phys. Usp. **25**, 257 (1982)].
2. K. Kawano and R. Nakata, in *Proceedings of the 1st Asia-Pacific EPR/ESR Symposium, Hong Kong, 1997*, p. 423.
3. C. W. E. van Eijk, in *Proceedings of the 10th Feofilov Symposium on Spectroscopy of Crystals Activated by Rare-Earth Transitional-Metal Ions*, Ed. by A. I. Ryskin and V. F. Masterov; Proc. SPIE **2706**, 158 (1996).
4. N. S. Sokolov and N. L. Yakovlev, in *Proceedings of the 10th Feofilov Symposium on Spectroscopy of Crystals Activated by Rare-Earth Transitional-Metal Ions*, Ed. by A. I. Ryskin and V. F. Masterov; Proc. SPIE **2706**, 57 (1996).
5. K. Kawano, H. Akahane, R. Nakata, and M. Sumita, J. Alloys Compd. **221**, 218 (1995).
6. V. A. Ulanov, M. M. Zaripov, V. A. Shustov, and I. I. Fazlizhanov, Fiz. Tverd. Tela (St. Petersburg) **40** (3), 445 (1998) [Phys. Solid State **40**, 408 (1998)].
7. B. Z. Malkin, Fiz. Tverd. Tela (Leningrad) **11** (5), 1208 (1969) [Sov. Phys. Solid State **11**, 981 (1969)].
8. Z. I. Ivanenko and B. Z. Malkin, Fiz. Tverd. Tela (Leningrad) **11** (7), 1859 (1969) [Sov. Phys. Solid State **11**, 1498 (1970)].
9. Yu. K. Voron'ko, A. L. Larionov, and B. Z. Malkin, Opt. Spektrosk. **40** (1), 86 (1976) [Opt. Spectrosc. **40**, 47 (1976)].
10. C. R. A. Catlow, Solid State Phys. **9**, 1845 (1976).
11. A. V. Bazhenov, I. S. Smirnova, T. N. Fursova, *et al.*, Fiz. Tverd. Tela (St. Petersburg) **42** (1), 40 (2000) [Phys. Solid State **42**, 41 (2000)].
12. A. E. Nikiforov and S. Yu. Shashkin, *Spectroscopy of Crystals* (Nauka, Leningrad, 1989), p. 274.
13. A. G. Gusev, V. G. Mazurenko, A. E. Nikiforov, and S. Yu. Shashkin, Fiz. Tverd. Tela (St. Petersburg) **36** (5), 1437 (1994) [Phys. Solid State **36**, 786 (1994)].
14. J. M. Leger, J. Haines, A. Atouf, and O. Schulte, Phys. Rev. B **52** (18), 13247 (1995).
15. J. Haines, J. M. Leger, and O. Schulite, Phys. Rev. B **57** (13), 7551 (1998).
16. J. R. Kessler, E. Monberg, and M. Nikol, J. Chem. Phys. **60** (12), 5057 (1974).
17. *Physics of Superionic Conductors*, Ed. by M. B. Salamon (Springer-Verlag, New York, 1979; Zinatne, Riga, 1982).
18. R. J. Elliott, W. Hayes, W. G. Kleppmann, *et al.*, Proc. R. Soc. London, Ser. A **360**, 317 (1978).
19. P. C. Allen and D. Lazarus, Phys. Rev. B **17** (4), 1913 (1978).

Translated by O. Moskalev

Physics of the Solid State, Vol. 44, No. 8, 2002, pp. 1519–1521. Translated from Fizika Tverdogo Tela, Vol. 44, No. 8, 2002, pp. 1452–1454.

PROCEEDINGS OF THE XI FEOFILOV WORKSHOP "SPECTROSCOPY OF CRYSTALS ACTIVATED BY RARE-EARTH AND TRANSITION-METAL IONS"

(Kazan, Tatarstan, Russia, September 24–28, 2001)

Phase Separation and Manifestation of Nanoscopic Nonuniformities in the Optical Spectra of Manganites

A. S. Moskvin*, E. V. Zenkov*, Yu. D. Panov*, N. N. Loshkareva, Yu. P. Sukhorukov**, and E. V. Mostovshchikova****

** Ural State University, pr. Lenina 51, Yekaterinburg, 620083 Russia*

e-mail: Eugene.Zenkov@usu.ru

*** Institute of Metal Physics, Ural Division, Russian Academy of Sciences, ul. S. Kovalevskoĭ 18, Yekaterinburg, 620219 Russia*

Abstract—The features observed in the frequency and temperature dependences of the optical spectra of doped manganites can be accounted for by assuming the latter to have inhomogeneous phase composition. The spectral response of the optical conductivity of the $La_{1-x}Sr_xMnO_3$ system was calculated in the effective-medium approximation over a broad range of x variation. *© 2002 MAIK "Nauka/Interperiodica".*

1. INTRODUCTION

Optical spectroscopy is a fundamental method for investigation of the electronic structure of condensed media. The optical conductivity $\sigma(\omega)$ of the doped manganites $La_{1-x}Sr_xMnO_3$ reveals interesting features which reflect a rearrangement of the low-energy electronic spectrum and the metal–insulator transition. The optical conductivity spectrum of the original dielectric $LaMnO_3$ in the 0- to 10-eV range consists of three bands centered at 2, 6, and 9 eV [1]. Even at low Sr concentrations, the $La_{1-x}Sr_xMnO_3$ system exhibits a complex redistribution of the spectral density (Fig. 1), accompanied by its shift to lower energies and the formation of a feature at about 4.5 eV [2]. At $x = 0.15$, a new absorption band forms in the region of the dielectric gap at about 1.5 eV, which evolves at high x into a Drude peak.

The temperature dependence of the optical conductivity of $La_{1-x}Sr_xMnO_3$ shows an anomalous behavior. Measurements performed on polycrystalline $La_{7/8}Sr_{1/8}MnO_3$ revealed that an additional absorption band appears near 0.4 eV at 210 K; its position remains unchanged but its intensity grows as the temperature decreases to 15 K [3]. While the available data on single-crystal compositions are controversial, they also indicate a substantial temperature dependence of $\sigma(\omega)$. For instance, it is reported in [4] that in the system with $x = 0.175$ ($T_c = 283$ K), the decrease in temperature from 290 to 9 K is accompanied by a noticeable transfer of spectral weight in the 0-to 3-eV interval toward lower energies, where σ becomes almost independent of frequency. On the other hand, the spectra obtained on a sample of the same composition in [5] look different and exhibit a smoother temperature behavior. It was pointed out that the reason for such a discrepancy may lie in the technology of sample preparation, in particular, in the grinding off of the surface layer [5].

2. PHASE INHOMOGENEITY EFFECTS IN MANGANITES

Taking into account the phase separation permits one to consider the characteristic features of the optical spectra of doped manganites from a different standpoint. Possible mechanisms of phase separation in the manganites have been discussed in the literature for a long time [6, 7]. In the energy functional

$$E = -znt\cos\theta/2 + zJS^2\cos\theta, \qquad (1)$$

where t is the transfer integral, n is the electron density, z is the number of nearest neighbors, and J is the exchange integral, the competition between double exchange and kinetic contribution makes nucleation of the conducting phase with a noncollinear spin ordering energetically preferable to the homogeneous state. The nucleus radius R, as estimated in the simplest way from the relation

$$\frac{4}{3}\pi\left(\frac{R}{a}\right)^3 = \frac{4}{3}\pi\left(\frac{\pi|t|}{4zJS^2}\right)^{3/5} \qquad (2)$$

(a is the lattice constant), yields a figure of the order of 10 Å [7, 8]. Equation (2) was derived under the assumption that the electrons in a drop of the conducting phase behave as free electrons.

Inhomogeneous media differ substantially from homogeneous ones in many respects. In particular, their absorption spectra exhibit additional features which relate to the so-called geometric or Mie resonances.

1063-7834/02/4408-1519$22.00 © 2002 MAIK "Nauka/Interperiodica"

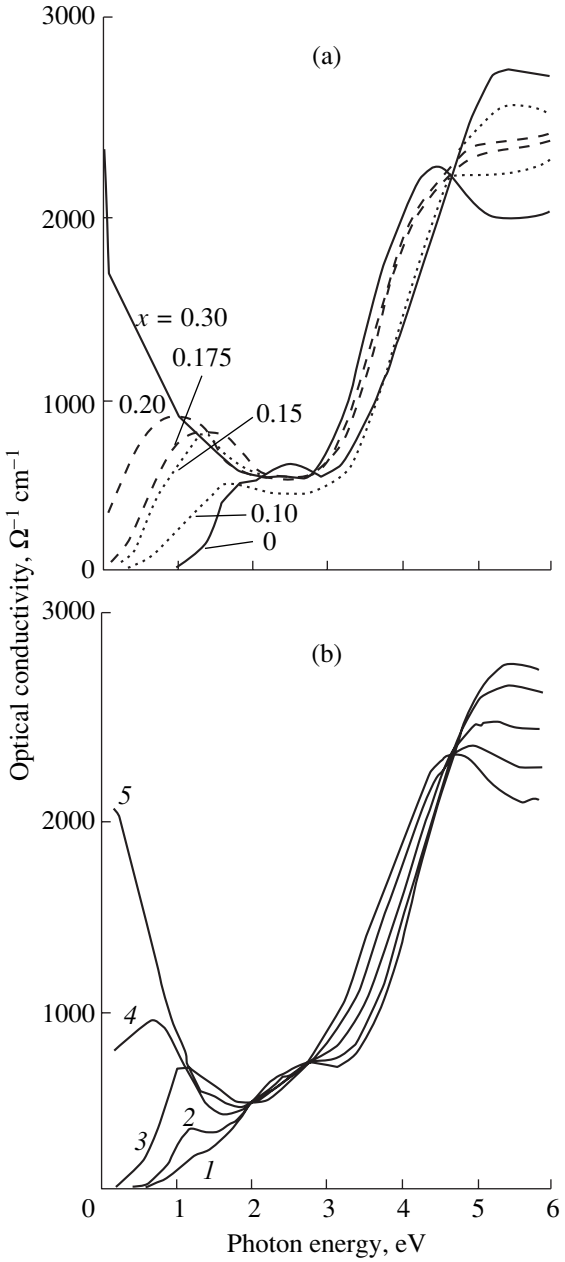

Fig. 1. Optical conductivity of single-crystal $La_{1-x}Sr_xMnO_3$ at room temperature: (a) experiment [2], and (b) effective-medium calculation made for different volume fractions of the conducting phase *p*: (*1*) 0.05, (*2*) 0.15, (*3*) 0.35, (*4*) 0.55, and (*5*) 0.75.

These resonances are not connected with electron transitions and are due to surface plasmon excitation at the boundaries of inhomogeneities, a feature that has no counterpart in homogeneous systems. The dispersion law of surface modes depends on the geometric shape of the particles of the inhomogeneous medium.

One can apply the formalism of the effective medium theory to interpret the properties of phase-inhomogeneous doped manganites phenomenologically. For instance, the observed properties of a binary mixture can be described by the effective dielectric permittivity, which, in the simplest form, can be written as

$$c_1\frac{\varepsilon_{\text{eff}}\varepsilon_1}{\varepsilon_{\text{eff}}+2\varepsilon_1}+c_2\frac{\varepsilon_{\text{eff}}\varepsilon_2}{\varepsilon_{\text{eff}}+2\varepsilon_2}=0, \qquad (3)$$

where ε_i is the dielectric permittivity of the *i*th component and c_i is its concentration. Equation (3) corresponds to the effective-potential approximation in the theory of disordered systems. This equation can be generalized to the case of an arbitrary ellipsoidal shape of the mixture particles by introducing depolarization factors, which are similar to demagnetizing factors.

3. EFFECTIVE-MEDIUM THEORY: COMPARISON WITH EXPERIMENT

We used the effective-medium theory [9] for a semiquantitative description of the concentration and temperature dependences of the properties of $La_{1-x}Sr_xMnO_3$. In the model used, the two components of a binary mixture represent the core and the envelope of fictive particles making up the composite. This model is similar to the cluster modification of the mean-field theory made in the spirit of the Bethe–Peierls approximation. We note that the effective-medium model has been employed to advantage [10] in interpreting the temperature dependence of the Seebeck coefficient for a related system, $La_{0.67}Ca_{0.33}MnO_3$.

The data on the bare dielectric permittivity of undoped $LaMnO_3$ were taken from [1, 2] and approximated by Lorentzians. The dielectric permittivity of drops of the conducting phase was expressed through the Drude relation

$$\varepsilon(\omega)=1-\frac{\Omega_p^2}{\omega(\omega+i\gamma)}, \qquad (4)$$

where the plasma frequency Ω_p and the reciprocal relaxation time γ were considered to be fitting parameters. To include the interband transition appearing near 4.5 eV for $x > 0.2$, a Lorentzian was added to Eq. (4). The particles of the conducting and dielectric phases were assumed to have spherical shape.

Figure 1 illustrates the calculations of the optical conductivity and the corresponding experimental spectra. The parameters of the Drude relation are Ω_p = 1.9 eV and γ = 0.5 eV. The curves are not the best fits and are shown for illustration. Nevertheless, they correctly reproduce, on the whole, the main features of the $\sigma(\omega)$ variation under doping.

The temperature dependence of optical conductivity can be described by properly varying the model parameters, more specifically, the concentration, plasma frequency, and reciprocal relaxation time of the metallic phase. Let us consider, for instance, the calculated spectra presented in Fig. 2 that simulates $\sigma(\omega, T)$ relations for polycrystalline $La_{7/8}Sr_{1/8}MnO_3$ in the T = 210- to 15-K range [3]. According to the phase diagram [11],

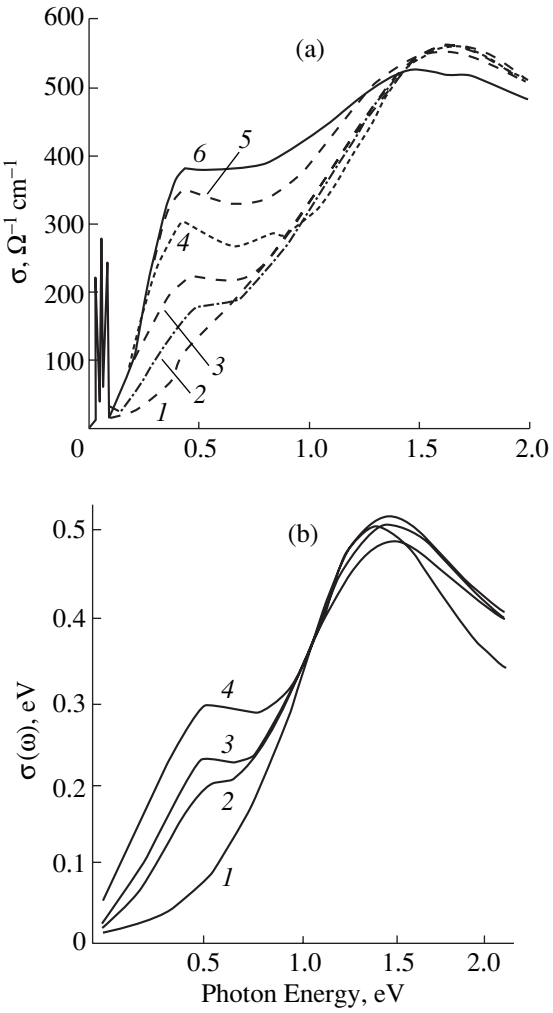

Fig. 2. (a) Spectral dependence of the optical conductivity of polycrystalline $La_{7/8}Sr_{1/8}MnO_3$ [3] at different temperatures T: (*1*) 210, (*2*) 180, (*3*) 160, (*4*) 120, (*5*) 80, and (*6*) 15 K; and (b) simulation by the effective-medium theory (see text for explanation): (*1*) $p = 0.01$, $\omega_p = 0.6$ eV, and $\gamma = 0.7$ eV; (*2*) $p = 0.3$, $\omega_p = 0.9$ eV, and $\gamma = 0.5$ eV; (*3*) $p = 0.35$, $\omega_p = 0.99$ eV, and $\gamma = 0.45$ eV; and (*4*) $p = 0.4$, $\omega_p = 1.0$ eV, and $\gamma = 0.47$ eV.

when the temperature is lowered down to the critical point ($T_c \sim 190$ K), the paramagnetic dielectric transforms into a ferromagnetic dielectric. Following the general concepts of the double-exchange theory, we assume that the transition to ferromagnetic ordering favors the formation of the metallic phase in the dielectric matrix; indeed, the concentration of the nuclei increases and the plasma frequency grows because of the proportionality $\Omega_p^2 \sim 1/m_{\text{eff}} \sim t\cos\theta$, where θ is the angle between the spins of the nearest neighbors and t is the transfer integral. As is evident from Fig. 2, by varying the parameters properly in accordance with the above reasoning, one succeeds in reproducing gradual growth of the spectral density in the band near 0.4 eV, which is in full agreement with experimental data [3]. At the same time, in our model, this maximum in absorption is due to geometric resonance, whose position is determined primarily by the shape of the metallic-phase nuclei. Thus, the constant position of this band pointed out in [3] also finds a consistent explanation.

4. CONCLUSION

Phase separation is one of the most interesting areas in the physics of strongly correlated systems, which is currently being actively pursued. In doped cuprates and manganites, phase separation finds experimental substantiation in the manifestation of the quasi-metallic free-carrier band in absorption spectra, which is centered at about $\omega = 0$ eV. A simple, informative phenomenology can be developed for nanoscopically inhomogeneous systems in terms of the effective-medium theory. We have applied this approach to describe the concentration and temperature dependences of the optical conductivity for the $La_{1-x}Sr_xMnO_3$ system and obtained reasonable agreement with experiment. We found that some spectral features are not associated with electron transitions and, being due to phase inhomogeneities in a doped system, can be related to surface plasmon excitation at phase boundaries (the Mie resonances).

ACKNOWLEDGMENTS

The partial support of CRDF (grant no. REC-005), of the Ministry of Education of the RF (grant no. E00-3.4-280), and of the Russian Foundation for Basic Research (project no. 01-02-96404) is gratefully acknowledged.

REFERENCES

1. J. H. Jung, K. H. Kim, D. J. Eom, *et al.*, Phys. Rev. B **55** (23), 15489 (1997).
2. K. Takenaka, K. Iida, Y. Sawaki, *et al.*, J. Phys. Soc. Jpn. **68** (6), 1828 (1999).
3. J. H. Jung, K. H. Kim, H. J. Lee, *et al.*, Phys. Rev. B **59** (5), 3793 (1999).
4. Y. Okimoto, T. Katsufuji, T. Ishikawa, *et al.*, Phys. Rev. Lett. **75** (1), 109 (1995).
5. K. Takenaka, K. Iida, Y. Sawaki, *et al.*, cond-mat/9905310.
6. É. L. Nagaev, Usp. Fiz. Nauk **165**, 529 (1995) [Phys. Usp. **38**, 497 (1995)].
7. D. I. Khomskii, Physica B (Amsterdam) **280**, 325 (2000).
8. Yiing-Rei Chen and Philip B. Allen, cond-mat/0101354.
9. Ping Sheng, Phys. Rev. Lett. **45** (1), 60 (1980).
10. M. Jaime, P. Lin, S. H. Chun, *et al.*, cond-mat/9808160.
11. A. Urushibara, Y. Moritomo, T. Arima, *et al.*, Phys. Rev. B **51** (20), 14103 (1995).

Translated by G. Skrebtsov

Physics of the Solid State, Vol. 44, No. 8, 2002, pp. 1522–1525. Translated from Fizika Tverdogo Tela, Vol. 44, No. 8, 2002, pp. 1455–1458.

PROCEEDINGS OF THE XI FEOFILOV WORKSHOP "SPECTROSCOPY OF CRYSTALS ACTIVATED BY RARE-EARTH AND TRANSITION-METAL IONS"

(Kazan, Tatarstan, Russia, September 24–28, 2001)

Nanoscale Inhomogeneities and Optical Properties of Doped Cuprates

A. S. Moskvin, E. V. Zenkov, and Yu. D. Panov

Ural State University, pr. Lenina 51, Yekaterinburg, 620083 Russia

e-mail: Eugene.Zenkov@usu.ru

Abstract—A new method is proposed for semiquantitative description of the optical properties of doped cuprates and related systems in the infrared region under the assumption of their phase inhomogeneity. The available experimental data are used to calculate the spectra of optical conductivity and electron-energy-losses for the $La_{2-x}Sr_xCuO_4$ system in the nonsuperconducting phase. © *2002 MAIK "Nauka/Interperiodica".*

1. INTRODUCTION

Experimental studies of the optical properties of cuprates and other low-dimensional oxides have revealed a number of nontrivial relations common to these systems. The main phenomenon associated with doping is the transfer of spectral weight from the region of interband transitions of the original undoped dielectric (1.5–2.0 eV for $La_{2-x}Sr_xCuO_4$) toward lower energies, which is accompanied by collapse of the dielectric gap, the appearance of a MIR absorption band, and the formation of a quasi-metallic peak in the *ab*-plane optical conductivity $\sigma(\omega)$. In some systems ($La_{2-x}Sr_xCuO_4$, $Nd_{2-x}Ce_xCuO_4$), this evolution exhibits an interesting feature: the $\sigma(\omega)$ curves obtained at different x intersect at almost one point [1]. The low-energy part (0–1000 cm^{-1}) of the optical conductivity of HTSCs, as well as of some nonsuperconducting oxides ($La_{8-x}Sr_xCu_8O_{20}$ [2]), has a complex structure and is characterized by an anomalous temperature behavior, which is traditionally described using the pseudogap concept.

We will show that many of the above unusual optical properties of doped cuprates can be explained in a straightforward way in terms of a semiempirical model based on the assumption that these systems possess phase inhomogeneities. The models of the spatially inhomogeneous state of cuprates belong to an area of HTSC science that is exhibiting explosive growth and are usually connected with the formation of structures of the type of stripes or electronic molecules [3]. Other approaches assume there to be an inhomogeneity in the reciprocal space, which is associated with hot and cold parts of the Fermi surface detected by angle-resolved photoelectron spectroscopy (ARPES).

2. EFFECTIVE-MEDIUM MODEL

The physical principles underlying the model developed by us are essentially as follows. A charge defect (nonisovalent substitution, oxygen vacancy) appearing in the original dielectric matrix gives rise to the formation of a potential well and creates conditions conducive to nucleation of a new conducting phase capable of efficiently screening the Coulomb potential of the impurity. This local metal–insulator transition occurring in the vicinity of an impurity can be qualitatively described in terms of the theory of Brinkman–Rice [4], in which the effective mass of a quasiparticle depends on the Hubbard potential U at the site, $m_{\text{eff}}/m = (1 - U^2/U_c^2)^{-1}$; this mass goes to infinity at the critical value U_c corresponding to localization. If a system is in the immediate vicinity of the metal–insulator transition, the Coulomb field of an impurity can lower the repulsion potential so that the quasiparticles will acquire a finite mass within a limited region. On the other hand, the stability of the new phase can be provided by its nontrivial topology [5].

It appears logical to assume that this transition primarily affects the low-energy part of the electronic spectrum. Therefore, the formation of a conducting phase should reduce the effective number of electrons near the fundamental absorption edge and transfer a part of the spectral weight toward lower energies.

When describing physical processes whose characteristic length is of the order of the inhomogeneity scale (spectroscopy at wavelengths λ = 0–2.0 μm), doped cuprates can be considered a granular system consisting of dielectric and metallic grains. This permits one to use the effective-medium approximation, whose development for calculation of the properties of composites proceeds from as far back as the 1920s.

1063-7834/02/4408-1522$22.00

The optical properties of a binary mixture are described in the effective-medium approximation through the dielectric permittivity ε_{eff}, which in the simplest case can be found from the equation

$$fD(\varepsilon_{eff}, \varepsilon_1) + (1 - f)D(\varepsilon_{eff}, \varepsilon_2) = 0, \quad (1)$$

where f is the concentration of the first component and $D(\varepsilon_{eff}, \varepsilon_i)$ is the polarizability of the ith component embedded in the effective medium and calculated from the Clausius–Mossotti relation. This version of the theory can actually be identified with the mean-field approximation.

To simulate the concentration dependence of the optical conductivity of the $La_{2-x}Sr_xCuO_4$ system, we made use of a modified effective-medium theory [6] in which the two components of a mixture represent either the core or the coating of the composite constituent particles. This improved version of the theory, which is similar to the mean-field cluster approximation (the Bethe–Peierls approximation in the Ising model), allows a more consistent description of the percolation transition and of some fine features in the optical spectrum.

It should be noted that representing a doped cuprate in the form of a composite and invoking the effective-medium formalism offers no more than a convenient phenomenology for description of its complex, spatially inhomogeneous electronic structure.

To calculate the effective dielectric permittivity, one has to prescribe the permittivity of each component of the mixture. The data for the dielectric permittivity of undoped La_2CuO_4 in the 0- to 2.5-eV region were taken from [1]. The imaginary part of $\varepsilon(\omega)$ was fitted by two Gaussians corresponding to the fundamental absorption edge and by a Lorentzian centered at 0.6 eV.

The conducting phase was simulated using the Drude relation

$$\varepsilon(\omega) = 1 - \frac{\omega_p^2}{\omega(\omega + i\gamma)}, \quad (2)$$

in which the plasma frequency and the relaxation rate are, in general, frequency-dependent, but for the simplest case were chosen to be constant: $\omega_p = 1.65$ eV and $\gamma = 0.5$ eV.

The fitting parameters of the theory, which determine the shape of the ellipsoidal particles of the dielectric and metallic phases, considerably affect the profile of the calculated optical conductivity spectra. The parameters are the ratio of the ellipsoid semiaxes in the *ab* plane (parameter α, $0 < \alpha < 1$) and the ratio of the out-of-plane semiaxis to the larger of the in-plane semiaxes (parameter β, $0 < \beta < 1$). These parameters enter the relations for the particle polarizabilities through the depolarization factors.

3. COMPARISON WITH EXPERIMENT

The calculated optical conductivity spectra of $La_{2-x}Sr_xCuO_4$ are displayed in Fig. 1a. They are shown for illustration and are not the best fits to the experimental curves presented in Fig. 1b. The figures adjoining the curves identify the volume fraction p of the metallic particles dependent on the doping level x. The calculation reproduces a fast decrease in the spectral

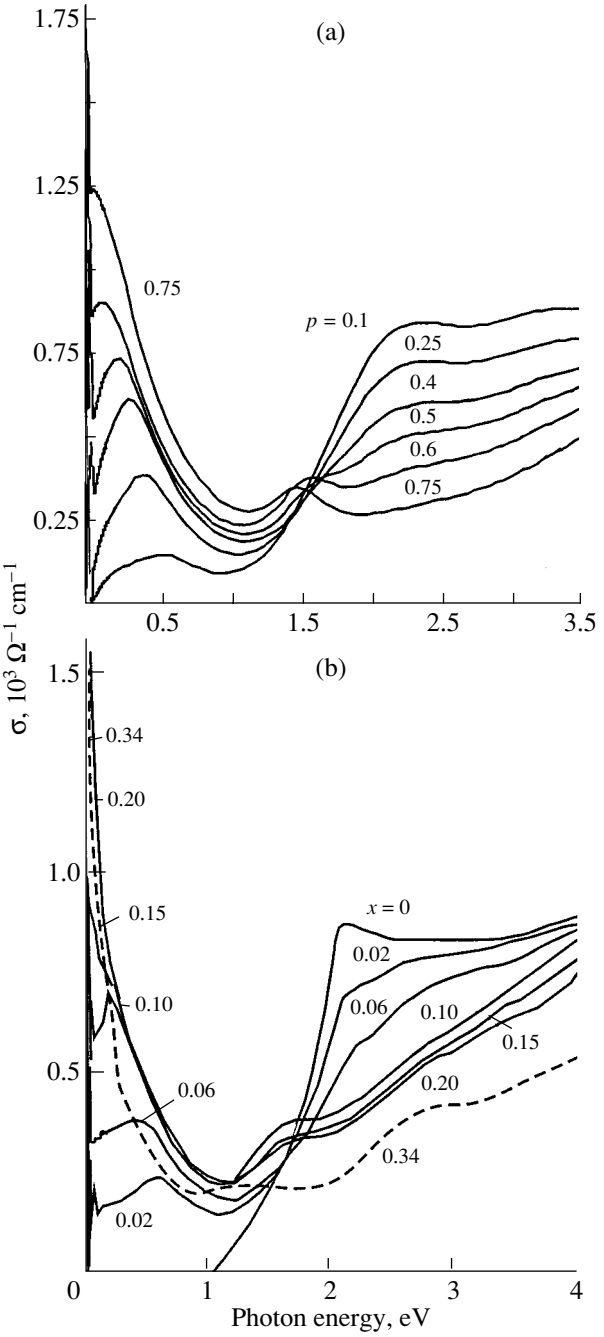

Fig. 1. Room-temperature optical conductivity spectra of $La_{2-x}Sr_xCuO_4$ in the *ab* plane: (a) calculation and (b) experiment [1]; p is the volume fraction of metallic particles dependent on the doping level x.

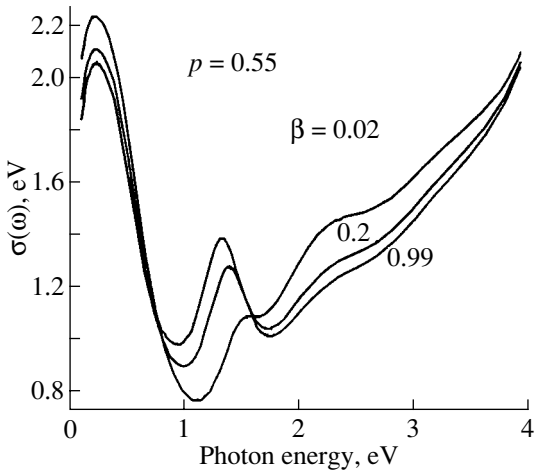

Fig. 2. Dependence of the optical conductivity on the shape of the metallic- and dielectric-phase regions. The smaller values of β correspond to more flattened particles.

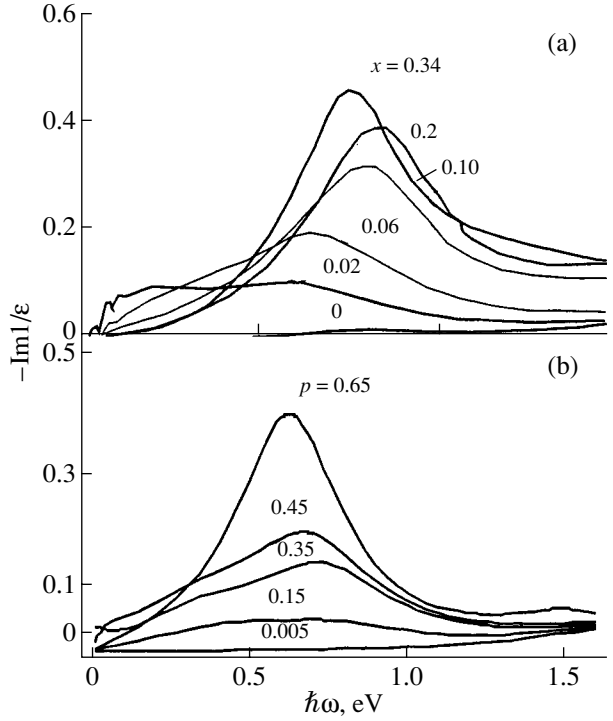

Fig. 3. (a) Experimental electron-energy-loss spectra for $k = 0$ [1] and (b) spectra calculated with the parameters used to obtain the optical conductivity response in Fig. 1a.

weight in the charge transfer band at about 2.2 eV and the formation of a Drude response, as well as the appearance of a new feature at 1.5 eV, starting from fairly large p. We assign this feature, which is indeed observed in the experimental spectrum, to surface plasmon excitation at the interface separating the metallic and dielectric phases. Resonance absorption of this type is specific of inhomogeneous media and is not related to transitions in the electronic spectrum of pure phases. Its parameters depend substantially on the geometry of the particles making up the composite medium. To demonstrate the effect of particle shape on the optical-conductivity profile, Fig. 2 presents three spectra calculated for fixed physical parameters and different particle shapes of the composite medium. Interestingly, the noticeably stronger resonance at 1.5 eV was observed in the transmission spectra of $La_{2-x}Sr_xCuO_4$ thin films [7]. Based on the geometric nature of the feature in question, this behavior can be readily explained, because the method of sample preparation, the internal stresses in it, etc. can affect the shape of the phase boundaries.

The theoretical spectra shown in Fig. 1a reproduce quite well another characteristic feature in the concentration dependence of the optical conductivity of $La_{2-x}Sr_xCuO_4$, namely, the intersection of $\sigma(\omega, x)$ curves corresponding to different x at the same point near 1.7 eV. The existence of this point follows naturally from the two-phase model. The curves drawn for the mixture should intersect at the point where the optical-conductivity curves of its pure metal and dielectric constituents cross, because at this frequency variation of the volume fraction of one phase at the expense of the other does not change the numerical value of the conductivity.

Figure 3a presents the experimental spectra, and Fig. 3b shows the calculated electron-energy-loss spectra (EELS) described by the relation $\mathrm{Im}[-1/\varepsilon(\omega)]$, which explicitly depends on both the imaginary and the real part of the dielectric permittivity. We note that, in contrast to traditional approaches, the EELS peak predicted by the effective-medium theory is not directly related to the plasma frequency, which enters the Drude formula.

While the simplest above model satisfactorily reproduces many characteristic features seen in the optical spectra above 0.2 eV, it requires modification to be applicable to the low-energy region; here, the optical conductivity spectra of various cuprates exhibit a universal behavior which is characterized by two components, at zero 0 and 1000 cm^{-1}, separated by a dip. This structure appears with decreasing temperature and is usually assigned to the formation of a pseudogap; recent publications suggest, however, the possibility that it may form as a result of a phase inhomogeneity [8].

To describe low-energy processes in this model, one has to take into account, first, the contribution of the various absorption mechanisms and, second, the inhomogeneity of the systems under study. While a charge defect becomes surrounded by a well-conducting screening phase, characterized by a low quasiparticle relaxation rate γ, in the peripheral regions, at the edge of the potential well, the quasiparticles are close to localization, with their relaxation rate γ increasing due to strong fluctuations. The magnitude of γ can also be affected by the small finite size of the quasi-metallic

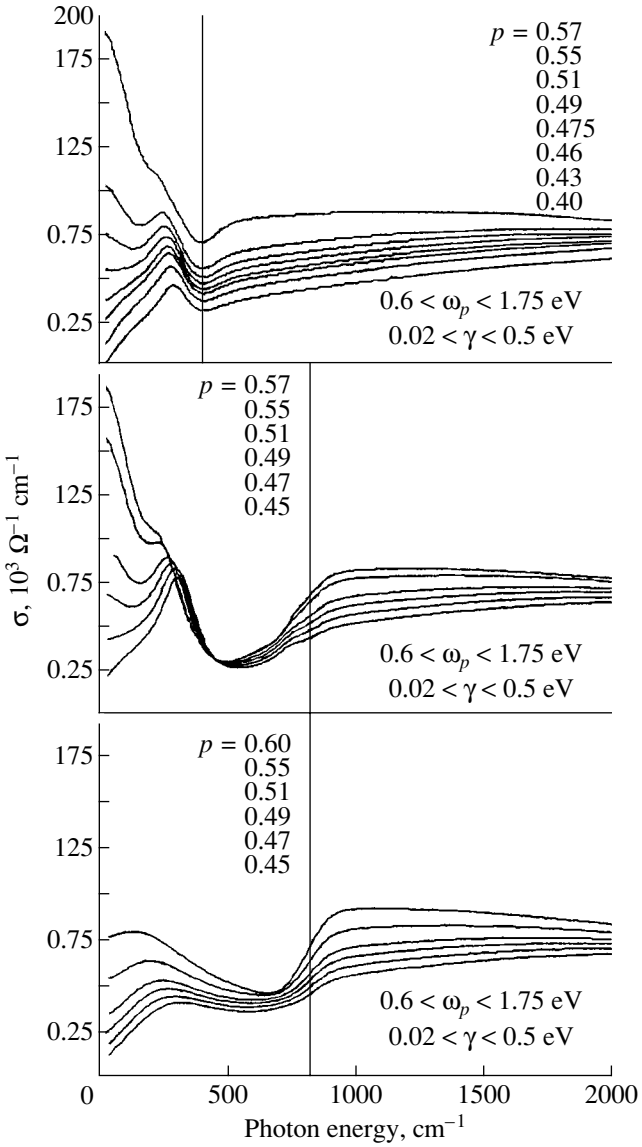

Fig. 4. Spectra of low-frequency optical conductivity calculated for various metallic-phase concentrations p and parameters ω_0, γ_1, and γ_2. The vertical line is the cutoff frequency ω_0 of the crossover from the low- to the high-frequency mode. The ranges of the effective relaxation rate $\gamma_1 < \gamma < \gamma_2$ and of the plasma frequency $\omega_{p1} < \omega_p < \omega_{p2}$ are specified in the figure.

droplet itself. The optical absorption of such a system is contributed by electron transitions inside the conducting-phase nucleus, as well as by mechanisms which, while not being associated with the internal structure of the nucleus, characterize this phase as a whole, for instance, the drift of the nucleus in an external field. This latter mechanism is a simplified notion. We believe that the formation of a collective mode in a system of nuclei (of the type of charge density waves) and the associated absorption are more probable.

The above factors can be taken into account in a simple phenomenological model by making the effective parameters in the Drude relation (2) frequency-dependent. We considered, in particular, stepwise $\gamma(\omega)$ and $\omega_p(\omega)$ dependences for which the "good"-metal mode ($\gamma_1 = 0.05$ eV, $\omega_{p1} = 0.6$ eV) crosses over to a "poor"-metal mode ($\gamma_2 = 0.5$ eV, $\omega_{p2} = 1.75$ eV) at a frequency ω_0. Experiment suggests a value of about 25 meV for ω_0. Figure 4 presents optical conductivity spectra calculated for various concentrations of the metallic phase and for various values of ω_0, γ_1, and γ_2. We readily see that only a slight complication of the model, which makes it more realistic, leads to a nontrivial optical conductivity response whose characteristic features are observed experimentally.

4. CONCLUSION

Thus, the phenomenological model proposed here is of a fairly general nature and is applicable to a broad class of strongly correlated systems comprising, for instance, various HTSC oxides and the lanthanum manganites. The model is based on the concept of the nuclei of the conducting phase forming at the minima of the potential relief, which is created by doping of the original dielectric. To describe the optical properties of such an inhomogeneous system, we have used the effective-medium theory, which permits one to simulate the dielectric permittivity of the system within a broad dopant concentration range. The optical conductivity and electron energy loss spectra of the $La_{2-x}Sr_xCuO_4$ system calculated in the 0.2- to 2-eV region agree reasonably well with the available experimental data and allow interpretation of many of the characteristic features in the spectra within a common framework.

ACKNOWLEDGMENTS

This study was partially supported by CRDF (grant no. REC-005), the Ministry of Education of the RF (project no. E00-3.4-280), and the Russian Foundation for Basic Research (project no. 01-02-96404).

REFERENCES

1. S. Uchida, T. Ido, H. Takagi, *et al.*, Phys. Rev. B **43**, 7942 (1991).
2. A. Lucarelli, S. Lupi, P. Calvani, *et al.*, cond-mat/0106402.
3. F. V. Kusmartsev, Europhys. Lett. **54**, 786 (2001).
4. W. F. Brinkman and T. M. Rice, Phys. Rev. B **2**, 4302 (1970).
5. R. J. Gooding, Phys. Rev. Lett. **66**, 2266 (1991).
6. Ping Sheng, Phys. Rev. Lett. **45**, 60 (1980).
7. M. Suzuki, Phys. Rev. B **39**, 2321 (1989).
8. D. Mihailovic, T. Mertelj, and K. A. Müller, Phys. Rev. B **57**, 6116 (1998).

Translated by G. Skrebtsov

Physics of the Solid State, Vol. 44, No. 8, 2002, pp. 1526–1528. Translated from Fizika Tverdogo Tela, Vol. 44, No. 8, 2002, pp. 1459–1461.

PROCEEDINGS OF THE XI FEOFILOV WORKSHOP "SPECTROSCOPY OF CRYSTALS ACTIVATED BY RARE-EARTH AND TRANSITION-METAL IONS"

(Kazan, Tatarstan, Russia, September 24–28, 2001)

Experimental and Theoretical Studies of Lattice Distortions Caused by Charged 3*d* Impurities in II–IV Semiconductors

V. I. Sokolov*, N. B. Gruzdev*, E. A. Shirokov*, V. N. Starovoĭtova*, A. V. Sokolov*, A. N. Kislov, and I. A. Nekrasov****

** Institute of Metal Physics, Ural Division, Russian Academy of Sciences, ul. S. Kovalevskoĭ 18, Yekaterinburg, 620219 Russia*

e-mail: visokolov@imp.uran.ru

*** Ural State Technical University, pr. Lenina 51, Yekaterinburg, 620083 Russia*

Abstract—The results of studies of photoinduced lattice vibration modes associated with charged 3*d* impurities (in particular, Ni) in II–IV semiconductors (ZnSe, ZnO) and solid solutions ZnSSe and ZnCdSe are presented. Experimental optical exciton–vibration spectroscopy studies revealed that the local vibration modes are coupled, which is due to strong anharmonicity of the local vibrations. Analysis of phonon replicas of the zero-phonon line in the spectra allows one to elucidate the nature of the anharmonicity. Model calculations performed for ZnSe : Ni and ZnO : Ni crystals revealed that the nearest neighbor environment of a charged Ni impurity is highly distorted. A change in the charged state of Ni leads to shifts in lines of calculated and experimentally measured x-ray emission spectra and, therefore, should be taken into account. © *2002 MAIK "Nauka/Interperiodica".*

1. INTRODUCTION

Photoinduced effects in semiconductors have been much investigated, because these effects have a considerable application potential in dynamic holography, ultrarapid communication, data processing, etc. Among these effects is the poorly investigated photoinduced lattice deformation in the vicinity of 3*d*-impurity atoms ionized under exposure to light. Local and quasi-local vibrations occur in the deformed regions of the crystal produced by illumination.

2. EXPERIMENTAL TECHNIQUE

The exciton–vibration spectroscopy study is based on the interaction of a vibrating system with so-called impurity excitons of 3*d*-impurity atoms [1]. In addition, charged impurity centers produce highly distorted regions in the crystal. In these regions, the vibration modes differ significantly from those of the host crystal (new vibration modes occur). These modes manifest themselves as phonon replicas of the zero-phonon line corresponding to the impurity exciton in the absorption spectrum (Fig. 1). In order to separate the exciton contribution to impurity absorption and to improve the sensitivity of the technique, we used electric-field modulation. Such a technique allows high-order processes to be recorded [2, 3].

3. RESULTS AND DISCUSSION

Model calculations of the lattice distortion near the charged Ni impurity show [4, 5] that only the ions of the first coordination shell are significantly displaced. The amount of displacement in ZnSe is roughly 4.5% of the lattice constant or 10% of the initial bond length (Fig. 2, $\Delta b/b = 0.1$). The nearest neighbor ions are shifted away from the defect in the case of Ni^{+} (acceptor) and toward the defect in the case of Ni^{3+} (donor). The displacement of atoms in the second coordination shell is 1% of the initial bond length (Fig. 2, $\Delta d/d = 0.01$). In ZnO, according to calculations of the lattice relaxation near the Ni^{+} impurity (which has a deficiency of positive charge with respect to the lattice), the nearest neighbor O^{-2} ion lying on the hexagonal axis *C* is shifted by 0.275 Å, which amounts to 14% of the Ni–O bond length; the other three nearest neighbor O^{-2} ions are shifted by 0.25 Å (13% of the bond length). These significant displacements are consistent with the notion that the distorted regions around impurities are distinct in properties from the other regions of the crystal and their vibration spectrum differs from that of undoped crystal.

We also calculated the x-ray emission spectrum (XES) for Ni in the ZnSe crystal with allowance for the displacements of Se ions (the change in the Ni–Se bond length in the first coordination shell by ±10%) caused by the change in the charge state of Ni $d^8 \longrightarrow d^7$ and

1063-7834/02/4408-1526$22.00 © 2002 MAIK "Nauka/Interperiodica"

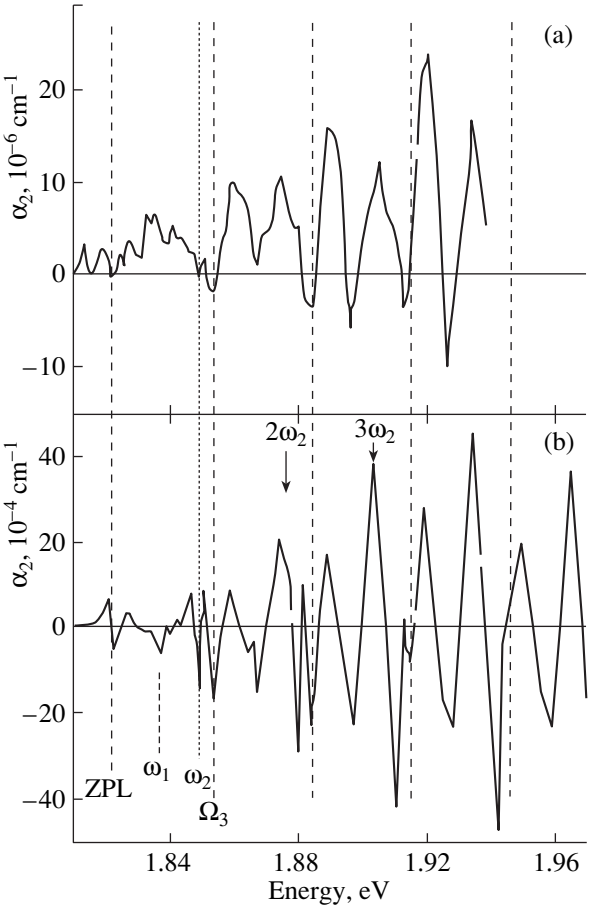

Fig. 1. (a) Exciton–vibration spectrum of the solid solution ZnS_ySe_{1-y} : Ni with $y = 0.02$ at $T = 4.2$ K. Allowance is made for the shift of the zero-phonon line (ZPL) due to the shift of the absorption edge of the solid solution. (b) Exciton–vibration spectrum of ZnSe : Ni in the region where the Ni-acceptor exciton exists; $T = 4.2$ K.

$d^8 \longrightarrow d^9$. The x-ray emission spectrum of Ni is found to have two peaks, L_2 and L_3, associated with the $4s3d \longrightarrow 2p_{1/2}$, $2p_{3/2}$ transitions. For the $Ni^+(d^9)$ ion with charge deficiency, the distance between the L_2 and L_3 peaks is larger: the L_2 peak shifts to higher energies. Tentative measurements of XES fluorescence from ZnSe : Ni samples with $Ni^+(d^9)$ revealed a shift of peak L_2 relative to the L_3 peak in comparison with the spectra of crystals doped only by Ni without a charge deficiency. These results suggest that the change in the charge state of the impurity should be taken into account when interpreting the experimental XES data.

An experimental exciton–vibration spectrum of a ZnSe : Ni crystal is shown in Fig. 1b. In the region of one-phonon replica, the zero-phonon line (ZPL) and peaks at frequencies ω_1, ω_2, and Ω_3 are clearly seen; in the region of many-phonon replicas, this structure is repeatedly reproduced at intervals equal to the frequency of the dominant mode [2, 3]. The difference in

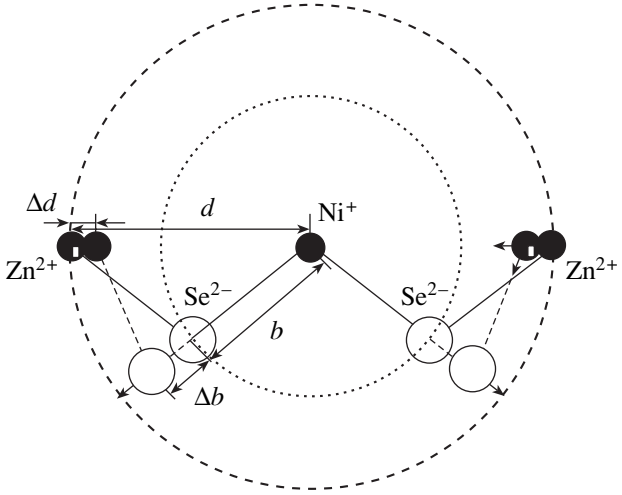

Fig. 2. Displacements of the ions of the first (Se^{2-}) and second (Zn^{2+}) coordination shells around the Ni impurity in ZnSe : Ni caused by a change in its charge state ($Ni^{2+} \longrightarrow Ni^+$). The directions of displacements are indicated by arrows.

intensity of the phonon replicas involving the dominant mode (at frequencies $n\Omega_3$, measured from the ZPL) and of the phonon replicas involving a combination of modes ($\omega_1 + n\Omega_3$) with different values of the replica repetition n is suggestive of energy transfer from one mode to another, that is, of intermode coupling and, therefore, strong anharmonism of vibrations of the impurity crystal. On the other hand, in an anharmonic potential, the vibrational energy levels are not equidistant, which qualitatively explains the increase in the efficiency of energy transfer with increasing replica repetition. The fact that there are no phonon replicas at frequencies $n\omega_2$ is also indicative of nonequidistance of vibrational energy levels and, therefore, of asymmetry of the potential curve corresponding to the vibrational mode with frequency ω_2, for which the one-phonon-replica is fairly strong.

A change in the nearest neighbor environment of the Ni impurity can affect anharmonic vibrations. We investigated this effect on the vibration spectrum of the crystal using a solid solution with different concentrations of foreign atoms. Figure 1a shows the exciton–vibration electroabsorption spectrum of the ZnS_ySe_{1-y} : Ni solid solution corrected for the shift of the zero-phonon line due to the shift of the impurity absorption edge in the solid solution. It is seen that all lines are much weaker than those in the exciton–vibration spectrum (electroabsorption spectrum [2]) of ZnSe : Ni. However, it is more important that the relationship between the line intensities has changed. The phonon replicas $n\Omega_3$ and ($\omega_1 + n\Omega_3$) are clearly seen, whereas the line Ω_2 and its phonon replicas ($\omega_2 + n\Omega_3$) are entirely absent. We also note that the relative intensities

of the phonon replicas $n\Omega_3$ differ essentially from the relative intensities of the corresponding phonon replicas for ZnSe : Ni. This difference can be explained by the fact that the change in the nearest neighbor environment of the Ni impurity (cluster $NiSe_4Zn_{12}$ transforms into $NiSe_3S_1Zn_{12}$) leads to a change in the anharmonicity of vibrations, which affects both the spectrum of vibration modes and their coupling.

In closing, we note that analysis of the experimental exciton–vibration spectroscopy data allows one to better understand the structure of anharmonic vibrations in distorted regions of the crystal lattice. However, one should also use other methods in order to obtain more detailed information on the amount and character of lattice distortions near charged impurity centers and extract such information from experimentally measured integral characteristics, which will allow one to take into account the effect of lattice deformation on the properties of impurity crystals.

REFERENCES

1. V. I. Sokolov, Fiz. Tekh. Poluprovodn. (St. Petersburg) **28** (4), 545 (1994) [Semiconductors **28**, 329 (1994)].
2. V. I. Sokolov, E. A. Shirokov, A. N. Kislov, and V. G. Mazurenko, J. Cryst. Growth **214/215**, 304 (2000).
3. V. I. Sokolov, E. A. Shirokov, A. N. Kislov, and V. G. Mazurenko, Phys. Status Solidi B **221**, 553 (2000).
4. A. N. Kislov, V. G. Mazurenko, V. I. Sokolov, and A. N. Varaksin, Fiz. Tverd. Tela (St. Petersburg) **39**, 2147 (1997) [Phys. Solid State **39**, 1921 (1997)].
5. A. N. Kislov, V. G. Mazurenko, V. I. Sokolov, and A. N. Varaksin, Fiz. Tverd. Tela (St. Petersburg) **41**, 986 (1999) [Phys. Solid State **41**, 897 (1999)].

Translated by Yu. Epifanov

Physics of the Solid State, Vol. 44, No. 8, 2002, pp. 1529–1531. Translated from Fizika Tverdogo Tela, Vol. 44, No. 8, 2002, pp. 1462–1464.

PROCEEDINGS OF THE XI FEOFILOV WORKSHOP "SPECTROSCOPY OF CRYSTALS ACTIVATED BY RARE-EARTH AND TRANSITION-METAL IONS"

(Kazan, Tatarstan, Russia, September 24–28, 2001)

Anomalous Abrupt Resonance-Type Change in the Low-Temperature Heat Conductivity in II–VI Semiconductors Doped with 3*d* Transition Metals

A. T. Lonchakov, N. B. Gruzdev, and V. I. Sokolov

Institute of Metal Physics, Ural Division, Russian Academy of Sciences, ul. S. Kovalevskoĭ 18, Yekaterinburg, 620219 Russia

e-mail: visokolov@imp.uran.ru

Abstract—The phonon heat conductivity in ZnSe : Ni and ZnS : Ni compounds is investigated. The temperature dependences of the heat conductivity coefficient for these crystals are measured by the method of stationary heat flux. It is found that the heat conductivity exhibits minima in the temperature range 15–20 K. It is assumed that the quasi-resonant behavior of the low-temperature heat conductivity is associated with the umklapp processes due to phonon scattering by anharmonic vibration modes of the cluster. © *2002 MAIK "Nauka/Interperiodica".*

1. INTRODUCTION

Impurities of 3*d* transition metals have attracted the particular attention of many researchers for a long time. These compounds have partially occupied 3*d* shells and, under exposure to light, can either donate an electron to the conduction band or accept an electron from the valence band, thus changing their charge state. For example,

$$Ni^{2+} + \hbar\omega \longrightarrow Ni^{3+} + \text{electron},$$

$$Ni^{2+} + \hbar\omega \longrightarrow Ni^{+} + \text{hole}.$$

In the case when impurity atoms substituting for a lattice cation are charged relative to the lattice, they cause a lattice distortion due to displacement of the nearest neighbor ions to new equilibrium positions. In turn, this gives rise to new vibration modes of the cluster. We observed these modes in ZnSe : Ni and ZnS : Ni materials with the use exciton oscillation spectroscopy. Analysis of the electroabsorption spectra revealed the fact that these modes intensively interact with each other (as the number of oscillation repetition increases, the energy is transferred from the dominant mode to the combined modes). The assumption was made [1, 2] that the coupling between these modes is caused by their strong anharmonicity of the third and fourth degrees. In order to verify this assumption, we investigated the phonon heat conductivity of our samples, because phonon scattering in a crystal is very sensitive to anharmonicity of the lattice vibrations. The heat conductivity was measured by the method of stationary heat flux in the temperature range 5–80 K. The measurements were performed with ZnSe : Ni samples (both undoped and doped with nickel at different concentrations) and ZnS : Ni.

Earlier [3], we obtained the temperature dependences of the heat conductivity coefficient for four ZnSe : Ni samples (samples 1–4 with nickel concentrations of 4.3×10^{17}, 5.4×10^{17}, 3.6×10^{19}, and 10^{20} cm^{-3}, respectively). These results demonstrated that, as the temperature increases, the heat conductivity of samples with high nickel concentrations (3.6×10^{19} and 1×10^{20} cm^{-3}) decreases drastically beginning with the lowest temperatures and has a minimum at a temperature $T_{\min} = 15 \pm 1$ K. It was found that the heat conductivity is approximately 40 times less in the former case and is more than 200 times less in the latter case than the maximum heat conductivity of pure ZnSe. With a further increase in the temperature, the heat conductivity increases and smoothly reaches the values corresponding to pure ZnSe. To the best of our knowledge, such a pronounced resonant behavior of the temperature dependence of the heat conductivity has never been observed in semiconductors and dielectrics. In this work, we obtained new temperature dependences of the heat conductivity coefficient both for ZnSe : Ni samples with a different nickel concentration and for ZnS : Ni samples. The results of measurements are represented in Figs. 1 and 2. For comparison, Fig. 1 shows the temperature dependence of the heat conductivity coefficient for pure ZnSe taken from [4].

2. RESULTS AND DISCUSSION

The results of the heat conductivity measurements indicate that the temperature dependence of the heat

1063-7834/02/4408-1529$22.00

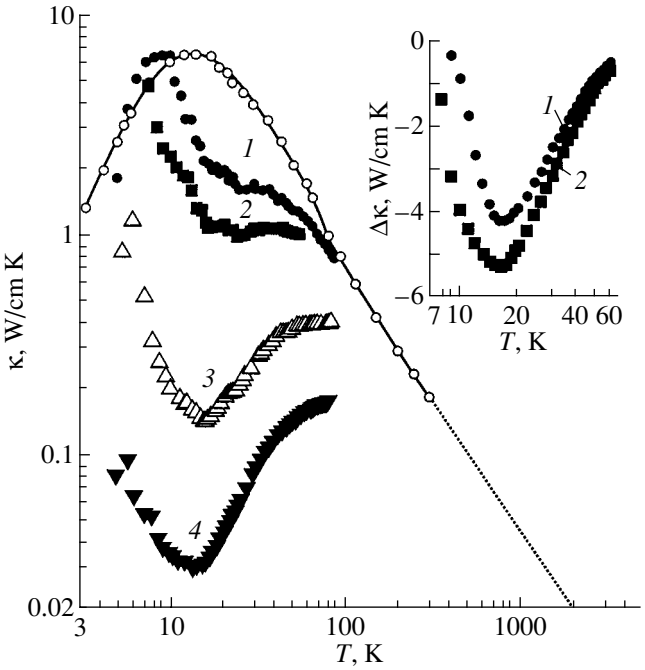

Fig. 1. Temperature dependences of the heat conductivity coefficient κ for four ZnSe samples with different nickel concentrations (samples 1–4). Numerals near the curves correspond to the sample numbers. The solid line represents the dependence for pure ZnSe [4]. The inset shows the differences Δκ between the heat conductivity coefficients of (*1*) sample 1 and pure ZnSe [4] and (*2*) sample 2 and pure ZnSe [4].

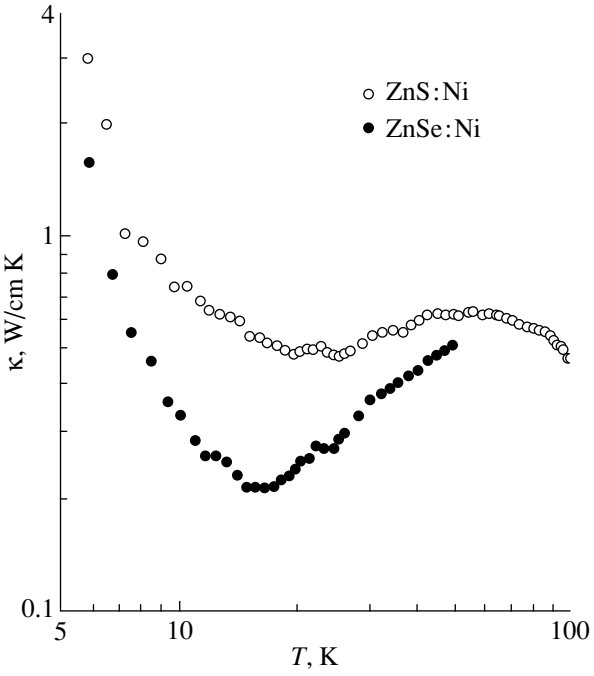

Fig. 2. Temperature dependences of the heat conductivity coefficient κ for ZnSe and ZnS samples with a nickel concentration of 3×10^{18} cm^{-3}.

conductivity coefficient for ZnS : Ni has a minimum at a temperature of 23 K. This minimum is less pronounced than the minimum of the heat conductivity for ZnSe : Ni. This difference can be due to a lower nickel concentration in ZnS as compared to that in samples 3 and 4. Such behavior of the temperature dependence of the heat conductivity can be explained by the coincidence of the phonon frequency either with the frequency corresponding to the energy gap between the states of the impurity center or with the frequency of the lattice vibrations. The first assumption was used to explain the temperature dependence of the heat conductivity in CdTe : Fe and ZnS : Fe samples, in which the separation between the impurity levels is equal to 2–2.5 eV and scattering of acoustic phonons inducing transitions between these levels becomes possible at the given frequency. However, the separation between the impurity levels for nickel is one order of magnitude larger than that for iron. As in [1], we assume that Ni^+ (d^9) impurity centers charged with respect to the lattice exist in ZnSe : Ni and ZnS : Ni crystals. The lattice undergoes deformation in the same manner as for the ionization of an impurity under exposure to light. In turn, this gives rise to new vibration modes of the $Ni^+Se_4Zn_{12}$ cluster which interact with each other due to pronounced anharmonicity [1, 2, 5]. It is these modes that bring about the strong phonon scattering responsible for the quasi-resonant behavior of the temperature dependence of the heat conductivity. In what follows, this scattering will be referred to as an A-process. Peierls [6] demonstrated that the heat conductivity is governed by the so-called umklapp processes. These processes manifest themselves if the anharmonic terms proportional to the third and fourth powers of the atomic displacements are taken into account in the potential energy of the interacting atoms. Hence, we can write the relationship $\mathbf{q} = \mathbf{g} + \mathbf{k} + \mathbf{k}'$, where $\mathbf{k}$ and $\mathbf{k}'$ are the wave vectors of the initial phonons and $\mathbf{q}$ is the wave vector of the new phonon. The vector $\mathbf{g}$ is equal either to zero or to a vector of the reciprocal lattice at which the vector $\mathbf{q}$ remains in the first Brillouin zone. In the case when $\mathbf{g} = 0$ (i.e., when $|\mathbf{k} + \mathbf{k}'| < 2\pi/a_0$, where a_0 is the lattice constant), no umklapp processes occur and thermal resistance of the sample is absent. If $\mathbf{g} \neq 0$, umklapp processes responsible for the heat conductivity proceed in the sample. The high efficiency of the A-process can be explained as follows. The anharmonic modes are associated with the motion of ions involved in the first two coordination spheres surrounding an impurity ion. These spheres are comparable in size to the unit cell (in the $Ni^+Se_4Zn_{12}$ cluster, the Ni–Se and Ni–Zn distances are estimated to be $b \approx 0.433a_0$ and $d \approx 0.707a_0$, respectively). Therefore, these modes correspond to the quasi-momenta $q_B = (2\pi/0.866a_0)$ and $(2\pi/1.414a_0)$, which are comparable to the reciprocal lattice vector. In the course of phonon scattering by these modes, the phonon momentum can become equal

to the reciprocal lattice vector. It is this circumstance that is responsible for the umklapp processes.

In order to explain the resonant behavior of the temperature dependence of the heat conductivity in our materials, we consider the form of the atomic potential energy. If the anharmonic terms of the third and fourth orders are taken into account, the form of the potential changes significantly. At low temperatures, the atom, as an oscillator, is located in the vicinity of the energy minimum and can be considered a harmonic oscillator. As the temperature increases, the fourth-order anharmonicity begins to manifest itself due to the higher energies in the interaction with phonons. The frequency of anharmonic modes in this range of energies depends on the amplitude. In most cases, this dependence is unknown; however, it should correspond to the condition of the generation of the resonant anharmonic mode. The oscillator can interact only with phonons whose energy corresponds to its frequency. However, only part of these phonons has quasi-momenta satisfying the necessary condition for the occurrence of umklapp processes: $|\mathbf{k} + \mathbf{k}'| \geq 2\pi/a_0$, where $\mathbf{k}$ and $\mathbf{k}'$ are the quasi-momenta of the oscillator and the phonon, respectively. The thermal resistance should be maximum at a temperature that corresponds to a maximum in the phonon distribution in the range satisfying the two aforementioned conditions. This explains the resonant behavior of the temperature dependence of the heat conductivity and the origin of the experimentally observed minima in the heat conductivity at certain temperatures: these minima correspond to selenium and sulfur ions (each of them has its own frequency; for the ZnS : Ni sample, the minimum is shifted to the right). In our case, the minima observed for the ZnSe : Ni and ZnS : Ni samples correspond to acoustic phonon frequencies of 0.5 and 0.6 THz, respectively.

3. CONCLUSION

Thus, the temperature dependence of the heat conductivity of ZnSe : Ni and ZnS : Ni crystals exhibits resonant behavior. This confirms the assumption made in our recent work [3] that phonon scattering by anharmonic modes occurs through the mechanism of the umklapp process. The efficiency of this process at two temperatures once more confirmed the inference regarding the strong anharmonicity of the modes of clusters of the materials under study. This mechanism calls for further investigation.

ACKNOWLEDGMENTS

This work was supported in part by the Russian Foundation for Basic Research, project no. 00-02-16299.

REFERENCES

1. V. I. Sokolov, E. A. Shirokov, A. N. Kislov, and V. G. Mazurenko, Phys. Status Solidi B **221**, 553 (2000).
2. V. I. Sokolov, E. A. Shirokov, A. N. Kislov, and V. G. Mazurenko, J. Cryst. Growth **214/215**, 304 (2000).
3. V. I. Sokolov and A. T. Lonchakov, Pis'ma Zh. Éksp. Teor. Fiz. **73** (11), 708 (2001) [JETP Lett. **73**, 626 (2001)].
4. G. A. Slack, Phys. Rev. B **6**, 3791 (1972).
5. A. N. Kislov, V. G. Mazurenko, V. I. Sokolov, and A. N. Varaksin, Fiz. Tverd. Tela (St. Petersburg) **39**, 2147 (1997) [Phys. Solid State **39**, 1921 (1997)].
6. R. E. Peierls, Ann. Phys. **3**, 1055 (1929).

Translated by O. Moskalev

Physics of the Solid State, Vol. 44, No. 8, 2002, pp. 1532–1535. Translated from Fizika Tverdogo Tela, Vol. 44, No. 8, 2002, pp. 1465–1468.

PROCEEDINGS OF THE XI FEOFILOV WORKSHOP "SPECTROSCOPY OF CRYSTALS ACTIVATED BY RARE-EARTH AND TRANSITION-METAL IONS"

(Kazan, Tatarstan, Russia, September 24–28, 2001)

On the Nature of the Energy Gap in Ytterbium Dodecaboride YbB_{12}

T. S. Al'tshuler* and M. S. Bresler**

** Zavoĭskiĭ Physicotechnical Institute, Sibirskiĭ trakt 10/7, Kazan, 420029 Russia*
e-mail: tatiana@dionis.kfti.kcn.ru
*** Ioffe Physicotechnical Institute, Russian Academy of Sciences, ul. Politekhnicheskaya 26, St. Petersburg, 194021 Russia*

Abstract—The YbB_{12} Kondo insulator was studied by EPR. The energy spectrum of YbB_{12} was established to have a gap of width $2\Delta \approx 12$ meV. The experimental data are interpreted in terms of the excitonic-dielectric model. The temperature behavior of the gap was determined; it was found that $\Delta(T) = 72$ K at absolute zero and vanishes at ~115 K. © *2002 MAIK "Nauka/Interperiodica".*

1. INTRODUCTION

The ytterbium dodecaboride YbB_{12} is an intermediate-valence material whose electronic excitation spectrum exhibits a gap 10–25 meV wide. Despite extensive application of various experimental methods (see, e.g., [1–5]), the origin of the electronic gap in Kondo insulators remains unknown. The experimental data on the unusual low-temperature properties of the Kondo insulator have been considered primarily in terms of the *f–d* hybridization gap, which is renormalized partially by correlation effects [5]. This model cannot, however, account for some fine details in the low-temperature behavior of this material; therefore, more advanced theories (the exciton-polaron model developed in [6, 7], the Wigner crystallization model [8]) have to be invoked. This communication reports on an EPR study of ytterbium dodecaboride; the method was found to be very appropriate for the investigation of the electronic band gap in SmB_6, which is a classical model Kondo insulator [9].

2. EXPERIMENT

EPR measurements were conducted on powder samples of ytterbium dodecaboride doped by gadolinium Gd^{3+} to concentrations $c = 0.1$, 0.5, and 1 at. % ($Yb_{0.999}Gd_{0.001}B_{12}$, $Yb_{0.995}Gd_{0.005}B_{12}$, $Yb_{0.99}Gd_{0.01}B_{12}$) and of lutecium dodecaboride doped by 1 at. % Gd^{3+} ($Lu_{0.99}Gd_{0.01}B_{12}$). The YbB_{12} compound was synthesized in an rf furnace in vacuum at 1700 K by barometrically reducing the Yb_2O_3 oxide. Next, it was melted in an arc furnace and dissolved in nitric acid to remove the remaining YbB_6. A single-phase sample in the form of a black powder was subjected to x-ray characterization. A lutecium dodecaboride sample was prepared in a similar manner. The powder grains were 10–20 μm in size, which is less than the skin-layer thickness of the YbB_{12} semiconductor and the LuB_{12} metal. To facilitate electromagnetic-field penetration into the grains, the powders were mixed with melted paraffin.

The measurements were carried out at a frequency $\nu = 9.4$ GHz in the 1.7- to 80-K temperature range.

All samples exhibited a strong EPR signal of the Gd^{3+} ion. Figure 1 displays the temperature dependence of the linewidth $\delta H(T)$ for the $Yb_{0.99}Gd_{0.01}B_{12}$ semiconductor and $Lu_{0.99}Gd_{0.01}B_{12}$, which has metallic conduction. $Lu_{0.99}Gd_{0.01}B_{12}$ produced an EPR signal due to the Gd^{3+} ions, which exhibited a linear linewidth temperature dependence $\delta H = a + bT$ typical of metals. The temperature slope was $b = \delta H/\delta T = 1.25$ Oe/K. For $Yb_{0.99}Gd_{0.01}B_{12}$, this relation is more complex: below 10 K, slight line broadening is observed, whereas above 20 K, the EPR linewidth grows nearly exponentially, reaches saturation at 50 K, then falls off, and above 80 K, the EPR signal linewidth cannot effectively be determined.

Samples with lower Gd concentrations (Fig. 2) exhibited EPR signals up to 17 K for $c = 0.1$ at. % and to 25 K for $c = 0.5$ at. %. The residual linewidth (δH at $T = 0$) increases with Gd concentration; however, this concentration dependence vanishes with the temperature increasing to 13–14 K. The values of δH for all three Gd concentrations fall on the same curve. This behavior implies that for $T > 14$–15 K, the linewidth is determined by pure relaxation processes. At 13–14 K, the samples exhibit a clearly pronounced kink in the linewidth δH.

Figure 3 shows a temperature dependence of the g factor of Gd^{3+} ions in LuB_{12} and YbB_{12}. Gadolinium

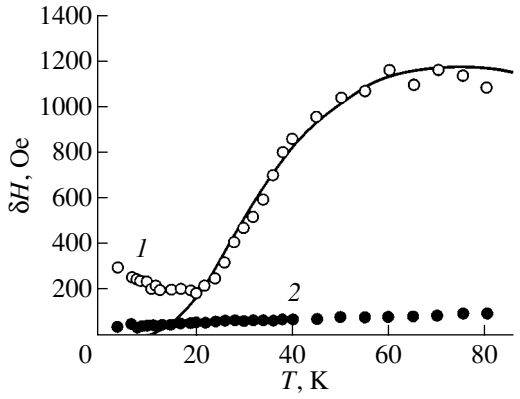

Fig. 1. Temperature dependence of the Gd^{3+} EPR linewidth in the dodecaborides of (*1*) ytterbium YbB_{12} and (*2*) lutecium LuB_{12}. Solid line is theory. Gd^{3+} concentration is 1 at. %.

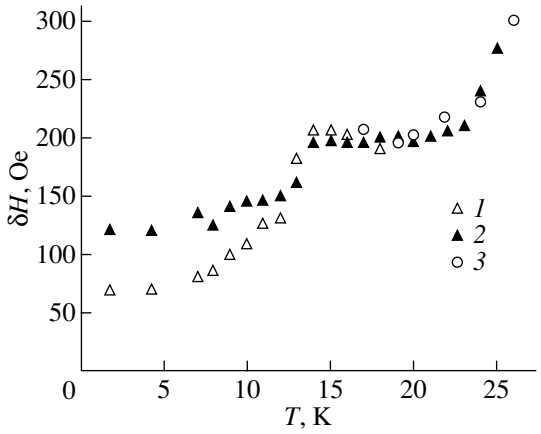

Fig. 2. Temperature dependence of the Gd^{3+} EPR linewidth in the ytterbium dodecaboride YbB_{12} at low temperatures. Gd^{3+} concentration (at. %): (*1*) 0.1, (*2*) 0.5, and (*3*) 1.

Gd^{3+} has a pure spin paramagnetism (the ground state $4f^7$, $^8S_{7/2}$); therefore, its *g* factor is close to 2.00. The Korringa metallic LuB_{12} does indeed exhibit a *g* factor close to 2.00, $g_{Lu} = 1.990 \pm 0.005$.

The behavior of the gadolinium *g* factor in YbB_{12} at low temperatures (<12 K) correlates fully with that of the linewidth; namely, the line broadening is accompanied by an increase in the *g* factor. This correlation is explained as being due to ferromagnetic ordering of the Gd ions.

For $T > 12$ K, the *g* factor does not depend on temperature and is 1.945 ± 0.015. The *g* factor of YbB_{12} (Fig. 3) is seen to be fairly strongly shifted ($\delta g_{Yb} = -0.045$) compared to δg in conventional metals (for $Lu_{0.99}Gd_{0.01}B_{12}$, $\delta g_{Lu} = -0.01$). It is well known that the density of states at Fermi level $N(\varepsilon_F)$ is substantially higher in Kondo insulators than in conventional metals because of the *sf* hybridization. Because $\delta g \sim N(\varepsilon_F)$, this shift implies that YbB_{12} exists in an intermediate state.

Indeed, the average valence state of a rare-earth ion correlates strongly with the *g*-factor shift in Kondo insulators; the average valency of Yb in YbB_{12} is 2.90, and the *g*-factor shift is $\delta g = -0.045$, whereas the average valency of Sm in SmB_6 is 2.65 for a *g*-factor shift $\delta g = -0.080$ [9]. In addition, the existence of intermediate valence in ytterbium dodecaboride is demonstrated by the semiconducting character of the $\delta H(T)$ temperature dependence. The latter is similar to the one observed in SmB_6, a classical Kondo insulator [9], and differs strongly from the linear $\delta H(T)$ relation for dodecaborides of other rare-earth elements, which is characteristic of metals.

3. DISCUSSION OF RESULTS

The ytterbium dodecaboride YbB_{12} is a cubic, narrow-band-gap Kondo insulator (Kondo semiconductor), unlike the lutecium dodecaboride LuB_{12} with metallic conduction, which is an isostructural compound. The Gd^{3+} EPR linewidths of these two compounds behave differently with temperature (Fig. 1). While LuB_{12} exhibits a linear $\delta H(T)$ dependence with a relatively small Korringa relaxation characteristic of metals, the exponential line broadening observed in YbB_{12} in the 14- to 80-K interval is due to the existence of a band gap in the electronic excitation spectrum of this semiconductor. This gap can form, for instance, as a result of the *s* conduction electrons being hybridized with the *f* electrons of the Yb valence band. The Gd^{3+} spin coupling with the spins of electrons and holes gives rise to EPR line broadening. Since the amount of *s–f* excitation grows exponentially with temperature, the $\delta H(T)$ dependence is also exponential.

There is, however, a variety of opinions on the origin of the gap. It has been attributed to *sf* hybridization [5],

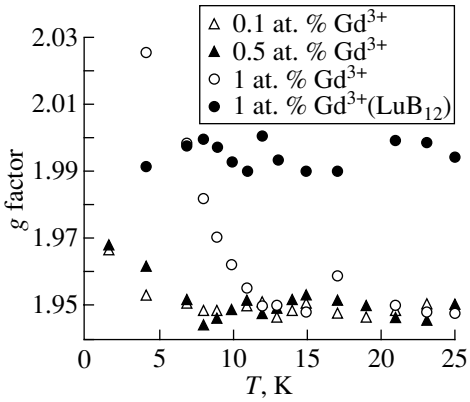

Fig. 3. Temperature dependence of the Gd^{3+} *g* factor in the dodecaborides of ytterbium YbB_{12} and lutecium LuB_{12}. See the figure for notation.

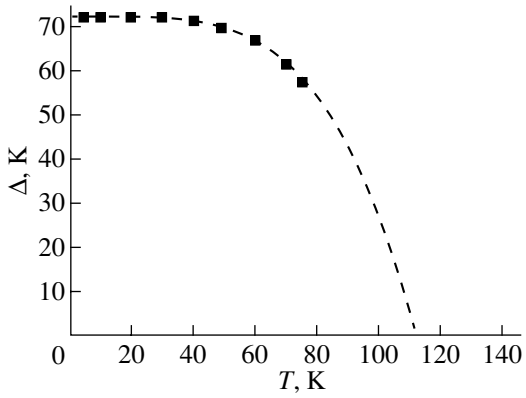

Fig. 4. Temperature dependence of the band gap width $\Delta(T)$ in the ytterbium dodecaboride YbB_{12}.

Wigner crystallization [8], and exciton coupling of *d* electrons with *f* holes [9, 10]. The results predicted by theory for finite temperatures differ substantially. For instance, the hybridization gap does not vary with temperature, whereas the excitonic one forms as a collective effect and disappears at temperatures of the order of the band gap itself. Calculations made within the *sf* hybridization model with a constant gap did not fit well to our experimental data.

The theory of the ground state and of the unusual properties of YbB_{12} has not been developed as comprehensively as for SmB_6; therefore, we shall draw from theoretical studies on samarium hexaboride.

The exciton-polaron model of Kikoin and Mishchenko [6] apparently provides the best description of the unusual properties of SmB_6, including the phonon spectrum anomalies [11] and the magnetic-excitation dispersion studied by inelastic neutron scattering [12]. The model is based on the idea that the ground state of the system is a superposition of the f^6 state of the Sm^{2+} ion with the f^5p state corresponding to the exciton in an intermediate coupling state, in which the hole is in the samarium ion *f* shell (Sm^{3+}) and the electron resides in an orbit representing a linear combination of the *p* states of the boron atoms surrounding the samarium (in the first coordination sphere). The exciton is in the singlet (i.e., nonmagnetic) state. The exciton states at different sites become correlated apparently through exciton interaction, which cannot exist in the mean-field approximation. This is how the macroscopically coherent state forms. The exciton formation gives rise to the opening of a gap in the electronic spectrum. Because the intermediate state fluctuates with phonon frequencies of 10^{12}–10^{13} Hz, there is nothing strange in that the fluctuations become coupled with lattice vibrations. This results in the softening of a phonon mode and renormalization of the electronic (excitonic) states, with the formation of a mixed exciton-polaron state. The phonon modes become mixed with both the charge excitations (the polaron) and the spin excitations (spin-polaron). It is the Jahn–Teller effect observed in SmB_6 that accounts for the latter [13, 14] (see also [15]).

Unfortunately, the spin relaxation rate in the Kondo insulator was not calculated in the Kikoin–Mishchenko model. Therefore, we had to analyze our results in terms of the calculations of Khaliullin and Khomskiĭ [9], who developed a model of an exciton dielectric with large-radius (Mott–Wannier) excitons consisting of a *d* electron and an *f* hole. Basically, the calculations of Khaliullin and Khomskiĭ followed the model of pair electron correlations in superconductors. As in the theory of superconductivity, a temperature-dependent gap opens naturally in the excitonic-dielectric spectrum and its temperature dependence can be determined from a comparison with experiment. The relation derived for the spin relaxation rate [9] can be written as

$$T_2^{-1} = 2\pi T f(\Delta)(b_d^2 + b_f^2)$$
$$\times\{1 + \alpha[1 - f(\Delta)](\Delta/2T)\ln 2\Delta\tau\},$$
$$f(\Delta) = [1 + \exp(\Delta/T)]^{-1},$$
$$b_i = J_i N_i, \quad \alpha = (b_d + b_f)^2/(b_d^2 + b_f^2),$$

where $\Delta = \Delta(T)$ is the excitonic gap; J_d and J_f are exchange integrals for Gd interaction with the *d* electron and the *f* hole, respectively; N_d and N_f are the densities of states of the respective bands at the Fermi level in YbB_{12}; and τ is the momentum relaxation time (the time in which the correlations vanish).

We obtained a satisfactory fit to the experimental values of T_2^{-1} (see the theoretical curve in Fig. 1) with the following values of the parameters:

$$b_d = -0.701 \times 10^{-2}, \quad b_f = -1.902 \times 10^{-2},$$
$$\alpha = 1.65, \quad \tau = 1.00\ \mathrm{K}^{-1}.$$

Although b_d, b_f, and τ are independent fitting parameters, they should also satisfy the other experimental data. It is known that πb_d^2 is of the order of the temperature slope of the Gd linewidth in LuB_{12}, namely, $\pi b_d^2 = 1.54$ Oe/K, $\delta H/\delta T(\mathrm{exp}) = 1.25$ Oe/K. The *g*-factor shift in Kondo dielectrics is proportional to the sum of b_d and b_f:

$$\delta g = b_d + \gamma b_f, \quad \gamma = [4/3J(J+1)]^{1/2};$$
$$\delta g = -0.09, \quad \delta g_{\mathrm{exp}} = -0.045.$$

As seen from the comparison, the agreement with experiment is quite good. It is possible that the difference between the effects that the intermediate-coupling and Mott–Wannier excitons produce on the Gd^{3+} spin relaxation rate T_2^{-1} does not radically affect the comparison of theory with experiment. Figure 4 presents the temperature behavior of the gap obtained by us. We

see that the gap $\Delta(T)$ is 72 K at the lowest temperatures reached and remains virtually constant up to 40 K, after which it decreases and possibly vanishes at 115 K. Because the gap width is $2\Delta = 140$ K, it is of about the same order of magnitude as $T_{cr} \sim 115$ K, which is in full agreement with theoretical predictions. Our results ($2\Delta = 12$ meV) should be compared with the experimental data on photoelectron emission [4] and optical conductivity [3] in YbB_{12}. The former study revealed a gap in the spectrum with an energy of 10 meV which opened below ~75 K when approached from the high-temperature side. In the latter study, a 25-meV-wide band gap also appeared below 70 K.

Thus, our results agree satisfactorily with the data obtained by other methods.

We note the kink in the temperature dependence of the EPR linewidth at low temperatures (Fig. 2). This kink is observed to exist at two levels of YbB_{12} doping by gadolinium. The kink is not seen at 1% Gd doping because of ferromagnetic ordering. Interestingly, we observed the same kink in SmB_6 at the same temperatures; it also did not depend on the impurity concentration. The increase in the linewidth at 13–14 K is apparently due to a nonzero electron density of states in the correlation gap, which is a point of considerable interest. The simplest explanation consists in the existence of impurity states in the gap, which, however, is at odds with our results revealing an independence from the gadolinium dopant concentration. A more promising suggestion connects this electron density of states with specific features of the ground state of the system, for instance, with the formation of a bound polaron, whose existence is discussed by Curnoe and Kikoin in [7]. At any rate, the available experimental data are insufficient for convincing conclusions to be made and the nature of the observed additional excitations requires more comprehensive study.

Our EPR investigation showed that the band gap in the Kondo dielectric YbB_{12}, as well as in SmB_6 [9], is of a cooperative nature rather than of single-particle origin, i.e., caused by *sf* hybridization alone. Unfortunately, our EPR measurements do not make it possible to choose between the excitonic-dielectric and Wigner crystallization models. We can, however, maintain that the gap is described satisfactorily in terms of the excitonic-dielectric model and, in view of the lack of experimental evidence on Wigner crystallization, we believe the excitonic-dielectric model to be preferable.

ACKNOWLEDGMENTS

This study was supported by the Russian Foundation for Basic Research, project no. 00-02-16080.

REFERENCES

1. T. Yoshino, T. Suzuki, Y. Bando, *et al.*, J. Magn. Magn. Mater. **177–181**, 277 (1998).
2. F. Iga, N. Shimizu, and T. Takabatake, J. Magn. Magn, Mater. **177–181**, 337 (1998).
3. H. Okamura, S. Kimura, H. Shinozaki, *et al.*, Phys. Rev. B **58**, R7496 (1998); H. Okamura, N. Shimizu, T. Takabatake, *et al.*, Physica B (Amsterdam) **259–261**, 317 (1999).
4. T. Suzaki, Y. Takeda, M. Arita, *et al.*, Phys. Rev. Lett. **82**, 992 (1999).
5. G. Aeppli and Z. Fisk, Comments Condens. Matter Phys. **16**, 155 (1992).
6. K. A. Kikoin and A. S. Mishchenko, Zh. Éksp. Teor. Fiz. **104**, 3810 (1993) [JETP **77**, 828 (1993)]; K. A. Kikoin and A. S. Mishchenko, J. Phys.: Condens. Matter **7**, 307 (1995).
7. S. Curnoe and K. A. Kikoin, Phys. Rev. B **61**, 15714 (2000).
8. T. Kasuya, J. Phys. Soc. Jpn. **65**, 2548 (1996).
9. T. S. Al'tshuler, G. G. Khaliullin, and D. I. Khomskiĭ, Zh. Éksp. Teor. Fiz. **90**, 2104 (1986) [Sov. Phys. JETP **63**, 1234 (1986)].
10. T. S. Al'tshuler, V. N. Mironov, G. G. Khaliullin, and D. I. Khomskiĭ, Pis'ma Zh. Éksp. Teor. Fiz. **40**, 28 (1984) [JETP Lett. **40**, 754 (1984)].
11. P. A. Alekseev, A. S. Ivanov, and B. Dorner, Europhys. Lett. **10**, 457 (1989).
12. P. A. Alekseev, J.-M. Mignot, J. Rossat-Mignot, *et al.*, J. Phys.: Condens. Matter **7**, 289 (1995).
13. H. Sturm, B. Elschner, and K. H. Hoeck, Phys. Rev. Lett. **54**, 1291 (1985); C. Weber, E. Sigmund, and M. Wagner, Phys. Rev. Lett. **55**, 1645 (1985).
14. T. S. Al'tshuler and M. S. Bresler, Zh. Éksp. Teor. Fiz. **115**, 1860 (1999) [JETP **88**, 1019 (1999)].
15. T. P. Nyhus, S. L. Cooper, Z. Fisk, and J. Sarrao, Phys. Rev. B **55**, 12488 (1997).

Translated by G. Skrebtsov

Physics of the Solid State, Vol. 44, No. 8, 2002, pp. 1536–1539. Translated from Fizika Tverdogo Tela, Vol. 44, No. 8, 2002, pp. 1469–1471.

PROCEEDINGS OF THE XI FEOFILOV WORKSHOP "SPECTROSCOPY OF CRYSTALS ACTIVATED BY RARE-EARTH AND TRANSITION-METAL IONS"

(Kazan, Tatarstan, Russia, September 24–28, 2001)

Effect of Defects on Ytterbium Ion Valency in YbB_{12}

T. S. Al'tshuler*, M. S. Bresler, Yu. V. Goryunov*, F. Iga***, and T. Takabatake*****

** Zavoĭskiĭ Physicotechnical Institute, Sibirskiĭ trakt 10/7, Kazan, 420029 Russia*
e-mail: tatiana@dionis.kfti.kcn.ru
*** Ioffe Physicotechnical Institute, Russian Academy of Sciences, ul. Politekhnicheskaya 26, St. Petersburg, 194021 Russia*
**** ADSM and MaRCH, Hiroshima University, 2-3-1 Kagamiyama, Higashi-Hiroshima, 739-8526 Japan*

Abstract—An EPR signal from ytterbium ions with an integer valence of +3 was detected in the YbB_{12} intermediate-valence compound. The measurements were carried out on an YbB_{12} single crystal in the 1.6- to 4.2-K temperature interval. The EPR spectrum is interpreted as being due to the existence of exchange-coupled ytterbium ion pairs. *© 2002 MAIK "Nauka/Interperiodica".*

The ytterbium dodecaboride YbB_{12} belongs to the class of Kondo insulators [1–8], whose classical representative is the samarium hexaboride SmB_6. The samarium valency fluctuates between the Sm^{2+} ($4f^6$) and Sm^{3+} ($4f^5$) valence states with a frequency of 10^{13}–10^{14} Hz. The average valency of the samarium ions is +2.6; i.e., for 40% of a time interval, one of the electrons is localized at the *f* level, and for 60% of the interval, it stays in the conduction band. The vacancies and defects were found to affect the stoichiometry of the system and to increase the average samarium valency [9, 10]. Only the SmB_6 metal sublattice deviates from stoichiometry, while the boron sublattice exhibits high stability. It was shown in [9] that when the concentration of vacancies *V* in $Sm_{1-x}V_xB_6$ reaches 30% ($x \sim 0.3$), the system crosses over completely to the integer valence state Sm^{3+}. The average samarium valency increases not through a change in the fluctuation frequency but rather through its stabilization. Even in high-quality single crystals with a low defect and vacancy density, one observes an EPR signal of samarium ions in the stabilized valence state Sm^{3+} ($c = 0.05$–0.1 at. %).

Recently, another intermediate-valence compound, the ytterbium dodecaboride YbB_{12}, became a subject of intense investigation. Its electrical properties [1, 2], magnetic susceptibility [1, 2], specific heat [3], and optical conductivity in the far infrared region [4] have been studied, and it has been investigated by inelastic neutron scattering [5, 6] and photoemission [7] and NMR [8] spectroscopy. We are not aware, however, of any study of the stoichiometry and valence-state stabilization of ytterbium in pure YbB_{12} samples at low temperatures. At the same time, valence-state stabilization of ions on the metal sublattice in a fluctuating system, besides being of interest in itself, offers a possibility of studying this compound by EPR without having to dope it by paramagnetic ions as markers. The EPR proved to be useful in studying the SmB_6 ground state; it was employed in detecting the Jahn–Teller effect [11, 12] and in measuring the temperature behavior of the electronic band gap [13].

This communication reports on an EPR study of single-crystal YbB_{12}.

The study was carried out on an YbB_{12} single crystal grown by the floating-zone technique with the use of four xenon lamps, which made it possible to stabilize a high temperature everywhere over the furnace at a level of 2200 ± 50°C. The homogeneity of the single-crystal phase was testified to by Laue patterns and powder diffraction analysis. The total amount of the rare-earth impurity did not exceed 0.05% [14]. The EPR studies were performed on a Bruker spectrometer at 10^{10} Hz in the 1.6- to 4.2-K temperature interval.

The rare-earth dodecaborides RB_{12} crystallize into an NaCl-type cubic fcc lattice, with the metal occupying the position of sodium and with a cubic octahedron of 12 boron atoms at the chlorine site. The Yb^{3+} ($4f^{13}$, $^8F_{7/2}$) multiplet is split by the cubic crystal field into a Γ_6 doublet, a Γ_8 quadruplet, and a Γ_7 doublet. In these conditions, the ground state in RB_{12} can be the Γ_6 or Γ_7 Kramers doublet and each of them can produce an EPR signal. YbB_{12}, however, is an intermediate-valence compound, with the valence-state fluctuation frequency (10^{13}–10^{14} Hz) being higher than the *X*-range EPR spectrometer frequency (10^{10} Hz); therefore, no EPR signal from the fluctuating ytterbium ions can be detected. However, an EPR signal was detected in the 1.6- to 4.2-K temperature interval. At 4.2 K, the spectrum consisted of two lines, with an additional, weaker

1063-7834/02/4408-1536$22.00 © 2002 MAIK "Nauka/Interperiodica"

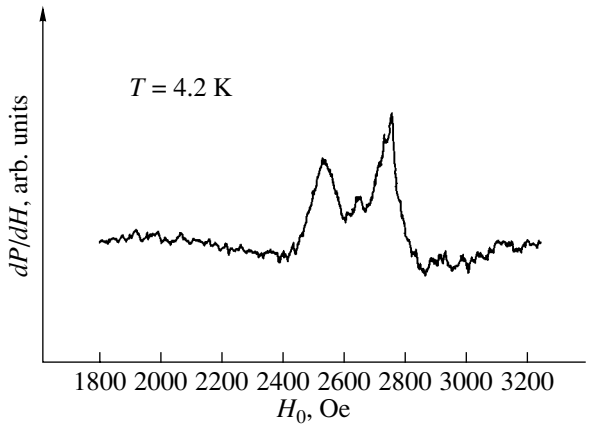

Fig. 1. EPR spectrum of a YbB_{12} single crystal for an angle $\phi = 0°$ between the magnetic field vector and the fourfold axis. $T = 4.2$ K.

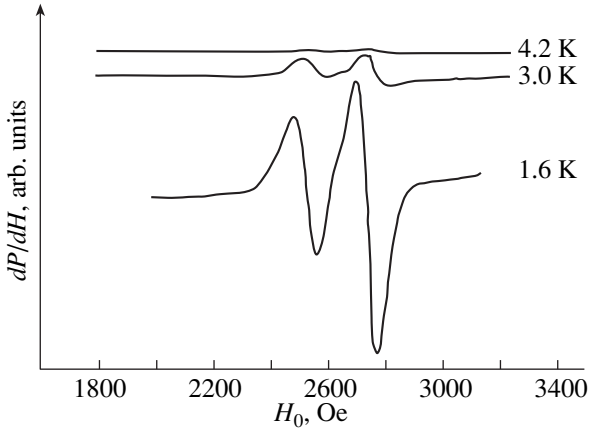

Fig. 2. EPR spectrum of a YbB_{12} single crystal for an angle $\phi = 0$ between the magnetic field vector and the fourfold axis. $T = 1.6$–4.2 K.

peak seen between them (Fig. 1). The peak separation does not exceed 100 Oe, the EPR linewidth is of the same order of magnitude ($\delta H \cong 80$ Oe), and the g factor of the central line is 2.57, which is close to $g = 2.59$ obtained for the Yb^{3+} Γ_6 doublet [15]. As the temperature was lowered down to 1.6 K, the intensity of the two side lines increased by more than an order of magnitude (Fig. 2) to mask the central peak. The average g factor of these two lines is 2.55, which is also close to $g = 2.59$ obtained for the Γ_6 doublet. A comparison with EPR signals of Gd and Er ions in known concentrations in YbB_{12} and DPPH powder samples showed the rare-earth concentration to be not less than 0.3%. This result, as well as the value of the g factor, provides a convincing argument for the EPR spectrum observed being indeed due to the Yb^{3+} ions. Here, apparently, defects and vacancies stabilize part of the ytterbium ions in their valence state, as they do in samarium hexaboride.

Figure 3 displays the dependence of the EPR line positions on the angle between the magnetic-field direction and the cubic axis, with the magnetic field vector rotated in the (110) plane. As could be expected, the position of the central peak of the Γ_6 doublet does not depend on the angle. The angular dependence of the two strongest lines, which lie symmetrically on both sides of the central peak, is well fitted by the function $H = 2635 \pm 14(5\cos 3\phi + 3\cos\phi)$. The figure 2635 Oe corresponds to $g = (7148\nu)/2635 = 2.55$. This value of the g factor and the virtually isotropic behavior of the average g factor (the anisotropy does not exceed 5%) permit one to identify the Yb^{3+} ground state, as already mentioned, with the Γ_6 state. The g factor modulation is described by a Legendre polynomial of the third kind, $Y_{30}(\cos\phi)$. At the same time, in place of one resonance line corresponding to the Γ_6 state, two lines are observed at resonance frequencies differing from the average frequency by the same value for opposite signs of the shift. This behavior directly indicates the presence of two identical coupled oscillators. This situation is well known in the EPR theory and corresponds to a pair of identical exchange-coupled ions [16]. The spin Hamiltonian of a pair of coupled spins ($S = 1/2$) can be written as

$$\begin{array}{c|cccc} & |++\rangle & |+-\rangle & |-+\rangle & |--\rangle \\ \hline |++\rangle & +G_z + (1/4)\Im_z & 0 & 0 & (1/4)(\Im_x - \Im_y) \\ |+-\rangle & 0 & -(1/4)\Im_z & (1/4)(\Im_x + \Im_y) & 0 \\ |-+\rangle & 0 & (1/4)(\Im_x + \Im_y) & -(1/4)\Im_z & 0 \\ |--\rangle & (1/4)(\Im_x - \Im_y) & 0 & 0 & -G_z + (1/4)\Im_z \end{array},$$

where $G_z = g\beta H_z$ is the Zeeman splitting of the Γ_6 state and $\Im_x$, $\Im_y$, and $\Im_z$ are the components of the exchange-integral tensor for the states of a pair of coupled spins. Exchange interaction of the pair spins gives rise to a level splitting and the appearance of two EPR lines at frequencies shifted by the same amount from the average frequency characteristic of the Γ_6 state: $h\nu = g\beta H_z \pm \frac{3}{4}\Im_z'$, where $\Im_z' = \Im_z - \frac{1}{3}(\Im_x + \Im_y + \Im_z)$.

The splitting of one resonance line into two induced by spin coupling in a pair is observed only if the exchange interaction is anisotropic; otherwise, the

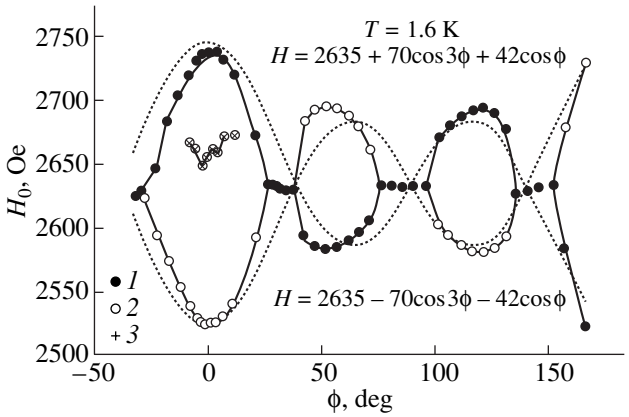

Fig. 3. Experimental (curves *1*, *2*) and theoretical (dashed lines) dependences of the positions of ytterbium ion pairs on the angle ϕ between the magnetic field vector and the fourfold axis, with the magnetic field rotated in the (110) plane. T = 1.6 K. Curve *3* describes the position of the central peak observed at T = 4.2 K.

terms of the pair split into a triplet and a singlet, but with no frequency shift in resonant transitions within the triplet. We note that in our experimental conditions, one might expect anisotropic exchange, but the frequency shift will be described in this case by the $\cos^2\phi$ function rather than by the Legendre polynomial of the third kind. Therefore, the model described by Abragam and Bleaney [16] does not interpret our results properly and needs to be complemented by an interaction having the symmetry required by the experiment.

If the Hamiltonian of our problem

$$H = g\beta H_z T_z + (1/2)(\tilde{\mathfrak{I}}_x' T_x^2 + \tilde{\mathfrak{I}}_y' T_y^2 + \tilde{\mathfrak{I}}_z' T_z^2) + (1/2)\tilde{\mathfrak{I}}\{T(T+1) - 3/2\}$$

is modified to include the term

$$a(3T_{1z}T_{2z} - \mathbf{T}_1\mathbf{T}_2)(\mathbf{T}_2\mathbf{H}),$$

where, using the notation of Abragam and Bleaney, $T_z = S_{1z} + S_{2z}$ is the projection of the total spin of the pair, then this Hamiltonian will transform as $(3\cos^3\phi - \cos\phi)$ with the rotation of the magnetic field. This expression differs somewhat from the Legendre polynomial of the third degree but can be complemented by an exchange correction $b(\mathbf{T}_1\mathbf{T}_2)(\mathbf{T}_2\mathbf{H})$, which transforms as $\cos^3\phi$.

It is assumed that the exchange between closely located spins forming a pair is isotropic.

The strong temperature dependence of the resonance intensity can be accounted for by the small exchange splitting of the ground-state triplet and the excited singlet, which brings about a nearly equal filling of all pair levels already at 4.2 K.

As far as we know, exchange pairs at Yb^{3+} ions have been observed only in $CsCdBr_3$ [17, 18]. The EPR spectrum of the even ^{170}Yb isotope generally resembles the one observed by us and shown in Fig. 1. There is, however, a substantial difference: in contrast to $CsCdBr_3$, where the pairs are in an anisotropic D_{6h}^4 crystal field, in our case, the pairs reside in a cubic O_h crystal field.

We note the absence of a hyperfine structure (hfs) due to the odd ytterbium isotopes. The reason for this is probably as follows. In YbB_{12}, the separation between the two lines is of the order of the linewidth itself and the linewidth δH is larger by nearly an order of magnitude than that for $CsCdBr_3$ and is apparently determined by inhomogeneous broadening, which is responsible for the mutual extinction of the hfs lines. It can also be conjectured that the hfs constants in Kondo insulators are smaller than those in conventional ones. At any rate, this problem requires further study.

The main results of this work can be summed up as follows.

(1) An EPR study of the YbB_{12} Kondo insulator revealed a signal of ytterbium ions in an integer-valence state Yb^{3+} at a concentration of not less than 0.3 at. %. The dependence of the EPR spectrum on the angle between the magnetic field vector and the fourfold axis in the (110) plane was measured at T = 4.2 and 1.6 K.

(2) The observed spectrum can be described if the formation of exchange-coupled ytterbium-ion pairs is taken into account. The reason for the ytterbium valence-state stabilization lies apparently in the samples having defects and vacancies.

ACKNOWLEDGMENTS

This study was supported by the Russian Foundation for Basic Research, project no. 00-02-16080.

REFERENCES

1. T. Yoshino, T. Suzuki, Y. Bando, *et al.*, J. Magn. Magn. Mater. **177–181**, 277 (1998).
2. F. Iga, N. Shimizu, and T. Takabatake, J. Magn. Magn. Mater. **177–181**, 337 (1998).
3. F. Iga, S. Hiura, J. Klijn, *et al.*, Physica B (Amsterdam) **259–261**, 312 (1999).
4. H. Okamura, S. Kimura, H. Shinozaki, *et al.*, Phys. Rev. B **58**, R7496 (1998); H. Okamura, N. Shimizu, T. Takabatake, *et al.*, Physica B (Amsterdam) **259–261**, 317 (1999).
5. A. Bouvet, T. Kasuya, M. Bonnet, *et al.*, J. Phys.: Condens. Matter **10**, 5667 (1998); T. Takabatake, A. Bouvet, A. Hiess, *et al.*, J. Phys. Chem. Solids **60**, 1193 (1999).
6. E. V. Nefeodova, P. A. Alekseev, J.-M. Mignot, *et al.*, Phys. Rev. B **60**, 13507 (1999); E. V. Nefeodova, P. A. Alekseev, J.-M. Mignot, *et al.*, Physica B (Amsterdam) **276–278**, 770 (2000).
7. T. Suzaki, Y. Takeda, M. Arita, *et al.*, Phys. Rev. Lett. **82**, 992 (1999).
8. K. Ikushima, Y. Kato, M. Takigawa, *et al.*, Physica B (Amsterdam) **281–282**, 274 (2000).

9. K. Niihara, Bull. Chem. Soc. Jpn. **44**, 963 (1971).
10. K. Kojima, M. Kasaya, and Y. Kay, J. Phys. Soc. Jpn. **44** (4), 1124 (1978).
11. H. Sturm, B. Elschner, and K. H. Hoeck, Phys. Rev. Lett. **54**, 1291 (1985); C. Weber, E. Sigmund, and M. Wagner, Phys. Rev. Lett. **55**, 1645 (1985).
12. T. S. Al'tshuler and M. S. Bresler, Zh. Éksp. Teor. Fiz. **115**, 1860 (1999) [JETP **88**, 1019 (1999)].
13. T. S. Al'tshuler, G. G. Khaliullin, and D. I. Khomskiĭ, Zh. Éksp. Teor. Fiz. **90**, 2104 (1986) [Sov. Phys. JETP **63**, 1234 (1986)].
14. F. Iga, N. Shimizu, and T. Takabatake, J. Magn. Magn. Mater. **177&181**, 337 (1998).
15. R. Yu. Abdulsabirov, A. A. Antipin, S. L. Korableva, and L. D. Livanova, Fiz. Tverd. Tela (Leningrad) **12**, 2497 (1970) [Sov. Phys. Solid State **12**, 2007 (1970)].
16. A. Abragam and B. Bleaney, *Electron Paramagnetic Resonance of Transition Ions* (Clarendon, Oxford, 1970; Mir, Moscow, 1973), Parag. 9.5.
17. B. Z. Malkin, A. M. Leushin, A. I. Iskhakova, *et al.*, Phys. Rev. B **62**, 7063 (2000).
18. V. Mehta and D. Gourier, J. Phys.: Condens. Matter **13**, 4567 (2001).

Translated by G. Skrebtsov

Physics of the Solid State, Vol. 44, No. 8, 2002, pp. 1540–1543. From Fizika Tverdogo Tela, Vol. 44, No. 8, 2002, pp. 1472–1474.

PROCEEDINGS OF THE XI FEOFILOV WORKSHOP "SPECTROSCOPY OF CRYSTALS ACTIVATED BY RARE-EARTH AND TRANSITION-METAL IONS"

(Kazan, Tatarstan, Russia, September 24–28, 2001)

High Coercivity Powders Based on Sm–Fe–Ta–N Prepared by a Novel Technique[1]

K. Zuzek, G. Drazić, P. J. McGuiness, and S. Kobe

Jozef Stefan Institute, Ljubljana, 1000 Slovenia

e-mail: spomenka.kobe@ijs.si

Abstract—Nitrided Sm_2Fe_{17}-based materials possess excellent intrinsic magnetic properties. In this study, we investigate two compositions, $Sm_{13.7}Fe_{86.3}$ and $Sm_{13.8}Fe_{82.2}Ta_{4.0}$. The stoichiometry of each phase was determined and the SmFeTa material was found to include Ta_3Fe_7, in addition to the Sm_2Fe_{17}, $SmFe_2$, and $SmFe_3$ phases observed in the SmFe alloy, but without the α-iron dendrites characteristic of the binary material. SEM and TEM studies revealed that in the cast structure, approximately 2.0% Ta is initially dissolved in the $Sm_2(FeTa)_{17}$ phase; however, HDDR processing causes the formation of Ta-based precipitates, leaving a 2 : 17 phase with much less dissolved Ta. The HDDR process, with subsequent nitrogenation, was used to prepare coercive powders. The coercivities of these powders were found to be very dependent on the HDDR conditions and Ta addition. The highest coercivity achieved was 1280 kA/m for the composition with Ta. © *2002 MAIK "Nauka/Interperiodica"*.

Because of their excellent intrinsic magnetic properties, SmFeN [1] magnets are being treated as potential candidates for certain types of high-energy permanent magnets. However, because of their instability at temperatures above 500°C, where they decompose into αFe and SmN, their production is limited to bonded magnets. The most common processes used for the preparation of highly coercive powder for bonded magnets are mechanical alloying [2, 3], melt spinning [4, 5], and conventional powder metallurgy [1, 6]; however, the HDDR process [7, 8] appears to be the most promising.

The Sm_2Fe_{17} phase is produced by a peritectic reaction, resulting in some unreacted αFe (up to 25%) [9], which, because it is magnetically soft, has an adverse effect on the hard magnetic properties. Regardless of the method used for the preparation of the alloy, the crystallization of αFe is difficult to avoid. As a result, a long and expensive heat treatment is necessary in order to remove the αFe phase. Previous studies, however, have shown that with the addition of a third element 4–5% Nb [10] or Ta [11] or 1% Zr [12], the primary αFe crystallization can, to a large extent, be avoided.

The HDDR process used for the preparation of highly coercive powders is based on the reaction of the alloy with hydrogen at different temperatures. The addition of a third element to the system causes significant changes in the behavior of the material: Ga [13], Zr [14], or Nb [15] have been observed to stabilize the 2 : 17 phase against disproportionation.

In this paper, we will attempt to explain the difference between SmFe and SmFeTa alloys arising from their different microstructures and phase composition.

1. EXPERIMENTAL PROCEDURE

SmFe and SmFeTa cast alloys were produced by conventional induction melting methods in 5-kg batches by Less Common Metals Ltd. The metals were carefully prepared using standard metallographic methods and examined by an energy dispersive x-ray spectroscopy (EDX)-equipped SEM. As-cast materials were also investigated using x-ray difractometry to determine their lattice parameters. The cast alloys and alloys which had been HDDR-treated once were investigated with TEM in order to explain the different behavior during the HDDR process between the binary material and the Ta-containing material. TEM samples of a powdered material were prepared using 3 to 5 wt % phenol-formaldehyde resin pressed at 0.5 to 1 MPa and cured at 180°C for a few minutes. The resulting pellet was mechanically very strong, so subsequent grinding, dimpling, and ion erosion proceeded without any problems. Due to the high proportion of powder particles, no liquid-nitrogen cooling during the ion erosion process was necessary and no charging effects were observed in the transmission electron microscope. Samples were examined using a Jeol 2000 FX TEM operating at 200 kV. The chemical composition was investigated using a Link AN-10000 EDX system with an Ultra-Thin Window Si(Li) detector mounted perpendicular to the electron beam. The samples were tilted at

[1] This article was submitted by the authors in English.

1063-7834/02/4408-1540$22.00 © 2002 MAIK "Nauka/Interperiodica"

Results of the lattice-parameter refinement calculations

SmFe alloy				SmFeTa alloy			
Phase	*a*, Å	*c*, Å	*V*, Å^3	Phase	*a*, Å	*c*, Å	*V*, Å^3
2 : 17	8.545 ± 0.002	12.428 ± 0.004	785.812 ± 0.364	2 : 17	8.558 ± 0.002	12.441 ± 0.005	789.096 ± 0.005

an angle of 30.5° during the EDXS spectrum collection. The Ta_3Fe_7 phase from the SmFeTa cast material and the Sm_2Fe_{17} phase from the binary cast material were used as standards for the *k*-ratio determination. The Cliff–Lorimer [16] method and absorption correction [17, 18] were used for the quantitative analysis. The sample thickness required for the absorption calculations was estimated using the contamination-spot method.

2. RESULTS AND DISCUSSION

2.1. X-ray Diffraction and EDX Spectroscopy

The SmFeTa material was found to contain significant amounts of Ta_3Fe_7, as well as the Sm_2Fe_{17}, $SmFe_2$, $SmFe_3$ phases observed in the SmFe material, but without the α-iron dendrites characteristic of the SmFe material. Analyses of the Sm_2Fe_{17} phase in the SmFeTa sample show that 2–3% of Ta is dissolved in this phase. More detailed information relating to this investigation has been published previously [19]. Results of the lattice-parameter refinement calculations are shown in the table. These refinements reveal that the presence of Ta in the Sm_2Fe_{17} phase, in agreement with Saje *et al.* [20], causes a significant lattice expansion. The volume of the 2 : 17 unit cell for the SmFeTa alloy was observed to be some 0.42% greater than that of the binary SmFe; this is somewhat smaller than the 0.7% expansion reported by Gutfleisch *et al.* [21] for a 4% Nb alloy.

2.2. TEM Investigations

In order to assess the influence of Ta on the different behaviour observed during the HDDR process, both materials were studied using analytical electron microscopy (TEM-EDX). First, the SmFeTa cast material was investigated (Fig. 1). The phase composition obtained using SEM-EDX analyses was confirmed. It was found that the 2 : 17 matrix phase has some Ta dissolved in it. In contrast, Ta can be found in the form of Ta-rich precipitates in the Sm-rich phases $SmFe_2$ and $SmFe_3$. In the $SmFe_2$ phase, some planar defects were observed. Using bright-field and dark-field experiments, it was confirmed that these defects are most probably antiphase boundaries (APB) (cf. Fig. 1).

Then, the SmFeTa sample subjected to the HDDR run (Fig. 2) was investigated and some differences were observed. It was found that the 2:17 matrix phase contains less Ta than the same phase in the cast material. The Ta was found in the form of Ta-based precipitates located within the original 2 : 17 phase. To find the exact difference in the Ta concentration in the Sm_2Fe_{17}

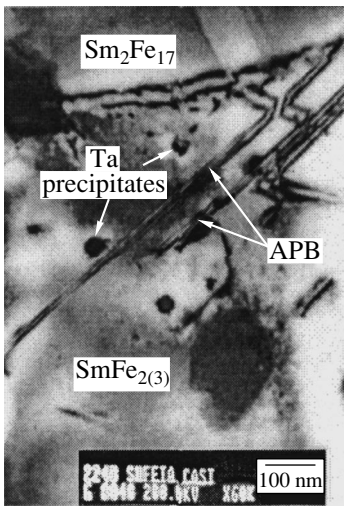

Fig. 1. A TEM image of the as-cast Sm–Fe–Ta alloy.

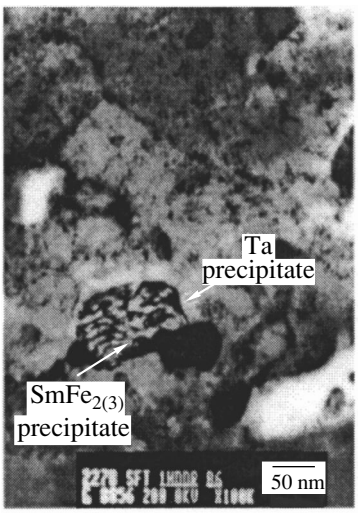

Fig. 2. A TEM image of the HDDR-processed Sm–Fe–Ta material.

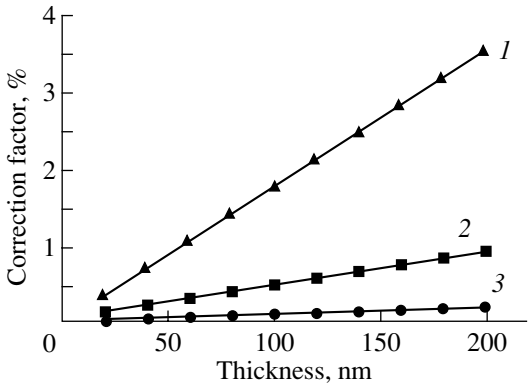

Fig. 3. Calculated absorption-correction and secondary fluorescence correction factors vs. foil thickness: (*1*) absorption-correction factors for Ta, (*2*) secondary fluorescence correction factors for Sm–Fe, and (*3*) for Fe–Ta.

phase between the cast material and in the samples after the HDDR run, we performed rigorous, quantitative EDXS analysis.

During the 5 min required for the collection of an EDXS spectrum, we observed that the drift of the sample and the sample contamination (carbon build-up) were relatively low. By limiting the time to 300 s and taking into account that around 5000 counts per Ta L_α peak for a 3% error limit (at a 95% confidence level) should be used, we found that the foil thickness at the measuring points had to be at least 150 nm. At this thickness, the influence of the amorphous contamination layer, originating from the ion erosion process, is also minimized. In addition, due to the relatively high mass absorption coefficient of Ta L_α lines in Sm (433.9 cm^2/g) [18], the influence of absorption should be tested if the errors are to be kept as low as possible. In Fig. 3, the calculated absorption-correction coefficients for Ta as a function of foil thickness in the Sm_2Fe_{17} phase are shown. For a thickness of around 150 nm, the correction factor is higher than 2.5%; thus absorption should not be neglected. We performed a similar calculation [22] for the secondary fluorescence correction (Fig. 3) and found that the effect is very low; therefore, this type of correction was not used.

From the measured concentrations we calculated the reproducibility (precision defined as the relative standard deviation of measurements) of the Ta concentration measurements in various phases. It was found that in the Ta_3Fe_7 phase (cast material), the reproducibility was better than 2%, justifying the use of this phase as a standard for Ta. In the $Sm_2(FeTa)_{17}$ phase in the cast alloy, the relative standard deviation of measurements was better than 5%, and in the same phase in the sample after a single HDDR cycle, it was around 12%. The relatively high value of the standard deviation in this case can be explained by the presence of Ta_3Fe_7 nanoprecipitates in the analyzed volume. After discarding the points where a high concentration of Ta indicates the presence of Ta-rich precipitates, it was found that in the Ta-containing cast material the concentration of Ta in the Sm_2Fe_{17} phase is 2.0 ± 0.1 at. %, while after the HDDR process, this phase contains 1.2 ± 0.1 at. % of Ta.

In summary, the introduction of Ta has a very significant and beneficial impact on the cast material: magnet-processing problems associated with the presence of iron dendrites are removed due to formation of the Ta_3Fe_7 phase rather than peritectic iron.

The Ta-containing alloy was also observed to be significantly more stable in terms of the resistance of the 2 : 17 hydride phase to disproportionation. This can be attributed to the dissolution of 2.0% of Ta into the 2 : 17 phase increasing its stability with respect to decomposition in a hydrogen atmosphere. SEM and TEM studies revealed that the Ta is initially dissolved in the $Sm_2(FeTa)_{17}$ phase in the cast structure; however, the HDDR process causes the formation of Ta-based precipitates leaving the 2 : 17 phase with 1.2% dissolved Ta.

ACKNOWLEDGMENTS

The financial support of the Ministry of Education, Science, and Sport of Slovenia is gratefully acknowledged.

REFERENCES

1. J. M. D. Coey and H. Sun, J. Magn. Magn. Mater. **87**, L251 (1991).
2. K. Schnitzke, L. Schultz, J. Wecker, and M. Katter, Appl. Phys. Lett. **57**, 2853 (1990).
3. M. Endoh, M. Iwata, and M. Tokunaga, J. Appl. Phys. **70**, 6030 (1991).
4. M. Katter, J. Wecker, and L. Schultz, J. Appl. Phys. **70**, 3188 (1991).
5. C. N. Christodoulou and T. Takeshita, J. Alloys Compd. **196**, 161 (1993).
6. M. Q. Huang, L. Y. Zhang, B. M. Ma, *et al.*, J. Appl. Phys. **70**, 6027 (1991).
7. T. Takeshita and R. Nakayama, in *Proceedings of the 11th International Workshop on Rare-Earth Magnets and Their Applications, Sankar and Wallace, Pittsburgh, USA, 1991*, p. 49.
8. P. J. McGuiness, X. J. Zhang, H. Forsyth, and I. R. Harris, J. Less-Common Met. **162**, 379 (1990).
9. S. A. Sinan, D. S. Edgely, and I. R. Harris, J. Alloys Compd. **226**, 170 (1995).
10. A. E. Platts, I. R. Harris, and J. M. D. Coey, J. Alloys Compd. **185**, 251 (1992).
11. B. Saje, A. E. Platts, S. Kobe Besenicar, *et al.*, IEEE Trans. Magn. **30**, 690 (1994).
12. B. Gebel, M. Kubis, and K.-H. Muller, J. Magn. Magn. Mater. **174**, L1 (1997).

13. M. Kubis, K.-H. Muller, and L. Schultz, J. Appl. Phys. **83**, 6905 (1998).
14. H. Nakamura, S. Sugimoto, T. Tanaka, *et al.*, J. Alloys Compd. **222**, L251 (1995).
15. S. Sugimoto, H. Nakamura, M. Okada, and M. Homma, in *Proceedings of the 6th International Conference on Ferrites (ICF 6), Tokyo and Kyoto, Japan, 1992*.
16. G. Cliff and C. W. Lorimer, J. Microsc. **103**, 203 (1975).
17. J. I. Goldstein, J. L. Costley, G. W. Lorimer, and S. J. B. Reed, in *SEM 1977*, Ed. by O. Johari (IITRI, Chicago, 1977), p. 315.
18. K. F. J. Heinrich, in *The Electron Microprobe*, Ed. by T. D. McKinley, K. F. J. Heinrich, and D. B. Wittry (Wiley, New York, 1964), p. 744.
19. K. Zuzek, P. J. McGuiness, and S. Kobe, J. Alloys Compd. **289**, 213 (1999).
20. B. Saje, S. Kobe-Besenič ar, Z. Samardžija, *et al.*, J. Magn. Magn. Mater. **146**, L251 (1995).
21. O. Gutfleisch, J. C. Clarke, A. C. Nieva, *et al.*, J. Alloys Compd. **233**, 216 (1996).
22. C. Nockolds, M. J. Nasir, G. Cliff, and G. W. Lorimer, Inst. Phys. Conf. Ser. **52**, 417 (1979).

Physics of the Solid State, Vol. 44, No. 8, 2002, pp. 1544–1549. Translated from Fizika Tverdogo Tela, Vol. 44, No. 8, 2002, pp. 1475–1479.

PROCEEDINGS OF THE XI FEOFILOV WORKSHOP "SPECTROSCOPY OF CRYSTALS ACTIVATED BY RARE-EARTH AND TRANSITION-METAL IONS"

(Kazan, Tatarstan, Russia, September 24–28, 2001)

Magnetic Properties of the Ising Dipole Ferromagnet $LiTbF_4$

I. V. Romanova*, **, B. Z. Malkin*, I. R. Mukhamedshin*, **, H. Suzuki, and M. S. Tagirov****

** Kazan State University, ul. Lenina 18, Kazan, 420008 Tatarstan, Russia*

*** Kanazawa University, Kanazawa, 920-11 Japan*

e-mail: Irina.Choustova@ksu.ru

Abstract—The field and temperature dependences of the magnetization of a $LiTbF_4$ single crystal are measured at temperatures ranging from 2 to 300 K in magnetic fields (up to 5 T) directed parallel and perpendicular to the crystallographic axis *c*. It is revealed that the temperature dependence of the induced (van Vleck) transverse magnetization exhibits nonmonotonic behavior with a maximum in the vicinity of the liquid-nitrogen temperature. The results of magnetization measurements are used to determine the parameters of the crystal field and interionic magnetic interactions. *© 2002 MAIK "Nauka/Interperiodica".*

1. INTRODUCTION

Lithium terbium tetrafluoride $LiTbF_4$ is an Ising dipole ferromagnet in which the magnetization axis is aligned parallel to the crystallographic axis *c*. Single-crystal $LiTbF_4$ undergoes a phase transition from the paramagnetic state to the ferromagnetic state with a decrease in temperature to T_c = 2.874–2.885 K [1, 2] due to the magnetic dipole–dipole interaction between non-Kramers Tb^{3+} ions. Different physical properties of $LiTbF_4$ crystals as a model system with the specific features of dipole–dipole ordering have been thoroughly investigated by many researchers. In particular, Christensen [3] measured optical absorption spectra and the energies of Stark sublevels for a number of multiplets (such as $^7F_6$, $^7F_3$, $^7F_2$, $^7F_1$, and $^5D_4$) of the Tb^{3+} $4f^8$ electron shell in the temperature range 2.3–150 K. Ahlers *et al.* [4] analyzed the temperature dependence of the heat capacity in the vicinity of the phase transition. In [5–7], the effects associated with the interaction between the 4*f* electrons localized on terbium ions and the lattice vibrations were studied using the Raman spectra. It was found that the magnetically ordered phase is characterized by spontaneous splitting of degenerate optical branches of the vibrational spectrum due to coupled electron–phonon excitations [5–7]. Als-Nielsen *et al.* [1] experimentally investigated magnetic scattering of neutrons and obtained the temperature dependence of the spontaneous magnetization. Holmes *et al.* [8] evaluated the exchange interaction constants. The Curie–Weiss paramagnetic temperature (3.6 K) and the characteristics of the ground state of terbium ions were determined from measurements of the magnetic susceptibility in weak magnetic fields [9] and from the electron paramagnetic resonance spectra [10]. Krotov *et al.* [11] investigated the magnetoelastic interaction, spontaneous magnetostriction, and forced magnetostriction in $LiTbF_4$ single crystals. The specific features of the magnetic properties of both the magnetically concentrated and diluted ($LiY_xTb_{1-x}F_4$) crystals in the vicinity of the Curie temperature were considered in [2, 12–15].

In the present work, we measured the longitudinal and transverse magnetizations in the paramagnetic and ferromagnetic phases of $LiTbF_4$ single crystals in external magnetic fields directed parallel and perpendicular to the symmetry axis of the corresponding crystal lattice with the aim of refining the data available in the literature on the parameters of the crystal field and interionic magnetic interactions.

2. EXPERIMENTAL TECHNIQUE

A single crystal of $LiTbF_4$ was grown by the Bridgman–Stockbarger method according to the procedure described in [16]. The single crystal was first oriented using an x-ray diffractometer and then shaped into a sphere approximately 2 mm in diameter. In order to exclude rotation of the single-crystal sample in strong magnetic fields (due to strong magnetic anisotropy), the crystal was fixed in a cryostat with the use of a Stycast 1266A low-temperature epoxy resin.

The magnetization measurements were performed on a SQUID quantum magnetometer (MPMS-2 Quantum Design), which made it possible to measure the magnetization of samples over wide ranges of magnetic fields (up to 5.5 T) and temperatures (2–400 K). However, for the single-crystal sample studied in this work, the linearity limit of the magnetometer used in measuring the magnetization was equal to 1.25 emu, because the quantum-mechanical amplifier went out of linear

operation when the magnetic flux changed drastically. For this reason, our attempts to measure the saturation magnetization were unsuccessful.

The experimental data obtained in this work were compared with the results of the theoretical analysis described below.

3. CALCULATION OF THE MAGNETIZATION AND DISCUSSION OF THE EXPERIMENTAL RESULTS

Crystals of the $LiLnF_4$ tetrafluoride series have a tetragonal structure of the $CaWO_4$ scheelite type with space-group symmetry $C_{4h}^6(I4_1/a)$. The unit cell parameters at a temperature of 100 K are as follows: a = 0.5181 nm and c = 1.0873 nm [1]. The unit cell contains two magnetically equivalent Ln^{3+} ions at sites with point-group symmetry S_4 [17]. The energy of interaction between the electrons localized on the 4*f* unfilled shell of the rare-earth ion and the static crystal field is determined by the parameters B_p^k of the single-electron Hamiltonian

$$H_{\rm cf} = \alpha B_2^0 O_2^0 + \beta[B_4^0 O_4^0 + B_4^4 O_4^4 + B_4^{-4}\Omega_4^{-4}] + \gamma[B_6^0 O_6^0 + B_6^4 O_6^4 + B_6^{-4}\Omega_6^{-4}], \quad (1)$$

where α, β, and γ are the reduced matrix elements (the Stevens coefficients) and O_p^k and Ω_p^k are the Stevens operators [18]. In the crystal field, the fundamental term $^7F_6$ of the Tb^{3+} ion is split into seven sublevels corresponding to the irreducible representations Γ_1 (three singlets), Γ_2 (four singlets), and Γ_{34} (three doublets) of point-group symmetry S_4. The ground state of the Tb^{3+} ion is characterized by a quasi-doublet consisting of two singlets Γ_2^k (k = 1, 2) with the initial splitting $\delta \approx 1$ cm^{-1}; in this case, the Δ energy of the nearest neighbor excited state (the Γ_{34} doublet) is of the order of 100 cm^{-1} [3]. At low temperatures ($k_BT \ll \Delta$, where k_B is the Boltzmann constant), only the fundamental quasi-doublet is virtually filled and, since sublevels of the Γ_2 symmetry are mixed only with the component of the external magnetic field $\mathbf{B}_0$ that is oriented along the [001] axis of the crystal lattice (in the present work, we used the crystal system of coordinates in which the z axis is aligned parallel to the c axis), the magnetic properties of the $LiTbF_4$ single crystal can be considered within the model of an Ising three-dimensional magnet in a transverse magnetic field whose role is played by the initial splitting δ of the quasi-doublet. The Hamiltonian of the system can be represented in terms of the operators of the effective spin moment components S_α of the ith Tb^{3+} ion (S = 1/2) in the following form:

$$H_{\rm eff} = -\frac{1}{2}\sum_{i,j}\left[\frac{(g_\parallel\mu_B)^2}{v}K_{ij} + J_{ij}\right]S_z^iS_z^j - \sum_i(\delta S_x^i + g_\parallel\mu_B B_{0z}S_z^i). \quad (2)$$

Here, μ_B is the Bohr magneton, the first sum corresponds to the pair magnetic dipole–dipole and exchange interactions, $K_{ij} = v(3z_{ij}^2 - r_{ij}^2)/r_{ij}^5$, $v = a^2c/2$ is the volume of the unit cell, and $\mathbf{r}_{ij}$ is the vector connecting two Tb^{3+} ions. The intrinsic magnetic moment of the Tb^{3+} ions is characterized by only the z component oriented along the symmetry axis of the crystal lattice. By virtue of the large effective g factor ($g_\parallel = 2g_L\langle\Gamma_2^1|J_z|\Gamma_2^2\rangle$ = 17.85 [10], where g_L = 3/2 is the Landé splitting factor and **J** is the total angular momentum of the ion), the magnetic dipole–dipole interaction plays a dominant role in magnetic ordering. Since the magnetic dipole–dipole interaction is a long-range interaction, the calculation of the low-temperature magnetic characteristics of the $LiTbF_4$ single crystal within the self-consistent field approximation is justified.

3.1. Exchange interaction. In the self-consistent field approximation, the local magnetic field acting on Tb^{3+} paramagnetic ions in a single-crystal sample along the [001] direction can be represented as the sum of the external magnetic field B_{0z}, the molecular field $B_M = \lambda M$, and the demagnetizing field $B_D = -DM$, where M is the magnetization of the sample, D is the demagnetizing factor (for a spherical sample, $D = 4\pi/3$), $\lambda = \lambda_D + \lambda_j$ is the molecular field constant, and $\lambda_D = \sum_j D_{ij}/2 = (4\pi/3) \times 1.3965$ is the Lorentz field constant, which is obtained by summation over the lattice (in our case, the unit cell contains two paramagnetic ions). The exchange field constant $\lambda_J = v\sum_j J_{ij}/2(g_\parallel\mu_B)^2$ is determined by the exchange interaction between the nearest neighbor ions. In particular, based on analyzing the data on quasi-elastic neutron scattering by a $LiTbF_4$ crystal, Holmes *et al.* [8] estimated the exchange integrals for interactions of terbium ions with the nearest neighbor ions (for four ions located at a distance of 0.375 nm, $J_1 = -0.3624 \pm 0.125$ cm^{-1}) and with the next-to-nearest neighbor ions (for ions located at a distance of 0.518 nm, $J_2 = 0.07 \pm 0.14$ cm^{-1}). In this case, the molecular field constant is estimated to be $\lambda = 5.23 \pm 0.56$. In the self-consistent field approximation, the molecular field constant λ can be related to the observed temperature of magnetic ordering through the relationship

$$1 = \lambda\frac{(g_\parallel\mu_B)^2}{v\delta}\tanh\left(\frac{\delta}{2k_BT_c}\right). \quad (3)$$

By substituting $\delta = 1.1$ cm^{-1} and $T_c = 2.88$ K into relationship (3), we can estimate the molecular field constant from below: $\lambda > 4.32$. For the paramagnetic phase at sufficiently low temperatures ($T_c < T \ll \Delta/k_B$) and in weak magnetic fields $B_{0z} \ll \delta/(g_{\|}\mu_B) \approx 0.1$ T, the magnetization of the studied sample along the crystallographic axis *c* of the lattice can be represented by the expression

$$M_z = B_{0z}\left[\lambda\left(\frac{\tanh(\delta/2k_BT_c)}{\tanh(\delta/2k_BT)} - 1\right) + D\right]^{-1}. \quad (4)$$

In the case when the dipole–dipole interaction between paramagnetic ions dominates in the crystal, a decrease in temperature below the Curie point leads to the formation of domains with a zero demagnetizing factor (i.e., long thin cylinders with a generatrix along the magnetization axis are formed) [3]. Note that the total magnetic moment of the crystal $\mathbf{M}V$ (V is the crystal volume) remains zero. In a weak external magnetic field, the domains are partially reoriented; as a result, the demagnetizing field B_{Dz} completely compensates for the external magnetic field B_{0z} and the magnetization of the crystal is equal to the limiting magnetization defined by expression (4); i.e., $M_z = B_{0z}/D$ at $T \longrightarrow T_c$ and under the condition $B_{0z} < M_0/D = B_c$. Here, M_0 is the spontaneous magnetization at a specified temperature of the sample, which satisfies the relationship

$$\frac{\delta}{[\delta^2 + (g_{\|}\mu_B\lambda M_0)]^{1/2}} \times \frac{\tanh\{[\delta^2 + (g_{\|}\mu_B\lambda M_0)]^{1/2}/2k_BT\}}{\tanh(\delta/2k_BT_c)} = 1. \quad (5)$$

Thus, the dependence of the induced magnetization on the external magnetic field is linear at $T < T_c$ and the saturation of magnetization occurs upon reorientation of all the domains involved. As can be seen from Fig. 1, the magnetization measured at a temperature of 2 K is a linear function of the external magnetic field (straight line *1*); in this case, the demagnetizing factor is estimated to be $D = 3.91 \pm 0.2$. The experimental temperature dependence of the magnetization measured in a very weak magnetic field is shown in Fig. 2 (curve *6*). The observed increase in the magnetization with a decrease in the temperature is adequately described by expression (4) with the molecular field constant $\lambda_{exp} = 4.525$ and demagnetizing factor $D = 4.11$, which correspond to the horizontal portion of the curve $M_z(T)$. The solid lines in Figs. 1 and 2 (except for curve *7* in Fig. 2) represent the results of our calculations with the same molecular field constant ($\lambda_{exp} = 4.525$). Therefore, the ratio of the energy of exchange (antiferromagnetic) interaction between the nearest neighbor ions to the energy of their magnetic dipole–dipole interaction can reach a value of –0.42. The derivative $(\partial M_z(T, B_{0z})/\partial T)_{B_{0z}}$ has a discontinuity at the point of intersection of the curves $M_z(T)$ and $M_0(T)$, which represent the temperature dependences of the induced magnetization and the spontaneous magnetization, respectively. Curve *7* in Fig. 2 depicts the temperature dependence of the spontaneous magnetization of the $LiTbF_4$ crystal according to the magnetic neutron scattering data obtained in [1]. It can be seen from the temperature dependences of the magnetization measured in magnetic fields of 0.0009 and 0.1 T (Fig. 2) that, in actual practice, similar information on the spontaneous magnetization of a dipole ferromagnet can be obtained from

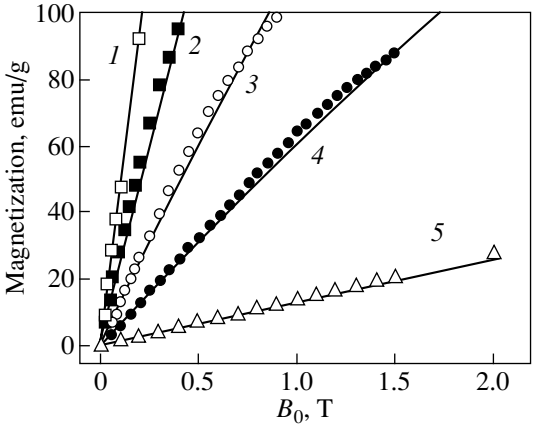

Fig. 1. Magnetization of the $LiTbF_4$ single crystal as a function of the external magnetic field strength ($\mathbf{M} \| \mathbf{B}_0 \| c$) at temperatures of (*1*) 2, (*2*) 5, (*3*) 10, (*4*) 20, and (*5*) 77 K. Symbols indicate the experimental data, and solid lines represent the results of calculations.

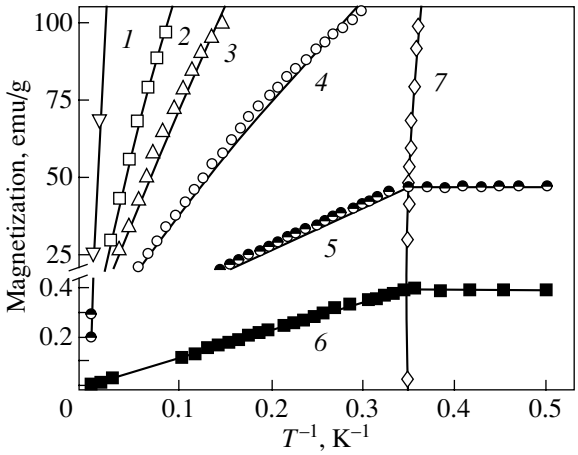

Fig. 2. Temperature dependences of the magnetization of the $LiTbF_4$ single crystal in the magnetic field $\mathbf{B}_0 \| c$. Magnetic field strength B_0: (*1*) 5, (*2*) 1, (*3*) 0.6, (*4*) 0.3, (*5*) 0.1, and (*6*) 0.0009 T. Symbols indicate the experimental data, and solid lines represent the results of calculations. (*7*) Spontaneous magnetization taken from [1].

significantly simpler measurements of the induced magnetization.

3.2. Parameters of the crystal field. For high temperatures (at which the populations of the excited Stark sublevels of the fundamental term $^7F_6$ for the Tb^{3+} ions should be taken into account) and strong magnetic fields with considerable mixing of the wave functions of the fundamental quasi-doublet and excited sublevels, the magnetization can be calculated as a function of the temperature and the local magnetic field $\mathbf{B}_{loc} = \mathbf{B}_0 + \mathbf{B}_M + \mathbf{B}_D$ in the framework of the single-ion approximation; that is,

$$\mathbf{M} = \frac{2g_L\mu_B}{v}\frac{\mathrm{Sp}[\mathbf{J}\exp(-H/k_BT)]}{\mathrm{Sp}[\exp(-H/k_BT)]}. \quad (6)$$

Here, H is the single-ion Hamiltonian operator involving the energy of the rare-earth ion in the crystal field and the energy of the Zeeman interaction:

$$H = H_{cf} + g_L\mu_B\mathbf{J}\mathbf{B}_{loc}. \quad (7)$$

The dependence of the magnetization on the external magnetic field $\mathbf{B}_0$ can be obtained from relationship (6) by comparing $\mathbf{M}(\mathbf{B}_{loc})$ and $\mathbf{B}_0 = \mathbf{B}_{loc} - (\lambda - D)\mathbf{M}(\mathbf{B}_{loc})$.

It should be noted that there is a wide scatter of the data available in the literature on the crystal field parameters for terbium ions in isostructural crystals $LiTbF_4$ [3, 11, 19] and $LiYF_4 : Tb^{3+}$ (Tb^{3+} ions substitute for Y^{3+} ions) [20]. Since the form of Hamiltonian (1) remains unchanged upon an arbitrary rotation of the coordinate system about the [001] quantization axis and, in particular, the x and y axes can be chosen in the basal plane of the crystal lattice in such a way that one of the four parameters B_4^{+4}, B_4^{-4}, B_6^{+4}, and B_6^{-4} becomes zero, information regarding the g factors and relative energies of the sublevels of the fundamental term of the paramagnetic ion, which is derived from investigations into the linear magnetic susceptibility and optical spectra, makes it possible to determine only six of the seven parameters B_p^k involved in the Hamiltonian operator (1). With the aim of determining the parameters of the crystal field in $LiRF_4$ crystals (R = Tb, Dy, Ho, Er, and Yb), Nevald and Hansen [19] studied the nonlinear magnetic susceptibility anisotropy in the basal plane of the crystal system and analyzed the results of magnetic measurements in terms of the single-ion Hamiltonian (7). However, the magnetic anisotropy of concentrated rare-earth paramagnets at low temperatures is characterized by a substantial contribution of the magnetoelastic interaction. Therefore, in the general case, the Hamiltonian operator (7) should contain terms accounting for the interaction between the rare-earth ion and the lattice strain induced by the magnetic field.

In $LiTbF_4$ crystals, the magnetoelastic interaction is suppressed by virtue of the large difference between the energy of the ground state (quasi-doublet) and the energy of the nearest neighbor excited states [11]; for the same reason, the van Vleck paramagnetic susceptibility in the ground state is small and its anisotropy in the basal plane is virtually absent. Nonetheless, the transverse magnetization can change significantly with an increase in the temperature and upon filling of excited non-Kramers doublet states, which are characterized by a considerable mixing with closely spaced singlet states in the magnetic field $\mathbf{B}_0 \perp c$. Figure 3 presents the results of our measurements of the transverse magnetization of the $LiTbF_4$ single crystal over a wide temperature range in magnetic fields with inductions of 1, 3, and 5 T. Owing to the very large difference (up to two orders of magnitude in a magnetic field with an induction of 1 T) between the longitudinal and transverse magnetic susceptibilities of the terbium ions, even an insignificant deviation of the sense of the external magnetic field from the basal plane may introduce large errors into the results of the magnetic measurements. We compared the results of magnetic measurements at different senses of the external magnetic field with respect to the symmetry axis of the crystal lattice and estimated the error $\delta\varphi < 0.8°$ in the orientation of the magnetic field with respect to the (x, y) plane in the experiments, the results of which are presented in Fig. 3. An insignificant increase in the magnetization with an increase in temperature from 3 to 20 K is caused by a decrease in the contribution from the longitudinal component of the magnetic moment of the terbium ions (cf. Fig. 2). With a further increase in temperature, the transverse magnetization increases substantially and reaches a maximum at a temperature of 80–90 K. The magnetization $\mathbf{M} \parallel \mathbf{B}_0 \perp c$ was calculated according to relationships (6) and (7). The results of

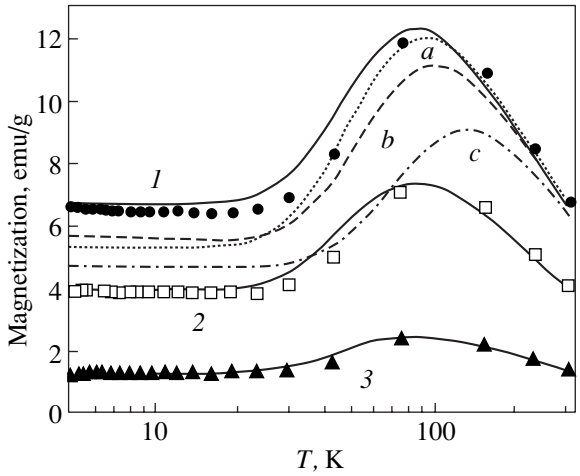

Fig. 3. Temperature dependences of the magnetization of the $LiTbF_4$ single crystal in the magnetic field $\mathbf{B}_0 \perp c$. Magnetic field strength B_0: (*1*) 5, (*2*) 3, and (*3*) 1 T. Symbols indicate the experimental data. Theoretical temperature dependences of the magnetization are calculated using the crystal field parameters obtained in this work (solid lines) and (at $B_0 = 5$ T) the parameters taken from (*a*) [20] (dotted line), (*b*) [3] (dashed line), and (*c*) [19] (dot-dashed line).

Crystal field parameters B_p^k (cm^{-1})

Parameter	Reference				
	[20] ($LiYF_4 : Tb^{3+}$)	[19]	[3]	[11]	This work
B_2^0	200	227.5	237	237	236
B_4^0	–100	–121.2	–54.1	–54.1	–58
B_6^0	–3.56	–30.3	4	4	–5
B_4^4	–1103	–946.5	–854.2	–854.2	–854.2
B_4^{-4}	0	0	–739	–739	–739
B_6^4	–529	–84.5	–526	–477	–477
B_6^{-4}	0	±93.8	–335	–291	–291

these calculations are presented in Fig. 3. The nonmonotonic behavior of the temperature dependence of the transverse magnetization can be explained by the anomalously large field-induced magnetic moment at the lower sublevel of the non-Kramers doublet Γ_{34} (nearest to the ground state) with an energy of 108 cm^{-1}. Figure 4 shows the splitting of this doublet as a function of the magnetic field in comparison with the shifts in the energy sublevels of the fundamental quasi-doublet. As can be seen from Fig. 3, the results of magnetization calculations with the use of the data available in the literature on the crystal field parameters (see table) differ significantly from the results of magnetization measurements. The small correction to the crystal field parameters calculated in [11] within the model of exchange charges made it possible to describe adequately both the energy of Stark sublevels of the $^7F_6$ term (in particular, we calculated the splitting of the fundamental quasi-doublet $\delta = 1.09$ cm^{-1}, the splitting factor $g_\parallel = 17.90$, and the energy of the nearest neighbor doublet $\Delta = 106.6$ cm^{-1}) and the temperature and field dependences of the magnetization. The results of our calculations are shown by solid lines in Figs. 1–3.

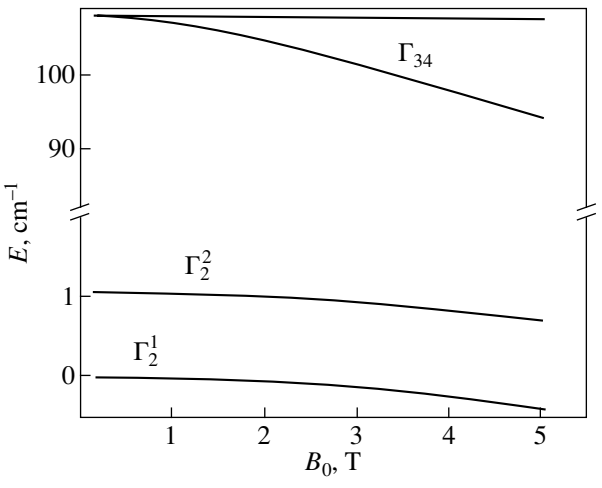

Fig. 4. Energy of the ground and nearest neighbor excited states of the Tb^{3+} ion as a function of the magnetic field strength ($\mathbf{B}_0 \perp c$).

In conclusion, we note that the results obtained in the present work can be useful in systematizing information on the exchange interaction and crystal field parameters for crystals of double rare-earth fluorides.

ACKNOWLEDGMENTS

We would like to thank S.L. Korableva and R.Yu. Abdulsabirov for growing the single crystals used in preparing the studied sample, V.A. Shustov and S.S. Tsarevskiĭ for the orientation of the sample used in our measurements, and D.A. Tayurskiĭ for his participation in discussions of the results and helpful remarks.

This work was supported by the Scientific and Educational Center of the Kazan State University (REC-007) and the Russian Foundation for Basic Research (project no. 99-02-17536).

REFERENCES

1. J. Als-Nielsen, L. M. Holmes, F. K. Larsen, and H. J. Giggenheim, Phys. Rev. B **12**, 191 (1975).
2. R. Frowein, J. Kotzler, B. Schaub, and H. Schuster, Phys. Rev. B **25**, 4905 (1982).
3. H. P. Christensen, Phys. Rev. B **17**, 4060 (1978).
4. G. Ahlers, A. Kornblit, and H. J. Guggenheim, Phys. Rev. Lett. **34**, 1227 (1975).

5. S. L. Korableva, A. K. Kupchenko, B. Z. Malkin, and A. I. Ryskin, Fiz. Tverd. Tela (Leningrad) **26**, 3700 (1984) [Sov. Phys. Solid State **26**, 2229 (1984)].
6. W. Dorfler, H. D. Hochheimer, and G. Schaack, Z. Phys. B **51**, 153 (1983).
7. W. Dorfler and G. Schaack, Z. Phys. B **59**, 283 (1985).
8. L. M. Holmes, J. Als-Nielsen, and H. J. Guggenheim, Phys. Rev. B **12**, 180 (1975).
9. L. M. Holmes, T. Johansson, and H. J. Geggenheim, Solid State Commun. **12**, 993 (1973).
10. J. Magarino, J. Tuchendler, P. Beauvillain, and I. Laursen, Phys. Rev. B **21**, 18 (1980).
11. V. I. Krotov, B. Z. Malkin, and A. A. Mittel'man, Fiz. Tverd. Tela (Leningrad) **24**, 542 (1982) [Sov. Phys. Solid State **24**, 305 (1982)].
12. J. A. Griffin and J. D. Litster, Phys. Rev. B **19**, 3676 (1979).
13. R. Frowein, J. Kotzler, and W. Assmus, Phys. Rev. Lett. **42**, 739 (1979).
14. P. Beauvillain, C. Chappert, and I. Laursen, J. Phys. C **13**, 1482 (1980).
15. K. Kjaer, J. Als-Nielsen, I. Laursen, and F. Krebs Larsen, J. Phys.: Condens. Matter **1**, 5743 (1989).
16. M. P. Davydova, S. B. Zdanovich, B. N. Kazakov, *et al.*, Opt. Spektrosk. **42**, 577 (1977) [Opt. Spectrosc. **42**, 327 (1977)].
17. L. K. Aminov, B. Z. Malkin, and M. A. Teplov, in *Handbook on the Physics and Chemistry of the Rare-Earths*, Ed. by K. A. Gschneidner and L. Eyring (North-Holland, Amsterdam, 1996), Vol. 22, p. 295.
18. S. A. Altshuler and B. M. Kozyrev, *Electron Paramagnetic Resonance in Compounds of Transition Elements* (Nauka, Moscow, 1972; Halsted, New York, 1975).
19. R. Nevald and P. E. Hansen, Physica B (Amsterdam) **86–88**, 1443 (1977).
20. G. K. Liu, J. Haung, R. L. Cone, and B. Jacquier, Phys. Rev. B **38**, 11061 (1988).

Translated by O. Borovik-Romanova

Physics of the Solid State, Vol. 44, No. 8, 2002, pp. 1550–1552. Translated from Fizika Tverdogo Tela, Vol. 44, No. 8, 2002, pp. 1480–1482.

PROCEEDINGS OF THE XI FEOFILOV WORKSHOP "SPECTROSCOPY OF CRYSTALS ACTIVATED BY RARE-EARTH AND TRANSITION-METAL IONS"

(Kazan, Tatarstan, Russia, September 24–28, 2001)

Isotropic and Anisotropic Exchange Interactions in the Orbitally Degenerate Excited ($^4A_2 \times {}^2T_2$) State of a Cr^{3+} Ion Pair Possessing D_{3h} Symmetry

V. V. Bannikov and V. Ya. Mitrofanov

Institute of Metallurgy, Ural Division of Russian Academy of Sciences, Yekaterinburg, 620016 Russia
e-mail: luda@imet.sco.ru

Abstract—Experimentally observed optical absorption spectra of isolated pairs of chromium ions in $Cs_3Cr_2Br_9$ corresponding to transitions of pairs from the ground ($^4A_2 \times {}^2A_2$) state to a singly excited ($^4A_2 \times {}^2T_2$) state are theoretically interpreted. It is shown that the position of the exchange multiplets in the excited ($^4A_2 \times {}^2T_2$) state is determined mainly by the resonance exchange interactions removing the degeneracy with respect to the exchange by an excitation within the pair. It is established that the observed fine structure of the pair in the ($^4A_2 \times {}^2T_2$) state is due to a superposition of the contributions from the one- and two-center spin–orbit interaction and resonance antisymmetric exchange. © *2002 MAIK "Nauka/Interperiodica".*

1. The $Cs_3Cr_2Br_9$ crystal (D_{6h}^4 symmetry group) is a concentrated two-nucleus system in which the chromium-ion dimers possess high local symmetry (D_{3h}) [1]. An investigation of the polarized absorption spectra in a wide interval of temperatures and magnetic fields [2] made it possible to reveal a great number of narrow lines in the range from 18500 to 19000 cm^{-1}. All the lines were identified and ascribed to the allowed zero-phonon electric-dipole transitions from the ground ($^4A_2 \times {}^2A_2$) state of the ion pair to a singly excited ($^4A_2 \times {}^2T_2$) state. The wavelengths of the identified lines and the energy-level diagram of the ion pair in the ($^4A_2 \times {}^2T_2$) state were also found in [2] (Table 1) by processing the experimental data.

This paper is devoted to investigation of the specific features of the exchange interactions in the excited ($^4A_2 \times {}^2T_2$) state of the Cr^{3+} ion pairs in $Cs_3Cr_2Br_9$. The positions and the fine structure of the exchange multiplets in the ($^4A_2 \times {}^2T_2$) state are calculated in the framework of the effective-Hamiltonian method. The parameters of the effective Hamiltonian are found by comparing the theoretically calculated and experimentally determined energy-level diagrams. The microscopic mechanisms responsible for the formation of the energy spectrum of the ion pair in the excited ($^4A_2 \times {}^2T_2$) state are established.

2. The ground state of a pair of Cr^{3+} ions ($^4A_2 \times {}^2A_2$) can be adequately described by the Heisenberg–Dirac–Van Vleck Hamiltonian

$$H = J_0(S_aS_b) + j(S_aS_b)^2, \qquad (1)$$

where the indices a and b refer to the ions and J_0 and j are the exchange parameters: $J_0 = 4.9 \pm 0.3$ cm^{-1} and $j = -0.21 \pm 0.06$ cm^{-1} [2].

The group-theoretical approach makes it possible to determine the allowed terms of the ion pair from the states of the isolated ions. This significantly simplifies calculation of the fine structure of the spectrum of the ($^2A_2 \times {}^2T_2$) state, whose degeneracy factor is 48. In this case, the set of the allowed multiplets of the pair is [3]

$$\begin{aligned} {}^4A_2 \times {}^2T_2 \longrightarrow {}& {}^3A_2' + {}^3A_1'' + {}^3E' + {}^3E'' \\ & + {}^5A_2' + {}^5A_1'' + {}^5E' + {}^5E'', \end{aligned} \qquad (2)$$

where $\Gamma = A_2'$, A_1'', E', E'' corresponds to irreducible representations of the D_{3h} group. Taking into account the spin–orbit and spin–spin interactions leads to additional splitting of the exchange multiplets in Eq. (2) (Table 1). When constructing the wave functions of the allowed terms of the ion pair and the effective Hamiltonian of one- and two-center interactions, it is very important to properly choose the local coordinate systems associated with individual ions and the pair coordinate system, which is necessary in writing out the spin-dependent pair interactions. We defined these systems of coordinates in the same way as was done for the first-order pair of Cr^{3+} ions in ruby [4].

3. The structure of the energy spectrum of the ion pair in the ($^4A_2 \times {}^2T_2$) state depends on the ratio between the energies of one-center (spin–orbit, trigonal field) and pair exchange interactions. In the case under consideration, the spin–orbit interaction and trigonal-field

Table 1. Fine-structure energy levels of the excited $({}^4A_2 \times {}^2T_2)$ states of a pair of chromium ions in $Cs_3Cr_2Br_9$

Term	Fine structure	Energy levels, cm^{-1}		Fine structure in terms of the effective Hamiltonian
		theory	experiment [2]	
${}^3A_2'$	$A_1'(0)$	18661	18661	$K_0 - 4D$
	$E''(\pm 1)$	18661		$K_0 + 2D$
${}^3A_1''$	$A_2''(0)$	18730	18730	$K_0 - 4D$
	$E'(\pm 1)$	18730		$K_0 + 2D$
${}^3E'$	$E''(\pm 1)$	18696	18696	$K_0 + \lambda + 2D$
	$E'(0)$	18699	18699	$K_0 - 4D$
	$A_1'' + A_2''(\pm 1)$	18701	18701	$K_0 + \lambda + 2D \pm 2\sqrt{6}\,\lvert B\rvert$
${}^3E''$	$E'(\pm 1)$	18768		$K_0 + \lambda + 2D$
	$E''(0)$	18787		$K_0 - 4D$
	$A_1' + A_2'(\pm 1)$	18802		$K_0 + \lambda + 2D \pm 2\sqrt{6}\,\lvert B\rvert$
${}^5A_2'$	$A_2'(0)$	18786	18786	$K_0 - 12D$
	$E'(\pm 2)$	18786	18786	$K_0 + 12D$
	$E''(\pm 1)$	18786		$K_0 - 6D$
${}^5A_2''$	$E'(\pm 1)$	18608	18608	$K_0 - 6D$
	$E''(\pm 2)$	18608	18608	$K_0 + 12D$
	$A_1''(0)$	18608		$K_0 - 12D$
${}^5E''$	$A_1'' + A_2''(\pm 2)$	18653		$K_0 + 2\lambda + 12D$
	$E'(\pm 1)$	18643	18645	$K_0 + \lambda - 6D$
	$E''(0)$	18635	18631	$K_0 - \lambda + ((12D - \lambda)^2 + 144B^2)^{1/2}$
	$E''(\pm 2)$	18621	18620	$K_0 - \lambda - ((12D - \lambda)^2 + 144B^2)^{1/2}$
	$A_1' + A_2'(\pm 1)$	18627	18630	$K_0 - \lambda - 6D \pm 6\sqrt{6}\,\lvert B\rvert$
${}^5E'$	$A_1' + A_2'(\pm 2)$	18878		$K_0 + 2\lambda + 12D$
	$E''(\pm 1)$	18892	18892	$K_0 + \lambda - 6D$
	$E'(0)$	18901	18901	$K_0 - \lambda - ((12D - \lambda)^2 + 144B^2)^{1/2}$
	$E'(\pm 2)$	18904	18904	$K_0 - \lambda + ((12D - \lambda)^2 + 144B^2)^{1/2}$
	$A_1'' + A_2''(\pm 1)$	18905	18905	$K_0 - \lambda - 6D \pm 6\sqrt{6}\,\lvert B\rvert$

in the ${}^2T_2(t_2^3)$ state do not appear in the first-order perturbational approximation. Therefore, the position of different multiplets ${}^{2S+1}\Gamma$ is determined mainly by the exchange interactions. The effective Hamiltonian can be represented in the form [3]

$$H = H_d + H_r,$$

$$H_d = K_1[X_{0a}(T_1) + X_{0b}(T_2)] + J_2(S_aS_b) + J_2[X_{0a}(T_2) + X_{0b}(B_2)](S_aS_b), \quad (3)$$

$$H_r = R_0\tau_{0a}(T_1)\tau_{0b}(T_1)(Q_aQ_b) + R_1\{\tau_{+a}(T_1)\tau_{-b}(T_1) + \tau_{-a}(T_1)\tau_{+b}(T_1)\}(Q_aQ_b).$$

Here, the Hamiltonian H_d describes the pair interaction in the case where the excitation is localized at one ion of the pair and the operator H_r is responsible for the exchange interactions removing the degeneracy with respect to the exchange by an excitation within the pair. The term with K_1 appears in the second-order approximation with respect to the trigonal field and spin-independent exchange interaction, and the term containing J_2 describes the orbital modification of the Hamiltonian. The matrices of the orbital operators τ_μ and $X_\mu(T_2)$ and of the spin operator Q were determined in [3].

The energy levels of the exchange multiplets in the $({}^4A_2 \times {}^2T_2)$ state are

$$E({}^{2S+1}\Gamma) = T_0 - K_1 + (J_1 + \eta J_2)\varphi(S) \pm R_i\nu(S), \quad (4)$$

Table 2. Parameters of the effective Hamiltonian (6) for different terms of the $({}^4A_2 \times {}^2T_2)$ state

Term	K_0, cm^{-1}	λ, cm^{-1}	D, cm^{-1}	B, cm^{-1}
${}^3A_2'$	18670			
${}^3A_1''$	18730			
${}^5A_2'$	18786			
${}^5A_1''$	18608			
${}^3E''$ (theory)	18786	–16.8	–0.27	0
${}^3E'$	18698	–2.5	–0.08	$\lvert B\rvert < 0.81$
${}^5E''$	18636	7.9	0.08	$\lvert B\rvert < 0.27$
${}^5E'$	18896	–6.5	–0.42	$\lvert B\rvert < 0.27$

where $\varphi(S) = [S(S+1) - 9/2]/2$ and $\nu(S) = S(S+1)/3$. Here, $\mu = -1$ and $R_i = R_1$ for $\Gamma = E', E''$and $\mu = 2$ and $R_i = R_0$ for $\Gamma = A_2', A_1''$.

The effective Hamiltonian describing the fine structure of the exchange multiplets can be written as

$$H_s = H_{ds} + H_{rs},$$

$$H_{ds} = \lambda_0[X_{0a}(T_1)S_{0a} + X_{0b}(T_1)S_{0b}] + \lambda_1[X_{0a}(T_1)S_{0b} + X_{0b}(T_1)S_{0a}] + (D + D_e[X_{0a}(T_2) + X_{0b}(T_2)])[S_aS_b]_0^{(2)}, \quad (5)$$

$$H_{rs} = D_1\{\tau_{+a}(T_1)\tau_{-b}(T_1) - \tau_{-a}(T_1)\tau_{+b}(T_1)\}[Q_aQ_b]_0^{(1)} + D_2\tau_{0a}(T_1)\tau_{0b}(T_1)[Q_aQ_b]_0^{(2)} + D_3\{\tau_{+a}(T_1)\tau_{-b}(T_1) + \tau_{-a}(T_1)\tau_{+b}(T_1)\}[Q_aQ_b]_0^{(2)}.$$

Along with the usual terms, the Hamiltonian H_s includes a number of new terms describing the spin–other-ion orbit (λ_1) and resonance antisymmetric exchange (D_1) interactions. At the first step, it is desirable to calculate the fine structure of the exchange multiplets by using the effective Hamiltonian in the total-pair-spin representation [3]:

$$H_{\text{eff}}({}^{2S+1}\Gamma_1) = K_0 + D_0S_0^{(2)},$$
$$H_{\text{eff}}({}^{2S+1}\Gamma_2) = K_0 + \lambda X(A_2)S_0^{(1)} + D_0S_0^{(2)} + B[X_{-}(E)S_{-2}^{(2)} - X_{+}(E)S_{+2}^{(2)}], \quad (6)$$

where $\Gamma_1 = A_2', A_1''$ and $\Gamma_2 = E', E''$. In the effective Hamiltonian (6), the constants corresponding to different terms do not necessarily coincide. In particular, for the parameters λ, we have

$$\lambda({}^3E'') = -\frac{1}{4\sqrt{2}}D_1 - \frac{(\lambda_0 + 5\lambda)}{4\sqrt{3}},$$
$$\lambda({}^3E') = +\frac{1}{4\sqrt{2}}D_1 - \frac{(\lambda_0 + 5\lambda)}{4\sqrt{3}},$$
$$\lambda({}^5E'') = +\frac{1}{4\sqrt{2}}D_1 + \frac{(\lambda_0 + 3\lambda)}{4\sqrt{5}}, \quad (7)$$
$$\lambda({}^5E') = -\frac{1}{4\sqrt{2}}D_1 + \frac{(\lambda_0 + 3\lambda)}{4\sqrt{5}}.$$

Agreement between the theoretically calculated energy-level diagrams and the energy diagrams experimentally found in [2] is achieved for the following values of the constants in Eq. (3):

$$|R_0| = 44.5 \text{ cm}^{-1}, \quad |R_1| = 65 \text{ cm}^{-1},$$
$$J_1 = 7.67 \text{ cm}^{-1}, \quad J_2 = -4.66 \text{ cm}^{-1},$$
$$K_1 = -19.5 \text{ cm}^{-1}.$$

The values of the constants involved in the effective Hamiltonian (6) and describing the fine structure of the multiplets of the $({}^4A_2 \times {}^2T_2)$ state are listed in Table 2.

It is seen that the parameters of the isotropic exchange in the ground and excited states are of the same sign and are comparable in magnitude. In this case, the resonance exchange interaction makes a dominant contribution to the formation of the energy spectrum of the pair. The relatively large value of the constant K_1 is due to the second-order contribution from the trigonal field V_{tr}: $K_1 \sim -V_{\text{tr}}^2/\Delta$, where $\Delta \sim 500$ cm^{-1} is the distance to the lowest excited state of $({}^4A_2 \times {}^2A_1)$.

The fine structure of the spectrum of the ion pair is determined mainly by the spin–orbit interactions and resonant antisymmetric exchange: $\lambda_0 = 28.9$ cm^{-1}, $\lambda = -7.6$ cm^{-1}, and $D_1 = 40.5$ cm^{-1}. The relatively large values of the constants in the effective Hamiltonian (6) and Eq. (7) are probably due to the uncertainty in the experimentally measured positions of the spectral lines.

ACKNOWLEDGMENTS

This work was supported by the Russian Foundation for Basic Research, project no. 00-03-32335.

REFERENCES

1. A. Ferrigato, K. J. Maxwell, and J. R. Owers-Bradley, J. Phys. Chem. Solids **51**, 157 (1990).
2. K. J. Maxwell and R. J. Turner, J. Phys. Chem. Solids **52**, 691 (1991).
3. V. Ya. Mitrofanov, A. E. Nikiforov, and V. I. Cherepanov, *Spectroscopy of Exchange-Bonded Complexes in Ionic Crystals* (Nauka, Moscow, 1985).
4. M. Naito, J. Phys. Soc. Jpn. **34**, 1491 (1973).

Translated by A. Poushnov

Physics of the Solid State, Vol. 44, No. 8, 2002, pp. 1553–1557. Translated from Fizika Tverdogo Tela, Vol. 44, No. 8, 2002, pp. 1483–1486.

PROCEEDINGS OF THE XI FEOFILOV WORKSHOP "SPECTROSCOPY OF CRYSTALS ACTIVATED BY RARE-EARTH AND TRANSITION-METAL IONS"

(Kazan, Tatarstan, Russia, September 24–28, 2001)

Local Structure of Titanium Pair Centers in SrF_2 Crystals: EPR and ENDOR Spectroscopic Studies

I. I. Fazlizhanov, V. A. Ulanov, M. M. Zaripov, and R. M. Eremina

Kazan Physicotechnical Institute, Russian Academy of Sciences, Sibirskiĭ trakt 10/7, Kazan 29, 420029 Tatarstan, Russia
e-mail: ulanov@dionis.kfti.kcn.ru

Abstract—The local structure of titanium pair centers in SrF_2 : Ti crystals is investigated using electron paramagnetic resonance (EPR) and electron–nuclear double resonance (ENDOR) spectroscopy. It is found that titanium pair centers with spin moment $S = 2$ and tetragonal symmetry of the magnetic properties are formed in SrF_2 : Ti cubic crystals under certain growth conditions and during annealing. The tensor components of the fine and ligand hyperfine structures in the EPR and ENDOR spectra are determined. A model of the Ti^+–Ti^{3+} paramagnetic dimer is proposed. This model provides an adequate interpretation of both the ferromagnetic nature of the exchange interaction and the observed displacements of four ligands in the first coordination sphere of titanium impurity ions in directions perpendicular to the impurity ion–ligand bonds. © *2002 MAIK "Nauka/Interperiodica".*

1. INTRODUCTION

Earlier, we investigated the conditions of the formation of different-type centers of transition metal impurity ions in crystals of the fluorite structural type (see, for example, [1, 2]) and demonstrated that crystals grown from a melt under certain conditions contain single-type stable clusters whose composition involves two or more impurity ions. It has been found that the formation of a cluster in the bulk of a growing crystal occurs through diffusion in the bulk of the already formed crystal lattice rather than through crystallization of a molecular cluster formed in the melt in the immediate vicinity of the crystallization front. This inference is confirmed by the results of electron paramagnetic resonance (EPR) investigations, according to which the concentration of clusters (dimers, trimers, etc.) formed upon annealing of a crystal activated by paramagnetic impurities increases at the expense of a decrease in the concentration of single impurity centers. We believe that the possibility of the solid-phase synthesis of stable impurity polymers proceeding in crystals of the fluorite structural type is determined by their physicochemical properties. As is known, these crystals belong to a large group of ionic compounds with the so-called superionic conductivity [3]. The effect of superionic conductivity resides in the fact that, at high temperatures (close to the melting temperature T_{melt}), the amplitude of lattice vibrations becomes large to such an extent that intensive processes of partially correlated ionic diffusion occur in the crystal. In this case, F^- lattice anions possess the highest mobility. It is evident that, under these diffusion conditions, stable impurity polymers can be formed only in the case when the lattice energy decreases as a result of coalescence of single impurity centers. It is this energy gain that determines the conditions of the formation of impurity clusters and their stability.

It is quite reasonable that the crystal lattice in the vicinity of an impurity polymer is distorted to such a degree that the lattice atoms nearest to the impurity ions will be displaced from positions corresponding to the impurity-free crystal. To the best of our knowledge, in all cases, the directions of these displacements are approximately collinear with respect to the directions of bonds between the impurity cations and the nearest neighbor anions. The novelty of the results obtained in the present work is as follows: in titanium impurity dimers, which we synthesized in SrF_2 : Ti cubic crystals under conditions providing impurity ion diffusion in the solid phase, four F^- anions involved in the first coordination sphere of one of the titanium impurity ions are displaced in the direction perpendicular to the impurity ion–ligand bonds. Prior to the above displacements, these four fluorine ions occupy vertices of a square fragment of one of the networks comprising the anionic sublattice whose plane is perpendicular to the axis of the impurity dimer. After synchronous displacements, the same four F^- fluorine ions occupy vertices of another square fragment that is rotated with respect to the initial square through 45°. This paper reports on the experimental results underlying the proposed interpretation of the unusual character of the lattice deformation observed in a SrF_2 : Ti crystal in the vicinity of a pair of titanium impurity ions.

1063-7834/02/4408-1553$22.00 © 2002 MAIK "Nauka/Interperiodica"

2. SAMPLE PREPARATION AND EXPERIMENTAL TECHNIQUE

Crystals of SrF_2 : Ti were grown by the Czochralski method in a helium atmosphere with small fluorine additives. The crucible used was produced from chemically pure graphite. Titanium impurities in the form of TiF_4 were introduced into the melt. Fluorine was added to the helium atmosphere used in the crystal growth for the purpose of preparing a melt of nonstoichiometric composition with an excess content of fluorine ions. This encouraged an increase in the equilibrium concentration of titanium ions dissolved in the melt. It turned out that the presence of excess fluorine ions in the melt is the necessary condition for the incorporation of titanium into the lattice of the growing crystal.

The grown crystals were examined by EPR spectroscopy. It was found that, depending on the growth conditions, the grown crystals contained either predominantly cubic centers of bivalent titanium (the temperature gradient in the vicinity of the crystallization front satisfied the condition $(dT/dz) \geq 50$ deg/cm, and the velocity of the crystallization dz/dt front was approximately equal to 20 mm/h) [4] or titanium centers of tetragonal symmetry with spin moment $S = 2$ ($(dT/dz) \leq 5$ deg/cm and $(dz/dt) \approx 20$ mm/h). The latter titanium centers were described for the first time in [5].

The electron paramagnetic resonance measurements were carried out on an E-12 Varian EPR spectrometer at temperatures of 4.2 and 77 K and at frequencies of 9.3 and 37 GHz. The angular dependence of the measured EPR spectra of titanium pair centers is typical of tetragonal paramagnetic centers with spin moment $S = 2$ and coincides with that obtained earlier in [5]. At a temperature of 4.2 K, the line width in the EPR spectrum is approximately equal to 15 Oe. At 77 K, the EPR lines in the spectrum are slightly broadened and the distances between the components of the fine structure decrease by approximately 10%.

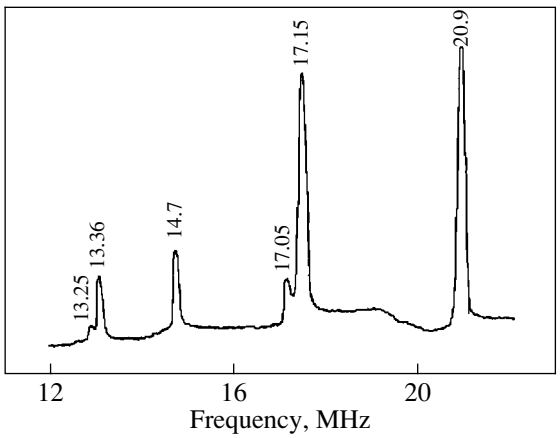

Fig. 1. ENDOR spectrum of a paramagnetic center formed by a pair of titanium ions in the SrF_2 crystal. The external magnetic field is aligned parallel to the C_4 crystallographic axis.

The electron–nuclear double resonance (ENDOR) investigations were performed at an electron paramagnetic resonance frequency of 9.3 GHz and at a temperature of 4.2 K. The ENDOR measurements were carried out on the same spectrometer equipped with a special nuclear pumping oscillator operating in the frequency range 1–100 MHz. The maximum input power of the pumping oscillator was 100 W.

The angular dependences of the ENDOR frequencies of titanium pair centers were measured in two crystallographic planes, namely, the (110) and (001) planes. The ENDOR spectra of titanium dimers were recorded for electronic states in which the electron spin had the following projections: $M_S = -2, -1, 1$, and 2.

3. EXPERIMENTAL RESULTS

Figure 1 shows the ENDOR spectrum for an electron transition ($|-2\rangle \longleftrightarrow |-1\rangle$) in one of the orientations of the SrF_2 : Ti sample with respect to the external magnetic field $\mathbf{B}_0$ ($\langle 001\rangle \parallel \mathbf{B}_0$). As can be seen from Fig. 1, the low-frequency portion of the ENDOR spectrum is similar to the high-frequency portion. This implies that the ENDOR transitions between nuclear sublevels of both electronic states, $|-2\rangle$ (the high-frequency portion of the spectrum) and $|-1\rangle$ (the low-frequency portion), occur simultaneously. The angular dependences of the ENDOR frequencies measured upon rotation of the stationary external magnetic field vector $\mathbf{B}_0$ in two crystallographic planes, namely, (001) and (110), are depicted in Figs. 2a and 2b, respectively. It is seen that from Fig. 2a that, for the sample orientation $\langle 001\rangle \parallel \mathbf{B}_0$, four ENDOR lines intersect at a point corresponding to $\nu = 20.9$ MHz and $\phi = 0°$ and eight ENDOR lines meet at $\nu = 17.15$ MHz and $\phi = 0°$. This indicates that the ENDOR spectrum is characterized by three groups of ^{19}F nuclei ($I = 1/2$). In the spectrum shown in Fig. 1, the ENDOR lines observed at frequencies of 20.9 and 14.7 MHz correspond to one of these three groups of ^{19}F nuclei that consist of four equivalent ligands, the lines at frequencies of 17.15 and 13.36 MHz are attributed to the second group composed of eight ligands, and the lines at frequencies of 17.05 and 13.25 MHz are assigned to the third group. The ENDOR lines that correspond to the third group of ligands exhibit a low intensity. For this reason, our attempts to determine the number of F^- anions in this group and their arrangement with respect to the titanium impurity cations were unsuccessful. As regards the first and second groups of ligands [Fig. 3, F(I) and F(II), respectively], we determined the parameters of the tensor components for the ligand hyperfine interaction. With knowledge of the parameters of the ligand hyperfine interaction tensors (see below) and the number of ENDOR lines, it is possible to determine the arrangement of these ligands

with respect to the titanium impurity ions and the number of ligands in the particular group, respectively. Apparently, the second group of ligands is formed by fluorine anions that are involved in the second coordination sphere of the anionic environment of one of the titanium impurity ions and belong to one of the anionic networks of the crystal lattice whose plane is perpendicular to the axis of the impurity dimer. Note that four ligands of the first group are involved in the first coordination sphere of this titanium ion. The plane passing through these ligands is also perpendicular to the dimer axis. However, the surprising thing is that the directions toward these four ligands do not coincide with those observed for the undistorted crystal lattice. Analysis of the angular dependences displayed in Figs. 2a and 2b indicates that these directions are rotated through 45° about the dimer axis.

Unfortunately, we cannot cite decisive evidence that ligands of the first and second groups belong to the same anionic network (this situation is illustrated in Fig. 3). However, our tentative calculations of the ligand hyperfine interaction parameters and the components of the g tensor predicted precisely this mutual arrangement of ligands involved in the first and second groups. These calculations will be described in detail in a separate work.

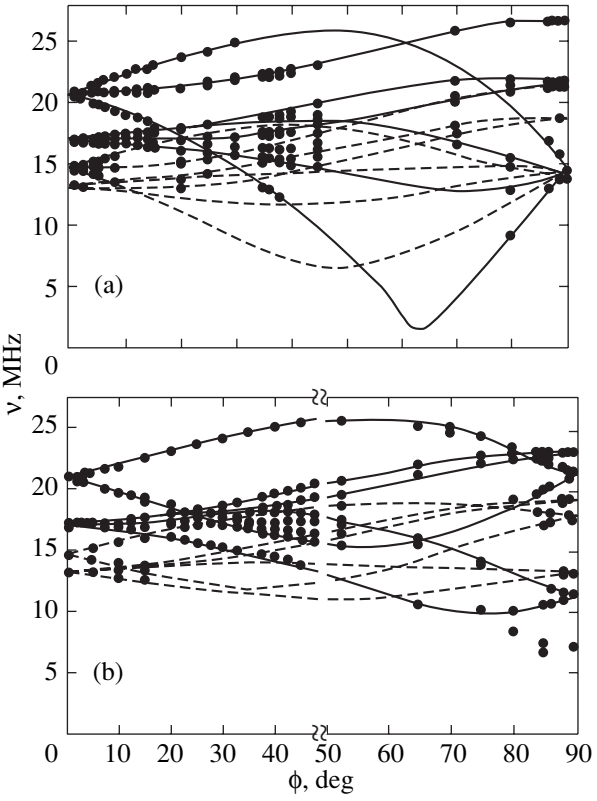

Fig. 2. Angular dependences of the ENDOR frequencies of a paramagnetic center formed by a pair of titanium ions in the SrF_2 crystal for electron spin projections $M_S = -2$ (solid lines) and $M_S = -1$ (dashed lines) and ϕ angles between the direction of the external magnetic field and the C_4 crystallographic axis in the planes (a) (001) and (b) (110).

4. THEORETICAL BACKGROUND

The spin Hamiltonian of an impurity dimer can be represented in the following form:

$$H = B_2^0 O_2^0 + g_\perp \beta (B_x S_x + B_y S_y)$$
$$+ g_\parallel \beta_e B_z S_z + \sum_i (S A_i I_i^F - g_N \beta_N B I_i^F),$$

where summation over i is performed over all ligands in the nearest environment of a given pair of titanium ions and A_i is the tensor of the ligand hyperfine interaction (for the other quantities, we used the universally accepted notation). From analyzing the angular dependence of the EPR spectra of titanium pair centers, we obtained the only nonzero component B_2^0 of the tensor of the fine structure in the EPR spectrum and the components $g_\parallel$ and $g_\perp$ of the g tensor: $B_2^0 = 356 \pm 16$ MHz, $g_\parallel = 1.883 \pm 0.005$, and $g_\perp = 1.975 \pm 0.005$.

For ligands of the first group, the ligand hyperfine interaction tensor can be represented in the coordinate system in which the Z axis is aligned parallel to the axis of the impurity dimer and the X axis is directed in such a way that the ligand under consideration is located in the XOZ coordinate plane. Reasoning from the symme-

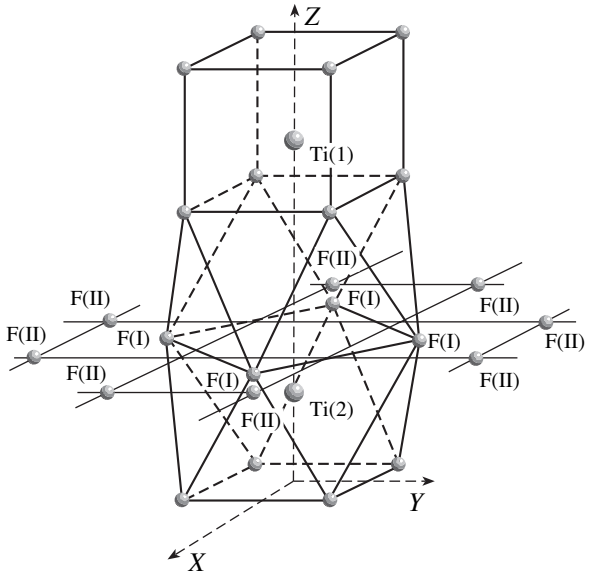

Fig. 3. Structure of the titanium impurity dimer in the SrF_2 crystal. Ligands of the first and second groups are designated as F(I) and F(II), respectively.

try of the impurity dimer, the ligand hyperfine interaction tensor for ligands of the first group in this system of the coordinates can be written in the form

$$A_1 = \begin{pmatrix} A_{xx} & 0 & A_{xz} \\ 0 & A_{yy} & 0 \\ A_{zx} & 0 & A_{zz} \end{pmatrix}.$$

Here, the experimental components obtained from analyzing the angular dependences of the ENDOR frequencies of titanium pair centers are given by

$$A_1 = \begin{pmatrix} 3.2 & 0 & -5.6 \\ 0 & -5.4 & 0 \\ -5.2 & 0 & -4.4 \end{pmatrix} \text{(in MHz)}.$$

The angular dependences of the ENDOR lines for eight fluorine anions involved in the second coordination sphere of the anionic environment of a titanium impurity cation are described by the axial tensor with the following parameters: $A_{\|} = 3.84$ MHz, $A_{\perp} = -4.08$ MHz, $\theta = 78.7°$, and $\phi = 28.1°$, where θ is the angle between the axis of the impurity dimer and the axis of the ligand hyperfine interaction tensor and φ is the angle between one of the $\langle 100 \rangle$ crystallographic axes lying in the plane perpendicular to the dimer axis and the projection of the axis of the ligand hyperfine interaction tensor onto the same perpendicular plane. Judging from the angles θ and φ, eight ligands of the second group belong to the second coordination sphere of the anionic environment of a pair of titanium impurity cations.

The angular dependences of the ENDOR frequencies calculated using the aforementioned components of the ligand hyperfine interaction tensor for the electronic states $|-2\rangle$ (solid lines) and $|-1\rangle$ (dashed lines) in the (001) and (110) planes are depicted in Figs. 2a and 2b, respectively. The calculated angular dependences shown in Fig. 2b have discontinuities, because the EPR frequencies in two portions of the corresponding angular dependences slightly differ from each other.

5. DISCUSSION

The basic experimental results obtained in the present work are as follows: (1) the total spin moment S of the titanium impurity center under investigation is equal to 2; (2) the intensity of the EPR spectra of the studied center in SrF_2 : Ti samples subjected to special annealing increases, whereas the intensity of the EPR spectra of titanium single cubic centers decreases; and (3) one of the groups of four fluorine anions involved in the nearest environment of titanium impurity cations proves to be rotated through 45° about the dimer axis.

As was noted above, the spin moment S of the titanium impurity center under investigation is equal to 2. This suggests that the studied center is formed by at least two titanium ions and that the exchange interaction between these ions has a ferromagnetic character. It is quite possible that the impurity center is formed by a Ti^{2+}–Ti^{2+} pair. However, we believe that, in this case, the formation of a Ti^{+}–Ti^{3+} pair is more probable. This assumption is confirmed by the fact that the concentration of titanium pair centers in SrF_2 : Ti crystals exceeds the concentration of titanium single cubic centers. In actual fact, nonisovalent substitution for a lattice cation gives rise to an uncompensated electric charge in the neighborhood of the impurity ion in the crystal bulk. In the case under consideration, an effective negative charge should be induced in the bulk of the coordination cube of one titanium ion and an effective positive charge should arise in the bulk of the coordination cube of the other titanium ion of the dimer. The Coulomb interaction between these charges can result in a decrease in the lattice energy upon clustering of two titanium single centers.

In our opinion, the formation of a Ti^{2+}–Ti^{2+} pair with spin moment $S = 2$ is questionable because, in this case, the orbital functions of the valence electrons of two titanium ions are not orthogonal (the overlap integral of these functions is nonzero); consequently, the ferromagnetic exchange between the titanium ions is unlikely. Moreover, since Ti^{2+} single centers are characterized by cubic symmetry and a singlet ground orbital level [4], there is no reason for the fundamental transformation of the crystal lattice in the vicinity of an impurity pair of Ti^{2+} ions isovalently substituted for two neighboring Sr^{2+} cations of the lattice. It should also be noted that the model of a Ti^{2+}–Ti^{2+} pair fails to explain why the resonance transitions revealed from the ENDOR spectra occur only between the nuclear sublevels of the ligands of one of the titanium impurity ions [in our case, the Ti(2) ion in Fig. 3], whereas the resonance transitions between the sublevels of the ligands of the other titanium ion [in our case, the Ti(1) ion] either are not observed at all or are characterized by entirely different interaction parameters (when these transitions manifest themselves as a low-intensity line in the ENDOR spectrum shown Fig. 1).

It is evident that the observed rotation of a square fragment of one of the anionic networks of the crystal lattice (Fig. 3) should lead to a decrease in the energy of the titanium pair center involved. This is most easily understood if the total energy of a pair of impurity ions is represented as the sum of the energy components:

$$W = W_1 + W_2 + W_{12} + W_{\text{lat}},$$

where W_1 is the energy of electron–electron and electron–nuclear interactions in one of the titanium single centers forming the given pair, W_2 is the energy of electron–electron and electron–nuclear interactions in the other titanium single center involved in the given pair, W_{12} is the energy of interactions between these centers,

and W_{lat} is the energy of interaction between the crystal lattice and the cluster as a whole.

It is clear that the rotation of one of the groups of four fluorine anions involved in the nearest environment of a titanium impurity cation should lead to an increase in the energy W_{lat}. Consequently, the total decrease in the lattice energy can occur only through considerable changes in the energies W_1, W_2, and W_{12}. We assume that the above rotation is associated with the mutual adjustment of the orbital motion of electrons in the outer shells of two titanium impurity ions and the nuclear configuration of the studied cluster. As a result of this adjustment, an increase in the energy W_{lat} is completely compensated for by a decrease in the energy W_{12}. In our opinion, the impurity pair can be formed by Ti^+ and Ti^{3+} ions whose ground orbital states are degenerate in the cubic crystal field. Therefore, the observed local static distortion of the crystal lattice can be explained by the static Jahn–Teller effect.

ACKNOWLEDGMENTS

This work was supported by the Russian Foundation for Basic Research, project no. 01-02-17718.

REFERENCES

1. M. M. Zaripov, M. V. Eremin, and V. A. Ulanov, in *Abstracts of XXIV Congress AMPERE on Magnetic Resonance and Related Phenomena, Kazan, 1994*, p. 424.
2. M. M. Zaripov, V. A. Ulanov, E. P. Zheglov, and G. N. Buchukuri, Fiz. Tverd. Tela (St. Petersburg) *36* (2), 411 (1994) [Phys. Solid State **36**, 224 (1994)].
3. J. B. Boyce and B. A. Huberman, Phys. Rep. **51** (4), 189 (1979).
4. N. V. Yunusov and V. P. Zentsov, Phys. Status Solidi B **88**, 87 (1978).
5. M. M. Zaripov, V. S. Kropotov, L. D. Livanova, and V. G. Stepanov, Fiz. Tverd. Tela (Leningrad) **10**, 3438 (1968) [Sov. Phys. Solid State *10*, 2722 (1968)].

Translated by O. Borovik-Romanova

Physics of the Solid State, Vol. 44, No. 8, 2002, pp. 1558–1563. Translated from Fizika Tverdogo Tela, Vol. 44, No. 8, 2002, pp. 1487–1491.

PROCEEDINGS OF THE XI FEOFILOV WORKSHOP "SPECTROSCOPY OF CRYSTALS ACTIVATED BY RARE-EARTH AND TRANSITION-METAL IONS"

(Kazan, Tatarstan, Russia, September 24–28, 2001)

Luminescence of Tl^+ Ions in a $KZnF_3$ Crystal

L. K. Aminov, S. I. Nikitin, N. I. Silkin, and R. V. Yusupov

Kazan State University, Kremlevskaya ul. 18, Kazan, 420008 Tatarstan, Russia

e-mail: Nikolai.Silkin@ksu.ru

Abstract—The luminescence spectra of a $KZnF_3 : Tl^+$ crystal are investigated in the energy range from 4.75 to 5.9 eV at temperatures of 10–300 K upon excitation into the *A* absorption band (5.7–6.3 eV). At $T = 300$ K, the luminescence spectra exhibit an intense band with a maximum at 5.45 eV, which is attributed to single Tl^+ ions substituted for K^+ ions. The 5.723-eV intense narrow band observed at $T < 20$ K is assigned to the ${}^3\Gamma_{1u}$–${}^1\Gamma_{1g}$ zero-phonon transition, which is weakly allowed by the hyperfine interaction. The luminescence decay is studied as a function of temperature. The main characteristics of the luminescence spectra are adequately described in terms of the semiclassical theory based on the Franck–Condon principle and the Jahn–Teller effect for an excited *sp* configuration of the Tl^+ ion with the use of the parameters obtained earlier from analyzing the absorption spectra of the system under investigation. © *2002 MAIK "Nauka/Interperiodica".*

1. INTRODUCTION

Fluoride crystals with a perovskite structure that are activated by transition metal ions are very promising for use in near-IR tunable solid-state lasers [1–3]. A few years ago, Furetta *et al.* [4] demonstrated that $KMgF_3 : Tl^+$ crystals are good scintillators. Owing to the broad transparent region, fluoride crystals activated by rare-earth ions (for example, $LiCaAlF_6 : Ce^{3+}$ crystals) can be used as active media in UV tunable lasers [5]. In particular, Pazzi *et al.* [6] studied CsI : In(Tl) crystals and obtained considerable amplification in the visible and UV ranges. In this respect, investigation of fluoride crystals activated by mercury-type ions for the purpose of producing materials promising for use in ultraviolet lasers is an urgent problem.

The first investigations into the absorption and photoluminescence spectra of $KMgF_3 : Tl^+$ crystals [7–9] revealed the similarity of this system to the previously studied alkali halide crystals containing mercury-type ns^2 ion impurities. Beginning in the 1930s, the latter crystals were thoroughly explored experimentally and theoretically. The results obtained in these investigations were summarized in a number of reviews (see, for example, [10, 11]). On this basis, theoretical treatment of the optical spectra of the systems involved can be performed using well-developed methods. For example, in our recent work [12], we simulated the shape of *A* absorption bands of Tl^+ ions in $KZnF_3$ and $KMgF_3$ crystals in the temperature range 10–300 K and achieved reasonable agreement between the calculated and experimental data.

In the present work, we investigated the luminescence of Tl^+ ions in a $KZnF_3$ crystal.

2. EXPERIMENTAL TECHNIQUE

Crystals of $KZnF_3$ activated by Tl^+ ions were grown by the Bridgman–Stockbarger method according to the procedure described earlier in [12]. The content of Tl^+ ions in the melt was equal to 0.5 wt %.

The luminescence and luminescence excitation spectra were measured upon excitation by a DKsÉl-1000 xenon lamp with the use of MDR-6 (in an excitation channel) and MDR-23 (in a recording channel) monochromators. The measured spectra were not corrected for spectral response. The luminescence decay was studied upon excitation with a DKSSh-150 lamp operating in a pulse mode (the pulse duration was ~30 ns). The luminescence was recorded using a FÉU-106 photomultiplier operating in a photon counting mode (the dead time of the recording system was 0.2 μs). The luminescence measurements in the temperature range 4.2–300 K were carried out using a CF-1204 cryostat (Oxford Instruments).

3. RESULTS

At $T = 300$ K, the luminescence spectrum measured upon excitation into the *A* absorption band of the $KZnF_3 : Tl^+$ crystal (Fig. 1, curve *a)* contains an intense band with a maximum at 5.45 eV (Fig. 1, curve *b*). The excitation spectrum of this luminescence band virtually coincides with the spectrum of the *A* absorption band. This allows us to make the inference that the lumines-

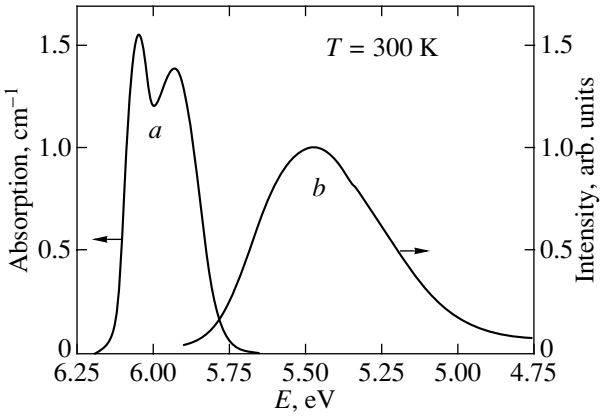

Fig. 1. (*a*) Absorption and (*b*) luminescence spectra of the $KZnF_3 : Tl^+$ crystal at $T = 300$ K.

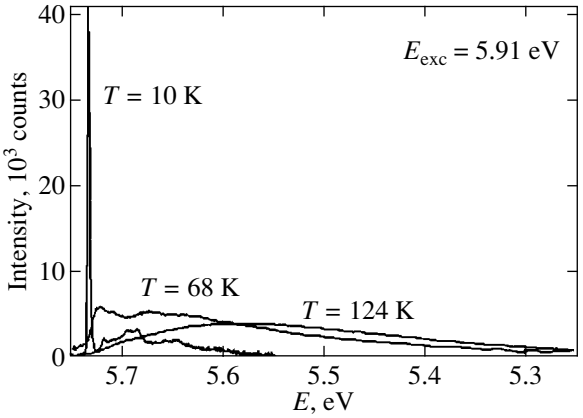

Fig. 2. Luminescence spectra of the $KZnF_3 : Tl^+$ crystal at temperatures of 10, 68, and 124 K.

cence band with a maximum at 5.45 eV is attributed to single Tl^+ ions.

At $T = 10$ K, the luminescence spectrum exhibits an intense zero-phonon line at an energy of 5.723 eV (Fig. 2). Analysis of the vibrational structure made it possible to distinguish vibrations with frequencies of 115 and 300 cm^{-1}. These values are in good agreement with the effective phonon frequencies of the ground-state modes Γ_5 and Γ_3, which we used earlier in [12] to simulate the absorption spectrum of the $KZnF_3 : Tl^+$ crystal.

In order to determine the energy spectrum of the excited state of Tl^+ ions in the studied crystal, we measured the luminescence decay. It was found that the luminescence involves two components, namely, fast and slow components, which are characteristic of mercury-type ions [11]. The temperature dependence of the lifetime of the slow component $\tau_s(T)$ is displayed in Fig. 3. As will be shown in Section 4, this dependence can be treated in the framework of the standard three-level model [11], which is schematically depicted in Fig. 3. For the given system of energy levels, the luminescence can be caused by transitions from level 2 immediately after excitation (the fast component) and transitions from states 2 and 1 after their thermalization (the slow component). The contributions of the transitions from these states to the stationary luminescence spectra depend on the transition probabilities k_1, k_2, k_{12}, and k_{21} and on the energy gap ΔE between these states (Fig. 3). Here, k_1 and k_2 are the rates of radiative transitions from states 1 and 2 to the ground state and k_{21} and k_{12} are the rates of nonradiative transitions between levels 1 and 2.

Under the commonly satisfied conditions $k_1 \ll k_2 \ll k_{21}$ [11], the temperature dependence of the lifetime of the slow component τ_s can be represented by the expression

$$\frac{1}{\tau_s} = \frac{k_1 + gk_2\exp(-\Delta E/kT)}{1 + g\exp(-\Delta E/kT)}, \qquad (1)$$

where g is the degeneracy ratio of the relaxed excited states 2 and 1 [in our case, $g = 2$ (see below)] and ΔE is the energy gap between these states. In the low-temperature range (of the order of 10 K), the lifetime of the slow luminescence component is determined only by the probability k_1, which, for the $KZnF_3 : Tl^+$ crystal, is equal to 85 s^{-1}. The fitting of the experimental data led to the following parameters: $k_2 = (7.1 \pm 0.1) \times 10^7$ s^{-1} and $\Delta E = 0.146 \pm 0.002$ eV. Let us now turn to the discussion of the results obtained.

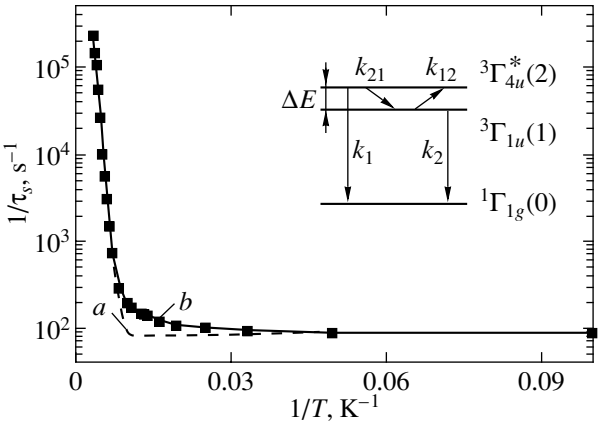

Fig. 3. Temperature dependence of the lifetime of the slow luminescence component for the $KZnF_3 : Tl^+$ crystal upon excitation into the *A* absorption band and the fit of this dependence according to (*a*) relationship (1) and (*b*) relationships (1) and (9). The inset shows the energy level diagram used in analyzing the experimental data.

4. DISCUSSION

The luminescence spectra, luminescence decay, and absorption spectra of impurity s^2 ions in crystal matrices can be satisfactorily described in terms of the semiclassical theory based on the Franck–Condon principle and the Jahn–Teller effect for an excited *sp* configuration [10, 11]. In many materials, including the system studied in the present work, impurity centers in the ground state have cubic symmetry. With due regard for the Coulomb interaction of electrons, the cubic crystal field, and spin–orbit interactions, 12 states of the excited *sp* configuration of the impurity center are distributed over four energy levels in order of increasing energy: $E_1({}^3\Gamma_{1u})$, $E_A({}^3\Gamma^*_{4u})$, $E_B({}^3\Gamma_{3u} + {}^3\Gamma_{5u})$, and $E_C({}^1\Gamma^*_{4u})$. Here, Γ_α are the indices of the irreducible representations of the octahedron group O_h according to which the states relating to the specified levels are transformed. The superscript on Γ_α indicates the multiplicity of the spin components of the electronic states. The states ${}^3\Gamma^*_{4u}$ and ${}^1\Gamma^*_{4u}$ are mixed through the spin–orbit interaction, which is designated by the asterisk.

Making allowance for the atomic displacements from equilibrium positions, we add the elastic energy H_L and the energy of vibronic interaction H_el to the electron energy of the impurity center. The energy of vibronic interaction H_el, as a rule, is treated in an approximation linear with respect to atomic displacements in the lattice and can be represented in the form

$$H_\mathrm{el}^{(1)} = \sum_{i=1\text{–}6} V_i Q_i. \tag{2}$$

Here, Q_i stands for interaction modes, i.e., the linear combinations of atomic displacements, which can transform upon rotation and reflection according to the irreducible representations of the symmetry group of the impurity center: $\Gamma_{1g}(Q_1)$, $\Gamma_{3g}(Q_2, Q_3)$, and $\Gamma_{5g}(Q_4, Q_5, Q_6)$. A rigorous treatment of only one excited *sp* configuration should include six interaction modes in the vibronic interaction $H_\mathrm{el}^{(1)}$. The vibronic interaction terms quadratic in the displacements Q_i can be taken into account without formal complication of the representation of the interaction Hamiltonian and the energy matrix. The matrix form $(H_\mathrm{el}^{(1)} + H_\mathrm{el}^{(2)})$ corrected for certain errors encountered in the literature in the representation of the matrix $H_\mathrm{el}^{(1)}$ was described in our previous work [12].

The elastic energy corresponding to the interaction modes in the ground state can be written as

$$H_L^{(g)} = \sum Q_i^2. \tag{3}$$

This expression implies the appropriate choice of the dimension of the coordinates Q_i and their scale which can differ for three types of mode (Γ_{1g}, Γ_{3g}, and Γ_{5g}), because the effective frequencies ω_i of these mode need not be identical. For the excited configuration, we obtain the relationship

$$\begin{aligned} H_L^{(\mathrm{exc})} &= a_1 Q_1^2 + a_2(Q_2^2 + Q_3^2) \\ &\quad + a_3(Q_4^2 + Q_5^2 + Q_6^2), \end{aligned} \tag{4}$$

in which the coefficients a_1, a_2, and a_3 account for the possible difference between the effective frequencies in the ground and excited configurations.

Upon inclusion of the energies $H_\mathrm{el}^{(1)}$ and $H_L^{(\mathrm{exc})}$, the excited levels E_A, E_B, and E_C are split and there arise 12 surfaces of the adiabatic potentials $E_n(Q_1, \ldots, Q_6)$. Minima of these potentials correspond to relaxed excited states into which the impurity centers excited by radiation are transformed after thermal relaxation from the ground state at relatively small Q_i; that is,

$$\langle Q_i^2 \rangle \approx kT_i^*/2 = (\hbar\omega_i/4)\coth(\hbar\omega_i/2kT). \tag{5}$$

As a rule, the luminescence is associated with the transitions from the relaxed excited states to the ground state. The appearance of several luminescence bands in the spectrum can be explained by the fact that, after excitation, the optical centers relax into states with different potential minima. For alkali halide crystals, one or two bands (A_T and A_X) are observed upon excitation into the A absorption band. The luminescence band A_T is assigned to impurity centers with tetragonal symmetry. The coexistence of minima of two types on the lower surfaces of the adiabatic potential, namely, $E_1(Q_1, \ldots, Q_6)$ and $E_A(Q_1, \ldots, Q_6)$, can be illustrated by considering the cross sections of these surfaces $E(Q_2, Q_3)$ when the other interaction modes Q_i are equal to zero [10, 11]. This treatment offers a satisfactory description of the experimental data provided the dominant contribution to the vibronic interaction is made by the coupling with the tetragonal modes Q_2 and Q_3 at the large parameter $b = \langle p_x|V_2|p_x\rangle$ (the excited molecular orbital p_x is similar to the atomic function $6p_x$).

Analysis of the absorption spectra of $KMgF_3 : Tl^+$ and $KZnF_3 : Tl^+$ crystals revealed that, in these systems, the interaction with the trigonal modes Q_4, Q_5, and Q_6 is predominant; i.e., $c^2 \gg b^2$, where $c = \langle p_y|V_4|p_z\rangle$ [8, 12]. Hence, as the basic approximation, it is reasonable to examine the minima of the functions $E(Q_4, Q_5, Q_6)$ and the system of equipotential surfaces $E(Q_4, Q_5, Q_6) = \mathrm{const}$. It should be noted that, if the functions $E(Q_2, Q_3) = \mathrm{const}$ on the (Q_2, Q_3) plane are characterized by the trigonal symmetry C_{3v}, the surfaces $E(Q_4, Q_5, Q_6) = \mathrm{const}$ in the (Q_4, Q_5, Q_6) three-dimensional space have the tetrahedral symmetry T_d: the points (Q_4, Q_5, Q_6) remain unchanged upon inversion in the real space; the fourfold rotations C_4 and S_4 in the Q space

are represented as the mirror rotation S_4 about the Q_4, Q_5, or Q_6 axes; etc.

We performed similar calculations for the $KZnF_3 : Tl^+$ system with the use of the parameters obtained in our earlier work [12] regarding the energy matrix of the excited *sp* configuration of the Tl^+ impurity center; more precisely, we used the mean energy positions of the absorption bands: $E_A = 6.03$ eV, $E_B = 7.2$ eV, and $E_C = 8.14$ eV. Moreover, the unperturbed energy of the lower level of this configuration was taken to be $E_1({}^3\Gamma_{1u}) = 5.72$ eV, which approximately coincides with the energy location of the zero-phonon line. In these calculations, we used the following parameters of the vibronic interaction (eV):

$$b^2 = 0.49, \quad b'^2 = 0.25, \quad c^2 = 1.69, \quad c'^2 = 1.$$

In the case when we restricted our consideration to the trigonal distortions Q_4, Q_5, and Q_6 of the impurity center, the parameters *b* and *b*' were not included in the calculation. The parameter $R = \mu^2/\nu^2$, which determines the degree of mixing of the states due to the spin–orbit interaction, was assumed to be equal to 7. The elastic constants a_i in relationship (4) were taken equal to unity.

Now, we consider the results of our calculations of the energy levels E_n for the *sp* configuration of the Tl^+ impurity center as functions of the displacements Q_4, Q_5, and Q_6 of this center from an equilibrium cubic position. It is assumed that the displacements Q_4, Q_5, and Q_6 satisfy the relationships $Q_4 = mQ$, $Q_5 = nQ$, and $Q_6 = kQ$ with $Q^2 = Q_4^2 + Q_5^2 + Q_6^2$; in this case, the coefficients *m*, *n*, and *k* are the direction cosines in the (Q_4, Q_5, Q_6) space.

Figure 4 displays the energies of the triplet ${}^3\Gamma_{4u}^*$ and the singlet ${}^3\Gamma_{1u}$ as functions of the trigonal distortion *Q* specified by the direction at $m = n = k$. The triplet ${}^3\Gamma_{4u}^*$ is split into a singlet and a doublet. The minimum energy of the doublet at $Q = -0.67$ approximately corresponds to the absolute minimum of the function $E_A(Q_1, \ldots, Q_6) \approx 5.88$ eV. The ground (optically inactive) state ${}^3\Gamma_{1u}$ of the *sp* configuration is characterized by a weakly pronounced minimum at the energy $E_1(Q = 0) = 5.72$ eV. At temperatures of ~100 K (0.01 eV), the distortion fluctuations responsible for the broadening of the line associated with the forbidden transition ${}^3\Gamma_{1u} \longrightarrow {}^1\Gamma_{1g}$ are estimated to be $\sqrt{\langle Q^2 \rangle} \approx 0.4$. Therefore, an approximate analysis of the luminescence can be performed on the basis of a three-level model (see Fig. 3) in which the second excited level is the trigonal doublet formed as a result of the splitting of the initial cubic triplet ${}^3\Gamma_{4u}^*$. The calculated spacing between the excited levels, $\Delta E = E_A(Q_{\min}) - E_1 \approx 0.16$ eV, is in reasonable agreement with the experimental data (0.146 eV).

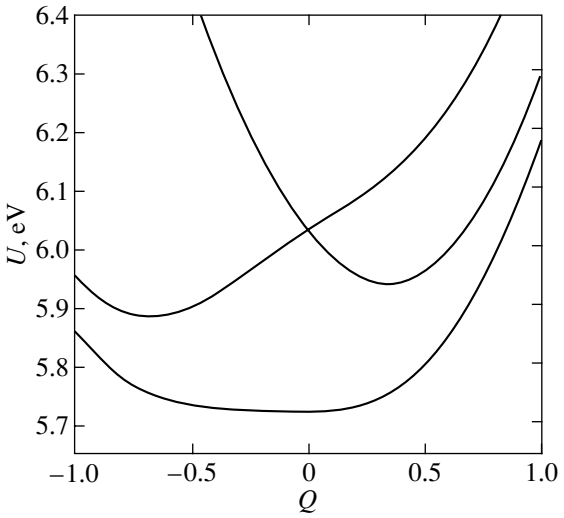

Fig. 4. Adiabatic potentials of the excited states ${}^3\Gamma_{1u}$ and ${}^3\Gamma_{4u}^*$.

The luminescence pattern for single Tl^+ centers can be represented as follows. The impurity centers are excited in a relatively narrow range of distortions *Q* corresponding to distortion fluctuations $Q^2 \leq kT^*$ in the ground state. Here, as was noted above, T^* is expressed through the effective frequency of the Γ_{5g}-type modes in the ground state ${}^1\Gamma_{1g}$ ($\omega \approx 100$ cm^{-1}). The ${}^3\Gamma_{4u}^*$ triplet states with energies close to 6.03 eV are populated upon excitation into the *A* absorption band. Upon distortion of the excited complex, the optical centers relax into the state corresponding to the minimum energy of the triplet. Some impurity centers undergo a dipole-allowed (fast) luminescent transition from this state to the ground state. The other centers are transformed into the singlet state ${}^3\Gamma_{1u}$ due to the vibronic interaction and, as a result of the reverse distortion, again go to the point $Q = 0$ in the (Q_4, Q_5, Q_6) space, which corresponds to the minimum energy of the singlet. The radiative transition with an energy of 5.72 eV from this state is allowed only through certain weak interactions. The transition from the triplet state is shifted toward the low-energy range and occurs at $E_{\min}(Q = -0.67) - Q^2 = 5.43$ eV. This agrees well with the observed location of the luminescence band at temperatures of ~100 K, at which the luminescence is governed primarily by transitions from the state ${}^3\Gamma_{4u}^*$.

At $T \leq 10$ K, the energy states of the impurity centers are predominantly located in the immediate vicinity of the minimum of the state ${}^3\Gamma_{1u}$ and the zero-phonon line

($^3\Gamma_{1u} \longrightarrow {}^1\Gamma_{1g}$) attributed to the transition between two minima has a very small width and a considerable peak intensity (Fig. 2). With an increase in the temperature, the Q fluctuations, as was noted above, increase significantly, the zero-phonon line becomes broadened, and its maximum shifts toward the low-frequency range. At $T \sim 100$ K, the estimated linewidth is of the order of $Q^2 \sim 0.16$ eV and the zero-phonon line is not observed. Furthermore, an increase in the temperature leads to a rapid increase in the probability of reverse vibronic transitions $^3\Gamma_{1u} \longrightarrow {}^3\Gamma^*_{4u}$, which, in turn, results in a decrease in the integral intensity of the forbidden line: $^3\Gamma_{1u} \longrightarrow {}^1\Gamma_{1g}$. Consequently, the slow luminescence is determined not by the direct transition $^3\Gamma_{1u} \longrightarrow {}^1\Gamma_{1g}$ but by the emission of the impurity centers in the metastable state $^3\Gamma_u$ through the active level $^3\Gamma^*_{4u}$. The rate of this process is governed primarily by the rate of the transition $^3\Gamma_{1u} \longrightarrow {}^3\Gamma_{4u}$ accompanied by phonon absorption. The latter rate almost exponentially depends on the reciprocal of the temperature; that is, $k_{12} = k_{21}\exp(-\Delta E/kT)$, where ΔE is the averaged spacing between the energy levels $E_1(^3\Gamma_{1u})$ and $E_A(^3\Gamma^*_{4u})$ [cf. relationship (1)].

The luminescence band attributed to the transition $^3\Gamma^*_{4u} \longrightarrow {}^1\Gamma_{1g}$ is characterized by a considerable width even at very low temperatures. Since the initial state corresponds to the energy minimum at $|Q| = -0.67$, the final state corresponds to a steep portion of the paraboloid representing the adiabatic potential of the ground state $^1\Gamma_{1g}$. Hence, the small fluctuations δQ observed at any temperature result in substantial variations in the final energies and a considerable linewidth. As the temperature increases, these fluctuations increase, the optical centers in the excited state occupy a progressively larger region in the (Q_4, Q_5, Q_6) space (for the most part, at large Q), the luminescence band becomes broader, and its maximum shifts toward the low-frequency range due to a decrease in the spacing $E_A(^3\Gamma^*_{4u}, Q) - E(^1\Gamma_{1g})$ with an increase in the distortion Q to within $\delta Q \sim kT$.

In the electric dipole approximation, the forbidden transition $^3\Gamma_{1u} \longrightarrow {}^1\Gamma_{1g}$ becomes allowed, for example, with inclusion of the admixture of the states $^3\Gamma^*_{4u}$ and $^1\Gamma^*_{4u}$ to the state $^3\Gamma_{1u}$ through the hyperfine interaction. Note that the main contribution to the hyperfine interaction is made by contact interaction between the 6*s* electron and the nuclear spin of the Tl^+ ion. This mechanism was considered earlier in [13, 14]. The hyperfine interaction Hamiltonian has the following form [15]:

$$H_{nf} = g_S\mu_B\gamma_n IN,$$
$$N = \sum\{(1-s)/r^3 + 3r(sr)/r^5 + (8\pi/3)s\delta(r)\}. \quad (6)$$

This Hamiltonian has a nonzero matrix element between the states $^3\Gamma_{1u}$ and $^1\Gamma^*_{4u}$. In particular, for the contact contribution, we have

$$\langle {}^3\Gamma_{4u}, z|N_z(\text{cont})|{}^3\Gamma_{4u}\rangle$$
$$= (8\pi/3\sqrt{6})\langle Z_+|\delta(r)|Z_-\rangle\langle S_0|s_z|S_Z\rangle \quad (7)$$
$$= (8\pi/3\sqrt{3})R^2_{6s}(0),$$

where $|Z_\pm\rangle = (1/\sqrt{2})(|s\,p_Z\rangle \pm |p_Z s\rangle)$, $|s\rangle$ and $|p_Z\rangle$ are the 6*s* and $6p_z$ one-particle orbitals, R_{6s} and R_{6p} are their radial parts, and $|S_{0,Z}\rangle = (1/\sqrt{2})(|1/2, -1/2\rangle - |-1/2, 1/2\rangle)$ are the spin functions [11]. The effective parameter A of the hyperfine interaction ($H_{hf} = AIS$) for the Tl^+ ion is of the order of 1–3 cm^{-1} (see, for example, [13]). The probability of emission from the metastable state can be estimated as

$$w(^3\Gamma_{1u}) \approx [A/(E_A - E_1)]^2 w(^3\Gamma^*_{4u}) \sim 10^{-6} w(^3\Gamma^*_{4u}). \quad (8)$$

This estimate approximately coincides with the ratio of radiative transition rates k_1/k_2 determined from the experimental data on the luminescence decay.

As was noted above, the temperature dependence of the slow luminescence component is well described by formula (1) (Fig. 3, curve *a*). A noticeable disagreement with the experimental data is observed in the vicinity of an inflection in the curve at $20 < T < 140$ K. It is quite possible that, in this range of temperatures, the transition from the state $^3\Gamma_{1u}$ becomes allowed through another mechanism, namely, due to the interaction of electrons with librational modes Γ_{4g} [16]. This mechanism leads to a temperature dependence of the radiative transition rate, and the coefficient k_1 in formula (1) can be represented as the sum of two contributions,

$$k_1(T) = k_{10} + k_{1d}\coth(\hbar\omega/2kT), \quad (9)$$

where ω is the frequency of the Γ_{4g} mode. The introduction of additional parameters makes it possible to describe adequately the dependence $\tau_s(T)$ over the entire temperature range (Fig. 3, curve *b*). However, the parameters k_{10}, k_{1d}, and ω become less definite.

5. CONCLUSION

It has been demonstrated that the simple theory described offers a qualitative description of the main features of the luminescence in the system under consideration. The energies of the luminescence bands

associated with single Tl^+ impurity centers are adequately described in terms of the vibronic interaction parameters determined from the absorption spectra of these centers.

Moreover, we investigated the optical properties of $KMgF_3 : Tl^+$ crystals. The results of our measurements of the *A* absorption band [12], for the most part, are in good agreement with the results of previous investigations into the optical properties of this system [7, 8]. However, our data on the luminescence spectra at low temperatures differ from the results obtained by Scacco *et al.* [9], because we observed an intense zero-phonon line. The results of these investigations and their theoretical interpretation will be described in a separate paper.

ACKNOWLEDGMENTS

This work was supported by the Russian Foundation for Basic Research (project no. 98-02-18037) and the Scientific and Educational Center of the Kazan State University (REC-007).

REFERENCES

1. M. V. Mityagin, S. I. Nikitin, N. I. Silkin, *et al.*, Izv. Akad. Nauk SSSR, Ser. Fiz. **54** (6), 1512 (1990).
2. K. R. German, U. Durr, and W. Kunzel, Opt. Lett. **11**, 12 (1986).
3. L. F. Johnson, H. J. Guggenheim, D. Bahnek, and A. M. Johnson, Opt. Lett. **8**, 371 (1983).
4. C. Furetta, C. Bacci, B. Rispoli, *et al.*, Radiat. Prot. Dosim. **33**, 107 (1990).
5. M. A. Dubinskii, V. V. Semashko, A. K. Naumov, *et al.*, J. Mod. Opt. **40** (1), 1 (1993).
6. G. P. Pazzi, M. G. Baldecchi, P. Fabeni, *et al.*, Opt. Commun. **43** (12), 405 (1982).
7. A. Scacco, S. Fioravanti, M. Missori, *et al.*, J. Phys. Chem. Solids **54**, 1035 (1993).
8. T. Tsuboi and A. Scacco, J. Phys.: Condens. Matter **7**, 9321 (1995).
9. A. Scacco, S. Fioravanti, U. M. Grassano, *et al.*, J. Phys. Chem. Solids **55**, 1 (1994).
10. A. Ranfagni, P. Mugnai, M. Bacci, *et al.*, Adv. Phys. **32**, 905 (1983).
11. P. W. M. Jacobs, J. Phys. Chem. Solids **52**, 35 (1991).
12. L. K. Aminov, A. V. Kosach, S. I. Nikitin, *et al.*, J. Phys.: Condens. Matter **13**, 6247 (2001).
13. Y. Merle d'Aubigne and Le Si Dang, Phys. Rev. Lett. **43** (14), 1023 (1979).
14. A. F. Éllerveé, A. I. Laĭsaar, and A.-M. A. Oper, Pis'ma Zh. Éksp. Teor. Fiz. **33**, 24 (1981) [JETP Lett. **33**, 21 (1981)].
15. A. Abragam and B. Bleaney, *Electron Paramagnetic Resonance of Transition Ions* (Clarendon, Oxford, 1970; Mir, Moscow, 1972).
16. S. Asano, Phys. Status Solidi B **105**, 613 (1981).

Translated by O. Borovik-Romanova

Physics of the Solid State, Vol. 44, No. 8, 2002, pp. 1564–1569. Translated from Fizika Tverdogo Tela, Vol. 44, No. 8, 2002, pp. 1492–1497.

PROCEEDINGS OF THE XI FEOFILOV WORKSHOP "SPECTROSCOPY OF CRYSTALS ACTIVATED BY RARE-EARTH AND TRANSITION-METAL IONS"

(Kazan, Tatarstan, Russia, September 24–28, 2001)

Infrared Spectroscopy of the Nd^{3+} Ion in Nd_2BaCuO_5 and Nd_2BaZnO_5

S. A. Klimin*, M. N. Popova*, and B. V. Mill**

**Institute of Spectroscopy, Russian Academy of Sciences, Troitsk, Moscow oblast, 142190 Russia*

e-mail: klimin@isan.troitsk.ru

***Moscow State University, Vorob'evy gory, Moscow, 119899 Russia*

Abstract—Absorption spectra of the Nd^{3+} ion in the Nd_2BaCuO_5 and Nd_2BaZnO_5 ternary oxides were measured within broad spectral (1500–17000 cm^{-1}) and temperature (4.2–200 K) intervals. The positions and widths of the Stark sublevels were determined. The exchange splittings of the Nd^{3+} Kramers doublets in several multiplets were found for the magnetically ordered state of Nd_2BaCuO_5 (T_N = 7.5 K). © *2002 MAIK "Nauka/Interperiodica".*

1. INTRODUCTION

The R_2BaCuO_5 cuprates related to high-temperature superconductors (R stands for a rare-earth element (RE) or yttrium) possess interesting magnetic properties. In particular, the so-called brown phase of Nd_2BaCuO_5 reveals quasi-one-dimensional magnetic fluctuations at temperatures of up to $\approx 10T_N$, where T_N = 7.5 K is the antiferromagnetic ordering temperature [1, 2]. A neutron scattering study [2] established the magnetic structure of Nd_2BaCuO_5 and showed that the quasi-one-dimensional magnetic properties of this compound, whose structure does not contain quasi-one-dimensional elements, are accounted for by the Dzyaloshinski–Moriya antisymmetric exchange being dominant in the ground state.

To gain a better understanding of the magnetic interactions in this compound, the positions of the Nd^{3+} Stark sublevels and their exchange splittings in the magnetically ordered state need to be known. The information that can be found in the literature on the spectroscopy of the Nd^{3+} ion in Nd_2BaCuO_5 is fragmentary. For instance, publication [1], on the detection of a magnetic-phase transition in Nd_2BaCuO_5 from the splitting of the Nd^{3+} Kramers doublets in the magnetically ordered state presents the energies of the Stark sublevels in the $^4I_{15/2}$ and $^4F_{3/2}$ multiplets. Data on the Stark structure of the $I_{11/2}$ and $^4F_{3/2}$ levels are presented [3].

We report on a study of Nd^{3+} spectra made in the 4.2- to 200-K temperature region throughout the infrared and, partially, the visible wavelength ranges, determination of the Stark sublevel positions, and measurement of the exchange splittings. To check the assignment of the Nd^{3+} spectral lines in Nd_2BaCuO_5, we recorded spectra of Nd_2BaZnO_5 in the same conditions. Replacement of the Cu^{2+} magnetic ion by the nonmagnetic Zn^{2+} ion results in a substantial line narrowing in the RE ion spectrum and in the disappearance of the interfering strong d–d transition band of the copper ion, which markedly facilitates identification of the spectra [4]. Earlier spectroscopic studies of Nd_2BaZnO_5 [3, 5–7] are incomplete, contradictory, and were performed with an inadequate spectral resolution.

2. ANALYSIS OF THE CRYSTAL STRUCTURE

Both Nd_2BaCuO_5 and Nd_2BaZnO_5 crystallize in the tetragonal structure. Their space groups, however, are

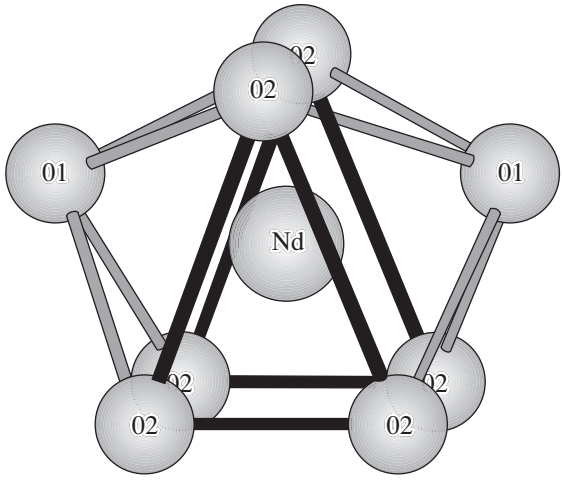

Fig. 1. Nearest neighbor environment of the Nd^{3+} ion in Nd_2BaCuO_5 and Nd_2BaZnO_5 (NdO_8 polyhedron). The data on the Nd_2BaCuO_5 structure are from [2].

1063-7834/02/4408-1564$22.00 © 2002 MAIK "Nauka/Interperiodica"

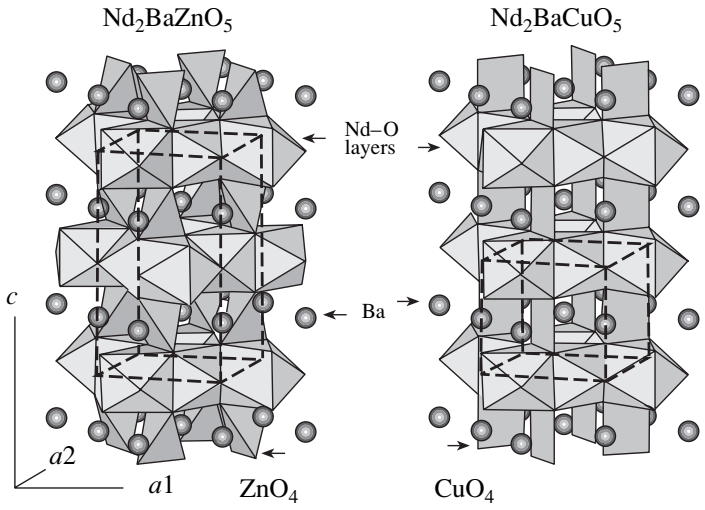

Fig. 2. Crystal structures of Nd_2BaCuO_5 and Nd_2BaZnO_5. The sketch shows the NdO_8 and MO_4 polyhedra. The unit cells are identified by a dashed line.

different: $P4/mbm$ (D_{4h}^5) for the copper compound [2, 8, 9] and $I4/mcm$ (D_{4h}^{18}) for the zinc compound [10, 11]. Nevertheless, the structures of the two compounds have much in common; in particular, the nearest neighbor environment of the Nd^{3+} ion is the same. In both oxides, the neodymium ion is surrounded by eight oxygen ions (Fig. 1). Six O^{2-} (2) ions make up a triangular prism with an isosceles triangle at the base and the neodymium ion at the prism's center. Two O^{2-} (1) ions face the two rectangular faces of the prism. The structure provides one position of C_{2v} symmetry for the Nd^{3+} ion. The Nd–O bond lengths are specified in Table 1. The bond lengths in the two compounds differ little, thus giving one grounds to expect that the crystal fields and, hence, the Stark splittings of the multiplets are also similar. The NdO_8 polyhedra are linked with one another to form Nd–O layers perpendicular to the c crystallographic axis (Fig. 2). The Ba^{2+} and Cu^{2+} (or Zn^{2+}) ions are located between the layers and are surrounded by four and ten oxygen ions, respectively. While the unit cell of the copper compound has only one Nd–O sheet, in the zinc compound, there are two sheets turned through 90° relative to one another about the screw axis passing through the Zn^{2+} position. Accordingly, the lattice constant along the c axis in the zinc compound is twice that in the copper compound (Table 1, Fig. 2). The copper and zinc ions have different environments. The copper is located inside rectangles; the zinc, inside tetrahedra. The coordination polyhedron for Ba^{2+} is a rectangular prism with two caps in the copper compound and an antiprism in the zinc compound.

Figure 3 shows the magnetic-moment orientation of the Nd^{3+} ion and of the nearest neighbor Cu^{2+} ions in magnetically ordered Nd_2BaCuO_5 [2]. The symmetric part of the exchange interaction

$$H = \sum_{j=1}^{4} (J_{xj} M_x S_{xj} + J_{yj} M_y S_{yj} + J_{zj} M_z S_{zj})$$

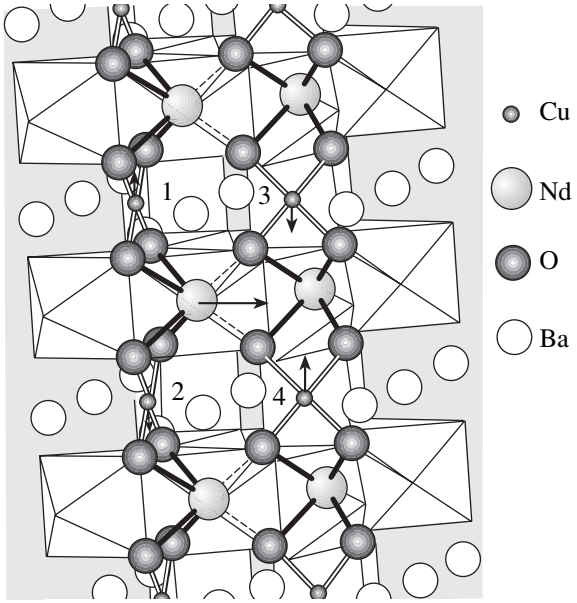

Fig. 3. Quasi-one-dimensional magnetic chains in Nd_2BaCuO_5. The arrows show the orientation and relative magnitude of the copper and neodymium ion magnetic moments in the magnetically ordered state [2].

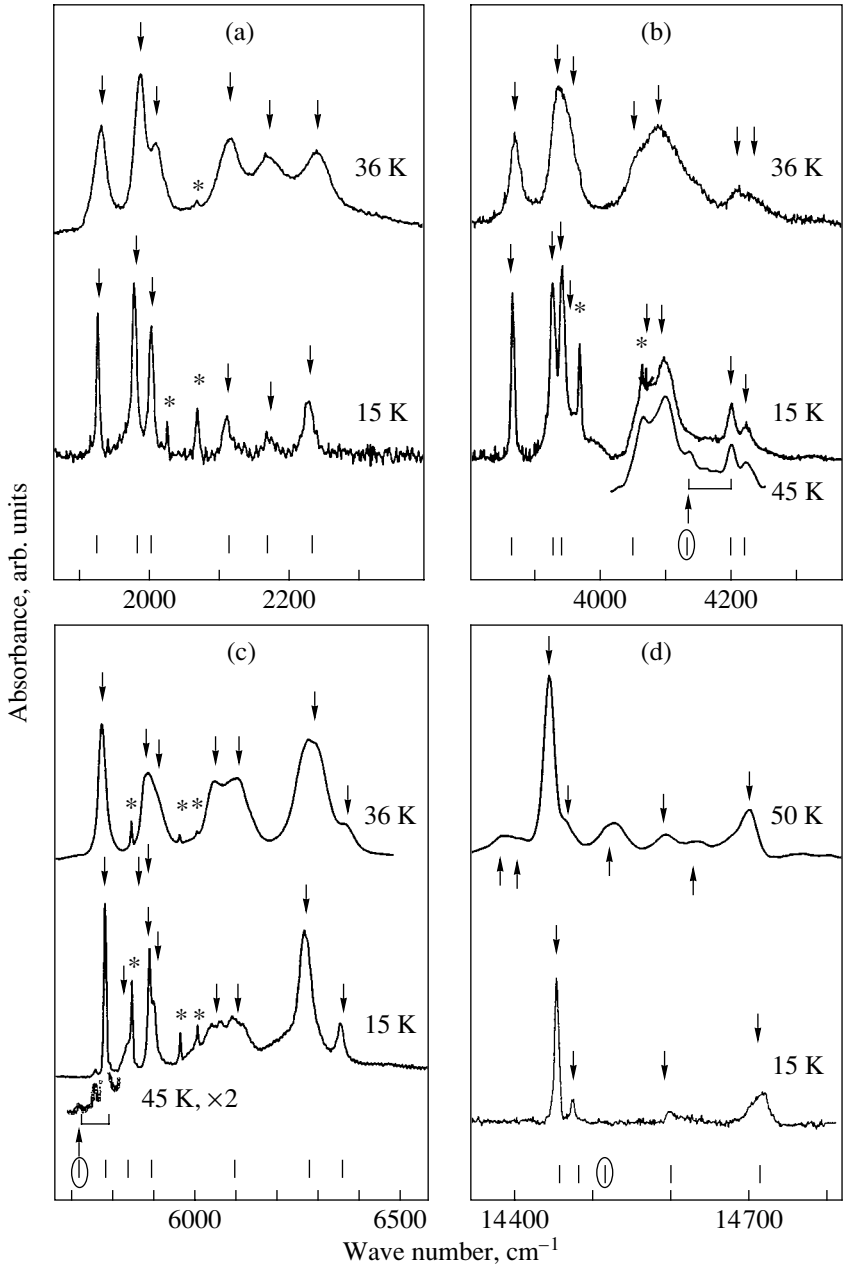

Fig. 4. Absorption spectra of the Nd^{3+} ion in Nd_2BaCuO_5 (top lines in each panel) and Nd_2BaZnO_5 (bottom lines) and the energy level diagrams of Nd_2BaZnO_5 taken from [3] (vertical bars under the arrows). The spectra contain regions corresponding to the transitions (a) $^4I_{9/2} \longrightarrow {}^4I_{11/2}$, (b) $^4I_{9/2} \longrightarrow {}^4I_{13/2}$, (c) $^4I_{9/2} \longrightarrow {}^4I_{15/2}$, and (d) $^4I_{9/2} \longrightarrow {}^4I_{9/2}$.

[where $\mathbf{M} = (M_x, M_y, M_z)$ is the neodymium-ion magnetic moment and $\mathbf{S}_j$ are the spins of the nearest neighbor copper ions] vanishes for each j, because vector $\mathbf{M}$ is perpendicular to vector $\mathbf{S}_j$. The antisymmetric part of the exchange interaction is dominated by the Dzyaloshinski–Moriya interaction [2]

$$H_{\text{as}} = \sum_j \mathbf{D}_j(\mathbf{M} \times \mathbf{S}_j),$$

where $\mathbf{D}_j$ is the Dzyaloshinski–Moriya vector

$$\mathbf{D}_j = d_j(\mathbf{r}_{0j} \times \mathbf{r}_j)$$

and $\mathbf{r}_{0j}$ and $\mathbf{r}_j$ are the position vectors connecting the oxygen ion in the Cu–O–Nd chain to the neodymium and copper ions, respectively. This term is other than zero only for the neodymium ion interaction with the Cu1 and Cu2 ions. The Dzyaloshinski–Moriya vectors for the copper ions denoted as 3 and 4 vanish, because the Cu–O–Nd bond angle is close to 180°. Thus, only

the anisotropic Dzyaloshinski–Moriya interaction is capable of accounting for the magnetic-moment ordering in the system, with the magnetic coupling being efficient only along Cu1–Nd–Cu2 chains aligned with the *c* axis.

3. EXPERIMENT

Nd_2BaCuO_5 and Nd_2BaZnO_5 polycrystalline samples were prepared from a stoichiometric mixture of chemically pure oxides (Nd_2O_3, CuO, or ZnO) and barium carbonate $BaCO_3$ by solid-phase synthesis in air at a temperature of 1100–1200°C. X-ray phase analysis revealed the presence of a small admixture of other phases in the Nd_2BaZnO_5 samples and no admixtures in Nd_2BaCuO_5.

The samples were mixed with ethanol, deposited on a sapphire substrate, and placed into a helium-vapor cryostat, where they were maintained at a temperature controlled within the 4.2-to 200-K interval. The transmission spectra of Nd_2BaCuO_5 and Nd_2BaZnO_5 were measured on a Bomem DA3.002 Fourier spectrometer in the 1800- to 18000-cm^{-1} range with a resolution of 2 cm^{-1}. In the 1800- to 5000-cm^{-1} interval, a KBr beam splitter, an MCT detector, and a globar as a light source were used; in the 4500-to 12000-cm^{-1} region, a quartz splitter, an InSb detector, and a globar were used; and in the 10000- to 18000-cm^{-1} region, a quartz splitter, a silicon detector, and a halogen lamp were used.

4. EXPERIMENTAL RESULTS AND DISCUSSION

Figure 4 presents the absorption spectra of Nd^{3+} in the two oxides studied. The spectra for Nd_2BaCuO_5 were obtained at a higher temperature than those for Nd_2BaZnO_5, because the magnetic phase transition occurring in the copper compound with decreasing temperature makes the spectral pattern very complicated. As a result of the relatively high temperature, the spectrum exhibits lines corresponding to transitions from excited Stark sublevels of the ground state. The lines disappear with decreasing temperature because of the upper Stark sublevels becoming depleted. These lines are indicated in the figures by up-headed arrows. As seen from Fig. 4, the assignment of some of these lines in Nd_2BaZnO_5 to ground-state transitions [3, 7], i.e., their interpretation as lines originating from the Stark sublevels of the upper multiplet (encircled in Fig. 4), is erroneous. We determined the positions of the Stark sublevels taking due account of the temperature dependence of the lines. The down-headed arrows specify these positions. From the temperature dependence, we also managed to derive the position of the lines corresponding to transitions from the upper Stark sublevels of the ground state, which are populated at a high temperature, and to reconstruct the positions of some Stark levels for the $^4I_{9/2}$ ground state from the difference between the line energies. All experimentally measured energy levels of the Nd^{3+} ion are given in Table 2.

Table 1. Nd–O bond lengths and lattice parameters (in nanometers) for $Nd_2Ba\mathit{M}O_5$

	M = Cu [9]	M = Zn [5]
Nd–O(1) × 2	0.248	0.249
Nd–O(2) × 2	0.232	0.230
Nd–O(2) × 4	0.259	0.263
a	0.670	0.675
c	0.582	1.154

A comparison of the spectra of the two compounds reveals an important point, that the Nd^{3+} levels in Nd_2BaCuO_5 and Nd_2BaZnO_5 are close in energy. This observation correlates well with the crystallographic data on the two compounds and suggests that the crystal

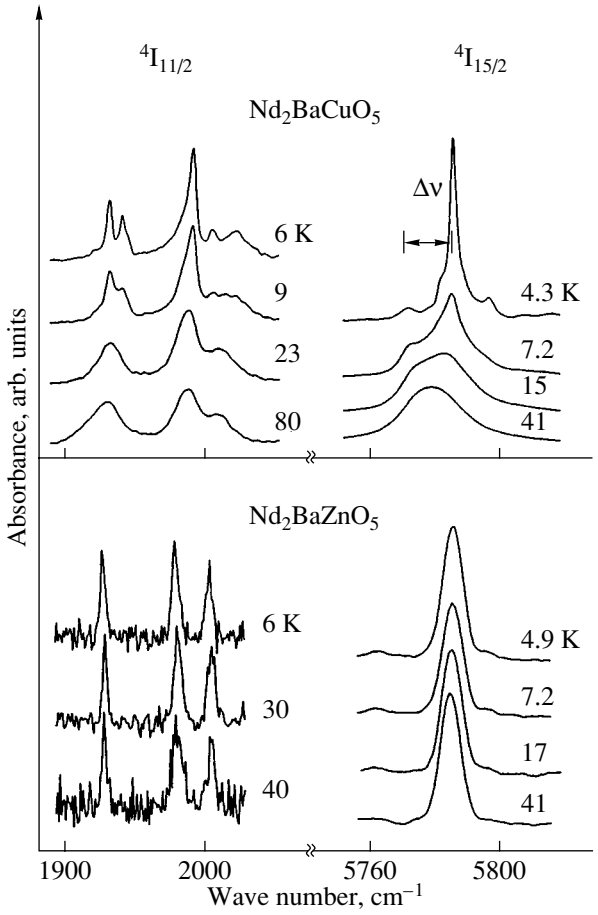

Fig. 5. Low-frequency part of the $^4I_{9/2} \longrightarrow {}^4I_{11/2}$ and $^4I_{9/2} \longrightarrow {}^4I_{15/2}$ transitions in Nd_2BaCuO_5 and Nd_2BaZnO_5 measured at different temperatures.

Table 2. Energy levels (E) and linewidths ($\delta\nu$) in Nd_2BaCuO_5 and Nd_2BaZnO_5 and Kramers doublet splittings ($\Delta\nu$) in magnetically ordered Nd_2BaCuO_5

Term	Nd_2BaZnO_5		Nd_2BaCuO_5			Term	Nd_2BaZnO_5		Nd_2BaCuO_5		
	E	$\delta\nu$	E	$\delta\nu$	$\Delta\nu$		E	$\delta\nu$	E	$\delta\nu$	$\Delta\nu$
	cm^{-1}						cm^{-1}				
$^4I_{9/2}$	0		0		7	$^4F_{5/2}$	12278	8	12265	18	8
	67		64				12293	7	12281	21	≈0
	228		–				12379	12	12373	25	≈0
	287		–			$^2H2_{9/2}$	12399	14	12386	25	1.5
	460		–				12474	18	12472	30	
							12510	21	12491	35	
$^4I_{11/2}$	1928	4	1935	20	8		12552		12548	30	
	1980	8	1991	20	≤1		12625	40	12620	39	
	2004	7	2012	17	18						
	2114		2120	37		$^4F_{7/2}$	13219	9	13206	24	6
	2176	28	2174	51			13306	12	13296	34	≈0
	2230	14	2242	43	7		13329	12	13322	34	7
							13375	18	13359	41	
$^4I_{13/2}$	3866	8	3870	20	4						
	3928	9	3936	27	6	$^4S_{3/2}$	13541		13539		
	3941	8	3961	17	≤2						
	4072	21	4054	40		$^4F_{9/2}$	14454	6	14447	16	≈0
	4096	35	4092	67			14475	4	14468	16	
	4198	9	4206	32			14595	11	14593	21	
	4223	18	4234	63			14698	20	14671	36	
							14714	20	14699	24	
$^4I_{15/2}$	5784	10	5779	19	7						
	–	24	5838	33		$^4G_{5/2}$	16540	15	16514	44	
	5891	24	5893	38			16770	22	16743	37	
	5910	29	5902	57			16974	18	16955	48	
	6061	23	6057	80							
	6119	38	6112	80		$^4G_{7/2}$	17056	22	17026	22	
	6278		6295				–		–		
	6362	19	6376	54							
						$^4G_{5/2}$	–		17161	46	
$^4F_{3/2}$	11262	9	11260	20	3		–		17205		
	11323	19	11319	31	32						

field is dominated by the nearest neighbor environment of the neodymium ion, which is the same in both compounds.

It should be noted that we did not detect any spectral lines that could be assigned to transitions in neodymium ions occupying barium sites [3]. Because the point symmetry group of the barium position in Nd_2BaCuO_5, C_{4h}, contains an inversion center, such transitions can be only magnetic-dipole allowed. The lines mentioned above should be the strongest for the $^4I_{9/2} \longrightarrow {}^4I_{11/2}$ transitions, which in a free ion are magnetic-dipole allowed. In Nd_2BaZnO_5, the barium position is noncentrosymmetric (D_4); therefore, the spectrum of neodymium in this position would be primarily due to electric-dipole transitions occurring in all the multiplets. For this reason, the additional narrow lines (identified by asterisks in Fig. 4), which are observed in nearly all multiplets in both the copper and the zinc compounds and coincide in frequency in both, cannot

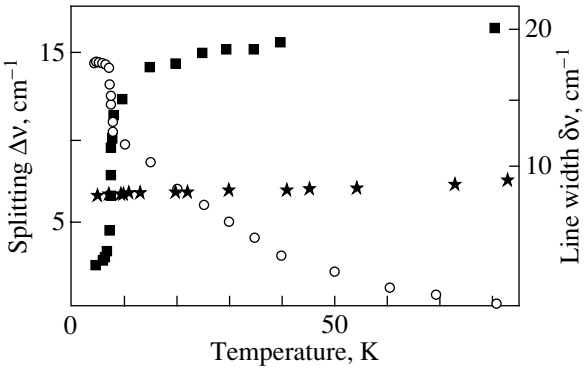

Fig. 6. Temperature dependences of the splitting of the lowest-frequency line corresponding to the $^4I_{9/2} \longrightarrow {}^4I_{15/2}$ transition in the Nd^{3+} ion in Nd_2BaCuO_5 (circles) and the halfwidth of this line in Nd_2BaCuO_5 (squares) and Nd_2BaZnO_5 (stars).

be assigned to neodymium being at the barium site; they are probably due to a parasitic phase. These lines are considerably stronger in Nd_2BaZnO_5, which correlates with the x-ray phase characterization of our samples. Obviously enough, RE ion spectroscopy is a more sensitive method of detecting small amounts of admixtures of other phases than x-ray phase analysis is.

Table 2 also lists the linewidths of transitions from the ground state to the corresponding Stark sublevels. Because the measurements were made on polycrystalline samples, these values should be considered to be tentative. Nevertheless, we see (Fig. 4, Table 2) that the spectral lines of the zinc compound are substantially narrower than those of the copper one. This is associated with the broadening caused by copper magnetic-moment disorder. Indeed, after the onset of magnetic order in Nd_2BaCuO_5, the absorption lines noticeably narrow (see below).

Figure 5 shows parts of the Nd^{3+} spectra in the copper and zinc compounds obtained at different temperatures. We readily see that some lines in Nd_2BaCuO_5 split and become much narrower with decreasing temperature, which is a consequence of magnetic ordering in Nd_2BaCuO_5 (T_N = 7.5 K). The copper magnetic-moment ordering brings about the creation of an internal magnetic field which splits the Kramers doublets of the neodymium ion. The depletion of the upper component of the split Kramers doublet with decreasing temperature is accompanied by line narrowing. The temperature dependence of the line parameters is presented graphically in Fig. 6 for both compounds. The changes in the splitting $\Delta\nu$ and the in linewidth $\delta\nu$ in the copper compound are the strongest at T_N = 7.5 K. However, splittings are also observed at temperatures considerably higher than T_N. This is a consequence of the quasi-one-dimensional magnetic correlations originating from specific features of the magnetic interactions [1, 2]. The zinc compound reveals neither line splitting nor a decrease in linewidth down to 4.2 K, which indicates the absence of magnetic order in Nd_2BaZnO_5. The exchange splittings measured experimentally on Nd_2BaCuO_5 are listed in Table 2.

ACKNOWLEDGMENTS

This study was supported by the Russian Foundation for Basic Research (project no. 01-02-16239) and INTAS (grant no. 990155).

REFERENCES

1. I. V. Paukov, M. N. Popova, and B. V. Mill, Phys. Lett. A **157** (4–5), 306 (1991).
2. I. V. Golosovsky, P. Böni, and P. Fischer, Phys. Lett. A **182** (1), 161 (1993).
3. B. Dareys, P. Thurian, M. Dietrich, *et al.*, Phys. Rev. B **55** (11), 6871 (1997).
4. M. N. Popova, S. A. Klimin, E. Antic-Fidancev, *et al.*, J. Alloys Compd. **284** (1), 138 (1999).
5. M. Taïbi, J. Aride, E. Antic-Fidancev, *et al.*, J. Solid State Chem. **74**, 329 (1988).
6. M. Taïbi, J. Aride, E. Antic-Fidancev, *et al.*, Phys. Status Solidi A **115**, 523 (1989).
7. A. de Andrés, S. Taboada, L. L. Martínez, *et al.*, Phys. Rev. B **55** (6), 3568 (1997).
8. C. Michel, L. Er-Rakho, and B. Raveau, J. Solid State Chem. **39**, 161 (1981).
9. J. K. Stalich and W. Wong-Ng, Mater. Lett. **9** (10), 401 (1990).
10. C. Michel and B. Raveau, J. Solid State Chem. **49**, 150 (1983).
11. M. Taïbi, J. Aride, L. Darriet, *et al.*, J. Solid State Chem. **86**, 233 (1990).

Translated by G. Skrebtsov

Physics of the Solid State, Vol. 44, No. 8, 2002, pp. 1570–1573. Translated from Fizika Tverdogo Tela, Vol. 44, No. 8, 2002, pp. 1498–1500.

METALS AND SUPERCONDUCTORS

The Mechanism of 4*f*–5*d* Hybridization in $Sm_{1-x}R_xS$ (*R* = Ce, Gd, and Y) Systems with Intermediate Valence

A. E. Sovestnov*, V. A. Shaburov*, Yu. P. Smirnov*, A. V. Tyunis*, and A. V. Golubkov**

** Konstantinov Institute of Nuclear Physics, Russian Academy of Sciences, Gatchina, St. Petersburg, 188300 Russia*

*** Ioffe Physicotechnical Institute, Russian Academy of Sciences, Politekhnicheskaya ul. 26, St. Petersburg, 194021 Russia*

e-mail: asovest@mail.pnpi.spb.ru

Received December 10, 2001

Abstract—For $Sm_{1-x}R_xS$ (*R* = Ce, Gd, Y) systems with intermediate valence, the population of Sm 4*f* states (valence) and populations of Ce 5*d*, Gd 5*d*, and Y 4*d* states are determined by the method of x-ray line displacement. It is found that, in all the systems under investigation, the valence of Sm upon transition to the intermediate valence state increases from $m \approx 2.5$ ($x \approx 0.15$–0.25) to $m \approx 2.65$ ($x \approx 0.8$) and then decreases. The populations of Ce, Gd, and Y *d* states remain nearly constant over the entire region of compositions: $\bar{n}_d = 0.78 \pm 0.03$, 0.43 ± 0.04, and 1.07 ± 0.04 for Ce, Gd, and Y, respectively. The experimental dependence of the Sm valence on the composition is explained under the assumption that the 4*f* electron of an Sm atom can be hybridized through two channels, namely, with the 5*d* electron of the neighboring Sm atom and with its own 5*d* electron. © *2002 MAIK "Nauka/Interperiodica".*

1. INTRODUCTION

It is known that, in Ce, Sm, Eu, and Yb rare-earth compounds, the states of localized 4*f* electrons are close in energy to the states of outer (5*d*, 6*s*) conduction electrons under certain conditions (composition, pressure, temperature, etc.); as a result, the so-called state of intermediate (fluctuating) valence is formed in the system [1, 2]. This state is treated as a resonance between the degenerate states $4f^n$ and $4f^{n-1}$ + a conduction electron; in other words, this state is a consequence of hybridization of localized 4*f* and collective 5*d* and 6*s* electrons. In fact, the specific mechanisms of mixing (hybridization) of the *f*, *s*, and *d* states and stabilization of the intermediate valence state have been the subject of discussions and experimental investigations. The phenomenon of intermediate valence is of particular interest because compounds with intermediate valence exhibit anomalies in virtually all their physical characteristics. Moreover, this phenomenon is associated with the fundamental problem of description of localized and collective states within a unified approach.

Substitutional solid solutions are convenient objects for investigation of the physics of intermediate valence. In these solutions, by varying the type and concentration of substituting atoms, it is possible to purposefully (gradually and over wide limits) change the characteristics of the system and to investigate their effect on the intermediate valence state. In their theoretical work, Kikoin *et al.* [3] assumed that the 4*f*–5*d* hybridization in $Sm_{1-x}R_xS$ solid solutions occurs through two mechanisms (channels), namely, two-center and one-center mechanisms. The first mechanism, which was proposed by Kaplan and Mahanti [4] for SmS under pressure, provides the hybridization of the 4*f* electron of an Sm atom with the 5*d* electron of a neighboring Sm atom. The second mechanism provides the 4*f*–5*d* hybridization within a single Sm atom and becomes impossible in the inversion symmetry field of pure SmS [4]. However, this mechanism manifests itself in $Sm_{1-x}R_xS$ due to distortion of the crystal field potential in a state of the Sm atom that is induced by substituting *R* ions.

Earlier [5], we studied the classical system $Sm_{1-x}Gd_xS$ with an intermediate valence. In addition to the universally known increase in the valence *m* from 2 to 2.5 at the critical concentration $x_{cr} \approx 0.15$, we revealed a decrease in the valence of Sm at small concentrations ($x \geq 0.9$) [5]. This effect was explained by the fact that the intermediate valence state arises from the hybridization of the 4*f* and 5*d* electrons of the neighboring Sm atoms. However, the observed decrease in the valence of Sm was substantially less than was expected for this mechanism ($m \longrightarrow 2$ at $x \longrightarrow 1$). It is known that parameters of the intermediate valence state of Sm in $Sm_{1-x}R_xS$ systems (such as the critical concentration of the transition, the valence of Sm, and the dependence of the valence of Sm on the concentration *x*) depend strongly on the type and concentration of *R* atoms substituting for samarium [2, 6]. For this reason, it is interesting and important in understanding the physics of the intermediate valence state to elucidate how the decrease in the valence of Sm in Sm(*R*)S systems depends on the characteristics of the substituting atoms.

In the present work, the electronic structures of Sm (the population of 4*f* states), Ce (populations of 5*d* and 6*s* states), and Y (populations of 4*d* and 5*s* states) in $Sm_{1-x}Ce_xS$ and $Sm_{1-x}Y_xS$ systems were investigated by the method of x-ray line displacement (for completeness and generality, we also considered the results of our previous work on the $Sm_{1-x}Gd_xS$ system [5]). The choice of $Sm_{1-x}R_xS$ (R = Ce, Gd, Y) systems as a subject of investigation was made for the following reasons. It is believed that the formation and stabilization of the intermediate valence state are determined primarily by the size effect (atomic or ionic radii r) and the electronic factor (the electronic structures of components of the compound). From the standpoint of the size effect, the Sm(Y)S and Sm(Ce)S systems are opposite to the Sm(Gd)S system (r^{3+}(Y) = 0.905 Å < r^{3+}(Gd) = 0.938 Å < r^{3+}(Ce) = 1.034 Å [7]). Consequently, yttrium should bring about a stronger intracrystalline contraction in the system as compared to gadolinium, whereas cerium should lead to a weaker contraction. As far as we know, the electronic factor (the electronic structures of Ce, Gd, and Y) in these systems has not been analyzed. In this work, primary attention was paid to the range of low Sm concentrations, because, according to [1–3], this range provides more valuable information for understanding the mechanism of 4*f*–*d* hybridization.

2. SAMPLES AND EXPERIMENTAL TECHNIQUE

The compounds to be studied were prepared by rf melting of SmS–CeS and SmS–YS mixtures in a hermetically sealed tungsten crucible. The batch concentrations of Sm, Ce, and Y were checked by fluorescence analysis. The samples were well-crystallized, single-phase, and, as can be seen from Fig. 1, which represents the results of an x-ray structure analysis of the compounds under investigation, are almost identical in lattice parameters to those studied earlier in [8, 9].

The method of x-ray line displacement is characterized by a high universality and selectivity and makes it possible to perform independent investigations of the electronic structures of components of the compound for a wide variety of elements and experimental conditions. The experimentally observed effects, which are caused by changes in the populations of the *f*, *d*, and *s* states, are significantly different in magnitude and exhibit characteristic dependences on the type of x-ray diffraction lines involved (facsimile [10]). This makes it possible to identify unambiguously the type of electrons involved in chemical bonding and to determine the population of the orbitals with an accuracy of ~0.01 electrons/atom for 4*f* electrons and ~0.03 electrons/atom for *d* and *s* electrons. It is important that the effects of x-ray line displacement can be calculated with a satisfactory accuracy in the framework of the self-consistent Dirac–Fock formalism [11]. The physical principles of the method of x-ray line displacement, the experimental setup, the measurement procedure, and data processing were described in detail in [10].

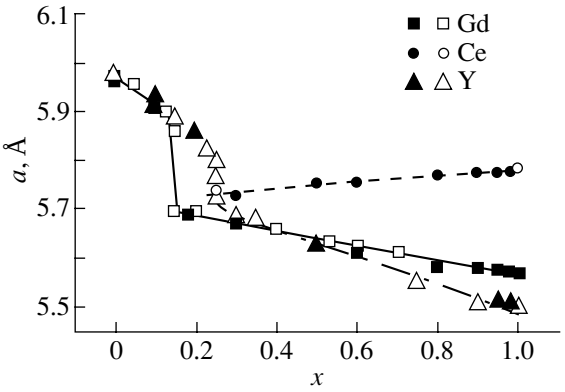

Fig. 1. Dependences of the lattice parameter on the composition of $Sm_{1-x}R_xS$ (R = Gd, Ce, Y). Closed symbols indicate our data, and open symbols represent the data taken from [8, 9].

In this work, the displacements of the Sm $K_{\beta 1}$, Ce $K_{\alpha 1}$, and Y $K_{\alpha 1}$ lines were measured with respect to reference substances, namely, ionic compounds of bivalent samarium (SmS) and trivalent compounds of cerium and yttrium (CeF_3 and YF_3). The valence of Sm was determined from the following simple relationship:

$$m = m_{\text{ref}} + \Delta E/\Delta E_{4f}.$$

Here, m_{ref} is the valence of Sm in the reference substance, ΔE is the experimental displacement of the x-ray line for the sample under investigation, and ΔE_{4f} is the normalization displacement of the same K line upon elimination of one 4*f* electron. For normalization, we used the averaged value for the trivalent compounds Sm_2O_3 and SmF_3 (with respect to SmS): $\Delta E_{4f} = -1485 \pm 7$ meV (hereafter, the errors are statistical). The electronic structure (the populations n_d and $n_s = 1 - n_d$ for the *d* and *s* states, respectively) for cerium, gadolinium (5*d* and 6*s* states), and yttrium (4*d* and 5*s* states) was determined from a comparison of the experimental displacements and those calculated from the Dirac–Fock–Koopmans (DFK) model:

$$\Delta E = \Delta E^{\text{DFK}}(n_d, n_s).$$

3. RESULTS AND DISCUSSION

The results of the determination of the valence of Sm and the populations of the outer 5*d* and 4*d* states of Ce, Gd, and Y are presented in Figs. 2 and 3, respectively.

It can be seen from Fig. 2 that, in the studied systems with $x \approx x_{\text{cr}} - 0.8$, the valence of Sm increases almost identically from $m \approx 2.5$ to $m \approx 2.65$, even though the intracrystalline contraction for samarium atoms increases in the Sm(Y)S and Sm(Gd)S systems and

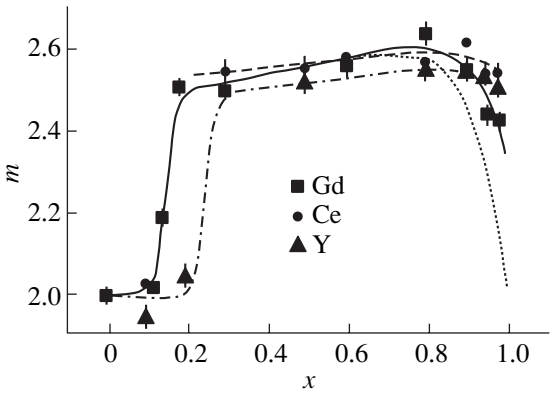

Fig. 2. Dependences of the valence m of samarium on the composition of $Sm_{1-x}R_xS$ (R = Gd, Ce, Y). The boundaries of transitions are plotted according to the structural data (Fig. 1).

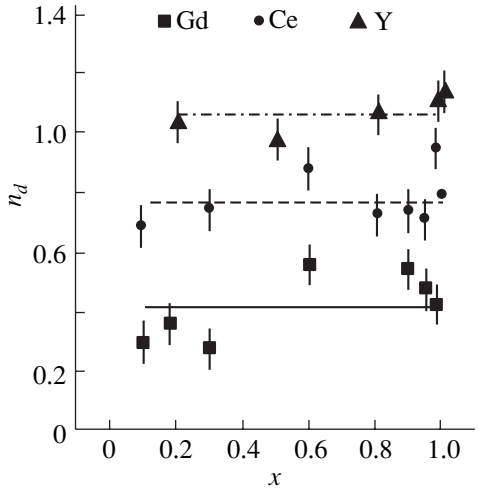

Fig. 3. Dependences of the population of Gd 5*d*, Ce 5*d*, and Y 4*d* states on the composition of $Sm_{1-x}R_xS$.

decreases in the Sm(Ce)S system with an increase in the concentration x (Fig. 1). With a further decrease in the Sm concentration, its valence somewhat decreases. This decrease is less pronounced in the Sm(Ce)S and Sm(Y)S systems as compared to the Sm(Gd)S system.

In [5], we proved that the decrease in the valence of Sm in Sm(R)S systems with concentrations x close to unity is associated with the formation of the intermediate valence state through the two-center mechanism of 4*f*–5*d* hybridization. However, upon the 4*f*–5*d* hybridization through only this mechanism, the valence of Sm should tend to $m = 2$ when x approaches unity due to a decrease in the probability of Sm–Sm pairs meeting (see the dotted curve[1] in Fig. 2). The residual intermediate valence of Sm at $x \approx 1$ suggests an additional mechanism of 4*f*–5*d* hybridization upon formation of the intermediate valence state, for example, the second (one-center) mechanism in terms of the theory proposed in [3]. At present, the x dependence of the probability of the second mechanism, unlike the first mechanism, remains unknown. For this reason, the contribution of the second mechanism to the formation of the intermediate valence state can be estimated only for $x \approx 1$, when the contribution of the first mechanism is insignificant.

As can be seen from Fig. 2, the valences of Sm in the Sm(Ce)S, Sm(Gd)S, and Sm(Y)S systems at $x = 0.95$–0.98 are as follows: $m^* = 2.54 \pm 0.02$, 2.43 ± 0.02, and 2.51 ± 0.01, respectively. Thus, we found that the valence m^* of Sm in the Sm(Ce)S system with intracrystalline stretching for samarium atoms is almost identical to that in the Sm(Y)S system with intracrystalline contraction for samarium atoms and is larger than that in the intermediate Sm(Gd)S system. Hence, it follows that this channel of the 4*f*–5*d* hybridization is unrelated to the size effects. Therefore, it is necessary to consider the electronic factor.

The population of the 5*d* and 4*d* states of Gd, Ce, and Y in these systems can serve as a quantitative estimate of the electronic factor (Fig. 3). It can be seen from Fig. 3 that, within the limits of experimental error, the populations of the outer *d* (and *s*) states are independent of x. The weighed-mean values are $\bar{n}_d = 0.43 \pm 0.04$, 0.78 ± 0.03, and 1.07 ± 0.04 electrons/atom for Gd, Ce, and Y, respectively. A comparison of the values m^* and $\bar{n}_d$ for the Sm(R)S (R = Gd, Ce, Y) systems under investigation indicates a weak correlation between the valence of Sm and the population of *d* states.

Thus, the experimental dependence of the valence of Sm on the composition of the $Sm_{1-x}R_xS$ solid solutions can be satisfactorily explained by the superposition of two channels (mechanisms) of hybridization of the Sm 4*f* electron: the first channel provides hybridization of the 4*f* electron of an Sm atom with the 5*d* electron of neighboring Sm atom, and the second channel provides hybridization of the 4*f* electron of an Sm atom with its own 5*d* electron. In the case when the concentration x approaches unity, the contribution of the first (two-center) channel to the formation of the intermediate valence state becomes small due to the low probability of Sm–Sm pairs meeting. Because of this circumstance, the Sm valence in the system somewhat decreases. However, owing to the second (one-center) mechanism, the intermediate valence state in the system is retained up to $x \approx 1$. The valence of Sm and, consequently, the efficiency of the 4*f*–5*d* hybridization within the same Sm atom, most likely, are governed by the electronic factor (the electronic structure of R atoms) and are independent of the size effects (the radii of R ions).

[1] This curve corresponds to the dependence $m(x) = 2 + (m_0 + kx)(1 - x^{12})$, where the multiplier $(m_0 + kx)$ accounts for the experimental linear increase in the valence of Sm in the concentration range $x \approx x_{cr} - 0.8$.

ACKNOWLEDGMENTS

We would like to thank O.I. Sumbaev and K.E. Kir'yanov for their participation in discussions of the results and helpful remarks.

This work was supported by the Russian Foundation for Basic Research, project no. 99-02-16633. A.V. Golubkov acknowledges the support of the Russian Foundation for Basic Research (project no. 99-02-18078) in synthesizing the samples used in this study.

REFERENCES

1. D. I. Khomskiĭ, Usp. Fiz. Nauk **129** (3), 443 (1979) [Sov. Phys. Usp. **22**, 879 (1979)].
2. J. M. Lawrence, P. S. Riseborough, and R. D. Parks, Rep. Prog. Phys. **44** (1), 1 (1981).
3. K. A. Kikoin, E. G. Goryachev, and V. A. Gavrichkov, Solid State Commun. **60** (8), 663 (1986).
4. T. A. Kaplan and S. D. Mahanti, Phys. Lett. A **51** (5), 265 (1975).
5. A. E. Sovestnov, V. A. Shaburov, Yu. P. Smirnov, *et al.*, Fiz. Tverd. Tela (St. Petersburg) **39** (6), 1017 (1997) [Phys. Solid State **39**, 913 (1997)].
6. A. E. Sovestnov, V. A. Shaburov, and V. I. Kozlov, Fiz. Tverd. Tela (Leningrad) **23** (11), 3457 (1981) [Sov. Phys. Solid State **23**, 2009 (1981)].
7. A. Iandelli and A. Palenzona, in *Handbook on the Physics and Chemistry of Rare Earths*, Ed. by K. A. Gschneider, Jr. and L. Eyring (North-Holland, Amsterdam, 1979), Vol. 2, Chap. 13, p. 22.
8. A. Jayaraman, P. Dernier, and L. D. Longinotti, Phys. Rev. B **11** (8), 2783 (1975).
9. M. Campagna, S. T. Chui, G. K. Wertheim, and E. Tosatti, Phys. Rev. B **14** (2), 653 (1976).
10. O. I. Sumbaev, in *Modern Physics in Chemistry* (Academic, New York, 1977), Vol. 1, No. 4, p. 33.
11. I. M. Band and V. I. Fomichev, Preprint LIYaF-498 (Leningrad, 1979).

Translated by N. Korovin

Physics of the Solid State, Vol. 44, No. 8, 2002, pp. 1574–1578. Translated from Fizika Tverdogo Tela, Vol. 44, No. 8, 2002, pp. 1501–1505.

SEMICONDUCTORS AND DIELECTRICS

Defect Samarium Ions and Electromotive-Force Generation in SmS

V. V. Kaminskiĭ, A. V. Golubkov, and L. N. Vasil'ev

Ioffe Physicotechnical Institute, Russian Academy of Sciences, ul. Politekhnicheskaya 26, St. Petersburg, 194021 Russia

e-mail: Vladimir.Kaminski@pop.ioffe.rssi.ru

Received November 29, 2001

Abstract—A model explaining electromotive-force generation in SmS under heating in the absence of external temperature gradients is considered. An analysis of data on the density of SmS single crystals with compositional deviations from stoichiometry in the homogeneity range suggests that excess samarium ions occupy vacancies on the sulfur sublattice. Possible concentrations of defect samarium ions are determined (up to 2.8×10^{21} cm^{-3}). The temperature interval within which electromotive force appears in various SmS samples (440–640 K) and the critical conduction-electron concentrations at which the generation sets in [$(6.0–8.5) \times 10^{19}$ cm^{-3}] are calculated. An expression permitting estimation of the magnitude of the observed effect is proposed. © *2002 MAIK "Nauka/Interperiodica".*

1. INTRODUCTION

Samarium sulfide (SmS) samples heated in the absence of external temperature gradients were found to generate an appreciable emf of 2.5 V in a 1.3-s pulse [1] and 0.6 V in a continuous regime [2]. The mechanism of the emf generation is related to the existence of defect samarium ions in this semiconductor material [1, 3]. When a sample is heated to the temperature at which the emf generation sets in (T_b), electrons excited primarily from impurity levels ($E_i \sim 0.045 \pm 0.015$ eV [4]) build up in the conduction band to a critical concentration n_b. These levels are associated with defect Sm^{2+} ions, whose position in the SmS lattice (NaCl type) is not fully clear [5]. The concentration n_b turns out to be high enough to screen the defect ion Coulomb potential to the extent necessary for complete delocalization of electrons from the E_i levels and crossover of the impurity samarium ions to the trivalent state. This collective process has a stepwise character. However, the defect ions are distributed nonuniformly over the sample; therefore, the above process does not occur simultaneously throughout the sample. This results in the creation of large conduction electron concentration gradients; it is this that accounts for the emf. Indeed, diffusion of carriers in a sample generates an electrical current with a density

$$j = eD\text{grad}n, \tag{1}$$

where D is the electron diffusion coefficient in SmS. Because the electrical resistivity of SmS at a time close to the onset of emf generation and in the sample region near that where the effect occurs is $\rho \approx (en_bu)^{-1}$, we can write for the associated electric field

$$E \approx \frac{D}{n_b u}\text{grad}n, \tag{2}$$

where u is the conduction electron mobility.

An analysis in terms of this model requires more accurate determination of the positions occupied by defect samarium ions in SmS and of the range of their possible concentrations. This will allow one to make calculations similar to those performed by us in [3] and to estimate the possible values of the emf generation parameters (T_b, n_b, etc.), as well as to choose the direction of research to be pursued.

2. DEFECT STRUCTURE OF SmS IN THE HOMOGENEITY RANGE

In stoichiometric SmS (even single-crystal samples), one observes, as a rule, inclusions of a second phase, Sm_3S_4, in amounts of ~1 vol % [6]. This means that the remainder of the sample, nominally pure SmS, should contain excess samarium ions. Because the homogeneity range of SmS extends toward excess samarium, one has to study the properties of SmS in the homogeneity range in order to learn the arrangement of the defect samarium ions in the lattice and their energy state.

It was established that samarium monosulfide is a one-sided variable-composition phase extending from 50 to 54 at. % Sm [7–9]. The Hall coefficient, electrical conductivity, thermopower, and lattice thermal conductivity vary strongly with composition within the range 50.0–50.5 at. % Sm and smoothly in the range from 50.5 to 54.0 at. % Sm. The density of the solid solution increases smoothly throughout the homogeneity range,

while the lattice constant varies very little. Within the homogeneity range, the properties of SmS change from semiconducting to semimetallic.

Figure 1 shows the experimental (points) and calculated density as a function of composition, the curves being constructed for the following three models of SmS crystallochemical structure: (1) the excess samarium occupies interstitial lattice sites (curve *1*); (2) in the SmS lattice with excess samarium, vacancies form on the sulfur sublattice in corresponding quantity (curve *2*); and (3) the excess samarium ions fill the vacancies on the sulfur sublattice (curve *3*) (see below).

As seen from Fig. 1, model *1* does not conform to the experimental composition dependence of the density. Model 2 is valid for low concentrations only. Model 3 is applicable throughout the concentration range covered. The deviation of the experimental density from that given by model *1* toward lower values indicates vacancy formation in the lattice. Vacancy formation through removal of sulfur atoms from the samarium monosulfide lattice is impossible in our case, because no sulfur-deficient SmS phase exists.

The mechanism of formation of an SmS-based solid solution in models 2 and 3 can be schematically conceived in the following way. Let us consider a sealed container housing an SmS crystal and a quantity of samarium. As the temperature is increased, sulfur atoms escape from the crystal surface with the formation of surface vacancies. After this, sulfur diffuses toward the surface and the vacancies move into the bulk of the crystal. As for the samarium vapors in the container, part of them react with the sulfur, diffusing out onto the surface to form new unit cells, while the remainder diffuse into the bulk. Curve *2* in Fig. 1 was drawn under the assumption that the number of sulfur vacancies is equal to that of the incorporated samarium atoms. This solid solution will have the following crystallochemical formula:

$$\frac{1}{1-p}\mathrm{Sm}_{1+p}\mathrm{S}_{1-p}V_p, \tag{3}$$

where $p = x/(2 + x)$ is the number of sulfur vacancies (V) and x is the samarium excess in the formula $\mathrm{Sm}_{1+x}\mathrm{S}$. By expressing p through x, we obtain

$$\mathrm{SmS} + x\mathrm{Sm} = \frac{2+x}{2} \times [\mathrm{Sm}_{1+x/(2+x)}\mathrm{S}_{1-x/(2+x)}V_{x/(2+x)}]. \tag{4}$$

The density calculated within model 2 can be written as

$$d_{\mathrm{calc}} = \frac{Z}{Na^3}\left[M_{\mathrm{Sm}}\left(1+\frac{x}{2+x}\right) + M_{\mathrm{S}}\left(1-\frac{x}{2+x}\right)\right], \tag{5}$$

where $Z = 4$ is the number of samarium and sulfur atoms in the SmS unit cell of stoichiometric composition; N is Avogadro's number; M_{Sm} and M_{S} are the atomic masses of samarium and sulfur, respectively;

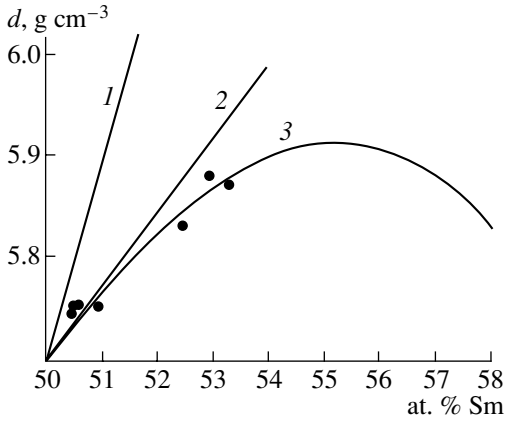

Fig. 1. Density of SmS samples with excess samarium vs. their composition. Points are experiment and curves *1–3* are calculations using models 1–3, respectively.

and $a = 5.97$ Å is the SmS unit-cell parameter. As seen from Fig. 1, the density calculated from this expression fits well (within the error of density determination) the experimental results for low samarium concentrations, ~50.0–50.5 at. % Sm.

The densities determined experimentally for the compositions ~50.5–54.0 at. % Sm lie below the values calculated using Eq. (5). This presupposes an increase in the fraction of vacancies in the real solid solution. We made an assumption that the number of vacancies is proportional not to the atomic fraction of sulfur, $1/(2 + x)$, but rather to that of samarium, $(1 + x)/(2 + x)$. The crystallochemical formula for this model takes on the form

$$\mathrm{SmS} + x\mathrm{Sm} = \frac{2+x}{2-x^2} \times [\mathrm{Sm}_{(1+x)(2-x^2)/(2+x)}\mathrm{S}_{(2-x^2)/(2+x)}V_{x(1+x)/(2+x)}], \tag{6}$$

and the density can be calculated from the expression

$$d_{\mathrm{calc}} = \frac{Z}{Na^3}\left[M_{\mathrm{Sm}}(1+x)\frac{2-x^2}{2+x} + M_{\mathrm{S}}\frac{2-x^2}{2+x}\right]. \tag{7}$$

As seen from curve *3* in Fig. 1, the calculated density agrees well with the experimental results throughout the solid-solution concentration region covered. Continuing the calculation with Eq. (7) beyond the homogeneity range, we find a maximum at a composition of 55.3 at. % Sm. Beyond this samarium concentration, the density of the solid solution decreases. The number of vacancies grows so rapidly that the solid-solution phase becomes unstable.

Thus, according to this model, excess samarium ions with a concentration $N_i = (4/a^3)x/(1 + x)$ (curve *1* in Fig. 2) occupy vacancies on the sulfur sublattice. As

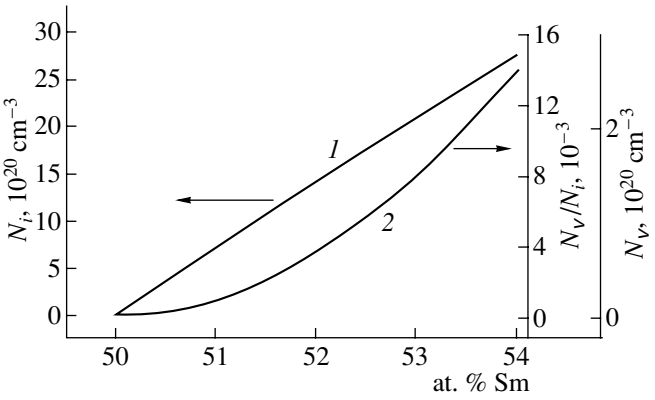

Fig. 2. Concentrations of (*1*) impurity (excess) samarium ions and (*2*) vacancies on the sulfur sublattice in SmS within the homogeneity range vs. deviation from stoichiometry.

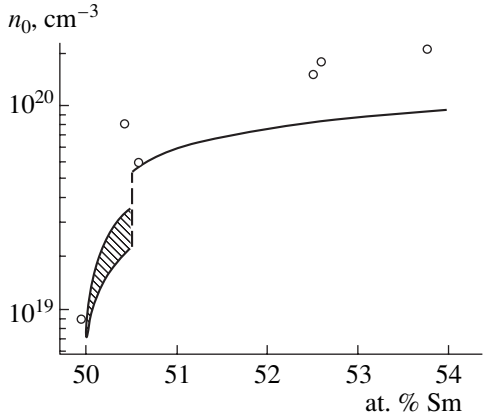

Fig. 3. Conduction electron concentration vs. composition plot in the SmS homogeneity range. Points are experiment, and curves are calculations (the area of calculated values of n_0 for $0.03 < E_i < 0.06$ eV is hatched).

seen from the ratio N_V/N_i, where $N_V = (4/a^3)x^2/(2 + x)$ (curve *2* in Fig. 2), part of the vacancies remain unfilled.

3. THE ENERGY STATE OF DEFECT SAMARIUM IONS IN SmS

The excess samarium ions are responsible for the carrier activation energy E_i derived from the temperature dependences of the electrical conductivity of SmS samples of various compositions measured in the homogeneity range at temperatures from 100 to 500 K. The activation energy E_i decreases from ~0.1 eV to 0 with increasing number of excess ions [6, 8, 10]. The value $E_i = 0$ is reached in the composition with 50.5 at. % Sm, which corresponds to $N_i \sim 4 \times 10^{20}$ cm^{-3} (Fig. 2), and remains unchanged in all compositions with higher samarium contents [6].

Stoichiometric SmS samples did not exhibit any features in the behavior of E_i. However, as follows from an earlier study by Zhuze *et al.* [11], the value of E_i in SmS varies in the 0.04- to 0.07-eV interval. It was shown later [4] that E_i in SmS can vary from sample to sample and is 0.045 ± 0.015 eV.

Let us use the concentration model developed by us for the piezoresistivity of SmS based on the solution to the charge neutrality equation [12]. Using the values of N_i from Fig. 2 and taking into account the above reasoning on the magnitude of E_i (E_i = 0.03–0.06 eV for $N_i < 4 \times 10^{20}$ cm^{-3} and $E_i = 0$ for $N_i > 4 \times 10^{20}$ cm^{-3}), we calculate the behavior of the conduction electron concentration n_0 for SmS samples in the homogeneity range. The curve obtained (Fig. 3) satisfactorily describes the experimental data of [8]. Thus, our values of N_i and E_i are realistic.

4. CALCULATION OF THE CRITICAL EMF GENERATION PARAMETERS FOR SmS SAMPLES OF STOICHIOMETRIC COMPOSITION

Determination of the temperature interval within which emf generation can take place and, primarily, of the lowest possible values of T_b is an important problem. It appears natural that these values should be reached in samples with the minimum E_i and maximum n_0. Figure 4 presents the dependence of the conduction electron concentration in SmS on the concentration of defect samarium ions (curve *1*). This dependence was calculated within the concentration model [12] for the following parameters: $m^* = m_0$, $E_i = 0.03$ eV, and the samarium 4*f* level depth $E_f = 0.23$ eV and density $N_f = 1.8 \times 10^{22}$ cm^{-3}. As shown by a large number of our measurements of the Hall concentration of carriers in SmS single crystals of stoichiometric composition, n_0 at $T = 300$ K cannot exceed 3.5×10^{19} cm^{-3}. Therefore, as follows from Fig. 4, the maximum value of N_i at $E_i = 0.03$ eV can be $\sim 5 \times 10^{20}$ cm^{-3}.

As shown in [3], as the temperature increases, emf generation sets in when the effective Bohr radius of the impurity a_B becomes equal to the Debye screening radius a_D of the impurity electric potential by the conduction electrons,

$$a_B = \frac{\varepsilon_0 \hbar^2}{m^* e^2},$$

$$a_D = \left[\frac{4\sqrt{2}e^2 m^{*3/2}(k_0 T)^{1/2}}{\pi \varepsilon_0 \hbar^3} F_{1/2}(\mu)\right]^{-1/2},$$

where $\varepsilon_0 = 18$ is the static dielectric permittivity of SmS [13], $F_{1/2}(\mu) = \int_0^\infty (-\partial f_0/\partial x) x^{1/2} dx$, $f_0(x, \mu) = [1 + \exp(x - \mu)]^{-1}$ is the Fermi integral, and μ is the reduced chemical potential. Using the condition $a_B = a_D$ with

the above values of m^*, E_i, and N_i, we numerically calculated the temperatures T at which electrons are delocalized from the E_i levels in the case of arbitrary degeneracy for various values of N_i. The functions $T_b(N_i)$ are presented in Fig. 4 for $E_i = 0.03$ and 0.06 eV (curves *2*, *3*, respectively). Recalling that $N_i = 5 \times 10^{20}$ cm^{-3}, we obtain from curve *2* the minimum value of $T_b \approx 440$ K. The maximum possible temperatures of the onset of generation $T_b \sim 640$ K, which can be derived from curves *2* and *3*, correspond to the minimum values of N_i and do not depend on E_i. Thus, our calculations show that the temperature T_b for SmS single crystals can range from 440 to 640 K in various samples. This conclusion is in accord with the experimentally observed values 435–455 [14], 375–405 [1], 455 [3], 390–670 [2], and 530 K [15].

Figure 4 also displays calculated critical concentrations n_b for $E_i = 0.03$ and 0.06 eV (curves *4*, *5*, respectively). As follows from these data, in SmS of stoichiometric composition, n_b can assume values in the interval $(6.0–8.5) \times 10^{19}$ cm^{-3}.

The calculated values of n_b can be compared with experiment. Delocalization of electrons from the impurity levels E_i not only accounts for the emf generation in SmS but plays, as it were, the role of a trigger for the semiconductor–metal phase transition driven in SmS by hydrostatic pressure. The latter was shown in [16]. It follows that the values of n_b should be equal to the critical concentrations of the conduction electrons n_c at which this phase transition occurs. The values of n_c were measured by us earlier [17]. Figure 5 shows experimental values of n_c (taken from [17]) together with the calculated n_b curves. Taking into account the error of ~15% with which the values of n_c were measured, the calculations can be considered to be in satisfactory agreement with experiment. This provides support for our model of the emf generation and for its intimate relation with the model of the semiconductor–metal phase transition in SmS, an observation that has already been pointed out [1, 14].

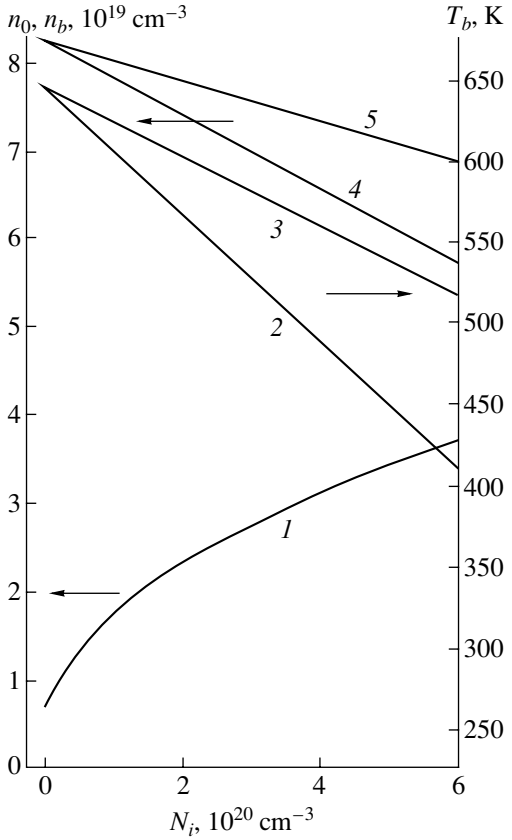

Fig. 4. SmS parameters calculated as functions of defect samarium ion concentration: (*1*) conduction electron concentration ($T = 300$ K) for $E_i = 0.03$ eV; (*2*, *3*) emf generation onset temperature for $E_i = 0.03$ and 0.06 eV, respectively; and (*4*, *5*) critical conduction electron concentrations for the onset of emf generation for $E_i = 0.03$ and 0.06 eV, respectively.

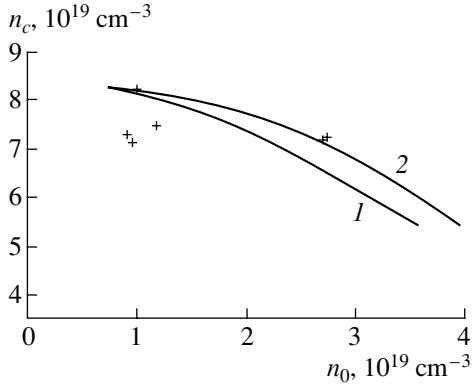

Fig. 5. Critical conduction electron concentration for the semiconductor–metal phase transition in SmS at $T = 300$ K (experimental points) and for the onset of emf generation (calculated curves *1* and *2* for $E_i = 0.03$ and 0.06 eV, respectively) plotted vs. conduction electron concentration at $T = 300$ K and $P = 0$.

5. DISCUSSION AND CONCLUSIONS

The above analysis of the electrophysical properties and of the structural features of SmS shows the presence of excess samarium ions to play a decisive role in the emf generation in SmS samples under heating in the absence of external temperature gradients. The generation onset temperature depends on the samarium ion concentration, and the emf amplitude depends on the gradient of this concentration. As follows from Eq. (2),

$$E = K \mathrm{grad} N_i. \quad (8)$$

The coefficient K depends in a complicated way on T, m^*, ε_0, N_i, and E_i, as well as on the actual conduction electron scattering mechanism, and, hence, requires empirical determination. The quantity $\mathrm{grad}N_i$ can be chosen by properly doping stoichiometric SmS by excess samarium atoms. As seen from Fig. 3, the magnitude of the effect under study (E) can be efficiently

increased by doping only to a level of 50.5 at. % Sm. When doped to higher concentrations, the excess Sm ions will play only a passive part under heating, because in this case $E_i = 0$. The latter is apparently due to the fact that $a_D < a_B$ already at room temperature and that the conduction electron concentration is above the critical level needed for the emf generation to set in. Thus, Eq. (8) is valid for stoichiometric SmS and compositions deviating from stoichiometry by up to ~0.5 at. % toward samarium excess.

Our analysis of the above model of emf generation in SmS suggests that similar effects can also be observed in other semiconducting compounds. The condition necessary for this effect to occur is the presence of a donor impurity distributed nonuniformly over the bulk of the sample at a concentration high enough for the equality $a_D = a_B$ to set in under the action of an external factor (temperature, pressure, etc.). Indeed, we observed emf generation under uniform heating of $Sm_{0.99}Gd_{0.01}S$ and $SmTe_xS_{1-x}$ with $x = 0.02$ and 0.05.

ACKNOWLEDGMENTS

The authors are indebted to M.M. Kazanin for helpful discussions and to M.V. Romanova for measurements on the SmS solid solutions.

This study was supported by the Russian Foundation for Basic Research, project no. 00-02-16947.

REFERENCES

1. V. V. Kaminskiĭ and S. M. Solov'ev, Fiz. Tverd. Tela (St. Petersburg) **43** (3), 423 (2001) [Phys. Solid State **43**, 439 (2001)].
2. V. V. Kaminskiĭ, in *Proceedings of the International Workshop on Results of Fundamental Research for Investments' 2001 "Nonconventional and Renewable Energy Sources," St. Petersburg, 2001*, p. 45.
3. V. V. Kaminskiĭ, L. N. Vasil'ev, M. V. Romanova, and S. M. Solov'ev, Fiz. Tverd. Tela (St. Petersburg) **43** (6), 997 (2001) [Phys. Solid State **43**, 1030 (2001)].
4. A. V. Golubkov, E. V. Goncharova, V. A. Kapustin, *et al.*, Fiz. Tverd. Tela (Leningrad) **22** (12), 3561 (1980) [Sov. Phys. Solid State **22**, 2086 (1980)].
5. A. V. Golubkov, N. F. Kartenko, V. M. Sergeeva, and I. A. Smirnov, Fiz. Tverd. Tela (Leningrad) **20** (1), 228 (1978) [Sov. Phys. Solid State **20**, 126 (1978)].
6. A. V. Golubkov and V. M. Sergeeva, Zh. Vses. Khim. O-va. **26** (6), 645 (1981).
7. V. M. Sergeeva, E. V. Goncharova, N. F. Kartenko, *et al.*, Izv. Akad. Nauk SSSR, Neorg. Mater. **8**, 2114 (1972).
8. V. P. Zhuze, E. V. Goncharova, N. F. Kartenko, *et al.*, Phys. Status Solidi A **18**, 63 (1973).
9. V. M. Sergeeva, Author's Abstract of Candidate's Dissertation (Leningr. Gos. Univ., Leningrad, 1972).
10. A. V. Golubkov, E. V. Goncharova, V. P. Zhuze, G. M. Loginov, V. M. Sergeeva, and I. A. Smirnov, *Physical Properties of Chalcogenides of Rare-Earth Elements* (Nauka, Leningrad, 1973).
11. V. P. Zhuze, A. V. Golubkov, E. V. Goncharova, *et al.*, Fiz. Tverd. Tela (Leningrad) **6** (1), 268 (1964) [Sov. Phys. Solid State **6**, 213 (1964)].
12. L. N. Vasil'ev and V. V. Kaminskiĭ, Fiz. Tverd. Tela (St. Petersburg) **36** (4), 1172 (1994) [Phys. Solid State **36**, 640 (1994)].
13. V. Zelezhy, J. Petzelt, V. V. Kaminski, *et al.*, Solid State Commun. **72** (1), 43 (1989).
14. M. M. Kazanin, V. V. Kaminskiĭ, and S. M. Solov'ev, Zh. Tekh. Fiz. **70** (5), 136 (2000) [Tech. Phys. **45**, 659 (2000)].
15. V. V. Kaminskiĭ and M. M. Kazanin, in *Proceedings of the VII Intergovernmental Workshop "Thermoelectrics and Their Applications," St. Petersburg, 2000*, p. 215.
16. V. V. Kaminskiĭ, V. A. Kapustin, and I. A. Smirnov, Fiz. Tverd. Tela (Leningrad) **22** (12), 3568 (1980) [Sov. Phys. Solid State **22**, 2091 (1980)].
17. S. I. Grebinskiĭ, V. V. Kaminskiĭ, A. V. Ryabov, and N. N. Stepanov, Fiz. Tverd. Tela (Leningrad) **24** (6), 1874 (1982) [Sov. Phys. Solid State **24**, 1069 (1982)].

Translated by G. Skrebtsov

Physics of the Solid State, Vol. 44, No. 8, 2002, pp. 1579–1586. Translated from Fizika Tverdogo Tela, Vol. 44, No. 8, 2002, pp. 1506–1512.

SEMICONDUCTORS AND DIELECTRICS

Specific Features of Anion Transfer in Superionic Conductors Based on MF_2 (M = Pb and Cd)

N. I. Sorokin*, B. P. Sobolev*, and M. W. Breiter**

** Shubnikov Institute of Crystallography, Russian Academy of Sciences, Leninskiĭ pr. 59, Moscow, 117333 Russia*

*** Technical University, Vienna, Austria*

Received December 13, 2001

Abstract—Fluoride-conducting superionic conductors in the PbF_2–CdF_2, PbF_2–SnF_2, PbF_2–ScF_3, CdF_2–HoF_3, and CdF_2–ErF_3 systems are studied over a wide range of temperatures (130–1073 K). The thermal stability of the electrical conduction characteristics and the smeared transition to the superionic state (10^{-1}–1 S/cm) are investigated in PbF_2, $Pb_{0.67}Cd_{0.33}F_2$, and $Pb_{1-x}Sc_xF_{2+x}$ (x = 0.01 and 0.1) single crystals and a $PbSnF_4$ polycrystalline sample. In the $Cd_{1-x}R_xF_{2+x}$ solid solutions (R = Ho and Er, $0.02 \le x \le 0.20$), the crossover from one mechanism of ion transfer to the other mechanism is revealed in the temperature range 600–800 K. The correlation between the anion transfer and specific features in the defect structure of crystals is discussed. © *2002 MAIK "Nauka/Interperiodica".*

1. INTRODUCTION

Solid solutions of $Pb_{1-x}Sc_xF_{2+x}$ ($0 \le x \le 0.15$), $Pb_{1-x}Cd_xF_2$ ($0 \le x \le 1$), and $Cd_{1-x}R_xF_{2+x}$ (R = La–Lu, $x \ge 0.1$) with a fluorite-type (CaF_2) structure and the $PbSnF_4$ compound with a fluorite-derivative structure are characterized by high fluorine anionic conductivities, which offers actual possibilities of using these materials in different devices of solid state ionics [1, 2]. The understanding of the mechanisms of anion transfer in superionic conductors based on MF_2 (M = Pb and Cd) calls for investigation over a wide range of temperatures. In the present work, we analyzed the specific features in the anionic conductivity σ of PbF_2, $Pb_{1-x}Sc_xF_{2+x}$ (x = 0.01 and 0.1), and $Pb_{1-x}Cd_xF_2$ (x = 0.33) single crystals in the temperature range 130–873 K; $Cd_{1-x}R_xF_{2+x}$ (R = Ho and Er, $0.02 \le x \le 0.2$) single crystals in the range 293–1073 K; and $PbSnF_4$ polycrystals in the range 140–597 K. The choice of the studied compositions of the fluorite solid solutions was made for the following reasons. The isovalent substitution $Pb^{2+} \longrightarrow Cd^{2+}$ in $Pb_{1-x}Cd_xF_2$ leads to the highest conductivity σ of the solid solution at x = 0.33 (the composition corresponding to a minimum in the melting curve) [1, 3]. The heterovalent substitution $Pb^{2+} \longrightarrow Sc^{3+}$ in $Pb_{1-x}Sc_xF_{2+x}$ results in the formation of a nonstoichiometric phase with the highest conductivity at x = 0.1 [1]. In $Cd_{1-x}R_xF_{2+x}$ solid solutions, a decrease in the ionic radius of rare-earth cations (from La to Lu) is attended by an increase in the anionic conductivity due to a decrease in the activation enthalpy of electrical conduction [4]. The preliminary results of investigations of these crystals in the temperature range from 293 to 500 K were published in our earlier papers [3–6].

2. SAMPLES AND EXPERIMENTAL TECHNIQUE

Single crystals of the $Pb_{0.67}Cd_{0.33}F_2$, $Pb_{1-x}Sc_xF_{2+x}$ (x = 0.01 and 0.10), $Cd_{1-x}Ho_xF_{2+x}$ (x = 0.02, 0.03, 0.04, and 0.11), and $Cd_{1-x}Er_xF_{2+x}$ (x = 0.03 and 0.20) solid solutions were grown by planar crystallization from melt at the Laboratory of Fluoride Materials of the Shubnikov Institute of Crystallography, Russian Academy of Sciences [3–5]. The crystals were free from scattering inclusions of oxygen-containing phases (the oxygen impurity content was of the order of 0.01–0.02 wt %) and had a fluorite-type structure (cubic crystal system, space group $Fm3m$), as was confirmed by x-ray diffraction.

The chemical composition of the solid solutions corresponded to that of the initial batches (the discrepancy did not exceed ±1 mol %). The content of impurity components in the single crystals was checked against the composition dependences of the lattice parameters of the solid solutions. The parameter of the cubic lattice a = 5.755 Å for $Pb_{0.67}Cd_{0.33}F_2$ coincides with the data available in the literature [3, 7]. The single-crystal samples suitable for electrical measurements were cut from transparent regions of the crystals grown under stationary conditions. The thickness of the samples was equal to 1–2 mm, and their surface area was 25–40 mm^2. The operating surfaces of the single-crystal samples were subjected to optical finishing and ultrasonic cleaning in acetone (Bransonic 221). The quality of the samples was examined using a Zeiss KL1500 optical microscope.

Samples of PbF_2 in the form of small-sized crystals (1–2 mm) and $PbSnF_4$ in the form of a finely crystalline powder were prepared by the hydrothermal method at

the Laboratory of Hydrothermal Synthesis of the Shubnikov Institute of Crystallography, Russian Academy of Sciences [6]. Crystals of PbF_2 and, especially, $PbSnF_4$ are characterized by a complex polymorphism; hence, their properties substantially depend on the synthesis procedure and thermal prehistory. As a consequence of this circumstance, there is disagreement between available data on the thermal, structural, and conductometric characteristics of these materials. X-ray powder diffraction analysis revealed that the samples prepared have a single-phase composition. Moreover, it was found that, prior to thermal analysis, the PbF_2 samples had an α-PbF_2 structure (orthorhombic crystal system, space group *Pcnm*, a = 7.652 Å, b = 6.439 Å, and c = 3.899 Å [6]) and the $PbSnF_4$ samples had an α'-$PbSnF_4$ structure (monoclinic crystal system, space group $P2_1/n$, a = 4.191 Å, b = 4.193 Å, c = 22.96 Å, and $\gamma = 91°72'$ [6]). The ionic conductivity of PbF_2 was examined using single-crystal samples. For measurements of the ionic conductivity in $PbSnF_4$, the powder of this compound was carefully ground and pressed into pellets 5 mm in diameter and 2–4 mm thick under a high pressure (4–5 MPa).

The thermal analysis was performed on a Setaram DTA/TG 92-12 instrument at a rate of 5–10 K/min in a flow of gaseous nitrogen in the temperature range from 293 to 1073 K. The electrical properties were measured on a Solartron 1260 impedometer under an alternating current in the frequency range from 10^{-1} to 10^7 Hz. The electrodes were fabricated from a silver paste. The voltage across the samples was equal to 30 mV. The impedance of the crystals was measured in a nitrogen flow at high temperatures (from 293 to 1073 K) and under vacuum (at a residual pressure of 10^{-3} Pa) at low temperatures (from 130 to 410 K). The experimental setups for high-temperature and low-temperature electrical measurements were described in detail in [8, 9]. The parameters of the anion transfer were calculated according to the formula $\sigma T = A\exp(-\Delta H/kT)$, where ΔH is the activation enthalpy of electrical conduction.

3. RESULTS AND DISCUSSION

3.1. Superionic conductors based on PbF_2. Figures 1 and 2 depict the temperature dependences of the anionic conductivity measured in the studied samples with the use of low-temperature and high-temperature techniques. Table 1 presents the electrical characteristics of the crystals and the data available in the literature for β-PbF_2 with a fluorite structure.

The electrical investigations of the low-temperature α-PbF_2 modification (space group *Pcnm*) were performed with two single crystals (oriented perpendicularly to the *c* axis) upon heating from 300 to 873 K and subsequent cooling to 327 K. As can be seen from Fig. 1, both samples are characterized by a good reproducibility of the results obtained upon heating and cooling. An increase in the temperature leads to a drastic increase in the anionic conductivity $\sigma(T)$ in the vicinity of 600 K due to an irreversible polymorphic transition from the orthorhombic (α) PbF_2 modification to the cubic (β) PbF_2 modification. The occurrence of the α–β irreversible phase transition is confirmed by a sharp narrow peak appearing in the thermograms at ~630 K upon first heating that is absent upon subsequent cooling and in the second heating–cooling cycle. The activation enthalpy of electrical conduction in the temperature range of the existence of the α-PbF_2 phase (300–600 K) is equal to 0.38 eV. This suggests that the ion transfer proceeds through the vacancy mechanism [11] associated with the presence of background impurities in the samples.

In the temperature range of the existence of the β-PbF_2 modification, the dependence $\sigma(T)$ at $T \approx 710$ K exhibits the second feature, which reflects a gradual transformation of the fluorite structure into the state with a high anionic conductivity (the so-called smeared

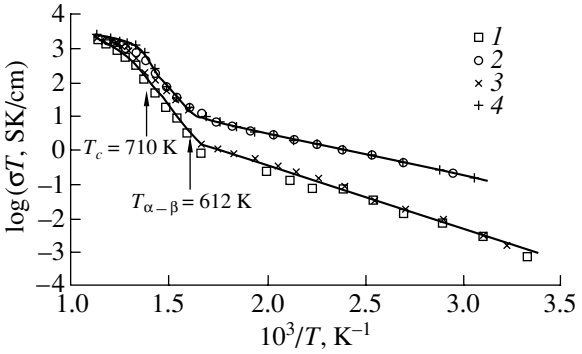

Fig. 1. Temperature dependences of the anionic conductivity measured normally to the *c* axis of α-PbF_2 single crystals upon (*1*, *3*) heating and (*2*, *4*) cooling: (*1*, *2*) sample 1 and (*3*, *4*) sample 2.

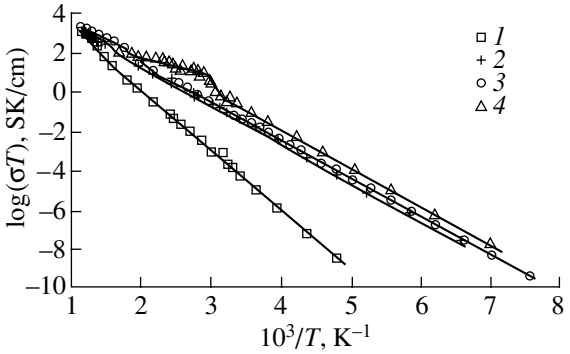

Fig. 2. Temperature dependences of the anionic conductivity of (*1*) $Pb_{0.99}Sc_{0.01}F_{2.01}$, (*2*) $Pb_{0.9}Sc_{0.1}F_{2.1}$, and (*3*) $Pb_{0.67}Cd_{0.33}F_2$ single crystals and (*4*) the β-$PbSnF_4$ polycrystalline sample.

Table 1. Electrical characteristics of PbF_2-based superionic conductors

Crystal	T_m, K*	T_c, K	σ, S/cm	ΔH, eV	σ, S/cm	ΔH, eV
			$T < T_c$, 293 K		$T < T_c$	
β-PbF_2	1098	711 ± 7	1×10^{-8} [10]	0.67 [10]	2 (873 K)	0.30
$Pb_{0.99}Sc_{0.01}F_{2.01}$	~1095	573–673	3×10^{-6}	0.60	1.2 (873 K)	0.30
$Pb_{0.9}Sc_{0.1}F_{2.1}$	~1085	573–673	1×10^{-4}	0.40	1.2 (873 K)	0.30
$Pb_{0.67}Cd_{0.33}F_2$	1023	513–621	2×10^{-4}	0.39	2.5 (873 K)	0.32
β-$PbSnF_4$	663–773	285–340	4×10^{-4}	0.39	0.2 (597 K)	0.16

* Melting temperature.

superionic transition in β-PbF_2 fluorite crystals [12]). The transformation of the fluorite structure into the superionic state is accompanied by disordering of the anionic sublattice (according to the data obtained by different methods, the concentration of mobile defects amounts to only several percent [12, 13]). This manifests itself in the behavior of the thermal properties of single-crystal samples upon thermal cycling: smeared thermal effects are observed at ~709 K (first heating), ~684 K (first cooling), ~706 K (second heating), and ~696 K (second cooling). In the superionic "phase" of the β-PbF_2 modification, the estimated enthalpy of ion transfer ΔH = 0.30 eV is in good agreement with the results obtained by other methods, namely, ΔH = 0.26 ± 0.05 eV [13] (neutron diffraction), 0.2 eV [14] (^{19}F NMR), and 0.25–0.30 eV [15] (conductometry). A subsequent decrease in the temperature of lead fluoride results in a crossover from the mechanism of intrinsic conduction through migration of anion Frenkel defects (F_i interstitial ions and V_F vacancies) to the vacancy mechanism of extrinsic conduction with the enthalpy ΔH = 0.24 eV (according to [10, 15], the enthalpy of migration of fluorine vacancies is equal to 0.23–0.26 eV).

The behavior of the dependence σ(T) changes in the range 573–673 K for $Pb_{1-x}Sc_xF_{2+x}$ (x = 0.01 and 0.1) single crystals and in the range 513–621 K for $Pb_{0.67}Cd_{0.33}F_2$ single crystals (Fig. 2), most likely, due to a superionic transition in the fluorite structures. The thermograms of the $Pb_{0.99}Sc_{0.01}F_{2.01}$ crystal exhibit broad peaks in three heating–cooling cycles: the initial portions of the thermal effect upon heating and cooling correspond to ~693 K and ~683 K, respectively. For the $Pb_{0.9}Sc_{0.1}F_{2.1}$ crystal, no thermal effects are revealed upon heating in two cycles and a very weak peak is observed at 638–643 K upon cooling. The thermograms of the $Pb_{0.67}Cd_{0.33}F_2$ crystal show no thermal effects in two cycles.

Upon introduction of ScF_3 impurities, additional anions are located at interstices of the fluorite matrix: ScF_3 (PbF_2) $\longrightarrow$ Sc_{Pb}^{+} + F_i^- + $2F_F$. The mechanism of ion transfer in anion-excessive solid solutions of $Pb_{1-x}Sc_xF_{2+x}$ is associated with the migration of F_i^- ions. An increase in the ScF_3 concentration in $Pb_{1-x}Sc_xF_{2+x}$ solid solutions by one order of magnitude (from 1 to 10 mol %) results in an increase in the anionic conductivity at 293 K by a factor of approximately 600. This change in the characteristics of ion transfer can be caused by the increase in the mobility of the impurity charge carriers F_i involved in the transfer due to the decrease in the height of the potential barriers [5, 16]. At $T < T_c$, the enthalpy of migration of F_i^- interstitial ions is estimated to be ΔH = 0.60 eV (210–640 K) for the $Pb_{0.99}Sc_{0.01}F_{2.01}$ crystal and ΔH = 0.40 eV (153–590 K) for the $Pb_{0.9}Sc_{0.1}F_{2.1}$ crystal.

The introduction of the CdF_2 component into the PbF_2 fluorite matrix does not bring about the formation of additional fluorine ions. At the same time, the mismatch between the ionic radii and the difference in the electronic configurations of Pb^{2+} and Cd^{2+} cations lead to a decrease in the cation–anion interaction coefficients (a weakening of ionic bonds) for $Pb_{1-x}Cd_xF_2$ solid solutions as compared to those for the β-PbF_2 matrix [17]. In turn, this results in a decrease in the energies of formation and migration of mobile defects and, eventually, is responsible for an increase in the conductivity. In the temperature range below T_c, the activation enthalpy of anion transfer in the $Pb_{0.67}Cd_{0.33}F_2$ crystal is estimated as ΔH = 0.388 ± 0.001 eV (132–532 K). This is in good agreement with the enthalpy ΔH = 0.38 ± 0.01 eV (293–480 K) determined in our earlier conductometric study [3].

In [18], the ion mobility and the structure of $Pb_{1-x}Cd_xF_2$ solid solutions were investigated by ^{19}F, ^{111}Cd, and ^{207}Pb NMR spectroscopy and x-ray diffraction. Analysis of the evolution of the ^{19}F NMR spectra (the appearance of a narrow line, a partial narrowing of a broad component, and a stepwise decrease in the second moment) revealed two types of F^- ions with different diffusion mobilities. The high mobility of a number of F^- ions (the mobile subsystem) and structural disordering of Pb^{2+} ions are responsible for the deficit of anions in general 8c positions (space group $Fm3m$). As the temperature increases, the number of F^- ions

increases in the immobile subsystem and, correspondingly, decreases in the mobile subsystem. According to x-ray diffraction analysis, a number of cations (for the most part, Cd cations) are displaced from the general 4*a* positions by a distance of ~0.2 Å along the fourfold and threefold axes. Most likely, this corresponds to the formation of clusters composed of defects (defect regions) in the solid solution crystal without a change in its cubic macrosymmetry. As a variant of these regions, the authors proposed an ordered (tetragonal) structure of the Ba_2ZnF_6 type which is misoriented with an equal probability over three possible directions of the fourfold axis in the general fluorite-type motif. The displacement of cations from the regular lattice sites in isovalent solid solutions provides space for anion motion and, thus, facilitates ion transfer in the nearest environment of the clusters.

The fluorine ionic conductivities in the superionic states of the β-PbF_2 fluorite matrix and the solid solutions on its base are close to each other and can be as high as 1–2 S/cm at 873 K. For these crystals, the activation enthalpies of electrical conduction virtually coincide with each other: ΔH = 0.30 eV for β-PbF_2, $\Delta H = 0.32 \pm 0.01$ eV for $Pb_{0.67}Cd_{0.33}F_2$ (640–873 K), and $\Delta H = 0.30 \pm 0.01$ eV for $Pb_{0.99}Sc_{0.01}F_{2.01}$ (800–873 K) and $Pb_{0.9}Sc_{0.1}F_{2.1}$ (620–873 K).[1] However, the mechanism of anion transfer in the superionic phase is still not clearly understood.

For $PbSnF_4$ polycrystalline samples subjected to first heating from 311 to 597 K, the dependence $\sigma(T)$ exhibits a feature in the range 350–370 K which is attributed to the transformation of the monoclinic (α') modification to the tetragonal (β) modification. In the thermograms measured for the $PbSnF_4$ compound in the heating–cooling cycle in the range from 293 to 573 K, the thermal effects manifest themselves at a temperature of ~348 K for the ceramic samples and at ~353 K for the small-sized crystals upon heating and are not observed upon cooling. The small enthalpy of the α(α')–β transition (440 cal/mol [19]) indicates that this transition is accompanied by an insignificant structural transformation. It is known that, upon cooling, the reverse transition from the β-$PbSnF_4$ modification to the α(α')-$PbSnF_4$ modification is hindered and occurs either at temperatures below 77 K or under mechanical actions (grinding) or a high hydrostatic pressure [20, 21]. Our x-ray powder diffraction data confirm that the ceramic sample after conductometric investigations (upon heating to 597 K) belongs to the β-$PbSnF_4$ modification (tetragonal crystal system, space group $P4/nmm$, $a = b = 4.215$ Å, and $c = 11.37$ Å). It should be noted that, under normal conditions, the metastable tetragonal β-$PbSnF_4$ modification was obtained by annealing at temperatures above 610 K [21, 22]. The unit cell of the tetragonal β-$PbSnF_4$ modification can be treated as a tetragonally distorted fluorite unit cell: $a_t = b_t = a_f/\sqrt{2}$ and $c_t = 2a_f$, where the subscripts *t* and *f* refer to the tetragonal and fluorite unit cells. According to Chernov *et al.* [22], the structure of $PbSnF_4$ can be represented as a heterostructure of the atomic level in which a Sn_4F_8 tetramer (an isolated fragment of the crystal lattice of the monoclinic α-SnF_2 modification) is located in the fluorite lattice of the β-PbF_2 phase.

Thus, the data on the ionic conductivity upon first cooling from 597 to 311 K and subsequent second heating from 293 to 410 K and second cooling to 143 K refer to the β-$PbSnF_4$ modification. It can be seen from Fig. 2 that, in the temperature range 285–340 K, the electrical conductivity of the β-$PbSnF_4$ phase gradually changes and the activation enthalpy of electrical conduction is characterized by a dispersion. These findings are in good agreement with the assumption made in [21, 22] that the tetragonal β-$PbSnF_4$ modification at temperatures of 190–340 K undergoes a smeared superionic transition similar to the phase transformation observed in the cubic β-PbF_2 modification. The estimated enthalpy of anionic conduction in the superionic phase is equal to 0.16 eV, which agrees with the previously determined enthalpies ΔH = 0.10–0.17 eV [1, 2, 19, 21].

The ^{19}F NMR [23], conductometric [19, 22], and structural [24, 25] data indicate that the fluorine ionic conduction in $PbSnF_4$ crystals occurs through the direct interstitial mechanism. The structure of the monoclinic α(α')-$PbSnF_4$ modification contains two types of F^- ions with different mobilities. Upon transition to the high-temperature β(β')-$PbSnF_4$ modification, F^- ions of both types become dynamically equivalent. In our recent work [6], we studied the fluorine ionic conductivity of α'-$PbSnF_4$ in single-crystal and ceramic samples in the temperature range 293–450 K. Owing to the perfect cleavage and the habit of the single crystals (thin plates), we succeeded in measuring the electrical conductivity of the α'-$PbSnF_4$ single crystals only along the crystallographic axis *c*. The results of electrical measurements performed with single-crystal and polycrystalline samples of the $PbSnF_4$ compound indicate a high anisotropy of fluorine transfer parallel and perpendicular to the *c* axis. Therefore, unlike the PbF_2 fluorite crystals and PbF_2-based solid solutions (three-dimensional superionic conductors), the tetragonal $PbSnF_4$ crystals can be characterized as two-dimensional superionic conductors in which fast transfer of F^- ions likely proceeds in the crystallographic planes perpendicular to the *c* axis.

3.2. Superionic conductors based on CdF_2. Earlier [4], we noted that, without resorting to special precautions at temperatures above 520 K, the pyrohydrol-

[1] For the last two crystals, the conductometric data were processed jointly.

ysis occurring on the surface of $Cd_{1-x}R_xF_{2+x}$ single crystals resulted in the formation of a conducting film. This hampered correct determination of the bulk resistivity. The formation of a CdO conducting layer on the surface of the CdF_2 crystal is caused by the presence of water or oxygen traces in the ambient atmosphere [26]. In our experiments, we took special precautions, such as ultrasonic cleaning of the sample surface, preliminary annealing of the samples followed by removal of the conducting layer, measurements in a flow of purified nitrogen and over a wider frequency range (in order to separate the contribution of the bulk resistivity of the single crystals from the contribution of the resistivity of the film), and others. These efforts made it possible for the first time to carry out high-temperature investigation of the electric properties of CdF_2-based single crystals.

The temperature dependences of the ionic conductivity of $Cd_{1-x}R_xF_{2+x}$ (R = Ho and Er) single crystals are plotted in Fig. 3. All the studied crystals are characterized by a good reproducibility of the ionic conductivities upon heating and cooling. No thermal effects are observed in the thermograms of the samples in the temperature range under investigation. The dependences $\sigma(T)$ at critical temperatures $T_c \sim 600$–800 K can be divided into two linear portions in accordance with different mechanisms of ion transfer. It should be noted that the activation enthalpy of ion transfer increases in the high-temperature range. Two similar portions in the curves $\sigma(T)$ were also observed for $Ca_{1-x}R_xF_{2+x}$ and $Na_{0.5-x}R_{0.5+x}F_{2+2x}$ solid solutions [8]. Table 2 lists the preexponential factors A and the activation enthalpies of electrical conduction ΔH for $Cd_{1-x}R_xF_{2+x}$ (R = Ho and Er) single crystals.

It should be noted that the ionic radii of Ho^{3+} and Er^{3+} cations are close to each other. For this reason, we jointly processed the experimental data on the $Cd_{1-x}Ho_xF_{2+x}$ and $Cd_{1-x}Er_xF_{2+x}$ solid solutions. Figure 4 depicts the concentration dependences $\sigma(x)$ and $\Delta H(x)$ in the low-temperature range ($T < T_c$). The obtained parameters of anion transfer in $Cd_{1-x}R_xF_{2+x}$ (R = Ho and Er) solid solutions agree well with the parameters determined in our earlier work [4] for $Cd_{0.78}Ho_{0.22}F_{2.22}$ and $Cd_{0.73}Er_{0.27}F_{2.27}$ crystals measured at temperatures no higher than 470 K. In the concentration range 3–27 mol % HoF_3 (ErF_3), the activation enthalpy linearly depends on the composition: $\Delta H = \Delta H_0 - Cx$, where $\Delta H_0 = 0.85 \pm 0.05$ eV and C is the proportionality factor. The concentration dependences $\sigma(x)$ and $\Delta H(x)$ can be explained within the model of defect regions, which we proposed earlier for $M_{1-x}R_xF_{2+x}$(M = Ca, Sr, and Ba) solid solutions [27, 28].

The nominally pure CdF_2 compound is characterized by the formation of point anti-Frenkel defects which are responsible for the sufficiently high ionic conductivity: $\sigma \sim 1 \times 10^{-7}$ S/cm at 400 K [26]. As follows from the results of density measurements [29], the

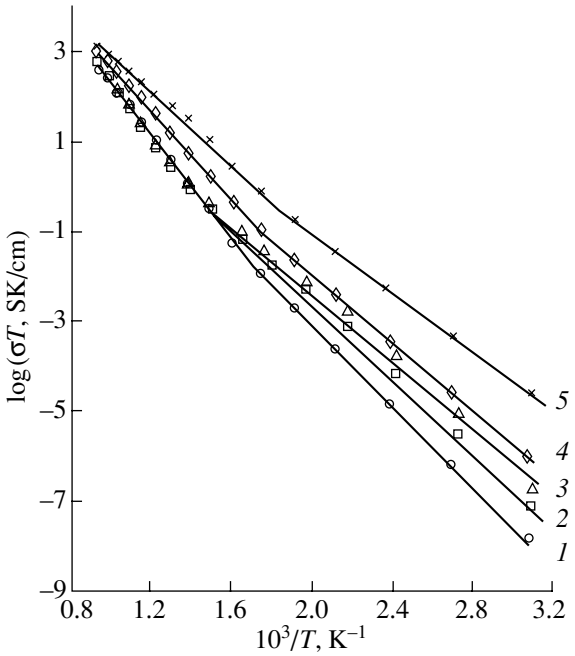

Fig. 3. Temperature dependences of the anionic conductivity of (*1*) $Cd_{0.98}Ho_{0.02}F_{2.02}$, (*2*) $Cd_{0.97}Er_{0.03}F_{2.03}$, (*3*) $Cd_{0.97}Ho_{0.03}F_{2.03}$, (*4*) $Cd_{0.89}Ho_{0.11}F_{2.11}$, and (*5*) $Cd_{0.8}Er_{0.2}F_{2.2}$ single crystals.

formation of $Cd_{1-x}R_xF_{2+x}$ solid solutions occurs through the replacement of Cd^{2+} by R^{3+} cations and the incorporation of additional fluorine ions (compensating for an excess charge of R^{3+} cations) into interstitial holes of the fluorite structure. It is known that, in $M_{1-x}R_xF_{2+x}$ (M = Ca, Sr, and Ba) solid solutions, an increase in the concentration of rare-earth trifluorides is accompanied by aggregation of isolated lattice defects into defect formations (clusters). According to the

Table 2. Parameters A and ΔH for $Cd_{1-x}R_xF_{2+x}$ (R = Ho and Er) single crystals

Crystal	ΔT, K	ΔH, eV	log(A, S/cm)
$Cd_{0.98}Ho_{0.02}F_{2.02}$	323–723	0.813 ± 0.007	5.65 ± 0.08
	773–1073	1.29 ± 0.03	8.78 ± 0.18
$Cd_{0.97}Ho_{0.03}F_{2.03}$	323–573	0.78 ± 0.02	5.59 ± 0.16
	673–1073	1.13 ± 0.04	7.97 ± 0.22
$Cd_{0.96}Ho_{0.04}F_{2.04}$	323–573	0.80 ± 0.02	5.83 ± 0.19
	823–1073	1.29 ± 0.03	8.91 ± 0.14
$Cd_{0.89}Ho_{0.11}F_{2.11}$	323–573	0.747 ± 0.007	5.54 ± 0.07
	623–1073	1.000 ± 0.008	7.72 ± 0.05
$Cd_{0.97}Er_{0.03}F_{2.03}$	323–573	0.863 ± 0.009	5.58 ± 0.11
	573–1073	1.118 ± 0.005	7.86 ± 0.03
$Cd_{0.8}Er_{0.2}F_{2.2}$	323–523	0.644 ± 0.007	5.20 ± 0.09
	573–1073	0.78 ± 0.02	6.60 ± 0.10

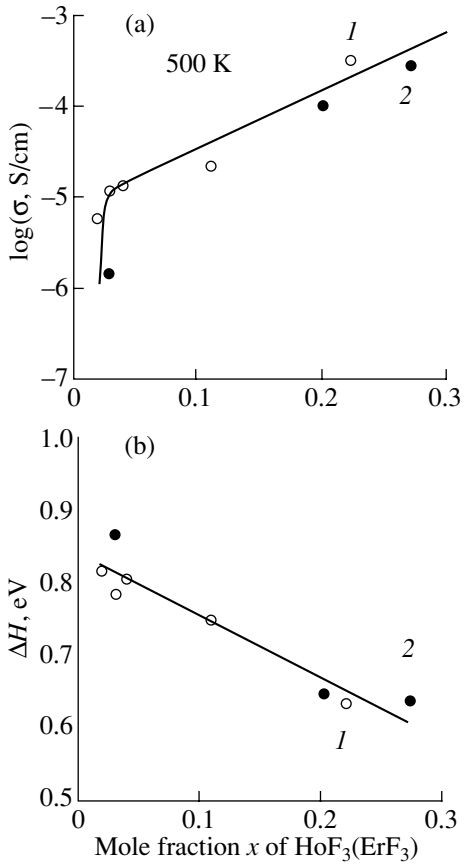

Fig. 4. Concentration dependences of (a) the conductivity at a temperature of 500 K and (b) the activation enthalpy of electrical conduction for (*1*) $Cd_{1-x}Ho_xF_{2+x}$ and (*2*) $Cd_{1-x}Er_xF_{2+x}$ single crystals in the low-temperature range ($T < T_c$).

NMR data [30], clusters containing two R^{3+} ions are revealed in $Cd_{0.9}Er_{0.1}F_{2.1}$ and $Cd_{0.94}Yb_{0.06}F_{2.06}$ single crystals. Unfortunately, to the best of our knowledge, no works dealing with a defect (cluster) structure of concentrated solid solutions based on CdF_2 have been performed.

As in the case of $M_{1-x}R_xF_{2+x}$ (M = Ca, Sr, and Ba) solid solutions, the experimental data on ion transfer in $Cd_{1-x}R_xF_{2+x}$ crystals can be consistently interpreted under the assumption that defect clusters are formed in their structures. As regards imperfection of the anionic motif, the $Cd_{1-x}R_xF_{2+x}$ solid solutions are similar to the anion-excessive fluorite solid solutions $Ca_{1-x}R_xF_{2+x}$. The results of structural investigations [31, 32] demonstrate that, in $Ca_{1-x}R_xF_{2+x}$ (R = Ho, Y, and Yb) solid solutions, defects located at 48*i* crystallographic positions of space group $Fm3m$ [$F_i(48i)$ defects] represent the dominant type of fluorine interstitial ions and R_6F_{36-37} cubic–octahedral clusters serve as cores of defect regions. This suggests that, at $T < T_c$, clusters of the R_6F_{37} type are formed in the structures of $Cd_{1-x}Ho_xF_{2+x}$ and $Cd_{1-x}Er_xF_{2+x}$ "impurity" fluorites. In disordered solid solutions with cubic–octahedral clusters, the percolation threshold of conduction is estimated to be x_p = 2–3 mol % RF_3 [28] and the activation enthalpy of ionic conduction at concentrations $x > x_p$ linearly depends on the composition. This situation is actually observed for $Cd_{1-x}R_xF_{2+x}$ (R = Ho and Er) single crystals (Fig. 4).

A fragment of the $[M_6F_{32}]$ structure can be distinguished in the MF_2 (M = Ca and Cd) fluorite matrix. In this case, the heterovalent substitution in the crystal lattice of the solid solutions can be represented by the following scheme: $[M_6F_{32}]^{20-} \longrightarrow [R_6F_{37}]^{19-} \longrightarrow F^-_{mob}$, where F^-_{mob} are fluorine interstitial ions located outside the R_6F_{37} clusters. According to Archer *et al.* [33], anion defects entering into the cluster composition do not participate in ion transfer; hence, it is these F^-_{mob} ions that are the most probable structural defects responsible for the anionic conduction in cadmium rare-earth fluorites at $T < T_c$. Within the model of defect regions, the enthalpy ΔH_0 corresponds to the mean activation enthalpy of F^-_{mob} mobile ions located around the periphery of defect regions in which defect clusters

Table 3. Experimental conductivities and calculated concentrations and mobilities of charge carriers (F^-_{mob} ions) at a temperature of 500 K for $Cd_{1-x}R_xF_{2+x}$ (R = Ho and Er) ionic conductors

Crystal	a, Å [35]	σ, S/cm	n, cm^{-3}	μ, $cm^2/V\,s$
$Cd_{0.98}Ho_{0.02}F_{2.02}$	5.394	5.7×10^{-6}	8.5×10^{19}	4.2×10^{-7}
$Cd_{0.97}Ho_{0.03}F_{2.03}$	5.398	1.2×10^{-5}	1.3×10^{20}	5.9×10^{-7}
$Cd_{0.96}Ho_{0.04}F_{2.04}$	5.401	1.4×10^{-5}	1.7×10^{20}	5.2×10^{-7}
$Cd_{0.89}Ho_{0.11}F_{2.11}$	5.423	2.1×10^{-5}	4.6×10^{20}	2.9×10^{-7}
$Cd_{0.78}Ho_{0.22}F_{2.22}$ [4]	5.458	3.2×10^{-4}	9.0×10^{20}	2.2×10^{-6}
$Cd_{0.97}Er_{0.03}F_{2.03}$	5.397	1.5×10^{-6}	1.3×10^{20}	7.4×10^{-8}
$Cd_{0.8}Er_{0.2}F_{2.2}$	5.448	1.0×10^{-4}	8.2×10^{20}	7.6×10^{-8}
$Cd_{0.73}Er_{0.27}F_{2.27}$ [4]	5.469	2.9×10^{-4}	1.1×10^{21}	1.6×10^{-6}

serve as a core. The activation enthalpy $\Delta H_0 = 0.85$ eV, which was determined for $Cd_{1-x}Ho_xF_{2+x}$ and $Cd_{1-x}Er_xF_{2+x}$ solid solutions in the present work, is rather close to the enthalpy of migration of host (thermal) F_i ions $\Delta H_{m,i} \approx 1.0$ eV [34] in the CdF_2 matrix.

In the framework of the above structural model of ionic conduction in $Cd_{1-x}Ho_xF_{2+x}$ and $Cd_{1-x}Er_xF_{2+x}$ solid solutions, the concentration n_F of charge carriers (F^-_{mob} ions) can be calculated from the formula $n_F = 2x/3a^3$, where a is the lattice parameter. The calculated concentrations and mobilities of charge carriers at 500 K are given in Table 3. The concentration of fluorine mobile ions varies from 9×10^{19} to 1×10^{21} cm^{-3} (with variations in the mole fraction of RF_3 from 0.02 to 0.27 and in the lattice parameter from 5.39 to 5.47 Å [35]). Note that the number of anionic current carriers constitutes only 0.2–2% of the total number of fluorine ions in the crystals under investigation. This agrees well with the available data for solid solutions based on other fluorite matrices MF_2 (M = Ca, Sr, Ba, and Pb) [12]. Therefore, the difference in the conductivities of the $Cd_{1-x}R_xF_{2+x}$ phases is associated with different concentrations of ionic current carriers and their different mobilities in the crystal lattice.

It is clear that the kinks observed in the dependences $\sigma(T)$ at critical temperatures $T_c \approx 600$–800 K reflect a transformation of the defect structure of $Cd_{1-x}R_xF_{2+x}$ crystals. Making allowance for the small coefficients of cation diffusion in fluorite structures [12, 34], we can draw the inference that the number of rare-earth cations in clusters apparently remains unchanged. It should be noted that the $Cd_{1-x}R_xF_{2+x}$ solid solutions (like the $Ca_{1-x}R_xF_{2+x}$ and $Na_{0.5-x}R_{0.5+x}F_{2+2x}$ solid solutions [8]) obey the relationship $\Delta H_2 > \Delta H_1$, where ΔH_1 and ΔH_2 are the activation enthalpies of electrical conduction at $T < T_c$ and $T > T_c$, respectively. According to [8, 33], the high-temperature portion of the dependence $\sigma(T)$ for $Ca_{1-x}R_xF_{2+x}$ and $Na_{0.5-x}R_{0.5+x}F_{2+2x}$ solid solutions is associated with the dissociation of F_i interstitial ions from clusters. As applied to the $Cd_{1-x}Ho_xF_{2+x}$ and $Cd_{1-x}Er_xF_{2+x}$ solid solutions, this process can be described by the following scheme: $[R_6F_{37}]^{19-} \longrightarrow [R_6F_{36}]^{18-} \longrightarrow F^-_{dis}$. The enthalpies of dissociation of F^-_{dis} interstitial anions are estimated to be $\Delta H_a = 2(\Delta H_2 - \Delta H_1) = 0.5$–$1.0$ eV. Note that the anionic conductivity at 1073 K can be as high as 0.5–1 S/cm.

Figure 5 shows the dependence of $\log A$ on ΔH for the $Cd_{1-x}R_xF_{2+x}$ (R = Ho and Er) single crystals under investigation. It is seen that the low-temperature and high-temperature conductivity parameters are characterized by the same compensation effect (with a correlation coefficient of 0.96): $\log A = \log A_0 + B_0\Delta H$, where $A_0 = 23$ S/cm and $B_0 = 5.83$ eV^{-1}. The temperature of the compensation effect $\theta = (2.3kB_0)^{-1} \approx 860$ K is in reasonable agreement with the critical temperatures $T_c \approx 600$–800 K determined directly from the experimental dependences $\sigma(T)$. The occurrence of the compensation effect for $Cd_{1-x}R_xF_{2+x}$ crystals indicates that ion transfer at low and high temperatures proceeds through interrelated mechanisms.

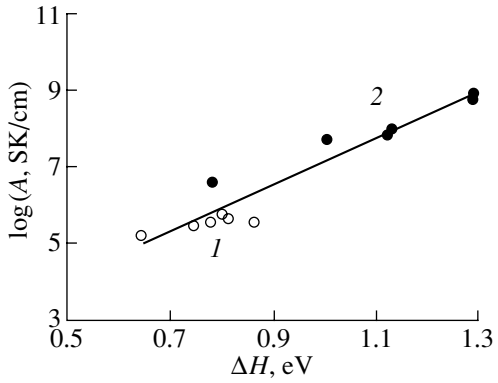

Fig. 5. Dependence of $\log A$ on ΔH for $Cd_{1-x}R_xF_{2+x}$ (R = Ho and Er) single crystals at temperatures (*1*) $T < T_c$ and (*2*) $T > T_c$.

4. CONCLUSIONS

Thus, the results obtained in the above investigation allowed us to make the following inferences. The PbF_2-based superionic conductors are promising fluoride-conducting solid electrolytes. Upon heating, the electrical characteristics are stable to a temperature of 873 K for $Pb_{1-x}Sc_xF_{2+x}$ (x = 0.01 and 0.1) and $Pb_{1-x}Cd_xF_2$ (x = 0.33) single crystals and to 597 K for $PbSnF_4$ ceramic samples. The temperature dependences of the anionic conductivity indicate the occurrence of smeared transitions to the crystalline state with superionic conductivity (10^{-1}–1 S/cm).

The specific features of anion transfer and the thermal stability of the electrical conduction characteristics were investigated for single crystals of the $Cd_{1-x}Ho_xF_{2+x}$ and $Cd_{1-x}Er_xF_{2+x}$ ($0.02 \le x \le 0.20$) fluorite solid solutions. Under standard conditions, all the single crystals studied are unstable at temperatures above 500 K. The crossover from one mechanism of ion transfer to the other mechanism is observed at temperatures $T_c \approx 600$–800 K. In the low-temperature range ($T < T_c$), the anionic conduction is determined by the migration of F_i interstitial ions and the conductivity σ (at 500 K) increases from 6×10^{-6} to 1×10^{-4} S/cm with an increase in the HoF_3 (ErF_3) content from 2 to 20 mol %. In the high-temperature range ($T > T_c$), the electrical conduction is likely associated with the dissociation of F_i ions from structural clusters and the conductivity σ at 1073 K is as high as ~1 S/cm.

ACKNOWLEDGMENTS

We are grateful to I.I. Buchinskaya, O.K. Nikol'skaya, M.A. Sattarova, and P.P. Fedorov for providing the crystals used in our measurements.

This work was supported by the L. Meitner Austrian Foundation, grant no. M00231-CHE.

REFERENCES

1. I. V. Murin, Izv. Sib. Otd. Akad. Nauk SSSR, Ser. Khim. Nauk, No. 1, 53 (1984).
2. J. M. Reau and J. Grannec, in *Inorganic Solid Fluorides Chemistry and Physics*, Ed. by P. Hagenmuller (Academic, London, 1985), p. 423.
3. N. I. Sorokin, I. I. Buchinskaya, and B. P. Sobolev, Zh. Neorg. Khim. **37** (12), 2653 (1992).
4. N. I. Sorokin, P. P. Fedorov, A. K. Ivanov-Shits, and B. P. Sobolev, Fiz. Tverd. Tela (Leningrad) **30** (5), 1537 (1988) [Sov. Phys. Solid State **30**, 890 (1988)].
5. N. I. Sorokin, P. P. Fedorov, and B. P. Sobolev, Neorg. Mater. **33** (1), 5 (1997).
6. O. K. Nikolskaya, L. N. Demianets, and N. I. Sorokin, High Press. Res. **20**, 195 (2001).
7. I. V. Murin and S. V. Chernov, Neorg. Mater. **18** (1), 168 (1982).
8. N. I. Sorokin and M. W. Breiter, Solid State Ionics **116**, 157 (1999).
9. J. R. Dygas and M. W. Breiter, Electrochim. Acta **41** (7–8), 993 (1996).
10. R. W. Bonne and J. Schoonman, J. Electrochem. Soc. **124** (1), 28 (1977).
11. C. C. Liang and A. V. Joshi, J. Electrochem. Soc. **122** (4), 466 (1975).
12. A. V. Chadwick, Solid State Ionics **8** (3), 209 (1983).
13. R. Bachmann and H. Schulz, Solid State Ionics **9–10**, 521 (1983).
14. R. E. Gordon and J. H. Strange, J. Phys. C **11**, 3213 (1978).
15. A. Azimi, V. M. Carr, A. V. Chadwick, *et al.*, J. Phys. Chem. Solids **45** (1), 23 (1984).
16. N. I. Sorokin, G. A. Shchavlinskaya, I. I. Buchinskaya, and B. P. Sobolev, Élektrokhimiya **34** (9), 1031 (1998).
17. I. Kosacki, Appl. Phys. A **49**, 413 (1989).
18. A. N. Matsulev, Yu. N. Ivanov, A. I. Livshits, *et al.*, Zh. Neorg. Khim. **45** (2), 296 (2000).
19. S. Vilminot, G. Perez, W. Granier, and L. Cot, Solid State Ionics **2**, 87 (1981).
20. G. Perez, S. Vilminot, W. Granier, *et al.*, Mater. Res. Bull. **15**, 587 (1980).
21. R. Kanno, S. Nakamura, and Y. Kawamoto, Mater. Res. Bull. **26**, 1111 (1991).
22. S. V. Chernov, M. Yu. Vlasov, and I. V. Murin, in *Proceedings of the IX All-Union Conference on Physical Chemistry and Electrochemistry of Ionic Melts and Solid Electrolytes, Sverdlovsk, 1987*, Vol. 3, p. 100.
23. A. V. Chadwick, E. S. Hammam, D. van der Putten, and J. H. Strange, Cryst. Lattice Defects Amorphous Mater. **15**, 303 (1987).
24. G. Debes, Y. H. Yu, T. Tyliszczak, and P. Hitchcock, J. Solid State Chem. **91**, 1 (1991).
25. Y. Ito, T. Mukoyama, and S. Yoshikado, Solid State Ionics **80**, 317 (1995).
26. Y. T. Tan and D. Kramp, J. Chem. Phys. **53** (9), 3691 (1970).
27. A. K. Ivanov-Shitz, N. I. Sorokin, P. P. Fedorov, and B. P. Sobolev, Solid State Ionics **31**, 253 (1989).
28. N. I. Sorokin, Kristallografiya **45** (5), 871 (2000) [Crystallogr. Rep. **45**, 799 (2000)].
29. M. Rubenstein and E. Banks, J. Electrochem. Soc. **106** (5), 404 (1959).
30. M. R. Mustafa, W. E. Jones, B. R. McGarvey, *et al.*, J. Chem. Phys. **62** (7), 2700 (1975).
31. L. P. Otroshchenko, V. B. Aleksandrov, N. N. Bydanov, *et al.*, Kristallografiya **33** (3), 764 (1988) [Sov. Phys. Crystallogr. **33**, 449 (1988)].
32. N. G. Grigor'eva, L. P. Otroshchenko, B. A. Maksimov, *et al.*, Kristallografiya **41** (4), 644 (1996) [Crystallogr. Rep. **41**, 607 (1996)].
33. J. A. Archer, A. V. Chadwick, I. R. Jack, and B. Zeqiri, Solid State Ionics **9–10**, 505 (1983).
34. A. B. Lidiard, *Crystals with the Fluorite Structure*, Ed. by W. Hayes (Clarendon, Oxford, 1974).
35. P. P. Fedorov and B. P. Sobolev, Kristallografiya **37** (5), 1210 (1992) [Sov. Phys. Crystallogr. **37**, 651 (1992)].

Translated by O. Borovik-Romanova

Physics of the Solid State, Vol. 44, No. 8, 2002, pp. 1587–1596. Translated from Fizika Tverdogo Tela, Vol. 44, No. 8, 2002, pp. 1513–1521.

SEMICONDUCTORS AND DIELECTRICS

Spin–Spin Interaction of Dy^{3+} Ions in $KY(WO_4)_2$

I. M. Krygin*, A. D. Prokhorov*, V. P. D'yakonov*, **, M. T. Borowiec, and H. Szymczak****

** Donetsk Physicotechnical Institute, National Academy of Sciences of Ukraine, Donetsk, 83114 Ukraine*

*** Institute of Physics, Polish Academy of Sciences, Al. Lotnikyw 32/46, Warsaw, 02-668 Poland*

e-mail: prohorov@pr.fti.ac.donetsk.ua

Received September 20, 2001

Abstract—The spin–spin interaction of Dy^{3+} ions in a $KY(WO_4)_2$ single crystal is investigated by electron paramagnetic resonance (EPR) spectroscopy at a temperature of 4.2 K and a frequency of 9.2 GHz. The EPR spectra of ion pairs located in different coordination shells are analyzed. It is revealed that the considerable contribution to the spin–spin interaction of the nearest neighbor ion pair *nn* is made not only by the magnetic dipole–dipole interaction but also by the isotropic exchange interaction with the parameter $\mathcal{J}_{nn} = (+601 \pm 17) \times 10^{-4}$ cm^{-1}. The exchange interaction in pairs of more widely spaced ions is substantially weaker: $\mathcal{J}_{5n} = (-38 \pm 3) \times 10^{-4}$ cm^{-1} and $\mathcal{J}_{9n} = (+18 \pm 4) \times 10^{-4}$ cm^{-1}. For the other ion pairs, the magnetic dipole–dipole interaction dominates. It is found that the EPR spectra of single ions and ion pairs exhibit a superhyperfine structure associated with tungsten nuclei. © *2002 MAIK "Nauka/Interperiodica".*

1. INTRODUCTION

The considerable interest expressed by researchers in crystals of double tungstates of monoclinic symmetry stems from a number of circumstances. First, these materials doped with rare-earth elements hold promise as a means for producing laser action with unique properties [1–4]. Second, $KDy(WO_4)_2$ and $RbDy(WO_4)_2$ crystals at low temperatures undergo structural phase transitions of the Jahn–Teller type during which lattice distortions occur without a change in symmetry [5–8]. At temperatures below 1 K, these crystals also undergo antiferromagnetic ordering [7, 9–11]. The electron paramagnetic resonance (EPR) parameters for concentrated $KDy(WO_4)$ [7] and diluted (0.1–1.0% Dy^{3+} in the diamagnetic analog $KY(WO_4)_2$) [12] crystals differ significantly. In crystals with a low dysprosium concentration, the g factor has ordinary values: $g_x = 0$, $g_y = 1.54$, and $g_z = 14.6$. In crystals with 100% Dy^{3+}, the g values are as follows: $g_x = 0$, $g_y = 0.82$, and $g_z = 3.13$ at temperatures above the phase transition point T_{spt} and $g_x = 0$, $g_y = 1.19$, and $g_z = 1.98$ at $T < T_{spt}$. Contradictory data on the g factor have been obtained from analyzing the susceptibility [10]. Such appreciable differences can be associated with the specific features of the spin–spin interaction. In turn, these features are determined by the crystallographic structure of the material. In this respect, we carried out a detailed investigation into the spin–spin interaction between dysprosium ions. For this purpose, we analyzed the EPR spectra of ion pairs located in different coordination shells.

Upon introduction of paramagnetic ions into a diamagnetic matrix, the impurity ions substitute for diamagnetic ions and can appear to be located sufficiently close to each other. In isomorphic crystals at low impurity concentrations, the probability of forming an ion pair is proportional to the impurity concentration squared. If the energy of spin–spin interaction between ions of the formed pair turns out to be comparable to the energy of microwave photons used in electron paramagnetic resonance, the possibility exists of obtaining information on the interaction forces on the microscopic level from the EPR spectrum.

Such investigations are important not only in the above specific case. These experiments are of general physical interest, because they make it possible to verify hypotheses relating the macroscopic magnetic properties of the studied materials to their microscopic characteristics. Detailed information on pair interactions allows one to calculate the magnetic structure of materials in a magnetically ordered state and to compare the results of calculations with the available data obtained by other independent methods. It should be noted that, as a rule, the isotropic exchange interaction makes the dominant contribution to the nondipole component of the spin–spin interaction. On this basis, the dependence of the isotropic exchange contribution to the spin–spin interaction on the interionic distance and the bonding direction can be investigated either by inducing strains in the sample under pressure and heat treatment or considering pairs of ions located in different coordination shells.

2. CRYSTAL STRUCTURE

Potassium yttrium and potassium dysprosium tungstates, $KY(WO_4)_2$ and $KDy(WO_4)_2$, are isomorphic crystals in the monoclinic system [13–15] with space-

Table 1. Unit cell parameters and rhombohedral angles in $KY(WO_4)_2$ and $KDy(WO_4)_2$ single crystals

Crystal	*a*, Å	*b*, Å	*c*, Å	β, deg	Reference
$KY(WO_4)_2$	8.11	10.35	7.54	93.3	[1]
$KDy(WO_4)_2$	8.05	10.32	7.52	94.4	[2]

Table 2. Coordinates of rare-earth ions in unit cells of $KY(WO_4)_2$ and $KDy(WO_4)_2$ crystals

Ion no.	*A*	*B*	*C*
1	0	0.2716	0.25
2	0.5	0.2284	0.25
3	0	0.7285	0.75
4	0.5	0.7716	0.75

group symmetry $C_{2h}^6 = C2/c$. The unit cell contains four formula units. The unit cell parameters for both crystals are listed in Table 1. The coordinates of rare-earth ions in the unit cell are presented in Table 2.

The rare-earth ions are located in the *ab* plane and form slightly bent chains lying along the line of intersection of the *ab* and *ac* planes. The nearest neighbor chains are in the line of intersection of the planes translated by 1/2*c* and 1/2*a* along the *c* and *a* axes. The next-to-nearest neighbor chains lie in the original plane *ac* at the distance *c*.

A paramagnetic impurity ion substituting for a diamagnetic ion brings about distortion of the unit cell (for example, due to a difference in the ionic radii). A pair of closely spaced impurity ions increases this distortion. Consequently, the distance between Dy^{3+} ions should differ from the distances between Y^{3+} ions in pure $[KY(WO_4)_2]$ or totally substituted $[KDy(WO_4)_2]$ matrices but will likely not exceed them. For this reason, the calculations were performed with unit cell parameters equal to the arithmetical means of the corresponding parameters for the above matrices, i.e., $a = 8.08 \pm 0.03$ Å, $b = 10.335 \pm 0.015$ Å, $c = 7.53 \pm 0.01$ Å, and $\beta = 93.85 \pm 0.55°$ for $Dy^{3+} : KY(WO_4)_2$. The calculated distances between the Dy^{3+} ions and the bonding directions for the first ten coordination shells in a rectangular laboratory system of coordinates are given in Table 3. The axes of this coordinate system are chosen as follows: the *y* axis coincides with the crystallographic axis *b* (C_2), and the *z* axis is aligned with the *ac* plane and emerges from the acute angle between the *a* and *c* axes at an angle of 20° to the *c* axis.

The nearest neighbor ion pairs *nn* and pairs 7*n* belong to the same chains. The bonding direction of the *nn* pair is aligned with the *ab* plane and makes an angle of 6.3° with the *ac* plane. The Dy^{3+} ions forming the pairs 2*n*, 3*n*, 4*n*, 6*n*, and 10*n* are located in the nearest neighbor chain, and the Dy^{3+} ions involved in the pairs 5*n*, 8*n*, and 9*n* are positioned in the next chain.

3. THEORY

Let us consider a Dy^{3+} ion with the $4f^9$ electron configuration ($S = 5/2$, $L = 5$, $J = 15/2$, Landé factor $g_J = 4/3$). The ground state $^6H_{15/2}$ is split by the crystal field of monoclinic tungstate into eight Kramers doublets, of which the lowest doublet exhibits an EPR spectrum. The first and second excited doublets lie 10 and 135 cm^{-1} above the ground doublet, respectively [5, 6]. The even dysprosium isotopes (the natural abundance $^e c$ is 56.1%) have a zero nuclear spin, whereas the odd isotopes ^{163}Dy ($^{163}c = 24.97\%$) and ^{161}Dy ($^{161}c = 18.88\%$) are characterized by the nuclear spin $U = 5/2$.

The EPR spectrum of a Dy^{3+} single ion can be described by the effective spin Hamiltonian

$$\hat{H} = \mu(\mathbf{B}\mathbf{g}\hat{S}) + \hat{S}\mathbf{A}\hat{I}, \quad (1)$$

where μ is the Bohr magneton, **B** is the magnetic induction vector, **g** is the tensor of spectroscopic splitting, **A** is the tensor of hyperfine interaction, $\hat{S}$ is the electron spin operator ($S = 1/2$), and $\hat{I}$ is the nuclear spin operator (for the even and odd isotopes, $I = 0$ and 5/2, respectively).

In the general case, Hamiltonian (1) cannot be directly diagonalized for odd isotopes. Let us consider a simpler situation: (i) the principal axes of the tensors **g** and **A** are aligned along the axes of the laboratory coordinate system, (ii) the external magnetic field is directed along the *z* axis, and (iii) the hyperfine interaction is axial in character (i.e., $A_z \gg A_x$ and A_y). In this simpler case, Hamiltonian (1) can be easily calculated because it includes only diagonal components. Moreover, the EPR spectrum should consist of a single line assigned to Dy^{3+} ions of the even isotopes and two sextets of equidistant hyperfine components attributed to the odd isotopes with relative line intensities $^eI : {}^{163}I : {}^{161}I = {}^e c : {}^{163}c/6 : {}^{161}c/6 = 56 : 25/6 : 19/6 = 100 : 7.4 : 5.6$. The separations between the nearest hyperfine components for each isotope are equal to $^{163}A_z$ and $^{161}A_z$. It should be noted that, in the case when the components of the tensor **g** are identical for Dy^{3+} ions of all the isotopes, the centers of all the spectra coincide with each other.

The absorption spectrum of a pair of interacting ions can be represented by the Hamiltonian

$$\hat{H} = \hat{H}_1 + \hat{H}_2 + \hat{H}_{12}. \quad (2)$$

Here, $\hat{H}_1$ and $\hat{H}_2$ are Hamiltonians (1) for single ions and $\hat{H}_{12}$ is the interaction Hamiltonian. Phenomeno-

Table 3. Interionic distances r (Å), direction cosines of bonding directions (n_x, n_y, and n_z), contributions of the magnetic dipole–dipole interaction to the components of the tensor **K**, and numbers N of magnetically equivalent centers in the first ten coordination shells involving Dy^{3+} : $KY(WO_4)_2$ ions (the energy parameters are given in terms of 10^{-4} cm^{-1})

Pair type	r	n_x	n_y	n_z	$K_{yy\,MDD}$	$K_{zz\,MDD}$	$K_{yz\,MDD}$	N
nn	4.06 ± 0.03	±0.906 ± 0.001	–0.1098 ± 0.0005	±0.408 ± 0.001	147 ± 2	6889 ± 122	–195 ± 2	2
2*n*	6.04 ± 0.02	±0.21325 ± 0.00004	0.78182 ± 0.00007	±0.58590 ± 0.00009	–38.9 ± 0.2	–125 ± 1	–607 ± 3	2
3*n*	6.76 ± 0.02	±0.19050 ± 0.00004	–0.83052 ± 0.00006	∓ 0.52340 ± 0.00009	–35.6 ± 0.1	532 ± 2	411 ± 2	2
4*n*	7.41 ± 0.02	±0.671 ± 0.001	–0.6970 ± 0.0003	∓ 0.697 ± 0.003	–11.5 ± 0.1	1827 ± 4	–127 ± 1	4
5*n*	7.53 ± 0.02	±0.34202 ± 0	0 ± 0	∓ 0.93969 ± 0	24.0 ± 0.1	–3564 ± 14	0 ± 0	2
6*n*	7.71 ± 0.04	±0.31089 ± 0.00009	∓ 0.670 ± 0.001	∓ 0.6738 ± 0.0009	–7.8 ± 0.1	–729 ± 2	–288 ± 2	4
7*n*	8.08 ± 0.06	±0.912 ± 0.001	0 ± 0	±0.410 ± 0.003	19.5 ± 0.2	866 ± 16	0 ± 0	2
8*n*	8.29 ± 0.02	±0.755 ± 0.002	–0.05385 ± 0.00003	∓ 0.654 ± 0.002	17.86 ± 0.06	–455 ± 8	–18.03 ± 0.09	2
9*n*	8.81 ± 0.04	±0.126 ± 0.001	–0.0506 ± 0.0001	±0.9908 ± 0.0008	14.8 ± 0.1	–2620 ± 20	–21.4 ± 0.2	2
10*n*	9.86 ± 0.05	±0.8777 ± 0.0006	0.479 ± 0.001	∓ 0.023 ± 0.001	3.350 ± 0.001	960 ± 7	3.3 ± 0.3	2

Note: The parameters K_{MDD} are calculated according to formula (10) at $g_x = 0$, $g_y = 1.54$, and $g_z = 14.6$. The parameters $K_{xx\,MDD}$, $K_{xy\,MDD}$, and $K_{xz\,MDD}$ are equal to zero.

logically, the interaction Hamiltonian $\hat{H}_{12}$ can be written as

$$\hat{H}_{12} = \hat{S}_1 \mathbf{K} \hat{S}_2, \tag{3}$$

where **K** is the spin–spin interaction tensor and $\hat{S}_1$ and $\hat{S}_2$ are the spin operators of the first and second Dy^{3+} ions, respectively.

In order to calculate Hamiltonian (2) to the first order in the perturbation theory, conditions (i)–(iii) should be complemented by the following conditions: (iv) the principal axes of the tensors **g** and **K** must be aligned with the axes of the laboratory coordinate system, and (v) the spin–spin interaction must be axial in character ($K_z \gg K_x$ and K_y). Then, we easily obtain the energy spectrum and the wave functions for this pair of interacting ions; that is,

$$\begin{aligned}
E_1 &= -g_z\mu B_z + K_z/4 - m'A_z'/2 - m''A_z''/2,\\
|1\rangle &= |-1/2, m', -1/2, m''\rangle,\\
E_2 &= -K_z/4 + m'A_z'/2 - m''A_z''/2,\\
|2\rangle &= |+1/2, m', -1/2, m''\rangle,\\
E_3 &= -K_z/4 - m'A_z'/2 + m''A_z''/2,\\
|3\rangle &= |-1/2, m', +1/2, m''\rangle,\\
E_4 &= g_z\mu B_z + K_z/4 + m'A_z'/2 + m''A_z''/2,\\
|4\rangle &= |+1/2, m', +1/2, m''\rangle,
\end{aligned} \tag{4}$$

where m' and m'' vary from –5/2 to +5/2 and A_z' and A_z'' take the value 0, $^{163}A_z$, and $^{161}A_z$. Therefore, each of the levels E_1–E_4 represents a singlet for even–even pairs, a sextet for even–odd pairs, or is split into 36 sublevels for odd–odd pairs.

Since only the energy-level transitions $E_1 \rightleftharpoons E_2$, $E_1 \rightleftharpoons E_3$, $E_2 \rightleftharpoons E_4$, and $E_3 \rightleftharpoons E_4$ with equal probability $W_{pq} = \left|\langle p|\hat{S}_{x1} + \hat{S}_{x2}|q\rangle\right|^2 = 0.25$ are allowed, we can calculate the absorption spectrum for high-energy photons ($h\nu > |K_z/2 - mA_z|$),

$$\begin{aligned}
E_1 \rightleftharpoons E_2, &\quad g_z\mu B_{1-6} = h\nu + K_z/2 - m'A_z',\\
E_1 \rightleftharpoons E_3, &\quad g_z\mu B_{7-12} = h\nu + K_z/2 - m''A_z'',\\
E_2 \rightleftharpoons E_4, &\quad g_z\mu B_{13-18} = h\nu - K_z/2 - m'A_z',\\
E_3 \rightleftharpoons E_4, &\quad g_z\mu B_{19-24} = h\nu - K_z/2 - m''A_z''
\end{aligned} \tag{5a}$$

and the absorption spectrum for low-energy photons ($h\nu < |K_z/2 - mA_z|$),

$$\begin{aligned} E_1 \rightleftharpoons E_2, \quad g_z\mu B_{1-6} &= K_z/2 - m'A'_z - h\nu, \\ E_1 \rightleftharpoons E_3, \quad g_z\mu B_{7-12} &= K_z/2 - m''A''_z - h\nu, \\ E_2 \rightleftharpoons E_4, \quad g_z\mu B_{13-18} &= K_z/2 - m'A'_z + h\nu, \\ E_3 \rightleftharpoons E_4, \quad g_z\mu B_{19-24} &= K_z/2 - m''A''_z + h\nu. \end{aligned} \tag{5b}$$

According to the above relationships, the experimental EPR spectrum should have the following form depending on the isotopic composition of the pairs:

(1) The even–even pair of Dy^{3+} ions. In this case, we have $A'_z = A''_z = 0$. The spectrum consists of two lines with the splitting $\delta B = K_z$ for a high-energy photon and $\delta B = 2h\nu$ for a low-energy photon. The spectrum is centered at $B_0 = h\nu/g_z\mu$ for the high-energy photon and at $B_0 = K_z/2$ for the low-energy photon. The intensity of each line is proportional to ${}^ec^2/2$.

(2) The even–odd pair (^{e}Dy–^{163}Dy or ^{e}Dy–^{161}Dy). Here, we have $A'_z = 0$ and $A''_z = A_z$ (where $A_z = {}^{163}A_z$ or ${}^{161}A_z$). The spectrum contains two singlets whose positions are identical to those in the spectrum of the even–even pair. Each singlet is at the center of the sextet of the equidistant components. The separation between the components is equal to A_z. The intensity of the central line is proportional to $2^ecc/4$, and the intensity of the line in the sextet is proportional to $\sim 2^ecc/24$ (where $c = {}^{163}c$ or ${}^{161}c$).

(3) The odd–odd pair of like ions (^{163}Dy–^{163}Dy or ^{161}Dy–^{161}Dy). In this case, $A'_z = A''_z = A_z$. The spectrum involves two sextets of equidistant components. The sextets are centered in the same manner as the lines in the spectrum of the ^{e}Dy–^{e}Dy pair. The separation between the nearest components in each sextet is equal to A_z, and the line intensity is proportional to $\sim c^2/12$.

(4) The odd–odd pair of unlike ions (^{163}Dy–^{161}Dy). Here, we have $A'_z = {}^{163}A_z$ and $A''_z = {}^{161}A_z$. The spectrum is composed of two groups of lines. Each group consists of two sextets with coinciding centers. The separations between the components in the sextets are $\delta B = {}^{163}A_z$ and $\delta B = {}^{161}A_z$. The positions of the centers of the groups and the center of the spectrum are similar to those in the spectrum of the ^{e}Dy–^{e}Dy pair. The intensities of 24 spectral lines each are proportional to $\sim 2^{163}c^{161}c/24$.

If conditions (i)–(v) are complemented by condition (vi), according to which the spin–spin interaction does not depend on the isotopic number, the spectra of different-type ion pairs coincide with each other and the overall spectrum contains two groups of lines. Each group consists of a central line and two hyperfine sextets. Note that the relative position of lines in each group and the relative intensity of the components coincide with those in the spectrum of single ions. Actually, the intensity of the central line is represented as

$$\begin{aligned} {}^0I &\sim {}^ec^2/2 + 2^ec^{163}c/4 + 2^ec^{161}c/4 \\ &= {}^ec({}^ec + 2^{163}c + 2^{161}c)/2. \end{aligned}$$

The intensity of the hyperfine component corresponding to the ^{163}Dy isotope in the spectrum of single ions can be written as

$$\begin{aligned} {}^{163}I &\sim 2^ec^{163}c/24 + {}^{163}c^2/12 + 2^{163}c^{161}c/24 \\ &= {}^{163}c({}^ec + {}^{163}c + {}^{161}c)/12. \end{aligned}$$

For the ^{161}Dy isotope, this intensity can be represented by the relationship

$${}^{161}I \sim {}^{161}c({}^ec + {}^{163}c + {}^{161}c)/12.$$

From these relationships, we obtain the relative line intensities in the overall spectrum:

$${}^0I : {}^{163}I : {}^{161}I = {}^ec : {}^{163}c/6 : {}^{161}c/6.$$

Judging from the line positions in the spectra of ion pairs, we can obtain directly only information on the magnitude of the spin–spin interaction tensor components. In order to determine the sign, it is necessary to examine the temperature dependence of the spectral line intensity. The calculations can be most easily carried out for even–even pairs exposed to high-energy photons ($h\nu > |K_z/2|$). In this case, expressions (4) take the form

$$\begin{aligned} E_1 &= -g_z\mu B_z + K_z/4, \quad |1\rangle = |-1/2, -1/2\rangle, \\ E_2 &= -K_z/4, \quad |2\rangle = |\pm 1/2, \mp 1/2\rangle, \\ E_3 &= g_z\mu B_z + K_z/4, \quad |3\rangle = |+1/2, +1/2\rangle. \end{aligned}$$

The intensity I of the absorption line is proportional to the difference between the energy level populations. By using the Boltzmann relationship, we obtain

$$\begin{aligned} I_{\text{high}} &= [1 - \exp(-D_{1\text{high}})]/[1 + \exp(-D_{1\text{high}}) \\ &\quad + \exp(-D_{2\text{high}})], \\ I_{\text{low}} &= [\exp(-D_{2\text{low}}) - \exp(-D_{1\text{low}})]/[1 + \exp(-D_{1\text{low}}) \\ &\quad + \exp(-D_{2\text{low}})], \end{aligned} \tag{6a}$$

$$\begin{aligned} &I_{\text{high}}/I_{\text{low}} \\ &= Q[1 - \exp(-D_{1\text{high}}/kT)]/[\exp(-D_{2\text{low}}/kT) \\ &\quad - \exp(-D_{1\text{low}}/kT)] \end{aligned}$$

at $K_z > 0$ and

$$\begin{aligned} I_{\text{high}} &= [\exp(-D_{2\text{high}}) - \exp(-D_{1\text{high}})]/[1 \\ &\quad + \exp(-D_{1\text{high}}) + \exp(-D_{2\text{high}})], \end{aligned}$$

$$I_{low} = [1 - \exp(-D_{1low})]/[1 + \exp(-D_{1low}) + \exp(-D_{2low})], \quad (6b)$$

$$I_{high}/I_{low} = Q[\exp(-D_{2high}) - \exp(-D_{1high})]/[1 - \exp(-D_{1low})]$$

at $K_z < 0$. Here, $Q = [1 + \exp(-D_{1high}) + \exp(-D_{2high})]/[1 + \exp(-D_{1low}) + \exp(-D_{2low})]$, $D_1 = (E_2 - E_1)/kT$, $D_2 = (E_3 - E_2)/kT$, and the subscript high (low) indicates that the magnetic induction B_z corresponding to the high-field (low-field) line is used in calculations of E_p.

As follows from relationships (6), the increase (decrease) in the ratio I_{high}/I_{low} upon cooling indicates that the parameter K_z has positive (negative) sign.

4. SAMPLES AND EXPERIMENTAL TECHNIQUE

The measurements were performed at a frequency of 9244.5 MHz and a temperature of 4.2 K. Single crystals of $KY(WO_4)_2$ doped with Dy^{3+} ions at concentrations of 0.02, 0.1, 1, 2, and 10% served as samples. The crystals were grown through spontaneous crystallization from a $K_2W_2O_7$ solution upon cooling from 950°C at a rate of 3 K/h. The linear dimensions of the grown crystals varied from 2 to 3 mm, and a number of crystals possessed a clearly pronounced faceting. The crystals were oriented using x-ray diffraction.

Analysis of the angular dependences of the EPR spectrum in the studied range of impurity concentrations demonstrates that the absorption spectrum is strongly anisotropic. The spectrum is observed at the lowest external field H_0 in the case when the field is aligned along the z axis of the laboratory coordinate system. The general view of the EPR spectrum for two characteristic impurity concentrations is displayed in Fig. 1.

At a low impurity concentration (0.02% Dy^{3+}), the absorption spectrum is well resolved (the linewidth ΔB is equal to 0.7 mT) and consists of the central singlet M and two sextets (A_1–A_6 and B_1–B_6) of equidistant lines (Fig. 2) with relative intensities corresponding to the natural abundance of dysprosium isotopes. The centers of the sextets coincide with the line M. The satellites m and S (not shown in Fig. 2) with substantially less intensities can be seen in the EPR spectrum at a larger amplification. The low-field (m_{low}) and high-field (m_{high}) satellites are equidistant from the line M. The satellites S are located at equal distances to the left (S_1 and S_2) and to the right (S_3 and S_4) of the A, M, and B lines each.

An increase in the impurity concentration is attended by the following changes in the spectra.

(1) 0.1% Dy^{3+} : $KY(WO_4)_2$. There arise the satellites a_1–a_4, b_1–b_4, s_2, and s_3 at low (Fig. 3a) and high (Fig. 3b) fields and the satellite f_{high} at even higher fields (Fig. 1). The positions of the satellites a_{2low}–a_{4low} and b_{1low}–b_{4low} with respect to the satellite m_{low} and the satellites a_{1high}–a_{4high} and b_{1high}–b_{4high} with respect to the satellite m_{high} and also their relative intensities (except for the intensities of the satellites b_2 and b_3) are similar to those observed in the spectrum depicted in Fig. 2. The separation between the satellites s_2 (s_3) and the satellites m is identical to that between the satellites S_2 (S_3) and the

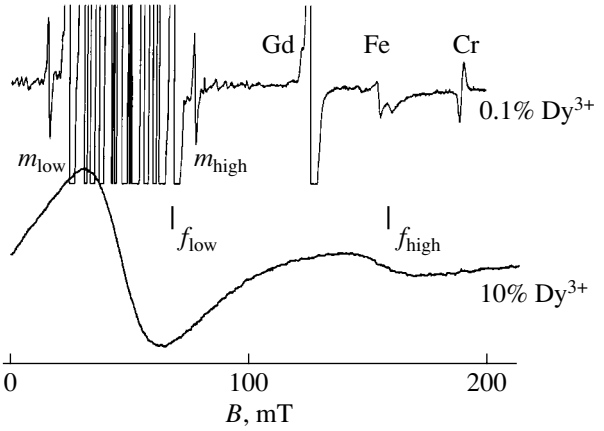

Fig. 1. A general view of the EPR spectra of Dy^{3+} ions in $KY(WO_4)_2$ at concentrations of 0.1 and 10% Dy^{3+}. The upper spectrum, in addition to the Dy lines, contains absorption lines assigned to Gd^{3+} and Fe^{3+} (uncontrollable impurities in the sample and sample holder). The signal with a reversed phase is attributed to Cr^{3+} ions in Al_2O_3 placed in the cavity for calibration. For $\mathbf{B}_0 \parallel z$, the satellite f_{high} coincides with the Fe^{3+} line (the upper and lower spectra are taken at $\Theta = 10°$ and 0°, respectively).

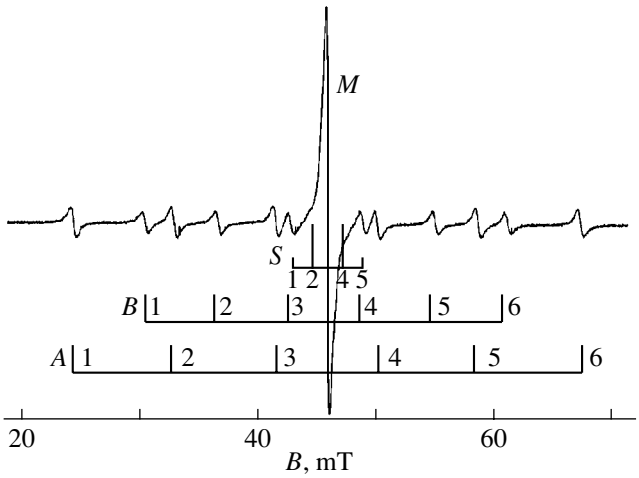

Fig. 2. EPR spectrum of 0.02% Dy^{3+} : $KY(WO_4)_2$ at $\Theta = 0°$. To avoid overloading of the figure, the satellites S of the hyperfine components and the satellites m are not shown.

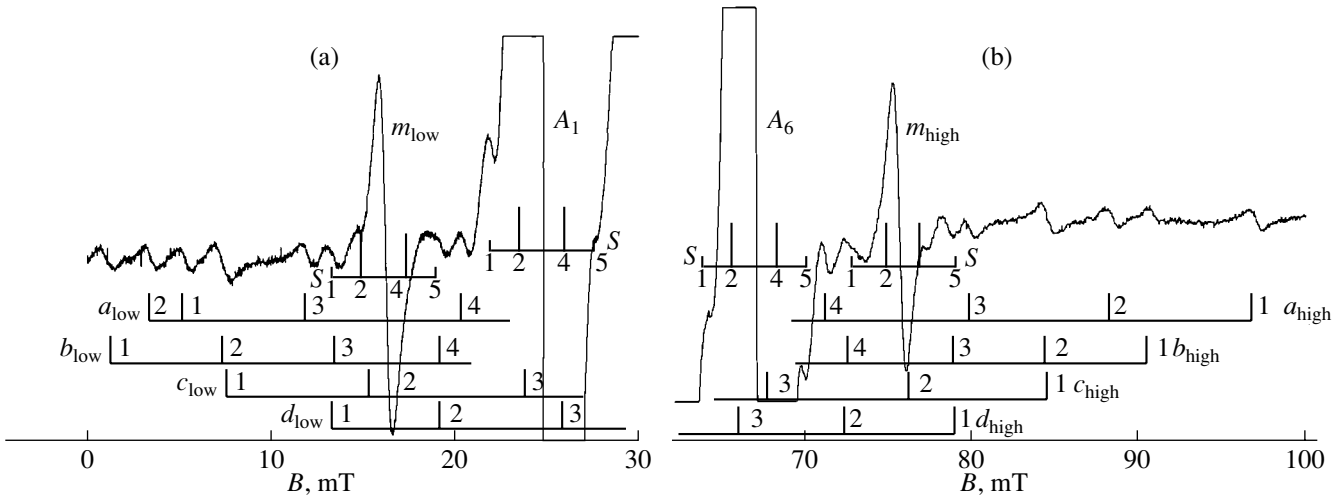

Fig. 3. (a) Low-field and (b) high-field parts of the EPR spectrum of 0.1% Dy^{3+} : $KY(WO_4)_2$ at $\Theta = 0°$.

lines *A*, *M*, and *B*. The symmetry is broken by the satellite a_1, because the satellite a_{low} has no analog in the high-field part of the spectrum, whereas an analog of the satellite a_{high} should be observed at negative fields. Moreover, the intensities of the low-field satellites a_{low}, b_{low}, and m_{low} exceed the intensities of the corresponding high-field satellites: $I_{low}/I_{high} = 1.14 \pm 0.03$. The satellite f_{high} also stands out in the spectrum. The single line of this satellite is noticeably broader ($\Delta B = 2.1$ mT) than the other lines ($\Delta B = 0.81$ mT).

(2) 2% Dy^{3+} : $KY(WO_4)_2$. The lines in the spectrum are broadened to $\Delta B = 2.6$ mT. As a result, the structure of the spectrum becomes substantially smeared.

(3) 10% Dy^{3+} : $KY(WO_4)_2$. The lines in the spectrum are so broadened that the fundamental spectrum with satellites transforms into a single line with the width $\Delta B = 33$ mT. The satellite f_{high} has the same width (Fig. 1).

Analysis of the concentration dependence of the spectral intensity demonstrates that the intensities of the lines *A*, *M*, and *B* and the satellites *S* increase in proportion to the impurity concentration. At the same time, the intensities of the satellites *a*, *m*, *b*, and *s* are proportional to the impurity concentration squared. The intensity of the satellite f_{high} increases even more steeply: $I_f/I_m = 0.2$ at 0.1% Dy^{3+} and 8.5 at 2% Dy^{3+}. At a concentration of 10% Dy^{3+}, the intensity of the satellite f_{high} becomes comparable to the intensity I_{sum} of the line representing the overall spectrum, including the other satellites: $I_{sum}/I_f = 7.8$.

5. DISCUSSION

5.1. The spectrum of single ions. The *AMB* spectrum (the fundamental spectrum) is assigned to the single Dy^{3+} ions. Analysis of the angular dependences shows that the spectrum is described by the spin Hamiltonian (1) with the parameters $g_x = 0$, $g_y = 1.54$, $g_z = 14.6$, $^{163}A_z = 582.8 \times 10^{-4}$ cm^{-1}, $^{161}A_z = 416.5 \times 10^{-4}$ cm^{-1}, $^{163}A_y = 146 \times 10^{-4}$ cm^{-1}, and $^{161}A_y = 104 \times 10^{-4}$ cm^{-1}. The axes are aligned parallel to the axes of the laboratory coordinate system.

In order to determine the spin–spin interaction tensor components, it is important to identify correctly the lines in the experimental spectrum. In this respect, the satellites *S* are noteworthy. The low intensity of these satellites (Figs. 3a, 3b) suggests that they belong to the spectrum of ion pairs. However, the linear concentration dependence of the intensity is a convincing reason to assume that the satellites *S* are attributed to the spectrum of single ions. Their origin can be explained by the superhyperfine interaction revealed in our recent work [12].

In the $KY(WO_4)_2$ crystal, ^{16}O nuclei do not possess magnetic moments. For this reason, the superhyperfine structure of the spectrum can be attributed to ^{39}K (^{39}c = 93.08%) and ^{41}K (^{41}c = 6.91%) nuclei with nuclear spin $I = 3/2$ and ^{183}W (^{183}c = 14.28%) nuclei with nuclear spin $I = 1/2$. The other even tungsten isotopes ^{e}W have zero nuclear spin. Since the rare-earth ion is located at the twofold rotation axis, there should exist two identical ligands responsible for the superhyperfine structure. By ignoring the interaction between the ligands, the analysis can be performed using Hamiltonian (1) with an additional term describing the interaction of each ligand with the Dy^{3+} ion; that is,

$$\hat{S}\mathbf{A}_S\hat{I}^{\mathrm{I}} + \hat{S}\mathbf{A}_S\hat{I}^{\mathrm{II}}, \qquad (7)$$

where $\hat{I}^{\mathrm{I}}$ and $\hat{I}^{\mathrm{II}}$ are the nuclear spin operators of the first and second ligands, respectively, and $\mathbf{A}_S$ is the tensor of the superhyperfine interaction. We assume that

this interaction is axial in character and does not depend on the mass of the ligand isotope. The calculations will be performed only for the even dysprosium isotopes, because the hyperfine components of the spectrum under the aforementioned assumptions (i)–(v) should exhibit a similar behavior.

First, let us assume that potassium ions are responsible for the superhyperfine structure. In this case, the EPR line is split into an octet with the relative intensities 1 : 2 : 3 : 4 : 3 : 2 : 1 and the separation between the nearest components $\delta B = A_{zS}$.

Now, we consider tungsten nuclei. There exist three possible combinations of isotopes: (1) ^{183}W–Dy^{3+}–^{183}W, (2) ^{183}W–Dy^{3+}–^{e}W, and (3) ^{e}W–Dy^{3+}–^{e}W.

It follows from relationship (7) that, in the first combination, the initial line is split into a triplet with the relative intensities 1 : 2 : 1 and the separation between the nearest components $\delta B = A_{zS}$. In the second case, the initial line is split into two components with identical intensities and the same separation. In the third case, the absorption line remains unchanged.

Feller [16] demonstrated that, if there are a sufficiently large number of objects of two sorts $\mathcal{A}$ and $\mathcal{B}$ and the concentration of objects of the $\mathcal{A}$th sort is equal to x, the probability V of finding m objects of the $\mathcal{A}$th sort in the sample of the volume n is defined as

$$V = C_m^n x^m (1-x)^{n-m}. \quad (8)$$

Hence, the probabilities of forming the above combinations are as follows: $V_1 = C_2^2$, $^{183}c^2 = {}^{183}c^2$, $V_2 = 2{}^{183}c(1 - {}^{183}c)$, and $V_3 = (1 - {}^{183}c)^2$. The relative intensities of the spectra are determined by the ratio $I_1 : I_2 : I_3 = V_1 : V_2 : V_3$. Since the centers of the spectra coincide with each other, the superposition of the spectra gives an equidistant pentad with the relative intensities $[{}^{183}c^2/4] : [{}^{183}c(1 - {}^{183}c)] : [{}^{183}c^2/2 + (1 - {}^{183}c)^2] : [{}^{183}c(1 - {}^{183}c)] : [{}^{183}c^2/4] = 1 : 24 : 146 : 24 : 1$ and the separation between the nearest components $\delta B = A_{zS}/2$.

As follows from the positions of the spectral lines, their relative intensities, and the concentration dependence in the experimentally observed spectrum *AMBS*, the satellites S_1–S_4 are the components of the superhyperfine structure with $A_{zS} = \pm(177 \pm 14) \times 10^{-4}$ cm^{-1} in the spectrum of individual ions and are associated with tungsten nuclei.

5.2. Pairs of Dy^{3+} ions. The dominant contribution to the spin–spin interaction tensor **K** (3) is made by the magnetic dipole–dipole (MDD) and isotropic exchange (Ex) interactions, that is,

$$K_{ij} = K_{ij\mathrm{MDD}} + K_{ij\mathrm{Ex}}, \quad i, j = x, y, z. \quad (9)$$

To sufficient accuracy, we can calculate only the contribution of the magnetic dipole–dipole interaction [17]:

$$K_{ij\mathrm{MDD}} = \mu^2/r^3(\delta_{ij} - 3n_i^2)g_i g_j, \quad (10)$$

where r is the interionic distance, n_i are the direction cosines of the bonding direction with respect to the corresponding axis, and $\delta_{ij} = 1$ at $i = j$ and $\delta_{ij} = 0$ at $i \neq j$.

The isotropic exchange interaction parameter $\mathcal{J}$ can be determined only experimentally. Note that this interaction can manifest itself in an anisotropic manner. By ignoring the admixture of excited states, the contribution (written in terms of effective spins) of the parameter $\mathcal{J}$ to the tensor **K** has the following form [17]:

$$K_{ij\mathrm{Ex}} = (g_{ij}/g_J)^2(g_J - 1)^2\mathcal{J}. \quad (11)$$

From relationships (10) and (11), it follows that the contributions of the interactions under consideration are quadratic in g_{ij}. Since $g_z \gg g_x$ and g_y, the spin–spin interaction is virtually axial and exhibits the characteristic spectrum described above. Therefore, taking into account the quadratic dependence of the intensity of the satellites *a*, *m*, and *b* on the concentration and disregarding the anomalously high intensities of the satellites b_2 and b_3, we can draw the inference that the satellites *a*, *m*, and *b* belong to the spectrum of Dy^{3+} ion pairs. The *amb* spectrum is represented by Hamiltonian (2) with the same parameters of the tensors **A** and **g** as for the single Dy^{3+} ion. Moreover, we have $K_{zamb} = -(4074 \pm 27) \times 10^{-4}$ cm^{-1} and condition (vi) is satisfied. The sign is determined with the use of relationships (6): at $T = 4.2$ K, the calculated ratio $I_{\mathrm{low}}/I_{\mathrm{high}}$ is equal to 0.906 at $K_z > 0$ and 1.12 at $K_z < 0$. The latter value almost coincides with that observed in the experiment.

The calculated *amb* spectrum of ion pairs is schematically depicted in Fig. 3. The asymmetric positions of the satellites a_1 stem from the fact that, for the satellite $a_{1\mathrm{low}}$, the strong field condition is not satisfied and its position should obey relationships (5b).

Within the limits of experimental error, the intensity of the satellite b_2 is equal to the sum of the intensities of the satellites a_1 and b_1 and the intensity of the satellite b_3 is twice as high as the intensity of the satellite b_1. This indicates a superposition of the *amb* spectrum and a spectrum that is characterized by the same intensities and relative positions of the components but is shifted toward the center of the spectrum of single ions, as can be seen from the *cd* spectrum in Fig. 3. In turn, this might suggest that the spectrum involves satellites of another pair with $K_{zcd} = \pm(2373 \pm 39) \times 10^{-4}$ cm^{-1}. The sign cannot be uniquely determined, because the *cd* spectrum overlaps with the *amb* satellites and the spectrum of single ions. Further arguments in support of the *cd* spectrum are given below.

Let us dwell on the satellites *s*. The spectrum of single ions contains additional lines due to the interaction of the Dy^{3+} ion with tungsten nuclei. It is not improbable that the same interaction manifests itself in the spectrum of ion pairs and is responsible for the satellites *s*.

For analyzing this situation, Hamiltonian (2) is complemented by the term

$$\hat{S}_1\mathbf{A}_s\hat{I}^{\mathrm{I}} + \hat{S}_1\mathbf{A}_s\hat{I}^{\mathrm{II}} + \hat{S}_2\mathbf{A}_s\hat{I}^{\mathrm{III}} + \hat{S}_2\mathbf{A}_s\hat{I}^{\mathrm{IV}}, \qquad (12)$$

which describes the interaction of the first and second ions of the pair with the corresponding four tungsten nuclei. Term (12) will be treated as a perturbation of the initial system. As before, we assume that the superhyperfine interaction tensor $\mathbf{A}_s$ is axial, ligands do not interact with each other, and the external constant magnetic field is aligned along the z axis.

The following combinations of tungsten isotopes and the Dy^{3+} ion pair with different absorption spectra become possible.

(1) All four ligands are odd isotopes. From formula (8), we obtain the probability of forming this combination $V_1 = {}^{183}c^4$. With due regard for the above assumptions, simple calculations of Hamiltonian (2) complemented by term (12) demonstrate that each line in the spectrum of ion pairs is split into a triplet with the relative intensities 1 : 2 : 1 and the separation between the nearest components $\delta B = A_{zs}$.

(2) One ligand is an even isotope, and the other ligands are odd isotopes. In this case, we have the probability $V_2 = 4(1 - {}^{183}c){}^{183}c^3$. Each satellite is split into a pentad with the relative intensities 1 : 2 : 2 : 2 : 1 and the separation between the nearest components $\delta B = A_{zs}/2$.

(3) Two ligands are even isotopes, and two ligands are ^{183}W isotopes. Here, there are two variants.

(3a) Each Dy^{3+} ion interacts with one even ^{e}W isotope. We obtain the probability $V_{3a} = 4[(1 - {}^{183}c){}^{183}c]^2$. The spectrum is represented by a doublet with the relative intensities 1 : 1 and $\delta B = A_{zs}$.

(3b) Both ^{183}W isotopes interact with one Dy^{3+} ion. In this case, we have the probability $V_{3b} = V_{3a}/2$ and a triplet with the relative intensities 1 : 6 : 1 and $\delta B = A_{zs}$.

(4) One ligand is a ^{183}W isotope, and the other three ligands are even isotopes. The probability V_4 is equal to $4{}^{183}c(1 - {}^{183}c)^3$. The spectrum consists of a triplet with relative intensities 1 : 2 : 1 and $\delta B = A_{zs}/2$.

(5) All four ligands are even isotopes. We have the probability $V_5 = (1 - {}^{183}c)^4$. The initial spectrum remains unchanged.

The overall spectrum is a pentad of equidistant lines with the separation $\delta B = A_{zs}/2$ and the relative intensities $[{}^{183}c^2/4] : [{}^{183}c(1 - {}^{183}c)] : [1 + {}^{183}c(3{}^{183}c/2 - 2)] : [{}^{183}c(1 - {}^{183}c)] : [{}^{183}c^2/4] = 1 : 24 : 146 : 24 : 1$. Judging from the spectrum calculated at $A_{zs} = A_{zS} = \pm 177 \times 10^{-4}$ cm^{-1} (Fig. 3), it is beyond question that the satellites s and S belong to the superhyperfine structure of the EPR spectrum.

It remains to elucidate the origin of the satellite f_{high}. At low impurity concentrations, the number of interacting triads of Dy^{3+} ions is proportional to the concentration cubed. Taking into consideration that the intensity of the satellite f_{high} increases steeply, it can be assumed that this satellite is associated with the spectrum of Dy^{3+} triads. However, this circumstance is not confirmed experimentally. Actually, if the interaction between the first and third ion is disregarded, the Hamiltonian of the triad, by analogy with Hamiltonian (2), can be written in the form

$$\hat{H} = \hat{H}_1 + \hat{H}_2 + \hat{H}_3 + \hat{H}_{12} + \hat{H}_{23}, \qquad (13)$$

where $\hat{H}_1$, $\hat{H}_2$, and $\hat{H}_3$ are Hamiltonians (1) of single Dy^{3+} ions and Hamiltonians $\hat{H}_{12}$ and $\hat{H}_{23}$ describe the interaction between the first and second ions and between the second and third ions, respectively [see formula (3)]. By calculating Hamiltonian (13) for even dysprosium isotopes under the above assumptions (i)–(vi), we found that the spectrum for a high-energy photon should be represented by a pentad with the relative intensities 1 : 4 : 2 : 4 : 1, the separation between the nearest components $\delta B = K_z/2$, and the center coinciding with the center of the spectrum of single ions. Since no considerable difference in the parameter K_z for a pair (for example, *amb*) and a triad can be expected, the second and fourth lines in the spectrum of triads should coincide with the satellites m_{low} and m_{high} and the first and fifth lines should be located in fields of 14.5 and 105 mT. However, this disagrees with the experimental data, according to which the satellite f_{high} occurs at 154.3 ± 0.5 mT. If the satellite f_{high} belongs to the spectrum of triads with a different parameter K_z, it is unclear how we can explain the absence of the other lines in the pentad.

Consequently, the satellite f_{high} cannot be attributed to the triad. We are forced to assume that this satellite is associated with an ion pair characterized by the parameter $K_{zf} = \pm(14900 \pm 110) \times 10^{-4}$ cm^{-1}. In this case, the low-field satellite f_{low} should be observed in a field of 63.8 mT and be overlapped with the fundamental spectrum, as can be seen from Fig. 1. This situation is consistent with our assumption but does not allow us to determine the sign of the parameter K_{zf}.

So far, we have not concentrated on the problem of the assignment of the experimental spectra to a particular type of pairs. In order to identify the spectra, we now consider the data on the calculated contributions of the magnetic dipole–dipole interaction to the spin–spin interaction (Table 3) for different types of pairs. First, let us assume that the interaction between Dy^{3+} ions occurs only through the magnetic dipole–dipole mechanism. In this case, the spectrum can contain satellites attributed to the pairs (in decreasing order of splitting) *nn*, 5*n*, 9*n*, 4*n*, and 10*n* (the satellites of the last pair are almost completely hidden by the spectrum of single ions). For the other types of pairs, the contribution of the magnetic dipole–dipole interaction is too small to

shift satellites from the range of the fundamental spectrum.

Now, we consider the additional effect of the isotropic exchange interaction. For pairs of closely spaced ions, this interaction rapidly weakens with an increase in the spacing; as a result, the spectrum can noticeably change compared to the spectrum associated only with the magnetic dipole–dipole interaction. However, it is highly improbable that the exchange interaction can substantially affect the spectra of the pairs of widely spaced ions, because the interionic distance r_{3n} even for the 3*n* pair is again half the distance r_{nn}. Therefore, the satellites *amb* and *cd* cannot belong to the spectra of the pairs *nn*, 2*n*, or 3*n*. Indeed, otherwise, the absence of the spectral lines attributed to the 5*n*, 4*n*, 9*n*, and 10*n* pairs of widely spaced ions can be explained only under the unrealistic assumption that the exchange interaction for all these pairs is not only sufficiently strong but also has a sign capable of compensating for the magnetic dipole–dipole interaction. Making allowance for the same intensities of the spectra *amb* and *cd*, these satellites also cannot be assigned to the 4*n* pair, because the probability of forming this pair is twice as high as that of forming the other pairs (Table 3). With the elimination method, we should also exclude the pair 10*n* from our consideration, because the contribution of the magnetic dipole–dipole interaction to K_{z10n} substantially differs in sign and magnitude from the contributions $K_{z\mathrm{MDD}5n}$ and $K_{z\mathrm{MDD}9n}$, whereas the difference between $|K_{zamb}|$ and $|K_{zcd}|$ is slightly larger than 50%. For the remaining pairs, we assign the *amb* spectrum to the 5*n* pair and the *cd* spectrum to the 9*n* pair. This choice is made for the following reasons. The parameter K_{zamb} coincides in sign with $K_{z\mathrm{MDD}5n}$ and differs from it in magnitude by only 13%. The difference between $K_{z\mathrm{MDD}5n}$ and $K_{z\mathrm{MDD}9n}$ is equal to 30%, which is close to the difference between $|K_{zamb}|$ and $|K_{zcd}|$. The parameter $K_{z\mathrm{MDD}9n}$ is less than the parameter $K_{z\mathrm{MDD}5n}$; hence, the *cd* spectrum with a smaller splitting should be attributed to the 9*n* pair. This suggests that K_{zcd} and K_{zamb} have the same sign. By using the experimental results, the data given in Table 3, and relationships (9) and (11), we obtain $\mathcal{J}_{5n} = (-38 \pm 3) \times 10^{-4}$ cm^{-1} and $\mathcal{J}_{9n} = (18 \pm 4) \times 10^{-4}$ cm^{-1}. A similar change in the sign of $\mathcal{J}$ for widely spaced neighbors was observed for pairs of Ni^{2+} ions in $ZnS : F_6 \cdot 6H_2O$ [18].

It only remains for us to identify the pair *nn* and the origin of the satellites *f*. Taking into account that r_{nn} is half as large as r_{5n} or r_{9n}, it can be expected that the spectrum of the nearest neighbor ion pair substantially differs from the spectrum associated only with the magnetic dipole–dipole interaction. Therefore, we can make the inference that the satellite f_{high} is attributed to the *nn* pair. In this case, the parameter $\mathcal{J}_{nn}$ is equal to $(601 \pm 17) \times 10^{-4}$ cm^{-1} at $K_{zf} > 0$ and $(-1636 \pm 17) \times 10^{-4}$ cm^{-1} at $K_{zf} < 0$. Both these values are appreciably larger than the parameters $\mathcal{J}$ for pairs of the other types. The sign of the parameter K_{zf} can be uniquely determined only from analyzing the EPR spectra at higher frequencies at which the satellite f_{low} appears to be located outside the range of the fundamental spectrum. However, with due regard for the fact that the magnetic properties of the compound studied are governed by the spin–spin interaction of the nearest neighbor ion pairs, the sign of the parameter K_{zf} can be predicted from indirect data. Our earlier investigation into the magnetic properties of $KDy(WO_4)_2$ [8] demonstrated that this compound is antiferromagnetically ordered; hence, the parameter $\mathcal{J}_{nn}$ should have positive sign; i.e., $\mathcal{J}_{nn} = (601 \pm 17) \times 10^{-4}$ cm^{-1} and $K_{zf} > 0$.

As was shown above, the experimental spectrum of Dy^{3+} ion pairs is a superposition of the spectra of pairs with different isotopic compositions. The spectrum of pairs has a sufficiently well-defined structure similar to that of the spectrum of single ions only in the case when the spin–spin interaction does not depend on the isotopic number. The dominant contribution to the spin–spin interaction of the pairs 5*n* and 9*n* is made by the magnetic dipole–dipole interaction, which is independent of the isotopic mass. Therefore, the spectra *amb* and *cd* are characterized by a rather high resolution. By contrast, the contribution of the isotropic exchange interaction energy for the *nn* pair is equal to more than half the total interaction energy. Hence, if the isotropic exchange interaction depends on the isotopic composition of the pair, smearing of the spectrum structure should occur, which is observed for the satellites *f*.

The isotropic exchange interaction primarily depends on two factors, namely, the interionic distance and the bonding direction. The bonding directions in the pairs 5*n* and 9*n* make angles $\Theta_{5n} = 20°$ and $\Theta_{9n} = 7.8°$ with the *z* axis. In pairs of the other types, the angles Θ are larger and vary from $\Theta_{4n} = 45.8°$ to $\Theta_{10n} = 88.7°$. Therefore, the absence of the considerable contribution from the exchange interaction for these pairs can be explained by the elongation of electron clouds along the *z* axis. On the other hand, the exchange interaction at short interionic distances can be sufficiently efficient even for an "unfavorable" direction, as is the case with the pair *nn* in which $\Theta_{nn} = 66°$. Note that, among all the types of pairs, only the pairs *nn*, 5*n*, and 9*n* are inside an ellipsoid with the semiaxes $a_x = a_y = 4$ Å and $a_z = 10$ Å.

6. CONCLUSIONS

Thus, it was established that the strongest interaction in the $KY(WO_4)_2$ crystal is observed between the nearest neighbor Dy^{3+} ions located along the crystallographic axis *a*. The isotropic exchange interaction ($\mathcal{J} = +601 \times 10^{-4}$ cm^{-1}) is comparable to the magnetic dipole–dipole interaction. The magnetic dipole–dipole interaction is predominant in pairs of widely spaced

ions. The contribution of the isotropic exchange interaction to the spin–spin interaction was determined for pairs $5n$ ($\mathcal{J} = -38 \times 10^{-4}$ cm^{-1}) and $9n$ ($\mathcal{J} = +18 \times 10^{-4}$ cm^{-1}). It should be noted that the g value for the Dy^{3+} ion up to a concentration of 10% remains constant. In order to answer the question as to why the concentrated crystal exhibits a different value of g, it is necessary to examine crystals with a gradually increasing impurity ion concentration. We assume that, in our previous work [7], we recorded only part of the spectrum due to the low-energy photons used in the experiments. The overall spectrum can be obtained at higher frequencies.

In the spectra of ion pairs, the superhyperfine structure attributed to tungsten nuclei was observed for the first time. The hypothesis was proposed that the isotopic composition of Dy^{3+} ions affects the exchange interaction. This effect manifests itself in a broadening of the lines in the spectrum of *nn* pairs. However, the problem cannot be considered to be solved conclusively. It is necessary to investigate crystals containing monoisotopic dysprosium impurities. The factor responsible for the drastic increase in the intensity of the lines in the spectrum of the nearest neighbor ion pairs remains to be revealed.

ACKNOWLEDGMENTS

We would like to thank G.Ya. Samsonova and L.F. Chernysh for growing the high-quality crystals of double tungstates and V.I. Kamenev for his assistance in the crystallographic orientation of the samples used in our investigation.

This work was supported in part by the Committee of Scientific Research of Poland (KBN), project no. 2 PO3B 141 18.

REFERENCES

1. A. A. Kaminskiĭ, H. P. Verdun, W. Koechner, *et al.*, Kvantovaya Élektron. (Moscow) **19**, 941 (1992).
2. M. C. Pujol, M. Rico, C. Zaldo, *et al.*, Appl. Phys. B **68**, 187 (1999).
3. A. A. Kaminskii, L. Li, A. V. Butahsin, *et al.*, Jpn. J. Appl. Phys. **36**, L107 (1997).
4. C. Zaldo, M. Rico, C. Cascales, *et al.*, J. Phys.: Condens. Matter **12**, 8531 (2000).
5. I. V. Skorbogatova and A. I. Zvyagin, Fiz. Nizk. Temp. **4** (6), 800 (1978) [Sov. J. Low Temp. Phys. **4**, 381 (1978)].
6. Yu. A. Popkov, V. I. Fomin, and L. N. Pelikh, Fiz. Nizk. Temp. **8** (11), 1210 (1982) [Sov. J. Low Temp. Phys. **8**, 614 (1982)].
7. M. T. Borowiec, V. Dyakonov, A. Nabialek, *et al.*, Physica B (Amsterdam) **240**, 21 (1997).
8. M. T. Borowiec, V. Dyakonov, V. Kamenev, *et al.*, Acta Phys. Pol. A **94**, 71 (1998).
9. V. P. D'yakonov, V. I. Markovich, V. L. Kovarskiĭ, *et al.*, Fiz. Tverd. Tela (St. Petersburg) **40** (4), 750 (1998) [Phys. Solid State **40**, 691 (1998)].
10. M. T. Borowiec, V. Dyakonov, E. Zubov, *et al.*, J. Phys. I **7**, 1639 (1997).
11. M. T. Borowiec, V. Dyakonov, A. Jedrzejczak, *et al.*, Phys. Lett. A **243**, 85 (1998).
12. M. T. Borowiec, V. P. Dyakonov, A. Prokhorov, and H. Szymczak, Phys. Rev. B **62**, 5834 (2000).
13. S. V. Borisov and R. F. Klevtsova, Kristallografiya **13** (3), 517 (1968) [Sov. Phys. Crystallogr. **13**, 420 (1968)].
14. P. V. Klevtsov and L. P. Kozeeva, Dokl. Akad. Nauk SSSR **185** (3), 571 (1969) [Sov. Phys. Dokl. **14**, 185 (1969)].
15. Yu. K. Vishakas, I. V. Molchanov, A. V. Mikhaĭlov, *et al.*, Litov. Fiz. Sb. **28** (2), 224 (1988).
16. W. Feller, *An Introduction to Probability Theory and Its Applications* (Wiley, New York, 1966; Mir, Moscow, 1967), Vol. 1.
17. A. Abragam and B. Bleaney, *Electron Paramagnetic Resonance of Transition Ions* (Clarendon, Oxford, 1970; Mir, Moscow, 1972), Vol. 1.
18. I. M. Krygin and A. D. Prokhorov, Fiz. Tverd. Tela (St. Petersburg) **41**, 1602 (1999) [Phys. Solid State **41**, 1469 (1999)].

Translated by O. Borovik-Romanova

Physics of the Solid State, Vol. 44, No. 8, 2002, pp. 1597–1603. Translated from Fizika Tverdogo Tela, Vol. 44, No. 8, 2002, pp. 1522–1528.

MAGNETISM AND FERROELECTRICITY

Effect of Electric Field on the Dielectric Permittivity of Betaine Phosphite Crystals in the Paraelectric Phase

E. V. Balashova*, V. V. Lemanov*, and A. Klöpperpieper**

**Ioffe Physicotechnical Institute, Russian Academy of Sciences, ul. Politekhnicheskaya 26, St. Petersburg, 194021 Russia*
e-mail: balashova@pop.ioffe.rssi.ru
***Saarland University, Saarbrücken, D-66123 Germany*

Received January 11, 2002

Abstract—Temperature dependences of the dielectric permittivity of betaine phosphite crystals are studied both without and under application of an electric bias. It is shown that, in view of the fact that the high-temperature improper ferroelastic (antiferrodistorsive) phase transition at T_{c1} = 355 K is nearly tricritical, the nonlinear temperature dependence of inverse dielectric permittivity in the paraelectric phase and the effect of the field on the dielectric permittivity can be described within a phenomenological model containing two coupled (polar and nonpolar) order parameters with a negative coupling coefficient. An analysis of the model revealed that, in the case where two phase transitions, a nonpolar and a ferroelectric one, can occur in the crystal, all of its dielectric properties, including the polarization response in a field, can be described by one dimensionless parameter a. For the crystal under study, we have $a = -2.5$. This value of the parameter corresponds to a second-order ferroelectric transition far from the tricritical point, at which $a = -1$. It is shown that the polarization response in the paraelectric phase in an electric field calculated within this model differs radically from that in the ferroelectric phase-transition model for which the Curie–Weiss law holds in the paraelectric phase. © *2002 MAIK "Nauka/Interperiodica".*

1. INTRODUCTION

Betaine phosphite (BPI) $(CH_3)_3NCH_2COO \cdot H_3PO_3$ belongs to a family of compounds based on the betaine aminoacid $(CH_3)_3N^+CH_2COO^-$ [1]. The BPI crystal consists of zigzag chains of HPO_3 inorganic tetrahedra coupled by hydrogen bonds. Each tetrahedron connects to a betaine molecule, also via a hydrogen bond. Two phase transitions were identified in BPI crystals, namely, an improper ferroelastic (antiferrodistorsive) $P2_1/m$, $Z = 2 \longrightarrow P2_1/c$, $Z = 4$ at T_{c1} = 355 K and a ferroelectric $P2_1/c$, $Z = 4 \longrightarrow P2_1$, $Z = 4$ at T_{c2} = 196–225 K [1–3]. Ferroelectric ordering sets in along chains parallel to the $Y(b)$ axis (Y is the twofold axis).

Studies of the temperature dependences of dielectric permittivity ε_b showed that the $\varepsilon_b(T)$ relation changes slope in the region of the structural phase transition at T_{c1} = 355 K [2]. In the phase stable at temperatures $T_{c2} < T < T_{c1}$, which we shall call the paraelectric antiferrodistorsive phase, the dielectric permittivity grows substantially faster with decreasing temperature than in the symmetric high-temperature phase for $T > T_{c1}$ and the dependence of its inverse dielectric permittivity on $(T - T_{c2})$ is nonlinear [2]. The ferroelectric phase-transition temperature in nominally pure BPI crystals varies within the interval T_{c2} = 196–225 K, apparently because of a residual impurity present in a small amount [2, 4–6]. Measurements of the lattice parameters of BPI crystals with different T_{c2} temperatures revealed only slight differences in the lattice parameter and monoclinic angle [4]. In some samples, additional anomalies in the dielectric permittivity were observed for $T < T_{c2}$, which are tentatively assigned to additional phase transitions [5].

The temperature behavior of the dielectric permittivity in the paraelectric antiferrodistorsive phase has been analyzed in terms of the quasi-one-dimensional Ising model [4, 6], as well as within Landau's theory, with a term proportional to $(T - T_{c2})^2$ introduced into the thermodynamic potential [6]. Another approach to the description of the BPI dielectric properties is based on Landau's theory with two coupled order parameters, polar and nonpolar [7]. The dielectric anomaly at the improper ferroelastic (antiferrodistorsive) phase transition (T_{c1} = 355 K) and the temperature behavior of dielectric permittivity in the paraelectric antiferrodistorsive phase ($T_{c2} < T < T_{c1}$) are described satisfactorily if an invariant $\xi\eta^2P^2$ (η is the nonpolar order parameter for the phase transition at T_{c1} = 355 K, P is the polarization) with a negative sign of the ξ coefficient is included into the thermodynamic potential and if it is recalled that the improper ferroelastic phase transition is close to the tricritical point [7, 8].

Investigation of the effect of a bias field on dielectric permittivity is an efficient method of studying phase transitions which permits one to obtain information on the phase-transition mechanism, establish the order of the phase transition, and determine some constants of the thermodynamic potential. The dielectric permittiv-

ity of BPI crystals under the application of a bias field was studied in [6]. It was shown that the shift of the maxima in the dielectric permittivity toward higher temperatures with increasing bias is described in terms of Landau's theory for second-order ferroelectric phase transitions. It should be pointed out, however, that studies of the effect of bias on the shift of the maxima in dielectric permittivity is limited to a narrow temperature region of about 10 K near T_c, where one may expect a noticeable manifestation, for instance, of the influence of defects. By contrast, investigation of the field-induced variation of ε in the paraelectric phase at temperatures more distant from the phase-transition point, while being more difficult experimentally, offers the possibility, by excluding or reducing the influence of defects or of other mechanisms near T_c, not only of establishing the order of the phase transition but also of more reliably estimating the parameters of the thermodynamic potential from the properties of the crystal in the paraelectric phase alone.

The purpose of this work was to perform an experimental study of the effect of an electric bias field on the dielectric permittivity of the BPI paraelectric antiferrodistorsive phase over a broad temperature range and a thermodynamic analysis of the polarization response in a bias field in terms of a model assuming coupled polar and nonpolar order parameters with a negative coupling coefficient.

2. EXPERIMENTAL RESULTS

For dielectric studies, we used samples measuring $4 \times 1 \times 5$ mm with the edges oriented along the *X*, *Y*, and *Z* axes, respectively. *Y*(*b*) is the twofold axis along which spontaneous polarization forms.

Figure 1 presents the temperature dependences of dielectric permittivity ε_b and $\tan\delta$ measured at 100 Hz, 1 kHz ($U_\sim$ = 2.5 V), and 1 MHz ($U_\sim$ = 0.25 V). The dielectric permittivity is seen to pass through a maximum at a temperature of 204 K, which almost coincides with the lower temperature limit for ferroelectric phase transitions in nominally pure BPI crystals. Above T = 204 K, as is evident from Fig. 1, the dielectric permittivity exhibits virtually no dispersion in the paraelectric phase and $\tan\delta$ is small.

Figure 2 displays the temperature dependence of inverse dielectric permittivity in the paraelectric phase; it does not follow the linear Curie–Weiss relation.

Figure 3 shows temperature dependences of the dielectric permittivity measured at 1 MHz in various bias fields. The maxima in dielectric permittivity are seen to decrease in magnitude with increasing bias and to shift toward higher temperatures.

The effect of an external electric field on dielectric permittivity of the paraelectric phase within a broad temperature range was investigated in the following way. The sample was cooled to a temperature *T*, and, after the temperature had stabilized, which was checked with high accuracy by the absence of variation of dielectric permittivity, an external bias *E* was applied to the sample. The difference between the values of dielectric permittivity in the field and without it, $\Delta\varepsilon = \varepsilon(E) - \varepsilon(0)$, was measured to within ±0.05 above the temperature at which the dielectric permittivity was maximum.

Figure 4 depicts $\Delta\varepsilon$ vs. $(T - T_{c2})$ dependences obtained in fields $E_1 = 4 \times 10^4$ and $E_2 = 10^5$ V/m. For temperatures $(T - T_{c2}) < 60$ K, we found the dielectric

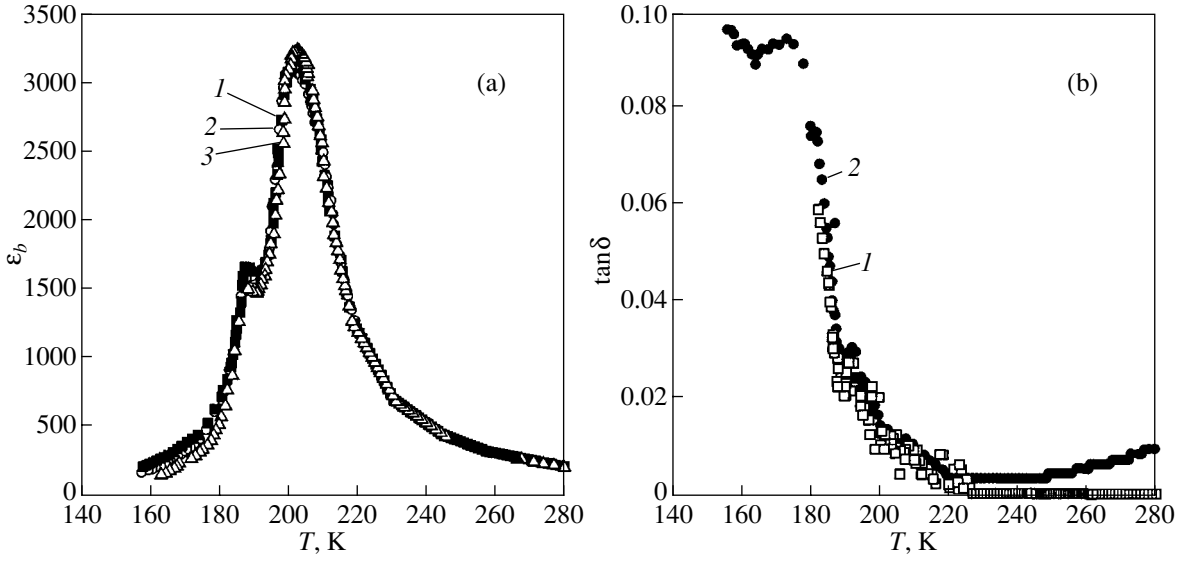

Fig. 1. Temperature dependences of (a) dielectric permittivity and (b) $\tan\delta$ measured at frequencies of (*1*) 100 Hz, (*2*) 1 kHz, and (*3*) 1 MHz.

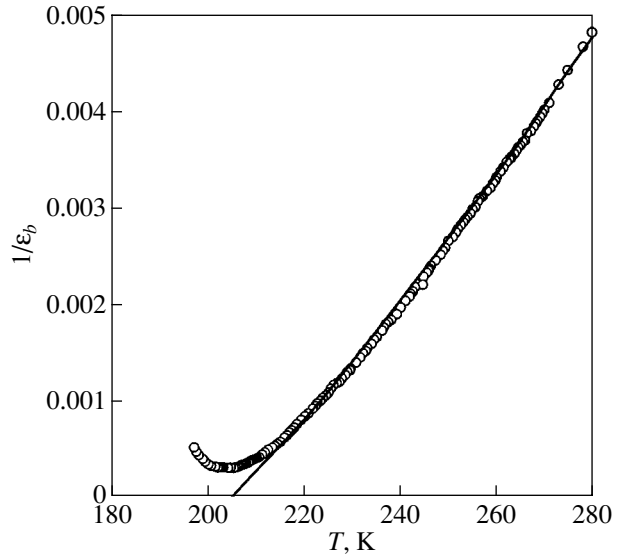

Fig. 2. Temperature dependences of inverse dielectric permittivity. The solid curve is a plot of Eq. (12).

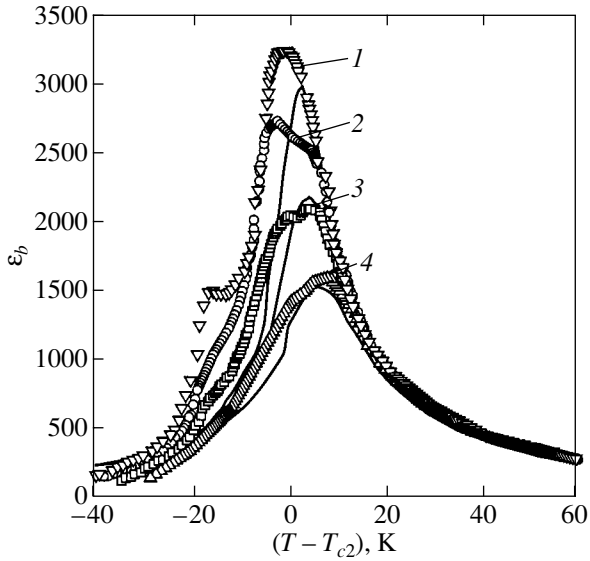

Fig. 3. Temperature dependences of dielectric permittivity measured at 1 MHz without and with application of an electric field E equal to (*1*) 0, (*2*) 4×10^4, (*3*) 10^5, and (*4*) 2×10^5 V/m. Solid curves are plots of Eq. (11) for $a = -3.5$.

permittivity to decrease under application of a bias. For $(T - T_{c2}) > 60$ K and up to room temperature, no changes in the dielectric permittivity were observed in the bias range covered.

3. ANALYSIS OF EXPERIMENTAL RESULTS

A specific feature of BPI crystals is that the temperature dependence of inverse dielectric permittivity in the paraelectric phase is not described by a linear relation (Fig. 2). As shown in [7], this deviation of the inverse dielectric permittivity from the Curie–Weiss law fits nicely into the thermodynamic model with two coupled order parameters and is accounted for by the high-temperature improper ferroelastic phase transition at $T_{c1} = 355$ K being close to the tricritical point.

The thermodynamic potential, including the relation between the polar and structural order parameters and the structural phase transition at the tricritical point, can be written as [7]

$$E = \frac{1}{2}\alpha_1\eta^2 + \frac{1}{6}\gamma_1\eta^6 + \frac{1}{2\chi_0}P^2 + \frac{1}{4}\beta_2 P^4 + \frac{1}{2}\xi\eta^2 P^2 - PE, \quad (1)$$

where $\alpha_1 = \lambda_1(T - T_{c1})$, $\beta_2 > 0$, $\xi < 0$, η is the nonpolar order parameter for the phase transition at T_{c1}, P is polarization, E is the macroscopic electric field, and χ_0 is the background dielectric susceptibility.

Thermodynamic potential (1) can be reduced to the dimensionless form

$$f = \frac{1}{2}ta^2q^2 + \frac{1}{6}q^6 - ap^2 + \frac{1}{2}p^4 - q^2p^2 + 2ape, \quad (2)$$

where $t = (T - T_{c1})/\Delta T$ is the reduced temperature; $\Delta T = \frac{\gamma_1}{\lambda_1\chi_0^2\xi^2}$ determines, as will be shown later, the region

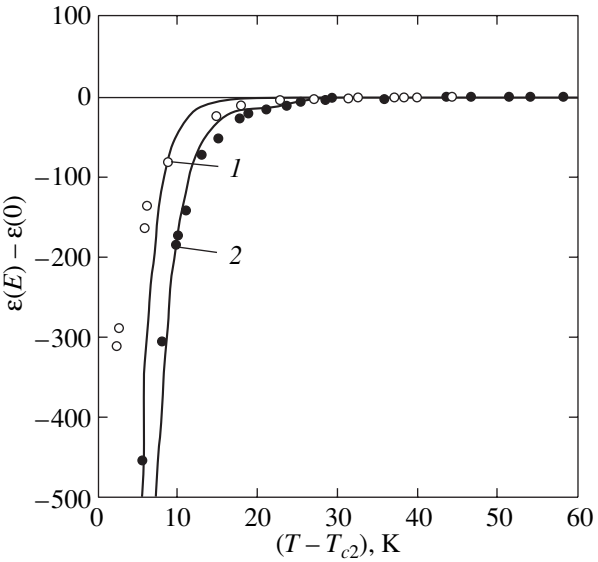

Fig. 4. Temperature dependences of the variation of dielectric permittivity at 1 MHz in the paraelectric phase with an electric field applied. E: (*1*) 4×10^4 and (*2*) 10^5 V/m. Solid curves are plots of Eq. (13) for $a = -3.5$.

of stability of the paraelectric antiferrodistorsive phase ($q \neq 0$, $p = 0$); $a = \dfrac{2\beta_2^2\gamma_1}{\chi_0\xi^3} < 0$ is a dimensionless parameter determining (see below) the region of stability of the polar phase ($q \neq 0$, $p \neq 0$); and

$$f = F\frac{8\beta_2^3\gamma_1^2}{\xi^6}, \quad q^2 = \frac{2\beta_2\gamma_1}{\xi^2}\eta^2,$$

$$p^2 = -\frac{2\beta_2^2\gamma_1}{\xi^3}P^2, \quad e = \frac{\sqrt{2\gamma_1}\beta_2\chi_0}{(-\xi)^{3/2}}E.$$

From Eq. (2), one can derive equations of state in the absence of a field:

$$\begin{aligned} q(ta^2 + q^4 - 2p^2) &= 0, \\ p(-a + p^2 - q^2) &= 0. \end{aligned} \tag{3}$$

As follows from Eq. (3), the system can reside in three states, namely, ($q = 0$, $p = 0$), ($q \neq 0$, $p = 0$), and ($q \neq 0$, $p \neq 0$) [in zero field, the ($q = 0$, $p \neq 0$) state cannot exist], whose regions of stability are determined by the inequalities

$$\begin{aligned} &\partial^2 f/\partial q^2 > 0, \quad \partial^2 f/\partial p^2 > 0 \\ &\text{and } [(\partial^2 f/\partial q^2)(\partial^2 f/\partial p^2) - (\partial^2 f/\partial q\partial p)^2] > 0. \end{aligned} \tag{4}$$

Equations (3) and (4) can be used to obtain expressions for the equilibrium values of the order parameters in the corresponding phases and the regions of stability of these phases.

Let us consider regions of the dimensionless parameter a which differ in the temperature interval of stability of the polar state ($q \neq 0$, $p \neq 0$).

Region I ($a < -1$)

In this region of values of parameter a, a sequence of a tricritical high-temperature phase transition and a continuous ferroelectric phase transition sets in. The phase sequence, the equilibrium values of the order parameters in the phases, and the regions of stability of the states can be presented in the following way:

(1) $q = 0$, $p = 0$ (high-temperature symmetric phase). The phase is stable for $t > 0$ in dimensionless units or for $T > T_{c1}$ in absolute units.

(2) $q \neq 0$, $p = 0$ (paraelectric antiferrodistorsive phase). The equilibrium value of the order parameter is

$$q^4 = -a^2 t. \tag{5}$$

The phase is stable for $-1 < t < 0$ or, in absolute units, for $T_{c2} < T < T_{c1}$, where $T_{c2} = T_{c1} - \Delta T$ is the temperature at which the ($q \neq 0$, $p = 0$) state loses stability.

(3) $q \neq 0$, $p \neq 0$ (polar phase). The equilibrium values of the order parameters can be written as

$$\begin{aligned} q^2 &= I + \sqrt{1 - ta^2 + 2a}, \\ p^2 &= a + 1 + \sqrt{1 - ta^2 + 2a}. \end{aligned} \tag{6}$$

The phase is stable for $t < -1$ or for $T < T_{c2}$. In this region of values of parameter a, T_{c2} is also the temperature of the continuous ferroelectric phase transition.

Region II ($-1 < a < -0.5$)

In this region of values of parameter a, a sequence of a tricritical structural phase transition and a first-order ferroelectric phase transition is realized. The phase sequence, the equilibrium values of the order parameters in the phases, and the regions of stability of the states can be presented in the following way:

(1) $q = 0$, $p = 0$ for $t > 0$ ($T > T_{c1}$);

(2) $q \neq 0$, $p = 0$ for $-1 < t < 0$ ($T_{c2} < T < T_{c1}$).

The equilibrium value of the order parameter is given by Eq. (5). In this region of values of parameter a, as in the preceding case, T_{c2} is the temperature at which the ($q \neq 0$, $p = 0$) state loses stability.

(3) $q \neq 0$, $p \neq 0$ for $t < (2a + 1)/a^2$ ($T < T_0 = T_{c1} + \Delta T(2a + 1)/a^2$),

where T_0 is the polar-state stability-loss temperature; in the region of values of parameter a at hand, this temperature lies within the interval of the ($q \neq 0$, $p = 0$) state stability ($T_{c2} < T_0 < T_{c1}$).

The equilibrium values of the order parameters are given by Eqs. (6). The temperature hysteresis of the first-order ferroelectric phase transition is described by the following expression (which also characterizes the closeness of the second-order ferroelectric phase transition to the tricritical point):

$$T_0 - T_{c2} = [(a + 1)/a]^2\Delta T. \tag{7}$$

For $T_{c2} < T < T_0$, the temperature of the first-order ferroelectric phase transition is found from the equality of the energies $f(q \neq 0, p = 0) = f(q \neq 0, p \neq 0)$.

As follows from Eq. (7), for $a = -1$, the temperature hysteresis of the transition is absent. This means that the value $a = -1$ corresponds to the tricritical point for the ferroelectric phase transition.

Region III ($0 > a > -0.5$)

For these values of parameter a, a first-order phase transition from the ($q = 0$, $p = 0$) phase to the ($q \neq 0$, $p \neq 0$) phase is possible (the trigger transition):

(1) $q = 0$, p = 0 for $t > 0$ ($T > T_{c1}$);

(2) $q \neq 0$, $p \neq 0$ for $t < (2a + 1)/a^2$ ($T < T_0 = T_{c1} + \Delta T(2a + 1)/a^2$).

In this region of values of parameter a, the temperature T_0 at which the polar state loses stability lies within the stability temperature interval of the ($q = 0$, $p = 0$) state, $T_0 > T_{c1}$. The temperature hysteresis of the first-order trigger ferroelectric phase transition is characterized by $T_0 - T_{c1} = \Delta T(2a + 1)/a^2$, and the temperature of the trigger phase transition is found by equating the energies of the two states, $f(q = 0, p = 0) = f(q \neq 0, p \neq 0)$, in the temperature region $T_{c1} < T < T_0$. (Note that, for $a \approx -0.5$, we have $f(q = 0, p = 0) < f(q \neq 0, p \neq 0)$ for $T > T_{c1}$ and the trigger transition does not occur.)

Because BPI crystals undergo two phase transitions and the ferroelectric transformation is of the second order of a first-order phase transition occurring very close to the tricritical point, we shall restrict our consideration to the region of parameter $a < -0.5$. In this case, the points of the improper ferroelastic and of the ferroelectric phase transitions permit one to immediately find the value of the parameter $\Delta T = T_{c1} - T_{c2}$, which defines the stability region of the ($q \neq 0$, $p = 0$) state and is used to reduce the temperature to a dimensionless form. All information concerning the polarization response of the crystal and the closeness of the ferroelectric phase transition to the tricritical point is contained in the value of parameter a.

Relations for the dielectric susceptibility can be derived from the equations of state in an electric field. In the presence of a bias field, the system under study can support two states:

(1) $q = 0$, $p \neq 0$. The equation of state in an electric field is

$$-ap + p^3 = -ae. \tag{8}$$

Equation (8) yields a relation for the dielectric susceptibility,

$$\chi = \frac{-a\chi}{-a + 3p^2}, \tag{9}$$

where the value of p is found numerically from Eq. (8). In the absence of a bias field ($e = 0$), Eq. (9) takes on the form

$$\chi = \chi_0 \quad \text{for} \quad T > T_{c1}.$$

(2) $q \neq 0$, $p \neq 0$. Using Eq. (2) for the potential, we obtain the following equations of state in an electric field:

$$\begin{aligned} ta^2 + q^4 - 2p^2 &= 0, \\ -ap + p^3 - pq^2 &= -ae. \end{aligned} \tag{10}$$

Equation (10) can be used to derive an expression for the dielectric susceptibility in an electric field,

$$\chi(E) = \frac{-a\chi_0(2p^2 - ta^2)^{1/2}}{(-a + 3p^2)(2p^2 - ta^2)^{1/2} + ta^2 - 4p^2}, \tag{11}$$

where the value of p is found numerically from the equations of state (10). With no external field present ($e = 0$), the expression for the dielectric susceptibility in the paraelectric antiferrodistorsive phase ($q \neq 0$, $p = 0$) has the form

$$\chi(0) = \frac{\chi_0}{1 - \sqrt{-t}}, \quad -1 < t < 0 \quad (T_{c2} < T < T_{c1}). \tag{12}$$

The field-induced variation of the dielectric permittivity in the paraelectric phase can be derived from Eqs. (11) and (12) to be

$$\begin{aligned} \Delta\varepsilon &= \varepsilon(E) - \varepsilon(0) \\ &= \varepsilon^*\left(\frac{-a(2p^2 - ta^2)^{1/2}}{(-a + 3p^2)(2p^2 - ta^2)^{1/2} + ta^2 - 4p^2} - \frac{1}{1 - \sqrt{-t}}\right), \end{aligned} \tag{13}$$

where the $p(t)$ relation is determined numerically from the equation of state (10) and $\varepsilon^* = 1 + 4\pi\chi_0$ is the background dielectric permittivity determined in the high-temperature symmetric phase for $T > T_{c1}$.

As follows from Eqs. (10) and (13), the field-induced variation of dielectric permittivity depends only on one dimensionless parameter, a, whose value can be found by comparing the experimental with the theoretical curves.

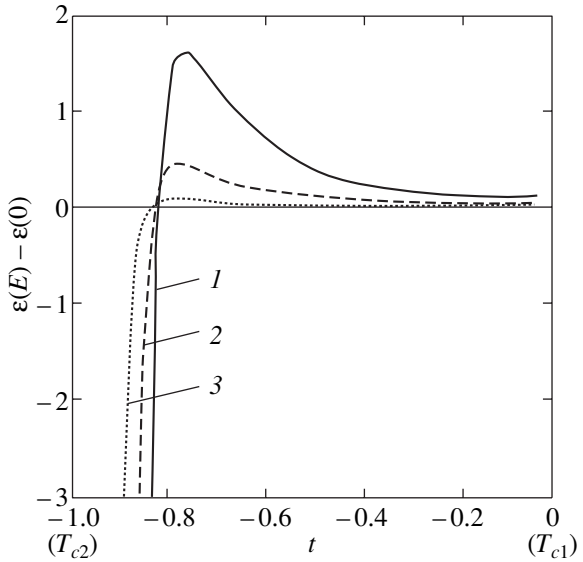

Fig. 5. Temperature dependences of the variation of dielectric permittivity in the paraelectric phase under various electric fields calculated from Eq. (13) for $a = -1.1$ and E equal to (*1*) 2.5×10^5, (*2*) 1.25×10^5, and (*3*) 5×10^4 V/m (t is the reduced temperature; $t = 0$ and -1 correspond in absolute units to the phase-transition temperatures T_{c1} and T_{c2}, respectively).

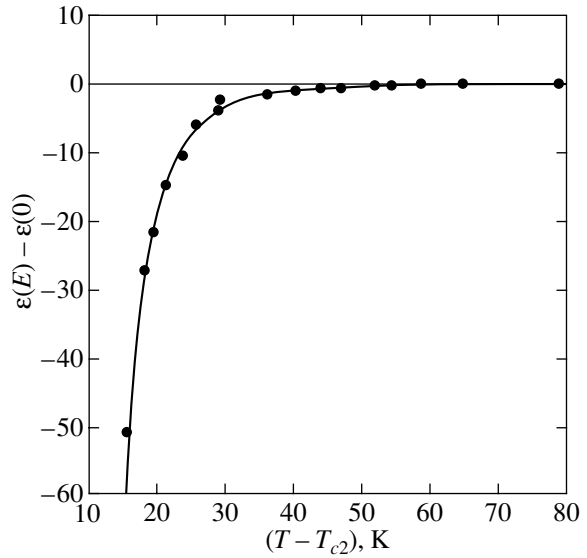

Fig. 6. Temperature dependences of the variation of dielectric permittivity at 1 MHz in the paraelectric phase measured in an electric field $E = 10^5$ V/m. The solid curve is a plot of Eq. (13) for $a = -2.5$.

Let us analyze the effect of electric bias on dielectric permittivity in the paraelectric phase in the case of continuous phase transition ($a < -1$). Figure 5 shows temperature dependences of the variation of the dielectric permittivity $\varepsilon(E) - \varepsilon(0)$ induced by electric fields $E_1 > E_2 > E_3$ calculated for parameter $a = -1.1$. As seen from Fig. 5, these dependences exhibit reversal of the sign of $\varepsilon(E) - \varepsilon(0)$ at a certain temperature which depends only weakly on the bias field. Positive values of the variation of dielectric permittivity relate to a field-induced increase in dielectric permittivity; the negative ones, to a decrease in the dielectric permittivity. The positive variation of dielectric permittivity increases with increasing field. We note that the value $a = -1.1$ corresponds to the second-order ferroelectric phase transition, whose closeness to the tricritical point is determined by Eq. (7) and is $T_0 - T_{c2} = 1.5$ K for $\Delta T \cong 150$ K.

Thus, the polarization response in the paraelectric phase with applied bias, considered within the model with coupled order parameters, differs radically in the case of the high-temperature nonpolar phase transition at the tricritical point from that in a model of ferroelectric phase transitions involving one polar mode. In the latter model, a field-induced increase in the dielectric permittivity is observed only in first-order phase transitions [9].

As the parameter a decreases, the effect of electric field on the dielectric permittivity retains its character but the region of positive changes in the dielectric permittivity shifts toward higher temperatures and the magnitude of the positive change in ε decreases to a level where it becomes difficult to experimentally detect an increase in ε in certain fields.

Now, let us analyze the experimental data in terms of the above model with coupled order parameters. Figure 2 presents the temperature dependence of the inverse dielectric permittivity calculated from Eq. (12) for $\Delta T = 151$ K and for a background dielectric permittivity in the high-temperature phase $\varepsilon^* = 62$. We readily see that the experimental relation is fitted well by the theoretical curve, except in a narrow temperature region of about 5 K near the phase-transition point, where the effect of crystal imperfections can be dominant. As follows from Eq. (12), in the absence of an electric field, the temperature behavior of dielectric permittivity in the paraelectric phase does not carry any information on the order of the phase transition. This information can be gained by analyzing the dielectric permittivity with an electric field applied. In our model, this information is contained in the magnitude of parameter a.

To determine the value of parameter a, we carried out numerical calculations of the temperature dependences of the dielectric permittivity and of the variation of dielectric permittivity in various fields in the paraelectric phase using Eqs. (11) and (13). The value of parameter a was determined by optimizing the deviations of all experimental curves obtained with the field, as displayed in Figs. 3 and 4, from the theoretical relations plotted in the same figures. The best fit of the experimental to calculated relations is observed for $a = -3.5$. This value of the parameter corresponds to the case of the second-order ferroelectric phase transition, whose closeness to the tricritical point, according to Eq. (7), is approximately 75 K. Let us estimate the bias which should be applied to the crystal in order to make the increase in the dielectric permittivity in the paraelectric phase for this value of a experimentally detectable. Calculations performed with Eqs. (10) and (13) show that, for $a = -3.5$, the region of positive field-induced changes in the dielectric permittivity shifts very strongly up in temperature, so that an increase in ε can be detected experimentally at temperatures $T_{c1} - 15$ K $< T < T_{c1}$ in fields $E > 4 \times 10^5$ V/m.

Because, as is evident from Fig. 2, at temperatures near T_{c2} (204–210 K), the experimental temperature dependence of the inverse dielectric permittivity deviates noticeably from the calculated curve, let us analyze the effect of an electric field on the dielectric permittivity in the paraelectric phase for $T > 215$ K, where the theoretical curve fits well to experiment. Figure 6 shows experimental and calculated temperature dependences of the dielectric-permittivity variation for $T - T_{c2} > 10$ K. It is seen that far from the ferroelectric phase transition, the experimental field-induced variation of the dielectric permittivity is fitted better by $a = -2.5$. The difference in determination of parameter a (–2.5 vs. –3.5) can be associated with the fact that far from the phase transition, some mechanisms, for instance, the effect of defects on dielectric permittivity, that are significant in the vicinity of the phase transition

were excluded; therefore, the value $a = -2.5$ appears more realistic.

Thus, our studies showed that the temperature dependence of dielectric permittivity with no electric field applied and with a field applied are described well by a phenomenological model in which there are two coupled, polar and nonpolar, order parameters with a negative coupling coefficient and which takes into account that the high-temperature improper ferroelastic phase transition is nearly tricritical. An analysis of the model revealed that in the case where two phase transitions, nonpolar and ferroelectric, can occur in the crystal, all its dielectric properties, including the polarization response in a field, are described by one parameter, a, which is –3.5 (or –2.5 far from the phase transition). This value of the parameter corresponds to a second-order ferroelectric phase transition sufficiently far from the tricritical point. Application of an electric field reduces the dielectric permittivity almost everywhere over the region of existence of the paraelectric phase (except in the temperature region near T_{c1}). As parameter a increases, i.e., as one approaches the tricritical point, where $a = -1$, calculations show the situation to change radically. In this case, the electric field increases the dielectric permittivity almost throughout the region of the paraelectric phase, despite the fact that the ferroelectric phase transition is continuous.

Considered within this model, the polarization response in the paraelectric phase under the application of an electric field differs radically from that in the case of a ferroelectric phase transition where the Curie–Weiss law holds in the paraelectric phase. In the latter case, a field-induced increase in the dielectric permittivity is possible only in a first-order phase transition, while in a continuous phase transformation, an electric field always decreases the dielectric permittivity in the paraelectric phase. By contrast, in the model of coupled order parameters, there exists a temperature region, determined by the magnitude of parameter a, in which an electric field increases the dielectric permittivity in the paraelectric phase even for a continuous phase transition. The reason for this unusual behavior of dielectric permittivity under an electric field to the paraelectric phase above a ferroelectric phase transition lies in the fact that the high-temperature nonpolar phase transformation is a phase transition at the tricritical point. The nonlinear effect of the nonpolar order parameter (through biquadratic coupling of the nonpolar order parameter and polarization with a negative coupling coefficient) on the polar instability brings about both a nonlinear temperature dependence of the inverse dielectric permittivity in the paraelectric phase in a zero electric field and the specific features of polarization response in an electric field considered above. It should be pointed out that investigation of crystalline betaine phosphite with higher ferroelectric phase transition temperatures can more clearly reveal the specific features of the polarization response in systems with coupled order parameters placed in an electric field.

ACKNOWLEDGMENTS

This study was supported by the Russian Foundation for Basic Research, project no. 01-02-17873.

REFERENCES

1. J. Albers, Ferroelectrics **78**, 3 (1988).
2. J. Albers, A. Klöpperpieper, H. J. Rother, and S. Haussühl, Ferroelectrics **81**, 27 (1988).
3. M. Dörffel, Th. Narz, A. Klöpperpieper, and S. Haussühl, Z. Kristallogr. **186**, 71 (1989).
4. I. Fehst, M. Paasch, S. L. Hutton, *et al.*, Ferroelectrics **183**, 1 (1993).
5. H. Bauch, J. Banys, R. Böttcher, *et al.*, Phys. Status Solidi B **187**, K81 (1995).
6. R. Cash, S. Dacko, and Z. Czapla, Phys. Status Solidi A **148**, 585 (1995).
7. E. V. Balashova and V. V. Lemanov, Ferroelectrics **247** (4), 269 (2000).
8. E. V. Balashov, V. V. Lemanov, J. Albers, and A. Klöpperpieper, Fiz. Tverd. Tela (St. Petersburg) **40**, 1090 (1998) [Phys. Solid State **40**, 995 (1998)].
9. L. P. Kholodenko, *Thermodynamic Theory of Ferroelectrics Related to Barium Titanate* (Znanie, Riga, 1971).

Translated by G. Skrebtsov

Physics of the Solid State, Vol. 44, No. 8, 2002, pp. 1604–1610. Translated from Fizika Tverdogo Tela, Vol. 44, No. 8, 2002, pp. 1529–1535.

FULLERENES AND ATOMIC CLUSTERS

Determination of the Activation Energy for Complicated Relaxation Processes

A. I. Slutsker*, Yu. I. Polikarpov, and K. V. Vasil'eva****

** Ioffe Physicotechnical Institute, Russian Academy of Sciences, Politekhnicheskaya ul. 26, St. Petersburg, 194021 Russia*

*** St. Petersburg State Technical University, Politekhnicheskaya ul. 29, St. Petersburg, 195251 Russia*

e-mail: Alexander.Slutsker@pop.ioffe.rssi.ru

Received October 19, 2001; in final form, October 23, 2001

Abstract—Different methods are considered for analyzing the temperature dependence of the relaxation rate in the Arrhenius form. It is emphasized that the possible changes in the barrier to elementary acts with variations in temperature should be taken into account in order to determine the relaxation activation energy correctly. Changes in the barrier to elementary acts are illustrated using experimental data on the temperature–frequency dependence of the dielectric relaxation in polymers. A theoretical approach offering realistic activation energies is proposed. © *2002 MAIK "Nauka/Interperiodica".*

1. INTRODUCTION

A large number of processes whose rates are characterized by a strong (exponential) temperature dependence are referred to collectively as relaxation processes. These are diffusion, evaporation, viscous flow, plastic deformation, fracture, and many other processes.

The activation energy is an important characteristic of these processes. The phenomenological meaning of the activation energy is that it determines the temperature dependence of the process rate. For this reason, the activation energy is used for describing the temperature dependences of the kinetics of processes.

However, since relaxation processes involve a sequence of elementary acts due to local fluctuations of the heat energy (in the classical limit), the activation energy has the meaning of a barrier whose height governs the probability of elementary acts. Hence, reliable (correct) determination of the activation energy is a necessary condition for in-depth analysis of elementary acts of processes.

In experimental studies on the kinetics of processes, different characteristics Φ_i (such as rates, frequencies, time parameters, and concentrations) are measured as a function of temperature *T*. When processing the experimental temperature dependences of Φ_i, it is common practice to represent the dependences $\Phi_i(T)$ in the Arrhenius form

$$\Phi_i(T) = A_i \exp(\pm U_i/kT). \quad (1)$$

This representation is based on a strong temperature dependence $\Phi_i(T)$ and justified concepts of the mechanisms of elementary acts, which rest on the basic principles of fluctuation dynamics [1].

Since the temperature range of measurements, as a rule, is relatively narrow and, consequently, the values of $\Phi_i(T)$ vary in a rather narrow range (most frequently, by one or two orders of magnitude), the dependence $\ln\Phi_i(1/T)$ appears to be virtually linear. This circumstance is considered to be evidence of the validity of relationship (1) as applied to analysis of the experimental data. The value of U_i, which is determined from the slope of the dependence $\ln\Phi_i(1/T)$, is termed the activation energy.

It should be noted that, as a rule, the preexponential factor A_i is not derived and is not even discussed in similar treatments.

When the activation energies U_i are determined in this manner, some doubts are cast upon the U_i values, which can be as large as 5–10 eV or higher; i.e., they can be considerably higher than the interatomic (intermolecular) interaction energies, which are of the order of 1 eV in condensed systems.

This situation is characteristic of molecular liquids in the solidification range and, especially, polymers in the glass transition range [2–5]. The high activation energies U_i thus obtained can be interpreted in the two following ways.

(1) The high activation energy U_i does not carry the meaning of the potential barrier to elementary acts and can be considered to be merely the temperature coefficient of the rate of the process involved. In this case, the quantity U_i is termed the apparent activation energy. Note that, in the framework of this interpretation, the obtained value of U_i is quite suitable for describing the temperature dependence of the process rate (but only in a limited temperature range).

1063-7834/02/4408-1604$22.00

(2) The high values of U_i account for the complex cooperative character of elementary acts; however, the quantity U_i itself retains the meaning of the barrier to elementary acts. In this case, either the value of U_i should be treated as the sum of the barriers related to partners of a cooperative act or it is necessary to take into account not only the potential barrier but also the entropy contribution.

It should be emphasized that the concept of cooperative character of elementary acts is undeniably reasonable and correct. On the other hand, the interpretation of the quantity $U_i = k(\Delta \ln \Phi_i(T)/\Delta(1/T))$ merely as a certain sum of partial barriers with subsequent quantitative inferences about specific features of elementary acts seems to be open to question. In many respects, this is associated with ignoring the preexponential factor in the case when the activation energy U_i is calculated from the slope of the dependence $\ln \Phi_i(1/T)$.

By analyzing experimental data in terms of relationship (1), it is assumed that the activation energy U_i (like the preexponential factor A_i) does not depend on the temperature. At the same time, there is evidence that the barriers to elementary acts vary with temperature (specifically in the range of structural and dynamical transitions in materials) and that this change affects the temperature dependence of the process rate [2, 3, 5]. However, an approach taking into account these findings has not been developed in detail.

In the present work, we developed this approach and, on its basis, proposed a method of processing and analyzing the dependence $\Phi_i(T)$. This allowed us to explain the increase in the slope of the dependence $\ln \Phi_i(1/T)$ and to derive more realistic results. In order to justify the proposed method, we analyzed the experimental data obtained for a compound that can be regarded as a model object.

2. PHYSICAL JUSTIFICATION

The mean expectation time for a local energy fluctuation E_{fl} (at one atom or a small group of atoms) as a function of the temperature can be represented in the form [1]

$$\tau_{\text{fl}} \cong \tau_0 \exp E_{\text{fl}}/kT, \tag{2}$$

where $\tau_0 \approx 10^{-12}$–10^{-13} s is the period of atomic vibrations in condensed materials.

Relationship (2) for energy fluctuations was directly confirmed by computer simulation of atomic dynamics in solids [6]. It was demonstrated that energy fluctuations are efficiently localized in time ($\sim\tau_0$) and space (virtually at one atom) [7].

In an elementary act, the barrier U is overcome at an energy $E_{\text{fl}} \geq U$. Then, the mean expectation time for the elementary act can be written as

$$\tau_e \cong \tau_0 \exp U/kT. \tag{3}$$

Since the processes involve a statistical sequence of elementary acts, relationship (3) leads to the following expressions.

(i) The process rate has the form

$$V = dN/dt \cong N/\tau_e \cong N/\tau_0 \exp(-U/kT),$$

where N is the concentration of particles that change their state (or position) in elementary acts.

(ii) The effective time a system takes to reach a state close to equilibrium (this attainment of equilibrium by the system is called relaxation) can be represented as

$$\tau_r \cong \tau_e \cong \tau_0 \exp U/kT.$$

In this case, the time τ_r is referred to as the relaxation time. However, it should be emphasized once again that this macroscopic characteristic of the system is close (within logarithmic accuracy) to a microscopic characteristic, namely, the mean expectation time for elementary acts.

(iii) When the system itself is in equilibrium but particles involved in the system undergo reversible local transitions between their states (positions), the mean frequency of these transitions for a particle is represented by the formula

$$\nu \cong \tau_e^{-1} \cong (1/\tau_0) \exp(-U/kT),$$

because the mean expectation time for a transition (the expectation time for the corresponding fluctuation) is equal to the mean time between two sequential transitions for the same particle.

Therefore, the characteristics of the system V, τ_r, and ν (collectively designated above as Φ_i) are directly related to such an important characteristic of the elementary act as the time τ_e. Consequently, by analyzing the dependence $\Phi_i(T)$ with due regard for relationship (3), it is possible to determine the barrier U to elementary acts and the preexponential factor. The preexponential factor either is directly taken equal to $\tau_0^{\pm 1}$ (from expressions for τ_r and ν) or can be obtained from the rate V at a known concentration N.

If the barrier to elementary acts remains unchanged (U = const) in the temperature range under consideration, the dependence $\ln \tau_e(1/T)$ obtained from measurements of $\Phi_i(T)$ should have the form depicted in Fig. 1 (line *1*), i.e., the form of a straight line extrapolated to $\sim 10^{-13}$ s at $1/T = 0$. The slope of this dependence $d \ln \tau_e/d(1/T)$ is equal to U/k.

Note that similar linear dependences $\ln \tau_e(1/T)$ extrapolated just to $\sim 10^{-13}$ s at $1/T = 0$ (what is especially important) were repeatedly observed (see, for example, the results given below and in [4, 8, 9]). Hence, the calculated value of U can be actually treated as the height of the potential barrier to elementary acts and the inferences that follow from a comparison of U with the energy parameters of interatomic (intermolecular) bonds are correct.

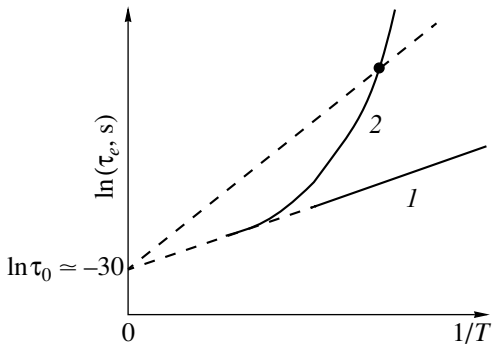

Fig. 1. Schematic temperature dependences of the mean expectation time for elementary acts: (*1*) temperature-independent barrier to transition and (*2*) barrier decreasing with an increase in temperature.

Let us now discuss the situation when the barrier changes with variations in the temperature; i.e., $U = U(T)$.

This situation can occur in materials with a molecular structure when the elementary act of a process involves a considerable number of atoms (i.e., an ensemble activated by thermal motion occupies a substantial volume and exhibits a large number of internal degrees of freedom). It can be expected that a decrease in the temperature leads to an increase in the "rigidity" and volume of the activated ensemble and to a rise in the barrier to elementary acts.

By consistently adhering to the concept of the fluctuation mechanism of elementary acts, for the barrier $U = U(T)$, we can write

$$\tau_e(T) \cong \tau_0 \exp\frac{U(T)}{kT}. \tag{4}$$

The validity of this relationship for $\tau_e(T)$ was considered in [3, 5].

It is essential that the same preexponential factor τ_0 is retained in the expression for $\tau_e(T)$.

Hence, the slope of the dependence $\ln\tau_e(1/T)$ can be represented in the form

$$\frac{d(\ln\tau_e)}{d(1/T)} = \frac{d[U(T)/kT]}{d(1/T)} = \frac{U(T)}{k} + \frac{1}{kT}\frac{dU(T)}{d(1/T)} = \frac{U(T)}{k} - \frac{T}{k}\frac{dU(T)}{dT}. \tag{5}$$

Therefore, the slope of the dependence $\ln\tau_e(1/T)$ is related not only to the barrier height $U(T)$ but also to the derivative of the barrier height with respect to the temperature. In particular, Kobeko [5] called attention to this circumstance.

Now, we introduce the following designations:

$$\frac{d(\ln\tau_e)}{d(1/T)} = \frac{U_f(T)}{k}, \quad \frac{dU(T)}{dT} = U'(T),$$

where U_f is the barrier determined from the slope of the dependence $\ln\tau_e(1/T)$. From relationship (5), we have

$$U_f(T) = U(T) - TU'(T). \tag{6}$$

According to this formula, the barrier to elementary acts at the temperature T is given by

$$U(T) = U_f(T) + TU'(T). \tag{7}$$

For $U'(T) < 0$ (the barrier to elementary acts increases with a decrease in the temperature), it becomes clear from expression (6) that increased values of U_f can be obtained as a result of changes in the barrier height.

By assuming that the barrier reaches a steady-state value U at sufficiently high temperatures and increases with a decrease in the temperature, the dependence $\tau_e(1/T)$ can be schematically represented in the form depicted in Fig. 1 (curve *2*).

The curvature of the dependence $\ln\tau_e(1/T)$ reflects an increase in the barrier U_f with a decrease in the temperature, i.e., the temperature dependence of the barrier. Since the mean expectation time for elementary acts τ_e can vary in a very narrow temperature range (as was already mentioned, this situation often occurs in experimental investigations), the impression can be gained that the barrier U_f is constant.

The linear extrapolation of a small quasi-linear portion of the curve $\ln\tau_e(1/T)$ from the point $\ln\tau_e(1/T)$ to $1/T = 0$ gives the quantity $\ln\tau_f = \ln\tau_e - \frac{U_f(T)}{k}\frac{1}{T}$. The deviation of $\ln\tau_f$ from $\ln\tau_0 \cong -30$ (the quantity τ_0 is expressed in seconds) toward smaller (!) values can serve as a criterion for deviation of the barrier U_f from the barrier U to elementary acts.

Under the above assumptions, the barrier $U(T)$ (an important parameter in physics) can be determined from the measured dependence $\ln\tau_e(1/T)$ according to formula (4); that is,

$$U(T) = kT\ln\tau_e/\tau_0. \tag{8}$$

This corresponds to the slope of the straight line passed from each point $\ln\tau_e(1/T)$ to the point $\ln\tau_0$ (Fig. 1).

In order to calculate the barrier to elementary acts $U(T)$ from expression (7) with the use of the quantity $U_f(T)$, the derivative $U'(T)$ must be known.

Thus, we justified that the slopes of the measured temperature dependences do not necessarily correspond to barriers to elementary acts. With the aim of confirming the aforementioned theoretical inferences, we now turn to analysis of the experimental data.

3. EXPERIMENTAL TECHNIQUE AND RESULTS

3.1. Experimental technique. In the present work, the relaxation processes were investigated by dielectric

loss spectroscopy. The advantage of this technique is that it provides a means for directly measuring the frequencies at which particles with electric moments reversibly transfer from one position to another. The technique is based on observations of maxima in the frequency and temperature (at specified frequencies of an external electric field) spectra of dielectric losses in polar dielectrics. In the case when the transition occurs through the fluctuation mechanism, the maximum in the dielectric loss spectrum corresponds to fluctuation resonance between the frequency ν of an applied electric field and the mean frequency of reversible transitions (hoppings) of polar particles. The latter frequency is equal to the temperature-dependent reciprocal of the mean expectation time for the transition τ_e^{-1} (see above). Therefore, the measured temperature dependence of the frequency ν_m, which corresponds to the maximum in the dielectric loss spectrum, can be used to determine the dependence $\tau_e(T) = \nu_m^{-1}(T)$.

In this work, the dielectric loss tangents ($\tan\delta$) were measured over wide ranges of frequencies (10^{-2}–10^7 Hz) and temperatures (120–420 K).

3.2. The object of investigation. Poly(vinyl acetate) was chosen as the object of investigation. The structure of a monomer unit of poly(vinyl acetate) is schematically depicted in Fig. 2.

The choice of poly(vinyl acetate) is governed by its following properties, which are favorable in the solution of the formulated problem.

First, poly(vinyl acetate) is a polar polymer owing to the considerable dipole moment of its side fragment ($-OCOCH_3$). As a consequence, this polymer is characterized by relatively high dielectric losses; hence, it is an appropriate object for investigation by dielectric loss spectroscopy.

Second, the static devitrification (glass transition) temperature of poly(vinyl acetate) $T_s \cong 300$ K [4] falls in a convenient temperature range; to be more specific, in the range of T_s, the polymer transforms from the solid state to the high-elasticity state in which polymer molecules are characterized by conformational dynamics (segmental mobility). Hence, the dielectric losses in poly(vinyl acetate) are conveniently measured in both solid (vitreous) and devitrified states (below and above the temperature T_s, respectively).

Third, the temperature spectrum of dielectric losses in poly(vinyl acetate) (as in a number of other polar polymers) exhibits two characteristic maxima (below and above the temperature T_s). A comparison between the parameters of these maxima allows one to judge the specific features of elementary acts (transitions).

Samples used for dielectric measurements were prepared in the form of plates from approximately one to several millimeters in thickness.

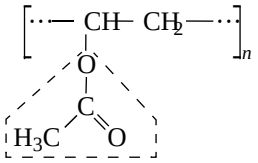

Fig. 2. Structure of a monomer unit of poly(vinyl acetate).

3.3. Experimental results. The temperature dependences of the loss tangent ($\tan\delta$) at two frequencies are shown in Fig. 3. The maxima in these dependences are observed at low (below T_s, Fig. 3a) and high (above T_s, Fig. 3b) temperatures. An increase in the frequency ν of the external field leads to a shift of the maxima toward the high-temperature range (to an increase in the temperature T_m corresponding to the loss tangent at a maximum). The dielectric measurements performed at a number of other frequencies result in dependences similar to those displayed in Fig. 3.

Since the transitions at $T < T_s$ and $T > T_s$ are conventionally termed the β and α transitions, respectively [4, 10], we denote the maximum of $\tan\delta$ at low temperatures by the β peak and the maximum of $\tan\delta$ at low temperatures by the α peak.

The temperature dependences $\tau_e(T) \cong \nu^{-1}(T)$ determined from the dependence of the frequency ν on the temperature T_m for each peak are plotted in Fig. 4 in the $\log\tau_e$–$(1/T)$ coordinates. As can be seen, the dependences $\log\tau_e(1/T)$ for the β and α peaks differ significantly.

The dependence $\log\tau_e(1/T)$ for the β peak appears to be linear (with a constant slope). It is worth noting that the extrapolation of this curve to $1/T = 0$ gives a value of $\sim 10^{-13}$ s, which is close to τ_0.

Therefore, the β peak can be described by the relationship $\tau_e \cong \tau_0 \exp U_\beta/kT$ under the condition $U_\beta = \text{const}$. From the slope $\dfrac{\Delta\log\tau_e}{\Delta(1/T)}$, we obtain $U_\beta \cong 0.37$ eV.

On this basis (judging from the linearity of the dependence $\ln\tau_e(1/T)$ and the extrapolated value of $\tau_0 \cong 10^{-13}$ s (Fig. 1)), we can draw the inference that the value of $U_\beta \cong 0.37$ eV determined from the slope of the dependence $\log\tau_e(1/T)$ actually corresponds to the barrier to elementary acts of the β transitions. This value of U_β is close to the activation energy obtained by other methods for the β transitions in poly(vinyl acetate) [4]. The temperature dependence of U_β is displayed in Fig. 5.

Compared to the β peak, the dependence $\log\tau_e(1/T)$ for the α peak appears to be substantially steeper and, what is particularly important, is nonlinear.

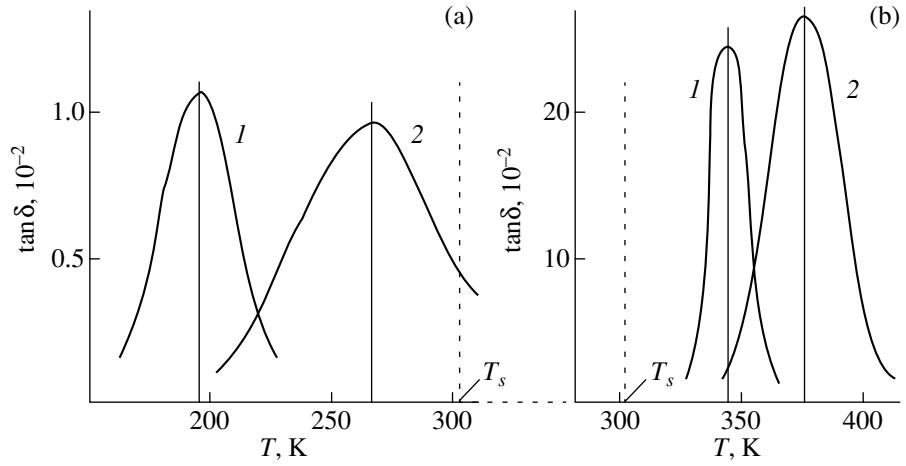

Fig. 3. Temperature dependences of the dielectric loss tangent in poly(vinyl acetate) at frequencies of (*1*) 3.2 kHz and (*2*) 1 MHz: (a) $T < T_s$ (β peak) and (b) $T > T_s$ (α peak).

The steepness of the curve $\log\tau_e(1/T)$ sharply increases as the glass transition temperature T_s is approached (Fig. 4). With an increase in the temperature, the incline decreases and the slope of the α dependence approaches the slope of the β dependence.

Therefore, the slope of the dependence $\log\tau_e(1/T)$ for the α peak is not constant. The linear extrapolation of different portions of this dependence to $1/T = 0$ leads to values that are many orders of magnitude less (!) than $\tau_0 \cong 10^{-13}$ s.

By calculating the particular barrier $U_{\alpha f}$ from the slope of the dependence $\log\tau(1/T)$ with the use of the formula $U_{\alpha f} = k\dfrac{d\ln\tau_e}{d(1/T)}$, we obtain the strong dependence $U_{\alpha f}(T)$ (Fig. 5). It is seen from Fig. 5 that the values of $U_{\alpha f}$ in the temperature range ~300–400 K are rather high (compared to U_β) and increase drastically as the temperature T_s is approached. With an increase in the temperature, the values of $U_{\alpha f}$ and U_β approach each other. In this respect, it is necessary to elucidate why the height of the barrier $U_{\alpha f}$ is high and depends on the temperature.

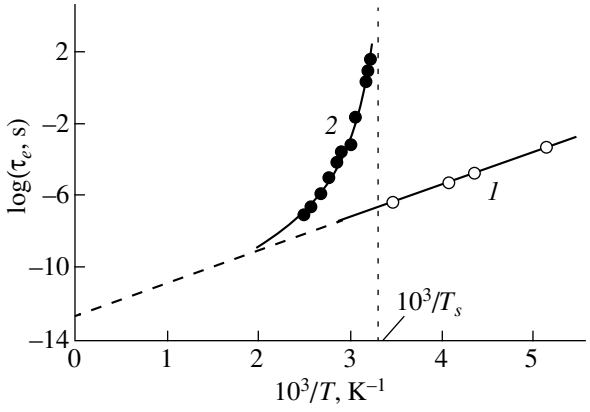

Fig. 4. Temperature dependences of the mean expectation time (the reciprocal of the frequency) for elementary acts of (*1*) β relaxation transitions and (*2*) α relaxation transitions in poly(vinyl acetate).

4. DISCUSSION

It should be noted that the experimental dependences shown in Fig. 4 are closely similar to the schematic graph that is depicted in Fig. 1 and reflects the influence of a change in the barrier with variations in the temperature on the mean expectation time for elementary acts. This behavior of the barrier to elementary acts is consistent with the modern concepts of molecular dynamics in polymers.

Below the glass transition temperature, the internal dynamics in polymers, as in conventional low-molecular solids, is governed primarily by atomic vibrations. However, low-molecular solids are also characterized by fluctuation diffusion events, dislocation motion (in crystals), and other processes. Similarly, fluctuation jumpwise motion of individual small-sized segments of macromolecules can also occur in vitreous polymers. This motion of individual polar fragments is responsible for the dielectric loss, i.e., the β peak [5, 11]. The barrier to these jumps (transitions) is determined by the interaction of a polar fragment with surrounding atoms (belonging to the same chain molecule and adjacent molecules). It is quite reasonable that a number of atoms (of the order of ten or more) should participate in the jumpwise change in the fragment position. However, judging from the data represented in Fig. 4 for the β peak, this collective character of the transition virtually does not manifest itself in the description of the process. The validity of relationship (3) for the polyatomic β transition implies that the transition occurs

only through energy fluctuations without a noticeable entropy contribution. Thus, the situation in the low-temperature range ($T < T_s$) seems to be sufficiently clear.

An increase in the temperature leads to devitrification of the polymer. As a result, virtually immobile skeletons of chain molecules can change their position and shape (conformational segmental mobility). Then, the transitions of adjacent side fragments [polar in the case of poly(vinyl acetate)] involved in the motion of their molecule appear to be correlated. It is these correlated transitions of polar fragments that are responsible for the α peak in the dielectric loss [5, 11].

At $T < T_s$, the correlated transitions cannot occur; hence, it can be assumed that the barrier to correlated transitions is infinitely high. At the initial stage of devitrification, the barrier becomes finite but remains sufficiently high. With a further increase in the temperature and the rate of segmental molecular motion, the correlation between transitions of the fragment involved should decrease and, correspondingly, the barrier to correlated transitions will decrease and tend to the barrier to the transition of a single fragment.

It is obvious that the above description is only a rough approximation; however, it allows us to elucidate the possible reasons for the changes in the barrier to transitions with variations in temperature for the α peak in the dielectric loss.

Let us now examine the dependence $\log\tau_e(1/T)$ for the α peak (Fig. 4) under the assumption that this dependence can be represented in the form $\tau_e \cong \tau_0 \exp\frac{U_\alpha(T)}{kT}$ [i.e., in the form given by relationship (4)]. The validity of the representation of the experimental dependence $\tau_e(T)$ in the form of relationship (4) for an elementary act is supported by the fact that this relationship turns out to be quite applicable to the description of the temperature behavior of the β peak. As was noted above, a large number of atoms are involved even in the β transition. Therefore, it is reasonable that an increase in the number of atoms involved in the correlated α transition should not radically change the description of the elementary act of the α transition in terms of the fundamental relationship (4) at the preexponential factor $\tau_0 \cong 10^{-13}$ s.

Consequently, from the dependence $\log\tau_e(1/T)$ for the α transition (Fig. 4) and relationship (8), we obtain the barrier to elementary acts of the α transition: $U_\alpha = kT\ln\frac{\tau_e}{\tau_0}$.

The dependence $U_\alpha(T)$ is displayed in Fig. 5. It can be seen that the barrier U_α is considerably less than the barrier $U_{\alpha f}$. As the difference between the temperature and T_s increases, the barrier U_α decreases and approaches the barrier U_β.

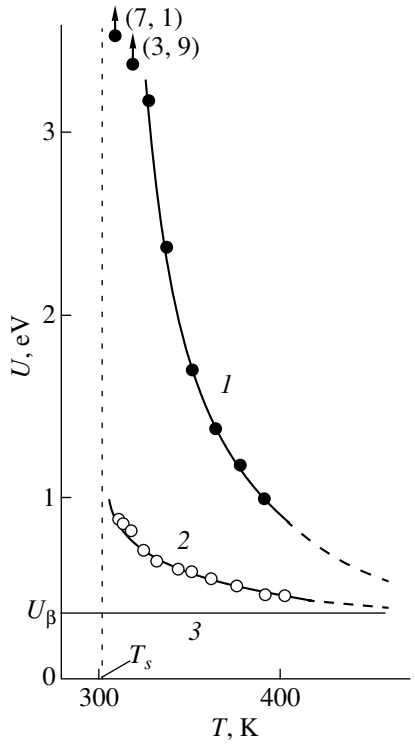

Fig. 5. Temperature dependences of the energy characteristics of relaxation transitions in poly(vinyl acetate): (*1*) $U_{\alpha f}$, (*2*) U_α, and (*3*) U_β.

The dependence $U_\alpha(T)$ obtained can be described analytically.

Ferry [12] proposed an empirical relationship between the barrier to the α transition and the temperature in the form

$$U(T) = U(T \longrightarrow \infty)\left(1 - \frac{T_s}{T}\right)^{-1}. \quad (9)$$

We constructed the dependence of $\log\frac{U_\alpha}{U_\beta}$ on $-\log\left(1 - \frac{T_s}{T}\right)$ according to formula (9) (see Fig. 6). This dependence exhibits virtually a linear behavior, which agrees with expression (9). However, the slope of the curve is approximately equal to 0.3 rather than to 1, as could be expected from expression (9). As a result, from the data on the barrier $U_\alpha(T)$ in Fig. 6, we obtain the relationship

$$U_\alpha(T) \cong U_\beta\left(1 - \frac{T_s}{T}\right)^{-0.3}. \quad (10)$$

Consequently, the derivative of the barrier height with respect to the temperature is determined as $U'_\alpha(T) = \frac{dU_\alpha(T)}{dT} \cong -0.3U_\beta\frac{T_s}{T^2}\left(1 - \frac{T_s}{T}\right)^{-1.3}$.

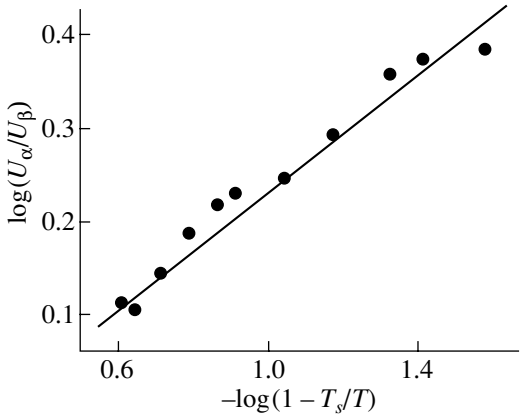

Fig. 6. Illustration of the validity of relationship (9) for $U_\alpha(T)$ in poly(vinyl acetate).

The use of the function $U'_\alpha(T)$ for determining the dependence $U_\alpha(T)$ from relationship (7) gives the same values of $U_\alpha(T)$ as those obtained from expression (8).

Certainly, relationship (10) is also empirical and has hitherto defied rigorous physical justification. However, the construction of even an empirical temperature dependence of the barrier to α relaxation (taking into account that the barrier to β relaxation is almost independent of temperature) is of considerable importance in further investigation.

5. CONCLUSIONS

In this work, we considered the problem concerning the influence of the temperature dependence of the barrier to elementary relaxation acts on the slope of the function $\ln\tau_e(1/T)$ and, consequently, on the method of determining the barrier height.

It was emphasized that the inferences regarding the "simple" [$U(T)$ = const] and "complex" [$U(T) \neq$ const] character of the elementary act should be made reasoning from an analysis of the preexponential factor in the temperature dependence of the relaxation rate of the process.

The actual barrier to complex elementary acts and the temperature dependence of the barrier were estimated for the specific case of relaxation phenomena—the dielectric loss in a polar polymer at temperatures above the glass transition point (the α relaxation).

It was found that, at $T = 320$ K, the obtained barrier to the α relaxation in poly(vinyl acetate) $U_a \cong 0.75$ eV is considerably less than the activation energy $U_{\alpha f} \cong$ 2.5 eV [4] determined without regard for the complex character of the α relaxation.

In many works devoted to the investigation of the α relaxation with the use of different methods [4, 10, 13], the available data, as a rule, were treated without considering both the possible temperature dependence of the barrier and the preexponential factor. This led to unjustifiably high activation energies.

We believe that the inclusion of these factors is required to examine thoroughly the kinetics of the processes involved and to obtain information on elementary acts—the main physical characteristic of the kinetics of processes.

REFERENCES

1. J. Frenkel, *Kinetic Theory of Liquids* (Clarendon, Oxford, 1946; Nauka, Moscow, 1975).
2. G. M. Bartenev and Yu. V. Zelenev, *Physics and Mechanics of Polymers* (Vysshaya Shkola, Moscow, 1983).
3. Yu. S. Lazurkin, in *Encyclopedia of Polymers* (Moscow, 1972), Vol. 1, p. 62.
4. V. A. Bershteĭn and V. M. Egorov, *Differential Scanning Calorimetry in the Physics and Chemistry of Polymers* (Khimiya, Leningrad, 1990).
5. P. P. Kobeko, *Amorphous Materials* (Akad. Nauk SSSR, Moscow, 1952).
6. A. I. Slutsker, A. I. Mikhaĭlin, and I. A. Slutsker, Usp. Fiz. Nauk **164** (4), 357 (1994) [Phys. Usp. **37**, 335 (1994)].
7. A. I. Slutsker, A. I. Mikhaĭlin, and I. A. Slutsker, *Problems of Theoretical Physics: A Collection of Articles* (PIYaF, St. Petersburg, 1994), p. 42.
8. P. F. Veselovskiĭ and A. I. Slutsker, Zh. Tekh. Fiz. **25** (5), 939 (1955).
9. V. R. Regel', A. I. Slutsker, and É. E. Tomashevskiĭ, *The Kinetic Nature of Solid Strength* (Nauka, Moscow, 1974).
10. *Transitions and Relaxations in Polymers*, Ed. by R. F. Boyer (Interscience, Easton, 1966; Mir, Moscow, 1968).
11. T. I. Borisova, in *Encyclopedia of Polymers* (Moscow, 1972), Vol. 1, p. 743.
12. J. D. Ferry, *Viscoelastic Properties of Polymers* (Wiley, New York, 1961; Inostrannaya Literatura, Moscow, 1963).
13. J. Heijboer, in *Static and Dynamic Properties of the Polymeric Solid State: Proceedings of the NATO Advanced Study Institute, Glasgow, 1981*, Ed. by R. A. Pethrick and R. W. Richards (Reidel, Dordrecht, 1982), p. 197.

Translated by O. Borovik-Romanova